IDENTIFICATION OF NONLINEAR DYNAMIC SYSTEMS USING THE FORCE-STATE MAPPING TECHNIQUE

By

Moufid Ajjan Al - Hadid

A thesis submitted for the degree of
Doctor of Philosophy in Engineering
(1989)

Department of Aeronautical Engineering

Queen Mary College

University of London

ABSTRACT

The identification of the dynamic characteristics of nonlinear systems is of increasing interest in the field of modal testing. In this work an investigation has been carried out into the force-state mapping approach to identification of nonlinear systems proposed by Masri and Caughey. They originally suggested a nonparametric identification technique based on curve fitting the restoring force in terms of the velocity and displacement using two dimensional Chebyshev polynomials. It has been shown that the use of Chebyshev polynomials is unnecessarily restrictive and that a simpler approach based on ordinary polynomials and special functions provides a simpler, faster and more accurate identification for polynomial and nonpolynomial types of nonlinearity. This simpler approach has allowed the iterative identification technique for multi-degree of freedom systems to be simplified and a direct identification approach, which is not subject to bias errors, has been suggested.

A new procedure for identifying both the type and location of nonlinear elements in lumped parameter systems has been developed and has yielded encouraging results.

The practical implementation of the force-state mapping technique required the force, acceleration, velocity and displacement signals to be available at the same instants of time for each measurement station. In order to minimise the instrumentation required, only the force and acceleration are measured and the remaining signals are estimated by integrating the acceleration. The integration problem has been investigated using several approaches both in the frequency and time domains.

An analysis of the sensitivity of the estimated parameters with respect to any amplitude and phase measurement errors has been carried out for single-d.o.f. linear systems. Estimates are shown to be extremely sensitive to phase errors for lightly damped

structures.

The estimation of the mass or generalised mass and modal matrices required for the identification of single or multi-d.o.f. nonlinear systems respectively, has also been investigated. Initial estimates were obtained using a linear multi-point force appropriation method, normally used for the excitation of normal modes. These estimates were then refined using a new technique based on studying the sensitivity of the mass with respect to the estimated system parameters obtained using a nonlinear model. This sensitivity approach seemed promising since accurate results were obtained. It was also shown that accurate estimates for the modal matrix were not essential for carrying out a force-state mapping identification.

Finally, the technique has been applied experimentally to the identification of a cantilevered T-beam structure with stiffness and damping nonlinearity. The cases of two well separated and then two fairly close modes were considered. Reasonable agreement between the behaviour of the nonlinear mathematical model and the structure was achieved considering inaccuracies in the measurement set-up.

Conclusions have been drawn and some ideas for future work presented.

CONTENTS.

Note : Tables appear within the text and figures are placed at the end of each chapter.

List of figures 9

Nomenclature 18

Acknowledgement 23

1. Introduction 25

2. Identification of single-d.o.f. nonlinear systems using the force-state mapping technique 39

2.1. Introduction 39

2.2. Basic philosophy of the force-state mapping technique 40

2.3. Curve fitting the restoring force 42

2.3.1. Masri/Caughey approach using Chebyshev polynomials 42

2.3.1.1. Interpolation/extrapolation of restoring force 47

2.3.1.2. Some further comments on Chebyshev polynomial approach 50

2.3.2. Ordinary polynomial approach 55

2.3.2.1. Conventional least squares solution 56

2.3.2.2. Solution using the singular value decomposition technique 59

2.3.3. The use of special functions 62

2.4. Examples 63

2.4.1. Linear case 64

2.4.2. Nonlinear cases 67

2.5. Conclusion 74

3. Application of the force-state mapping technique to multi-d.o.f. nonlinear systems 91

3.1. Identification procedure for simple chain-like multi-d.o.f. nonlinear lumped parameter systems 93
3.2. Formulation of the identification procedure for arbitrary multi-d.o.f. nonlinear lumped parameter systems 94
3.3. Mathematical modelling of the modal restoring force vector 98
3.3.1. Step-by-step approach (iterative approach) 89
3.3.2. Single-step approach (direct approach) 103
3.3.3. Two d.o.f. system example 107
3.4. Method for identification of the type and physical location of nonlinearities for arbitrary lumped parameter systems 111
3.4.1. Two d.o.f.example with several nonlinearities 117

4. Estimation of the unmeasured states 124

4.1. Measurement considerations 124
4.2. A brief review 124
4.3. Integration procedures 125
4.3.1. Time domain integration 126
4.3.1.1. Standard integration formulae 126
4.3.1.2. Cubic spline approach 128
4.3.2. Frequency domain integration 130
4.4. Integration problems 131
4.4.1. Low frequency components 131
4.4.2. Roundoff errors 133
4.4.3. Truncation errors in time domain integration 133
4.4.4. High frequency components 136
4.4.5. Leakage errors in frequency domain integration 137
4.5. Integration of linear data 138
4.6. Trend removal 143
4.6.1. Trend removal in the time domain 143
4.6.1.1. Least squares curve fitting 144
4.6.1.2. High pass digital filtering 145

4.6.2. Trend removal in the frequency domain 146
4.6.3. Further comments on least squares trend removal 148
4.7. Sensitivity of integration to measurement noise 151
4.8. Integration of nonlinear data 154
4.9. Conclusion 158

5. Sensitivity of the force-state mapping technique to measurement errors 179

5.1. Introduction 179
5.2. Sensitivity of parameters of a linear single-d.o.f. system to systematic measurement errors 180
5.2.1. Amplitude errors only 184
5.2.2. Phase errors only 184
5.2.3. Amplitude and phase errors 186
5.3. Sensitivity of parameters of a linear single-d.o.f. system to random measurement noise 187
5.4. Discussion 190

6. The estimation of the mass and mode shape parameters 195

6.1. Introduction 195
6.2. Effect of mass error on the force-state mapping technique 198
6.3. Mass estimation for single-d.o.f. linear systems 202
6.3.1. Linear example 204
6.3.2. Nonlinear example 205
6.4 Mass estimation for single-d.o.f. nonlinear systems 206
6.4.1. Crawley and O'Donnell approach 207
6.4.2. Worden and Tomlinson approach 211
6.5. Sensitivity approach for mass estimation of single-d.o.f. nonlinear systems 211
6.5.1. Basic philosophy for a linear system 212
6.5.2. Extension of approach to a system with cubic stiffness nonlinearity 215
6.5.3. Examples of the sensitivity approach 217

6.5.4. Application of the sensitivity approach using nonparametric curve fit 221
6.5.5. Effect of systematic errors on the sensitivity approach 222
6.5.6. Effect of noise errors on the sensitivity approach 226
6.6. Estimation of generalised mass and modal matrices for multi-d.o.f. systems 227
6.7. Estimation of the mass matrix for multi-d.o.f. nonlinear systems 234
6.8. Effect of using an incorrect modal matrix in the force-state mapping technique 238
6.9. Conclusion 245

7. Application of the force-state mapping technique to the identification of a T-beam structure 258

7.1. Introduction 258
7.2. Description of test structure 259
7.3. Description of experimental set-up 260
7.3.1. Computer 261
7.3.2. Analogue Interface unit 261
7.3.3. Other equipment 263
7.4. Experimental procedure 265
7.5. Sources of experimental errors 267
7.5.1. Quantization error 267
7.5.2. Multiplexer error 268
7.5.3. Channel mismatch errors 269
7.5.4. Transducer errors 272
7.6. Experimental application of the force-state mapping technique to the identification of well separated modes 275
7.6.1. Identification of bending mode 275
7.6.2. Identification of torsion mode 281
7.7. Experimental application of the force-state mapping to the identification of two fairly close modes 283
7.7.1. Initial estimation of generalised mass

and modal matrices 283
7.7.2. Refinement of generalised mass matrix using the sensitivity approach 287
7.7.3. Identification of model 288
7.8. Conclusion 293

8. Conclusion and suggestions for future work 321

9. References 326

List of Figures

Chapter 1.

Figure 1.1. Classification of nonlinear methods.

Chapter 2.

Figure 2.1. Single d.o.f. nonlinear system.

Figure 2.2. Sample time histories for a 1 d.o.f. simulated system.

Figure 2.3. Force-state map of raw data for a 1 d.o.f. system obtained using sweep excitation

Figure 2.4. Force-state map of raw data obtained using steady state excitation.

Figure 2.5. Projection of the force-state map onto the (f,x) and (f,y) planes.

Figure 2.6. Projection of the force-state map onto the $(\bar{x},\bar{y})$ and (θ,ϕ) planes.

Figure 2.7. Projection of the force-state map onto the (f,x) and (f,y) planes for a piecewise stiffness nonlinearity.

Figure 2.8. Illustration of the effective change of origin introduced by the normalisation process.

Figure 2.9. Variations of Chebyshev polynomials against ϕ.

Figure 2.10. Illustration of the steep undulations introduced by the use of Chebyshev polynomials.

Figure 2.11. Variation of the time to calculate the C_{mn} values for a linear system with the number of integration points.

Figure 2.12. Variation of the goodness of Chebyshev fit for a linear system against the number of integration points.

Figure 2.13. Illustration of the increase in the extrapolation required due to the transformation to the (θ,ϕ) plane.

Figure 2.14. Two dimensional force-state map of raw data for a linear system obtained using sweep excitation.

Figure 2.15. Force-state map for the fitted model of a linear system.

Figure 2.16. Force-state map for the fitted model of a system with cubic stiffness nonlinearity.

Figure 2.17. Force-state map of raw data for the Van der Pol oscillator.

Figure 2.18. Two dimensional force-state map of raw data for the Van der Pol oscillator.

Figure 2.19. Projection of force-state map onto the $(\bar{x},\bar{y})$ and (θ,ϕ) planes for the Van der Pol oscillator.

Figure 2.20. Exact force-state map surface for the Van der Pol example.

Figure 2.21. Force-state map of interpolated and extrapolated values, taken from reference 2, for the Van der Pol example.

Figure 2.22. Force-state map for the fitted model of the Van der Pol example, taken from reference 2.

Figure 2.23. Force-state map for the fitted model of the Van der Pol example, obtained via ordinary polynomial curve fitting within bins.

Figure 2.24. Force-state map of raw data for the quadratic damping example.

Figure 2.25. Two dimensional force-state map of raw data for the quadratic damping example.

Figure 2.26. Force-state map for the fitted model of the quadratic damping example.

Figure 2.27. Sample time histories for the Coulomb friction example.

Figure 2.28. Force-state map of raw data for the Coulomb friction example.

Figure 2.29. Two dimensional force-state map of raw data for the Coulomb friction example.

Figure 2.30. Force-state map for the fitted model of the Coulomb friction example.

Figure 2.31. Force-state map of raw data for the dead space example.

Figure 2.32. Force-state map for the fitted model of the dead space example.

Chapter 3.

Figure 3.1. The two d.o.f. nonlinear example considered in section (3.3.3).
Figure 3.2. Illustration of the step-by-step procedure.
Figure 3.3. FRF of the two d.o.f. example considered in section (3.3.3), obtained at 2 force levels.

Chapter 4.

Figure 4.1. Comparison between transfer functions of single-stage integration for Trapezium and Simpson rules.
Figure 4.2. Comparison between transfer functions of two-stage integration for Trapezium and Simpson rules and the Cubic Spline approach.
Figure 4.3. Variations of truncation and roundoff errors with number of points for a particular example, taken from reference [57].
Figure 4.4. Comparison between exact and estimated displacement signals for the 4 time domain integration rules and he cubic spline approach.
Figure 4.5. Variations of velocity and displacement errors with time for Bode's rule.
Figure 4.6. Variations of velocity and displacement errors with time for Bode's rule after maintaining the excitation over the entire window.
Figure 4.7. Comparisons between exact and estimated displacement signals for the analytical expression using 2 different sampling rates.
Figure 4.8. Amplitudes of acceleration, velocity and displacement spectra for the linear example of section (4.5).
Figure 4.9. Comparisons between exact and estimated displacement signals obtained using the frequency domain integration approach.

Figure 4.10. Flowchart of time domain integration and least squares trend removal.
Figure 4.11. Flowchart of time domain integration and high pass filtering trend removal.
Figure 4.12. Comparisons between exact and estimated displacement signals for the least squares trend removal case.
Figure 4.13. A sample comparison between exact and estimated displacement signals after trend was removed by applying a high pass filter in one direction.
Figure 4.14. A sample comparison between exact and estimated displacement signals after trend was removed by applying a filter in two directions.
Figure 4.15. Flowchart of frequency domain integration.
Figure 4.16. Comparisons between exact and estimated displacement signals after adding 0.2% DC to the acceleration.
Figure 4.17. Displacement signal after removing trends of Fig. (4.16) by the least squares approach, using 2nd and 3rd order polynomials.
Figure 4.18. A sine wave with a parabolic trend.
Figure 4.19. A comparison between exact and estimated signals after removing the parabolic trend of Fig. (4.18) by the least squares approach.
Figure 4.20. Results from time domain integration after adding a noise sequence to the acceleration.
Figure 4.21. A sample comparison between exact and estimated displacement after removing trend by least squares approach for the example with added noise.
Figure 4.22. Results from time domain integration and high pass filtering trend removal for the example with added noise.
Figure 4.23. A comparison between the exact displacement with added noise and the estimated displacement obtained using frequency domain integration.
Figure 4.24. Force-state map for the nonlinear example.

Chapter 5.

Figure 5.1. Sensitivity of stiffness to measurement amplitude errors for a linear system.
Figure 5.2. Sensitivity of damping to measurement phase errors for a linear system.
Figure 5.3. Sensitivity of damping to integration phase errors in velocity and displacement for a linear system.
Figure 5.4. Sensitivity of damping to measurement and integration phase errors for a linear system.

Chapter 6.

Figure 6.1. Variation of eigenvalue with frequency for a single-d.o.f. linear system.
Figure 6.2. Real and imaginary parts used for estimating the mass for a single-d.o.f. linear system.
Figure 6.3. FRF of the nonlinear example given in section (6.3.2) for different force levels.
Figure 6.4. Real part of FRF of the nonlinear example at 3 force levels.
Figure 6.5. Variation of mass, obtained using Crawley's approach, with frequency for a linear example.
Figure 6.6. Variation of mass, obtained using Crawley's approach, with frequency for the nonlinear example of section (6.3.2).
Figure 6.7. Variations of stiffness with mass for a linear system, for frequencies below, at and above the natural frequency.
Figure 6.8. Illustration of the sensitivity approach procedure.
Figure 6.9. Mass estimation using the sensitivity approach for a linear system.
Figure 6.10. Mass estimation using the sensitivity approach for a cubic stiffness nonlinearity.
Figure 6.11. Mass estimation using the sensitivity approach for a nonlinear example with cubic stiffness and quadratic damping nonlinearity.
Figure 6.12. Effect of noise on the mass obtained by the

sensitivity approach for a linear system.
Figure 6.13. Variations of eigenvalues of the two d.o.f. nonlinear example, considered in section (6.6), with frequency for 2 force levels.
Figure 6.14. Eigenvectors corresponding to the eigenvalues of Fig. (6.13.b).
Figure 6.15. Sample plots used to estimate the first mode shape of the 2 d.o.f. example.
Figure 6.16. Sample plot of the S_{11} function used to estimate the generalised mass for mode 1.
Figure 6.17. Sample plots for the T_{11} and T_{21} functions used to estimate the first column of the generalised damping matrix of the 2 d.o.f. example.
Figure 6.18. Estimation of generalised mass matrix of the 2 d.o.f. example using the sensitivity approach.
Figure 6.19. Comparisons of the exact responses of the 2 d.o.f. example and the responses of a model identified using an incorrect modal and the exact mass matrices.
Figure 6.20. Comparison of exact response of the 2 d.o.f. example and the response of a model identified using an incorrect modal matrix but a mass matrix obtained using the sensitivity approach.

Chapter 7.

Figure 7.1. Photograph of experimental T-beam configuration.
Figure 7.2. Block diagram of experimental set-up.
Figure 7.3. Flowchart of programme used for carrying out tests.
Figure 7.4. Illustration of quantization error problem.
Figure 7.5. Amplitude and phase mismatch errors between channels for the 32 points/cycle case.
Figure 7.6. Amplitude and phase mismatch errors between channels for the 1024 points/cycle case.
Figure 7.7. Transducer calibration set-up.
Figure 7.8. Apparent mass and phase plots measured at 3 force levels.
Figure 7.9. Apparent mass and phase plots for the 2

accelerometers used in the test.
Figure 7.10. Sketch of the T-beam structure with the added lumped masses.
Figure 7.11. FRF of T-beam before and after adding a lumped mass at its junction.
Figure 7.12. A sample FRF of bending mode at 3 force levels.
Figure 7.13. Mass estimation plot for the bending mode obtained using the sensitivity approach.
Figure 7.14. Sample portions of steady-state time histories at 3 force levels.
Figure 7.15. Force-state map generated at 3 force levels using steady-state excitation.
Figure 7.16. Sample measured and integrated time histories for sweep excitation.
Figure 7.17. Force-state map generated using sweep excitation.
Figure 7.18. Comparison between FRFs of structure and identified steady-state model at 4 force levels.
Figure 7.19. Comparison between FRFs of structure and identified sweep model at 4 force levels.
Figure 7.20. Comparison between responses of structure and steady-state model for sweep excitation.
Figure 7.21. Comparison between responses of structure and steady-state model for random excitation.
Figure 7.22. Comparison between FRFs generated from models using different mass values.
Figure 7.23. Comparison between FRFs generated from models using parametric and nonparametric approaches.
Figure 7.24. Mass estimation plot for torsion mode.
Figure 7.25. Two dimensional force-state map generated at 4 force levels for torsion mode.
Figure 7.26. Comparison between FRFs of structure and model for torsion mode.
Figure 7.27. Comparison between responses of structure and model for random excitation.
Figure 7.28. Variation of measured resonance frequencies with added mass for the 2 modes.

Figure 7.29. Photograph of experimental configuration for the 2 close mode case.

Figure 7.30. A sample FRF of 2 close mode configuration at 3 force levels.

Figure 7.31. Variation of Trail Nash eigenvalues with frequency for the 2 d.o.f. case.

Figure 7.32. Variation of normalised eigenvector elements with frequency for the 2 d.o.f. case.

Figure 7.33. Variation of the S_{11} function with frequency for the primary bending mode.

Figure 7.34. Variation of S_{22} function with frequency for the torsion mode.

Figure 7.35. Variation of the mode shape parameter with frequency for the bending mode.

Figure 7.36. Variation of the mode shape parameter with frequency for the torsion mode.

Figure 7.37. A sketch of the estimated mode shapes for the 2 d.o.f. configuration.

Figure 7.38. Variations of T_{11}, T_{21} and T_{12}, T_{22} functions with frequency for the 2 d.o.f. case.

Figure 7.39. Variation of generalised mass estimates for both modes with force level.

Figure 7.40. Sample time histories for the acceleration and integrated signals corresponding to first station.

Figure 7.41. Mass estimation using the sensitivity approach for the 2 d.o.f. case.

Figure 7.42. Sample sweep time histories used for identification of the 2 d.o.f. case.

Figure 7.43. Sample sweep map used for identification of the 2 d.o.f. case.

Figure 7.44. Comparison between FRFs of structure and identified sweep model at 3 force levels.

Figure 7.45. Comparison between FRFs of structure and identified single-frequency sweep model at 3 force levels.

Figure 7.46. Sample comparisons between responses of structure and identified single-frequency sweep model using random excitation at

low force level.

Figure 7.47. Sample comparisons between responses of structure and identified single-frequency sweep model using random excitation at high force level.

NOMENCLATURE

$A(\omega)$ Real part of FRF

A_{ij} Coefficients of two dimensional ordinary polynomial

A^b_{ij} Coefficients of two dimensional ordinary polynomial fitted to data within bins

A_1 Effective change of origin introduced by normalisation

$B(\omega)$ Imaginary part of FRF

$\underset{\sim}{B}$ Vector of unknown least squares parameters

B_i Coefficients of basis functions

BL_i Coefficients of basis functions of step L in the multi-step curve fitting approach

C Physical damping matrix

C_u Generalised damping matrix

CA(I,K) Contribution of the Kth term in the Ith step to the accumulative fit so far

C(I,K) Contribution of the Kth term in the fitted series to the Ith step

CT(I) Contribution of the Ith step to the accumulative fit

C_{ij} Coefficients of two dimensional Chebyshev series

c Viscous damping constant of a single d.o.f. system

[D] Design matrix of the least squares curve fitting process

D_{ij} Relative physical displacement between stations i and j

d Clearance value of a piecewise stiffness

e Number of exciters (chapter 6)

F_i Basis functions introduced in section (2.3.2.1)

FL_i Basis functions of step L in the multi-step curve fitting approach

$\underset{\sim}{f}$ Physical restoring force vector

$\underset{\sim}{\hat{f}}$ Fitted restoring force vector

$f_D(\bar{x})$ Displacement dependent function used for interpolation and extrapolation of restoring force (Masri/Caughey)

$f_v(\bar{y})$ Velocity dependent function

f Frequency (Hz)

$f(\dot{x},x)$	Restoring force of a single-d.o.f. system
f_b	Restoring force within each bin (chapter 2)
f_n	Natural frequency (Hz)
G	Goodness of fit
G_y	Goodness of estimating a signal y by integration
H	FRF of a single d.o.f. system
$\underset{\sim}{h}$	Modal restoring force vector
$h_i^{(L)}$	Fitted modal restoring force of mode i , step L
J	Least squares cost function
K	Physical stiffness matrix
K_u	Generalised stiffness matrix
k	Stiffness of a single-d.o.f. system
M	Physical mass matrix
M_u	Generalised mass matrix
M_c	Generalised consistent mass matrix (chapter 6)
M_s	Generalised mass matrix obtained by sensitivity approach
M_d, M_v	Number of points in the two dimensional numerical integration used to evaluate Chebyshev coefficients
m	Mass of a single-d.o.f. system or number of cycles in a sinusoid (chapter 4) or number of response stations (chapter 6)
N_p	Number of points per cycle
N_d, N_v	Number of terms in a two dimensional Chebyshev series
NF	Number of frequency points in ADC test
P	Amplitude of a sinusoidal excitation
$\underset{\sim}{p}(t)$	Input force vector
$\underset{\sim}{q}$	generalised coordinates obtained using wrong modal matrix
R	Transformation matrix defined in section (3.2)
R_T	Integration performance of Trapezium rule
R_S	Integration performance of Simpson's rule
R_{CS}	Integration performance of the Cubic Spline approach
T_i	One dimensional Chebyshev polynomial of order i
TI	Transducer calibration factor of channel I
$w(\bar{x})$	Weighting function of Chebyshev orthogonality relationship
U	An orthogonal matrix obtained by the singular value decomposition technique

$\underset{\sim}{u}$ Modal displacement vector

V An orthogonal matrix obtained by the singular value decomposition technique

V_{ij} Relative physical velocity between stations i and j

W Matrix containing the singular values of the design matrix or scaling matrix (chapter 6)

X Amplitude of a sinusoidal displacement

$X(\omega)$ Fourier transform of x(t)

$x(t)$ Displacement time history

$\underset{\sim}{x}$ Displacement vector

$\bar{x}$ Normalised displacement to the region [-1,+1]

$|x|$ Absolute value of x

y Velocity used in place of $\dot{x}$ for convenience

z Acceleration (chapter 4)

α Coefficient of friction force element or measurement amplitude error (chapter 5)

$\alpha(I)$ Percentage amplitude error for channel I with respect to 1st channel

β Coefficient of cubic stiffness element

γ Coefficient of quadratic damping element

$\Delta h_i^{(L)}$ Residual modal restoring force error of mode i , step L

Δt Sampling interval of time signals

$\Delta\theta$ Equally spaced increment in θ

$\Delta\tau$ Multiplexer time delay between channels

ε Coefficient of Van der Pol oscillator or measurement phase error (chapter 5)

$\varepsilon(I)$ Absolute phase error of channel I with respect to 1st channel

ζ Damping ratio

η Time variable measured from the beginning of the interval

θ Arccosine transformation of normalised displacement (chapter 2)

λ Frequency ratio

μ Eigenvalue of Trail Nash method

Φ Modal matrix

ϕ Arccosine transformation of normalised velocity (chapter

2)

or Phase of FRF of a single-d.o.f. system

ψ Characteristic phase lag

ω Frequency (rad/sec)

ω_n Natural frequency (rad/sec)

ω_s Sampling frequency

Papers written in relation to this research work.

1) M. Ajjan Al-Hadid and J. R. Wright. Developments in the Force-State Mapping Technique for Nonlinear Systems and the Extension to the Location of Non-linear Elements in a Lumped Parameter System. Mechanical Systems and Signal Processing, 3(3), pp. 269-290, June 1989.

2) M. Ajjan Al-Hadid and J. R. Wright. Application of the Force-State Mapping Approach to the Identification of Nonlinear Systems. European Forum on Aeroelasticity and Structural Dynamics. Aachen, 17-19 April 1989. (Also selected for publication in a special issue of Mechanical Systems and Signal Processing).

3) M Ajjan Al- Hadid and J. R. Wright. Sensitivity of the Force-State Mapping Identification Procedure to Measurement Errors. To be submitted for publication shortly.

ACKNOWLEDGEMENT

I would like to thank Dr. Jan Wright deeply for his supervision of this research work. Dr. Wright is endowed with great kindness and patience which I always felt through the help and guidance he provided me with during the 4 year period spent for carrying out this work.

I am most grateful to Mr. K. Worden and Professor G. R. Tomlinson of the University of Manchester for many helpful discussions and suggestions.

Many thanks are also due to Mr. D. J. Sharp and Dr. R. Vepa for their useful remarks and to Mr. Ian Bater for making and setting up the experimental rig.

I would especially like to thank the Scientific Studies and Research Centre of Syria for all the financial support I was given throughout this study.

To my lovely wife

Words can not express what you have experienced during the 4 long years you spent away from home, family and friends, looking after a very busy husband and two wonderful naughty little children.

Thank you so much.

1. INTRODUCTION

It is common practice to measure the dynamic characteristics of structures so as to obtain a mathematical model which will represent the dynamic behaviour as accurately as possible. This process is known as "Modal Testing" because models are usually expressed in terms of the natural frequency, damping, generalised mass and shapes of each mode of the structure [1].

The process of obtaining mathematical models for dynamic systems is usually carried out in two steps. Firstly, the system under consideration is excited and its response measured. Secondly, the measured data are analysed in some way so as to yield a mathematical model for the test system.

Mathematical models obtained using experimental data can have many applications in various technical disciplines such as mechanical, aeronautical and structural engineering. Some of these applications [1] are,

(i) the validation of theoretical mathematical models,
(ii) the prediction of response of structures to different excitation types and magnitudes, and
(iii) the modification of some structural components to change the behaviour of the structure.

However, the main assumption on which "Modal Testing" is based is that the test structure is linear. This assumption has two main implications :

(i) The transfer or frequency response function (FRF) relating the response to the excitation is not dependent on the excitation level (i.e. if the excitation amplitude is doubled then the

response doubles and thus the same FRF will be obtained) and
(ii) The principle of linear superposition holds.

Unfortunately, most real structures show some nonlinear behaviour. Depending on the significance of this behaviour, the above two implications may no longer be valid. As a result the amplitude and phase of the frequency response functions will vary with the excitation force level. Ewins [1] presented some signs of nonlinear behaviour as,

(i) natural frequencies varying with position and strength of excitation,
(ii) FRFs varying with force level,
(iii) distorted FRFs and
(iv) unstable or unrepeatable data.

However, most conventional modal testing methods [1] are based on extracting the modal parameters of the system by curve fitting the FRF data using a linear model which has only three parameters, namely, mass, damping and stiffness. Such a linear model, if derived from a system having significant nonlinear behaviour, would be an approximation to that behaviour at the force level for which the data were generated. The model would clearly not characterise the system behaviour at other force levels. The parameters would be biased i.e. the linear model would not be equivalent to the linear part of the exact nonlinear model.

Indeed, Ewins showed that even slight structural nonlinearities, which are usually considered as insignificant, may yield large errors in the modal model obtained from FRF data. The same arguments would apply to other linear methods such as those in the time domain.

The problem of nonlinearity in modal testing has been the subject of fairly extensive research during the last couple of decays by many researchers from various technical disciplines. However the

subject is extremely wide and difficult and therefore still requires further consideration, particularly in regard to the mathematical modelling of single and multi-d.o.f. nonlinear dynamic systems using experimental data.

This particular topic will be the main theme of this thesis where an attempt will be made to extend the studies of other workers who have presented some interesting ideas for nonlinearity identification in the time domain [2].

Before proceeding with the study in depth, a brief review of the identification methods of nonlinear systems will be given. The term "identification" can refer to simply detecting the presence of nonlinear behaviour right through to obtaining a full mathematical description of the system.

Tomlinson [3] has presented a review in which the identification methods relevant to modal testing are classified according to whether sinusoidal or random excitation was used. The methods suitable for sinusoidal excitation were subdivided as follows :

(i) Superposition and reciprocity methods
(ii) Nyquist plot distortion / Frequency isochrones methods [4,5]
(iii) Damping distortion method [1]
(iv) Harmonic distortion methods, in particular
  - Locus of beat frequency method
  - "Sig-Function" method [6-8]
(v) Hilbert Transform method [9-11]

The second category, relevant particularly to random excitation, was subdivided as follows :

(i) Optimum FRF method [11]
(ii) Functional series methods such as
  - Volterra series [11-13]
  - Bispectral analysis methods [11,14,15]

- Time-series analysis methods such as that using the NARMAX model (Nonlinear AutoRegressive Moving Average model with Xogenous inputs) [16]

More recently, Natke et al [17] have published a review on the identification of nonlinear systems. Although there are very many references, taken from both the engineering and control fields, the review is rather brief. Further review papers have been presented by Tomlinson [11] and Billings [12].

Some of the methods presented in the above reviews and believed to be of interest will now be discussed. It is perhaps helpful to consider the classification of these methods according to the extent of the identification (i.e. detection or mathematical representation) and the domain in which the identification is carried out (i.e. time or frequency), as seen in Fig. (1.1).

(a) Detection methods.

In modal testing, it is vital for the modal analyst to know whether the test system behaves either linearily or nonlinearily before proceeding with extracting the system modal parameters from the measured data. Obtaining such an insight into the system behaviour at an early stage of the test may avoid later problems which could occur if the system behaves nonlinearily. If the system is known to be nonlinear then the measurement process may be carried out under different, more linear, conditions [18] so that the extracted linear parameters may be more accurate, or under conditions where the nonlinear behaviour is emphasised [2,19] so that a nonlinear model may be estimated with more confidence.

A variety of methods concerned with detection of nonlinear behaviour of vibrating structures is available. All methods allow the presence of nonlinearity to be detected but some also provide some indication about the type of nonlinearity.

The simplest of these methods ia based on checking for linearity by repeating the measurements at several excitation levels using steady-state sinusoidal excitation under controlled conditions; in particular, the actual force applied to the structure must be kept constant at all the frequency increments within the bandwidth of interest. This process must be implemented to avoid the drop out in the force spectrum caused by the interaction between the structure and the electrodynamic exciter at the excitation point [20,21].

The FRF plots obtained at various levels of constant force excitation will be different if the system is behaving nonlinearily. The variation in the FRF with force has been shown [7] to be systematic for some common nonlinearities; it can also provide an indication of the type of nonlinearity when modes are fairly well separated.

The use of the Nyquist or vector plot is one of the earliest techniques for detecting nonlinearity during a modal test [3-5] because the well known near-circular vector locus for linear systems may become distorted due to the presence of nonlinearity in the system. In general, the distortion is dependent upon the type of nonlinearity and the excitation force level. The use of constant frequency lines (isochrones) joining points of the same frequencies obtained for different force levels may also be useful for nonlinearity detection [3]. In reference [3] it is pointed out that these lines are more sensitive to distortion than the actual vector locus and are therefore more able to characterise the type of nonlinearity present in the system.

The principle of superposition may also be used for detection of nonlinearity. A major drawback is that it should be checked for all response and excitation stations as well as for a range of force levels before linearity is assumed, a very time consuming process. Furthermore, no idea about the type of nonlinearity can

be deduced [3].

The damping distortion method has been proposed [1,18] to asses the quality of the FRF data used for estimating the modal parameters of the system. The method is based upon constructing a three dimensional carpet plot representing the variation of the estimated modal damping with the frequencies defining the points on the locus used for the damping estimation. Ideally, if the system is linear, there will be no variation and the carpet plot will be flat. However if the system is nonlinear the carpet will not be flat. The distortion may in some cases be systematic so that the type of nonlinearity may be inferred from the shape of the plot. The main limitation of this approach is that it can only be implemented satisfactorily with well separated modes since the method is based on single-d.o.f. theory. However in reference [18] it has been suggested that the approach may also be used with closely-coupled modes providing the effects of the close modes are extracted, a very difficult process for nonlinear systems [3].

A technique that makes use of time domain data for detecting and characterising nonlinearity during a modal test makes use of the "Sig-Function" [6-8]. The technique is based upon the energy loss caused by filtering out the sub and super harmonics from the response to steady-state sinusoidal excitation. The Sig-Function is frequency dependent and is defined as the mean square value of the difference between the total response (fundamental plus sub and super harmonics) and the filtered response (fundamental only) divided by the mean square value of the total response. It has been shown [6] that the Sig-Function can be used as a measure of the nonlinear behaviour of the structure and in some cases be capable of indicating the type of nonlinearity. This idea was shown to work for a single-d.o.f. with a stiffness nonlinearity.

The Hilbert transform technique has been developed and recommended by Tomlinson et al [3, 9-11, 23-29] for detecting and characterising nonlinearity during a modal test. The theory of the

Hilbert transform and its applications to nonlinear systems are very well documented in the above references. However, an attempt will be made to discuss briefly some of its practical aspects.

For this particular application, the Hilbert transform offers a means of checking the FRF generated during a modal test for linearity. Basically, the technique relies on the concept of the causality of physically realisable linear and nonlinear systems; causality implies that systems do not start vibrating before they are excited. From an analytical point of view it has been shown that if a system is linear then the real and imaginary parts of its FRF are related uniquely by the Hilbert transform. Also when a test structure behaves nonlinearily then the inverse Fourier transform of its FRF is non-causal and the above relationship between the real and imaginary parts of the FRF does not hold. Thus a comparison of the FRF and its Hilbert transform can show whether nonlinearity is present.

The Hilbert transform technique has been used successfully for detecting nonlinearity in single and multi-d.o.f. systems, though residual effects can be a problem.

In references [27-29] it was suggested that the type of nonlinearity for a single-d.o.f. may be deduced from the difference between the FRF and its associated Hilbert transform at different force levels. The nature of the difference was quantified via the statistical moments about the frequency and amplitude or real and imaginary axes resulting, for example, in a function known as the Hilbert Transform Describer [28]. This function could also indicate the force level at which the FRF would be essentially linear.

The main limitation of any of the above detection methods is that they must be applied to all the individual elements of the FRF matrix to ensure that the linearity assumption is completely valid. However, the principal component analysis approach [26,28]

reduces the number of FRFs which need to be processed by transforming to fewer linearly independent principal FRFs. This is particularly useful when the number of stations exceeds the effective number of modes in order to identify mode shapes accurately.

Once nonlinear behaviour has been detected and possibly characterised using one of the above methods, it remains to obtain a nonlinear mathematical model of the test structure.

(b) Mathematical modelling methods.

The dynamic behaviour of a system is by no means simple, especially when the behaviour is nonlinear. The implementation of a "parametric" concept of modelling, which assumes that the type of the mathematical model of the structure is known a priori and that only the parameter values need to be estimated, is an impractical concept. Consequently, most attention has been given to methods which do not assume that the form of the model is known but which seek to represent the nonlinear behaviour of the system as closely as possible. This "nonparametric" modelling approach is the subject which will be dealt with in this research work.

One of the traditional nonparametric identification techniques is known as the Volterra series approach. Most of the applications of the Volterra series has been in the field of control engineering and recent studies [12, 13, 30-32] have attempted to use the Volterra series in identification of nonlinear systems in modal analysis.

The Volterra series expresses the response of a nonlinear system as a sum of terms each of which is a function of the input and some function called the Volterra kernel. The Volterra kernel corresponding to the first term in the series represents the impulse response of the linear part of the system and so characterises its linear behaviour, while the kernels present in

the higher order terms of the series characterise the nonlinear behaviour. Thus, the problem here is to find the Volterra kernels purely from input and response data.

The estimation of the higher order Volterra kernels is outside the scope of this review but is a difficult task and requires a large amount of computer storage and time. A modified Volterra series known as the Wiener series has been developed in order to alleviate the problem of estimating the Volterra kernels. When the excitation is an uncorrelated white Gaussian time signal then the Wiener series will be a series of orthogonal functions the estimation of which is less involved.

The equivalent of the higher order Volterra kernels in the frequency domain are the higher order frequency response functions [13,31], which show the effect of excitation at more than one frequency simultaneously and can apparently help to understand the nonlinear system behaviour. An interesting development is the attempt to curve fit the higher order FRFs [33] so as to obtain a nonlinear mathematical model for the system.

A further class of methods aim to fit a difference equation model (rather like a digital filter) to discrete time domain data. A well known method uses the NARMAX model [16]. The models can be used to predict response to other excitations.

Identification of nonlinearities in vibrating systems using the optimal control deconvolution technique is another new area of study developed by Hammond et al [34-36]. In this technique the linear part of the system is assumed to be known and only the form of the model of the nonlinear part of the system and its associated parameters are sought and estimated.

The method solves the tracking problem in which an input is estimated such that when it is applied to the assumed linear model, it yields a response as close as possible to the original

nonlinear response. The difference between the true input and the estimated input is a measure of the nonlinear restoring force of the system. The restoring force could then be plotted against the velocity and displacement in a 3 dimensional form; a curve fit would then be possible.

The main limitation of implementing the technique is that the linear part of the nonlinear system will need to be estimated so any errors in the linear part will bias the results. Also the method is involved and computationally intensive.

An earlier and interesting technique for modelling nonlinear systems was suggested by Masri and Caughey [2,19,37,38]. Given an estimate of the system mass, the restoring force time history is calculated by subtracting the inertia force from the excitation force. The resulting restoring force is then represented by a surface over the measured velocity-displacement plane and a two dimensional fit to the surface is carried out using an orthogonal polynomial series expression. The technique was extended by the same authors for the identification of multi-d.o.f. systems by transforming to modal space using assumed generalised mass and modal matrices.

The Masri and Caughey technique is considered to be nonparametric since it assumes that no prior knowledge of the type of mathematical model to be fitted to the restoring force is required. In addition it has advantages over other methods [2] some of which will be mentioned in the next chapter. It is the Masri/Caughey technique which will be considered in detail in this research.

In an independent study, Crawley et al [39-42] have developed a variant of the Masri/Caughey single-d.o.f. approach for investigation of joints in space structures. A method for identifying the nonlinear parameters of the joints known as the force-state mapping technique was introduced. This technique

represents the force transmitted through the joint as a function of its relative velocity and displacement. However, unlike the Masri/Caughey approach, the force-state mapping technique has used a least squares algorithm for the curve fitting process using ordinary polynomials [43]. Nevertheless, their representation of the force in terms of the measured states in 3 dimensional form looked similar to the Masri/Caughey representation. The potential of the force-state mapping technique has been shown when Crawley et al [41] applied the technique successfully to experimental data from an idealised test article and a simple nonlinear joint. The application was restricted to single-d.o.f. systems. It is interesting considering the similarity between the approaches, that neither of the authors has referenced the other! In this work the method will also be referred to as the force-state mapping for convenience.

These recent developments of the force-state mapping method for identification of single and multi-d.o.f. nonlinear systems have attracted attention from other researchers namely, Yang and Ibrahim [44], Worden and Tomlinson [45-47], Argoul [48] and Hunter et al [49]. Their work is considered later on.

It may be seen from the above attempt to review some of the methods of identification of nonlinear systems that the subject is wide and interesting. However, it seems that no single method can yet encompass all the aspect of the problem so research in many areas could be fruitful and any method would be complementary to the others.

In this research, the simple and potentially useful technique suggested by Masri et al and Crawley et al will be investigated and developed further, both for single and multi-d.o.f. systems.

In chapter 2, the implementation of the force-state mapping approach of Masri and Caughey to the identification of single-d.o.f. nonlinear systems is considered. In particular, it

is shown that the use of two dimensional orthogonal polynomials is unnecessarily restrictive and that a simpler approach based on ordinary polynomials and special functions provides a faster and more accurate identification for polynomial and nonpolynomial types of nonlinearity.

The extension of the force-state mapping approach to the identification of multi-d.o.f. nonlinear systems is considered in chapter 3. It is shown that the use of the Masri/Caughey iterative approach will yield biased models unless some of the steps are repeated several times to correct for the bias. In addition, the problem of bias can be removed by carrying out the entire curve fit of the restoring force in a single step. A new approach for identifying the type and location of discrete nonlinear elements in lumped parameter systems is also presented.

The practical implementation of the force-state mapping technique demands that the force, acceleration, velocity and displacement signals are available at the same instants of time for each measurement station. Because it is impractical to measure all these signals simultaneously, the problem of estimating a full set of states from partial measurements is considered in chapter 4.

Chapter 5 is concerned with a study of the sensitivity of the identified parameters with respect to amplitude and phase measurement errors for single-d.o.f. identification.

The estimation of the mass required for single-d.o.f. identification and generalised mass and modal matrices for multi-d.o.f. identification, is investigated in some detail in chapter 6 where a new approach is presented for estimating the mass for nonlinear systems. The effect of the accuracy of the modal matrix is also considered.

The application of the force-state mapping technique to a real T-beam structure is considered in chapter 7 where some results for

two well separated modes and two fairly close modes are presented.

Finally, chapter 8 presents some conclusions and suggestions for further work.

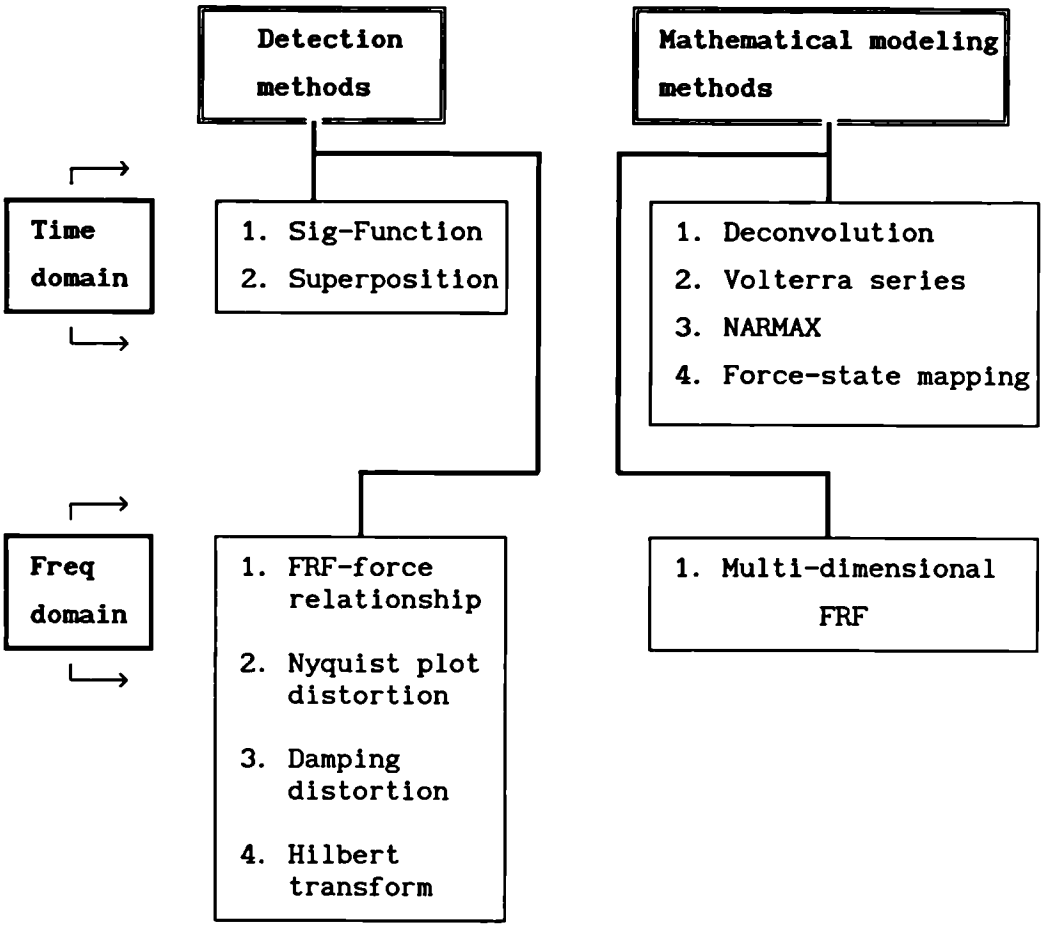

Figure 1.1. Classification of nonlinear methods.

2. Identification of Single Degree of Freedom Nonlinear Systems Using the Force-State Mapping Technique

2.1. Introduction.

About a decade ago Masri and Caughey presented an interesting technique for identification of single-degree of freedom nonlinear dynamic systems [2]. In their technique they argued that since the model structure in most practical dynamic problems is by no means clear , the use of parametric identification methods, which assume that the type of the model of the test structure is known and only its associated parameter values need to be identified, may be impractical and inappropriate. Accordingly, they presented their technique as a nonparametric technique which does not require such knowledge about the type of the model to be identified. The technique claimed to have some advantages over the traditional nonparametric methods such as the Volterra/Weiner approach in that (a) it does not include restrictions on the nature of the dynamic system to be identified, (b) it has also no restriction on the excitation signal that can be used as long as the signal can excite any nonlinearity present in the system, (c) it has less mathematical complexity and requires less storage and computations and (d) it is faster and has relatively rapid convergence.

In this chapter, the basic philosophy of the force-state mapping technique used for identifying single-degree of freedom nonlinear dynamic systems will be presented. The problem of curve fitting the restoring force of the test system in terms of its states will be investigated. In particular, the Masri/Caughey approach which approximates the restoring force by a function expressed in terms of two dimensional orthogonal polynomials, will be considered in some detail. It will be shown that the use of these orthogonal

polynomials is unnecessarily restrictive and causes some complications which may be avoided by implementing an alternative approach based on ordinary polynomials and special functions.

The applications in this chapter will be restricted to simulated systems whereas real structures are considered in chapter 7.

2.2. Basic philosophy of the force-state mapping technique.

The dynamics of the single-degree of freedom nonlinear system shown in Fig. (2.1) may be represented by the following differential equation,

$$m\ddot{x} + f(x,\dot{x}) = p(t) \quad \ldots\ldots\ldots\ldots\ldots\ldots \quad (2.1)$$

where m is the mass, $\ddot{x}$ is the acceleration, p(t) is the applied force and $f(x,\dot{x})$ is the overall restoring force which contains both the linear and nonlinear parts of the system and is a function of the velocity $\dot{x}$ and displacement x. For a linear system, it is clear that

$$f(x,\dot{x}) = c\dot{x} + kx$$

where c is the viscous damping constant and k is the stiffness, whereas for a nonlinear system with a cubic stiffness element, then

$$f(x,\dot{x}) = c\dot{x} + kx + \beta x^3$$

with coefficient β defines the degree of hardening or softening. It is possible to rearrange equation (2.1) into the form,

$$f(x,\dot{x}) = p(t) - m\ddot{x} \quad \ldots\ldots\ldots\ldots\ldots\ldots (2.2)$$

and therefore it can be seen that an estimate of the restoring

force may be obtained if a good estimate of the mass is available and if the acceleration and excitation force signals are measured for a particular test. It should be pointed out here that any excitation may be used (for example random or sine sweep) as long as it is large enough to cause the system to behave nonlinearily.

The aim of the force-state mapping technique is to express the estimated restoring force $f(x,\dot{x})$ as a mathematical function of $\dot{x}$ and x, which can be referred to as the "states" of the system, by some curve fitting process. In order to carry out such a curve fit it is necessary to obtain $f(x,\dot{x})$, $\dot{x}$ and x as functions of time. In practice test data are digitized and so the three values must be available at the same sampling instants. Sample time histories for one degree of freedom simulated data are shown in Fig. (2.2). The velocity and displacement may be found by direct measurement [41] or by careful integration of the acceleration [42,45] (see chapter 6).

Once a sufficient number of values of the restoring force, velocity and displacement have been obtained at discrete times the particular characteristics of the nonlinearity may be seen before any curve fitting by selecting values of each of the $f(x,\dot{x})$ $\dot{x}$ and x time histories at the same instants and plotting them in a three dimensional form called a force-state map of the raw data as shown in Fig. (2.3).

The selection of the $f(x,\dot{x})$, $\dot{x}$ and x values to construct the map is not restricted to any particular rule as long as they are taken at the same instant of time. It is particularly interesting to note that pure sinusoidal excitation with response measured after reaching the steady-state condition may lead to a circular map with a "hole" in the surface as shown in Fig. (2.4). To get a spiral map, however, a transient response starting from zero or ending at zero amplitude should be used. Points from the $f(x,\dot{x})$, $\dot{x}$ and x signals which overlap on the map may be omitted and thus

allowing for different points to be selected from different parts of the time signals so that map may be filled uniformly. This is made possible since there is no requirement of equal sample interval on the time scale for constructing the map. Note that points around peak regions are particularly important since they are usually associated with the significant nonlinear behaviour of the system, apart from friction nonlinearity for which points around low amplitude regions are important.

It is often particularly helpful for lightly damped structures to plot the projection of the map onto the force-displacement plane as shown in Fig. (2.5.a). The force-velocity projection shown in Fig. (2.5.b) is not normally as useful.

Crawley et al [39-42] constructed a regular grid map from the raw data by dividing the area covered by these data into small squares and then averaging the restoring force values at the points contained in each square. The average value of each square was then located in the centre of the square. If a square was empty from data points, the restoring force at its centre was calculated by averaging points surrounding the square. The resulting shapes of the force-state map were then used for characterizing nonlinearities and it was shown that these shapes are unique and recognizable for most structural nonlinearities.

2.3. Curve fitting the restoring force.

Once the restoring force $f(x,\dot{x})$, velocity $\dot{x}$ and displacement x are obtained as a set of values at discrete time instants, it remains to fit a suitable mathematical model to the restoring force in terms of the states.

2.3.1. Masri/Caughey approach using Chebyshev polynomials.

The approach adopted by Masri and Caughey in their development of

this nonparametric identification procedure [2] is to approximate the restoring force $f(x,\dot{x})$ by a function expressed in terms of two dimensional polynomials. Thus

$$f(\bar{x},\bar{y}) \approx \hat{f}(\bar{x},\bar{y}) = \sum_{i=0}^{N_d} \sum_{j=0}^{N_v} C_{ij}\, T_i(\bar{x})\, T_j(\bar{y}) \qquad \ldots\ldots\ldots (2.3)$$

where C_{ij} are unknown coefficients to be determined by a least squares curve fitting procedure, T_i, T_j are Chebyshev polynomials, and N_d, N_v are number of terms in the two dimensional series. Note that for convenience of notation, y will be used in place of $\dot{x}$ throughout some of the following sections. The values $\bar{y}$ and $\bar{x}$ are velocity and displacement normalised to the region [-1,+1] using,

$$\bar{x} = \frac{x - A_1}{A_2} \qquad \ldots\ldots\ldots\ldots\ldots\ldots (2.4)$$

where $A_1 = \dfrac{x_{max} + x_{min}}{2}$ and $A_2 = \dfrac{x_{max} - x_{min}}{2}$

and similarly for $\bar{y}$.

In fact, this normalisation of data is necessary since it will be shown that the Chebyshev polynomials are only orthogonal in the interval [-1,+1].

The Chebyshev polynomial of degree i can be defined as

$$T_i(\bar{x}) = \cos\,(i \cos^{-1} \bar{x}\,) \qquad \ldots\ldots\ldots\ldots (2.5)$$

Using the identity

$\cos\,(i+1)\theta + \cos\,(i-1)\theta = 2 \cos\,\theta \cos\, i\theta$ and setting $\theta = \cos^{-1}\bar{x}$ the following expression can be obtained

$$T_{i+1}(\bar{x}) = 2\,\bar{x}T_i(\bar{x}) - T_{i-1}(\bar{x}) \quad \ldots\ldots\ldots\ldots (2.6)$$

which is known as the three-term recurrence expression for the Chebyshev polynomials (where $i \geq 1$). Thus, Chebyshev polynomials can be written as ordinary polynomial series expansions, namely

$$T_0 = 1$$
$$T_1(\bar{x}) = \bar{x}$$
$$T_2(\bar{x}) = 2\,\bar{x}^2 - 1$$
$$T_3(\bar{x}) = 4\,\bar{x}^3 - 3\,\bar{x}$$
$$\ldots\ldots\ldots\ldots\ldots$$
etc

which alternate between being even and odd functions of $\bar{x}$.
The important property of Chebyshev polynomials is that they are orthogonal. Since it is well known that

$$\int_0^{\pi} \cos i\theta \cos j\theta \, d\theta = \begin{cases} 0 & (i \neq j) \\ \pi/2 & (i=j\neq 0) \\ \pi & (i=j=0) \end{cases} \quad \ldots\ldots\ldots (2.7)$$

then substituting $\theta = \cos^{-1}\bar{x}$ can be shown to yield

$$\int_{-1}^{+1} w(\bar{x})\, T_i(\bar{x})\, T_j(\bar{x})\, d\bar{x} = \begin{cases} 0 & (i \neq j) \\ \pi/2 & (i=j\neq 0) \\ \pi & (i=j=0) \end{cases} \quad \ldots\ldots\ldots (2.8)$$

where $w(\bar{x}) = \dfrac{1}{\sqrt{1 - \bar{x}^2}}$ is a weighting function.

Thus, the Chebyshev polynomials satisfy a weighted orthogonality relationship over the interval [-1,+1]. This orthogonality property of Chebyshev polynomials means that additional terms could be introduced into the series in equation (2.3) without needing to recompute earlier coefficients. An additional feature

is the equal ripple approximation for the error within an interval of interest. In fact, Chebyshev polynomials were chosen by Masri and Caughey because of their orthogonal property and the equal ripple approximation for the error.

The coefficients C_{ij} of the curve fit in equation (2.3) may now be found by multiplying both sides of the equation by

$$w(\bar{x})\ w(\bar{y})\ T_m(\bar{x})\ T_n(\bar{y}) \qquad \text{where} \quad m = 0,1\ldots N_d,\ n = 0,1\ldots N_v$$

and integrating with respect to $\bar{x}$ and $\bar{y}$ between -1 and +1. Thus

$$\int_{-1}^{+1}\int_{-1}^{+1} f(\bar{x},\bar{y})\ w(\bar{x})\ w(\bar{y})\ T_m(\bar{x})\ T_n(\bar{y})\ d\bar{x}\ d\bar{y} \approx$$

$$\int_{-1}^{+1}\int_{-1}^{+1} \left[\sum_{i=0}^{N_d}\sum_{j=0}^{N_v} C_{ij}\ T_i(\bar{x})\ T_j(\bar{y})\right] w(\bar{x})w(\bar{y})T_m(\bar{x})T_n(\bar{y})\ d\bar{x}\ d\bar{y} \qquad \ldots\ldots\ldots (2.9)$$

Using the orthogonality property given in equation (2.8) then, the right hand side of equation (2.9) only exists for i=m and j=n and is given by

$$C_{mn}\int_{-1}^{+1} w(\bar{x})\ T_m(\bar{x})\ T_m(\bar{y})\ d\bar{x}\int_{-1}^{+1} w(\bar{y})\ T_n(\bar{y})\ T_n(\bar{y})\ d\bar{y}$$

$$= C_{mn}\frac{\pi^2}{4} \qquad \text{for m and n} \neq 0$$

$$= C_{mn}\frac{\pi^2}{2} \qquad \text{for m or n} \neq 0 \qquad \ldots\ldots\ldots (2.10)$$

$$= C_{mn}\,\pi^2 \qquad \text{for m and n} = 0$$

Hence, combining equations (2.9) and (2.10) leads to

$$C_{mn} \approx A_{mn} \int_{-1}^{+1} \int_{-1}^{+1} f(\bar{x},\bar{y})\, w(\bar{x})\, w(\bar{y})\, T_m(\bar{x})\, T_n(\bar{y})\, d\bar{x}\, d\bar{y} \quad \ldots.(2.11)$$

where

$$A_{mn} = \begin{cases} 4/\pi^2 & \text{for m and } n\neq 0 \\ 2/\pi^2 & \text{for m or } n \neq 0 \\ 1/\pi^2 & \text{for m and } n=0 \end{cases} \quad \ldots\ldots\ldots(2.12)$$

In fact integrating equation (2.11) between -1 and +1 is not possible in this form since the weighting functions are infinite at the boundaries of the integrals. Therefore the following transformations must be used in equation (2.11)

$\bar{x} = \cos\theta$ and $\bar{y} = \cos\phi$ leading to

$$C_{mn} = A_{mn} \int_{\theta=0}^{\pi} \int_{\phi=0}^{\pi} f(\theta,\phi)\, T_m(\theta)\, T_n(\phi)\, d\theta\, d\phi \quad \ldots\ldots\ldots(2.13)$$

To obtain C_{mn} the integrals have to be evaluated numerically. The simplest way is to write equation (2.13) in a discrete form as, approximately

$$C_{mn} = A_{mn} \sum_{k=1}^{M_d} \sum_{l=1}^{M_v} f_{kl} \cos(m\,\theta_k) \cos(n\,\phi_l)\, \Delta\theta\, \Delta\phi \quad \ldots.(2.14)$$

where the equally spaced increments in θ and ϕ are given by

$$\Delta\theta = \frac{\pi}{(M_d-1)}, \quad \Delta\phi = \frac{\pi}{(M_v-1)} \quad \text{and}$$

$$f_{kl} = f(\theta_k, \phi_l)$$

$$\theta_k = (k-1)\ \Delta\theta$$

$$\phi_l = (l-1)\ \Delta\phi$$

It is clear from equation (2.14) that in order to calculate the coefficients C_{mn}, the values of the restoring force must be available at equally spaced increments in θ and ϕ over the entire region defined by $\theta, \phi = 0$ to π. The integers M_v and M_d define the number of points used for the numerical integration.

Unfortunately the measured data will only cover part of the region defined by $\bar{x}, \bar{y} = -1$ to $+1$ and therefore only part of the required (θ, ϕ) region as shown in Fig. (2.6). In general the measured data will not appear at the equi-spaced values of θ and ϕ even within the region covered by the measurements. Therefore a two dimensional interpolation/extrapolation scheme is needed to generate the restoring force at the required equally spaced locations. It is clear from Fig. (2.6.b) that the region over which extrapolation is required is quite considerable.

Before proceeding with the next phase, it is worthwhile to consider the interpolation/extrapolation problem in some detail and to give an idea about the relevant work done by different researchers in this area.

2.3.1.1. Interpolation/extrapolation of restoring force.

Masri and Caughey do not specify which two dimensional interpolation scheme they use but their extrapolation procedure [2] is based on the assumption that

$$f(\bar{x}, \bar{y}) = f_D(\bar{x}) + f_V(\bar{y}) \quad \ldots\ldots\ldots\ldots (2.15)$$

is a valid approximation outside the region of measured data. This expression implies that the restoring force is made equal to the sum of two functions, one displacement dependent and the other velocity dependent. This assumption of no coupling between displacement and velocity is probably not too unreasonable in practice but it would not apply to more complicated nonlinearities such as the Van der Pol oscillator.

Masri and Caughey then expand the two functions $F_D(\bar{x})$ and $f_v(\bar{y})$ as one dimensional Chebyshev polynomial series, namely

$$f(\bar{x},\bar{y}) \approx \sum_{i=0}^{n_D} a_i \, T_i(\bar{x}) + \sum_{j=0}^{n_v} b_j \, T_j(\bar{y}) \quad \ldots\ldots\ldots (2.16)$$

The coefficients of the series for $f_D(\bar{x})$ and $f_v(\bar{y})$ are obtained by curve fitting the data located between two narrow bands around $\bar{y}=0$ and $\bar{x}=0$ (or around ϕ, $\theta = \pi/2$) respectively, as shown in Fig. (2.6). It should be noted that the evaluation of these coefficients requires interpolation for generating equally spaced points along the $\bar{x}$ and $\bar{y}$ axes.

Once the coefficients a_i and b_j are estimated, the expression (2.16) may be used to extrapolate into the empty corner regions shown in Fig. (2.6) and so evaluate the restoring force values required.

Worden and Tomlinson [45-47] used an interpolation procedure for the irregularly spaced points based on the construction of the so-called Dirichlet tessellation and the associated Delaunay triangulation. The process is rather involved and time consuming for this particular application. However, because the method will not cope with extrapolation, the data zone has to be reduced until there are no empty corner regions. Obviously normalisation must then be referred to this reduced data area. there is clearly a

major problem in the procedure since a large quantity of data may be rejected and it is the very data that is associated with the significant nonlinear excursions.

Argoul [48] has also implemented the method of curve fitting using Chebyshev polynomials but has adopted an iterative approach to the extrapolation procedure. A series is first fitted within the reduced data region used by Worden and Tomlinson. The fitted series is then used to extrapolate into a somewhat larger region and the fit repeated to update the series. Eventually the whole data area is covered. Argoul claims better results than Masri and Caughey for the Van der Pol example in reference [2].

In the work carried out by the author on the Chebyshev representation, a simpler approach was adopted for the interpolation and extrapolation process. No data was discarded. Instead the $(\bar{x},\bar{y})$ plane was divided up into a number of equal size square "bins" as shown in Fig. (2.6.a). Within each bin a two dimensional fit using an ordinary polynomial series of first, second or third order was used to represent the restoring force variation. Thus,

$$f_b(\bar{x},\bar{y}) \approx \hat{f}_b(\bar{x},\bar{y}) = \sum_{i=0}^{N}\sum_{j=0}^{N} A_{ij}^{b}\,\bar{x}_b^{i}\bar{y}_b^{j} \qquad \ldots\ldots\ldots (2.17)$$

where the value of N may be selected as 1,2 or 3 by examination of the force-state map plot of the raw data for example, f_b is the restoring force, $\bar{x}_b$ and $\bar{y}_b$ are the normalised displacement and velocity values contained in each bin and A_{ij}^{b} are two dimensional coefficients applying to each bin to be found by an ordinary least squares algorithm. The resulting series was used to generate equi-spaced data values within the appropriate bin, using equation (2.17), ready for the subsequent overall Chebyshev fit. The total number of bins (typically 4 to 9) was chosen to ensure that there

were sufficient data points within each bin.

It can be seen that, unlike the other methods, this procedure can be used to interpolate and extrapolate even in the presence of displacement-velocity coupling since the series in equation (2.17) contains basic coupling terms. Furthermore, if the actual restoring force surface is discontinuous, as seen in Fig. (2.7) for a piecewise stiffness case, then it is possible in principle to divide the surface up into bins with boundaries located at the discontinuities. Then each bin will contain a continuous surface. Note that in this case the bins may be of different sizes. The procedure described worked fairly well as will be seen later when some examples are considered.

2.3.1.2. Some further comments on the Chebyshev polynomial approach.

The practical implementation of Chebyshev polynomial representation of the restoring force has several significant drawbacks which are important and will be discussed below.

(i) Firstly the normalisation from (x,y) to $(\bar{x},\bar{y})$ is required to bring the displacement and velocity data into the range $[-1,+1]$ and was defined in equation (2.4) by, for example,

$$\bar{x} = \frac{x - A_1}{A_2}$$

where $A_1 = \frac{x_{max} + x_{min}}{2}$ and $A_2 = \frac{x_{max} - x_{min}}{2}$

In fact this kind of normalisation process involves an effective change of origin equal to A_1, as seen in Fig. (2.8) for the displacement direction. This results in the loss of any odd or even behaviour of the function to be fitted if the A_1 value is significant. This feature may be illustrated by considering the

following simple example where the restoring force is given by the odd function,

$$f(x) = kx + \beta x^3 \quad \ldots\ldots\ldots\ldots\ldots\ldots (2.18)$$

Using the normalisation equation then it can be shown that

$$f(\bar{x}) = (kA_1 + \beta A_1^3) + (kA_2 + 3\beta A_1^2 A_2)\,\bar{x} + (3\beta A_1 A_2^2)\,\bar{x}^2 + (\beta A_2^3)\,\bar{x}^3$$

which is of the form

$$f(\bar{x}) = a_0 + a_1\bar{x} + a_2\bar{x}^2 + a_3\bar{x}^3 \quad \ldots\ldots\ldots\ldots\ldots (2.19)$$

Thus, it may be seen that the normalisation process has effectively introduced two new even terms (a_0 and $a_2\bar{x}^2$) to the function and hence a larger series needs to be fitted than if the unnormalised function were fitted. This feature may be significant in practice since most nonlinearities display a nominal odd behaviour against both displacement and velocity.

The change in origin described above depends upon the difference in the absolute values of the maximum and minimum displacements or velocities. This will be small for steady-state oscillations but could be significant if a transient response is used to construct the map. Also, since the curve fit yields coefficients of Chebyshev polynomial terms, then in order to relate the fitted series back to the physical states (x,y) the Chebyshev polynomial series has to be converted back into an ordinary polynomial series in $(\bar{x},\bar{y})$ and denormalisation process has to be carried out. The physical system parameters such as k and β in the example above could then be determined.

Having said that, it should be pointed out, however, that Masri et al were not interested in obtaining the original parameters of the test system but rather in obtaining a nonparametric mathematical

model in terms of 2 dimensional orthogonal polynomials which would respond in a similar way to the true system when both were subjected to a different input.

(ii) Secondly it was shown earlier that because a weighting function is involved in the orthogonality integrals for the Chebyshev polynomials, the data must be transformed from the $(\bar{x},\bar{y})$ plane to the (θ,ϕ) plane using

$$\theta = \cos^{-1}(\bar{x}) \qquad \text{and} \qquad \phi = \cos^{-1}(\bar{y})$$

In fact this transformation of the data will result in the need to use a significant number of integration points in the double integral approximation of equation (2.14) in order to evaluate the C_{ij} coefficients accurately, even for a simple linear system. To illustrate this point, consider again the double integral approximation for C_{mn} in equation (2.14) but written in a different form,

$$C_{mn} = A_{mn} \sum_{k=1}^{M_d} \sum_{l=1}^{M_v} f^{mn}(\theta_k,\phi_l)\ \Delta\theta\ \Delta\phi \qquad \ldots\ldots\ldots (2.20)$$

where $f^{mn}(\theta_k,\phi_l) = f(\theta_k,\phi_l)\ \cos m\theta_k\ \cos n\phi_l$

Thus, it may be seen from equation (2.20) that each of the coefficients C_{mn} is evaluated by working out the value of a volume bounded by the surface $f^{mn}(\theta_k,\phi_l)$ using a simple two dimensional numerical integration rule. Clearly the accuracy of the integration result will increase by using a larger number of points M_d and M_v within the integration boundaries. The surfaces for integration are in general much more complicated than the original force-state map surface since the integration function $f^{mn}(\theta_k,\phi_l)$ consists of the restoring force surface firstly defined by the transformation and then multiplied by Chebyshev polynomials

given as cosine terms (ie. cos $m\theta_k$ cos $n\phi_l$), shown in Fig. (2.9). This will tend to make the integration function $f^{mn}(\theta_k,\phi_l)$ vary rapidly with θ_k and ϕ_l in some regions of the (θ,ϕ) plane, and hence a significant number of points would be required for the double summation of equation (2.20) to be evaluated accurately.

An example of a surface requiring integration is given in Fig. (2.10). The function $f^{31}(\theta_k,\phi_l)$ is plotted in a two and three dimensional form for the simple nonlinear restoring force

$$f(\bar{x},\bar{y}) = \bar{x} + \bar{y} + \bar{x}^3 \quad \ldots\ldots\ldots\ldots\ldots\ldots \quad (2.21)$$

It may be seen that the surface has fairly steep undulations caused by the cos 3θ term, and hence it requires a large number of points for accurate numerical integration.

The requirement for a significant number of integration points (typically $M_d = M_v = 100$) will clearly increase the computational effort involved. Fig. (2.11) shows a variation of the time used by the CA-Alpha 2-40 mini-computer in calculating the C_{mn} values for a linear system against the number of integration points M_d $(=M_v)$ used in the double summation of equation (2.20). The time includes the interpolation/extrapolation process, as proposed earlier, carried out using 256 measured data points.

Fig. (2.12) shows a variation of the corresponding "goodness of fit" G, defined by

$$G = 1 - \frac{\text{(R.M.S. of error in fit)}}{\text{(R.M.S. of restoring force)}} = 1 - \frac{\text{R.M.S.}(f_k - \hat{f}_k)}{\text{R.M.S.}(f_k)} \quad (2.22)$$

where $\text{R.M.S}\ (f_k) = \sqrt{\frac{1}{N}\sum_{k=1}^{N} f_k^2}$

is the root mean square value of a signal f_k defined at N points,

f_k is the measured restoring force time history and $\hat{f}_k$ is the time history of the fitted model generated at the same displacement and velocity values. For a perfect fit G would be equal to one.

Thus, it can be seen that in order to obtain an acceptable goodness of fit a considerable number of points (about 100x100) must be used in calculating each of the C_{mn} values by equation (2.20). This will result in a time consuming process even for the identification of a simple linear system.

(iii) Finally, it has been shown that the numerical integration procedure used in obtaining the coefficients C_{mn} required restoring force data at equal intervals within the (θ,ϕ) plane. In principle this in turn requires both interpolation and extrapolation in two dimensions. In fact, the requirement for interpolation and extrapolation is by far the most important disadvantage associated with the use of Chebyshev polynomials for this particular application. However, although interpolation in region covered by the measured data should be fairly accurate, extrapolation into the empty corner regions will give opportunity for significant errors to be introduced. The problem is exaggerated because the arccosine transformation from the $(\bar{x},\bar{y})$ to the (θ,ϕ) plane changes the shape of the projection of the map and hence makes the proportion of the plane over which extrapolation is required increase significantly. For example, in the linear case the proportion changes from around 21% in the $(\bar{x},\bar{y})$ plane to around 50% in the (θ,ϕ) plane as seen in Fig. (2.13). Note that The proportion may become even more than 50% for some nonlinear systems such as the Van der Pol oscillator.

Moreover, apart from giving opportunity for significant errors to be introduced, the interpolation/extrapolation scheme required would probably consume a relatively long time in order to generate the required data.

2.3.2. Ordinary polynomial approach.

The significant disadvantages of the Chebyshev method adopted by Masri and Caughey led the author to consider whether the alternative simpler approach, which makes use of ordinary polynomials for curve fitting the restoring force, would be any better.

It was later found that other authors, namely Crawley et al [39-42] and Yang and Ibrahim [44] had also attempted the force-state mapping process and had in fact used ordinary polynomials. However the author is not aware of any real attempt to compare the two polynomial approaches and considers it valuable to do so since several workers have used or are still using the Chebyshev approach.

In the ordinary polynomial approach the series representation of the restoring force involves polynomials with powers of x and y, namely

$$f(x,y) \approx \hat{f}(x,y) = \sum_{i=0}^{N_d} \sum_{j=0}^{N_v} A_{ij}\, x^i\, y^j \qquad \ldots\ldots\ldots\ldots (2.23)$$

where A_{ij} are unknown coefficients to be determined by fitting the series in equation (2.23) to the measured f(x,y), x and y data by a linear least squares algorithm. This is simple and rather obvious but nevertheless will be seen to be an important modification to the implementation of Masri and Caughey's idea. It is believed that the use of Chebyshev polynomials has been an unnecessary restriction which has limited other workers in this area as well as the author. In fact, there are a number of advantages to using ordinary polynomials, namely

(i) there is no need to interpolate and extrapolate because

equi-spaced data points are not required and hence the associated errors are avoided, leading to a better goodness of fit,
(ii) the process is much faster and has lower computer storage requirements,
(iii) the approach uses the raw data in the curve fitting algorithm and hence the series produced is easier to interpret since it can be related directly to physical parameters without the need for denormalisation, and
(iv) any odd or even behaviour of the restoring force function is preserved.

However there are disadvantages since the terms in the series are not orthogonal which means that the entire calculation has to be repeated when the number of terms in the series is modified. Nevertheless, the fit in the ordinary polynomial case is so much faster than in the Chebyshev polynomial case that this is not really a problem. Another feature of this lack of orthogonality is that ill-conditioning of the least squares solution can become a problem when the number of terms in the series and the number of points in the time signals are large especially for computers with poor precision. This problem will be considered after formulating the solution of the general least squares problem.

2.3.2.1. Conventional least squares solution.

Consider that there are N data points in each of the restoring force, displacement and velocity time histories and the restoring force will be approximated by an Mth degree polynomial given in terms of displacement x and velocity y, namely,

$$f_k(x_k,y_k) \approx \hat{f}_k(x_k,y_k) = \sum_{i=1}^{M} B_i \, F_i(x_k,y_k) \qquad \ldots\ldots\ldots\ldots\ldots\ldots (2,24)$$

where k=1,N. Obviously, this expression is the same as equation

(2.23) but given in a different form where the two dimensional power polynomials have been combined in a series of functions $F_i(x_k, y_k)$ called "basis functions". For example a viscously damped system with a cubic stiffness nonlinearity would require at least M= 3 with, say, $F_1 = x$, $F_2 = y$ and $F_3 = x^3$.

Equation (2.24) can be written in a matrix form, namely

$$\underset{\sim}{f} \approx \hat{\underset{\sim}{f}} = [D]\ \underset{\sim}{B} \qquad \ldots\ldots\ldots\ldots\ldots\ldots (2.25)$$

where $\underset{\sim}{B}$ is an (Mx1) vector containing the unknown system parameters, $\underset{\sim}{f}$ is an (Nx1) vector containing the restoring force data points, and [D] is an (NxM) matrix called the design matrix of the fitting problem. Note that in general D has more rows than columns, since there must be at least as many data points as parameters to be estimated (i.e. N≥M). Equation (2.25) may be solved algebraically in order to obtain the unknown system parameters $\underset{\sim}{B}$ using the classical least squares approach.

In order to see how well the model matches the data the least squares cost function

$$J = \sum_{k=1}^{N} \left\{ f_k - \hat{f}_k \right\}^2$$

$$= (\underset{\sim}{f} - \hat{\underset{\sim}{f}})^T (\underset{\sim}{f} - \hat{\underset{\sim}{f}})$$

$$= (\underset{\sim}{f} - D\ \underset{\sim}{B})^T (\underset{\sim}{f} - D\ \underset{\sim}{B}) \qquad \ldots\ldots\ldots\ldots\ldots\ldots (2.26)$$

is used. To obtain the parameters $\underset{\sim}{B}$ which minimize J then its derivative with respect to $\underset{\sim}{B}$ is set to zero so

$$\partial J/\partial \underset{\sim}{B} = -2\ D^T \underset{\sim}{f} + 2\ D^T D\ \underset{\sim}{B} = 0 \qquad \ldots\ldots\ldots\ldots\ldots\ldots (2.27)$$

hence

$$D^T D \underset{\sim}{B} = D^T \underset{\sim}{f} \quad \ldots\ldots\ldots\ldots\ldots\ldots (2.28)$$

which is called the normal equation of the least squares problem. Notice that this equation can be obtained directly by premultiplying equation (2.25) by D^T.

Equation (2.28) may be solved for the vector $\underset{\sim}{B}$ by one of the standard methods such as the Gauss-Jordan elimination method [50]. Thus

$$\underset{\sim}{B} = [D^T D]^{-1} D^T \underset{\sim}{f} \quad \ldots\ldots\ldots\ldots\ldots\ldots (2.29)$$

Having obtained the least squares solution, it should be pointed out that in some practical cases the normal equations might be nearly singular or even singular. In this case the equations may be described as ill-conditioned and the solution accuracy will depend upon the precision of the computer used. Results could be significantly in error. The likelihood of ill-conditioning occurring can be reduced by

(a) simple normalisation of the data by dividing through by maximum values, namely

$$\bar{f}_k = \frac{f_k}{|f_{max}|}$$

$$\bar{x}_k = \frac{x_k}{|x_{max}|}$$

$$\bar{y}_k = \frac{y_k}{|y_{max}|} \quad \ldots\ldots\ldots\ldots\ldots\ldots (2.30)$$

In this case all the normalised values will fall within the range

[-1,+1] and this will make the $[D^TD]$ matrix well conditioned for the solution process. Obviously, the least squares algorithm will result in normalised coefficients $\bar{A}_{ij}$ but the original physical coefficients can be easily recovered using

$$A_{ij} = \frac{|f_{max}|\ \bar{A}_{ij}}{|x_{max}|^i\ |y_{max}|^j} \qquad \ldots\ldots\ldots\ldots\ldots\ldots (2.31)$$

(b) selection of odd or even powers of x and y in the series if appropriate, in order to reduce the number of terms in the fit, and hence the size of the $[D^TD]$ matrix, and

(c) the use of the singular value decomposition technique [50] which will be considered in the following section.

2.3.2.2. Solution by use of the Singular Value Decomposition technique.

In this section the use of the Singular Value Decomposition technique (henceforth referred to as SVD) is considered. In particular, the technique can be used for working out the pseudo-inverse of a rectangular matrix and so for solving the least squares problem when it is suspected that the equations are ill-conditioned, such as might occur if the least squares fitting model were over specified. The method will be used particularly in identification of multi-degree of freedom systems as will be seen in the next chapter.

The SVD technique allows any (NxM) matrix D in which ($N \geq M$) to be decomposed into three matrices related by the following equation

$$D = U\ W\ V^T \qquad \ldots\ldots\ldots\ldots\ldots\ldots (2.32)$$

where U is an (NxM) orthogonal matrix

V is an (MxM) orthogonal matrix

and W is an (MxM) diagonal matrix with elements greater than or equal to zero called the singular values of the D matrix.

The columns of the matrices U and V are orthonormal so they satisfy the equation

$$U^T U = V^T V = 1 \quad \ldots\ldots\ldots\ldots\ldots (2.33)$$

Assume at this stage that all the singular values of matrix D are finite so that it is of rank M and can be inverted. Using equations (2.25) and (2.32) the curve fit problem is the solution of

$$D \underset{\sim}{B} = \underset{\sim}{f} \quad \text{or} \quad U W V^T \underset{\sim}{B} = \underset{\sim}{f} \quad \ldots\ldots\ldots\ldots\ldots (2.34)$$

Now assume that the solution is given as a linear combination of the right singular vectors of D, namely,

$$\underset{\sim}{B} = V \underset{\sim}{b} \quad \ldots\ldots\ldots\ldots\ldots\ldots\ldots (2.35)$$

then substituting for B and premultiplying by U^T leads to

$$U^T U \; W \; V^T V \; \underset{\sim}{b} = U^T \underset{\sim}{f}$$

or from orthogonality equation (2.33)

$$W \; \underset{\sim}{b} = U^T \underset{\sim}{f}$$

$$\underset{\sim}{B} = V \; W^{-1} U^T \underset{\sim}{f} \quad \ldots\ldots\ldots\ldots\ldots\ldots\ldots (2.36)$$

is the solution and $[V \; W^{-1} U^T]$ is the pseudo-inverse of D. The inversion of W is straightforward since it is diagonal, so

$$W^{-1} = \text{diag}\,[1/w_1, 1/w_2 \ldots\ldots 1/w_M]$$

It can be shown that the solution (2.36) is identical to the standard least squares solution when the D matrix is well-conditioned.

If the D matrix is poorly-conditioned or singular then one or more of the singular values will be extremely small or zero. If the singular values w_j are presented in descending order of magnitude then the condition number of the matrix is defined by the ratio w_1/w_M. A matrix is singular if its condition number is infinite, and it is ill-conditioned if its condition number is too large. In reference [50] a measure for ill conditioning is recommended and given as the reciprocal of the condition number when it approaches the machines floating point precision (for example, less than 10^{-6} for single precision or 10^{-12} for double).

If the D matrix is singular or ill-conditioned then it is possible to repeat the analysis given above using partitioned matrices but the final result is in fact equivalent to using equation (2.36) but putting $1/w_j$ to zero in W^{-1} if the ratio w_j/w_1 is less than N times the machine precision. This process of "editing" the singular values leads to a sensible solution but the estimated parameters will not be exact.

2.3.3. The use of special functions.

There is a further benefit to the adoption of ordinary polynomial approach rather than the Chebyshev polynomial approach in this particular application. Because each Chebyshev polynomial is essentially an ordinary polynomial series expansion, (eg. $T_3=4x^3-3x$), then only polynomial type nonlinearities such as cubic stiffness can be accurately represented. Nonpolynomial nonlinearities such as friction, velocity squared damping, piecewise stiffness (eg. dead space) etc can only be approximated by using a significant number of terms in the fitted model.

However, removing the Chebyshev polynomial restriction allows the ordinary polynomial expansion of equation (2.23) to be written more generally as equation (2.24) in which the basis functions $F_i(x,y)$ may include not only the ordinary polynomial power terms (eg. x, y, x^2, x^3..etc) but also special functions chosen to represent nonpolynomial nonlinearities.

A velocity-squared damping term could be represented by

$$F_j(x,y) = y^2 \text{ sign}(y) \quad \text{.....(2.37)}$$

and a coulomb friction term by

$$F_k(x,y) = y/|y| \quad \text{or} \quad \text{sign}(y) \quad \text{.....(2.38)}$$

A piecewise nonlinearity such as a dead space of $x = \pm d$ would require

$$F_l(x,y) = 0 \qquad \text{for } |x| \leq d$$

$$F_l(x,y) = x - d \text{ sign}(x) \quad \text{for } |x| > d \quad \text{.....(2.39)}$$

and clearly a value of d would need to be estimated, for example from the force-state map. Other nonlinearities may be dealt with in a similar way, except for memory dependent hysteresis. The curve fitting of such nonpolynomial nonlinearities has also been illustrated by Crawley et al [41,42]. Obviously, these special functions can be included in the design matrix D of equation (2.29) for a least squares curve fitting. For example a system with a restoring force

$$f(x,y) = kx + cy + \beta x^3 + \gamma\, y^2 \text{ sign}(y) + \delta \text{ sign}(y)$$

would lead to a design matrix such as

$$D = \begin{bmatrix} x_1 & y_1 & x_1^3 & y_1^2 \text{sign}(y_1) & \text{sign}(y_1) \\ x_2 & y_2 & x_2^3 & y_2^2 \text{sign}(y_2) & \text{sign}(y_2) \\ \cdots & \cdots & \cdots & \cdots & \cdots \\ x_N & y_N & x_N^3 & y_N^3 \text{sign}(y_N) & \text{sign}(y_N) \end{bmatrix}$$

where N is number of intervals in each of the measured time signals.

2.4. Examples.

In this section, the identification of simulated one degree of freedom linear and nonlinear systems will be considered. This investigation aims to show some of the practical restrictions and disadvantages associated with the use of two dimensional Chebyshev polynomials and also to show that the rejection of these orthogonal polynomials and the adoption of the ordinary polynomial and special function approach provides a faster, simpler and a more accurate identification for both polynomial and nonpolynomial types of nonlinearity.

Various common types of nonlinearity are considered. It will be shown that each type of nonlinearity has a distinctive, unique and recognizable force-state map. The force-state maps will be presented both for raw and fitted data in various forms.

The excitation signal chosen for this exercise was a linear swept sine, starting from a frequency below the natural frequency and ending at a frequency above the natural frequency, although in principle any excitation signal could have been used. The response signals (x, $\dot{x}$ and $\ddot{x}$) were calculated by integrating the equation of motion using a fourth order Runge Kutta algorithm and values at 256 sampling instants were obtained. The mass of the system was assumed to be known; its estimation will be considered in a later chapter.

For the sake of comparison, several of the examples chosen are those used by Masri and Caughey in reference [2].

2.4.1. Linear case.

The equation of motion is given by

$$m\ddot{x} + c\dot{x} + kx = p(t)$$

where the parameters were chosen to be

m = 1 Kg
c = 0.1 N/m/s
k = 1 N/m

corresponding to 5% critical damping and an undamped natural frequency of 0.159 Hz (1 rad/s). Therefore the exact restoring force is given by

$f(x,y) = 0.1\ y + x$ (where as before $y = \dot{x}$)

The excitation frequency range of 0.1 to 0.2 Hz was covered by the sweep in 128 seconds. In order to obtain 256 response values, the nature of the integration algorithm used meant that 512 excitation values at 0.25 second intervals, were required. The force level was 1 N peak. The parameters obtained from different curve fitting approaches are shown in Table (2.1). The approaches referred to in the table are

A. Results deduced from the Chebyshev coefficients, obtained by Masri and Caughey in reference [2], by denormalizing the identified Chebyshev series using equations (2.4) and (2.6). Since the identified Chebyshev coefficients in reference [2] were

Approach	Description	c	k	G*	T(sec)
-	Exact values	0.100	1.000	-	-
A	Chebyshev polynomials $N_d = N_v = 2$ (ref. 2)	0.082	0.999	0.923	-
B	Chebyshev polynomials (Bins approach)	0.103	1.030	0.969	288
C	Ordinary polynomials	0.100	1.000	1.000	4

* G stands for goodness of fit

Table (2.1). Parameters identified for the linear case.

$$c = \begin{bmatrix} -0.22 & 0.65 \\ 7.64 & 0.003 \end{bmatrix}$$

and $x_{max} = 7.57$ $x_{min} = -7.72$

$y_{max} = 7.97$ $y_{min} = -7.89$

then the identified model can be written as

$$\hat{f}(\bar{x},\bar{y}) = c_{00}\, T_0(\bar{x})\, T_0(\bar{y}) + c_{01}\, T_0(\bar{x})\, T_1(\bar{y}) + c_{10}\, T_1(\bar{x})\, T_0(\bar{y}) + c_{11}\, T_1(\bar{x})\, T_1(\bar{y})$$

or $$\hat{f}(\bar{x},\bar{y}) = -0.22 + 0.65\,\bar{y} + 7.64\,\bar{x} + 0.003\,\bar{x}\,\bar{y}$$

When this series is denormalized then the fitted result is,

$$\hat{f}(x,y) = -0.1483 + 0.0819\,y + 0.9993\,x + 4.948E\text{-}05\,x\,y$$

B. Results obtained from the Chebyshev fit, but using ordinary polynomial curve fitting of first order within 4 equal size of

bins to interpolate and extrapolate the data. (see section (2.3.1.1)).

Here, the identified Chebyshev coefficients are given by

$$c = \begin{bmatrix} 0.0291 & 0.8696 \\ 8.4145 & 0.0007 \end{bmatrix}$$

and $x_{max} = 8.196$ $\quad x_{min} = -8.134$

$y_{max} = 8.418$ $\quad y_{min} = -8.468$

Following the same procedure as above yields the following denormalized model

$$\hat{f}(x,y) = -0.00041 + 0.1029\ y + 1.03\ x + 1.086E\text{-}05\ x\ y$$

and it may be seen that the offset and coupling terms are smaller.

C. Results obtained from the ordinary polynomial fit to the raw data, given in section (2.3.2) using a model

$$f(x,y) = a_0 + a_1 y + a_2 x + a_3 x\ y$$

In the approaches A and B the two interpolation/extrapolation schemes were used to generate a 100x100 point grid in the (θ,ϕ) plane. In all A, B and C cases the goodness of fit is defined by reference to the response data points as given in equation (2.22). The timings refer to the mini-computer used and quoted to allow comparison of Chebyshev and ordinary polynomial approaches.

It can be seen that the results in Table (2.1) indicate an improvement in the Chebyshev fit when the alternative interpolation/extrapolation approach B was used. Moreover, the ordinary polynomial approach C results are more accurate and take considerably less time.

The force-state map for the raw data is shown in Fig. (2.14) in a two dimensional form. The linear force-displacement behaviour is somewhat obscured by the effect of damping. The force-state map for the fitted model obtained by the ordinary polynomial approach is shown in Fig. (2.15).

2.4.2. Nonlinear cases.

The above process was also carried out for some nonlinear systems but with slight differences in the linear damping of each system, the force level and the sweep range used. The linear damping coefficient was reduced to c = 0.04 (2% critical) so as not to obscure the nonlinear behaviour.

2.4.2.1. Cubic hardening stiffness.

In this case the stiffness restoring force component includes a term which varies with the cube of the displacement, so that

$$m\ddot{x} + c\dot{x} + kx + \beta x^3 = p(t)$$

The exact restoring force for this example was chosen to be

$$f(x,\dot{x}) = 0.04\,\dot{x} + x + 0.003\,x^3$$

and the excitation from 0.1 to 0.3 Hz used a 4 N peak force.
The restoring force, displacement and velocity time histories were shown in Fig. (2.2) and the force-state map for the raw data was presented in Fig. (2.3) in a three dimensional form and in Fig. (2.5) in a two dimensional form. The cubic stiffness behaviour can clearly be seen in the two dimensional restoring force-displacement plot of Fig. (2.5). The fitted surface is shown in Fig. (2.16) to have a characteristic shape.

The identified parameters are presented in Table (2.2) and show a

similar behaviour to the linear case but the time spent for the Chebyshev polynomial approach has increased to 672 seconds due to increasing the number of terms in the series. This may well indicate that the Chebyshev approach is time consuming although care was taken to reduce the running time of the program used for calculating the coefficients of Chebyshev series.

Approach	Description	c	k	β	G	T (sec)
-	Exact values	0.0400	1.000	0.0030		-
A	Chebyshev polynomials N_v=2, N_d=4 (ref. 2)	0.0430	0.975	0.0029	0.991	-
B	Chebyshev polynomials N_v=2, N_d=4, Bins=4	0.0404	1.008	0.0030	0.993	672
C	Ordinary polynomials	0.0400	1.000	0.0030	1.000	8

Table (2.2). Parameters identified for the cubic stiffness case.

2.4.2.2. Van der Pol oscillator.

This rather unusual nonlinearity has become a fairly classical case for investigating and testing nonlinear identification schemes since velocity and displacement are coupled via an amplitude dependent damping force. The equation of motion is

$$m\ddot{x} + \varepsilon(x^2-1)\,\dot{x} + kx = p(t)$$

The exact restoring force for this example was chosen to be

$$f(x,\dot{x}) = -0.2\,\dot{x} + 0.2\,x^2\dot{x} + x$$

and the excitation from 0.1 to 0.3 Hz used a 4 N peak force. Various views of the force-state map for the raw data are shown in Figs. (2.17) and (2.18).

This is a particularly difficult identification for the Chebyshev polynomial approach because if all data are to be used then there is a large amount of extrapolation necessary, as shown in Fig. (2.19) which represents a projection of the force-state map onto the $(\bar{x},\bar{y})$ and (θ,ϕ) planes.

As might be expected, the ordinary polynomial fit only required 3 terms in the series and yielded almost the exact surface (goodness of fit G = 0.999999) shown in Fig. (2.20). However, the results obtained using the Chebyshev representation in reference [2] were rather poor due to errors caused by the extrapolation scheme used which relied upon uncoupled velocity and displacement condition. The surface of interpolated and extrapolated values shown in Fig. (2.21) (obtained from reference [2]) shows severe undulations which required a high order model to provide a reasonable quality of fit. Indeed a total of 64 Chebyshev coefficients had to be evaluated in order to achieve the fit shown in Fig. (2.22). It is clear that this differs significantly from the exact surface. The equivalent 64 term Chebyshev fit, obtained via ordinary polynomial curve fitting within bins to interpolate and extrapolate the data, gave a much more realistic fit as seen in Fig. (2.23), but still not as good as the fit obtained by the ordinary polynomial approach.

It is clear from the examples shown that the ordinary polynomial approach seems superior to the Chebyshev representation in many ways and that the advantages outweigh the orthogonality and equal error ripple properties of the Chebyshev polynomials in the particular application of force-state mapping.

The remaining examples illustrate the use of special functions to

identify nonpolynomial nonlinearities and the difficulty of identifying such nonlinearities when the ordinary polynomial power series given in equation (2.23) is used. Note that the Chebyshev approach will not be used in these examples.

2.4.2.3. Velocity squared (or quadratic) damping.

This type of damping may arise due to the action of fluid drag forces upon a body. The equation of motion is of the form

$$m\ddot{x} + c\dot{x} + \gamma\,\dot{x}^2\,\mathrm{sign}(\dot{x}) + kx = p(t)$$

The exact restoring force for this example was chosen to be

$$f(x,\dot{x}) = 0.04\,\dot{x} + 0.04\,\dot{x}^2\,\mathrm{sign}(\dot{x}) + x$$

and the excitation from 0.1 to 0.3 Hz used a 2.8 N peak force. Two views of the force-state map for the raw data are given in Figs. (2.24) and (2.25).

An attempt was first made to curve fit the restoring force using the ordinary polynomial series given in equation (2.23). The fitted model was chosen to be

$$f(x,\dot{x}) = A_1 x + A_2\dot{x} + A_3\dot{x}^3$$

where the cubic term was included since $\dot{x}\,\mathrm{sign}(\dot{x})$ is an odd function of $\dot{x}$.

The identified parameters were A_1=0.999, A_2=0.15 and A_3=0.0031 and the goodness of fit G=0.98. Obviously, using the ordinary polynomial approach for identifying nonpolynomial nonlinearity does not yield the correct parameters of the system but the fit for this example is surprisingly good. However, the parameters identified using a model which includes the corresponding special

function (section 2.3.3) were obtained almost exactly ($\hat{k}$=1, $\hat{c}$=0.04002, and $\hat{\gamma}$=0.03997) and the goodness of fit was G = 0.99999. The force-state map of the fitted model obtained using a special function is shown in Fig. (2.26).

2.4.2.4. Coulomb friction.

This common nonlinearity leads to the equation of motion of the form

$$m\ddot{x} + c\dot{x} + \alpha \text{ sign } (\dot{x}) + kx = p(t)$$

where α is a constant friction force. The exact restoring force for this example was chosen to be

$$f(x,\dot{x}) = 0.04\ \dot{x} + 0.08\ \text{sign}(\dot{x}) + x$$

and the excitation from 0.1 to 0.3 Hz used a 0.14 N peak force. Note that unlike the previous nonlinear cases this type of nonlinearity requires a low force level in order to be excited properly since the friction force would be highlighted at a low force level and the larger the input force level is compared to the friction force then the smaller and more difficult to identify will be the nonlinear effect. If the system contained , in addition to the friction, a different nonlinear element then the identification would become more difficult and would need that the system is excited twice, once with a low force level for identifying the friction and once with a high force level for identifying the other nonlinear element.

The restoring force, displacement and velocity time histories are shown in Fig. (2.27) and the two views of the force-state map for the raw data are presented in Figs. (2.28) and (2.29). The combination of friction and the stiffness restoring force gives

rise to the classical hysteresis loop and the force-velocity variation also shows up the presence of friction.

The ordinary polynomial series used for curve fitting the restoring force was chosen to be

$$\hat{f}(x,\dot{x}) = A_1 x + A_2 \dot{x} + A_3 \dot{x}^3 + A_4 \dot{x}^5 + A_5 \dot{x}^7$$

since the step in the map of Fig. (2.29) clearly indicates an odd behaviour in the $\dot{x}$ direction. However the goodness of fit was only 0.656.

The parameters identified using a model which includes the corresponding special function were again obtained almost exactly ($\hat{c}$=0.0424, $\hat{\alpha}$=0.0794 and $\hat{k}$=1.00001) and the fitted map of this model is shown in Fig. (2.30). It can be seen that, unlike the special function approach, using the polynomial fit approach with friction type nonlinearity yields a poor model. Clearly a lot of terms would need to be included to model the step in the map.

2.4.2.5. Clearance type nonlinearity.

This common nonlinearity which is sometimes termed "backlash" and may be encountered in aircraft structures, can be described by the equation of motion

$$m\ddot{x} + c\dot{x} + kx + F(x) = p(t)$$

where $F(x) = 0$ for $|x| \leq d$

$F(x) = k_c(x - d\ \mathrm{sign}(x))$ for $|x| \geq d$

where d is the clearance (dead space) value and k_c the piecewise stiffness to be identified. The exact restoring force was considered to be

$$f(x,\dot{x}) = 0.04\,\dot{x} + x + 2\,(x - 20\,\text{sign}(x))$$

The excitation from 0.1 to 0.4 Hz used a 5.7 N peak force. Notice that k_c can be identified only if the input force causes the system to displace beyond the clearance value.

The two views of the force-state map for the raw data are given in Fig. (2.7) and (2.31). It can be seen that the clearance value can be estimated directly from the force-displacement plot.

The ordinary polynomial series used for curve fitting the restoring force was chosen to be

$$\hat{f}(x,\dot{x}) = A_1 x + A_2 \dot{x} + A_3 x^3 + A_4 x^5 + A_5 x^7$$

since the force-state map of Fig. (2.7) indicates an odd behaviour in the x direction. The goodness of fit was G = 0.9427.

The parameters identified using a model which includes the corresponding special function were obtained exactly ($\hat{c}$=0.04, $\hat{k}$=1 and $\hat{k}_c$=2), assuming the exact d value is available from the force-state map. The force-state map of this model is shown in Fig. (2.32).

Thus, it can be seen from the above nonpolynomial type nonlinearity examples that the use of a nonpolynomial type curve fitting approach is more appropriate and yields a much better goodness of fit as well as the correct physical linear and nonlinear parameters of the system.

2.5. Conclusion.

Some of the practical restrictions and drawbacks associated with the use of the orthogonal Chebyshev polynomials in the identification of nonlinear systems using the force-state mapping,

have been demonstrated. Consequently, it has been shown that the use of the alternative ordinary polynomial approach avoids all those restrictions and drawbacks and provides a faster, easier and a more accurate identification procedure.

Furthermore, extending the fitted model to include special functions can cater for nonpolynomial nonlinearities such as friction, quadratic damping, dead space etc and provides a more accurate identification than the ordinary polynomial approach.

Finally, a set of force-state maps representative of the raw data were given in various views for some common nonlinear elements. The associated maps of the identified models were given in a carpet plot form . It is hoped that those raw and carpet plots may assist for nonlinearity characterization of some nonlinear elements when present individually in single-degree of freedom systems.

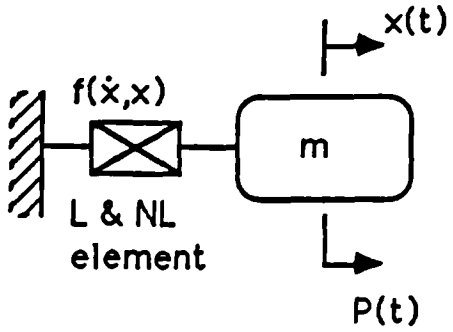

Figure 2.1. Single d.o.f. nonlinear system.

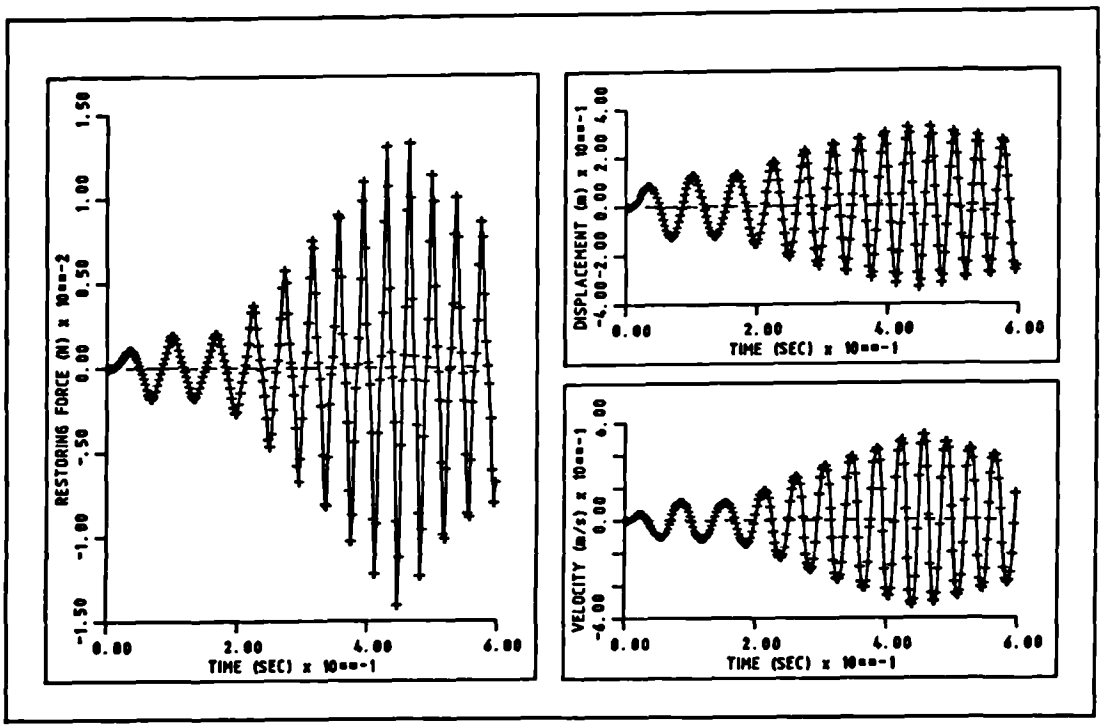

Figure 2.2. Sample time histories for a 1 d.o.f. simulated system.

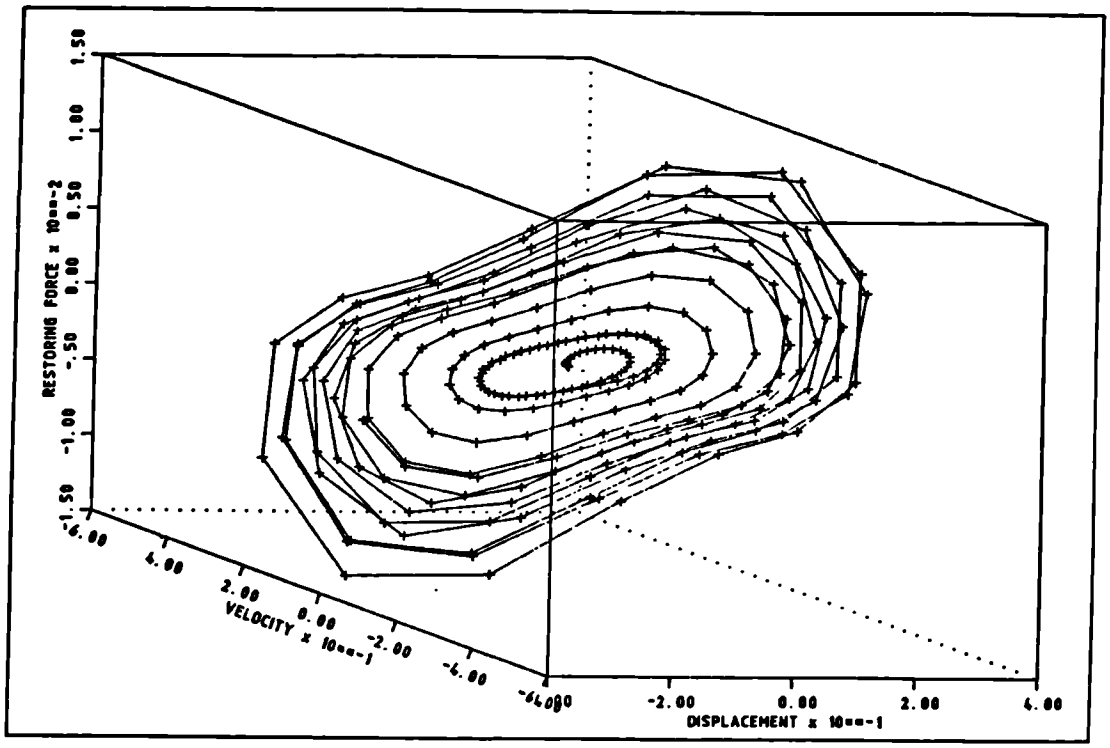

Figure 2.3. Force-state map of raw data for a 1 d.o.f. system obtained using sweep excitation

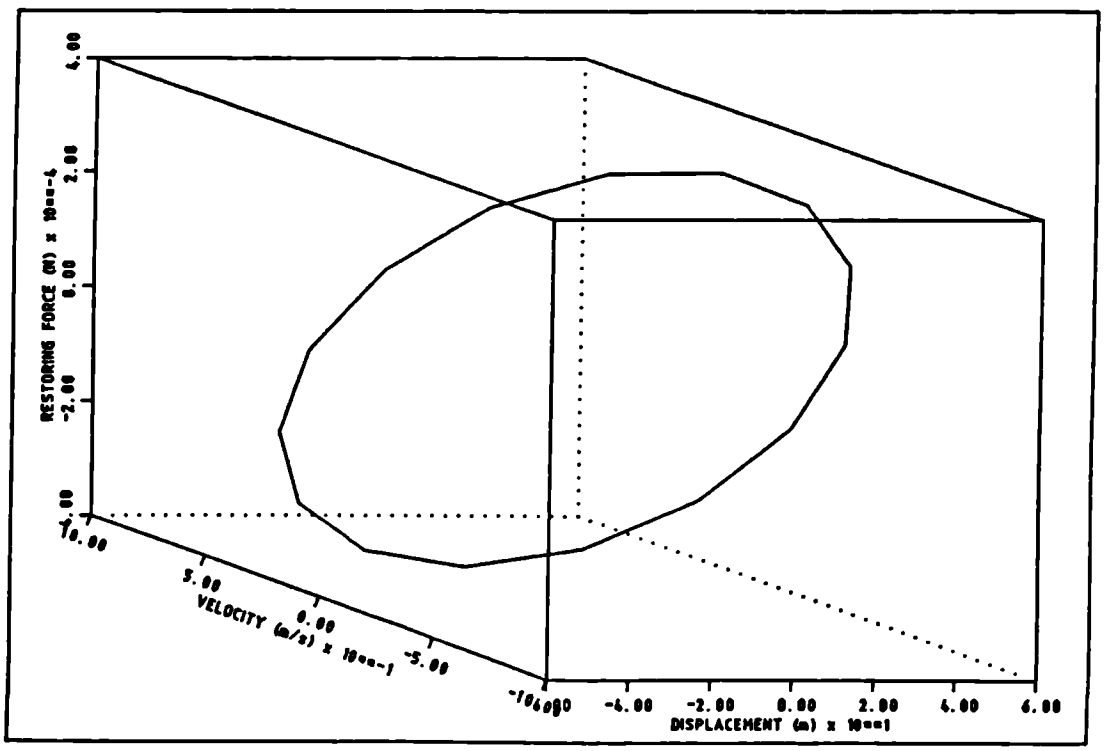

Figure 2.4. Force-state map of raw data obtained using steady state excitation.

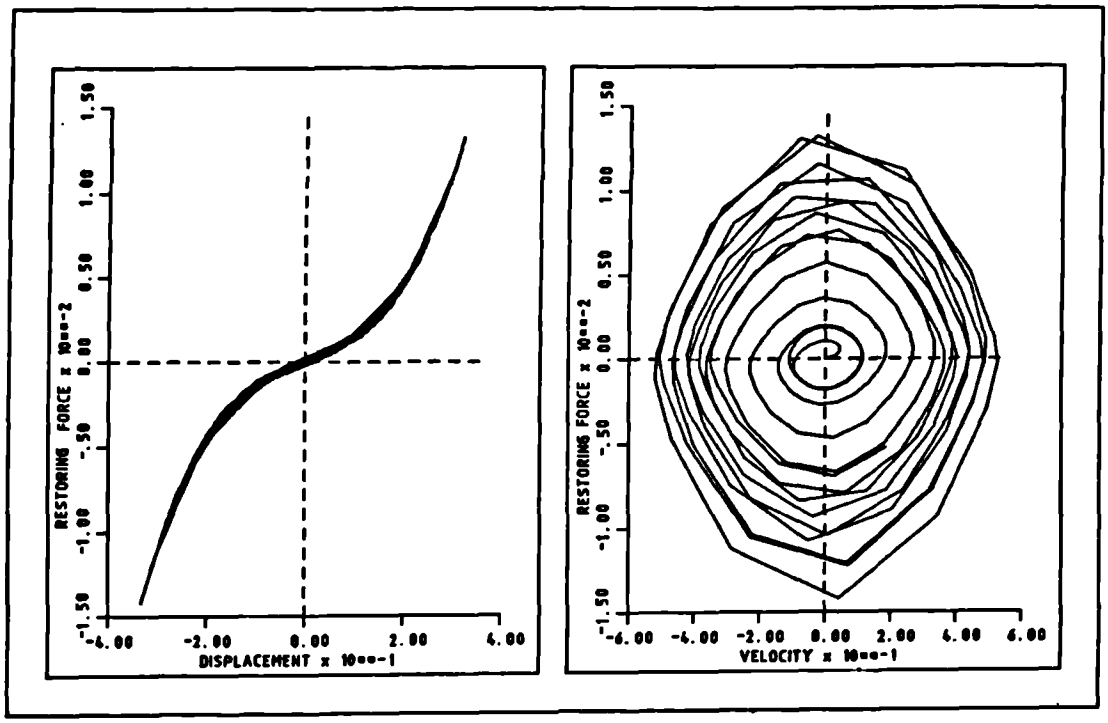

a b

Figure 2.5. Projection of the force-state map onto the (f,x) and (f,y) planes.

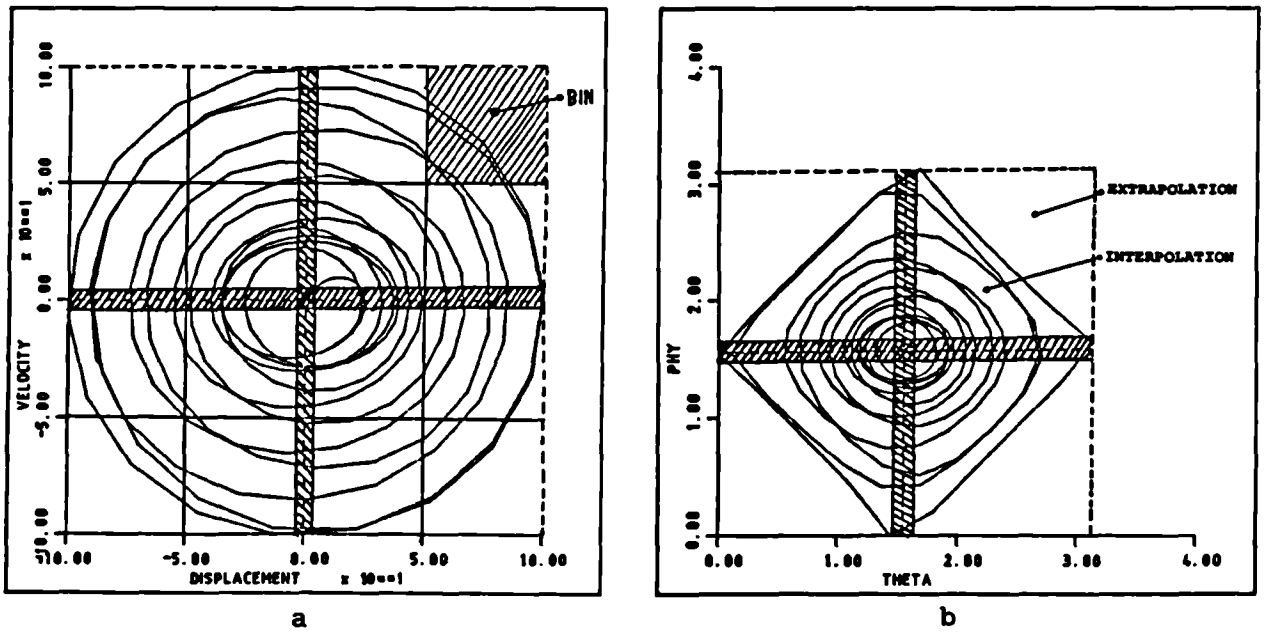

a b

Figure 2.6. Projection of the force-state map onto the (x,y) and (θ,ϕ) planes.

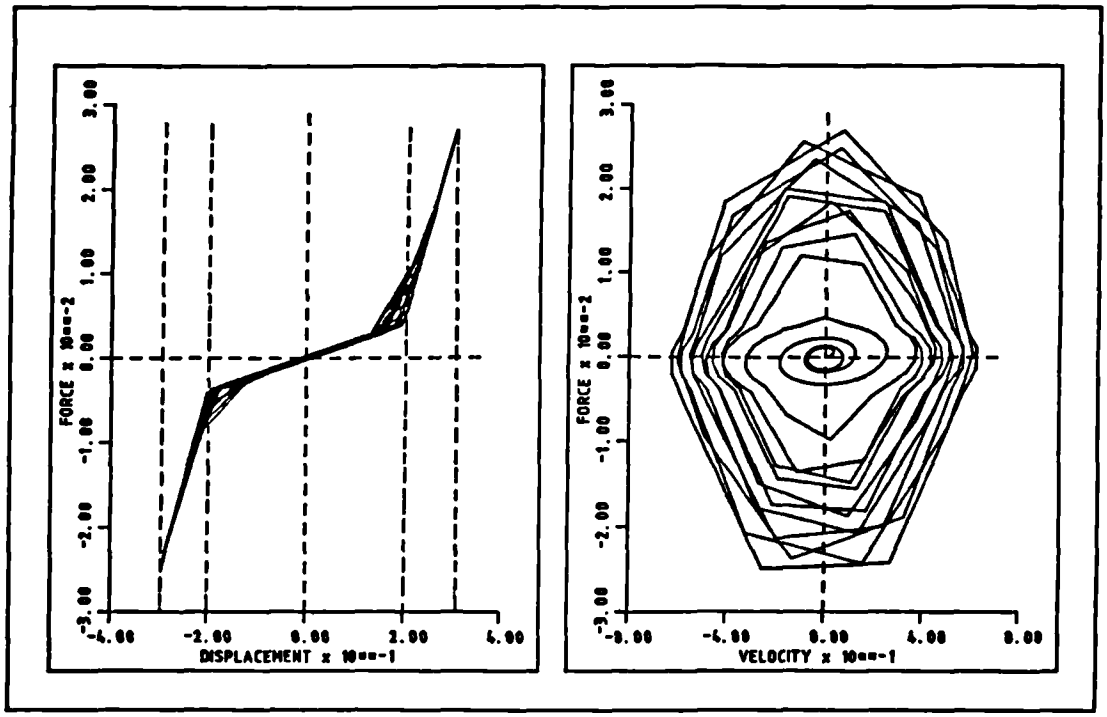

Figure 2.7. Projection of the force-state map onto the (f,x) and (f,y) planes for a piecewise stiffness nonlinearity.

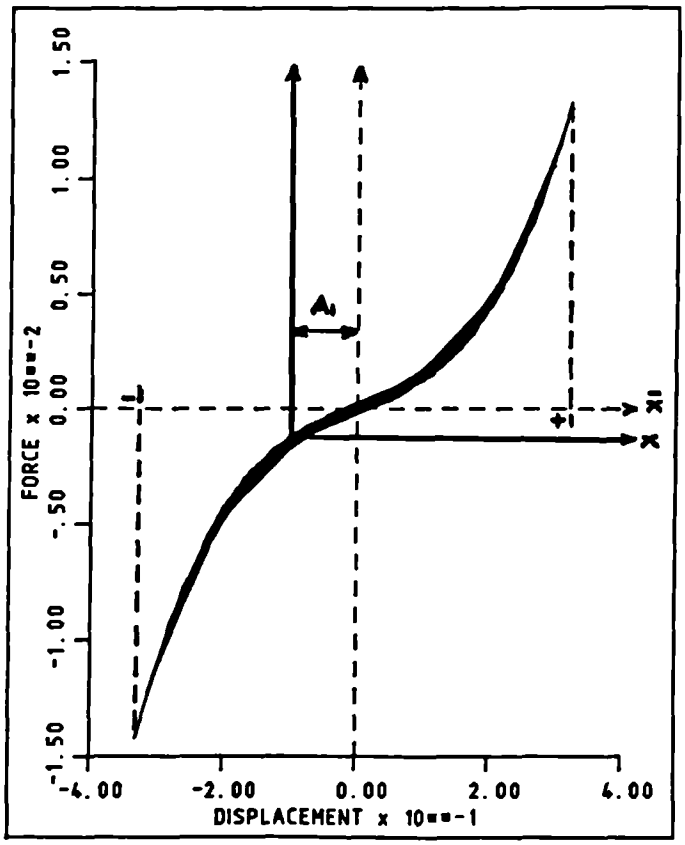

Figure 2.8. Illustration of the effective change of origin introduced by the normalisation process.

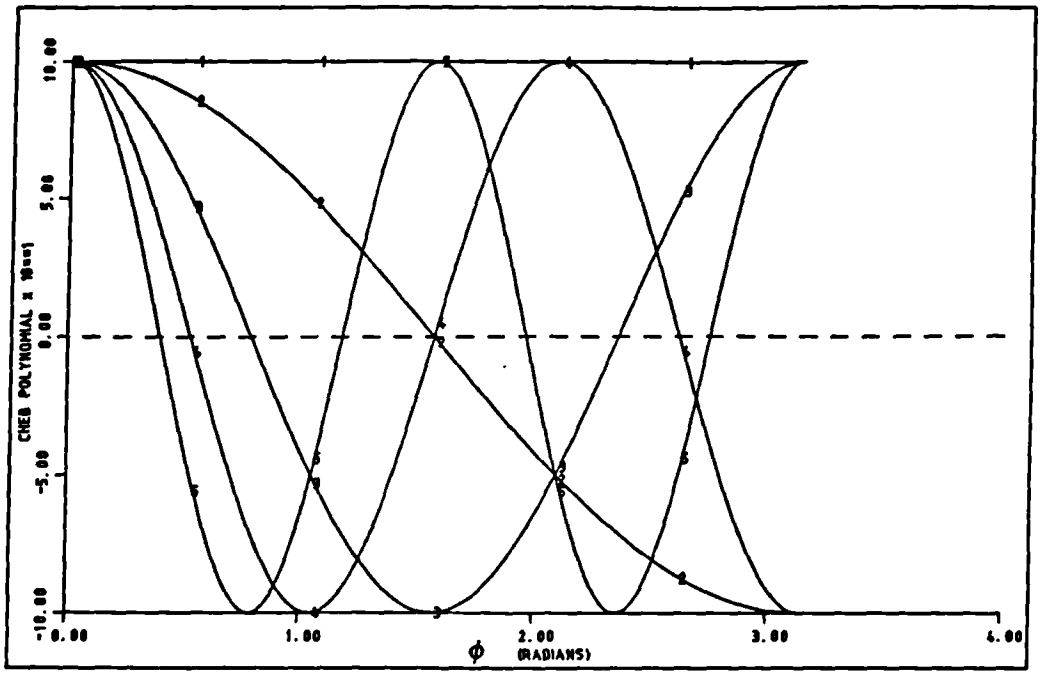

Figure 2.9. Variations of Chebyshev polynomials against ϕ.

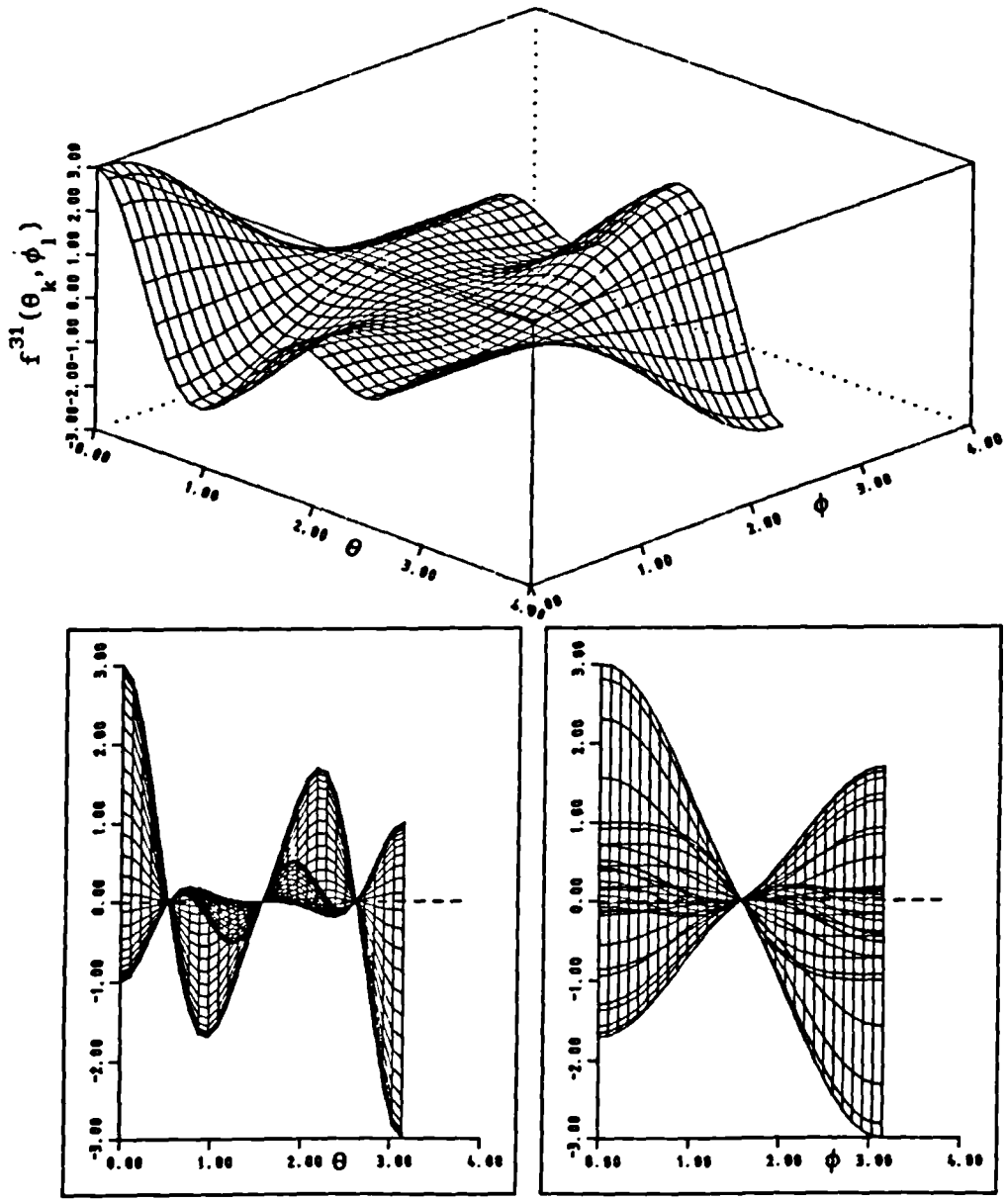

Figure 2.10. Illustration of the steep undulations introduced by the use of Chebyshev polynomials.

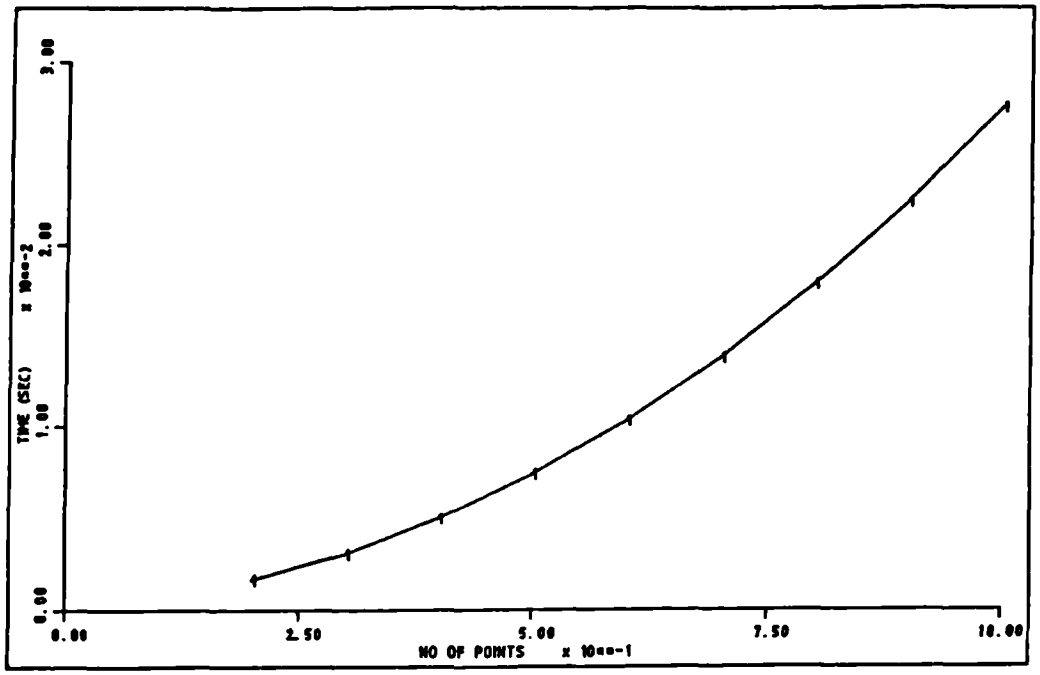

Figure 2.11. Variation of the time to calculate the C_{mn} values for a linear system with the number of integration points.

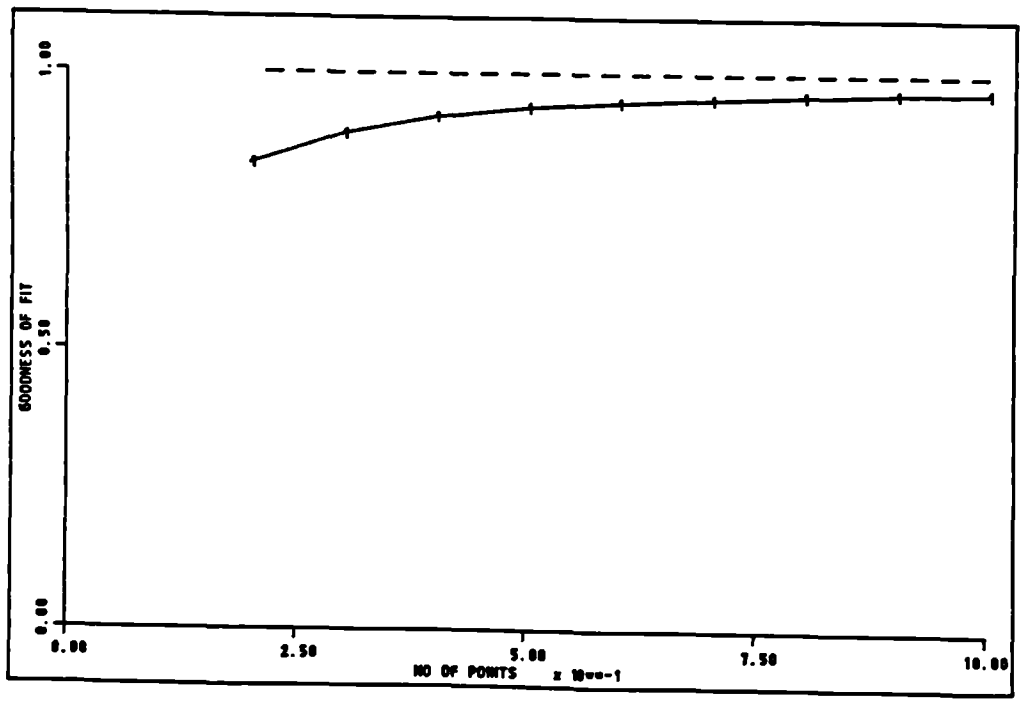

Figure 2.12. Variation of the goodness of Chebyshev fit for a linear system against the number of integration points.

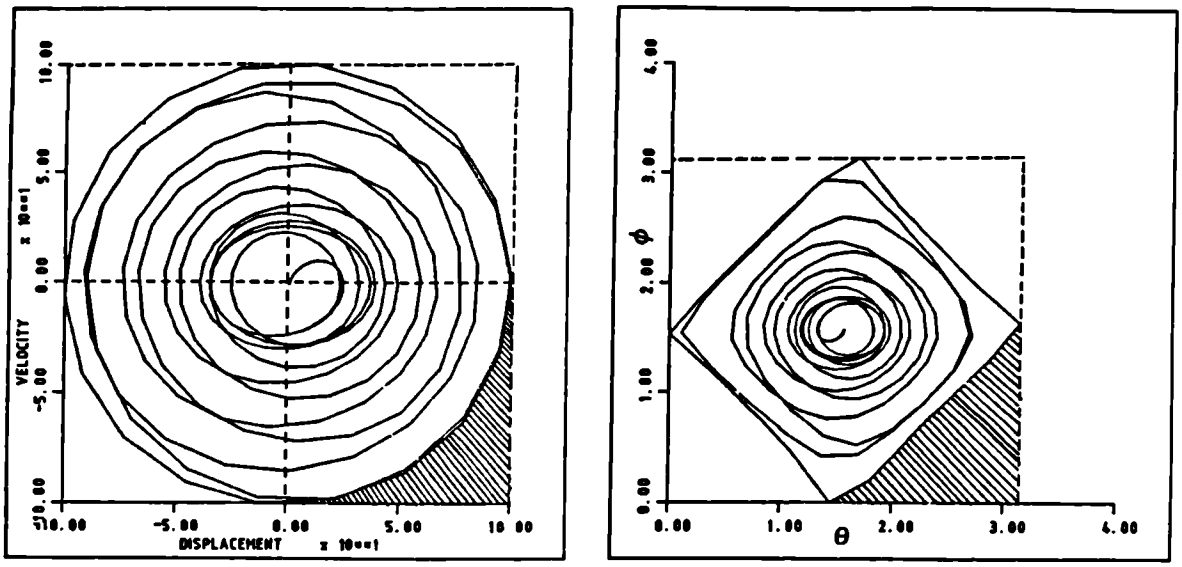

Figure 2.13. Illustration of the increase in the extrapolation required due to the transformation to the (θ, ϕ) plane.

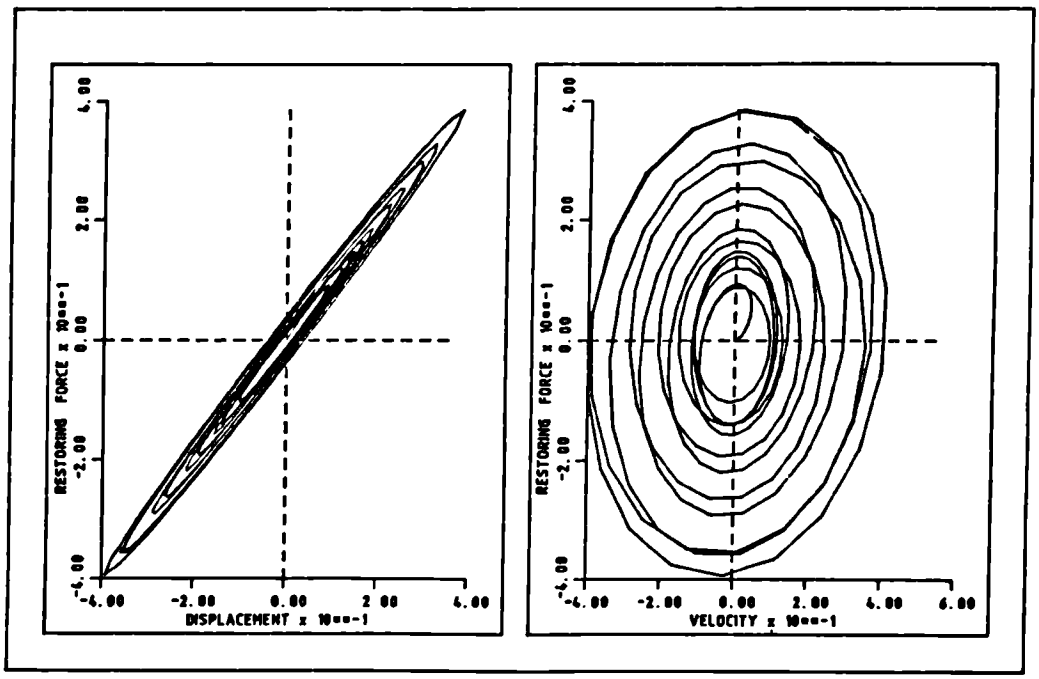

Figure 2.14. Two dimensional force-state map of raw data for a linear system obtained using sweep excitation.

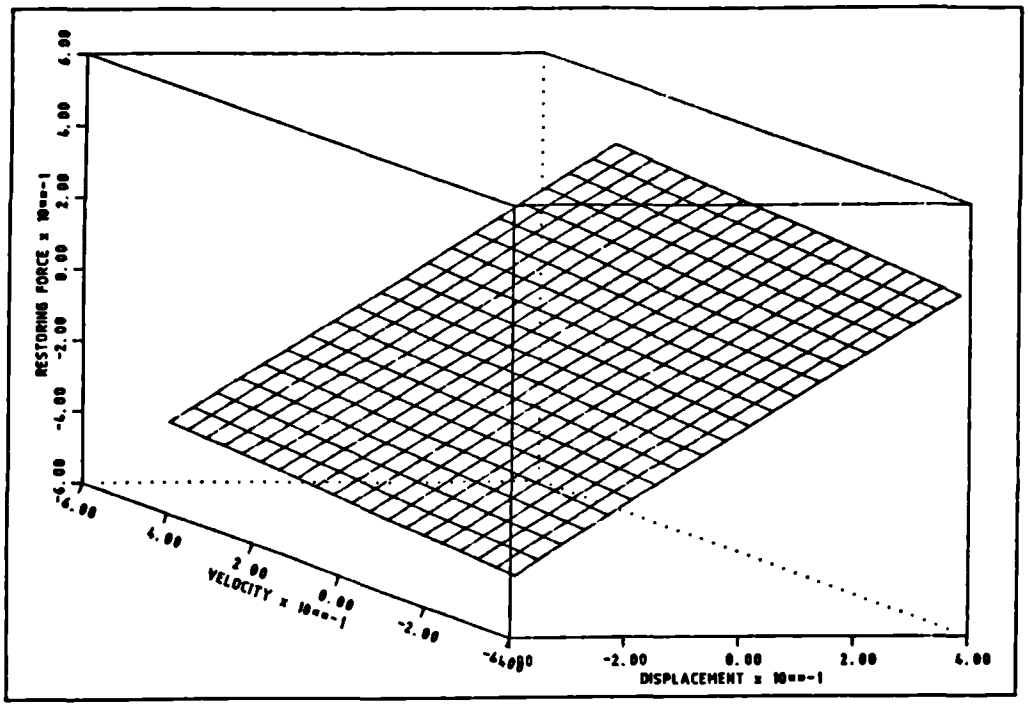

Figure 2.15. Force-state map for the fitted model of a linear system.

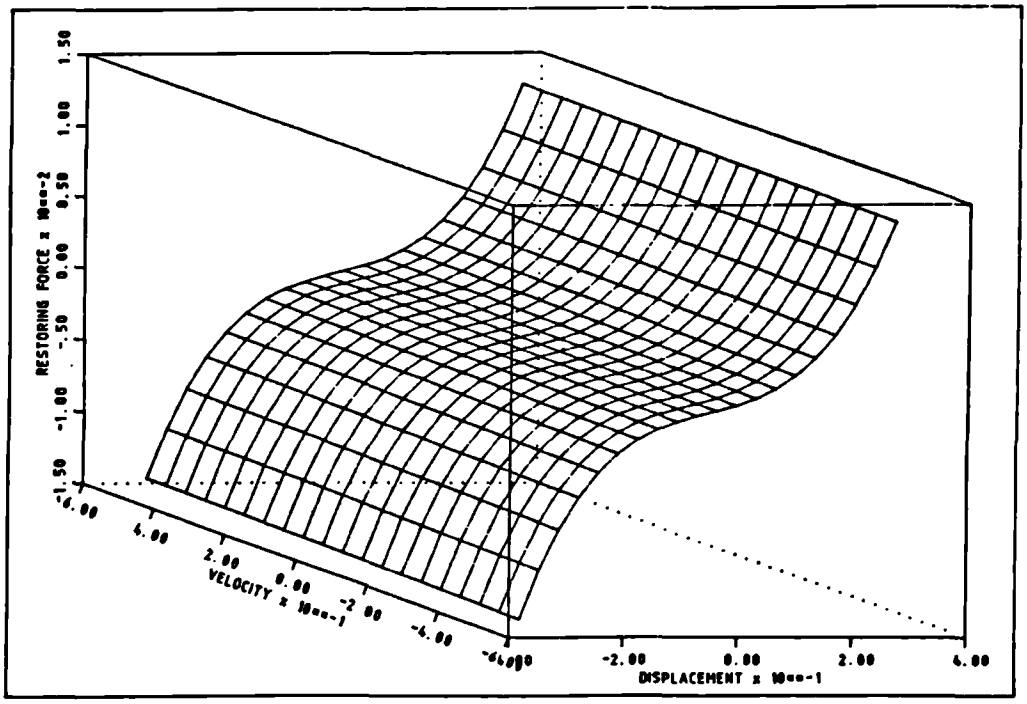

Figure 2.16. Force-state map for the fitted model of a system with cubic stiffness nonlinearity.

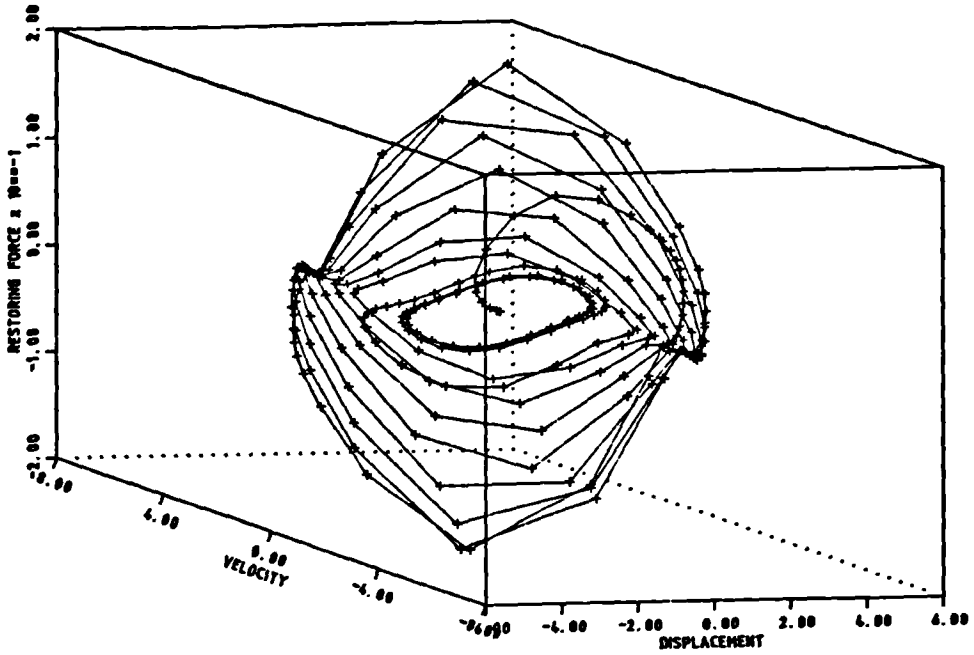

Figure 2.17. Force-state map of raw data for the Van der Pol oscillator.

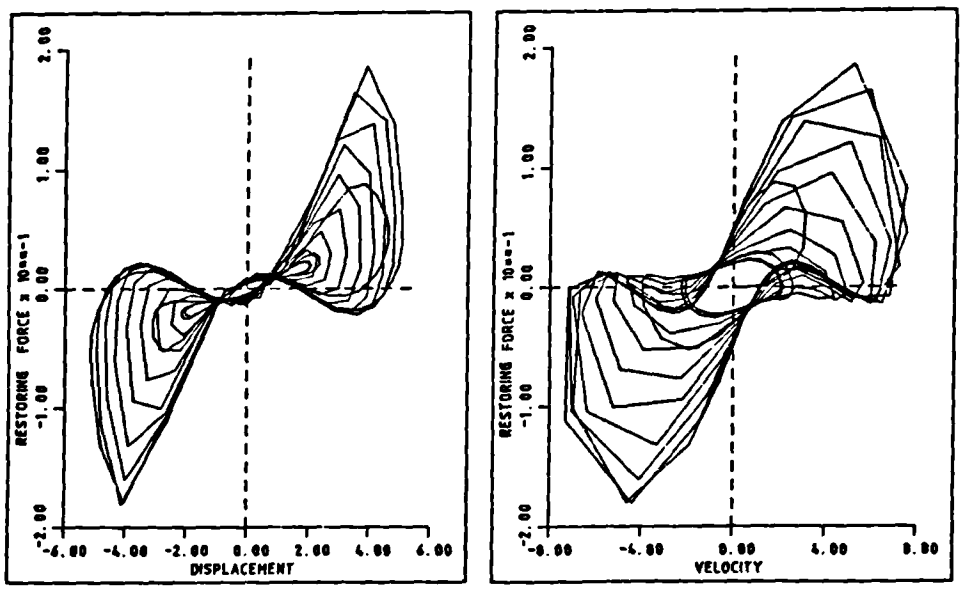

Figure 2.18. Two dimensional force-state map of raw data for the Van der Pol oscillator.

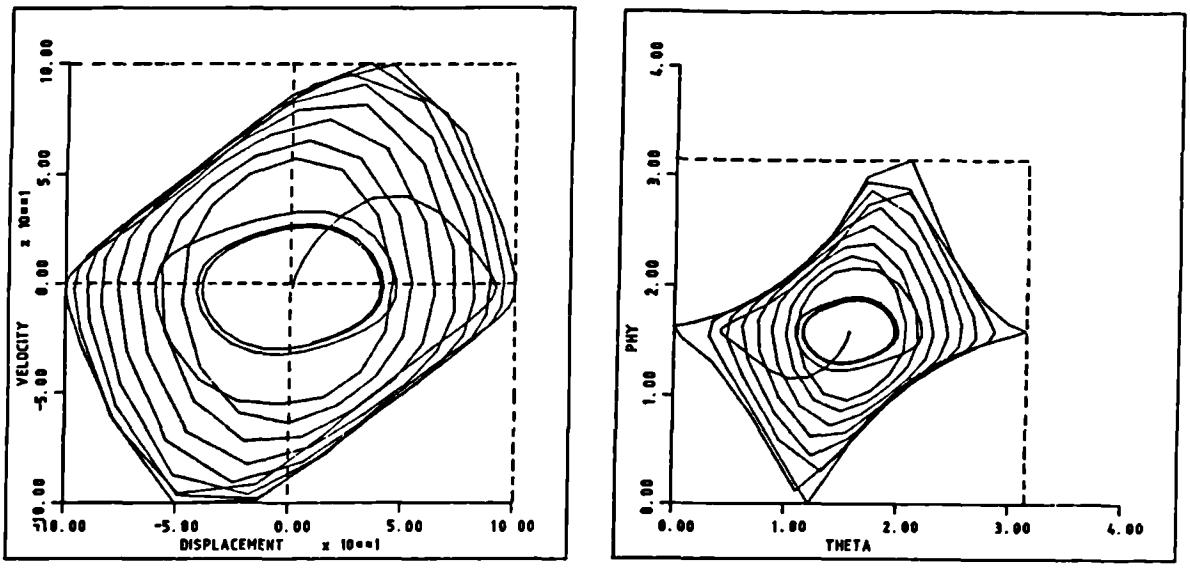

Figure 2.19. Projection of force-state map onto the $(\bar{x},\bar{y})$ and (θ,ϕ) planes for the Van der Pol oscillator.

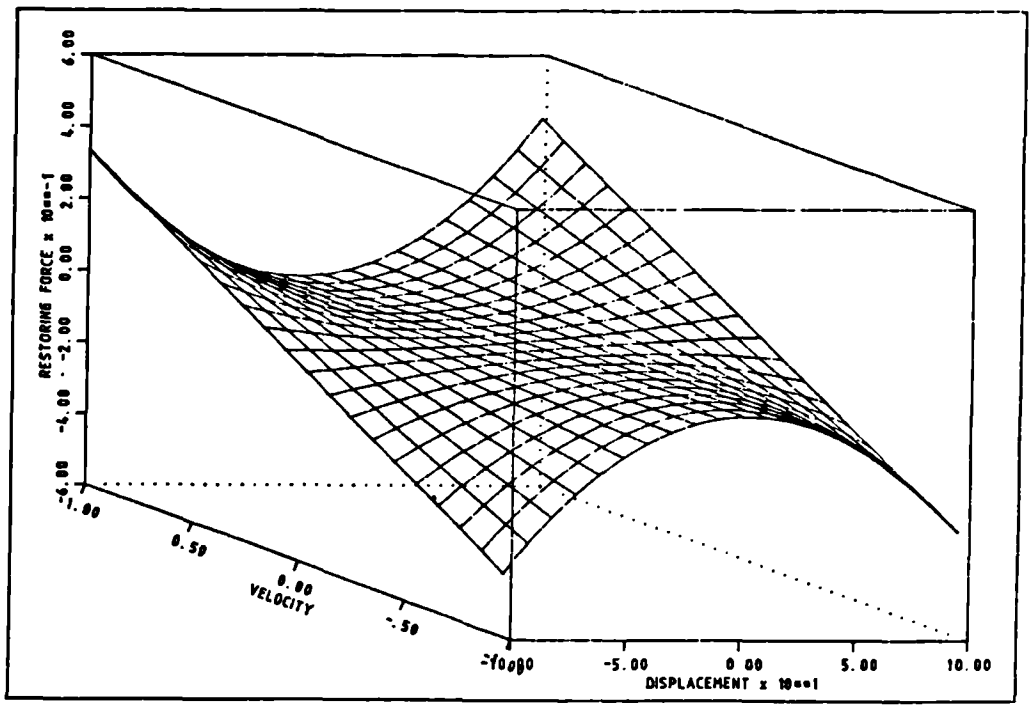

Figure 2.20. Exact force-state map surface for the Van der Pol example.

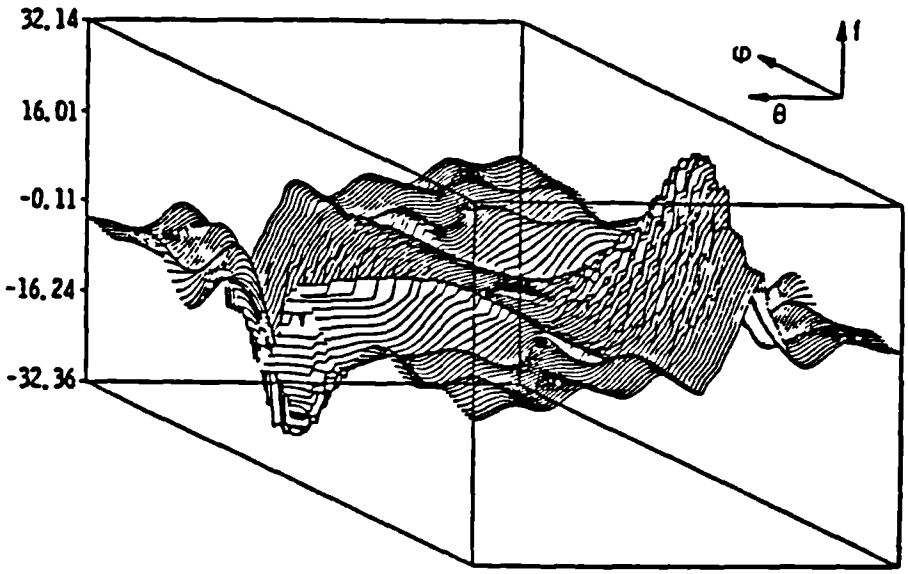

Figure 2.21. Force-state map of interpolated and extrapolated values, taken from reference 2, for the Van der Pol example.

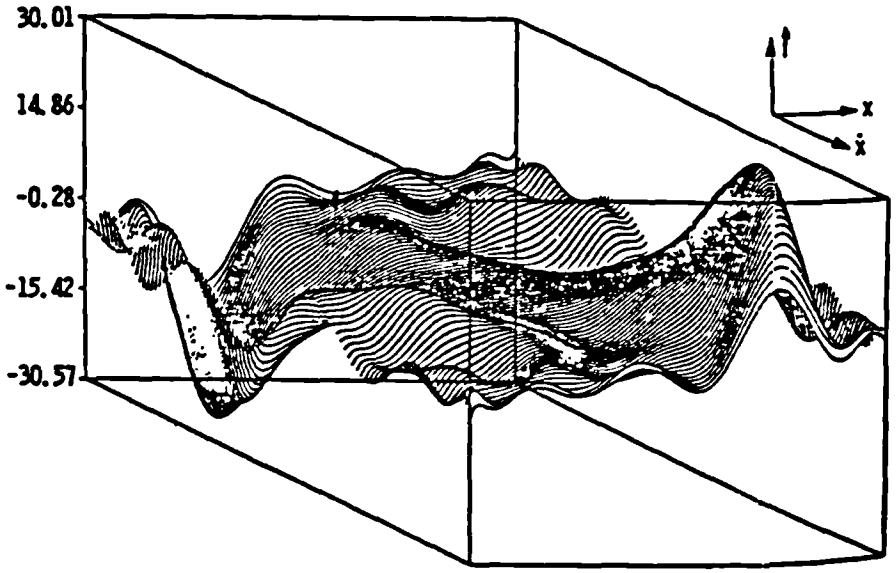

Figure 2.22. Force-state map for the fitted model of the Van der Pol example, taken from reference 2.

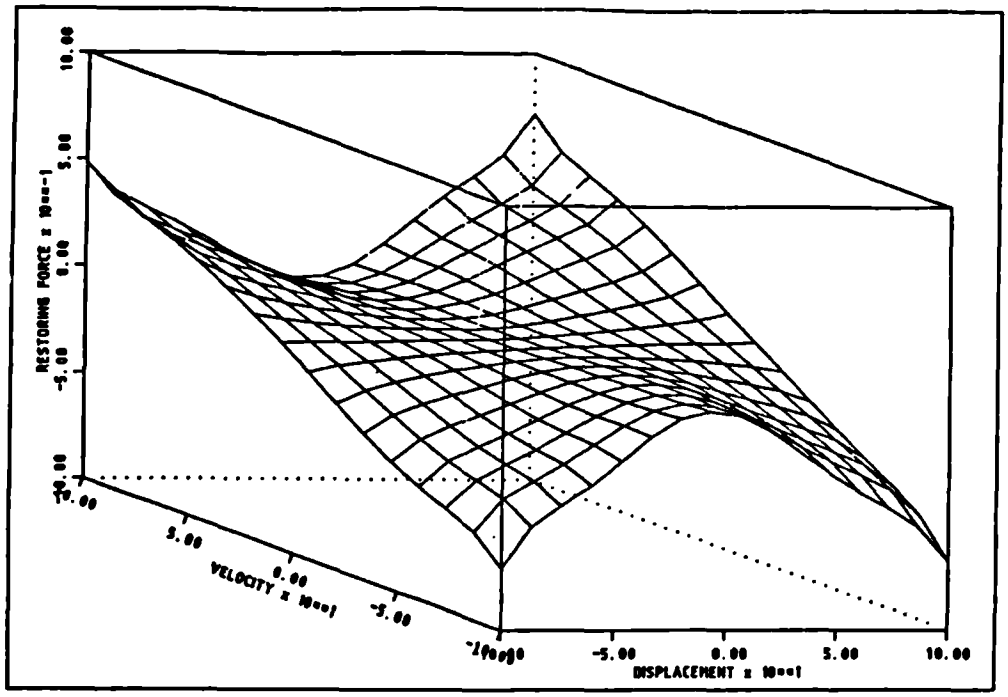

Figure 2.23. Force-state map for the fitted model of the Van der Pol example, obtained via ordinary polynomial curve fitting within bins.

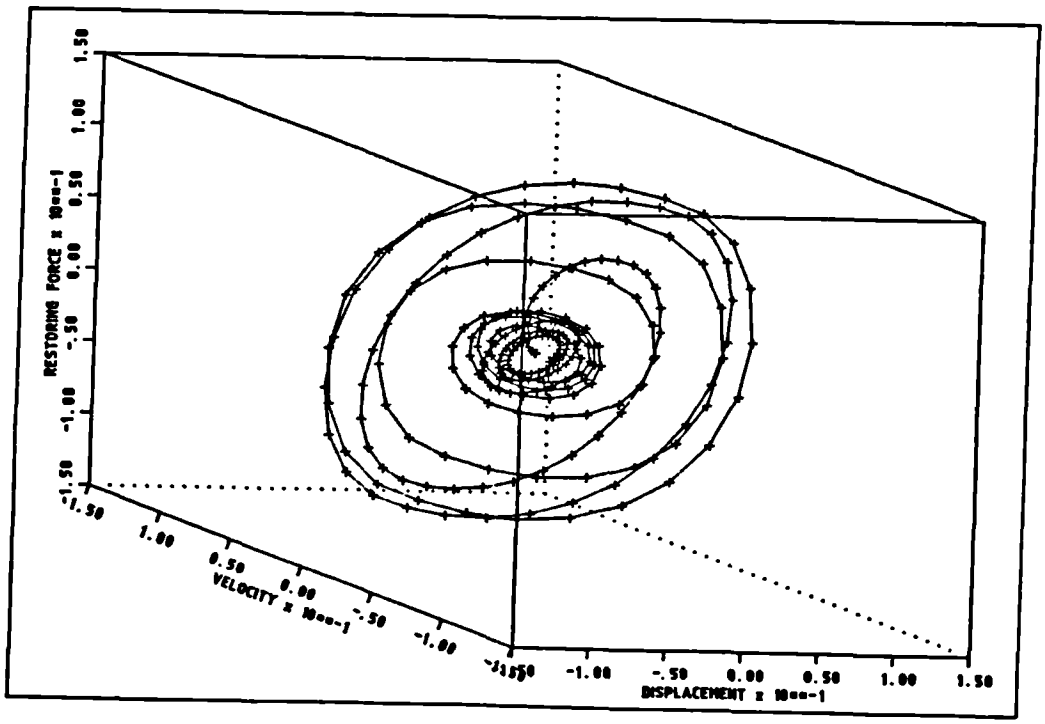

Figure 2.24. Force-state map of raw data for the quadratic damping example.

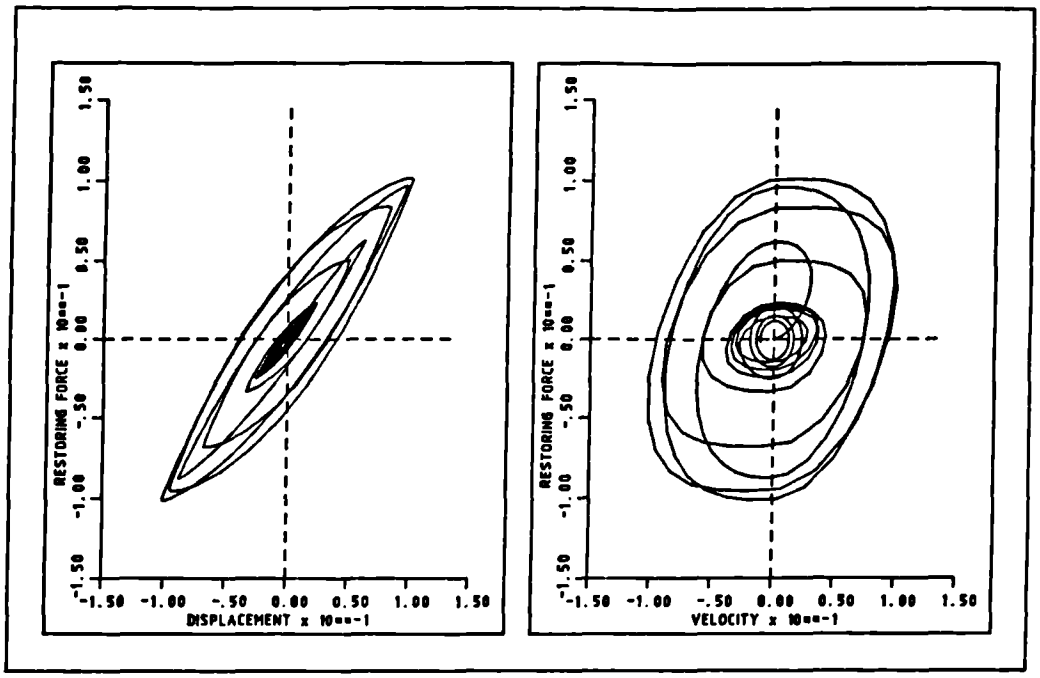

Figure 2.25. Two dimensional force-state map of raw data for the quadratic damping example.

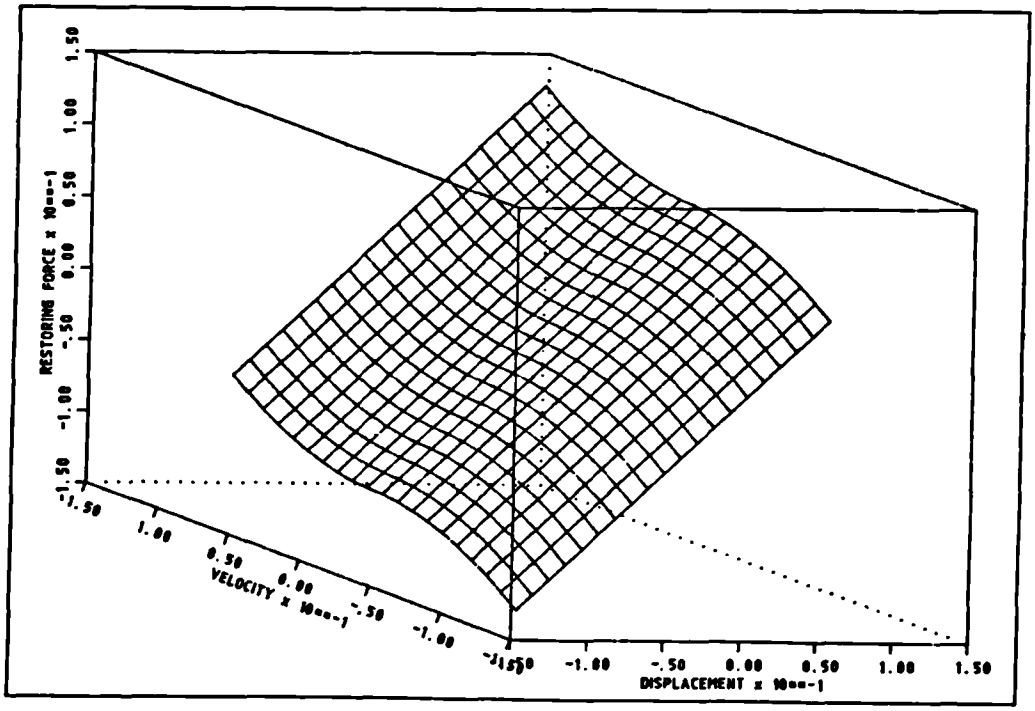

Figure 2.26. Force-state map for the fitted model of the quadratic damping example.

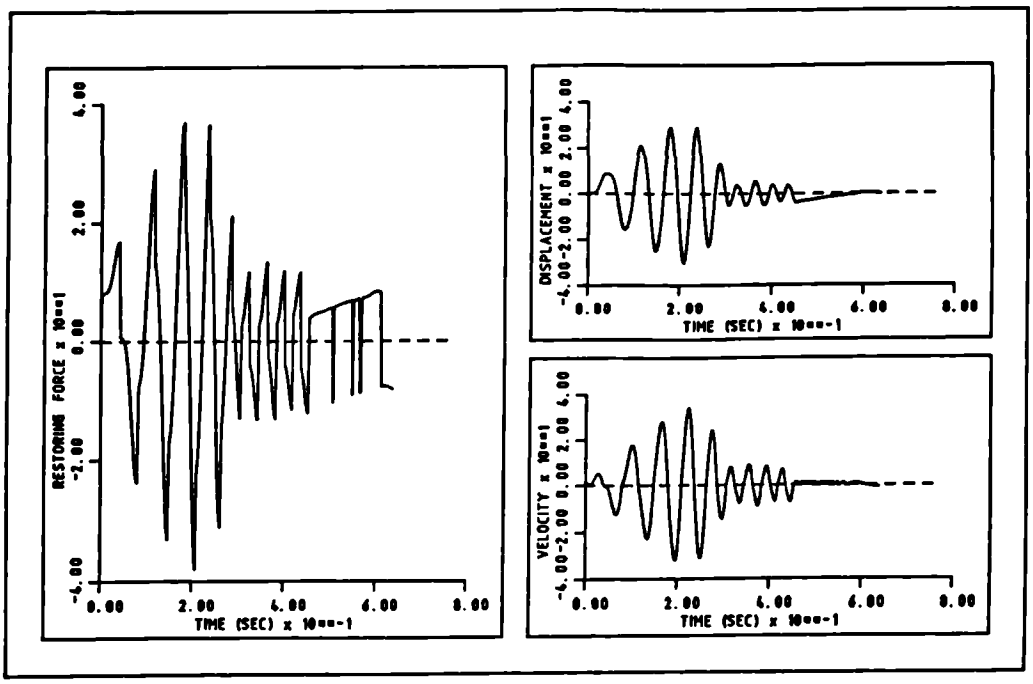

Figure 2.27. Sample time histories for the Coulomb friction example.

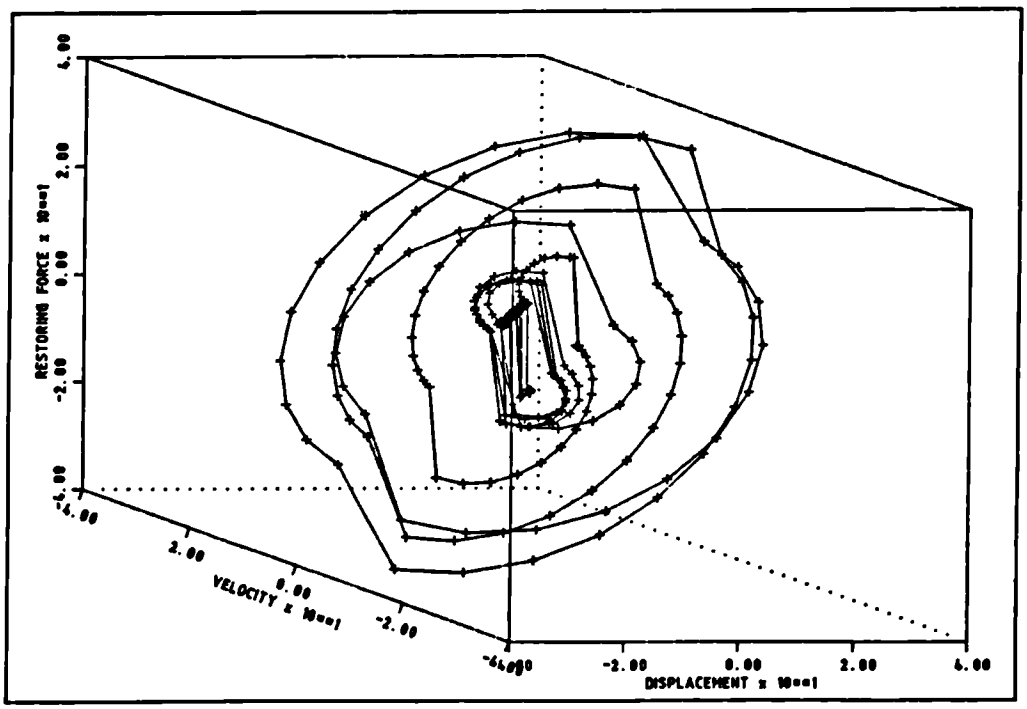

Figure 2.28. Force-state map of raw data for the Coulomb friction example.

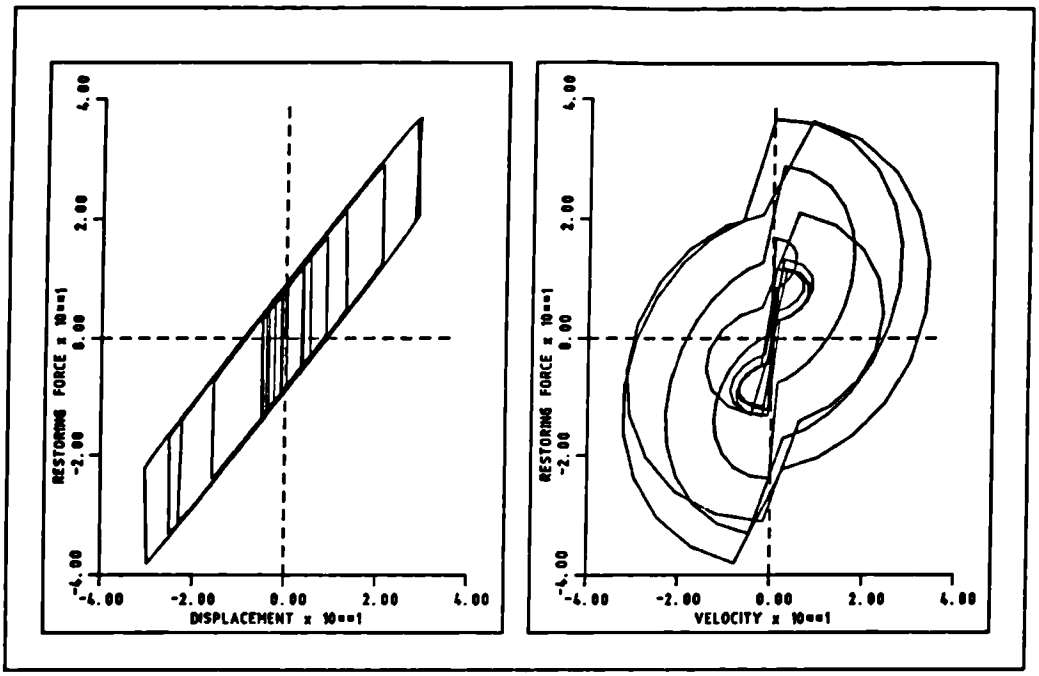

Figure 2.29. Two dimensional force-state map of raw data for the Coulomb friction example.

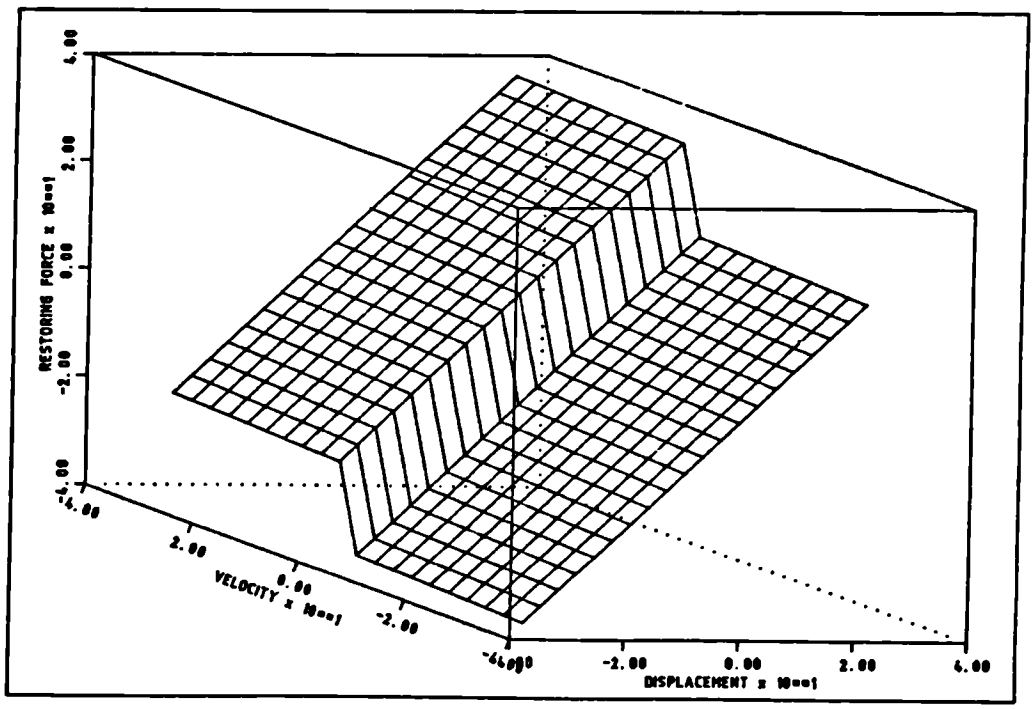

Figure 2.30. Force-state map for the fitted model of the Coulomb friction example.

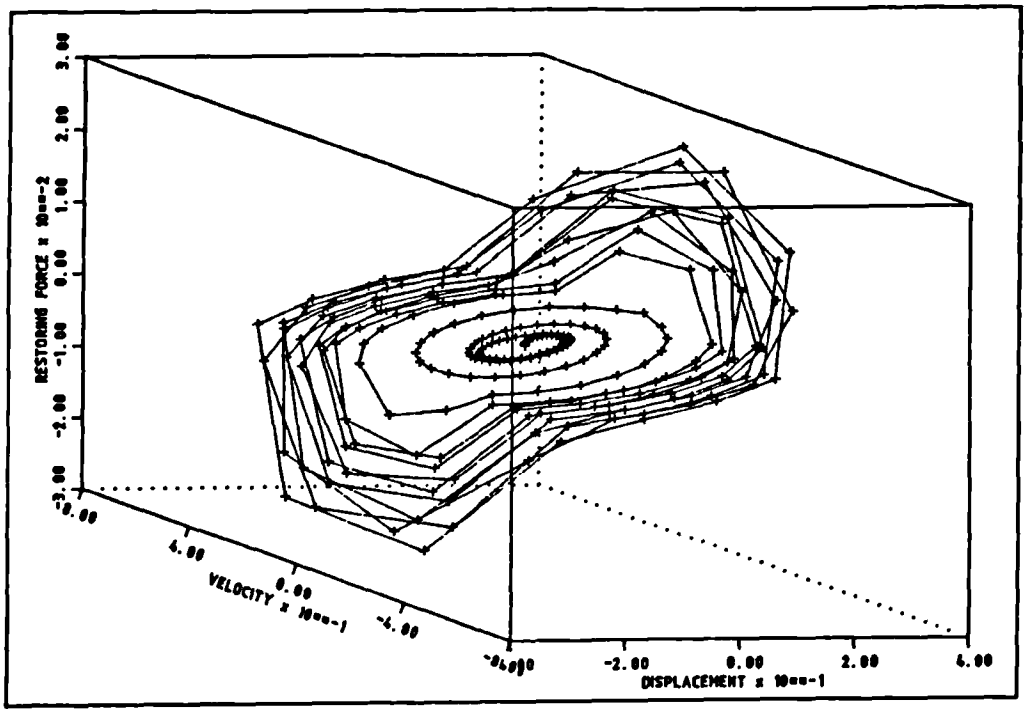

Figure 2.31. Force-state map of raw data for the dead space example.

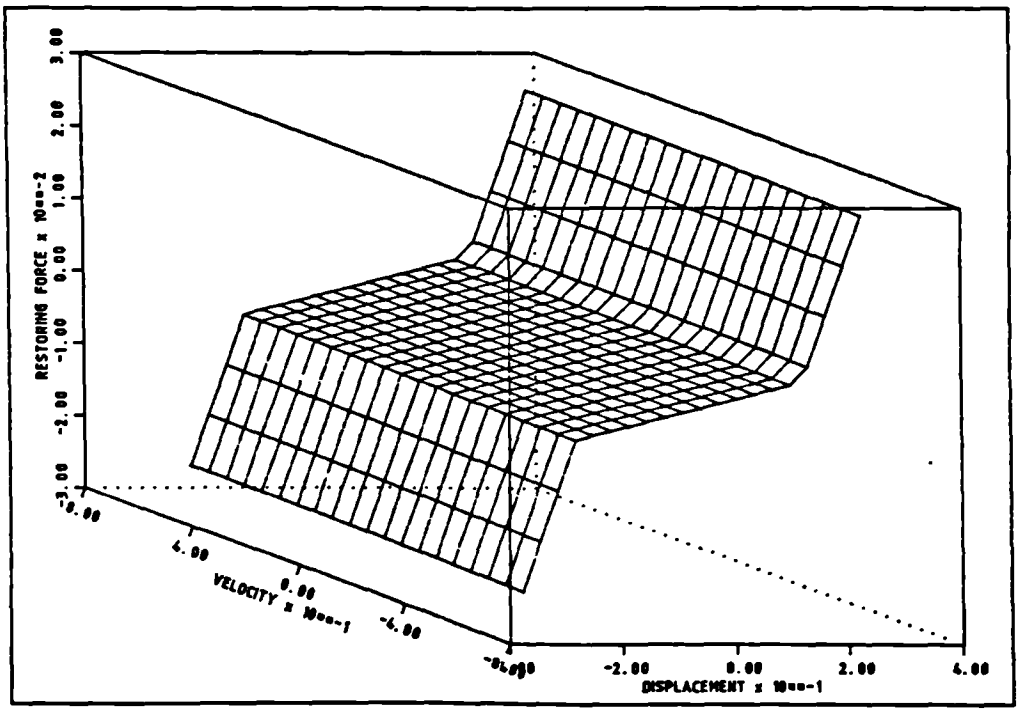

Figure 2.32. Force-state map for the fitted model of the dead space example.

3. Application of the Force-State Mapping Technique to Multi-Degree of Freedom Nonlinear Systems

The possibility of identifying single-degree of freedom nonlinear systems is useful, either for systems where there is one dominant mode or where multiple modes are so well separated that they have no significant coupling and therefore each may be analysed separately. However it is natural to wish to be able to identify multi- d.o.f. nonlinear systems where the modes are significantly close to interact in some way.

The identification of multi- d.o.f. linear systems has received a great deal of attention. Methods can be classified as "phase separation", where multi-d.o.f. mathematical models are fitted to measured data in the frequency or time domain, or "phase resonance", where appropriated multi-point excitation is used to isolate "pure" normal modes. Linear identification encounters problems when the modes are very close.

Part of the basis for linear multi-d.o.f. systems is that the equation of motion can be transformed into uncoupled form in modal space provided the damping is proportional. However once a system includes some nonlinearity, it is not generally possible to find transformations that yield an uncoupled form of equations and when the usual linear transformations are applied, the resulting equations can have significant and complex nonlinear couplings. Also the idea of a "mode" is no longer strictly appropriate for a nonlinear system. For convenience it is helpful and reasonable to think of the modes of a nonlinear system as being the undamped modes of the system with its nonlinear forces put to zero. For some nonlinearities this is equivalent to the behaviour of the undamped system as the amplitude tends to zero but this is not true for other nonlinearities, such as friction.

In relatively recent studies Masri and Caughey [19,37,38,51] have presented approaches for extending their single-d.o.f. idea to the identification of multi-d.o.f. nonlinear lumped parameter systems. For simple "chain-like" systems where masses move in one direction and are separated by linear/nonlinear elements, the identification procedure can be simplified so that each element can be identified in turn by modeling the force in that element using two dimensional orthogonal polynomials expressed in terms of the appropriate relative physical velocities and displacements. The values of each of the lumped masses need to be known.

On the other hand, for arbitrary lumped parameter systems where the masses are coupled together in a more complicated manner this simple approach can not be used. Masri and Caughey carried out the identification by transforming to modal space and curve fitting the modal restoring force vectors using two dimensional orthogonal polynomials expressed in terms of various combinations of modal velocities and displacements; the process is carried out in a step-by-step fashion since only two variables may be included at a time.

In this chapter the implementation of the Masri/Caughey approaches will be considered. Although the simple method for "chain-like" systems will be introduced briefly for completeness, the main emphasis will be placed upon the method for arbitrary system in modal space.

It will be shown that the restriction of using two modal variables at a time in the step-by-step approach of Masri and Caughey will result in parameters being biased by the influence of terms not included in each step of the fit and that this requires some of the steps to be repeated several times in order to correct for the bias. This is true even when ordinary polynomials are used instead of orthogonal polynomials as discussed in the last chapter.

To avoid the problem of bias in the step-by-step approach a direct approach is suggested so that the entire curve fit can be carried out in a single step by including all possible modal coupling terms in one model.

Finally, an approach for identifying not only the type but also the location of discrete nonlinearities within arbitrary lumped parameter systems is introduced.

3.1. Identification procedure for simple "chain-like" multi-d.o.f. nonlinear lumped parameter systems.

The simplest kind of multi-d.o.f. nonlinear lumped parameter system to identify is the so called "chain-like" system referred to by Masri and Caughey in [51]. The equation of motion for a two d.o.f. chain-like system may be written as

$$\begin{aligned} m_1 \ddot{x}_1 + f_1(D_{10}, V_{10}) - f_2(D_{21}, V_{21}) &= p_1(t) \\ m_2 \ddot{x}_2 + f_2(D_{21}, V_{21}) &= p_2(t) \end{aligned} \qquad \ldots\ldots\ldots (3.1)$$

where $f_i(D_{ij},V_{ij})$ is the linear/nonlinear restoring force located between stations i and j and given in terms of the relative displacement $D_{ij} = x_i - x_j$ and velocity $V_{ij} = \dot{x}_i - \dot{x}_j$. Note that when j is zero then the restoring force element is located between mass i and the support (or "earth"). Note also that $f_i(D_{ij},V_{ij}) = -f_i(D_{ji},V_{ji})$.

Equations (3.1) may be rearranged and written in the form

$$\begin{aligned} f_2(D_{21}, V_{21}) &= p_2(t) - m_2\ddot{x}_2 \\ f_1(D_{10}, V_{10}) &= p_1(t) - m_1\ddot{x}_1 + f_2(D_{21}, V_{21}) \end{aligned} \qquad \ldots\ldots\ldots (3.2)$$

It is assumed here that the lumped mass values and a full set of force, acceleration, velocity, and displacement signals are available. This would allow that the restoring force time histories $f_2(t)$ and $f_1(t)$ to be estimated in the manner shown in

equations (3.2). Once this has been done it remains to curve fit the restoring forces f_1 and f_2 in terms of the corresponding relative displacement and velocity signals.

The main advantage of this approach is that, because relative velocities and displacements are used, each restoring force element can be treated essentially as an element of a single-d.o.f. system. This would simplify the curve fitting process quite significantly since only one pair of relative displacement / velocity terms need be included in each fit.

The main drawback of the approach is the restriction that the system be "chain-like" which means that no mass can be attached to more than two elements and that one of the masses must only be joined to a single element. Thus the approach may not be used even for the simple system shown in Fig. (3.1), let alone for arbitrary lumped parameter systems involving more complex arrangements of mass and interconnecting elements.

For the more general problem, a transformation of all or part of the equation to modal space can be useful and this is considered in the following sections.

3.2. Formulation of the identification procedure for arbitrary multi-d.o.f. nonlinear lumped parameter systems.

In principle, any discrete (or lumped parameter) structure consists of a number of lumped masses, interconnected by discrete elements which may be linear (eg. stiffness and damping elements) or nonlinear. The equation of motion of such a structure can be written as,

$$M \ddot{\underset{\sim}{x}}(t) + \underset{\sim}{f}(\dot{\underset{\sim}{x}}(t), \underset{\sim}{x}(t)) = \underset{\sim}{p}(t) \quad \ldots\ldots\ldots\ldots\ldots (3.3)$$

where M is an (nxn) diagonal mass matrix,

$\underset{\sim}{x}(t)$ is an (nx1) displacement vector,

$\underset{\sim}{f}$ is an (nx1) linear/nonlinear restoring force vector,

$\underset{\sim}{p}(t)$ is an (nx1) excitation vector

and n is the total number of degrees of freedom for the lumped masses. For a linear system then

$$\underset{\sim}{f} = C \dot{\underset{\sim}{x}} + K \underset{\sim}{x} \qquad \text{.....(3.4)}$$

where C is the damping matrix and K is the stiffness matrix. The idea of the Masri/Caughey approach is to transform equation (3.3) into modal coordinates (or modal space) for the r modes of interest using

$$\underset{\sim}{x} = \Phi \underset{\sim}{u} \qquad \text{.....(3.5)}$$

where Φ is the (nxr) modal matrix corresponding to the linear part of the nonlinear system and $\underset{\sim}{u}$ is an (rx1) modal displacement vector. Substituting equation (3.5) into (3.3) and premultiplying by Φ^t yields

$$\Phi^t M \Phi \ddot{\underset{\sim}{u}} + \Phi^t \underset{\sim}{f} (\Phi \dot{\underset{\sim}{u}}, \Phi \underset{\sim}{u}) = \Phi^t \underset{\sim}{p} \qquad \text{or}$$

$$M_u \ddot{\underset{\sim}{u}} + \underset{\sim}{h} (\dot{\underset{\sim}{u}}, \underset{\sim}{u}) = \Phi^t \underset{\sim}{p} \qquad \text{.....(3.6)}$$

where M_u is the (rxr) diagonal modal or generalised mass matrix corresponding to the underlying linear part of the system and $\underset{\sim}{h} = \Phi^t \underset{\sim}{f}$ is the (rx1) restoring force vector expressed in modal space.

For a linear system then

$$\underset{\sim}{h} = C_u \dot{\underset{\sim}{u}} + K_u \underset{\sim}{u} \qquad \text{.....(3.7)}$$

where C_u and K_u are diagonal generalised damping and stiffness matrices unless the damping is non-proportional in which case C_u is in general fully-populated.

The transformation to modal space may only decouple the underlying linear system but the nonlinear part of the system remains coupled. However the transformation is worthwhile because it provides some simplification.

From equation (3.6) it is possible to obtain an expression for the modal restoring force vector

$$\underset{\sim}{h}(\dot{\underset{\sim}{u}},\underset{\sim}{u}) = \Phi^{t}\,\underset{\sim}{p} - M_{u}\,\ddot{\underset{\sim}{u}} \qquad \ldots\ldots\ldots\ldots\ldots\ldots (3.8)$$

and this is the multi degree of freedom equivalent of equation (2.2). Provided that estimates are available for the linear generalised mass and modal matrices, the modal state vectors $\ddot{\underset{\sim}{u}}$, $\dot{\underset{\sim}{u}}$ and $\underset{\sim}{u}$ and the excitation vector $\underset{\sim}{p}$, then a mathematical model for $\underset{\sim}{h}$ may be sought.

The modal displacements $\underset{\sim}{u}$ may be related to the physical displacements $\underset{\sim}{x}$ using equation (3.5). Firstly, if r=n, then Φ is a square non-singular matrix and so

$$\underset{\sim}{u} = \Phi^{-1}\,\underset{\sim}{x} \qquad \ldots\ldots\ldots\ldots\ldots\ldots\ldots (3.9)$$

or if the orthogonal properties of Φ are involved,

$$\underset{\sim}{u} = \Phi^{t}\,\underset{\sim}{x} \qquad \ldots\ldots\ldots\ldots\ldots\ldots\ldots (3.10)$$

Alternatively, if $r < n$ then premultiplying equation (3.5) by Φ^{t} leads to

$$\Phi^{t}\,\underset{\sim}{x} = \Phi^{t}\,\Phi\,\underset{\sim}{u}$$

and if the (rxr) $[\Phi^{t}\Phi]$ matrix is nonsingular then

$$\underset{\sim}{u} = [\Phi^{t}\Phi\,]^{-1}\,\Phi^{t}\,\underset{\sim}{x} \qquad \ldots\ldots\ldots\ldots\ldots\ldots (3.11)$$

Thus in general the transformation from physical to modal

coordinates may be expressed in the form

$$\underset{\sim}{u} = R\,\underset{\sim}{x} \qquad \ldots\ldots\ldots\ldots\ldots\ldots\ldots\ldots (3.12)$$

where $R = [\Phi^t\Phi]^{-1}\Phi^t$ is an (rxr) transformation matrix. In reference [19], Masri et al propose the transformation for $r < n$ of

$$\underset{\sim}{u} = \Phi_r^{-1}\,\underset{\sim r}{x} \qquad \ldots\ldots\ldots\ldots\ldots\ldots\ldots\ldots (3.13)$$

where Φ_r is an (rxr) submatrix of Φ and $\underset{\sim r}{x}$ is a vector containing the corresponding r components of $\underset{\sim}{x}$. This has the advantage of only requiring r measurements whereas if more than r measurements are available then equation (3.11) provides a least squares type estimate for $\underset{\sim}{u}$.

Worden and Tomlinson [46] point out that if the Φ matrix is assumed to be orthogonal and equation (3.10) used, then errors occur in the overall identification process if there are errors in the Φ matrix which means that it is not actually orthogonal.

The transformation in equation (3.12) may also be used for velocity and acceleration so the modal restoring force may now be written from equation (3.8) as

$$\underset{\sim}{h} = \Phi^t\,\underset{\sim}{p} - M_u\,R\,\ddot{\underset{\sim}{x}} \qquad \ldots\ldots\ldots\ldots\ldots\ldots (3.14)$$

and modal velocities and displacement may also be estimated. Clearly, before the modal restoring force, velocity and displacement vectors can be obtained, it is necessary to specify the number of modes r for which a mathematical representation is required.

It will be assumed in this chapter that a full set of excitation and response data $\underset{\sim}{p}$, $\ddot{\underset{\sim}{x}}$, $\dot{\underset{\sim}{x}}$ and $\underset{\sim}{x}$ can be measured simultaneously and so values will be available at discrete time intervals. Because

this is an impractical assumption the case where only the force and acceleration signals are measured simultaneously while the velocity and displacement signals are estimated by integration, is considered in chapter 4.

Note that the excitation vector $\underset{\sim}{p}$ may have several null elements provided it is able to excite the system adequately. It is also assumed in this chapter that the Φ and M_u matrices are available. The estimation of these matrices from measured data is possible and will be discussed in detail in chapter 6.

The process of obtaining values of the modal restoring force, velocity and displacement vectors at discrete time intervals may be referred to as the data preparation phase. The next phase involves the curve fitting of $\underset{\sim}{h}$ to produce a mathematical model of the system.

3.3. Mathematical modelling of the modal restoring force vector.

Two approaches to obtaining a mathematical model for $h_i(\dot{\underset{\sim}{u}}, \underset{\sim}{u})$, the component of the modal restoring force vector defining generalised linear and nonlinear restoring forces for the ith mode, will be considered.

3.3.1. Step-by-step approach (iterative approach).

This approach was proposed by Masri and Caughey [19] as an extension to their previous single-d.o.f. work, already discussed in chapter 2. The approach seeks to build up a series representation of $h_i(\dot{\underset{\sim}{u}}, \underset{\sim}{u})$ by carrying out a sequence of Chebyshev type curve fits using two modal variables at a time. These two modal variables are selected at each step of the sequence so as to attempt to account for all possible linear and nonlinear modal couplings between the ith mode and the other nearby modes. It is possible to introduce ordinary polynomials instead of Chebyshev polynomials as was considered in chapter 2 without altering the

idea of the approach.

The First step of the step-by-step approach is to curve fit $h_i(\dot{\underset{\sim}{u}}, \underset{\sim}{u})$ against the direct modal velocity $\dot{u}_i$ and displacement u_i via a series

$$h_i(\dot{\underset{\sim}{u}}, \underset{\sim}{u}) \approx h_i^{(1)}(\dot{u}_i, u_i) = \sum_{k=1}^{N1} B1_k \, F1_k(\dot{u}_i, u_i) \qquad \ldots\ldots\ldots (3.15)$$

where $F1_k$ are the basis functions introduced earlier and $h_i^{(1)}$ is the first estimate of h_i. This first series must clearly include the dominant direct linear stiffness and damping terms.

Since the modes will in general be coupled both linearly and nonlinearly then there will be some error in this curve fit because the parameter values of the fitted model will be biased by the influence of terms present in the restoring force but not included in the fit.

Since values of h_i are available at discrete time intervals, the corresponding values of $h_i^{(1)}$ may be calculated from the series once the fit has been carried out and the residual $\Delta h_i^{(1)}$ time history from this fit may be found from

$$\Delta h_i^{(1)} = h_i - h_i^{(1)} \qquad \ldots\ldots\ldots\ldots\ldots\ldots\ldots (3.16)$$

Note that this residual will be biased due to bias in the parameter values. The goodness of fit at this step may be calculated using

$$G^{(1)} = 1 - \frac{\text{R.M.S. } [\Delta h_i^{(1)}]}{\text{R.M.S. } [h_i]} \qquad \ldots\ldots\ldots\ldots\ldots (3.17)$$

where R.M.S. [.] refers to the root mean square taken over all the values available at discrete time intervals.

Subsequent steps in the sequence seek to include coupling terms in

the model. For example the second step could include the modal displacement coupling between u_i and u_j ($j \neq i$) by curve fitting the residual $\Delta h_i^{(1)}$ from the first fit using

$$\Delta h_i^{(1)} \approx h_i^{(2)}(u_i, u_j) = \sum_{k=1}^{N2} B2_k \, F2_k(u_i, u_j) \qquad \ldots\ldots (3.18)$$

where the basis functions will in general be different. The parameter j could typically be i-1 or i+1 on the assumption that the dominant coupling will be with modes nearest in frequency. The residual from this second curve fit may be found using

$$\Delta h_i^{(2)} = \Delta h_i^{(1)} - h_i^{(2)}(u_i, u_j) \qquad \ldots\ldots\ldots\ldots\ldots\ldots (3.19)$$

Because this is actually the net residual from the first two steps, the cumulative goodness of fit can be examined using

$$G^{(2)} = 1 - \frac{\text{R.M.S. } [\Delta h_i^{(2)}]}{\text{R.M.S. } [h_i]} \qquad \ldots\ldots\ldots\ldots\ldots (3.20)$$

The third step would aim to account for a different coupling combination, for example $\dot{u}_i$ and $\dot{u}_j$, by curve fitting the second residual $\Delta h_i^{(2)}$ with a suitable model $h_i^{(3)}(\dot{u}_i, \dot{u}_j)$, calculating the next residual $\Delta h_i^{(3)}$ and examining the new cumulative goodness of fit $G^{(3)}$. The procedure is shown schematically in Fig. (3.2).

The process continues in this fashion until the cumulative goodness of fit is adequate, which means that its value has become close to unity or that it has converged to a value it can not exceed even though some further coupling combinations are included. In other words if all the coupling terms that should have been present in the system have already been included in the fit then the residual of the restoring force would merely be some kind of unsystematic noise which can not be curve fitted by any further series and hence the value of the cumulative goodness of

fit can not increase significantly.

In choosing the model at each step of the process it is helpful to have some measure for assessing the contribution of each of the terms included in the fitted series to the overall fit. Then, if some of the terms in the series have very small contribution, the fit could be repeated with these terms omitted and perhaps with other terms included. The contribution of the kth term in the series to the Ith step can be defined by

$$C(I,k) = \frac{\text{R.M.S. } [BI_k \,.\, FI_k]}{\sum_{j=1}^{NI} \text{R.M.S. } [BI_j \,.\, FI_j]} \times 100\ \% \quad \ldots\ldots \quad (3.21)$$

where NI is the number of terms in the Ith step series. Alternatively the contribution of the kth term in the Ith step to the cumulative fit so far is

$$CA(I,k) = \frac{\text{R.M.S. } [BI_k \,.\, FI_k]}{\sum_{L=1}^{S} \left\{ \sum_{j=1}^{NL} \text{R.M.S. } [BL_j \,.\, FL_j] \right\}} \times 100\ \% \quad \ldots (3.22)$$

where S is the number of steps so far and NL is the number of terms in the series for the Lth step. Finally the contribution of the Ith step to the cumulative fit is

$$CT(I) = \sum_{k=1}^{NI} CA(I,k) \quad \ldots\ldots\ldots\ldots\ldots\ldots \quad (3.23)$$

In fact, this last contribution value could show whether the series selected at a particular step has contributed significantly, or rather sufficiently, to the fit so far. If it has not, then this would mean that the selection of this

particular series at this step was not successful and an alternative series or coupling combination should be considered.

The final approximate representation for the ith modal restoring force is the sum of the separate fitted models, namely

$$h_i(\dot{\underset{\sim}{u}},\underset{\sim}{u}) \approx h_i^{(1)}(\dot{u}_i,u_i) + h_i^{(2)}(u_i,u_j) + h_i^{(3)}(\dot{u}_i,\dot{u}_j) + \ldots \quad (3.24)$$

In the published work on this approach [19,37,38], it seems to have been assumed that, once sufficient coupling combinations have been included, the fit will be good and the parameters in the model accurate. However the above process does not account for bias in the parameter estimates encountered because only two variables at a time are fitted to a function of many variables. It is possible that the bias was not seen in the simulations carried out by Masri and Caughey because the errors associated with the use of Chebyshev polynomials would obscure the bias errors. However the use of ordinary polynomials gives more accurate identification and hence allows bias errors to be seen. It has been the experience of the author that a cumulative bias error would result unless some of the steps are repeated several times in order to correct for the bias. This point will be illustrated in an example later in this chapter.

Having obtained a mathematical model for the ith restoring force, the whole process explained above is repeated for each of the remaining modes of interest until a complete nonlinear model for the modal restoring force vector $\underset{\sim}{h}(\dot{\underset{\sim}{u}},\underset{\sim}{u})$ has been obtained.

Finally, the resulting model may be solved numerically to predict the response of the system to some excitation such as stepped sine, swept sine or random. It is best to carry out this numerical solution using the equations in modal space and then to transform the resulting response into physical coordinates using equation (3.5). This is considered preferable to attempting to transform the nonlinear modal model back to physical coordinates.

The particular problem of bias has arisen primarily from the restriction of fitting only two modal variables at a time which is an outcome of using two dimensional Chebyshev polynomials. However the simpler and more accurate curve fit philosophy adopted for single degree of freedom identification in chapter 2 can also be extended to overcome the bias problem in the iterative approach and so to simplify the procedure for identification of multi degree of freedom nonlinear systems.

3.3.2. Single-step approach (direct approach).

The problem of bias in the step-by-step procedure can be removed in principle by carrying out the entire curve fit to $h_i(\dot{\underset{\sim}{u}}, \underset{\sim}{u})$ in a single step. This is made possible by increasing the number of modal variables present in the fitted model to more than two with all possible couplings between these variables are included in the model. In essence, the restoring force for a well separated mode i would be mainly a function of the direct modal displacement u_i and velocity $\dot{u}_i$. The terms for inclusion in the fitted series corresponding to this model, for an ordinary polynomial representation of nonlinearity, could be selected using Pascal's triangle, namely

$$
\begin{array}{ccccccc}
 & & & 1 & & & \\
 & & u_i & & \dot{u}_i & & \\
 & u_i^2 & & u_i\dot{u}_i & & \dot{u}_i^2 & \\
u_i^3 & & u_i^2\dot{u}_i & & u_i\dot{u}_i^2 & & \dot{u}_i^3
\end{array}
$$

Here it is assumed that ordinary polynomials up to the third order are sufficient to characterise most physical types of polynomial nonlinearity. Terms to allow for other nonlinearities could be added if required. Thus h_i could be approximated by the complete series

$$h_i(u_i,\dot{u}_i) = a_1 + a_2u_i + a_3\dot{u}_i + a_4u_i^2 + a_5u_i\dot{u}_i + a_6\dot{u}_i^2 + a_7u_i^3 +$$

$$a_8u_i^2\dot{u}_i + a_9u_i\dot{u}_i^2 + a_{10}\dot{u}_i^3 \quad \ldots\ldots\ldots(3.25)$$

though it may be argued from physical considerations that some of the terms are unnecessary. However, if the ith mode was not well separated then the coupling effect of the adjacent modes should be considered. For example, if the ith mode is only coupled with the jth mode then the series given in equation (3.25) should also include coupling terms that should be selected from the following possible Pascal's triangles corresponding to

i) Cross product terms for (u_i,u_j) displacement coupling are,

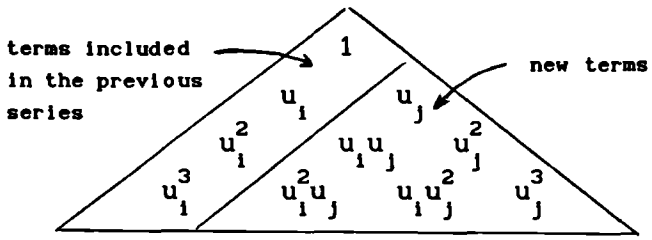

$$h_i(u_i,u_j) = a_{11}u_j + a_{12}u_iu_j + a_{13}u_j^2 + a_{14}u_i^2u_j + a_{15}u_iu_j^2 + a_{16}u_j^3$$

$$\ldots\ldots\ldots\ldots\ldots\ldots\ldots\ldots(3.26)$$

where only the terms that have not been included in the previous series are considered here

ii) Cross product terms for $(u_i,\dot{u}_j)$ displacement-velocity coupling are,

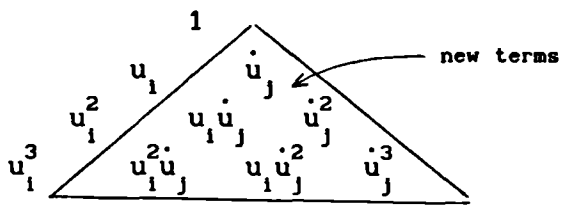

$$h_i(u_i,\dot{u}_j) = a_{17}\dot{u}_j + a_{18}u_i\dot{u}_j + a_{19}\dot{u}_j^2 + a_{20}u_i^2\dot{u}_j + a_{21}u_i\dot{u}_j^2 + a_{22}\dot{u}_j^3$$

$$\ldots\ldots\ldots\ldots\ldots\ldots\ldots\ldots(3.27)$$

iii) Cross product terms for $(\dot{u}_i, u_j)$ velocity-displacement coupling are,

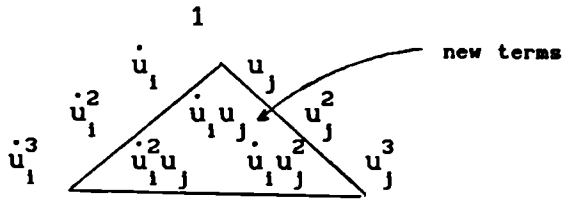

$$h_i(\dot{u}_i, u_j) = a_{23}\dot{u}_i u_j + a_{24}\dot{u}_i^2 u_j + a_{25}\dot{u}_i u_j^2 \quad \ldots\ldots\ldots (3.28)$$

iv) Cross product terms for $(\dot{u}_i, \dot{u}_j)$ velocity coupling are

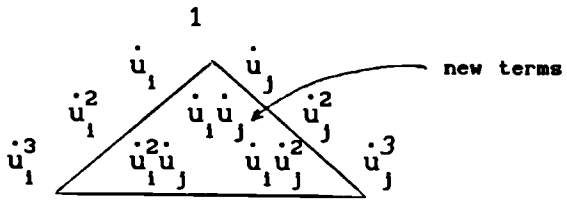

$$h_i(\dot{u}_i, \dot{u}_i) = a_{26}\dot{u}_i \dot{u}_j + a_{27}\dot{u}_i^2 \dot{u}_j + a_{28}\dot{u}_i \dot{u}_j^2 \quad \ldots\ldots\ldots (3.29)$$

The final 28 term third order model for the ith mode, coupled to the jth mode would be the sum of the individual series given in equations (3.25) to (3.29), namely,

$$h_i(u_i, \dot{u}_i, u_j, \dot{u}_j) = h_i(u_i, \dot{u}_i) + h_i(u_i, u_j) + h_i(u_i, \dot{u}_j) + h_i(\dot{u}_i, u_j) + h_i(\dot{u}_i, \dot{u}_j) \quad \ldots\ldots\ldots\ldots\ldots (3.30)$$

Now, if the ith mode is coupled with two modes (jth and kth modes) then the coupling effect of the third mode must also be considered. In fact, the remaining term that should be considered is given by

$$h_i(u_i, \dot{u}_i, u_k, \dot{u}_k) = h_i(u_i, u_k) + h_i(u_i, \dot{u}_k) + h_i(\dot{u}_i, u_k) + h_i(\dot{u}_i, \dot{u}_k)$$

$$\ldots\ldots\ldots\ldots\ldots\ldots (3.31)$$

where the terms in the right hand side of this equation are given by replacing index j by k in equations (3.26) to (3.29). Thus the final complete third order series that may be fitted to the modal restoring force for the ith mode, which is coupled mainly to modes j and k, would be

$$h_i(\underset{\sim}{u},\dot{\underset{\sim}{u}}) = h_i(u_i,\dot{u}_i,u_j,\dot{u}_j) + h_i(u_i,\dot{u}_i,u_k,\dot{u}_k) \quad \ldots\ldots\ldots (3.32)$$

At this point it will be assumed that considering the coupling effect of the closest two modes to the mode to be identified would be sufficient. This assumption may not be too impractical for many systems apart from some complex structures which may have several close modes within a narrow frequency range. In this case the fitted series could in principle be extended so that all possible coupling terms are included.

Having determined the form of the full series to be used in the fit, then the parameters of the series may be identified by a least squares approach. If all significant terms are included in the fit then parameter bias should not occur.

However, a major disadvantage of this technique is that ill-conditioning of the least squares solution can become a problem when the number of terms in the series and the number of data points are large. This problem was considered in section (2.3.2). The number of terms in the complete third order series which is 46 for this case of one mode coupled with two others may appear to be somewhat excessive, although results from Masri and Caughey's work [2,19] sometimes showed direct fits to only two variables with up to 64 Chebyshev terms.

Once parameters have been obtained from the fit, the contribution of each term in the series to the total fit may be estimated using equation (3.21) to see which are negligible. If necessary the fit may be repeated with an appropriately reduced model to obtain

better results. Clearly, the goodness of fit must be also estimated and examined. If its value is not close to unity this would mean that some terms are probably missing and the full series need to be extended even further to include the missing terms or the coupling effect of some other modes.

3.3.3. Two d.o.f. system example.

The above step-by-step and single-step identification procedures will now be illustrated on the simple two degree of freedom lumped parameter model shown in Fig. (3.1). In fact, the choice of such a simple model may be justified since the aim here is to investigate the applicability of the procedures and to demonstrate their associated problems using simple mathematical expressions that may be easily understood. Accordingly it is felt that any consideration of a more complicated system is not necessary at this stage of the investigation. The parameter values are chosen to be

$m_1 = 1$ kg $\qquad c_1 = 1.41$ N/m/s $\qquad k_1 = 3553$ N/m

$m_2 = 1$ kg $\qquad c_2 = 7.92$ N/m/s $\qquad k_2 = 35619.3$ N/m

It can be easily shown that the equations of motion for such a lumped parameter model may be written in terms of its physical coordinates in the following matrix form

$$\begin{bmatrix} 1 & 0 \\ 0 & 1 \end{bmatrix}\begin{bmatrix} \ddot{x}_1 \\ \ddot{x}_2 \end{bmatrix} + \begin{bmatrix} 9.33 & -1.41 \\ -1.41 & 9.33 \end{bmatrix}\begin{bmatrix} \dot{x}_1 \\ \dot{x}_2 \end{bmatrix} + \begin{bmatrix} 35619.3 & -3553 \\ -3553 & 35619.3 \end{bmatrix}\begin{bmatrix} x_1 \\ x_2 \end{bmatrix} + \begin{bmatrix} 35530 \\ 0 \end{bmatrix} x_1^3 = \begin{bmatrix} F_1 \\ F_2 \end{bmatrix} \qquad \text{.....(3.33)}$$

where it is assumed that a nonlinear cubic stiffness element with coefficient $\beta = 35530$ N/m^3 is located between the first mass and the fixed support (earth).

The undamped free vibration of the linear part of the model can be solved to yield the eigenvalues and eigenvectors which represent the natural frequencies and normal mode shapes of the model, namely,

$f_{n1} = 28.5$ Hz, $f_{n2} = 31.5$ Hz and

$$\Phi = \begin{bmatrix} 1 & 1 \\ 1 & -1 \end{bmatrix}$$

A sample frequency response function, obtained using single frequency excitation at the first mass, is shown in Fig. (3.3) for two different force levels namely 50 N (solid line) and 500 N (dashed line). It is possible to transform equations (3.33) into their modal form using equation (3.5), thus we get

$$\begin{bmatrix} 2 & 0 \\ 0 & 2 \end{bmatrix}\begin{bmatrix} \ddot{u}_1 \\ \ddot{u}_2 \end{bmatrix} + \begin{bmatrix} 15.84 & 0 \\ 0 & 21.48 \end{bmatrix}\begin{bmatrix} \dot{u}_1 \\ \dot{u}_2 \end{bmatrix} + \begin{bmatrix} 64132.6 & 0 \\ 0 & 78344.6 \end{bmatrix}\begin{bmatrix} u_1 \\ u_2 \end{bmatrix} +$$

$$\begin{bmatrix} 35530 & 106590 & 106590 & 35530 \\ 35530 & 106590 & 106590 & 35530 \end{bmatrix}\begin{bmatrix} u_1^3 \\ u_1^2 u_2 \\ u_1 u_2^2 \\ u_2^3 \end{bmatrix} = \begin{bmatrix} P_{u1} \\ P_{u2} \end{bmatrix} \quad \ldots\ldots (3.34)$$

and the damping is clearly proportional. The linear dampings in modes 1 and 2 are 2.21 % and 1.57 % critical respectively. It can be seen that the transformation from physical to modal space has been able to decouple the linear part of the system, but the nonlinear part has increased in complexity, with the two modes coupled nonlinearly in quite a complicated manner. Note that if the nonlinear element was placed between the two masses then only the second mode would behave nonlinearily due to the linear mode shapes and so the nonlinear part would also be decoupled. This is unlikely to be the case in general.

Data for identification were obtained by applying a frequency sweep from 27 to 35 Hz with 2000 N peak force to mass 1 and evaluating the responses numerically to provide 256 data points. The modal responses were computed using the exact modal and generalised mass matrices.

(1) The step-by-step approach was applied to the data using ordinary polynomials. The sequence of steps used the following pairs of modal quantities for the first modal restoring force (h_1), namely ($u_1,\dot{u}_1$), (u_1,u_2) and ($\dot{u}_1,u_2$) where sufficient terms were included in the second step of each sequence to allow for the nonlinear coupling present between the modal displacements u_1 and u_2. The sequence was repeated more than five times and the cumulative parameter values after each step were calculated, by simply adding the identified parameters to the corresponding parameters of the previous steps.

The process is shown in table (3.1) from which it is seen that the sequence needs to be repeated in order to improve the identified linear and a sample nonlinear parameter values and thus to allow for the main effect of bias to be overcome.

(2) The direct approach was applied to the h_1 data using the rather large model given in equation (3.30) which would be written for the 1st modal restoring force as

$$\begin{aligned} h_1(\underset{\sim}{u},\dot{\underset{\sim}{u}}) = {} & a_1 + a_2u_1 + a_3\dot{u}_1 + a_4u_1^2 + a_5u_1\dot{u}_1 + a_6\dot{u}_1^2 + a_7u_1^3 + a_8u_1^2\dot{u}_1 + \\ & a_9u_1\dot{u}_1^2 + a_{10}\dot{u}_1^3 + a_{11}u_2 + a_{12}u_1u_2 + a_{13}u_2^2 + a_{14}u_1^2u_2 + a_{15}u_1u_2^2 + \\ & a_{16}u_2^3 + a_{17}\dot{u}_2 + a_{18}u_1\dot{u}_2 + a_{19}\dot{u}_2^2 + a_{20}u_1^2\dot{u}_2 + a_{21}u_1\dot{u}_2^2 + \\ & a_{22}\dot{u}_2^3 + a_{23}\dot{u}_1u_2 + a_{24}\dot{u}_1^2u_2 + a_{25}\dot{u}_1u_2^2 + a_{26}\dot{u}_1\dot{u}_2 + a_{27}\dot{u}_1^2\dot{u}_2 + \\ & a_{28}\dot{u}_1\dot{u}_2^2 \qquad \ldots\ldots\ldots\ldots\ldots\ldots (3.35) \end{aligned}$$

modal variable	K_{11}^{*}	C_{11}^{*}	βu_1^{3} *	cumulative (G)+	CT** (%)
u_1 $\dot{u}_1$	76255.6	32.671	-	0.7888	55.130
u_1 u_2	64097.4	-	33864.5	0.9691	36.300
$\dot{u}_1$ u_2	-	20.217	-	0.9841	2.444
u_1 $\dot{u}_1$	64033.9	20.228	-	0.9843	0.130
u_1 u_2	64122.4	-	35096.2	0.9919	3.753
$\dot{u}_1$ u_2	-	16.983	-	0.9958	0.666
u_1 $\dot{u}_1$	64122.4	16.980	-	0.9958	0.000
u_1 u_2	64130.1	-	35415.3	0.9978	0.976
$\dot{u}_1$ u_2	-	16.136	-	0.9988	0.172
u_1 $\dot{u}_1$	64125.8	16.138	-	0.9989	0.016
u_1 u_2	64131.5	-	35499.9	0.9994	0.263
$\dot{u}_1$ u_2	-	15.917	-	0.9996	0.050
u_1 $\dot{u}_1$	64131.5	15.917	-	0.9996	0.000
u_1 u_2	64132.1	-	35521.6	0.9998	0.068
$\dot{u}_1$ u_2	-	15.859	-	0.9998	0.012

** Contribution of step to cumulative fit (see equation (3.23))

+ Cumulative goodness of fit.

* Exact values: K_{11}=64132.6 C_{11}=15.84 β=35530

Table (3.1). Results obtained using the step-by-step approach.

In fact, a model of this or similar form was easily constructed in a program by specifying four arrays representing the power values of the u_1, $\dot{u}_1$, u_2 and $\dot{u}_2$ signals in the model, given for this example by the following table,

u_1	0 1 0 2 1 0 3 2 1 0	0 1 0 2 1 0	0 1 0 2 1 0	0 0 0	0 0 0
$\dot{u}_1$	0 0 1 0 1 2 0 1 2 3	0 0 0 0 0 0	0 0 0 0 0 0	1 2 1	1 2 1
u_2	0 0 0 0 0 0 0 0 0 0	1 1 2 1 2 3	0 0 0 0 0 0	1 1 2	0 0 0
$\dot{u}_2$	0 0 0 0 0 0 0 0 0 0	0 0 0 0 0 0	1 1 2 1 2 3	0 0 0	1 1 2
	$h_1(u_1,\dot{u}_1)$	$h_1(u_1,u_2)$	$h_1(u_1,\dot{u}_2)$	$h_1(\dot{u}_1,u_2)$	$h_1(\dot{u}_1,\dot{u}_2)$

However, because of memory constraints in the mini-computer used, the number of points in the time histories had to be reduced from 256 to 128 points for this large model and hence it was decided to select a time window from the data within which the response to the sweep reached its peak value. The results of the fit using the singular value decomposition approach are represented in table (3.2). Significant terms are obvious, having been identified accurately and quickly. Results are also presented in the table for a smaller model which included only the terms that have significant contribution values in the large model.

3.4. Method for identification of the type and physical location of nonlinearities for arbitrary lumped parameter systems.

In the previous section it was shown that a simple two degree of freedom lumped parameter system behaved in quite a complicated manner when its equations of motion were transformed into modal space; the extra complexity of the model was caused by the transformation of the nonlinear cubic stiffness term. In fact, for systems with more degrees of freedom the complexity of the model in modal space would increase, in some cases, to a level at which the two identification approaches discussed earlier in section 3.3 would become impractical or very difficult to apply.

For the sake of illustration, consider a three degree of freedom chain-like lumped parameter system with a single cubic stiffness

a_i	True value	$\hat{a}_i$ (large model)	C^+	$\hat{a}_i$ (small model)	C^+
a_1	0	0.1826	**	-	-
a_2	64132.60	64123.10	57.69	64132.00	68.52
a_3	15.84	15.7780	2.85	15.83	3.89
a_4	0	-0.0136	**	-	-
a_5	0	-0.1500	**	-	-
a_6	0	*	**	-	-
a_7	35530.00	35547.70	5.10	35530.50	5.09
a_8	0	0.1554	0.002	-	-
a_9	0	*	**	-	-
a_{10}	0	*	0.003	-	-
a_{11}	0	1.1718	0.002	-	-
a_{12}	0	0.1320	**	-	-
a_{13}	0	-0.6230	**	-	-
a_{14}	35530.00	35525.40	11.98	35529.60	11.98
a_{15}	106590.00	106583.00	10.57	106591.00	10.57
a_{16}	106590.00	106606.00	11.78	106580.00	11.77
a_{17}	0	0.0025	**	-	-
a_{18}	0	0.0046	**	-	-
a_{19}	0	*	**	-	-
a_{20}	0	*	**	-	-
a_{21}	0	-0.0342	**	-	-
a_{22}	0	0.0002	**	-	-
a_{23}	0	0.0026	**	-	-
a_{24}	0	0.0002	**	-	-
a_{25}	0	0.1330	**	-	-
a_{26}	0	*	**	-	-
a_{27}	0	*	**	-	-
a_{28}	0	*	**	-	-

+ C is contribution of each term to the fit.

* identified parameter value < 0.0001. ** Contribution < 0.001

Table (3.2). Results obtained using the single-step approach.

nonlinear element between the first mass and a fixed point (earth). The contribution of this nonlinear element to the equations of motion expressed in physical space would be

$$\begin{bmatrix} \beta \\ 0 \\ 0 \end{bmatrix} x_1^3$$

where β is the nonlinear coefficient and x_1 the displacement of the first mass. If it is assumed that the first row of the modal matrix is simply {1 1 1} then the contribution of this nonlinear element to the equations expressed in modal space would be

$$\begin{bmatrix} \beta \\ \beta \\ \beta \end{bmatrix} (u_1+u_2+u_3)^3$$

which is clearly far more involved. Thus the equation for each mode would include a nonlinear polynomial term given by

$$\beta\ (u_1^3 + u_2^3 + u_3^3 + 3\ u_1u_2^2 + 3\ u_1u_3^2 + 3\ u_2u_1^2 + 3\ u_2u_3^2 + 3\ u_3u_1^2 + 3\ u_3u_2^2 + 6\ u_1u_2u_3)$$

Moreover, if the cubic stiffness elements were replaced by a quadratic damping element introducing a force $\gamma\ \dot{x}_1^2\ \text{sign}(\dot{x}_1)$ at the first mass, then the equivalent nonlinear term in each modal equation would be

$$\gamma\ (\dot{u}_1^2 + \dot{u}_2^2 + \dot{u}_3^2 + 2\ \dot{u}_1\dot{u}_2 + 2\ \dot{u}_1\dot{u}_3 + 2\ \dot{u}_2\dot{u}_3 + \dot{u}_1 + \dot{u}_2 + \dot{u}_3)\ \text{sign}\ (\dot{u}_1 + \dot{u}_2 + \dot{u}_3)$$

Obviously, identifying such a system in modal space would be extremely tedious especially if the step-by-step procedure of the previous section were to be implemented, even assuming that the form of the model to be fitted were known.

The problems of the involved equations in modal space and the lack of any sort of indication as to the physical locations of the identified nonlinear elements using earlier approaches, have led the author to develop an alternative approach. This can be used not only for identifying the nonlinearities present in the system but also for locating them within the physical system itself.

To illustrate the new approach consider an n degree of freedom lumped parameter system with each mass free to move in one dimension only. Let there be m possible locations for nonlinear elements. The equation of motion may then be written with linear and nonlinear terms separated as follows

$$M \ddot{\underset{\sim}{x}} + C \dot{\underset{\sim}{x}} + K \underset{\sim}{x} + \delta \underset{\sim}{q} = \underset{\sim}{p}(t) \quad \ldots\ldots\ldots\ldots\ldots\ldots (3.36)$$

where M, C and K are the mass, damping and stiffness matrices, δ is an (nxm) matrix of parameters defining the magnitude of the coefficients in the physical nonlinear elements and $\underset{\sim}{q}$ is an (mx1) vector containing functions of the relative physical velocities and displacements corresponding to each of the possible locations for nonlinearity.

In order to illustrate the form of equation (3.36), then for simplicity reconsider a two degree of freedom example of the type used earlier in section (3.3.3). However now let there be cubic stiffness elements in all three possible locations. The equation of motion in physical space could be written in the form of equation (3.36) with

$$\delta = \begin{bmatrix} \beta_1 & 0 & -\beta_3 \\ 0 & \beta_2 & \beta_3 \end{bmatrix} \quad \ldots\ldots\ldots\ldots\ldots\ldots (3.37)$$

$$\underset{\sim}{q} = \begin{bmatrix} (x_1-x_0)^3 \\ (x_2-x_0)^3 \\ (x_2-x_1)^3 \end{bmatrix} \quad \ldots\ldots\ldots\ldots\ldots\ldots (3.38)$$

where β_1, β_2 and β_3 are the nonlinear coefficients and x_0 corresponds to the displacement of "earth" so is actually zero. Note that the δ matrix will have null columns corresponding to any location where there is no nonlinearity actually present.

Now having established the equation written in this particular form, the transformation to modal space may be carried out as shown in section (3.2) except that the nonlinear terms are left expressed in relative physical coordinates. Thus the result is

$$M_u \ddot{u} + C_u \dot{u} + K_u u + \Phi^t \delta q = \Phi^t p(t) \quad \ldots\ldots\ldots (3.39)$$

where M_u , C_u and K_u are the generalised mass, damping and stiffness matrices. The modal restoring force vector may then be written as

$$h(\dot{u}, u) = C_u \dot{u} + K_u u + \Delta q \quad \ldots\ldots\ldots\ldots\ldots\ldots (3.40)$$

where $\Delta = \Phi^t \delta$ is an (rxm) matrix, and r is the number of modes of interest. For the two d.o.f. example, if

$$\Phi = \begin{bmatrix} 1 & 1 \\ 1 & -1 \end{bmatrix} \quad \text{then}$$

$$\Delta = \begin{bmatrix} \beta_1 & \beta_2 & 0 \\ \beta_1 & -\beta_2 & -2\beta_3 \end{bmatrix} \quad \ldots\ldots\ldots\ldots\ldots\ldots (3.41)$$

where it is clear that each column corresponds to a particular location of a nonlinear element. Note that the null value indicates that β_3 has no influence on the first mode.

In equation (3.40) the restoring force has a linear component expressed in terms of modal quantities and a nonlinear component expressed in terms of relative physical velocities and

displacements. Thus once the modal restoring force vector $\underset{\sim}{h}$ has been obtained using equation (3.14), a model may now be fitted for each mode in order to identify C_u , K_u and Δ. For the above two d.o.f. example, assuming proportional damping, then the ith modal restoring force would be of the form,

$$h_i(\dot{\underset{\sim}{u}}, \underset{\sim}{u}) \approx \hat{h}_i(\dot{\underset{\sim}{u}}, \underset{\sim}{u}) = C_{ii}\,\dot{u}_i + K_{ii}\,u_i + \Delta_{i1}\,(x_1 - x_0)^3 + \Delta_{i2}(x_2 - x_1)^3$$

$$+ \Delta_{i3}(x_2 - x_0)^3 \qquad \ldots\ldots\ldots\ldots\ldots\ldots (3.42)$$

and the curve fit is possible because information about both the physical and modal states is assumed to be available. Obviously, for a nonproportional damping case, linear velocity dependent coupling terms would also be included in equation (3.42).

Once the Δ matrix has been identified, the likely locations of nonlinearities will then correspond to positions of columns where the identified parameters are of significant magnitude compared to other columns in the matrix. Note that for a general n d.o.f. discrete system it may be possible to identify the locations of nonlinear elements using only r ($r < n$) modal equations, where even $r = 1$ is possible. However this relies upon the relative displacements for each possible nonlinear location being non-zero in the modes chosen. It is safer to examine all the modes (r=n), as seen in equation (3.41) where β_3 would not be located if only the first mode were curve fitted. The other advantage of using all the modes (r=n) is that the actual nonlinear coefficients could be found from Δ using

$$\delta = [\Phi^t]^{-1}\,\Delta \qquad \ldots\ldots\ldots\ldots\ldots\ldots\ldots\ldots (3.43)$$

For other types of nonlinearity the form of the $\underset{\sim}{q}$ vector would be different. In the friction case a typical element in the vector might be sign $(\dot{x}_i - \dot{x}_j)$. If more than one type of nonlinearity is thought to be present the $\underset{\sim}{q}$ vector would need to be extended to include all possible terms. Any nonlinearity included in the

fitted model but not actually present in the real system should have small coefficient in the fit. Hopefully the length of the $\underset{\sim}{q}$ vector could be reduced if certain locations and types of nonlinearity were eliminated, prior to curve fitting, using other arguments.

Note that a cubic stiffness type of model should give an indication of the presence of other types of stiffness nonlinearity such as piecewise stiffness since there would be a dominant cubic term in the fit. Once the nonlinearities have been located, the curve fit could be repeated with the behaviour at those locations modelled more thoroughly.

The idea of the approach has been illustrated by means of a two d.o.f. example. The extension to systems having a larger number of d.o.f. is straightforward but the number of possible locations increases.

However, the form of the curve fit is much simpler when the nonlinear contribution is left in relative physical coordinates than when the entire system is expressed in modal coordinates. This is especially true when nonpolynomial nonlinearity such as quadratic damping or friction are considered.

3.4.1. Two degree of freedom example with several nonlinearities.

To demonstrate the simplicity and effectiveness of the approach the above procedure was carried out on the two degree of freedom example with a single cubic stiffness element considered in section (3.3.3). This time it was assumed in the analysis that information regarding the type and location of the system nonlinearities were not available. Therefore the $\underset{\sim}{q}$ vector was extended to include functions of relative displacements and velocities to allow for various types of nonlinearities at all possible locations. These types were selected to be cubic stiffness, quadratic damping, friction and Van der Pol so the

extended vector was

$$\underset{\sim}{q}^t = [D_{10}^3, D_{21}^3, D_{20}^3, V_{10}^2\ \mathrm{sgn}(V_{10}), V_{21}^2\ \mathrm{sgn}(V_{21}), V_{20}^2\ \mathrm{sgn}(V_{20}), \mathrm{sgn}(V_{10}),$$

$$\mathrm{sgn}(V_{21}),\ \mathrm{sgn}(V_{20}),\ D_{10}^2 V_{10},\ D_{21}^2 V_{21},\ D_{20}^2 V_{20}] \quad \ldots\ldots\ldots (3.44)$$

where $D_{ij} = x_i - x_j$

and $V_{ij} = \dot{x}_i - \dot{x}_j$

Although the presence of the Van der Pol nonlinearity in the fitted model may seem unreasonable it was included in order to introduce cross-product term nonlinearity into the model, regardless of its physical meaning, and hence to see whether the approach can cope with such a model. The identified matrices, obtained using the same data as for the previous example, were

$$C_u = \begin{bmatrix} 15.78 & -0.106 \\ 0.003 & 21.482 \end{bmatrix}$$

$$K_u = \begin{bmatrix} 64130 & 0 \\ 0 & 78343.7 \end{bmatrix}$$

and

$$\Delta = \begin{bmatrix} 35533 & 0.5 & -1.9 & * & * & * & 2.7 & * & 0.1 & * & * & * \\ 35530 & * & -0.1 & * & * & * & * & * & * & * & * & * \end{bmatrix}$$

* value is ≤ 0.01

From these matrices it is apparent that the damping is essentially proportional and that there is a nonlinearity corresponding to the first element in the $\underset{\sim}{q}$ vector, namely a cubic stiffness between the first mass and "earth". Also the coefficient values are accurately determined. However in order to ensure that no other terms in the Δ matrix have a significant contribution even though they appear small, the R.M.S. contributions of each were checked and shown to be insignificant as expected.

Furthermore, in order to show that the method works when several nonlinearities of different types are present, the two degree of freedom example was considered again. The simulation included three different nonlinear elements; a piecewise stiffness element located between the first mass and earth and quadratic damping and cubic stiffness elements located between the two masses.

Once again, apart from the clearance value of the piecewise stiffness element, it was assumed that no information regarding the type and location of the system nonlinearities was available and hence a model was used in which four different nonlinear elements were located at all possible locations. These elements were of the types cubic stiffness, quadratic damping, piecewise stiffness and Van der Pole and accordingly the $\underset{\sim}{q}$ vector was

$$\underset{\sim}{q}^t = [D_{10}^3, D_{21}^3, D_{20}^3, V_{10}^2\ \mathrm{sgn}(V_{10}), V_{21}^2\ \mathrm{sgn}(V_{21}), V_{20}^2\ \mathrm{sgn}(V_{20}), F(D_{10}),$$

$$F(D_{21}),\ F(D_{20}),\ D_{10}^2 V_{10},\ D_{21}^2 V_{21},\ D_{20}^2 V_{20}]$$

where $F(D_{ij})$ represents the piecewise stiffness function between stations i and j. The resulting matrices identified were

$$C_u = \begin{bmatrix} 15.866 & -0.38 \\ 0.019 & 21.59 \end{bmatrix}$$

$$K_u = \begin{bmatrix} 64141.4 & 0 \\ 0 & 78336 \end{bmatrix}$$

$$\Delta = \begin{bmatrix} 1144 & -6816 & -1348 & * & 0.02 & * & 29969.9 & 16.6 & 1.1 & * & 198 & 3 \\ -104 & 220664 & 13 & * & 50.01 & * & 29993.8 & -28.7 & 7.2 & 3.3 & -76.5 & 3 \end{bmatrix}$$

* value is ≤ 0.01

In order to pinpoint the significant terms in this model the R.M.S. contribution of each of the identified parameters to the total fit for each mode was calculated. Thus the equivalent

damping, stiffness and nonlinear contribution matrices to those quoted above are,

$$C_c = \begin{bmatrix} 3.467 & 0.008 \\ 0.007 & 0.775 \end{bmatrix} \%\ ,$$

$$C_k = \begin{bmatrix} 66.89 & 0 \\ 0 & 14.49 \end{bmatrix} \%\ ,$$

and

$$C_\Delta = \begin{bmatrix} 0.09 & * & 0.1 & 0.05 & * & 0.05 & 29.27 & * & * & * & * & 0.02 \\ * & 0.25 & * & 0.03 & 34.17 & 0.02 & 50.10 & * & * & 0.04 & * & 0.04 \end{bmatrix} \%$$

* value is ≤ 0.01

Clearly the damping contribution matrix indicates that the system has proportional damping. The nonlinear contribution matrix shows that there are three significant columns (2nd, 5th and 7th) which, by reference to the $\underset{\sim}{q}$ vector, correspond to cubic stiffness, quadratic damping and piecewise stiffness. Also the locations of these elements are between stations 1-2, 1-2 and 1-0 respectively.

As was pointed out earlier, terms with small contributions can now be left out and the identification repeated in order that better parameter estimates may be obtained. The final matrices obtained after reducing the size of the $\underset{\sim}{q}$ vector to include only the three significant terms were

$$C_u = \begin{bmatrix} 15.837 & 0.004 \\ 0.0002 & 21.477 \end{bmatrix}$$

$$K_u = \begin{bmatrix} 64125.8 & 0 \\ 0 & 78343.2 \end{bmatrix}$$

$$\Delta = \begin{bmatrix} 91 & -0.0005 & 30003.1 \\ 199996 & 50 & 30000.1 \end{bmatrix}$$

Since Φ is assumed to be known, the nonlinear physical coefficient matrix was obtained, using equation (3.43), as

$$\delta = \begin{bmatrix} 100043.5 & 24.999 & 30001.6 \\ -99952.5 & -25.000 & 1.5 \end{bmatrix}$$

compared to the exact value of

$$\delta = \begin{bmatrix} 100000 & 25 & 30000 \\ -100000 & -25 & 0 \end{bmatrix}$$

Obviously, by comparison with the exact values, the parameters are obtained very accurately and the locations of the identified elements are correct. The larger errors in some of the parameters seen for the results using the large model are due to computational precision and the resulting small bias effect of the additional terms.

Note that identifying such a system using the previous multi-step or single-step approaches would be significantly more difficult and would not yield information regarding the locations of the identified nonlinear elements.

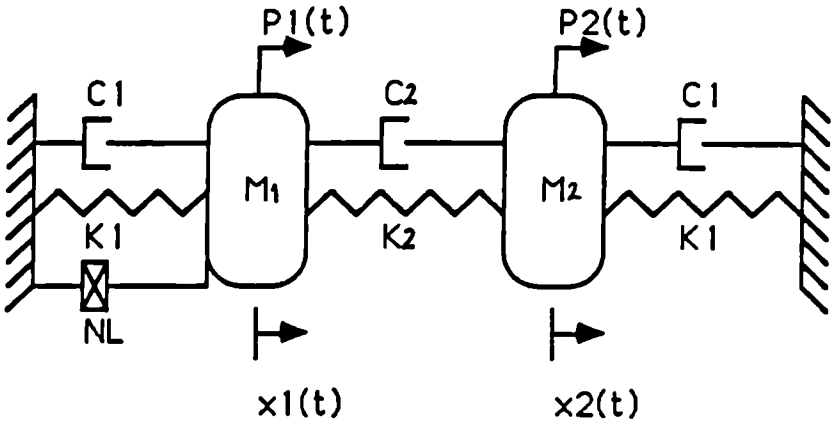

Figure (3.1). The 2 d.o.f. example considered in section (3.3.3).

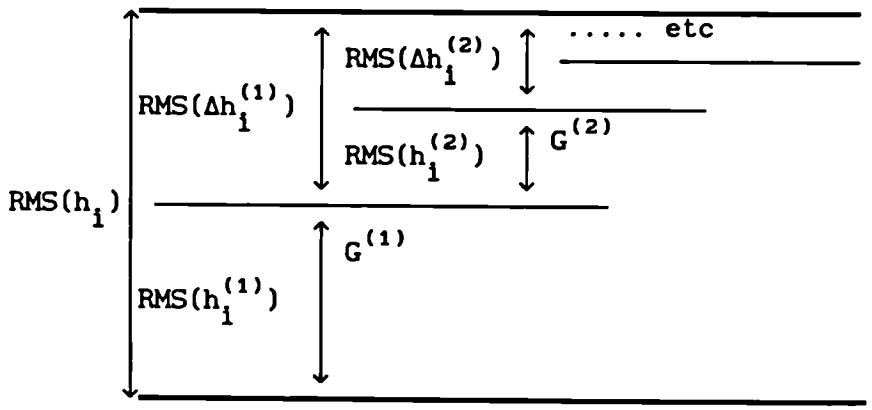

Figure (3.2). Illustration of the step-by-step procedure.

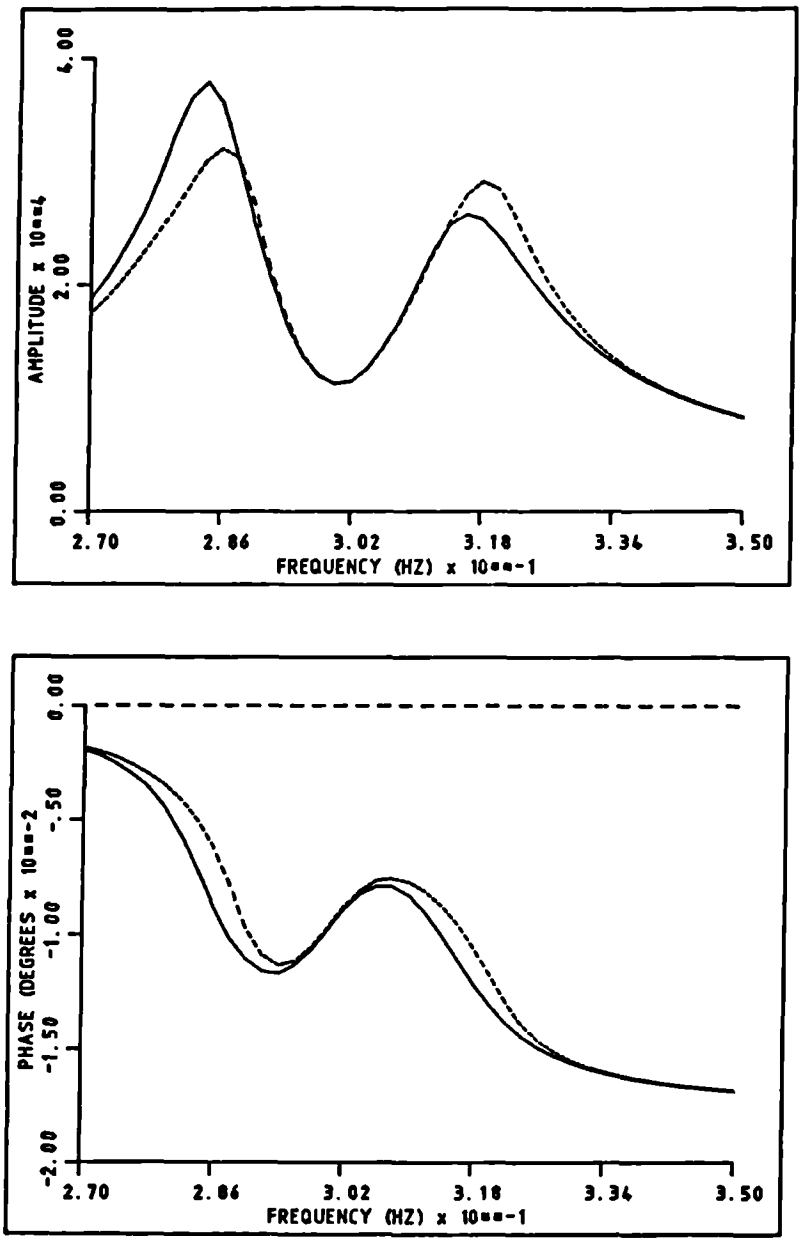

Figure 3.3. FRF of the two d.o.f. example considered in section (3.3.3), obtained at 2 force levels.

4. Estimation of the Unmeasured States

4.1. Measurement considerations.

As was indicated earlier the implementation of the force-state mapping technique implies that the force, acceleration, velocity and displacement signals must be available at the same instants of time. To obtain these synchronised signals, four different transducers with similar phase characteristics would be needed. This is somewhat impractical since instrumentation effort and cost would increase significantly. Ideally, it does not matter which of the acceleration, velocity and displacement signals are measured in an experimental investigation since they are all interrelated by an integration or differentiation operation. However, in reality there are certain restrictions imposed on the process used. The integration process will be very sensitive to the presence of low frequency components in the original signal and any DC offset can introduce considerable errors if particular care is not taken. On the other hand the differentiation process is very sensitive to high frequency noise and therefore to the high frequency performance of the transducer used for the actual measurement.

4.2. A brief review.

The problem of obtaining a complete set of states from partial measurements was not considered by Masri and Caughey since the analysis and application of their techniques was restricted to the identification of simulated systems [2,19,37,38]. However Crawley et al [39-42] applied the force-state mapping technique experimentally. Initially they evaluated the approach on a single-d.o.f. mass-spring system and in fact measured all the states independently. Later they sought to identify the nonlinear characteristics of joints in space structures and needed to

develop methods for estimating the unmeasured states. Their objective was to obtain accurate state estimates which incorporated as much measurement information as possible since this would provide estimates which were not solely dependent on the measurements from any single transducer. Consequently they assumed that both the acceleration and displacement signals were measured and the velocity signal estimated in some optimal way using a technique based on optimal control theory to minimise noise in the measurements. The theory of the technique is documented in reference [40] and will not be repeated here. Suffice it to say that this approach would double up the instrumentation and would thus make the experimental set up more expensive and arguably impractical for multi- d.o.f. structures.

Obviously the most attractive practical approach is to measure only one state and to use analogue or digital integration and differentiation to estimate the other two states. Since accelerometers are the most common form of transducers used in modal testing and since estimation of velocity and displacement from acceleration would only require integration, this approach has been favoured by other researchers. It has been attempted digitally with some success on simulated and experimental data by Worden and Tomlinson [52,53], Hunter et al [49] and the author [54]. Worden [53] also investigated the use of differentiation but considered it less suitable.

The digital integration of acceleration will be considered in this chapter.

4.3. Integration procedures.

Integration of digital signals may be carried out either in the time or frequency domain. Time domain integration makes use of well known numerical integration rules based on approximating the integrand by some polynomial and estimating the area under the polynomial. These rules vary from the very simple trapezoidal

rule, which incorporates a peicewise linear function, to some extended and more involved rules, which incorporate polynomials of higher order.

Frequency domain integration involves the implementation of forward and inverse Fourier transform so that the integration process can be carried out by dividing Fourier components by $(j\omega)$.

The basic philosophy of the two approaches is quite simple but nevertheless the practical implementation of the techniques is important and will be considered in some detail.

4.3.1. Time domain integration.

It will be assumed here that the acceleration time history z(t) is measured and sampled at N points z_i [i= 1,2,...N], each separated by a time interval Δt. The aim is to obtain the corresponding velocity and displacement values y_i and x_i using integration. Two approaches will be considered, firstly the use of standard integration formulae and then the use of the "cubic spline".

4.3.1.1. Standard integration formulae [50].

These formulae are derived by fitting a polynomial through several of the known data values and integrating the resulting function over the corresponding interval. The simplest is the Trapezoidal rule which assumes a linear variation of acceleration over each sampling interval. It can be shown easily that the resulting formula for velocity is

$$y_i = y_{i-1} + \Delta t\ (z_{i-1} + z_i)/2 \quad \ldots\ldots\ldots\ldots\ldots\ldots (4.1)$$

where i= 2,3,...N. Clearly the integration process is not self-starting since the initial value of the velocity y, is required. This is not a problem provided the system starts from rest and the first sample corresponds to this initial condition.

The trapezoidal rule is only exact for integration of signals which have a linear variation.

The well known Simpson's rule assumes a quadratic variation over two intervals using three data values to define the coefficients and it is exact for signals having a parabolic variation. The corresponding expression for velocity is

$$y_i = y_{i-2} + \Delta t \, (z_{i-2} + 4 z_{i-1} + z_i)/3 \quad \ldots\ldots\ldots\ldots (4.2)$$

where i =3,4,....N. It can be seen here that both y_1 and y_2 values are needed to start the integration process. It is possible to make use of the trapezoidal rule to obtain y_2 since y_1 may be assumed zero if the system starts from rest.

There are many more rules available [50] but those which have been considered for investigation in this work, in addition to the above two, are Simpson's 3/8 rule

$$y_i = y_{i-3} + \Delta t \, (3z_{i-3} + 9z_{i-2} + 9z_{i-1} + 3z_i)/8 \quad \ldots\ldots (4.3)$$

where i= 4,5 ....N, which assumes a cubic variation over three sampling intervals, and Bode's rule

$$y_i = y_{i-4} + \Delta t \, (14z_{i-4} + 64z_{i-3} + 24z_{i-2} + 64z_{i-1} + 14z_i)/45$$

$$\ldots\ldots\ldots\ldots\ldots\ldots (4.4)$$

where i=5,6, ...N, which assumes a quartic variation over four sampling intervals. Obviously, these two rules require three and four initial values respectively in order to get the computation process started. Once again simpler rules can be used to obtain the initial values needed.

Clearly the displacement values x_i can be estimated from the resulting velocity values y_i by repeating the integration process so a two stage operation is necessary.

4.3.1.2. Cubic spline approach.

A different approach known as the cubic spline allows the displacement to be estimated directly from the measured acceleration in a single stage integration. The term spline was originally adopted and used by engineers for studying flexible beams in the field of structural analysis. Mathematicians used the concept to interpolate smoothly between data points [50] while others used it for removal of trends from random sequences [55].

Firstly the mathematical concept will be considered briefly. Later the results will be compared with those obtained using standard integration formulae in two stages.

Assume initially that displacement values $x_i = x(t_i)$ are available at N data points (i=1,N), then consider two adjacent intervals $[t_{i-2}, t_{i-1}]$ and $[t_{i-1}, t_i]$. It is possible that a cubic polynomial can be fitted between two successive ordinates such that the values of slope at these two ordinates are equal to those of different cubic polynomials fitted through the adjacent intervals. For the interval $[t_{i-1}, t_i]$ then the polynomial can be written as

$$x = a + b\,\eta + c\,\eta^2 + d\,\eta^3 \qquad \text{.....(4.5)}$$

where a,b,c and d are the coefficients and $\eta = t - t_{i-1}$ is the time variable measured from the beginning of the interval. This transformation is made for convenience later on. Then since $\eta_{i-1}=0$ and $\eta_i = \Delta t$,

$$x_{i-1} = a$$
$$x_i = a + b\,\Delta t + c\,\Delta t^2 + d\,\Delta t^3 \qquad \text{.....(4.6)}$$

Therefore it can be seen that the slopes (i.e. velocities) at each end of the interval are

$$y_{i-1} = b \qquad \text{.....(4.7)}$$

$$y_i = b + 2c\,\Delta t + 3d\,\Delta t^3$$

and the curvatures (i.e. accelerations) are

$$z_{i-1} = 2c \qquad \text{.....(4.8)}$$

$$z_i = 2c + 6d\,\Delta t$$

Since a relationship between displacement x and acceleration (or curvature) z is sought then equations (4.6) and (4.8) may be written as

$$\begin{bmatrix} x_{i-1} \\ z_{i-1} \\ x_i \\ z_i \end{bmatrix} = \begin{bmatrix} 1 & 0 & 0 & 0 \\ 0 & 0 & 2 & 0 \\ 1 & D & D^2 & D^3 \\ 0 & 0 & 2 & 6D \end{bmatrix} \begin{bmatrix} a \\ b \\ c \\ d \end{bmatrix} = [\,\Gamma\,] \begin{bmatrix} a \\ b \\ c \\ d \end{bmatrix} \quad \text{... (4.9)}$$

where $D=\Delta t$. If a similar process is carried out for the interval $[t_{i-2}, t_{i-1}]$ then

$$\begin{bmatrix} x_{i-2} \\ z_{i-2} \\ x_{i-1} \\ z_{i-1} \end{bmatrix} = [\,\Gamma\,] \begin{bmatrix} \bar{a} \\ \bar{b} \\ \bar{c} \\ \bar{d} \end{bmatrix} \qquad \text{.....(4.10)}$$

where $\bar{a}$, $\bar{b}$, $\bar{c}$ and $\bar{d}$ are the polynomial coefficients corresponding to this interval and [Γ] is the same matrix as in equation (4.9).

Now on the assumption that z_{i-2}, z_{i-1} and z_i are known by measurement and that x_{i-2} and x_{i-1} are available from previous integration steps then there are 9 unknowns, namely a-d , $\bar{a}$-$\bar{d}$ and x_i. Since there are only 8 equations in (4.9) and (4.10) a further equation is required. This is found from the condition that the slope (or velocity) at the common point (i-1) is the same for each

polynomial. Thus

$$\bar{b} + 2\bar{c}\,D + 3\bar{d}\,D^3 = b \qquad \ldots\ldots\ldots\ldots\ldots\ldots (4.11)$$

and using the equations to solve for x_i, it may be shown that

$$x_i = 2\,x_{i-1} - x_{i-2} + \Delta t^2\,(z_{i-2} + 4z_{i-1} + z_i)/6 \qquad \ldots . (4.12)$$

This equation allows the estimation of displacement signal directly from the acceleration signal z in a similar step-by-step fashion to the earlier well known integration rules. The difference is that only one stage is required. Obviously, in order to get the computation process started x_2 can be estimated using the trapezium rule, so

$$x_2 = x_1 + \Delta t\,[\,2y_1 + \Delta t\,(z_1 + z_2)/2\,]/2 \qquad \ldots\ldots\ldots\ldots (4.13)$$

where the initial values x_1 and y_1 are assumed available. Note that it is possible to obtain a single stage integration formula relating acceleration and velocity using the above approach. It can be shown that this would yield Simpson's rule.

4.3.2. Frequency domain integration.

As regards the frequency domain integration, a periodic acceleration signal can be transformed into the frequency domain using the discrete Fourier transform. Because this transform resolves the signal into harmonic components then each of these components can be integrated simply by dividing it by $j\omega$. Thus

$$Y(\omega_k) = \frac{Z(\omega_k)}{j\omega_k}$$

$$X(\omega_k) = \frac{Y(\omega_k)}{j\omega_k} = \frac{-\,Z(\omega_k)}{\omega_k^2} \qquad \ldots\ldots\ldots\ldots\ldots\ldots (4.14)$$

where $\omega_k = 2\pi k/N\Delta t$, $k=1,2,\ldots .N/2$ and X, Y and Z are the Fourier transform of x_i, y_i and z_i. Thus the division in equation (4.14)

must be carried out for each frequency component except at zero frequency where it must be assumed that Z(0)=0 i.e. that the acceleration has zero mean. Clearly this must be the case in practice for a supported system. A DC acceleration component implies a ramped velocity in which case the periodic assumption breaks down.

Clearly, the corresponding velocity and displacement time histories can be obtained by transforming $Y(\omega_k)$ and $X(\omega_k)$ back into the time domain using the inverse Fourier transform.

4.4. Integration problems.

4.4.1. Low frequency components.

Digital integration of signals is not as straight as it may seem at first sight. This is primarily due to the fact that integration is very sensitive to the presence of any low frequency components in the original signal. These may be genuine noise or else due to quantisation or roundoff errors.

This sensitivity problem can be demonstrated by considering a simple example of integration in the frequency domain. Suppose that an acceleration spectrum $Z(\omega)$ has only two harmonic components $Z(\omega_1)$ and $Z(\omega_2)$ corresponding to measurement noise and signal respectively. If the ratio of these components is

$$R_z = \frac{|Z(\omega_1)|}{|Z(\omega_2)|} \qquad \ldots\ldots\ldots\ldots\ldots\ldots (4.15)$$

then the ratio of integrated displacement components will be

$$R_x = \frac{|X(\omega_1)|}{|X(\omega_2)|} = \left(\frac{\omega_2}{\omega_1}\right)^2 R_z \qquad \ldots\ldots\ldots\ldots (4.16)$$

Thus if $R_z = 0.01$ and $\omega_1/\omega_2 = 50$ then $R_x = 25$ and so the noise component has been amplified by the integration process relative

to the signal by a factor of 2500 ! Obviously, this would introduce considerable errors into the integration result since the first component will be seen as a large drift in the time history of the displacement after transforming $X(\omega)$ back into the time domain.

Time domain integration methods are also very sensitive to the presence of low frequency components in the acceleration signal. For example, if the measurement process introduces a non-zero mean value ν to the acceleration signal z then the measured acceleration is $z_m = z + \nu$ and the integration will introduce a linear trend into the velocity signal and a parabolic trend into the displacement signal. Note that the sampled version of a zero-mean continuous signal can have a non-zero mean. It can easily be seen that the correct velocity and displacement signals may be obtained using

$$y(t) = y_m(t) - \nu\, t - y_m(0)$$

$$x(t) = x_m(t) - \nu\, t^2/2 - y_m(0)\, t - x_m(0)$$

where $y_m(t)$ and $x_m(t)$ are the signals resulting from integrating $z_m(t)$, $y_m(0)$ and $x_m(0)$ are the corresponding values at t=0 and ν needs to be found from z_m. Alternatively the trends may be removed by curve fitting as will be shown in section (4.6)

More generally, low frequency components in the acceleration other than at zero frequency would introduce different and rather more complicated trends. In any event, any trends must either be removed from the integrated velocity and displacement signals or prevented from occurring in the first place.

The problem of sensitivity of the integration to low frequency components can be dealt with in various ways, mainly involving the use of some sort of digital filtering which can be carried out in the time or frequency domain. This process will be discussed

later.

4.4.2. Roundoff errors.

Estimating the displacement from an acceleration signal having N data points would involve the execution of a number of algebraic multiplications and additions. In the time domain this number varies from one rule to another and is given in table (4.1) for the double application of the standard integration formulae and for the single-stage cubic spline approach.

Rule	Trapezium rule	Simpson's rule	3/8 rule	Bode's rule	Cubic spline approach
No of operations	6N	10N	18N	22N	7N

Table (4.1). Number of algebraic operations used by time domain integration methods.

Depending upon the computational precision used, roundoff errors may be a problem. The table indicates that the trapezium rule and the cubic spline approach would accumulate minimum roundoff error compared with the other rules for a given number of data points. Clearly roundoff errors may be reduced by increasing the precision or reducing the number of points, provided the integration accuracy is not significantly impaired (see next section).

In the frequency domain, roundoff errors can also be a problem. The number of operations for the forward and inverse Fourier transforms is $2N \log_2 N$, let alone the division by $-\omega^2$, and this soon exceeds the number of operations required by time domain methods. In addition, when integer rather than real arithmetic is used for the transform, roundoff errors increase.

4.4.3. Truncation errors in time domain integration.

A different type of error is the integration error which is mainly

caused by the fact that numerical integration in the time domain is merely an approximation of the area under the integrand curve. This error is sometimes called the truncation error [50,56] and will be so referred to henceforth in this work. It does not occur for frequency domain integration.

Hamming [56] has shown how the integration performance and therefore truncation error may be investigated as a function of sampling rate. For example, using the trapezoidal rule and assuming an input z(t) of $e^{j\omega t}$ and output y(t) of $A(j\omega)e^{j\omega t}$, then by substituting into equation (4.1) and noting that $z_i = e^{j\omega(i\Delta t)}$ etc an expression for the transfer function of the integration process $A(j\omega)$ may be obtained. This can be divided by the exact transfer function $(1/j\omega)$ to obtain a ratio between the approximate and exact performance. For the trapezoidal rule the ratio is

$$R_T = \frac{\omega\,\Delta t}{2} \cot \frac{\omega\,\Delta t}{2} \qquad \ldots\ldots\ldots\ldots\ldots\ldots (4.17)$$

and when the same process is carried out using equation (4.2) the ratio for Simpson's rule is

$$R_S = \frac{\omega\,\Delta t}{3} \left[\frac{2 + \cos \omega\Delta t}{\sin \omega\Delta t} \right] \qquad \ldots\ldots\ldots\ldots (4.18)$$

The variation of these ratios with (ω/ω_s), where $\omega_s = 2\pi/\Delta t$ is the sampling frequency, is shown in Fig. (4.1). Note that $\omega/\omega_s = 1/N_p$ where N_p is the number of points per cycle in the frequency component being integrated. The truncation error increases as the number of points per cycle reduces. The integration is overestimated using Simpson's rule and underestimated using the Trapezoidal rule.

When the same process was carried out for the single stage integration from acceleration to displacement using the cubic spline approach in equation (4.12) then the ratio between the resulting transfer function and the exact transfer function $(-1/\omega^2)$ may be shown to be

$$R_{cs} = \frac{\omega^2 \Delta t^2}{6} \left[\frac{2 + \cos \omega\Delta t}{1 - \cos \omega\Delta t} \right] \quad \ldots\ldots\ldots\ldots\ldots (4.19)$$

This ratio is compared to R_T^2 and R_S^2 , the corresponding ratios for the other two rules for two stage integration, in Fig.(4.2). Simpson's rule provides the most accurate integration of these three rules when more than 4 points/cycle are used. The higher order Simpson's 3/8 and Bode's rules will be even more accurate for reasonable sampling rates.

Thus in general the truncation error can be reduced by selecting a smaller time step and so increasing the number of points per cycle. This would clearly increase the total number of points in the response time histories for a given total time but also increase any roundoff error. In other words, increasing the number of points reduces the truncation error but increases the roundoff error. Thus the integration process will tend to reach a saturation point after which any increase in the number of points would increase the total error, now dominated by the roundoff error. This point is illustrated in Fig.(4.3), taken from reference [57], where the truncation and roundoff error values of a particular example are plotted against the number of data points used by the Trapezoidal and Simpson's rules. Obviously the use of extended precision allows a larger number of points to be used before the saturation point is reached.

On the other hand too large a time step should not be tolerated since this would certainly increase the error for all the integration rules. It will be shown later that the use of an inadequate time step may introduce instability into the output from integration rules which incorporate high order polynomials.

Some involved integration approaches are called adaptive stepsize control techniques [50]. They are based on adjusting the time step of the response signals according to some error criterion. These

techniques could be implemented on-line but this would make the data acquisition process too involved and therefore they are not considered in this work.

4.4.4. High frequency components.

Just as the presence of frequency components below the frequency band of interest can cause problems, so any noise components at higher frequencies can lead to serious difficulties in integration. This is fortunately not true for frequency domain integration since the division by $j\omega$ and $-\omega^2$ will tend to attenuate higher frequency components considerably.

However for some time domain integration approaches high frequency components may be actually amplified significantly. This is because the components will have fewer points per cycles than the components of interest for which the truncation error is being kept within acceptable limits. Then the ratio of approximate to exact integration transfer functions shown in Figs. (4.1) and (4.2) can be considerably different to unity. The trapezoidal rule attenuates high frequency components and so is a robust rule though it does require a high number of points per cycle for accuracy. However Simpson's, and Simpson's 3/8 and Bode's rule too, will actually magnify high frequency components because the ratio tends to infinity at the sampling frequency. This unstable type of behaviour will be seen later and can be a real drawback of these higher order rules unless some low pass filtering is used. A double application to obtain displacement from acceleration will just make matters worse.

Note that for any number of points/cycle, the single-stage cubic spline approach actually performs better than a double application of Trapezoidal rule and does not magnify high frequency components, as seen in Fig. (4.2). It would therefore seem a reasonable compromise to use for obtaining displacement from acceleration. In fact it turns out from equations (4.17) to (4.19)

that

$$R_{cs} = R_T R_s \quad \ldots\ldots\ldots\ldots\ldots\ldots\ldots\ldots (4.20)$$

and therefore the derived cubic spline is equivalent to a combination of the Trapezoidal and Simpson's rules, applied in a single stage without the disadvantage of the high frequency behaviour of Simpson's rule!

4.4.5. Leakage errors in frequency domain integration.

The requirement of a periodic acceleration for the frequency domain approach is important and influences the type of excitation which may be used. One approach to produce a periodic response is to stop the forcing input (sweep, burst random etc) early enough in order to allow the acceleration signal to die away before the end of the time window is reached. However, this may not work well for very lightly damped systems since the response takes longer to die away and so a larger time window and hence more points are required. Also the excitation may be tailored in some way to help to minimise transient response and thus obtain a periodic acceleration. This will be considered later in chapter 7. Another approach is to use a single frequency sinusoidal excitation, allow the response to reach a steady-state and to acquire an integer number of cycles of data. A periodic excitation such as cyclic random should also provide a periodic response.

If the signal is nonperiodic for some reason then the integration results will suffer in accuracy due to leakage errors in the Fourier transform. A well known remedy to the leakage problem is to multiply the response signal by a time window such as Hanning, Hamming, Flat-top etc [58] so that the signal is forced to start and end with zero values. obviously the measured input signal should be multiplied by the same window too. For a nonlinear system this windowing may modify the nonlinear law of the system governing the relationship between the input and response signals.

Therefore it is clearly preferable that the leakage problem be avoided altogether by a suitable choice of excitation.

The following sections will be concerned with investigating the use of the above time and frequency domain methods for integrating the acceleration of linear and nonlinear single-d.o.f. simulated systems. The main advantages and drawbacks of both approaches will be explored by examining,

(i) how well the estimated signals match the exact signals,
(ii) how well the estimated system parameters agree with their exact values,
(iii) how easily and effectively the problem of sensitivity to low frequency components can be solved and finally
(iv) how sensitive to measurement noise both methods are.

4.5. Integration of linear data.

For the example considered in this section the problem of sensitivity to low frequency components and removal of trends will be investigated and the most effective way of reducing the sensitivity and removing the trends will be sought. Note that the use of single-d.o.f. systems can be considered adequate to illustrate the integration and its associated problems.

The excitation signal will be restricted here to sinusoidal sweep excitation. Random excitation has been considered extensively by Worden [53].

The response of the system will be generated using a fourth order Runge-Kutta algorithm. This allows a comparison between the integrated and the exact velocity signals to be carried out using

$$G_y = 1 - \frac{\text{R.M.S.}[y(t)-\hat{y}(t)]}{\text{R.M.S.}[y(t)]} \qquad \ldots\ldots\ldots\ldots\ldots (4.21).$$

where y(t) is the exact velocity provided by the Runge-Kutta

algorithm, $\hat{y}(t)$ is the estimated velocity signal obtained by integrating the exact acceleration and G_y is the "goodness of velocity estimation" and has a value of unity for a perfect estimation. A similar equation can be written for the displacement comparison. A linear single-d.o.f. system having parameters

m = 1 kg
k = 100000 N/m (f_n = 50.32 Hz)
c = 30 N/m/s (ζ = 4.74% critical damping)

was subjected to a 47 to 53 Hz sinusoidal sweep excitation with p= 10N R.M.S. The total time of 0.634 sec and sampling interval of 0.00124 sec were chosen such that 512 data points were produced by the simulation for each of the acceleration, velocity and displacement time histories. The sweep excitation only occupied 50% of the total time window in order to allow the response to die out and thus to minimise any leakage effect for frequency domain integration.

(a). Time domain integration.

The five time domain integration algorithms introduced earlier in section (4.3.1) were used first and the corresponding goodness of velocity and displacement estimation, henceforth referred to as G_y and G_x respectively, are given in table (4.2).

It can be seen that the velocity estimation is quite good since values of G_y are close to unity. However displacement estimation is significantly more in error. A comparison between the estimated and exact displacement signals corresponding to each of the four integration rules and the cubic spline approach is shown in Fig (4.4.a-e). For all but the trapezoidal integration, the agreement

	Trapezium rule	Simpson's rule	Simpson's 3/8 rule	Bode's rule	Cubic spline approach
G_y	0.987	0.997	0.997	0.996	0.997
G_x	0.842	0.819	0.809	0.799	0.822

Table (4.2). G_y and G_x values for time domain integrations.

seems to be very good over the first half of the time window but then deteriorates as an apparently linear trend causes the estimated signal to deviate from the exact value. Also for the Simpson, Simpson 3/8 and Bode rules there is a higher frequency component superimposed upon the signals. The results for the Trapezoidal rule behave differently in that the error is evident over the first half of the time window, appearing as a slight attenuation in amplitude as might be expected plus a growing trend affecting the mean; in the second half of the window the error remains as an apparently constant DC shift. It is interesting that in all cases the behaviour of the error appears to alter at the point where the excitation ceases and the response is allowed to decay freely. It is therefore unlikely that the appearance of a drift and higher frequency oscillation is due to roundoff errors in the integration; indeed when the integration was started half way through the time window using the simulated values to start the process, a similar behaviour was seen.

In order to investigate the behaviour of the error in the estimated signals further the difference between the exact and the estimated signals, normalised with respect to the maximum value of the exact signal, was calculated for the velocity using

$$EY_i = \frac{y_i - \hat{y}_i}{y_{max}} \times 100\ \% \qquad \ldots\ldots\ldots\ldots\ldots (4.22)$$

where y_i and $\hat{y}_i$ are the exact and estimated values at the ith time step. A similar expression was used for the displacement error

EX_1. The variation of these errors with time is shown in Fig. (4.5) for Bode's rule integration as an example. Over the first half of the time window there is a small almost linear drift in the displacement error reaching a maximum of about 1.5% plus a small higher frequency oscillation, neither visible in Fig. (4.4.d). The velocity error is very small but has a DC component which causes the linear drift in the displacement error. However there is a dramatic change in behaviour half way through the window when the force ceases where there is a step change in the DC component of the velocity error, causing a significant increase in the drift of the displacement error. Also the oscillatory component amplitude is constant for the velocity but grows steadily for the displacement error.

A further confirmation of the significance of stopping the excitation may be seen by maintaining the excitation throughout the entire time window; the equivalent results to those already shown in Fig. (4.5) for Bode's rule integration show a much more regular error behaviour although the total drift is also large. This error behaviour is shown in Fig. (4.6).

It would appear therefore that the rapid growth in the displacement error is triggered off by some discontinuity in the acceleration associated with the excitation stopping suddenly. It is not yet certain whether this problem is due to the discontinuity in the slope of the acceleration signal associated in the excitation or to errors caused by inadequate step size in the Runge-Kutta simulation used to generate the so-called "exact" data. In order to answer this point, a signal corresponding to a steady-state sinusoidal response followed by a free decay was computed from analytical expression without any numerical simulation process. The exact and integrated displacements for two different sampling rates are shown in Fig. (4.7). Since the same sort of behaviour is seen as before, it may be concluded that the discontinuity in the slope of the acceleration is responsible. It would appear that the linear drift and growing oscillation are due

to a velocity error associated with the inability of the integration to follow the discontinuity. Alternatively the discontinuity may be viewed as higher frequency "noise" superimposed upon a "smooth" signal. Clearly the error is reduced by increasing the sampling rate but could be reduced in practice by "tailoring" the excitation so as to minimise any discontinuity or by low pass filtering.

It is surprising to note that when the integrated signals in Fig. (4.1) were used to produce a force-state map, without correction, the fitted parameters were within 2.5% of the true values, as shown in table (4.3).

% error	Trapezium	Simpson	3/8	Bode	Cubic spline
Stiffness	2.15	-2.01	-2.09	-2.53	-0.52
Damping	1.80	-0.12	-0.20	0.01	-0.22

Table (4.3). Errors of parameters obtained using estimated signals.

The errors would be expected to be larger for a nonlinear example or if the drift were to affect more of the map than the low amplitude region. Clearly the drift and higher frequency oscillation should be avoided or reduced.

(b). Frequency domain integration.

The above linear example will now be approached using frequency domain integration. The discrete acceleration signal was transformed into the frequency domain and then divided by $j\omega$ twice to give the transforms of the velocity and displacement signals. The corresponding amplitudes of acceleration, velocity and displacement spectra are shown in Fig. (4.8). The estimated velocity and displacement are obtained by transforming back into the time domain. A sample comparison between the exact and estimated displacement signals is shown in Fig. (4.9). The accuracy of the integration is indicated by G_y and G_x values of

0.983 and 0.532 respectively. The poor displacement accuracy is clearly due to the low frequency behaviour superimposed upon the desired signal. The low frequency components are clearly visible in the displacement spectrum in Fig. (4.8) but not in the acceleration spectrum. However, as pointed out earlier, low frequency noise in the acceleration need not be large to be significant after double integration.

The low frequency components in the acceleration must have been introduced because the nominally exact floating point values produced by the simulation were converted into integer format to represent the sampling process and because the discrete Fourier transform was carried out using 16 bit integer arithmetic. The divisions by $j\omega$ and $-\omega^2$ were carried out in floating point arithmetic and the results scaled and converted to integer again for the inverse Fourier transformation. However, the estimation of parameters from the resulting force-state map yielded an unacceptable 18% error in the stiffness so clearly the low frequency behaviour needs to be removed.

4.6. Trend removal.

So far low frequency behaviour and trends (or drifts) in the integrated results have not been corrected for. The trends introduced in the time domain may be linear or parabolic whereas in the frequency domain the trends are likely to be of higher order. In this section the removal of trends is considered.

4.6.1. Trend removal in the time domain.

The problem of trend removal from time signals has been dealt with in this work using two approaches, namely least squares curve fitting and high-pass digital filtering. The flow charts for these two approaches are shown in Figs. (4.10) and (4.11).

4.6.1.1. least squares curve fitting.

The idea of this approach is simply based on carrying out a standard least squares curve fit to the estimated signals in order to identify the polynomial which characterises the trend as closely as possible. The estimated signal can then be refined using

$$\hat{y}_k = y_k - \sum_{i=0}^{M} a_i \, t_k^i \qquad (k=1,2,\ldots N) \qquad \ldots\ldots\ldots (4.23)$$

where M is the number of terms in the curve fitted polynomial, a_i are the identified parameters, y_k is the estimated signal before removing the trend and $\hat{y}_k$ is the refined signal after removing the trend. The polynomial order must be chosen carefully; too high and real data will be removed or too low and some trend will remain.

When this approach was used for removing the trends from the estimated signals, shown in Fig. (4.1), the G_x values improved quite well as can be seen in table (4.4). The order of the fitted polynomial was 2 for the velocity and 4 for the displacement. A comparison between the exact and estimated displacement time histories is shown in Fig. (4.12) for all the time domain integration cases. The removal is fairly effective considering that there was a discontinuity in the trend for this particular excitation.

	Trapezium rule	Simpson's rule	Simpson's 3/8 rule	Bode's rule	Cubic spline approach
G_y	0.987	0.997	0.997	0.996	0.997
G_x	0.971	0.952	0.971	0.918	0.976

Table (4.4). G_y and G_x values after removing trends by least squares approach.

Having removed the undesired trends from the integrated signals the force-state maps were constructed and the system parameters were identified. Errors are presented in table (4.5).

% error	Trapezium	Simpson	3/8	Bode	Cubic spline
Stiffness	2.57	-0.28	-0.16	-0.68	1.23
Damping	1.30	0.07	0	0.22	-0.03

Table (4.5). Errors in parameters for least squares trend removal case.

The results for the higher order integration rules improved but the stiffness estimates for the trapezoidal and cubic spline approaches were actually slightly less accurate than without the trend removal; the reason for this is unclear but the result of the removal is imperfect and the force-state mapping is a complex process. It will be shown later that this least squares curve fitting approach can actually lead to biased results when subtracting trends from oscillatory signals.

4.6.1.2. High pass digital filtering.

The digital filtering approach was also applied using a 6-pole Butterworth high pass digital filter [22] with a 10 Hz cut-off frequency. As can be seen from Fig. (4.11) the filter is applied before each integration process is carried out. This ensured that each signal to be integrated contained no low frequency components before the integration and was thus intended to minimise the trends in the estimated signals. It is essential to note that the filter must be applied, not only to the integrated signals, but also to the measured force and acceleration signals to ensure similar phase shift characteristics for all the signals used in the subsequent analysis. A sample comparison between estimated and exact displacement time histories is shown in Fig. (4.13) for the trapezium rule integration case. It can be seen that the filtering process has been able to remove the trends. Obviously, the G_y and

G_x values will not be helpful in this case due to the large phase shift between the estimated and exact signals. However, the identified parameters showed similar quality to those obtained when using the least squares approach. Errors are presented in table (4.6).

% error	Trapezium	Simpson	3/8	Bode	Cubic spline
Stiffness	2.58	-0.17	-0.16	-0.55	1.24
Damping	1.30	0.03	0.01	0.19	-0.04

Table (4.6). Errors in parameters for high pass filtering case

The phase shift introduced by the implementation of a digital filter for the removal of the undesired trends can in principle be eliminated by applying the filter to the signal both in the forward and backward directions so allowing negative and positive phase shifts to cancel out [53]. A comparison between the exact and estimated displacement time histories for the trapezium rule case in Fig. (4.14) shows that the phase shift introduced previously by the filter no longer exists in the integrated signal. Because the filter is applied twice, it needs not be of such-high order.

The elimination of the phase shift problem means that the G_y and G_x values are useful parameters for assessing the quality of the integrated signals. The results of using this approach are shown in table (4.7). Once again the identified parameters are of similar quality to those obtained earlier. Errors are presented in table (4.8).

4.6.2. Trend removal in the frequency domain.

In the frequency domain integration approach the removal of trends from the estimated velocity and displacement signals can be carried out by simply suppressing or reducing the low frequency

	Trapezium rule	Simpson's rule	Simpson's 3/8 rule	Bode's rule	Cubic spline approach
G_y	0.987	0.997	0.997	0.996	0.997
G_x	0.973	0.956	0.980	0.920	0.986

Table (4.7). G_y and G_x values for the high pass filtering case.

% error	Trapezium	Simpson	3/8	Bode	Cubic spline
Stiffness	2.58	-0.26	-0.14	-0.66	1.24
Damping	1.30	0.07	-0.004	0.22	-0.04

Table (4.8). Errors in parameters after using filter in both directions.

components present in the frequency spectra of these signals before the inverse Fourier transformations are carried out. This is equivalent to using a high-pass digital filter but has the advantage of maintaining the amplitude and phase characteristics of the unfiltered frequency components of interest.

A simple and rather obvious way is to multiply the frequency spectra by a rectangular frequency window which is zero below the cut-off frequency. The process is merely a convolution of two time signals but is carried out in the frequency domain using, for example,

$$\hat{X}(\omega) = F(\omega) * X(\omega) \quad \ldots\ldots\ldots\ldots\ldots\ldots\ldots (4.24)$$

where $F(\omega) = 0$ for $\omega \leq \omega_c$

$= 1$ for $\omega > \omega_c$

and ω_c is the chosen cut-off frequency and X and $\hat{X}$ are the raw and the filtered spectra. The phase is clearly unaffected.

A flow chart of the integration and the trend removal process in the frequency domain is shown in Fig. (4.15). Once the velocity and displacement spectra are obtained, the displacement amplitude spectrum is plotted in order to select the cut-off frequency of the frequency window to be used for suppressing the low frequency components. Note that the same filtering process is also applied to the acceleration and force spectra so that all the signals used in the force-state mapping are filtered in the same way. The rectangular window proposed is actually not physically realisable because it is non-causal (i.e. its impulse response is finite for negative time). Alternative window shapes could be used too, for example a window varying linearly from zero at $\omega=0$ to unity at $\omega=\omega_c$ or true high pass filter shapes.

The cut-off frequency should be selected with care. Too high an ω_c would suppress some frequency components in the signal itself and too low an ω_c would leave some trend in the signal. Also the amplitude of the spectrum at the cut-off frequency should be small enough to minimise the "ringing" effect which could be introduced into the time signal by the artificial windowing.

When the example data shown in Fig. (4.9) was filtered using a cut-off frequency of 18 Hz (5% of Nyquist frequency), the G_y value improved from 0.983 to 0.997 and the G_x value from 0.532 to 0.991. The stiffness and damping parameters were obtained with errors -0.03% and 0.04% respectively. The results are a considerable improvement upon those obtained without filtering and are in fact the best so far.

4.6.3. Further comments on least squares trend removal.

In the process of testing the use of least squares curve fitting to remove trends from time signals, a rather interesting feature emerged. Consider the earlier example and allow a very small DC value of 0.2% of the maximum to be added artificially to the

acceleration signal. The resulting velocity and displacement signals are compared to the exact signals in Fig. (4.16); the linear and parabolic trends clearly need to be removed before further analysis.

The velocity trend was removed successfully using a first order (i.e. linear) polynomial, the G_y value being 0.998. However the resulting displacement signal after removing trend using second and third order polynomials is shown in Fig. (4.17). The results are surprisingly poor, the best being for the second order polynomial with a G_x value of only 0.892. However the result was improved to $G_x = 0.976$ by further removing a linear trend from the signal in what is then a two-stage trend removal process. Using higher order polynomials was no better.

The significant errors in the trend removal are rather puzzling since the process is simple and least squares routines had been tested and precautions against rounding off errors and ill-conditioning taken (i.e. data normalisation). It was discovered that the results of the curve fit were biased because an oscillatory signal was superimposed upon the trend to be removed. This behaviour will be illustrated using a simple example.

Consider a sinusoidal displacement signal which has a parabolic trend present due to errors in the acceleration. Let the signal be described by

$$x(t) = a_0 + a_1 t + a_2 t^2 + a_3 \sin \omega t \quad \ldots\ldots\ldots\ldots (4.25)$$

In order to determine the trend, let a second order polynomial of the form $x_T = b_0 + b_1 t + b_2 t^2$ be fitted to the above signal. The least squares process seeks to minimise the sum of the squares of the residual error between the fitted curve x_T and the signal x by suitable choice of the parameters b_0, b_1 and b_2. The parameters are normally evaluated numerically using discrete values of the

data x_i at time t_i. The equations to solve are

$$\begin{bmatrix} \Sigma 1 & \Sigma t_i & \Sigma t_i^2 \\ & \Sigma t_i^2 & \Sigma t_i^3 \\ & & \Sigma t_i^4 \end{bmatrix} \begin{Bmatrix} b_0 \\ b_1 \\ b_2 \end{Bmatrix} = \begin{Bmatrix} \Sigma x_i \\ \Sigma x_i t_i \\ \Sigma x_i t_i^2 \end{Bmatrix} \quad \ldots.(4.26)$$

where all summations are for i=1,2,.. N and N is the number of data points. It is possible, however, to calculate b_0, b_1 and b_2 analytically rather than numerically be replacing the summations by integrations over the cycles of the sinewave; for example $\sum x_i t_i$ becomes $\int_0^T x\ t\ dt$ where $T= 2\pi m/\omega$ and m is number of cycles in the sinusoid.

Using the true expression for x(t) in equation (4.25), evaluating the integrals and solving the simultaneous equations (4.26) yields

$$b_0 = a_0 + \frac{3}{\pi\ m}\ a_3$$

$$b_1 = a_1 - \frac{3\omega}{\pi^2\ m^2}\ a_3 \qquad \ldots\ldots\ldots\ldots\ldots(4.27)$$

$$b_2 = a_2$$

Clearly the values of b_0 and b_1 are biased since if the trend had been determined correctly then $b_0 = a_0$ and $b_1 = a_1$. When the parameters are used to remove the trend from x(t) the resulting signal is

$$x_r(t) = x(t) - x_T(t) = a_3 \sin \omega t - \frac{3}{\pi\ m}\ a_3 + \frac{3}{\pi^2\ m^2}\ a_3 t \qquad \ldots(4.28)$$

and the bias has led to a residual linear trend which could be removed largely by a further curve fit.

The bias effect clearly depends upon the number of cycles m of the sinusoid. The worst case occurs for a single cycle (m=1) in which

case it can be seen from equation (4.28) that the bias is of the same order as the sine wave amplitude.

An example of a sine wave with a parabolic trend is shown in Fig. (4.18) for $a_0=a_1=a_2=a_3=10$, $\omega=4\pi$ and m=8. The fitted quadratic curve is shown and can be seen to be slightly biased by examining each end of the signal. The identified parameters were $b_0=11.174$, $b_1=9.413$ and $b_2=10.0001$ for 256 data points and these are very close to the results expected from equations (4.27). When the fitted curve was removed from the original signal, the result is compared to the exact sine wave in Fig. (4.19) and still seen to include a linear trend as expected. Other examples with different trends and different order fitted models also show bias, getting worse for higher order models.

The reason behind this bias effect is rather obvious. When a cycle of a sine wave is added to a low order polynomial then the contribution of the positive half cycle to terms such as $\sum x_i t_i$ will not be "balanced" by the negative half cycle at a later time. The effect for the entire signal will be more significant when only a few cycles are used and higher order fits which included values of x_i weighted by higher powers of t_i. This is presumably the reason behind the result in Fig. (4.17) being worse for the third order polynomial case. This is clearly a drawback in using least squares curve fitting to remove significant trends.

When the example in Fig. (4.16), with the artificial DC acceleration error, was tackled using digital high pass filtering in two directions then the results were extremely accurate. Similarly the frequency domain approach gave excellent results because the zero frequency spectral line for the acceleration is actually set to zero so the DC offset has no effect.

4.7. Sensitivity of integration to measurement noise.

So far, the acceleration signal has been generated as a nominally

noise-free signal and thus the integration techniques have not been tested in the presence of measurement noise in the acceleration. This is believed to be an important point and should be considered in this investigation since noisy acceleration signals may well be encountered when dealing with real structures.

Measurement noise is usually of random nature and it is generally valid, when dealing with theoretical examples, to generate a sequence of random numbers with a Gaussian distribution and add it to the system response.

The linear single-d.o.f. example considered earlier in section (4.5) was used here. The measurement noise sequence was added to the acceleration signal generated using the simulation such that the noise R.M.S. was 2% of the acceleration R.M.S.

(a). Time domain integration.

The resulting displacement signals from time domain integration are shown in Figs. (4.20.a-e); the trends are far larger than those for the noise-free data in Figs. (4.4.a-e). Note that the presence of higher frequency noise is evident early in the sweep for the higher order integration rules.

An attempt was made to remove these large trends by using the least squares approach to fit a straight line to the velocity and a parabola to the displacement. The quality of the integration improved but was still unacceptable as shown for the Trapezoidal rule in Fig. (4.21). The use of higher order polynomials or successive fits did not improve the situation. This behaviour is believed to be a combination of bias problem mentioned in section (4.6.3) and the fact that the difference between the approximate and exact signals may not be represented by a simple polynomial.

It was therefore decided to use the high pass digital filtering approach instead. The resulting signals are presented in Figs

(4.22.a-e); they are compared with the exact signals which are also corrupted by 2% measurement noise as if they had been measured separately. The G_y and G_x values are presented in table (4.9).

	Trapezium rule	Simpson's rule	Simpson's 3/8 rule	Bode's rule	Cubic spline approach
G_y	0.972	0.971	0.970	0.968	0.971
G_x	0.948	0.789	0.795	0.717	0.952

Table (4.9). G_y and G_x values for the added noise case.

It would appear from the table and Figs. (4.22.a and e) that the trend has been removed successfully for the Trapezoidal and cubic spline approaches. However the results for the higher order integration rules are still rather poor due to the way they amplify any high frequency content; the results could be improved by low pass filtering but it really seems that these rules are unsuitable in practice.

The errors in the parameters estimated from the force-state map are shown in table (4.10).

% error	Trapezium	Simpson	3/8	Bode	Cubic spline
Stiffness	2.49	-4.27	-4.08	-7.74	1.14
Damping	1.31	0.84	2.17	1.19	-0.05

Table (4.10). Errors in parameters for the added noise case.

These results indicate that the Trapezoidal rule is less sensitive to the presence of noise in the acceleration than the other standard integration rules since it is free from the "unstable" behaviour introduced by the other rules. However the cubic spline approach yielded the best identified parameters and showed to be insensitive to the presence of noise in the acceleration too.

(b). Frequency domain integration.

It might be expected that the frequency domain integration approach would be less sensitive to noise since the nature of the integration process implies that the higher frequency components in the noise are reduced significantly relative to the components of interest. However lower frequency noise content would require filtering to prevent large trends. In fact the frequency domain integration approach gave quite good results when it was applied to the above example. The cut-off frequency of the window used for removing the low frequency components from the frequency spectra of the signals was 5% of the Nyquist frequency (i.e. 18 Hz). The G_y and G_x values were 0.977 and 0.970 respectively. A comparison between the exact displacement with noise added and the estimated displacement is shown in Fig. (4.23). Clearly the integration process has attenuated the higher frequency noise components.

An interesting point is that the identified system parameters obtained using the estimated velocity and displacement signals were actually closer to the exact values than those obtained using the exact signals with noise added as can be seen in table (4.11). The results are also better than those obtained using time domain integration.

% error	Exact signals with noise used	Estimated signals used
Stiffness	-0.11	-0.035
Damping	-0.99	0.038

Table (4.11). Errors in parameters for exact signals with noise and estimated signals used.

4.8. Integration of nonlinear data.

So far the work in this chapter has been concerned with the

integration of the acceleration response of a linear system, the response being proportional to the input force. However the response of a nonlinear system is not proportional to the input force and contains more information about the system since it no longer can be characterised by only three parameters (mass, stiffness and damping). It is therefore essential to investigate how the parameters of a nonlinear system might be affected by any shortcomings in the integration process used.

The single-d.o.f. system considered for this purpose has the following linear and nonlinear parameters

$m = 1$ kg
$k = 100000$ N/m $\quad (f_n = 50.33$ Hz$)$
$c = 20$ N/m/s $\quad (\zeta = 3.1\%)$
$\beta_1 = -10^9$ N/m^3
$\beta_2 = 20$ N/m^2/s^2

where β_1 and β_2 are the coefficients of cubic stiffness and quadratic damping elements respectively. The excitation used was a sinusoidal sweep from 47 to 53 Hz with a time step of 0.00062 sec. The force was stopped after 50% of the time window as before. The number of points in the force signal was 1024 points which yielded 512 point response signals. The corresponding two dimensional force-state map for the exact raw data is shown in Fig. (4.24). Clearly the nonlinear stiffness and damping behaviour is significant.

(a). Time domain integration.

When the acceleration response of the nonlinear system was integrated using time domain methods, the results showed similar behaviour to those seen for the linear system in Fig. (4.4) and therefore trend removal was necessary. The undesired trends were firstly removed by curve fitting using a first order polynomial for the velocity and a second order polynomial for the

displacement. The resulting G_y and G_x values for the estimated signals are given in table (4.12). and the errors in the system parameter estimates obtained from the force-state map are shown in table (4.13).

	Trapezium rule	Simpson's rule	Simpson's 3/8 rule	Bode's rule	Cubic spline approach
G_y	0.987	0.995	0.995	0.994	0.995
G_x	0.966	0.923	0.956	0.867	0.974

Table (4.12). G_y and G_x values for the nonlinear example.

% error	Trapezium	Simpson	3/8	Bode	Cubic spline
Stiffness	2.64	-2.95	-0.91	-8.51	1.26
Damping	-0.67	6.19	4.02	13.32	-0.15
Cubic stiffness	8.94	-19.10	-5.50	-55.73	4.29
Quadratic damping	4.45	-5.73	-3.87	-11.96	-0.01

Table (4.13). Errors in parameters for the nonlinear example.

Once again, in general, the errors were larger for the higher order integration rules; the nonlinear coefficients seem especially sensitive to the "unstable" behaviour of these rules which is not surprising. The best results were obtained using the cubic spline approach.

Similar results were also obtained using high pass filtering with a 10 Hz cut-off frequency. However it should be noted that high pass filtering has the potential of altering the nonlinear

relationship between the input and response signals because of the imperfection nature of digital filters which have a finite cut-off rate and thus modify the amplitude characteristics of the filtered signals significantly if the cut-off frequency is too high.

When the procedure was repeated using half the step size for the simulation and integration the results improved significantly, especially for the higher order rules because much smaller errors were introduced at the point where the acceleration ceased.

(b). Frequency domain integration.

When the acceleration response of the nonlinear system was integrated using the frequency domain approach and lower frequency components suppressed by a cut-off at 5% of the Nyquist frequency , the G_y and G_x values were 0.995 and 0.985 respectively. The errors in the system parameter estimates were -0.02, -0.20, -0.06 and 0.14 % for the stiffness, damping, cubic stiffness and quadratic damping respectively. These are far better than the corresponding results for the time domain integration but are actually of similar quality to those obtained for the higher order integration rules when the step size was halved.

Finally, in order to see how frequency domain integration coped with larger time steps the procedure was repeated with $\Delta t=0.002$ sec, almost four times the nominal value. This corresponded to only 8 or 9 points per cycle over the frequency range of interest. The G_y and G_x values were 0.996 and 0.989 and the errors in the parameter estimates were -0.41, 1.55 -1.44 and 0.04 % for the stiffness, damping, cubic stiffness and quadratic damping respectively. The results are quite good although have deteriorated slightly probably due to imperfection in the suppression process of the undesired low frequency components. The cut-off frequency used was 8% of the Nyquist frequency.

The possibility of using larger time steps with the frequency

domain integration approach is very useful since an increase in the length of the data acquisition window is possible. Thus it is more likely for lightly damped structures that the acceleration response signal will die away sufficiently before the end of the window is reached. This means that a leakage-free frequency domain integration may be carried out. Note that none of the time domain integration methods was able to cope with such a large time step and the results were very poor.

4.9. Conclusion.

It has been shown that it is possible to obtain reasonable quality parameter estimates from the force-state mapping approach where the velocity and displacement signals are estimated from the acceleration by time or frequency domain integration.

All the time domain methods suffer from the problem that trends can be introduced due to measurement noise, errors in the initial conditions, sudden change in the acceleration and a non-zero mean in the sampled acceleration. These trends can be largely removed using least squares curve fitting or preferably digital high-pass filtering in both directions because the least squares approach can suffer from a bias problem and is ineffective when the trend is not a fairly simple polynomial. On the other hand care needs to be taken when filtering because the nonlinear relationship between the signals can be corrupted if the cut-off frequency is too high.

A more serious problem is that the transfer functions for the higher order integration rules (Simpson, Simpson 3/8 and Bode) show that high frequency content in the signals can be significantly amplified. In the examples considered, where the sweep excitation was suddenly stopped and the discontinuity in the acceleration slope triggered off a response at half the sampling frequency, the results could be improved by increasing the sampling rate. However this is somewhat artificial because any measurement noise would lead to a high frequency oscillation which

would gradually grow unless low pass filtering was used.

For this reason the most suitable time domain methods considered in this work seem to be the Trapezoidal rule and the cubic spline approach. Although they suffer from a larger truncation error than the higher order rules, this can be reduced by a suitable choice of sampling rate. It is considered that the use of the cubic spline approach to obtaining the displacement directly from the acceleration is the most suitable compromise since it is more accurate than a double application of the Trapezoidal rule and does not have the sensitivity to higher frequency components of the higher order rules. It is also computationally quite efficient.

Finally it is considered that it may be more attractive to use frequency rather than time domain integration provided that the acceleration signal is essentially periodic which imposes certain restrictions upon the excitation. Only a swept sinusoidal excitation has been considered in this chapter but there is no particular reason why steady-state sine, cyclic random or even burst random excitation should not be used. The technique has the advantage over the time domain integration approach in that it is much less sensitive to the size of the time step and does not suffer from the "instability" problem because it is insensitive to the presence of high frequency measurement noise in the acceleration signal. The spurious low frequency components amplified by the integration process can be effectively removed by using a window in the frequency domain but care needs to be taken in selecting the cut-off frequency so as to minimise the ringing effect and the suppression of main components in the signals.

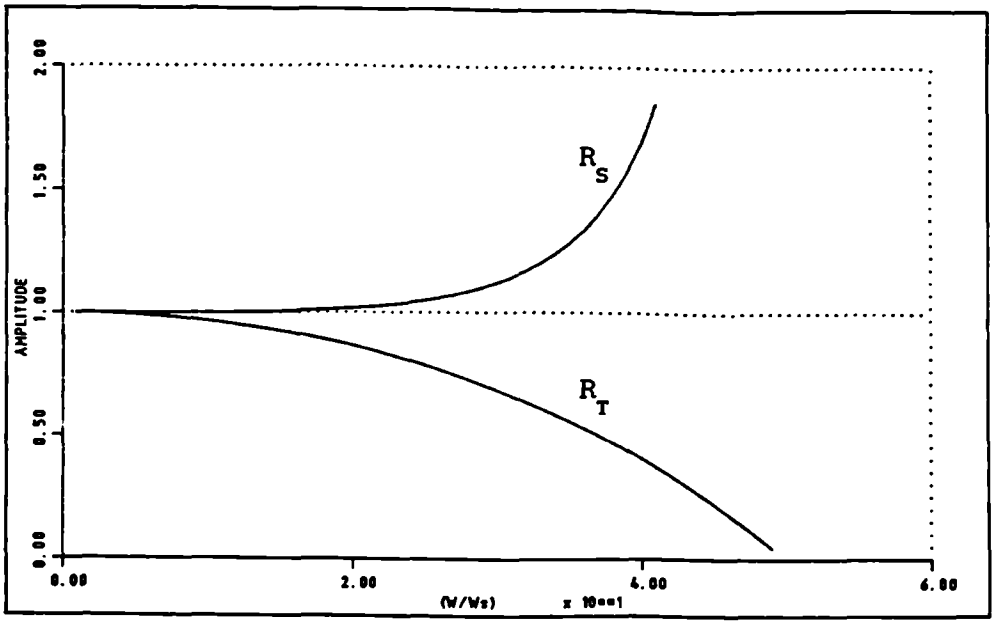

Figure 4.1. Comparison between transfer functions of single-stage integration for Trapezium and Simpson rules.

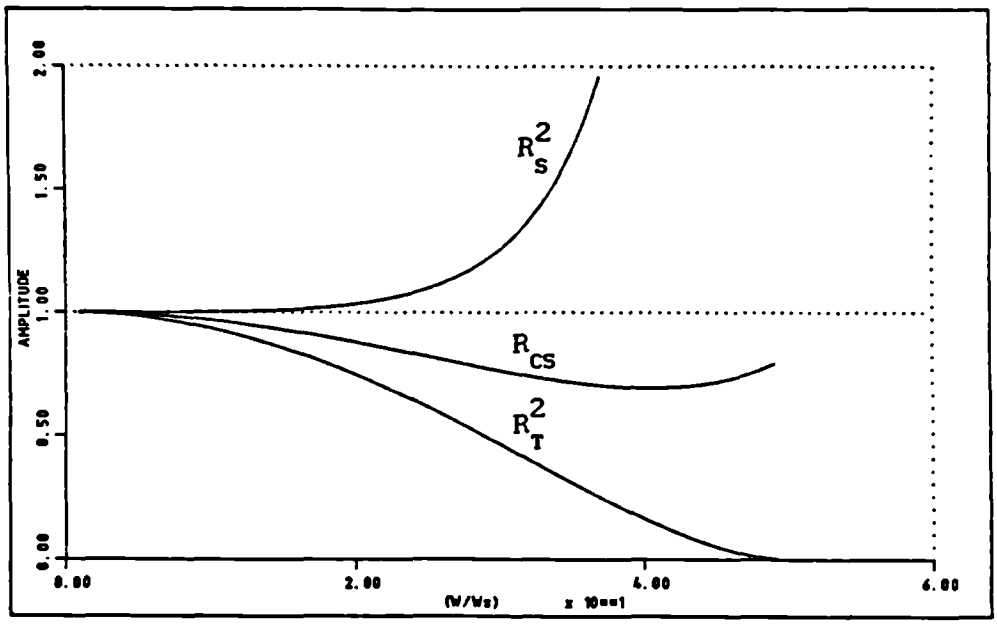

Figure 4.2. Comparison between transfer functions of two-stage integration for Trapezium and Simpson rules and the Cubic Spline approach.

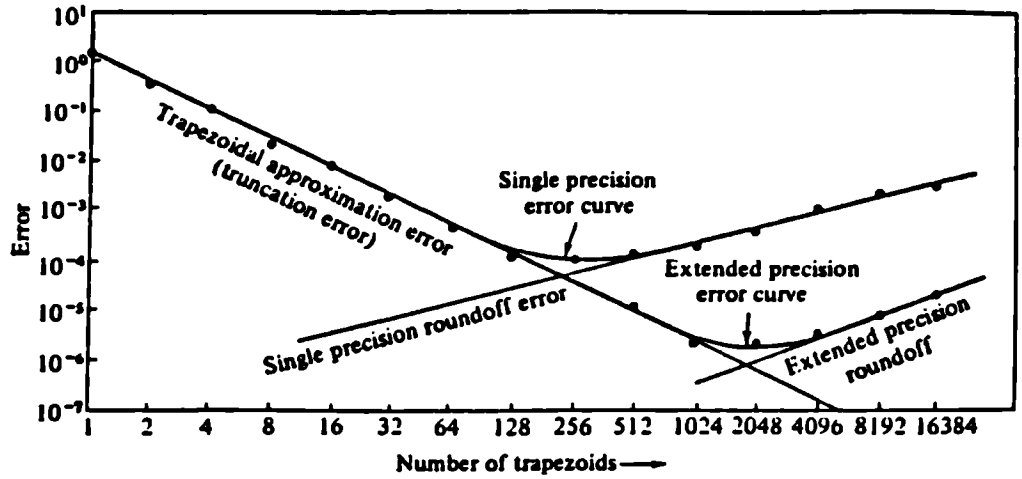

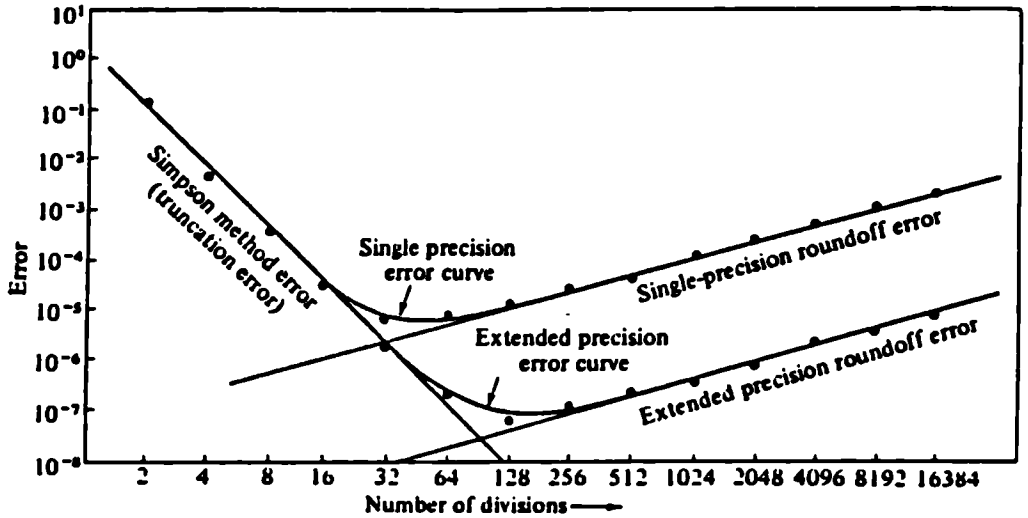

Figure 4.3. Variations of truncation and roundoff errors with number of points for a particular example, taken from reference [57].

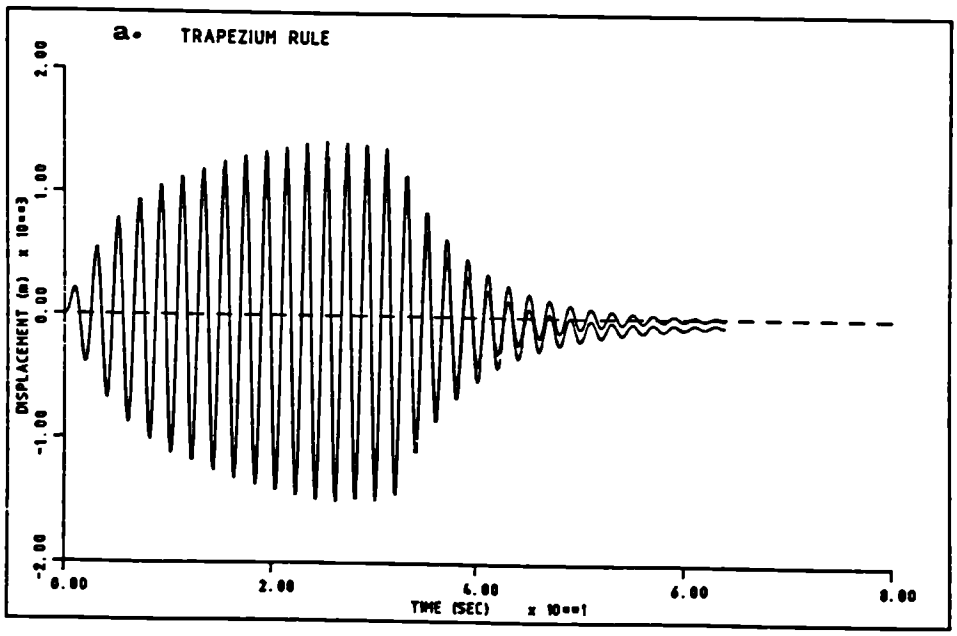

Figure 4.4.a. See next page for title.

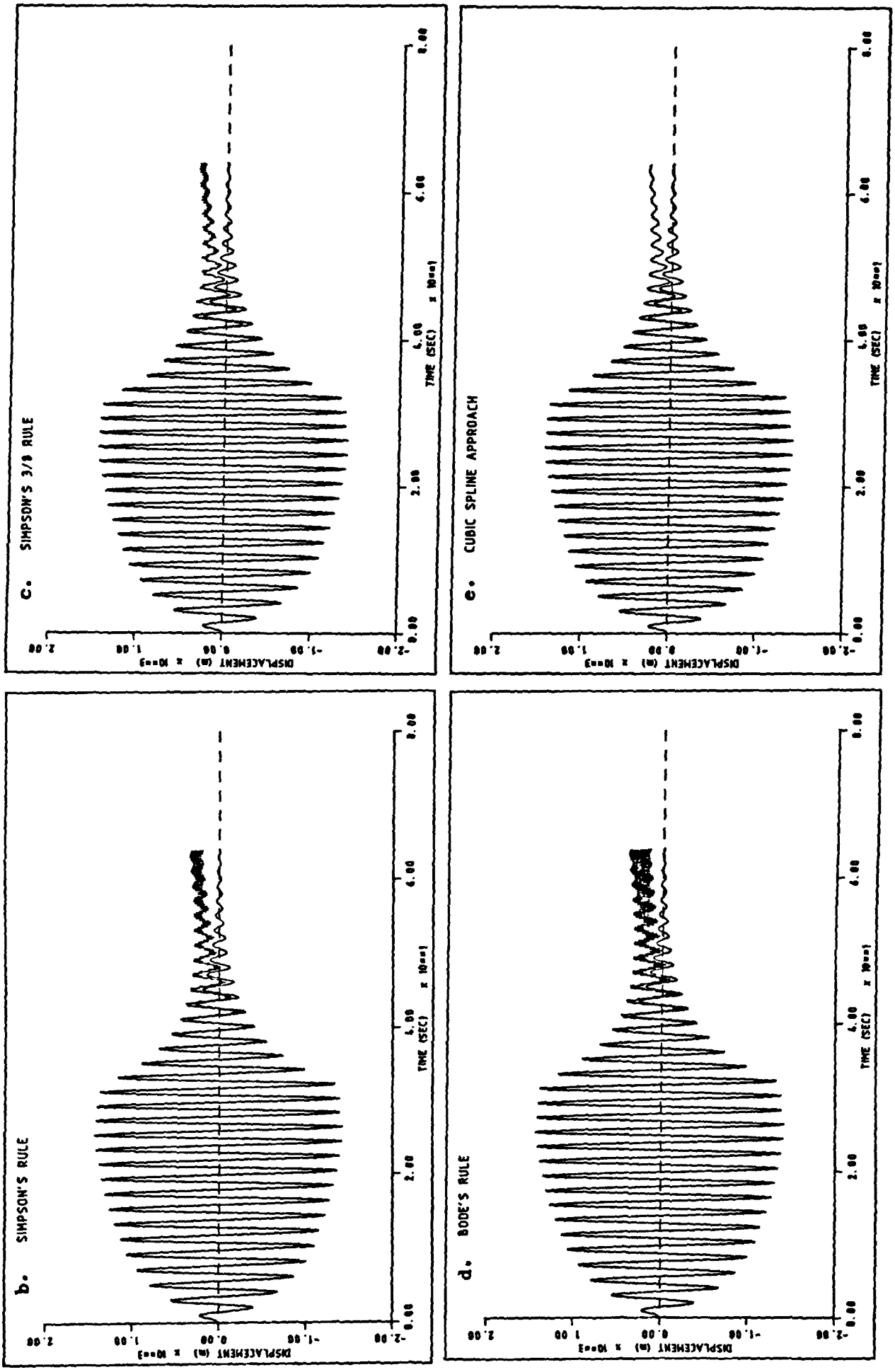

Figure 4.4. Comparison between exact and estimated displacement signals for the 4 time domain integration rules and the cubic spline approach.

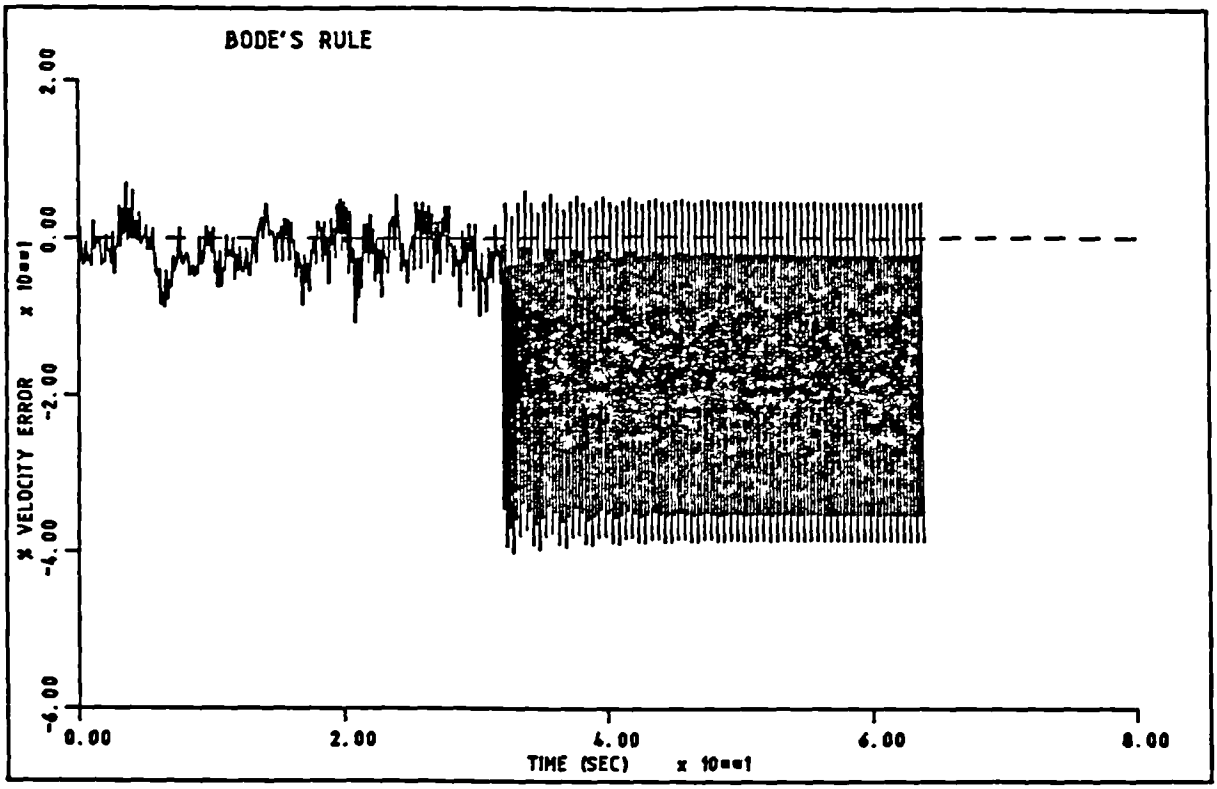

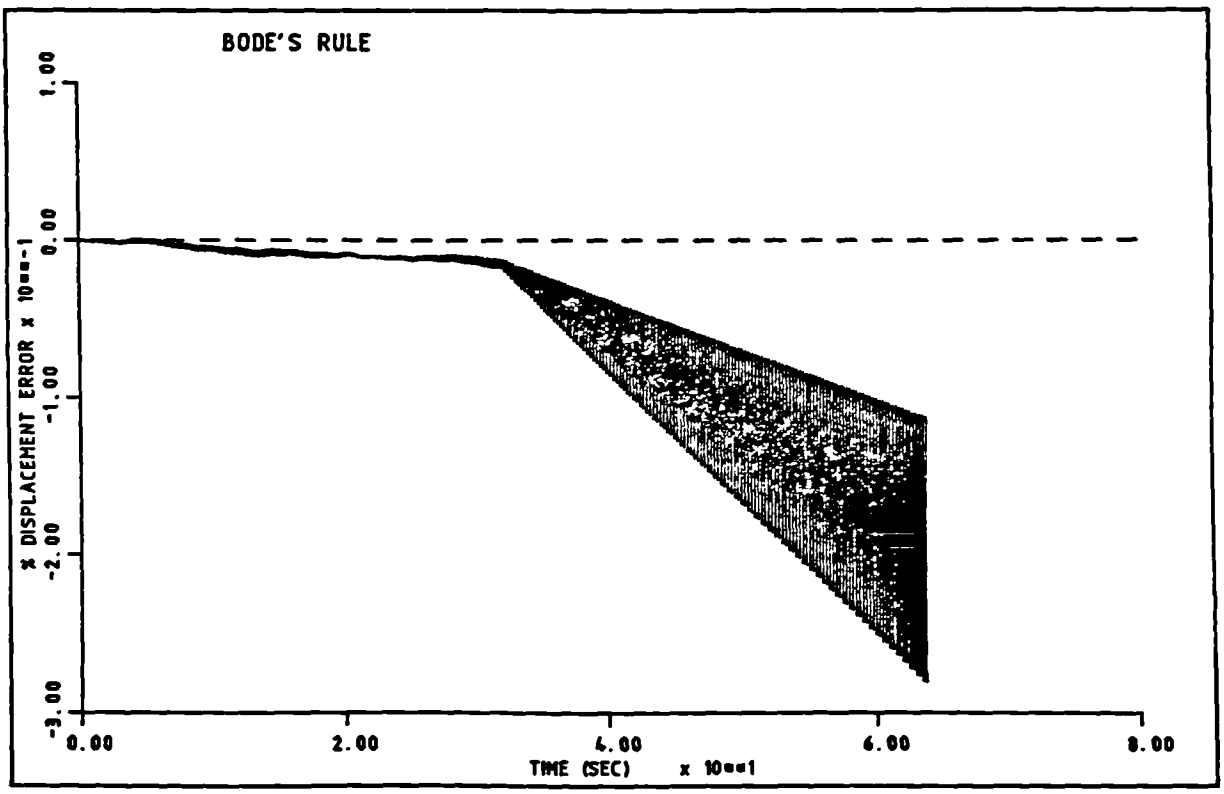

Figure 4.5. Variations of velocity and displacement errors with time for Bode's rule.

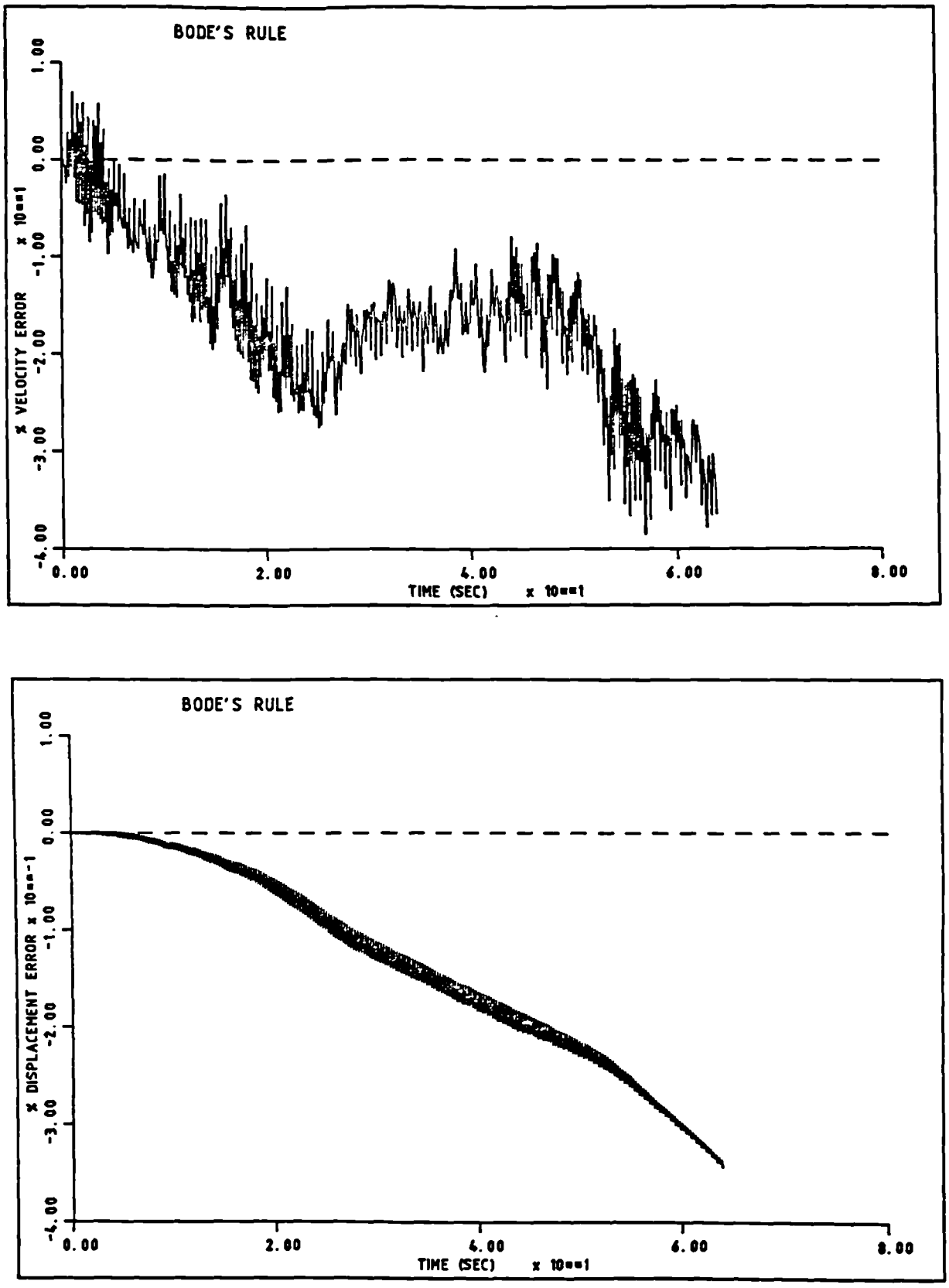

Figure 4.6. Variations of velocity and displacement errors with time for Bode's rule after maintaining the excitation over the entire window.

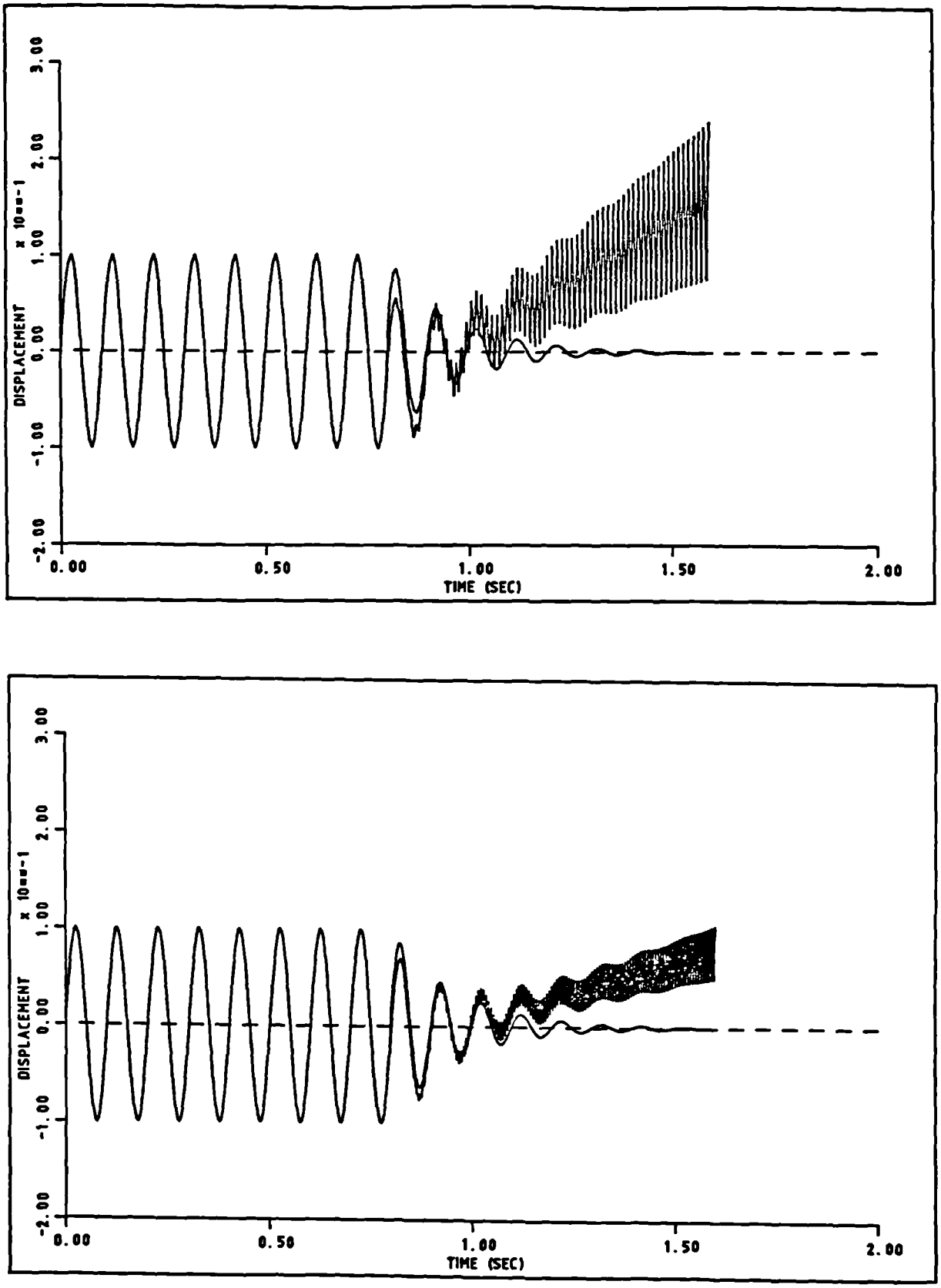

Figure 4.7. Comparisons between exact and estimated displacement signals for the analytical expression using 2 different sampling rates.

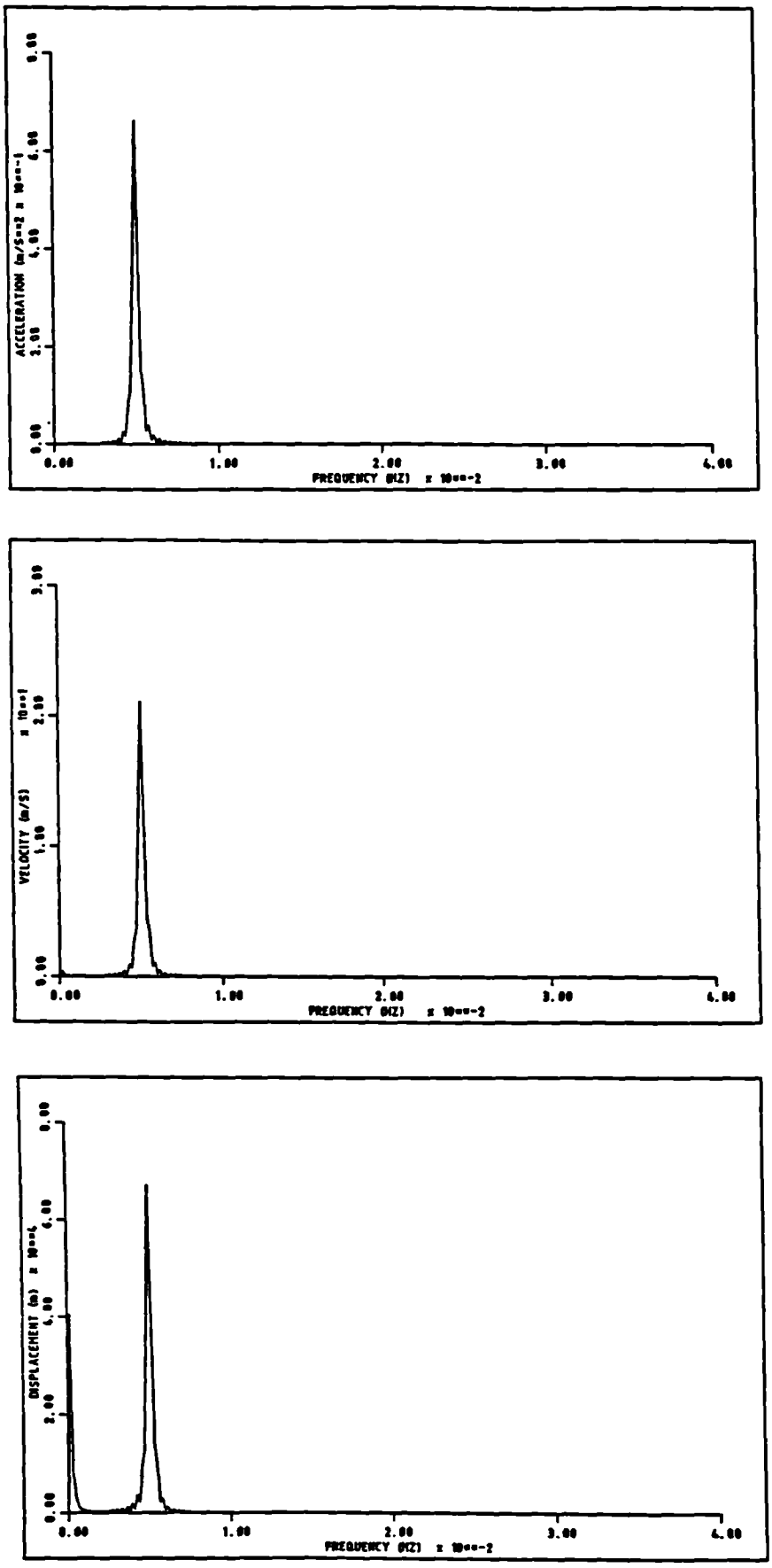

Figure 4.8. Amplitudes of acceleration, velocity and displacement spectra for the linear example of section (4.5).

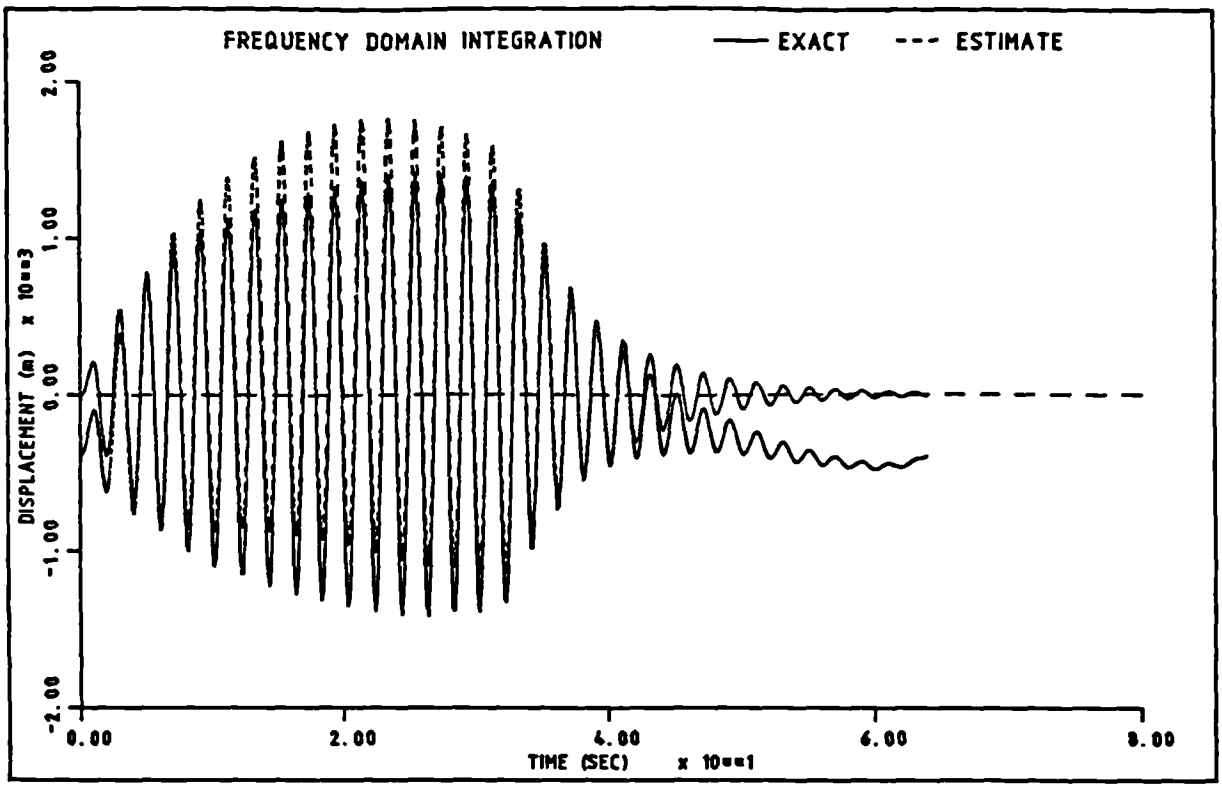

Figure 4.9. Comparison between exact and estimated displacement signals obtained using the frequency domain integration approach.

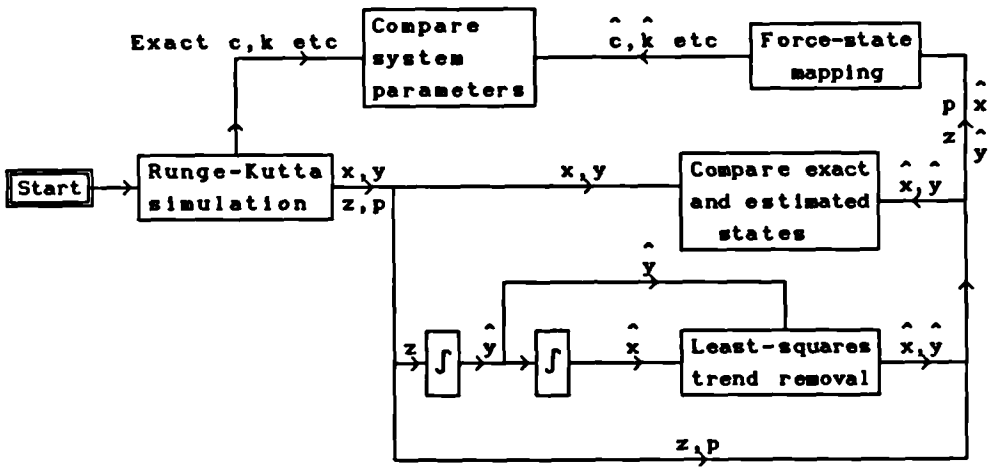

Figure 4.10. Flowchart of time domain integration and least squares trend removal.

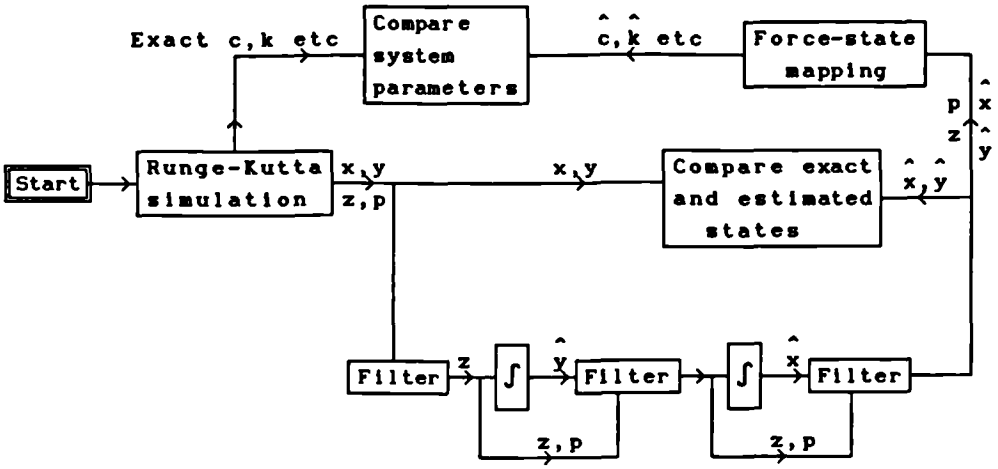

Figure 4.11. Flowchart of time domain integration and high pass filtering trend removal.

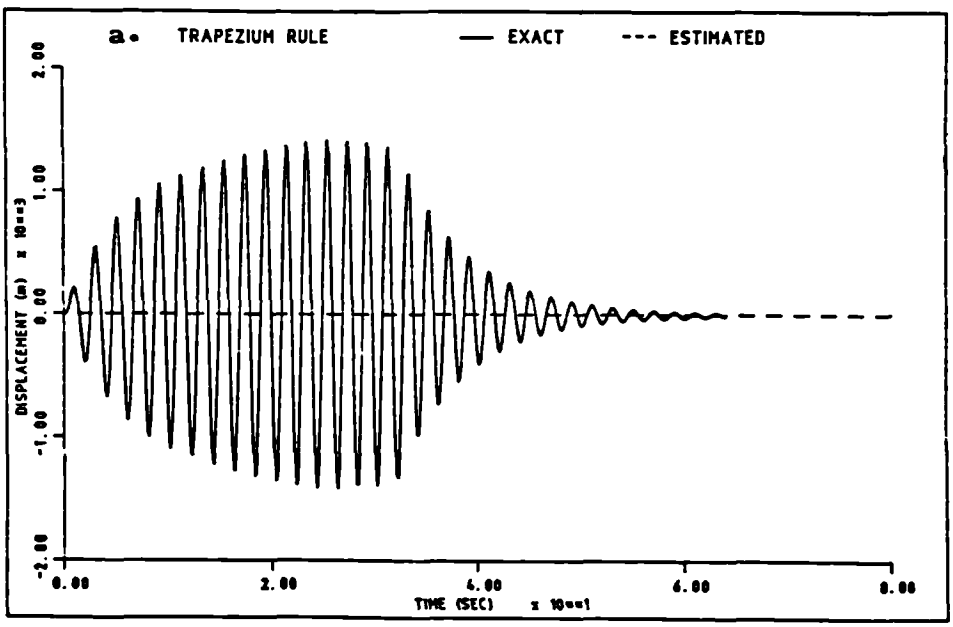

Figure 4.12.a. See next page for title.

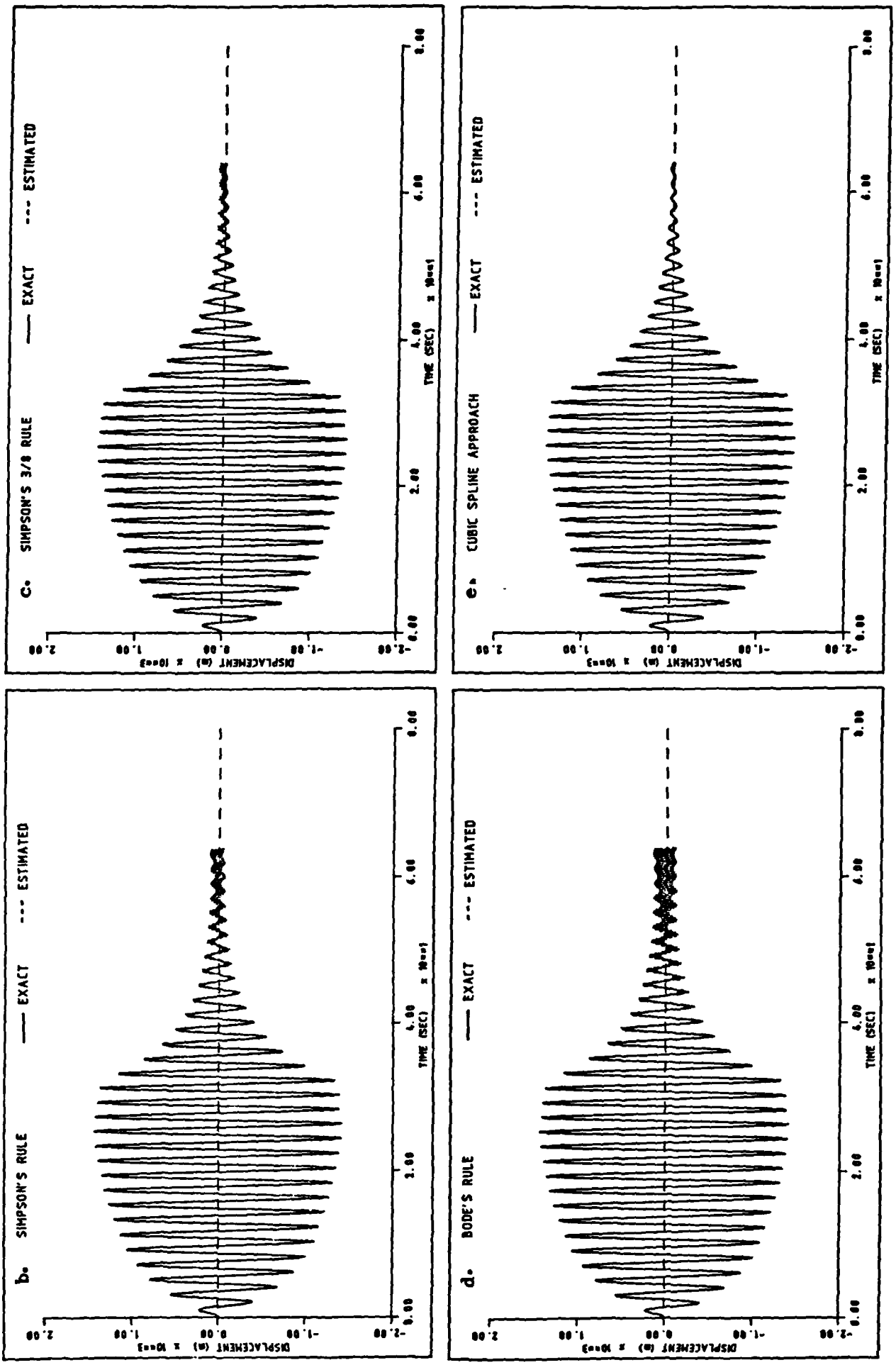

Figure 4.12. Comparisons between exact and estimated displacement signals for the least squares trend removal case.

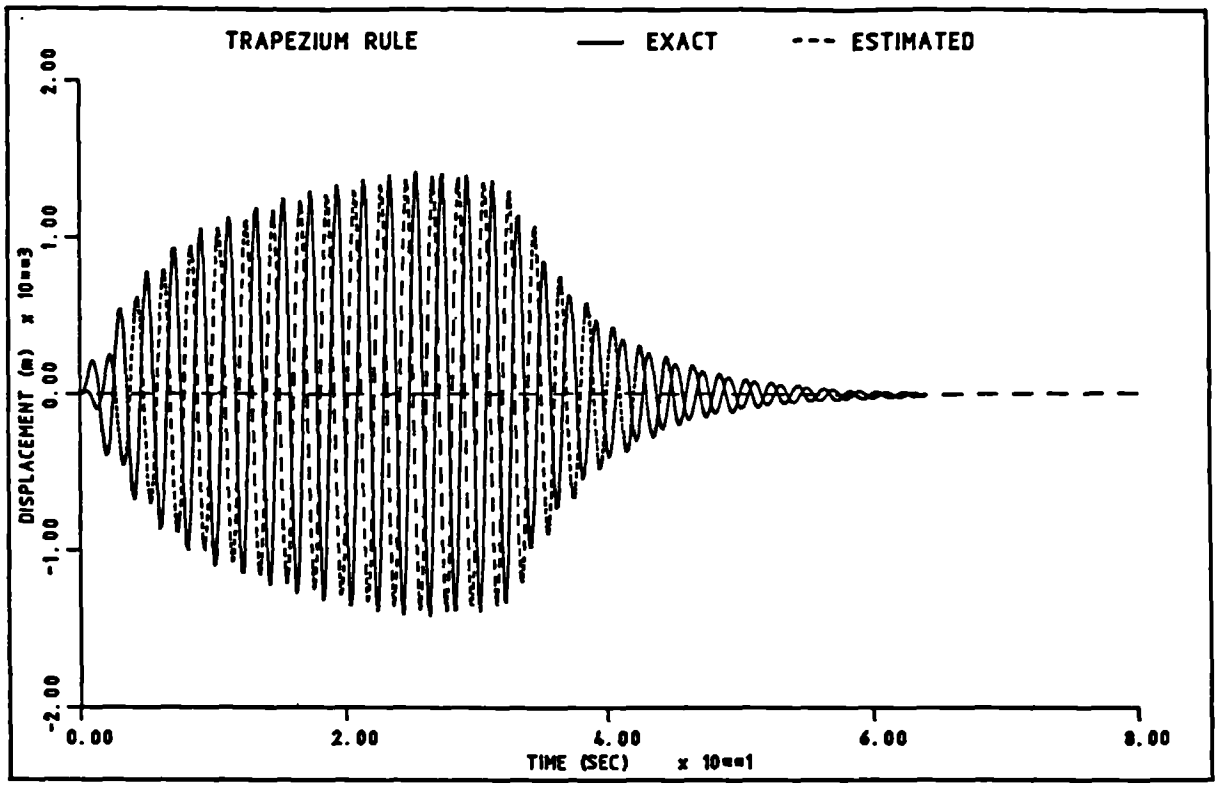

Figure 4.13. A sample comparison between exact and estimated displacement signals after trend was removed by applying a high pass filter in one direction.

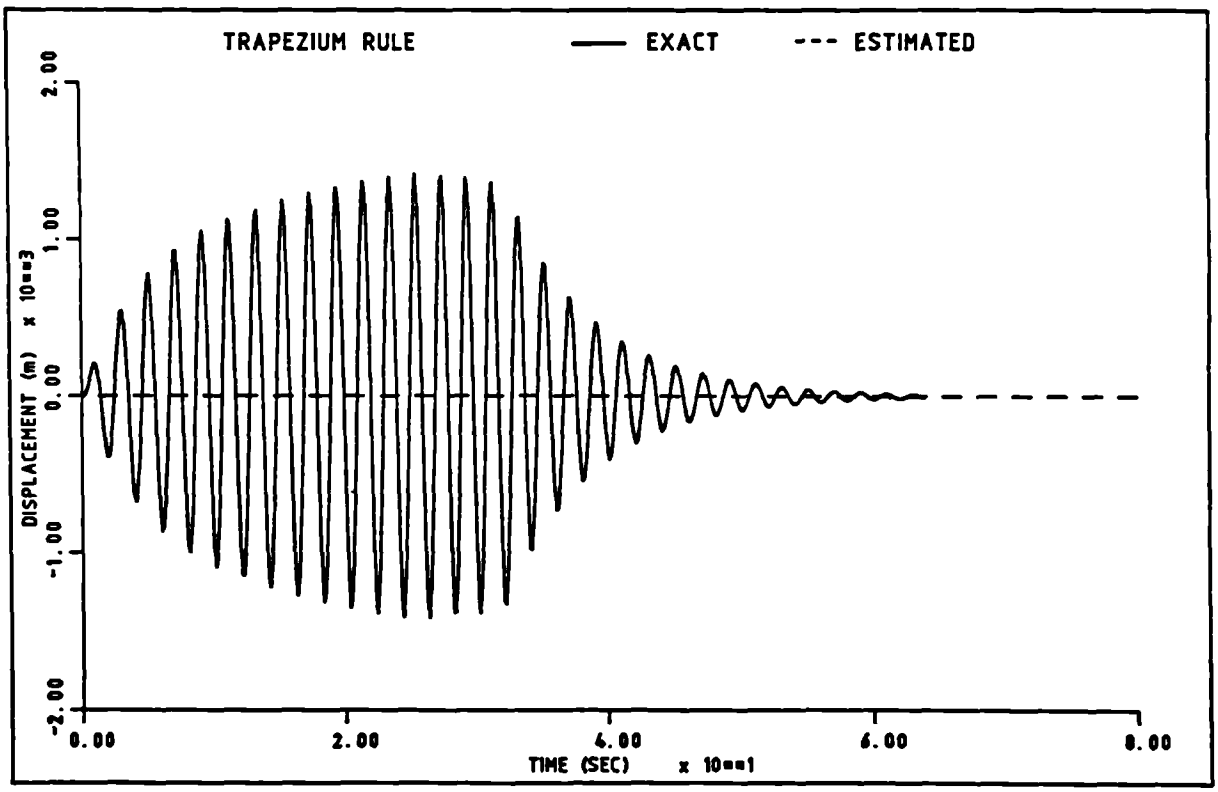

Figure 4.14. A sample comparison between exact and estimated displacement signals after trend was removed by applying a filter in two directions.

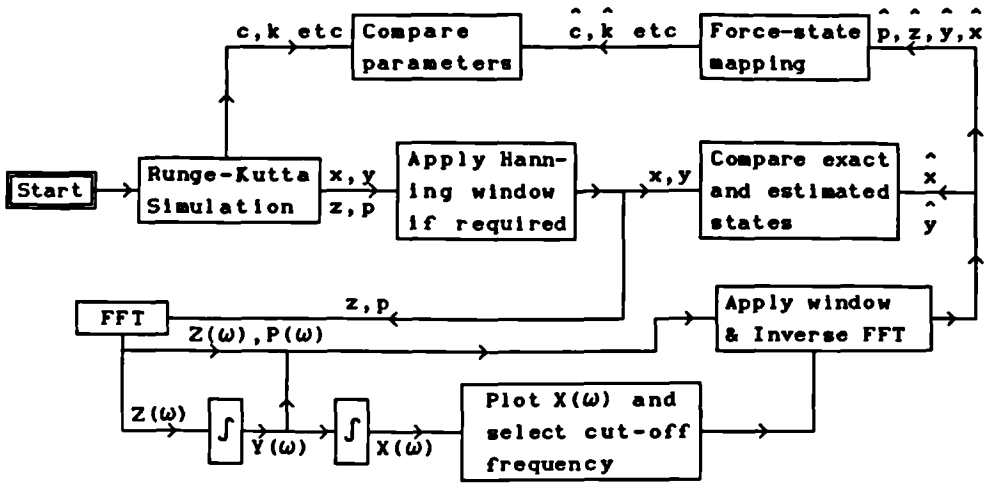

Figure 4.15. Flowchart of frequency domain integration.

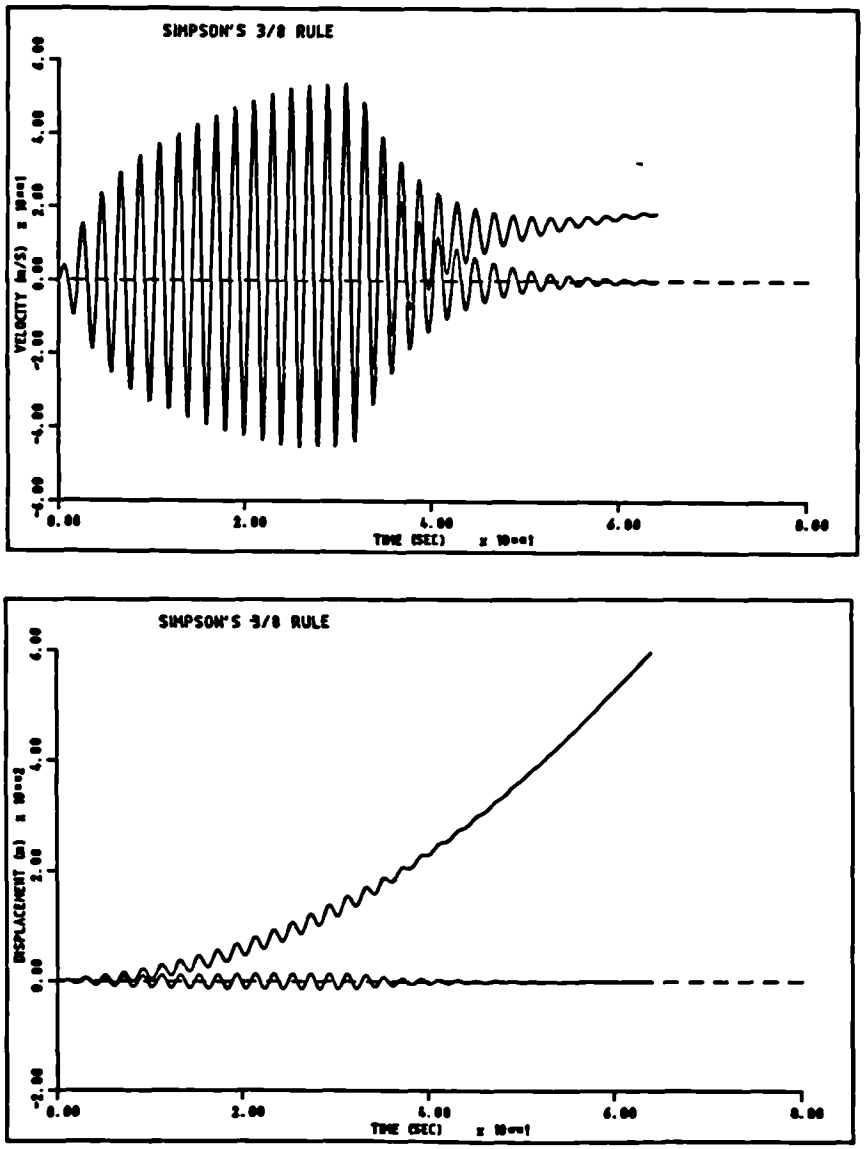

Figure 4.16. Comparisons between exact and estimated signals after adding 0.2% DC to the acceleration.

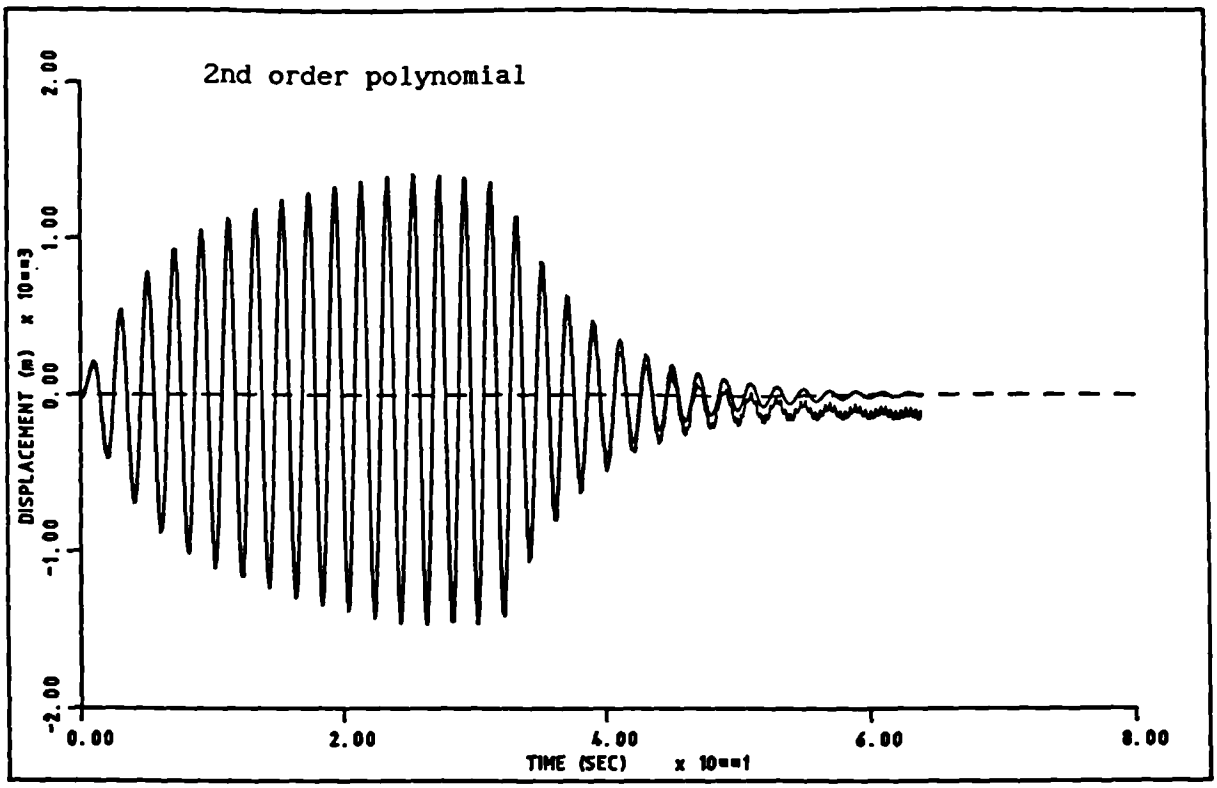

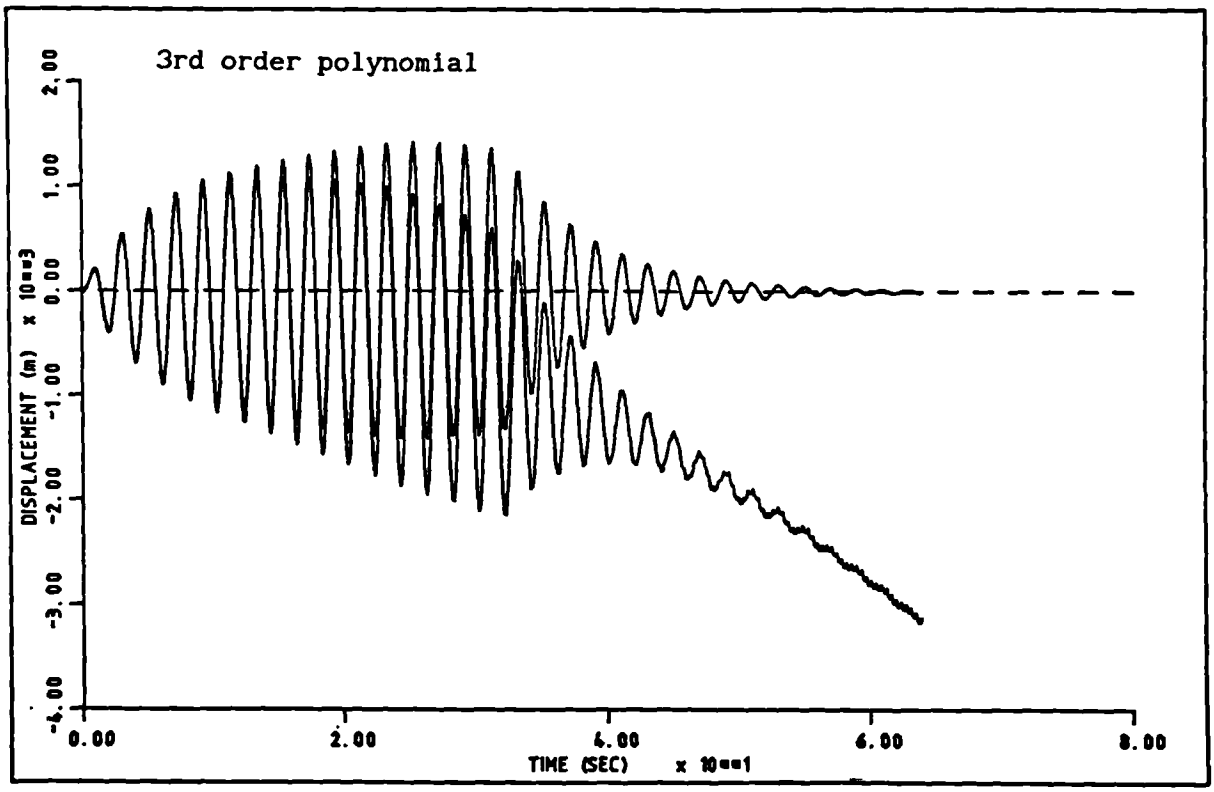

Figure 4.17. Displacement signal after removing trends of Fig. (4.16) by the least squares approach, using 2nd and 3rd order polynomials.

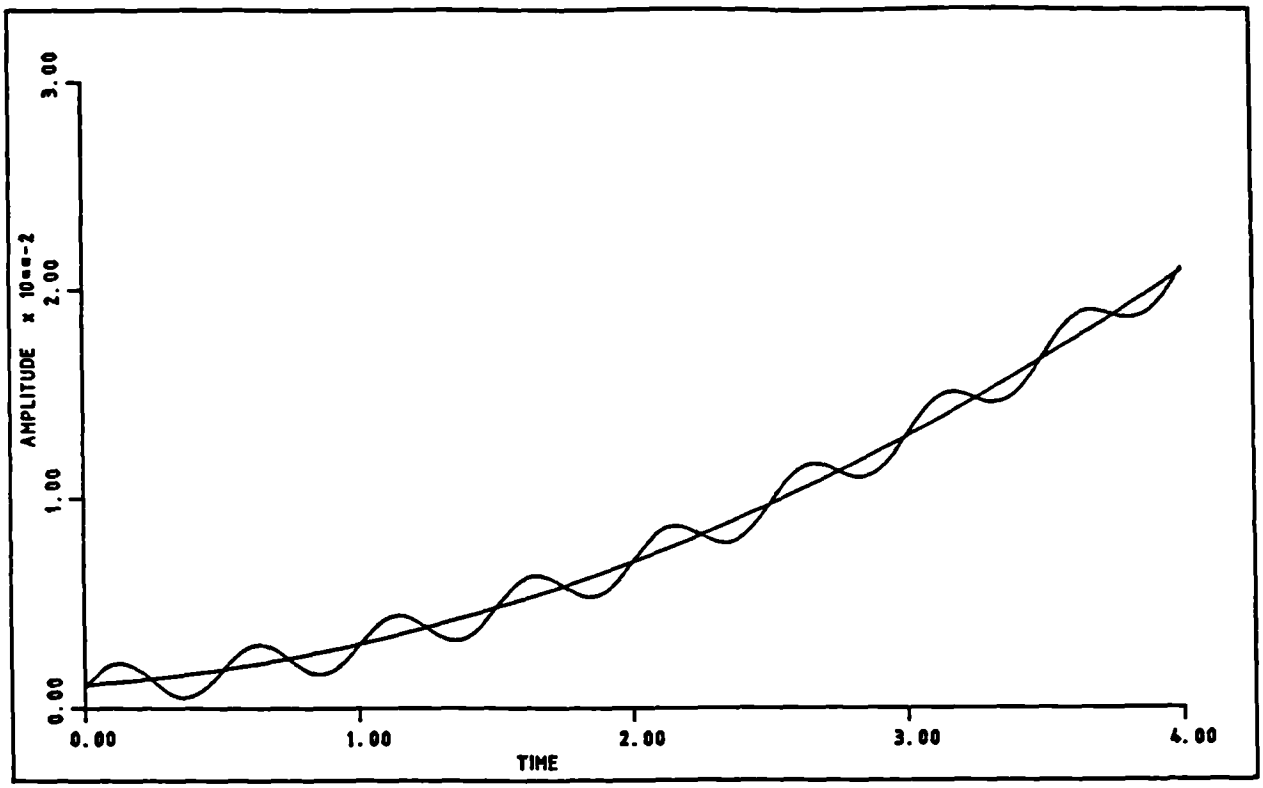

Figure 4.18. A sine wave with a parabolic trend.

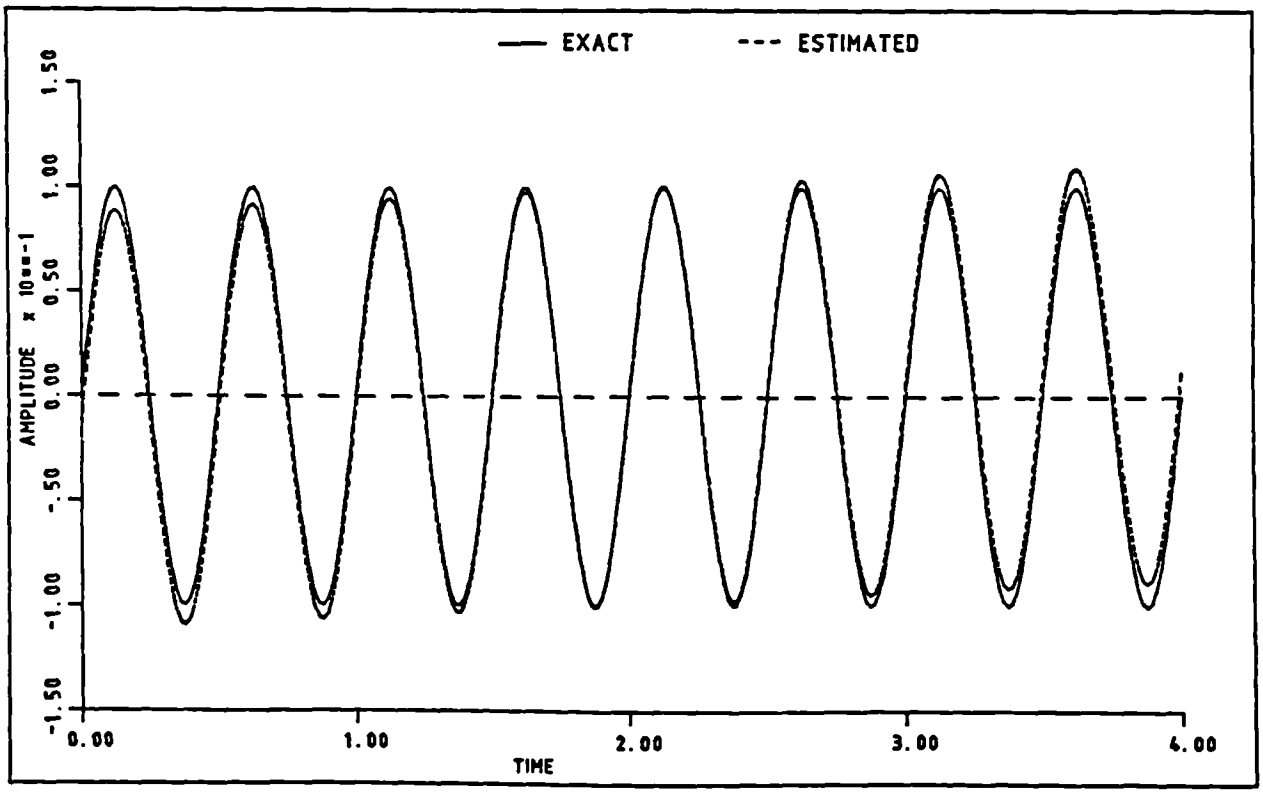

Figure 4.19. A comparison between exact and estimated signals after removing the parabolic trend of Fig. (4.18) by the least squares approach.

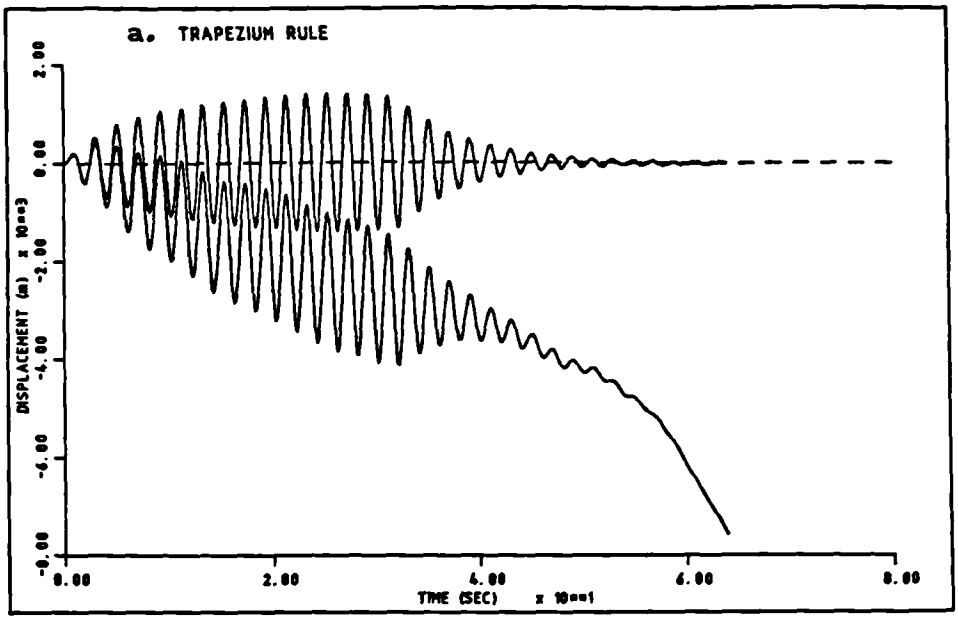

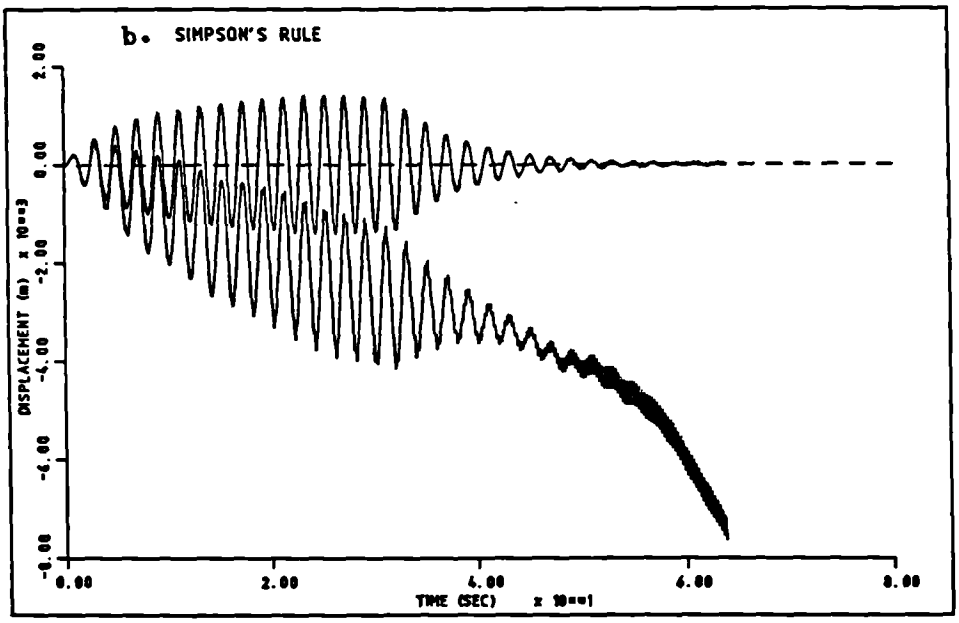

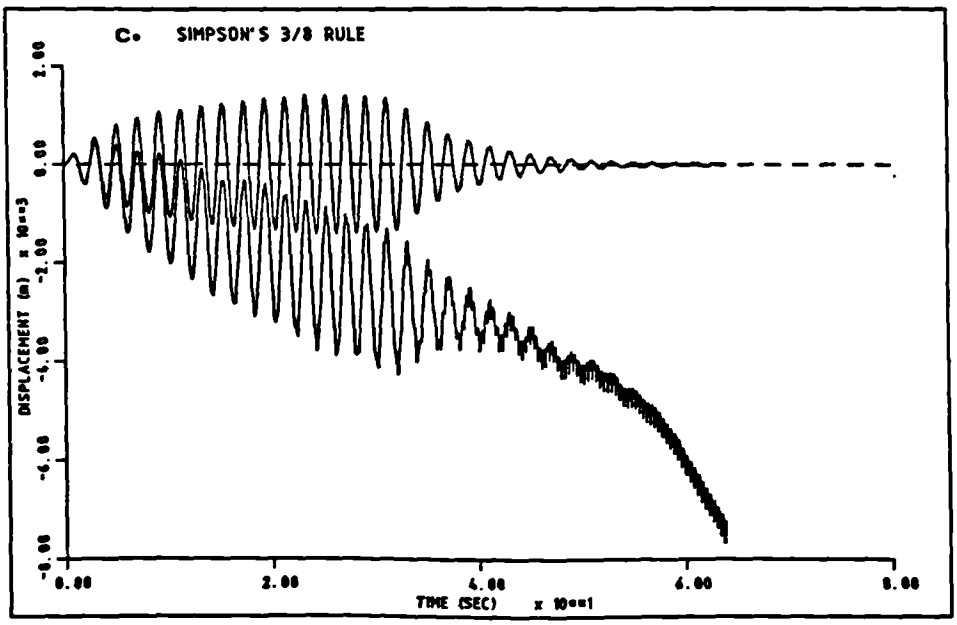

Figure 4.20.a-c. See next page for title.

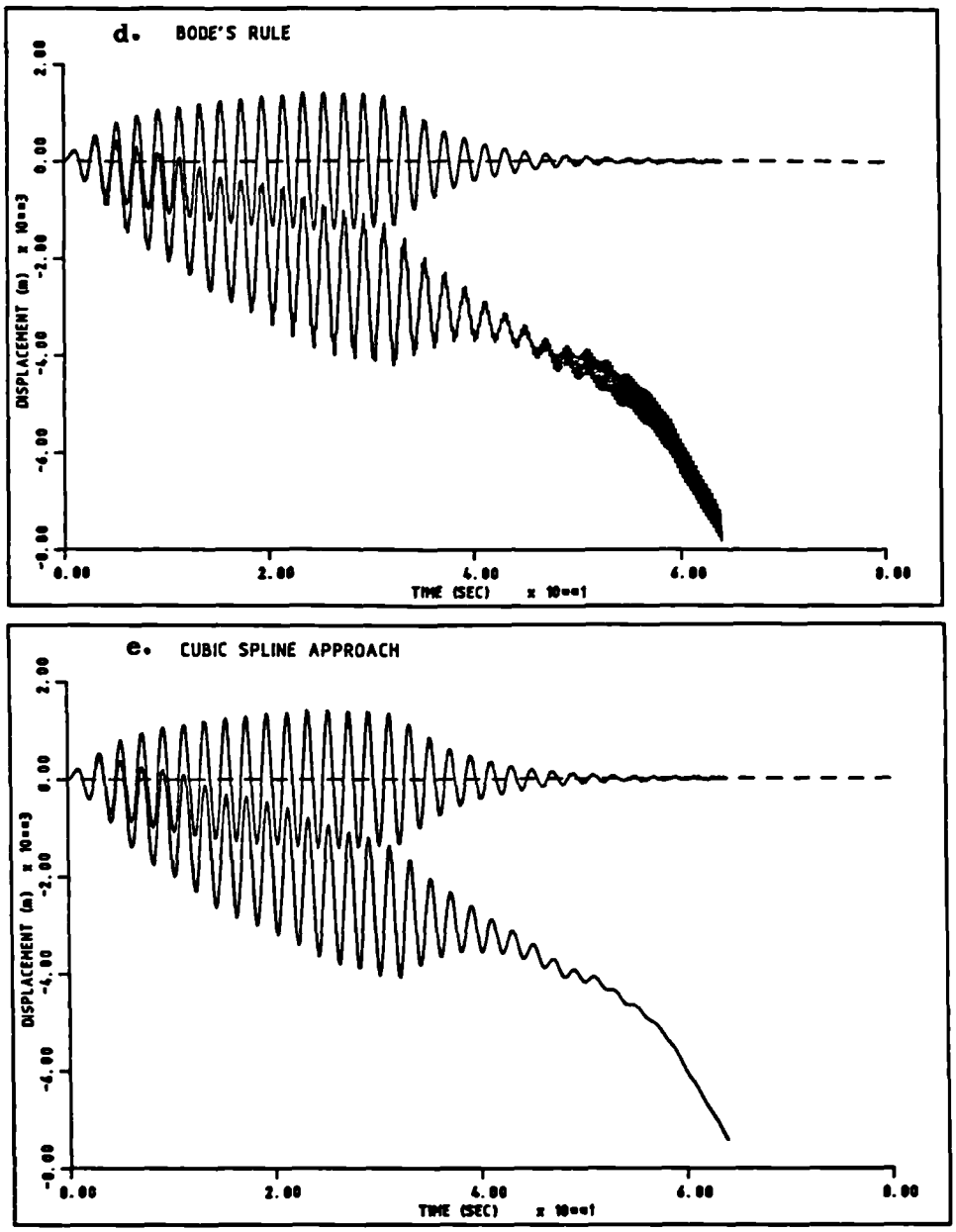

Figure 4.20. Results from time domain integration after adding a noise sequence to the acceleration.

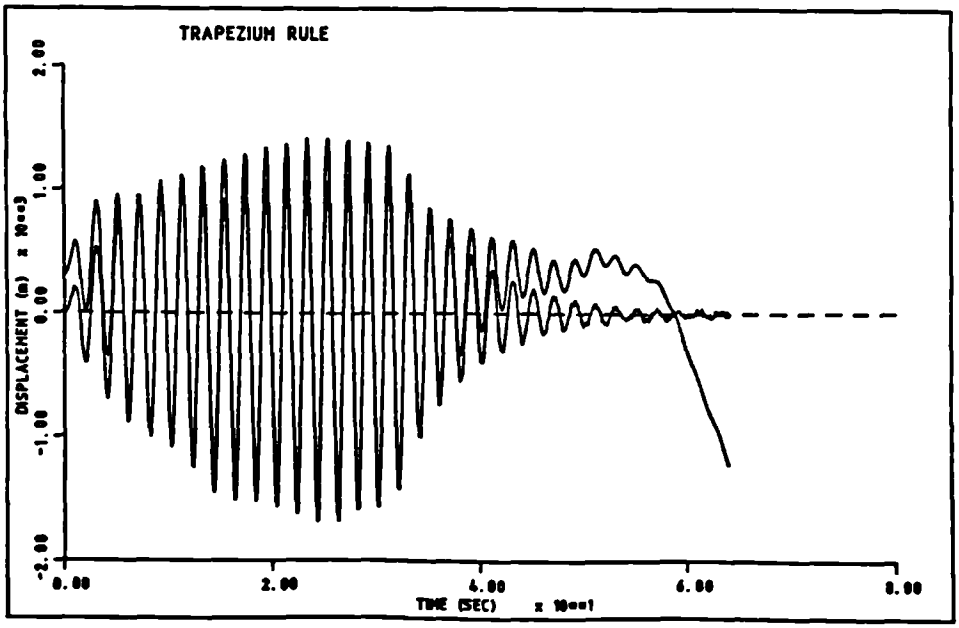

Figure 4.21. A sample comparison between exact and estimated displacement after removing trend by least squares approach for the example with added noise.

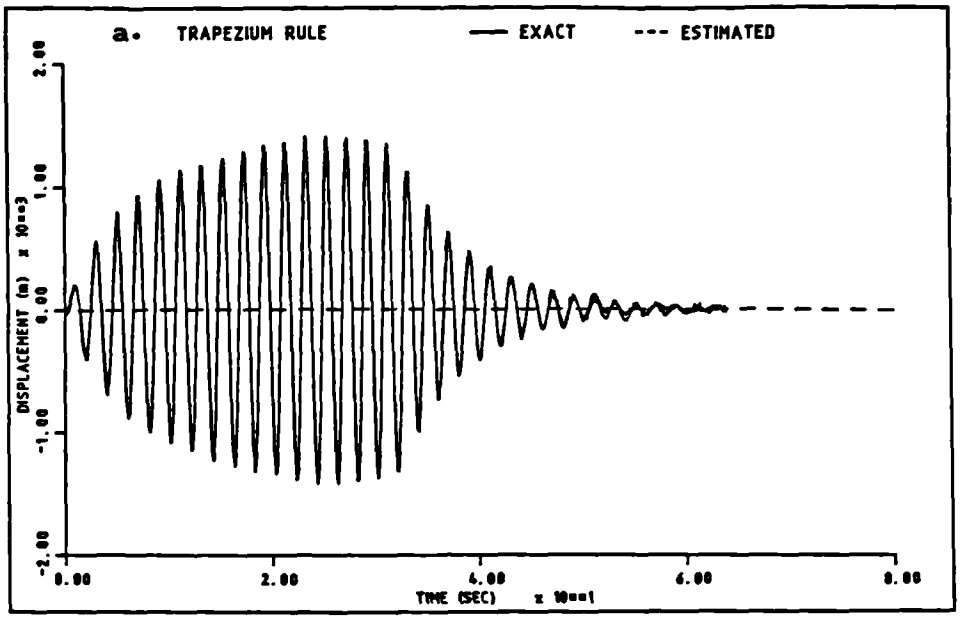

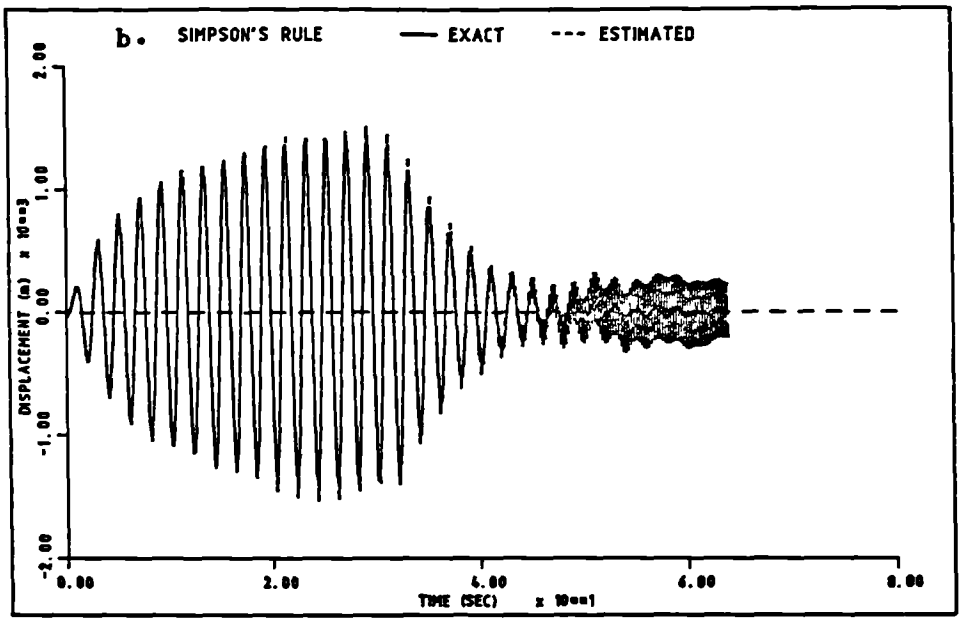

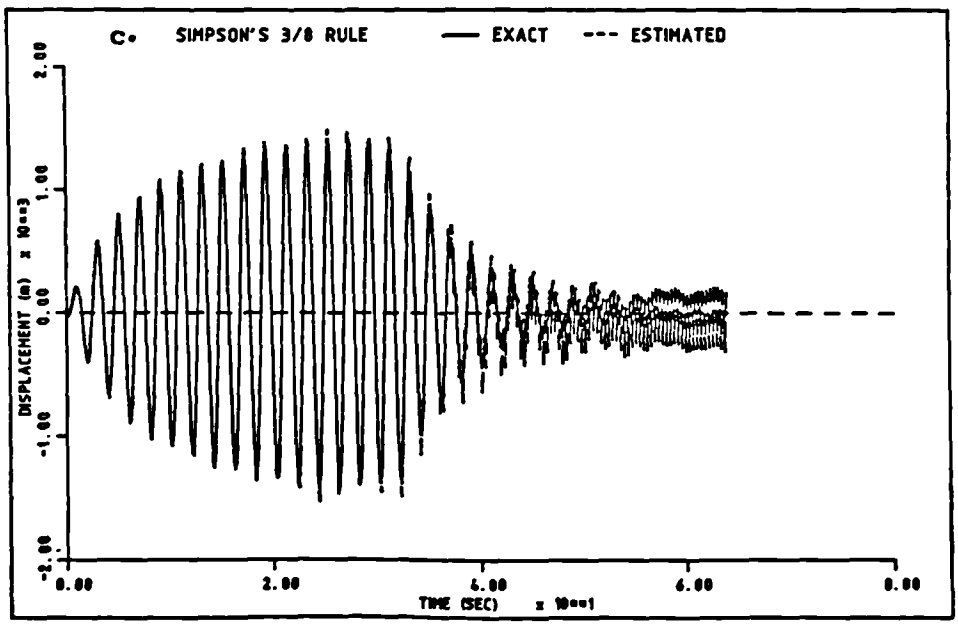

Figure 4.22.a-c. See next page for title.

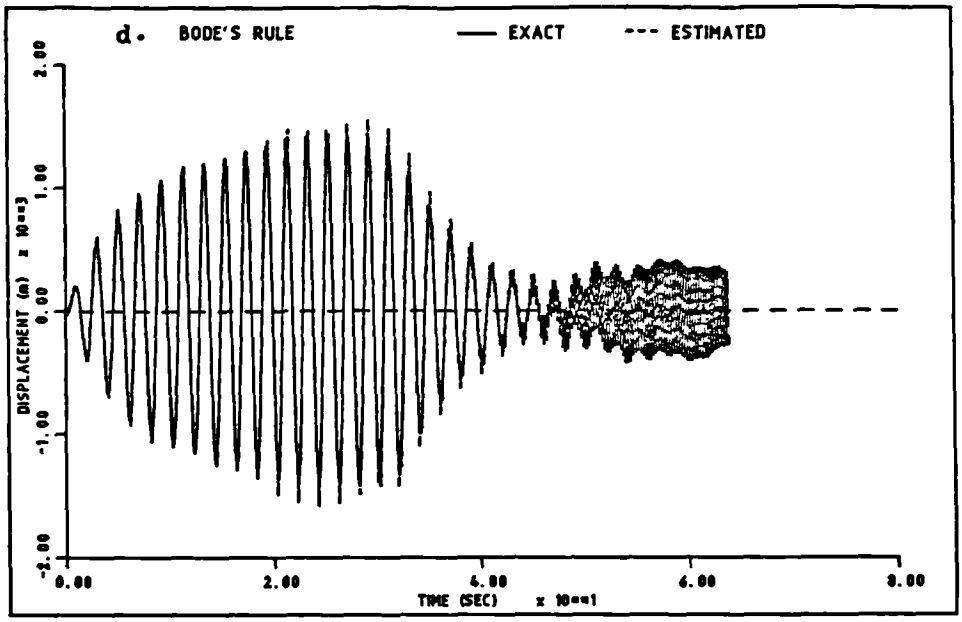

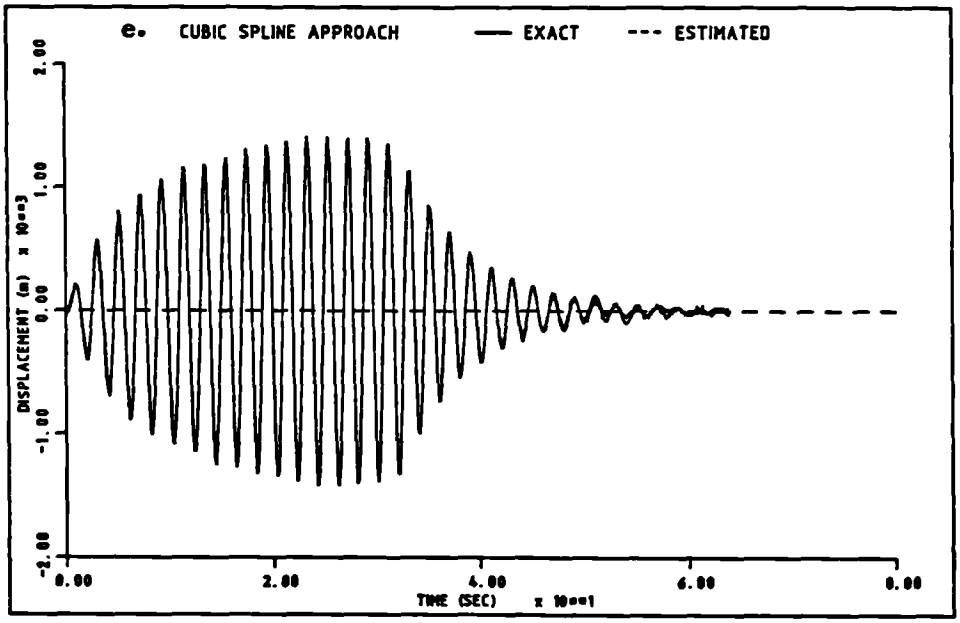

Figure 4.22. Results from time domain integration and high pass filtering trend removal for the example with added noise.

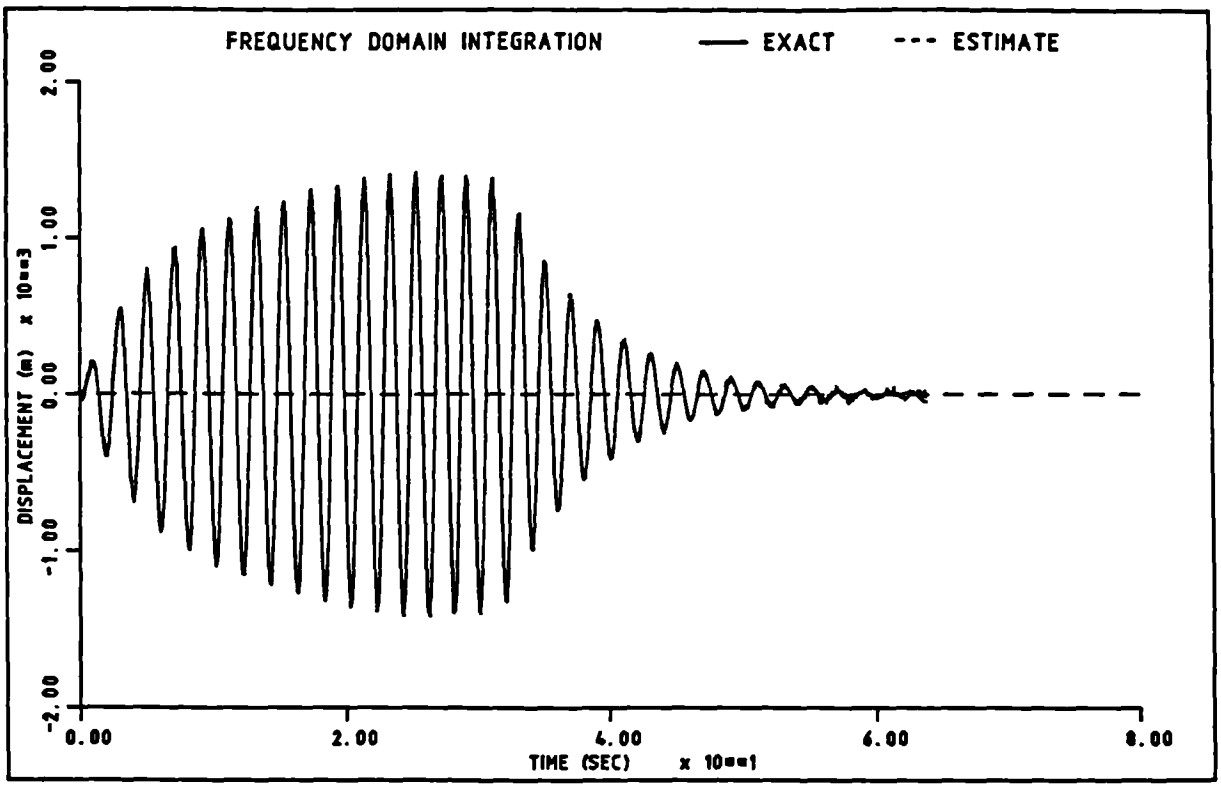

Figure 4.23. A comparison between the exact displacement with added noise and the estimated displacement obtained using frequency domain integration.

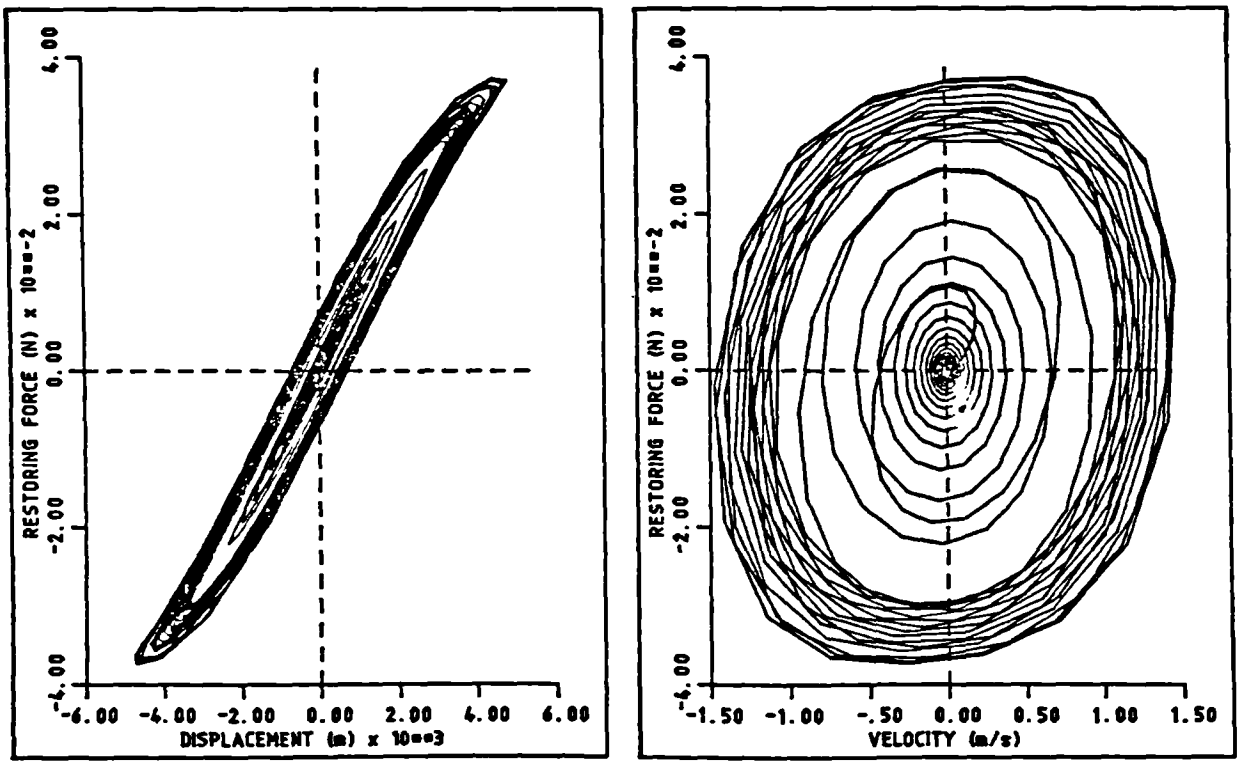

Figure 4.24. Force-state map for the nonlinear example.

5. Sensitivity of the Force-State Mapping Technique to Measurement Errors

5.1. Introduction.

Implicit in the force-state mapping procedure is the assumption that the values of $\ddot{x}$ and p may be measured accurately at the same instants of time. Thus the data acquisition system should employ a simultaneous sample and hold for all the measured data channels. If such a facility is not available then sampling the channels sequentially will introduce phase errors which will depend upon the ratio of the delay $\Delta\tau$ between channels and the period T of the frequency content of the signals i.e. a phase error of $(360\ \Delta\tau/T)$ degrees between two channels. In addition, it will be shown in chapter 7 that other phase errors can occur due to the characteristics of the transducers used and, perhaps more importantly, due to mismatch in the phase lags introduced by different channels of anti-aliasing filters; a quoted phase mismatch between channels of $\pm\ 0.5^{\circ}$- 2° is common in commercial analogue or switched capacitor filters.

Amplitude errors can also occur in the measured data due to errors in transducer calibration factors and in any amplifier gain values and due to alteration by anti-aliasing filters. The sampling process itself introduces quantisation errors due to representing the analogue data by digital values at a discrete number of levels, typically + 2048 to - 2047 for 12 bit accuracy.

Provided that the mass is known accurately, the final possible source of errors in the force-state map prior to curve fitting is associated with the practice of estimating one or more of the states rather than measuring them directly. As was shown in the previous chapter typically $\dot{x}$ and x are estimated from measured

acceleration by integration in the time or frequency domains. This process can itself introduce amplitude and phase errors, especially due to the problem of removing apparent drift which can be created by the integration of the low frequency content in the sampled acceleration data.

It is therefore of interest to gain some appreciation of the sensitivity of identified parameters to amplitude and phase errors in the data.

5.2. Sensitivity of parameters of a linear single-d.o.f. system to systematic measurement errors.

The sensitivity of identified parameters to measurement errors may be carried out by analysis or by simulation. It is considered at this stage that an analytical approach to a linear single-degree of freedom system under steady-state sinusoidal excitation will provide some useful indications as to the conditions under which the force-state mapping approach is particularly sensitive. For a weakly nonlinear system the linear restoring forces dominate the curve fit and so similar conclusions may be expected. Also the estimation of linear damping is extremely important if a model that can accurately reproduce the behaviour of the measured system is required; the author [54] and Crawley and O'Donnell [40] have experienced difficulty in damping estimation when using this method experimentally.

The restriction to steady-state sinusoidal excitation has been imposed in this chapter in order to permit an analytical approach. It is considered that the results obtained will have some relevance to force-state maps obtained from other forms of excitation such as narrow band frequency sweeps and transient sine (i.e. using the transient prior to steady-state for a single frequency excitation) since sine waves are the basic response components. Random excitation would be expected to display similar sensitivity problems but a simulation would really be necessary to

demonstrate this.

Consider the linear single-degree of freedom system governed by the equation

$$m\ddot{x} + c\dot{x} + kx = p(t) \quad \ldots\ldots\ldots\ldots\ldots\ldots (5.1)$$

where the excitation force is $p(t) = P \sin \omega t$. It is well known that the steady-state response is given by

$$x = X \sin (\omega t - \phi) \quad \ldots\ldots\ldots\ldots\ldots\ldots (5.2)$$

where $X = P/\sqrt{(k-\omega^2 m)^2 + (\omega c)^2}$ and $\phi = \tan^{-1}\left(\omega c / k-\omega^2 m\right)$

Now, in order to examine the sensitivity of the method, consider the force and the steady-state displacement, velocity and acceleration signals to be subject to amplitude and phase errors, namely

$$\begin{aligned} p &= \alpha_p P \sin (\omega t - \varepsilon_p) \\ x &= \alpha_d X \sin (\omega t - \phi_d) \\ \dot{x} &= \omega \alpha_v X \cos (\omega t - \phi_v) \\ \ddot{x} &= -\omega^2 \alpha_a X \sin (\omega t - \phi_a) \end{aligned} \quad \ldots\ldots\ldots\ldots\ldots\ldots (5.3)$$

where

$$\begin{aligned} \phi_d &= \phi + \varepsilon_d \\ \phi_v &= \phi + \varepsilon_v \\ \phi_a &= \phi + \varepsilon_a \end{aligned}$$

and α and ε allow for amplitude and phase errors, nominally different for each signal. The form of the errors is chosen to be systematic for simplicity so each signal is magnified by a factor α and shifted by a phase ε over its entire period. Values of $\alpha = 1$ and $\varepsilon = 0$ correspond to no error.

Now the restoring force can be obtained from equation (2.2) as

$$f(\dot{x}, x) = \alpha_p P \sin(\omega t - \varepsilon_p) + m\omega^2 \alpha_a X \sin(\omega t - \phi_a) \quad \ldots\ldots\ldots\ldots (5.4)$$

and this will be assumed to be fitted with a simple linear model

$$\hat{f}(\dot{x},x) = \hat{c}\dot{x} + \hat{k}x \qquad \ldots\ldots\ldots\ldots\ldots\ldots\ldots\ldots (5.5)$$

where $\hat{c}$ and $\hat{k}$ will be estimates of c and k. If sampled data were available at L discrete time intervals then the normal least squares solution would be obtained by minimising

$$J_d = \sum_{j=1}^{L} (f_j - \hat{f}_j)^2 \qquad \ldots\ldots\ldots\ldots\ldots\ldots\ldots\ldots (5.6)$$

leading to the equations

$$\begin{bmatrix} \Sigma\dot{x}_j^2 & \Sigma x_j\dot{x}_j \\ \Sigma x_j\dot{x}_j & \Sigma x_j^2 \end{bmatrix} \begin{Bmatrix} \hat{c} \\ \hat{k} \end{Bmatrix} = \begin{Bmatrix} \Sigma f_j\dot{x}_j \\ \Sigma f_j x_j \end{Bmatrix} \qquad \ldots\ldots\ldots\ldots\ldots (5.7)$$

However in order to obtain analytical expressions for sensitivity it is reasonable to consider the minimisation carried out over N cycles for the continuous signals using the cost function

$$J_c = \int_0^{NT} (f - \hat{f})^2 dt \qquad \ldots\ldots\ldots\ldots\ldots\ldots\ldots\ldots (5.8)$$

leading to the equations,

$$\begin{bmatrix} \oint\dot{x}^2 dt & \oint x\dot{x} dt \\ \oint x\dot{x} dt & \oint x^2 dt \end{bmatrix} \begin{Bmatrix} \hat{c} \\ \hat{k} \end{Bmatrix} = \begin{Bmatrix} \oint f\dot{x} dt \\ \oint f x dt \end{Bmatrix} \qquad \ldots\ldots\ldots\ldots (5.9)$$

where $\oint$ indicates that the integration is carried out between limits [0,NT] with $T=2\pi/\omega$.

The expressions for f in equation (5.4) and for $\dot{x}$ and x in equation (5.3) may now be substituted into (5.9) which, after evaluation of the integrals and dividing through by $\pi NX^2/\omega$, becomes

$$\begin{bmatrix} \omega^2\alpha_v^2 & \omega\alpha_v\alpha_d\sin\varepsilon_{vd} \\ \omega\alpha_v\alpha_d\sin\varepsilon_{vd} & \alpha_d^2 \end{bmatrix} \begin{Bmatrix} \hat{c} \\ \hat{k} \end{Bmatrix} = \begin{Bmatrix} \omega\alpha_p\alpha_v/H \sin(\phi+\varepsilon_{vp}) - m\alpha_a\alpha_v\omega^3\sin\varepsilon_{av} \\ \alpha_p\alpha_d/H \cos(\phi+\varepsilon_{dp}) + m\alpha_a\alpha_d\omega^2\cos\varepsilon_{ad} \end{Bmatrix}$$

.....(5.10)

where $\varepsilon_{vd} = \varepsilon_v - \varepsilon_d$, $\varepsilon_{va} = \varepsilon_v - \varepsilon_a$ etc are relative phase errors and H = X/P is the amplitude of the exact FRF.

The ratio $\hat{c}/c$ and $\hat{k}/k$ may be obtained by solving equation (5.10). It is convenient to introduce the undamped natural frequency $\omega_n = \sqrt{k/m}$ and the damping ratio $\zeta = c/2m\omega_n$ in order to eliminate H, m, c, k and ϕ in the solution. The sensitivity ratios can be shown to be

$$\frac{\hat{c}}{c} = \frac{\alpha_p}{\alpha_v}\left[\Phi_{c1} + \frac{1}{2\zeta}\left(\frac{1}{\lambda} - \lambda\right)\Phi_{c2}\right] - \frac{\alpha_a}{\alpha_v}\left[\frac{\lambda}{2\zeta}\Phi_{c3}\right] \quad .....(5.11)$$

$$\frac{\hat{k}}{k} = \frac{\alpha_p}{\alpha_d}\left[(1-\lambda^2)\Phi_{k1} - 2\zeta\lambda\,\Phi_{k2}\right] + \frac{\alpha_a}{\alpha_d}\left[\lambda^2\,\Phi_{k3}\right] \quad .....(5.12)$$

where $\lambda = \omega/\omega_n$ is the frequency ratio and the phase dependent factors are given by

$$\Phi_{c1} = (\cos\varepsilon_{vp} + \sin\varepsilon_{dp}\sin\varepsilon_{vd})/\cos^2\varepsilon_{vd}$$

$$\Phi_{c2} = (\sin\varepsilon_{vp} - \cos\varepsilon_{dp}\sin\varepsilon_{vd})/\cos^2\varepsilon_{vd}$$

$$\Phi_{c3} = (\sin\varepsilon_{av} + \sin\varepsilon_{vd}\cos\varepsilon_{ad})/\cos^2\varepsilon_{vd}$$

$$\Phi_{k1} = (\cos\varepsilon_{dp} - \sin\varepsilon_{vd}\sin\varepsilon_{vp})/\cos^2\varepsilon_{vd}$$

$$\Phi_{k2} = (\sin\varepsilon_{dp} + \sin\varepsilon_{vd}\cos\varepsilon_{vp})/\cos^2\varepsilon_{vd}$$

$$\Phi_{k3} = (\cos\varepsilon_{ad} + \sin\varepsilon_{vd}\sin\varepsilon_{av})/\cos^2\varepsilon_{vd}$$

The value of these factors clearly depend upon the relative phase errors between the different signals.

The sensitivity of the estimates of the damping and stiffness coefficients to amplitude and phase errors may be examined by comparing the expressions (5.11) and (5.12) to unity.

5.2.1. Amplitude errors only.

If there are no phase errors at all or if all the signals have the same phase error then the phase dependent factors Φ are either unity or zero and equations (5.11) and (5.12) become

$$\frac{\hat{c}}{c} = \frac{\alpha_p}{\alpha_v} \qquad \ldots\ldots\ldots\ldots\ldots\ldots\ldots\ldots\ldots\ldots\ldots\ldots\ldots\ldots (5.13)$$

$$\frac{\hat{k}}{k} = (1-\lambda^2)\frac{\alpha_p}{\alpha_d} + \lambda^2\frac{\alpha_a}{\alpha_d} = \frac{\alpha_p + \lambda^2(\alpha_a - \alpha_p)}{\alpha_d} \qquad \ldots\ldots\ldots (5.14)$$

The damping sensitivity is independent of the frequency ratio and of the system damping. It only depends upon the force and velocity amplitude errors. Since the values of α are likely to be very close to unity (within 1% say) then the damping errors will not be very large (within 2% say).

The stiffness sensitivity is also independent of the system damping but increases with the frequency ratio provided that the force and acceleration amplitude errors are different. An example for the case when $\alpha_p = 1$ and $\alpha_a = \alpha_d \neq 1$ (i.e. no integration error) is shown in Fig. (5.1) in which the error values varied from 0.98 to 1.02. It should be pointed out that the estimated stiffness is based upon the assumption of using the correct mass; if the mass were estimated from inaccurate data then the estimated stiffness would be modified.

5.2.2. Phase errors only.

If on the other hand there are no amplitude errors then equations (5.11) and (5.12) are simplified somewhat since α values are unity. When phase errors are present then potentially all the Φ

values will depart from their ideal values of zero or unity and errors in the parameter estimates will result.

It is clear from equation (5.12) that the stiffness sensitivity is likely to increase significantly with increase in excitation frequency unless for example $\Phi_{k1} \approx \Phi_{k3}$ and Φ_{k2} is small. An example for this case is when $\varepsilon_p = 0$ and $\varepsilon_d = \varepsilon_v = \varepsilon_a \neq = 0$ (i.e. no integration error). Results for this example where the errors varied from -0.4° to 0.4° and λ varied from 0.3 to around 2 showed that $\hat{k}/k$ was almost unity.

However the system damping is extremely significant in determining the damping sensitivity as may be seen by examining equation (5.11). The factor $1/2\zeta$, equivalent to the 'Q' magnification factor of the system, will mean that the phase factors Φ_{c2} and Φ_{c3} have an increasing effect on the damping sensitivity as the system damping reduces; since mechanical structures can have damping values typically in the range 0.2 - 2% critical then magnification factors of 25-250 are possible.

The effect of frequency on the damping sensitivity is less obvious. The influence of the Φ_{c3} term will increase as λ increases but the $(1/\lambda - \lambda)$ factor multiplying the Φ_{c2} term is zero for excitation at the natural frequency and increases in magnitude at frequencies above or below the natural frequency. Thus the damping estimate will become more sensitive as frequency departs from the natural frequency of the system.

It is obvious that there is a very large number of possible combinations of phase errors associated with the four signals. However only a few examples will be given in order to indicate the magnitude of damping errors which are possible.

Firstly the case when $\varepsilon_p = 0$ and $\varepsilon_d = \varepsilon_v = \varepsilon_a \neq 0$ (i.e. no integration error) is shown in Fig. (5.2) for 2% (dashed lines)and 0.2% (solid lines) critical damping and a range of frequencies and possible phase errors (between -0.4° to 0.4°). It is clear that

the accuracy of the damping coefficient estimate deteriorates considerably for frequency ratios different to unity. The large increase in sensitivity as damping reduces is also apparent. It is interesting that it is quite possible for a negative damping estimate to be obtained which must imply that the phase errors have caused the force-state map to be tilted about the x axis. Such a result was found by Crawley and O'donnell [40] in their experimental study of a linear single-degree of freedom system but was not adequately explained.

Another possible case is for the measurement to be accurate, namely $\varepsilon_p = \varepsilon_a = 0$, but the integration process to introduce phase errors so that ε_v , $\varepsilon_d \neq 0$. For simplicity the case where a similar error is introduced at each integration ($\varepsilon_d = 2\varepsilon_v$ and ε_d varied between -0.4° to 0.4°) is shown in Fig. (5.3) for 2% (dashed lines) and 0.2% (solid lines) critical damping. Similar features to those seen in the previous results are evident but the damping estimate is also sensitive at the natural frequency.

Finally, for a combined measurement and integration error case an example with $\varepsilon_d = 2\varepsilon_v$ (ε_d varied between -0.4° to 0.4°) and $\varepsilon_v = 2\varepsilon_a$ is considered. The results are shown in Fig. (5.4) for the above two damping values. High damping sensitivity to errors is also obvious for the low damping case.

The sensitivity corresponding to other combinations of phase errors could be deduced from equations (5.11) and (5.12) if required.

5.2.3. Amplitude and phase errors.

When both amplitude and phase errors are present the situation is more complex but similar features to those discussed above will be observed. Because of the significant magnification of phase errors possible for lightly damped structures, the sensitivity of damping estimates to phase errors is likely to be the most important feature.

5.3. Sensitivity of parameters of a linear single-degree of freedom system to random measurement errors.*

In order to examine the effect of random errors upon the estimated parameters consider the signals to include some measurement noise, namely

$$\begin{aligned} p &= P \sin \omega t + n_p \\ x &= X \sin(\omega t - \phi) + n_d \\ \dot{x} &= \omega X \cos(\omega t - \phi) + n_v \\ \ddot{x} &= -\omega^2 X \sin(\omega t - \phi) + n_a \end{aligned} \qquad \ldots\ldots\ldots\ldots\ldots\ldots (5.15)$$

where n refers to the measurement noise. Assume in each case that the noise is uncorrelated with the true part of the signal. When these signals are substituted into the least squares equation (5.9) then

$$\begin{bmatrix} \pi N\omega X^2 + R_v & R_{vd} \\ R_{vd} & \frac{\pi N X^2}{\omega} + R_d \end{bmatrix} \begin{Bmatrix} \hat{c} \\ \hat{k} \end{Bmatrix} = \begin{Bmatrix} \pi NXP \sin\phi - mR_{av} \\ \frac{\pi NXP}{\omega} \cos\phi + \pi Nm\omega X^2 - mR_{ad} \end{Bmatrix} \ldots (5.16)$$

where $$R_v = \int_0^{NT} n_v^2 \, dt$$

$$R_{vd} = \int_0^{NT} n_v n_d \, dt$$

and so on are essentially zero lag auto and cross-correlations of the noise components. It has been assumed that correlations between n_p and n_v or n_d and also between the noise and the true part of the signal are zero; the integration interval could be extended to make this more realistic without changing the essence of equation (5.16).

---

* The author is grateful to Dr. Wright for providing him with the theory of this section.

(i) If the velocity and displacement signals were measured independently then all the cross-correlations in equation (5.16) could be put to zero, leaving only n_v and n_d to corrupt the estimates. Now the mean square of the noise on the velocity is

$$m_v^2 = \frac{1}{NT}\int_0^{NT} n_v^2 dt = \frac{\omega}{2\pi N} R_v \qquad \ldots\ldots\ldots\ldots\ldots\ldots (5.17)$$

and if a noise to signal ratio is defined as

$$\gamma_v = \frac{\text{R.M.S. of noise}}{\text{R.M.S. of signal}} = \frac{m_v}{\omega X/\sqrt{2}} \qquad \ldots\ldots\ldots\ldots\ldots\ldots (5.18)$$

then from equations (5.17) and (5.18) it may be shown that

$$R_v = \gamma_v^2\, \pi N \omega X^2 \qquad \ldots\ldots\ldots\ldots\ldots\ldots\ldots\ldots (5.19)$$

Using a similar definition for the displacement noise then equation (5.16) becomes, after dividing by $\pi N X^2/\omega$

$$\begin{bmatrix} \omega^2[1+\gamma_v^2\,] & 0 \\ 0 & [1+\gamma_d^2\,] \end{bmatrix} \begin{Bmatrix} \hat{c} \\ \hat{k} \end{Bmatrix} = \begin{Bmatrix} \omega \sin\phi/_H \\ \cos\phi/_H + m\omega^2 \end{Bmatrix} \qquad \ldots\ldots (5.20)$$

This equation may be solved and simplified to give

$$\frac{\hat{c}}{c} = \frac{1}{1+\gamma_v^2} \qquad \ldots\ldots\ldots\ldots\ldots\ldots (5.21)$$

$$\frac{\hat{k}}{k} = \frac{1}{1+\gamma_d^2} \qquad \ldots\ldots\ldots\ldots\ldots\ldots (5.22)$$

so the errors in the parameter estimates are likely to be fairly small for realistic levels of noise in a vibration test ($\gamma < 2\%$).

(ii) If however the velocity and displacement signals are obtained from the noisy acceleration signal by integration then n_v and n_d will be related to n_a and so the cross-correlation terms will not necessarily be zero. However it may be shown [59]that a signal is statistically uncorrelated with its integral; this is because any

harmonic component is shifted by 90° phase upon integration and the resulting correlation is zero if taken over a sufficient time. Thus R_{av} and R_{vd} may be ignored. Unfortunately the correlation R_{ad} between acceleration and displacement is not zero because the double integration simply shifts the phase of each frequency component by 180° and amplifies the noise on the acceleration by the factor $(1/\text{frequency})^2$ over the frequency range considered. As was shown in chapter 4 any low frequency noise components in the acceleration signal will be magnified considerably and will introduce large errors unless some filtering is used as part of the integration process.

If it is assumed that the power spectral density of the acceleration noise is constant over the bandwidth ω_L to ω_u (ω_L and ω_u are lower and upper frequencies), and made zero outside this band prior to integration, then by making use of the relationships between correlations and spectra [59] it may be shown that

$$R_{ad} = -R_a/\omega_L\omega_u \qquad \ldots\ldots\ldots\ldots\ldots\ldots\ldots (5.23)$$

It can be shown further that the noise to signal ratios for velocity and displacements are related to that for acceleration, because of the integrations, by

$$\gamma_v^2 = \mu\gamma_a^2 \qquad \ldots\ldots\ldots\ldots\ldots\ldots\ldots (5.24)$$

$$\text{and} \quad \gamma_d^2 = \frac{1}{3}\left(1 + \beta + \frac{1}{\beta}\right)\mu^2\gamma_a^2 \qquad \ldots\ldots\ldots (5.25)$$

$$\text{where } \mu = \omega^2/\omega_L\omega_u \quad \text{and} \quad \beta = \omega_u/\omega_L$$

If equation (5.23) is used in equation (5.16) then it can be shown that the damping expression given in equation (5.21) is unchanged, apart from the dependence of γ_v^2 on γ_a^2, but that the stiffness estimate becomes

$$\frac{\hat{k}}{k} = \frac{1 + \mu\lambda^2\gamma_a^2}{1 + \gamma_d^2} \qquad \ldots\ldots\ldots\ldots\ldots\ldots (5.26)$$

where γ_d^2 is given by equation (5.25). If for example the excitation frequency is the geometric mean of the upper and lower frequency bounds of the noise then $\mu = 1$ so equation (5.24) gives $\gamma_v = \gamma_a$ and the damping estimate should be fairly accurate. However the accuracy of the stiffness estimate will depend upon the frequency ratio λ and the ratio β. It can be seen that the displacement noise will not be too large for reasonable β (e.g. $\beta = 9$ implies $\omega_L = \omega/3$, $\omega_u = 3\omega$ and $\mu = 1$) and so the stiffness errors should not be excessive. Clearly for single frequency sine excitation ω_L and ω_u can be quite close to ω ($\beta \approx 1$) but for broader band excitation the truncation values must be chosen with care.

All the above analysis for random noise has assumed that sufficient data is used for certain correlations (or expected values) to be zero. In practice other correlations will not be zero so there will be errors in the estimates but these errors should average out if a number of tests are carried out. It is difficult to quantify such errors without carrying out a number of simulations.

5.4 Discussion.

The significant influence of systematic phase errors upon the accuracy of damping estimates from the force-state mapping approach for lightly damped structures has been observed. Systematic errors in amplitude are far less important.

Since the damping in the mathematical model derived from experimental data is arguably the most critical factor in being able to reproduce the behaviour of the structure to various excitations, this high sensitivity is very unsatisfactory. This is especially true when the application to nonlinear and to multi degree of freedom systems is contemplated since the models to be

fitted are more complex and data accuracy is more important.

There are various possible approaches to take in seeking to overcome this problem. The first and best solution is to eliminate the problem by using extremely high quality and well matched instrumentation at every stage of the process. However the phase matching requirements are quite severe for very lightly damped structures.

A second approach is to seek to calibrate the instrumentation for the force and acceleration channels and then to compensate for phase errors digitally by shifting the measured signals. However this is difficult to do unless an extremely high sampling rate is used since data will only be available at discrete intervals. Also such a correction could only be contemplated for steady-state sinusoidal excitation where the wave form is periodic unless maybe a digital filter with the desired phase shift could be employed.

A further approach is to accommodate the errors by considering the instrumentation as part of the system under test, at least for early trials of the force-state mapping approach. The sampled data are then considered to be accurate once transducer calibration factors have been applied. The quality of any fitted mathematical model would then be assessed by comparing its response to various measured excitations with the corresponding measured and sampled response of the actual system. Unfortunately even with perfect integration this approach will not really cope with the phase error problem. As an extreme illustration of this consider the case where $\varepsilon_p = 0$ but $\varepsilon_d = \varepsilon_v = \varepsilon_a \neq 0$ and the errors are such that a negative damping estimate is obtained. There is no way that the simulated response of this model would resemble the actual response of the system including instrumentation errors. A less severe example would obviously provide a closer match and this approach to the errors may be the best that can be done with an inadequate measurement system.

Although the analysis presented has been carried out for

steady-state sinusoidal excitation at one frequency, the conclusions might well be expected to apply to other forms of excitation since very accurate data appear to be a basic requirement for the force-state mapping approach for lightly damped systems. However, because of the excitation frequency depending on the damping and stiffness sensitivity, it is possible that the superposition of steady-state results from several frequencies around the resonance, or the use of a sinusoidal sweep, might mean that the total error is reduced in certain circumstances; for example, when $\hat{c}/c > 1$ for $\lambda < 1$ but $\hat{c}/c < 1$ for $\lambda > 1$ so some cancellation might be possible. Such fortuitous behaviour is unlikely to be anticipated in advance of any experiment. Note that in general, when measurement errors are present, the results from different types and band widths of excitation will be different, even for the same measurement system. Any one excitation may be best in a particular test.

Finally a study of the effect of random errors upon the estimates indicated that for fairly high quality data (low noise-to-signal ratio) the estimates would be reasonably accurate.

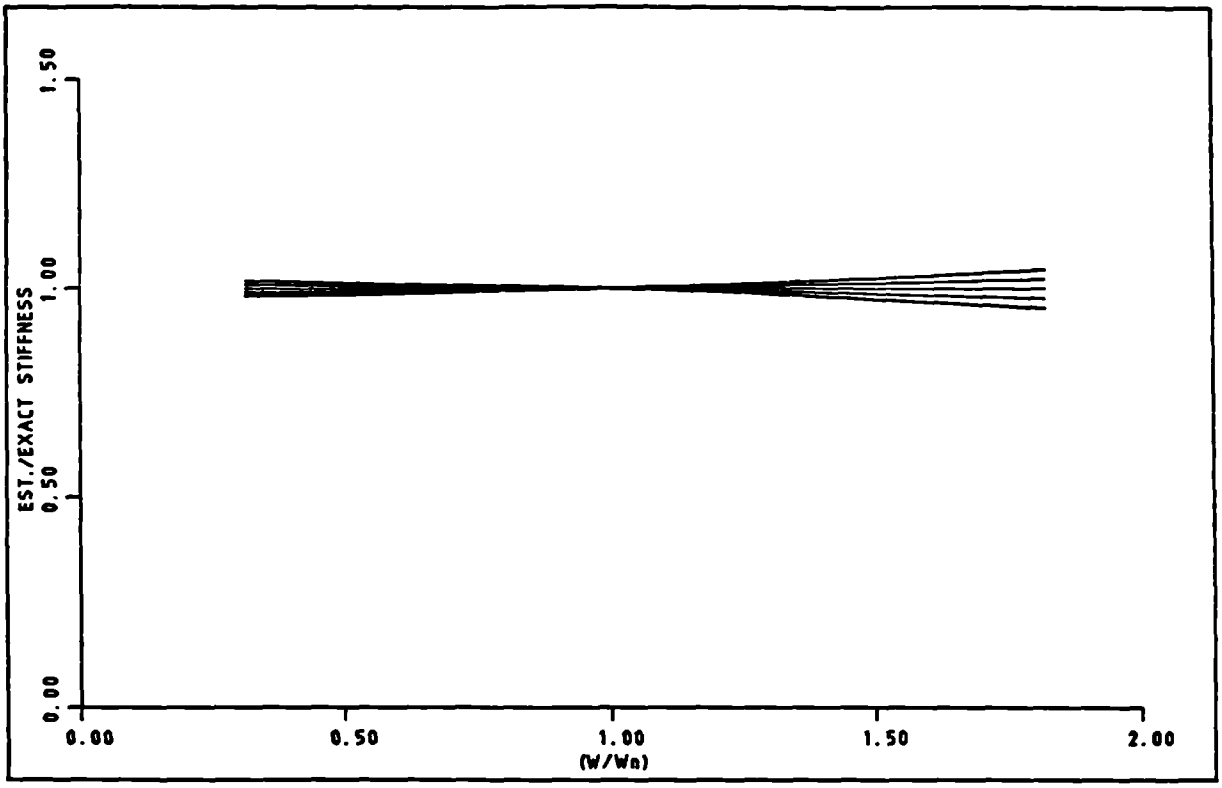

Figure 5.1. Sensitivity of stiffness to measurement amplitude errors for a linear system.

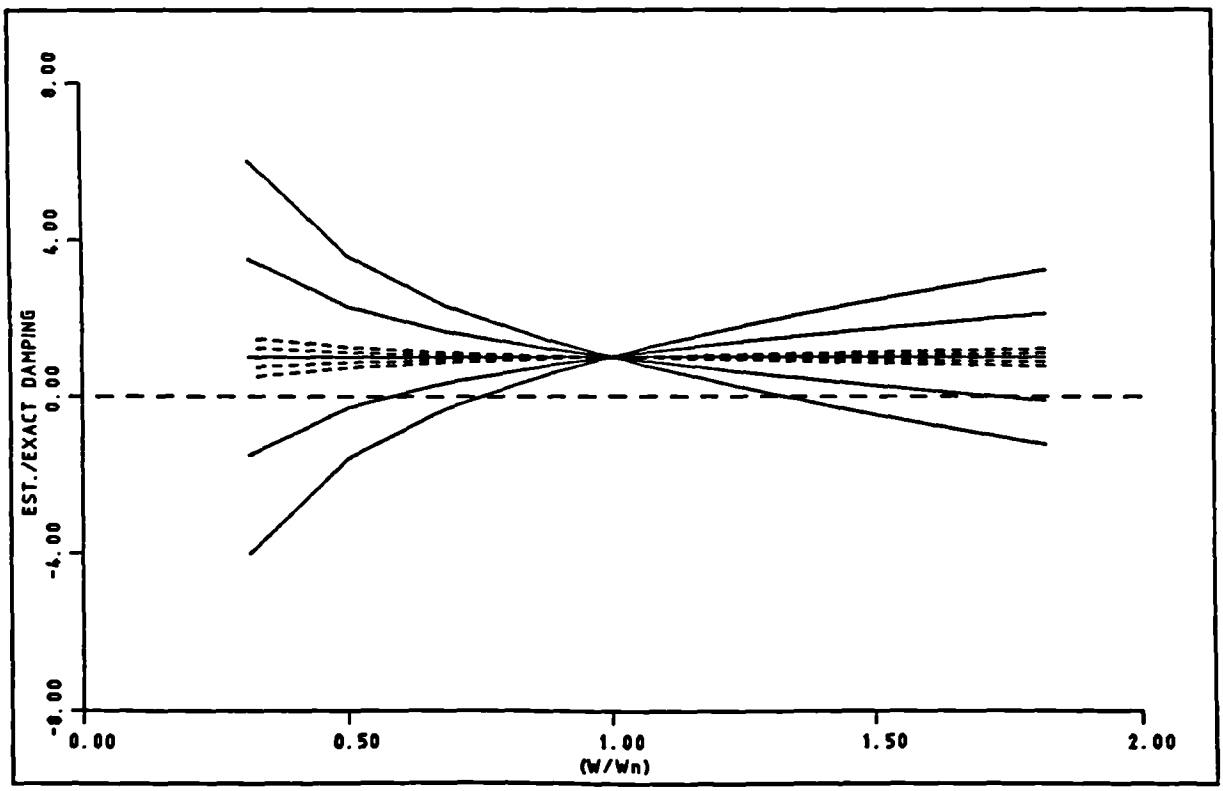

Figure 5.2. Sensitivity of damping to measurement phase errors for a linear system.

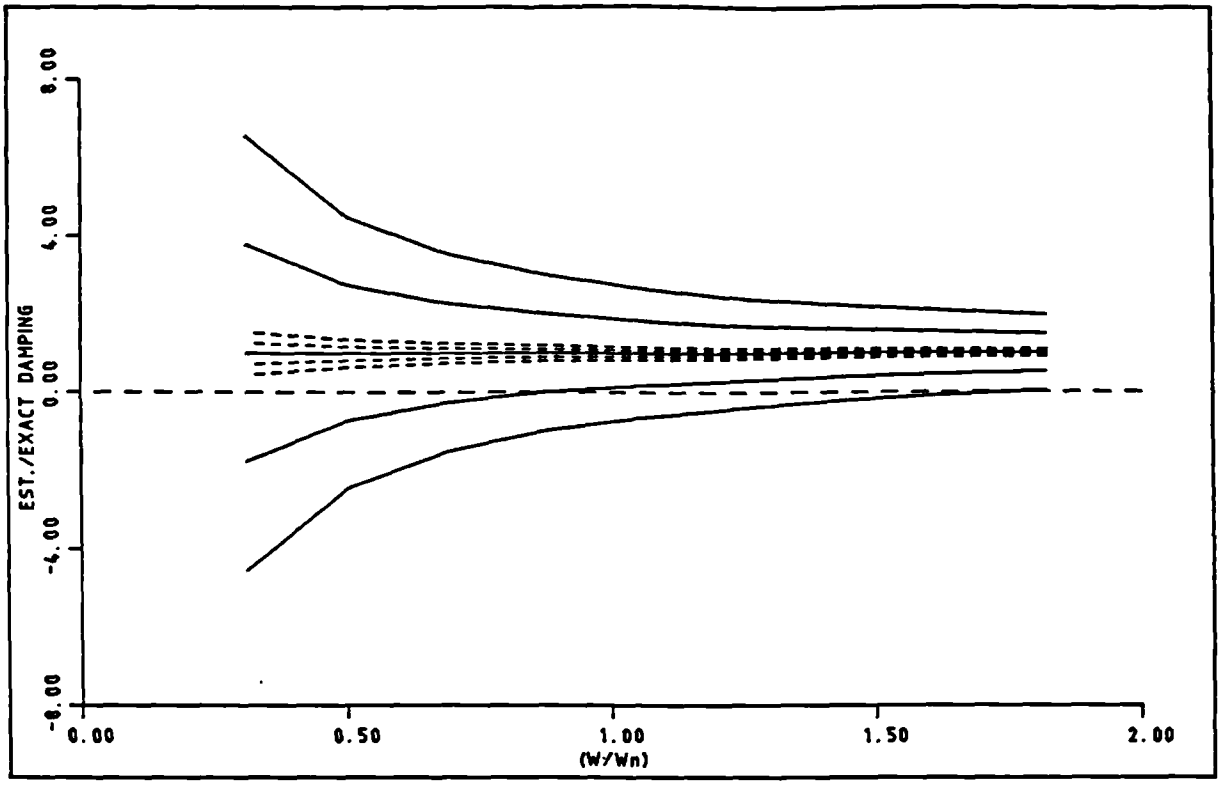

Figure 5.3. Sensitivity of damping to integration phase errors in velocity and displacement for a linear system.

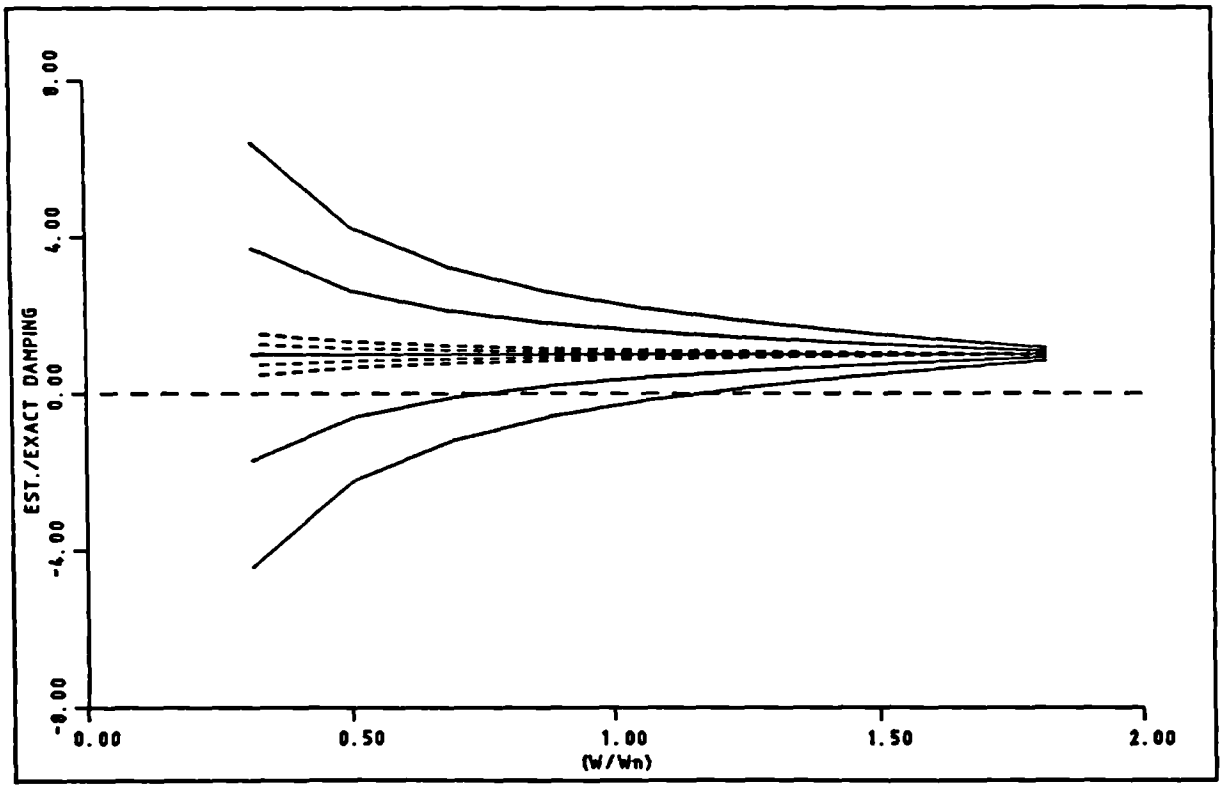

Figure 5.4. Sensitivity of damping to measurement and integration phase errors for a linear system.

6. The Estimation of the Mass and Mode shape Parameters.

6.1. Introduction.

In all the examples considered so far, it has been assumed that the mass and, where appropriate, mode shape parameters are known. Because this is not true in practice, it is essential for a proper application of the force-state mapping technique to investigate how these parameters may be estimated from measured data, such as input and response time histories or FRF data.

There are various methods for estimating the mass and mode shape parameters for linear systems but it is likely that they would yield different estimates at different input force levels for a nonlinear system.

The problem of using a wrong mass estimate in the force-state mapping technique can be rather serious and it is therefore necessary to investigate the effect of mass errors and how the mass may be correctly estimated for nonlinear systems. In this chapter the mass estimation for single and multi-d.o.f. nonlinear systems will be the main subject of consideration though some attention will be paid to mode shape estimation.

In their early work, Crawley and O'Donnell [40] suggested a method for evaluating the effective mass of single-d.o.f. nonlinear systems. Their procedure was based on a least squares curve fit of the input rather than restoring force in terms of the acceleration, velocity and displacement signals. The robustness of the least squares solution with respect to the amplitude and frequency of the excitation signal was considered and it was shown that the approach is sensitive to the unmodeled system features (e.g. noise) at frequencies below or around the resonance frequency.

In conjunction with developing the nonparametric identification approach, Masri et al [37] introduced a technique for estimating the effective physical lumped masses in a multi-d.o.f. lumped parameter system. The technique was based on applying an impulsive force at the required location and using the impulse-momentum relationship; it was shown that the accuracy of the estimate is dependent upon the pulse duration which must be a small fraction of the smallest system period. The approach was said to be quite insensitive to the presence of nonlinearities but no attempt was made to study the sensitivity of the estimated mass to noise in the measurements.

Very recently, Masri et al [38] have further extended their nonparametric identification by generalising the approach to handle arbitrary nonlinear multi-d.o.f. dynamic lumped parameter systems with multiple inputs and outputs. The method was based on the use of a linear time domain least squares technique to identify the physical mass, damping and stiffness matrices of an equivalent linearised version of the nonlinear system. The mass matrix was then used for estimating the restoring force vector and the eigenvalue problem associated with the mass and stiffness matrices was solved to provide an estimate of the modal matrix Φ which would then be used for transforming from physical to modal space. However, their original philosophy of curve fitting the restoring force was slightly modified in that the acceleration was included with the velocity and displacement signals in the curve fit. They once again recommended the use of Chebyshev polynomials. It would appear that the inclusion of the acceleration in the curve fit may be attributed to the fact that the estimation of the mass matrix using a linearised approach would not be correct for nonlinear systems; thus the identified parameters corresponding to the acceleration terms could attempt to compensate for the error in the mass. However, this point was not discussed in the reference.

Yang and Ibrahim [44] presented a method for obtaining the physical mass matrix of lumped parameter models, providing that the sum of the masses is known. The method was based on curve fitting the acceleration time history of each mass in terms of the relative velocities and displacements measured between it and all the other masses. It was assumed that the external force at the mass under consideration should be zero, its acceleration being caused by applying a force at a different station. Clearly the identifications were all carried out in physical not modal space.

Worden and Tomlinson [52,60] showed that errors in the mass introduce a scaling factor into the estimated parameters. They also showed that including the acceleration signal, when curve fitting the restoring force estimated using an incorrect mass, would allow the estimation of the error in the mass since it would be the coefficient of the fitted acceleration term. The mass could then be corrected and the procedure repeated until the mass converges to the correct value. Ideally the mass value should converge after one iteration. For multi-d.o.f. lumped parameter systems they introduced a technique based on implementing the concept of transmissibility in physical space which allowed the identification of the coefficients of the system up to a scaling factor. Thus the estimation of the mass was not needed [52].

In this chapter the estimation of the mass for one d.o.f. and of the generalised mass matrix for multi-d.o.f. will be considered. The approaches of Crawley and O'Donnell and Worden and Tomlinson will be investigated. A new "sensitivity approach" based on the refinement of linear estimates for a nonlinear system will be presented and shown to perform very well; the determination of the initial linear estimates will be discussed. The effect of noise upon the methods will be considered.

A by-product of the linear method used to estimate the generalised mass matrix is that an estimate of the modal matrix is also obtained from the experimental data and not from a theoretical

model. The effect of an incorrect modal matrix upon the identification will be considered and it will be shown that the sensitivity approach to mass estimation will compensate for the mode shape errors and lead to a correct model.

6.2. Effect of mass error on the force-state mapping technique.

It may be recalled from chapter 2 that the restoring force of a single-d.o.f. system may be estimated using

$$f = p - m\ddot{x} \qquad \ldots\ldots\ldots\ldots\ldots\ldots\ldots (6.1)$$

In order to carry out a simple analytical investigation into the sensitivity of the force-state mapping technique to errors in the mass, it is convenient to consider here that the excitation force is sinusoidal and the system is linear. Thus, let the excitation be

$$p = P\, e^{j\omega t} \qquad \ldots\ldots\ldots\ldots\ldots\ldots\ldots (6.2)$$

where P is the force amplitude. The linear response would be given by

$$x = \tilde{X}\, e^{j\omega t} \qquad \ldots\ldots\ldots\ldots\ldots\ldots\ldots (6.3)$$

$$\text{where } \tilde{X} = X\, e^{-j\phi} \qquad \ldots\ldots\ldots\ldots\ldots\ldots (6.4)$$

and X and ϕ are the response amplitude and phase lag between the input and response signals respectively.

The sensitivity of the restoring force with respect to the mass may be shown from equations (6.1) and (6.3) to be

$$\frac{\partial f}{\partial m} = \omega^2\, \tilde{X}\, e^{j\omega t} \qquad \ldots\ldots\ldots\ldots\ldots\ldots (6.5)$$

If the mass error is given by

$$\Delta m = \hat{m} - m \qquad \ldots\ldots\ldots\ldots\ldots\ldots (6.6)$$

where $\hat{m}$ is the estimated mass value, then the restoring force would have an error Δf which can be normalised with respect to the exact restoring force and written as

$$\frac{\Delta f}{f} = \frac{1}{f}\frac{\partial f}{\partial m}\Delta m = \frac{\Delta m}{m + \dfrac{1}{\omega^2 H}} \qquad \ldots\ldots\ldots\ldots (6.7)$$

where $H = \dfrac{\tilde{X}}{P}$ is the complex FRF of the system. Since for a linear system

$$\frac{1}{H} = k - \omega^2 m + i\omega c \qquad \ldots\ldots\ldots\ldots\ldots\ldots\ldots (6.8)$$

then substituting equation (6.8) into (6.7) and simplifying yields the magnitude of the error as

$$\left|\frac{\Delta f}{f}\right| = \frac{\lambda^2}{\sqrt{1 + 4\zeta^2\lambda^2}}\,\frac{\Delta m}{m} \qquad \ldots\ldots\ldots\ldots\ldots (6.9)$$

where $\lambda = \omega/\omega_n$, ω_n is the undamped natural frequency and ζ is the damping ratio.

From equation (6.9) it can be seen that the modulus of the restoring force error is proportional to the mass error and that the constant of proportionality is dependent upon the excitation frequency and the damping of the system.

For lightly damped systems ($\zeta < 0.05$) and moderate values of λ equation (6.9) may reduce to

$$\left|\frac{\Delta f}{f}\right| = \lambda^2\,\frac{\Delta m}{m} \qquad \ldots\ldots\ldots\ldots\ldots\ldots (6.10)$$

From which it can be seen that for a particular mass error the

restoring force error simply increases with the square of the frequency i.e., as expected, it depends on the magnitude of the acceleration. Crawley and O'Donnell [40] showed a similar result in a different way.

Worden and Tomlinson [52,60] showed that the estimated restoring force could be written

$$\hat{f} = \frac{\hat{m}}{m} f - \frac{\Delta m}{m} p \qquad \ldots\ldots\ldots\ldots\ldots\ldots\ldots\ldots (6.11)$$

so that errors in the mass lead to a scaling factor $\hat{m}/m$ and a bias of $-(\Delta m/m)p$ on the restoring force. The effect on the fitted parameters will depend upon the excitation and the system itself. They showed that for random excitation the bias term introduces "noise" into the restoring force, but this is not true for sinusoidal type excitation.

Another way of writing the error is to note that

$$\Delta f = \hat{f} - f = -\Delta m \ddot{x} \qquad \ldots\ldots\ldots\ldots\ldots\ldots\ldots\ldots (6.12)$$

If the system is linear and a simple polynomial fitted to f then it is possible to write

$$\Delta f = \Delta c \dot{x} + \Delta k x$$

For steady-state sinusoidal excitation the acceleration is proportional to the displacement and so it can be shown that the errors in the fitted parameters are $\Delta c = 0$ and $\Delta k = +\omega^2 \Delta m$ so only the stiffness is affected. However for other excitations or nonlinear systems the effects will be more complex and all parameters would be in error.

In order to illustrate the effect of a mass error on a nonlinear system, a single-d.o.f. system with quadratic damping nonlinearity was simulated using the following parameters

$m = 1$ kg

$c = 5$ N/m/s (2.5% critical damping)

$k = 10000$ N/m ($f_n = 15.91$ Hz)

$\gamma = 5$ N/m^2/s^2 (coefficient of quadratic damping term)

The estimated mass value used to calculate the restoring force was assumed to be 0.5 kg and the force-state mapping identification was carried out for excitation frequencies below, at and above the natural frequency, namely

$f_1 = 10$ Hz , $f_2 = 15.91$ and $f_3 = 20$ Hz.

The excitation signal for each case was a single frequency sine wave having an R.M.S. value of 20 N and the simulated response was allowed to reach a steady-state. The identified system parameters corresponding to each excitation frequency are shown in table (6.1) together with their percentage errors.

Frequency (Hz)	$\hat{k}$	$\hat{c}$	$\hat{\gamma}$	k_e(%)	c_e(%)	γ_e(%)
10.00	7951	6.85	-0.39	-20.5	37.0	-108
15.91	5000	7.56	-0.49	-50.0	51.2	-110
20.00	2458	8.41	-0.39	-75.4	68.3	-108

Table (6.1). Parameters identified using wrong mass.

It can be seen that there is a systematic increase in the stiffness and damping errors with excitation frequency whereas the quadratic damping estimate was fairly independent of frequency but badly in error, even the sign being incorrect. The errors in the stiffness are very close to those expected for a linear system using $\Delta k = -\omega^2 \Delta m$ but the presence of nonlinearity has modified the signals such that the damping error is now significant and not zero. Note that the natural frequency of the fitted model is quite

different to the true value so the results would not be of any use.

When the same example was analysed using a frequency sweep over the frequency range covered by the 3 discrete frequencies, the errors in the parameters were k_e=48% , c_e=41% and γ_e=29.8% so errors of a similar magnitude occur.

Notice that Crawley and O'Donnell [40] recommended that the restoring force should be measured well below the natural frequency in order that the effect of any possible error in the mass may be reduced. A major drawback of such an argument is that the use of data well below resonance would probably not allow a strong excitation of the nonlinearity present in the system. Also the acceleration signal would be small and subject to larger measurement errors. It is believed therefore that rather than attempting to reduce the effect of the mass error on the restoring force, it would be more appropriate to investigate how to obtain a correct mass value.

6.3. Mass estimation for single-d.o.f. linear systems.

In this section, the estimation of the mass for single-d.o.f. linear systems is considered. However, the main aim of the study is to show that the use of methods based on linear theory for estimating the mass of nonlinear systems is inappropriate and may yield unacceptable results. It will therefore be necessary to seek alternative methods which take into consideration the nonlinear behaviour of the system, thus yielding more reasonable mass values. Some such methods can actually use incorrect estimates from linear system approaches to act as the starting point for refinement when the system is nonlinear.

The approach considered here is believed to be a fairly typical way of estimating the mass for a single-d.o.f. linear system. The analysis is based on using real and imaginary FRF data, preferably

obtained using steady-state excitation. The FRF of a single-d.o.f. linear system may be written in the form

$$\frac{\tilde{X}}{P} = A(\omega) + i\,B(\omega) = \frac{(k-\omega^2 m) - i\omega c}{(k-\omega^2 m)^2 + \omega^2 c^2} \qquad \ldots\ldots\ldots (6.13)$$

where $A(\omega)$ and $B(\omega)$ are the real and imaginary parts of the FRF respectively, P is the amplitude of the input force and $\tilde{X}$ is the complex amplitude of the response. Differentiating $A(\omega)$ with respect to ω yields

$$\frac{dA}{d\omega} = -2\omega m\, S + (k-\omega^2 m)\,\frac{dS}{d\omega}$$

where $$S = \frac{1}{(k-\omega^2 m)^2 + \omega^2 c^2}$$

At the undamped natural frequency $\omega=\omega_n$, then

$$\left[\frac{dA}{d\omega}\right]_{\omega_n} = \frac{-2\,\omega_n\, m}{(\omega_n c)^2} \qquad \ldots\ldots\ldots\ldots\ldots (6.14)$$

and also

$$\left[\,B\,\right]_{\omega_n} = \frac{-1}{\omega_n\, c} \qquad \ldots\ldots\ldots\ldots\ldots (6.15)$$

Substituting (6.15) into (6.14) yields

$$m = \frac{-\left[\frac{dA}{d\omega}\right]_{\omega_n}}{2\,\omega_n\,[B^2]_{\omega_n}} \qquad \ldots\ldots\ldots\ldots\ldots (6.16)$$

from which it can be seen that the mass may be estimated using the imaginary part and the slope of the real part at the natural frequency.

Notice that it is also possible to estimate the mass from the slope of the real part of the inverse FRF at the natural frequency or from the behaviour of the FRF well above the natural frequency where the inertia force dominates.

There are various possible ways of obtaining the natural frequency, needed in equation (6.16), for single-d.o.f. systems. However, in order to be consistent with the later multi- d.o.f. work, presented in section (6.6), the following parameter is considered, namely

$$\mu(\omega) = \frac{A(\omega)}{B(\omega)} = -\left(\frac{k-\omega^2 m}{\omega c}\right) = \frac{-1}{\tan \phi} \qquad \ldots\ldots\ldots (6.17)$$

and it can be seen that plotting $\mu(\omega)$ against ω would yield the natural frequency at which $\mu = 0$.

6.3.1. Linear example.

The example given in the last section was reconsidered with the coefficient of the quadratic damping term set to zero. The FRF of the resulting linear system was obtained using a stepped-sine steady-state excitation with an R.M.S. value of 10 N.

In order to estimate the natural frequency of the system the parameter μ (referred to later in section 6.6 as an "eigenvalue") was plotted against the frequency as shown in Fig. (6.1). A straight line was then fitted through the four points nearest to the frequency axis and the natural frequency was obtained as the frequency corresponding to the point at which the fitted line crossed the frequency axis. The resulting value was 15.91 Hz which is equal to the exact natural frequency.

The mass value was obtained by curve fitting a third order polynomial through the corresponding four points on each of the real and imaginary parts shown in Fig. (6.2). The fitted equation for the real part was then differentiated with respect to the frequency and evaluated, together with the imaginary part, at the estimated natural frequency. The resulting values were then used in equation (6.16) to yield a mass value of 0.9975 kg, only 0.25% in error. Clearly the approach has coped well with such a linear

system but requires a reasonable frequency resolution for the slope to be evaluated.

6.3.2. Nonlinear example.

In order to demonstrate the effect of nonlinearity on the mass estimated using an approach based on linear theory, a cubic stiffness term with $\beta=-10^6$ N/m^3 was added to the linear system considered above. The FRF of the resulting system is shown in Fig. (6.3) for three force levels having R.M.S. values of 7.5, 10 and 12.5 N and compared to the FRF of the linear part of the system (curve 1).

Clearly, adding a nonlinear term into the system has affected the FRF dramatically by shifting the peaks to the left, indicating a softening stiffness behaviour. The jump phenomena is also apparent for the largest force level. It would be expected that the use of such data will certainly result in a different mass value for each force level. In fact, when μ was plotted against frequency for the 3 force levels the crossing point of μ on the frequency axis was shifted to the left as the force level increased and so 3 different values for the natural frequency were obtained, namely 15.63, 15.40 and 15.17 Hz (all wrong).

Fig. (6.4) shows the real part of the FRF corresponding to the three force levels and clearly the slope changes with force level. The use of equation (6.16) yielded the following mass estimates corresponding to the three force levels, namely

$\hat{m}$ = 0.965 kg (m_e = -3.5%) P = 7.5 N

$\hat{m}$ = 1.110 kg (m_e = 11.0%) P = 10 N

$\hat{m}$ = 2.578 kg (m_e =157.8%) P = 12.5 N

and clearly the error increases as the contribution of the nonlinearity to the response increases. The mass estimates at the

lowest two force levels are surprisingly reasonable but the estimate at the highest force level is likely to have been affected by the jump phenomena.

Clearly some way of accounting for the nonlinearity of the system when estimating the mass would be helpful in order to obtain reasonable accuracy. One possibility would be to observe the trend of the estimated mass with force level and extrapolate back to zero force where the system is arguably linear for this type of nonlinearity (but not for friction). However the above results indicate that the variation is not simple.

6.4. Mass estimation for single-d.o.f. nonlinear systems.

In the literature concerned with the development of the force-state mapping approach there have been two attempts to estimate the mass for single-d.o.f. systems. Both use a similar philosophy in that, the acceleration is involved in some way in a curve fit so that its coefficients would be either an estimate for the mass or an error in the mass which can be used to correct its initial value. The two independent approaches are those of crawley and O'Donnell [40] and Worden and Tomlinson [52] as mentioned briefly in section (6.1). These methods will be considered within this section.

In the course of this work, a variant approach has been developed. In this approach the philosophy is different, in that the acceleration is used only for estimating the restoring force. The sensitivity of the identified parameters to errors in the mass is studied in some way, leading to an estimate for the mass. For this reason the approach has been called the sensitivity approach and will be presented in some detail in section (6.5). Unfortunately, the theory of this approach has not yet been published, due to time restrictions, but it has been used successfully with real data as pointed out in reference [54].

6.4.1. Crawley and O'Donnell approach.

Crawley and O'Donnell [40] carried out some investigation into curve fitting the input force, rather than the restoring force, using a model given in terms of the acceleration, velocity and displacement signals. In essence, the fitted model is

$$p \approx \hat{m}\,\ddot{x} + \hat{c}\,\dot{x} + \hat{k}\,x + \sum_{i=0}^{M} B_i F_i(x,\dot{x}) \qquad \ldots\ldots\ldots\ldots (6.18)$$

where the basis functions F_i defined earlier in chapter 2 allow for nonlinearity in the data. This model allows the estimation of the mass as being the coefficients of the acceleration term. The technique may seem promising at first glance but unfortunately the robustness of the least squares solution depends heavily on the amplitude and frequency content of the excitation signal. Crawley and O'Donnell analysed the robustness of the solution to the frequency and amplitude for the linear part of equation (6.18) when it is excited by a sinusoidal force. They found that the approach is sensitive to the unmodeled system errors (e.g. noise) and suggested that high frequency tests enhance the inertia effect with respect to the stiffness and are better for identifying the mass whereas low frequency tests reduce the inertia effect and are better for identifying the stiffness.

The inclusion of the acceleration in the model leads to a significant problem, when steady-state sinusoidal excitation is used, as kindly pointed out to the author by K. Worden who found that wrong mass estimates were obtained. Worden showed that by artificially adding a term of the form ($\alpha x - \alpha x$), actually zero, into the equation of motion for a linear single-d.o.f. system with sinusoidal excitation then

$$(m - \alpha/\omega^2)\,\ddot{x} + c\,\dot{x} + (k - \alpha)\,x = p \qquad \ldots\ldots\ldots\ldots\ldots (6.19)$$

A fit of the form proposed by Crawley and O'Donnell would lead to the estimated parameters

$$\hat{m} = m - \alpha/\omega^2$$
$$\hat{c} = c$$
$$\hat{k} = k - \alpha$$

from which it can be seen that the identified mass will be biased by a frequency dependent term and thus the least squares problem has a family of solutions for the mass each of which corresponds to an arbitrary value of α. The problem is due to the linear dependence of the displacement and acceleration signals. In such a case, the data can not distinguish between the two basis functions x and $\ddot{x}$ used in the design matrix for the least squares solution [50].

The author has since examined the problem by considering the equations involved in the least squares solution for the linear part of equation (6.18), using sinusoidal excitation. The equations are

$$\begin{bmatrix} \omega^3 & 0 & -\omega \\ 0 & \omega & 0 \\ -\omega & 0 & 1/\omega \end{bmatrix} \begin{Bmatrix} \hat{m} \\ \hat{c} \\ \hat{k} \end{Bmatrix} = \begin{Bmatrix} (\omega/H)\sin\phi \\ (1/H)\sin\phi \\ (1/\omega H)\cos\phi \end{Bmatrix} \quad \ldots\ldots\ldots (6.20)$$

where H is the modulus of the FRF and ϕ is its phase. On inspection it may be seen that the matrix is singular for any excitation frequency which means that there is no unique solution in this least squares problem for the $\hat{m}$ and $\hat{k}$ parameters as found by Worden.

If however the excitation was a swept sine or random signal then the matrix would be different and a unique solution would exist. Also, for a nonlinear system, the matrix is different and the presence of sub/super harmonics in the response could destroy the linear dependence of displacement and acceleration so a unique

solution should exist even for steady-state sinusoidal excitation.

(a). Linear example.

The above approach was applied to the linear system considered earlier in section (6.3.1). The system was excited at discrete frequencies from 13 to 19 Hz in steps of 1 Hz using a sinusoidal force with R.M.S. value of 10 N. As was expected, when steady-state data were used, the approach yielded wrong parameters (e.g. $\hat{m}$= -0.12, $\hat{c}$= 5.01 and $\hat{k}$= -304 at a frequency of 15 Hz).

However, when data were taken from the start of the excitation, then due to the transient in the response, the signal contained the damped natural frequency of the system in addition to the excitation frequency. In this case the identified parameters were exact for all the above frequency cases since the linear dependence of displacement and acceleration no longer existed and so the design matrix became nonsingular.

(b). Linear example with measurement noise.

In order to examine how sensitive the approach is to measurement noise, the force and acceleration signals were contaminated using a Gaussian noise sequence having an R.M.S. value of 2% of each signal. To make the simulation closer to a practical problem, the two noise sequences of the force and acceleration were generated using two different seed values. The displacement and velocity signals were assumed to be uncorrupted so in essence only the restoring force was corrupted. In practice the noise content on these signals would depend upon whether they were directly measured or obtained by integration. The latter has been considered in this work and it has been shown in chapter 4 that the frequency domain integration would reduce the higher frequency noise content significantly from both the velocity and displacement signals due to the division by $j\omega$ and $-\omega^2$ respectively.

At each frequency the input force was curve fitted to the linear part of the model given in equation (6.18), the transient part of the response being used. The identification of the system parameters was carried out for 20 noise cases, each of which used a different noise sequence, and the results were then averaged. Fig. (6.5) shows a plot of the average mass against the frequency of excitation, compared with the noise-free mass estimate. Clearly the approach seems very sensitive to measurement noise particularly around the natural frequency where the results show a relatively large bias. This may be because the two frequencies present in the transient response are closer together in this region and therefore the acceleration and displacement signals are more nearly linear dependent, thus making the design matrix more nearly singular. The "standard deviation" value of the mass estimate was around 0.01 for all frequency cases indicating that the scatter on the estimates was small.

When the above process was repeated but for a sine sweep from 13 to 19 Hz, the mean value of the 20 mass estimates corresponding to 20 noise cases was 0.965 with a standard deviation of 0.009. Thus the approach is less sensitive for sweep excitation since the linear dependence of acceleration and displacement is removed.

(b). Nonlinear example with measurement noise.

In order to apply the approach to a nonlinear system, a cubic stiffness element with $\beta = -10^6$ N/m^3 was added into the above linear system and the identification process repeated in exactly the same manner using similar noise data except that the force level was increased to 20 N in order to excite the nonlinearity strongly. Fig. (6.6) shows a plot of the average mass against the excitation frequency, compared to the noise-free mass estimate. The mass values are definitely better than those obtained for the above linear case around the resonance region of the system. The errors are smaller probably because any near linear dependence of

the acceleration and displacement in this region will be less due to the nonlinearity in the data.

6.4.2. Worden and Tomlinson approach.

Worden and Tomlinson [52] showed that when using an incorrectly estimated mass value $\hat{m}$, the estimated restoring force would be given by

$$\hat{f} = f - \Delta m \ddot{x} \qquad \text{.....(6.21)}$$

where f is the exact restoring force and Δm is the mass error. This equation implies that in order to obtain unbiased system parameters, an acceleration term should be included in the model fitted to the estimated restoring force. For a perfect fit, the coefficient of the acceleration would be the error in the mass and the other estimates would be unbiased. If necessary the procedure could be repeated until convergence is obtained but in an ideal situation one step is sufficient. The idea is interesting and yielded accurate estimates of mass for linear and nonlinear simulated examples. However when it was applied to the above examples with noise it yielded similar results to those obtained using the above approach. Clearly, this approach suffers from the same problem of linear dependence of acceleration and displacement for sinusoidal excitation, but it is also less sensitive to noise for sweep excitation.

6.5. Sensitivity approach for mass estimation of single-d.o.f. nonlinear systems.

This approach has been developed in this work and is based on studying the sensitivity of the parameters identified by force-state mapping with respect to the mass. In order to illustrate the approach the theoretical analysis will firstly be given for a linear system and then extended to account for the presence of a cubic stiffness term in the same system. Because it

would be extremely difficult to include other types of nonlinearity in the analysis, the validity of the approach for other nonlinearities as well as multiple nonlinearities will be examined by considering some simulated examples once the basic philosophy has been presented.

6.5.1. Basic philosophy for a linear system.

If it is supposed that an incorrect estimate of the mass $\hat{m}$ for a single-d.o.f. linear system is available then the estimated restoring force will also be incorrect and given by

$$\hat{f}(x,\dot{x}) = p - \hat{m}\,\ddot{x} \qquad \ldots\ldots\ldots\ldots\ldots\ldots\ldots (6.22)$$

As was shown in the previous chapters, the usual force-state mapping procedure is to curve fit the estimated restoring force in terms of the states x and $\dot{x}$ in order to obtain estimates for the parameters of the system. Thus

$$\hat{f}(x,\dot{x}) \approx \hat{f}_c(x,\dot{x}) = \hat{c}\,\dot{x} + \hat{k}\,x \qquad \ldots\ldots\ldots\ldots\ldots (6.23)$$

where $\hat{f}_c$ is the curve fitted restoring force which would satisfy

$$\hat{f}_c(x,\dot{x}) = p - \hat{m}\,\ddot{x} \qquad \ldots\ldots\ldots\ldots\ldots\ldots\ldots\ldots (6.24)$$

for a perfect fit. In such a case then, from equations (6.23) and (6.24), it is possible to write

$$\hat{k}\,x = p - \hat{m}\,\ddot{x} - \hat{c}\,\dot{x} \qquad \ldots\ldots\ldots\ldots\ldots\ldots (6.25)$$

If it is assumed that the excitation is sinusoidal at frequency ω the input and steady-state response signals can be described by

$$p = P\cos\omega t \qquad \text{and} \qquad x = X\cos(\omega t - \phi)$$

Substituting p and x into equation (6.25) and equating terms in sin ωt and cos ωt leads to the equations

$$\hat{k}\ X \cot \phi = \frac{P}{\sin \phi} + \omega^2\ \hat{m}\ X \cot \phi + \omega\ \hat{c}\ X \quad .....(6.26.a)$$

$$\hat{k}\ X \tan \phi = \omega^2\ \hat{m}\ X \tan \phi - \omega\ \hat{c}\ X \quad .....(6.26.b)$$

Then adding these two equations yields

$$\hat{k} = \frac{1}{H} \cos \phi + \omega^2\ \hat{m} \quad .....(6.27)$$

where H=X/P and ϕ are the exact amplitude and phase values of the FRF of the system at a frequency ω. By substituting for H and ϕ it may be shown that the equation may be rewritten as

$$\hat{k} = (k-\omega^2 m) + \omega^2\ \hat{m} \quad .....(6.28)$$

where m and k are the exact mass and stiffness respectively. These equations describe the estimated stiffness $\hat{k}$ as a function of the estimated mass $\hat{m}$. For a particular excitation frequency ω_0 then the corresponding values of the amplitude H_0 and phase ϕ_0 would be constant and hence the relationship between $\hat{k}$ and $\hat{m}$ would be linear. If $\hat{k}$ was then plotted against $\hat{m}$ for this frequency a straight line would be obtained having a slope equal to ω_0^2 and an intercept equal to $(\cos \phi_0/H) = k(1-\lambda_0^2)$, where $\lambda_0=\omega_0/\omega_n$.

To illustrate the behaviour of equation (6.27), consider three excitation cases, namely

(i) a resonance where $\lambda_0 = 1$ and the intercept is zero,
(ii) below resonance where $\lambda_0 < 1$ and the intercept would be positive, and
(iii) above resonance where $\lambda_0 > 1$ and the intercept would be negative.

Plotting $\hat{k}$ against $\hat{m}$ for these three cases gives the three

straight line graph shown in Fig.(6.7). Now, on each of these lines there is a single point at which the estimated mass and stiffness parameters are exact, namely $\hat{m} = m$ and $\hat{k} = k$. Therefore all three lines must meet at this point and this provides the basis of the sensitivity approach.

The idea of the approach is to determine the intersection point by plotting lines for two or more different excitation frequencies. Because the lines are straight then only two points on the line for each frequency are required. These two points can correspond to two initial mass estimates $\hat{m}_1$ and $\hat{m}_2$ which should be selected such that they embrace an initial mass estimate $\hat{m}$ obtained using, for example, the approach given in section (6.3). The general procedure of the sensitivity approach can be carried out as follows :

1) The system is excited at frequency $\omega_1 < \omega_n$ and the response is measured so the restoring force may be estimated using the first initial mass value $\hat{m}_1 < \hat{m}$, namely

$$\hat{f}_1 = p - \hat{m}_1 \ddot{x}$$

2) The corresponding force-state map is produced and curve fitted in terms of the states x and $\dot{x}$ to yield a model for the system from which $\hat{k}_1$ becomes available.

3) For the other mass estimate $\hat{m}_2 > \hat{m}$ or $\hat{m}_2$ typically 2-3 times $\hat{m}_1$, the restoring force is estimated and step 2 is repeated so that $\hat{k}_2$ becomes also available.

4) The values $(\hat{k}_1, \hat{m}_1)$ and $(\hat{k}_2, \hat{m}_2)$ determine a straight line L1 in the $[\hat{k}, \hat{m}]$ plane.

5) For the same initial mass estimates $\hat{m}_1$ and $\hat{m}_2$, steps 1-4 are repeated at a different frequency $\omega_2 > \omega_n$ and thus another straight line L2 with a different slope and intercept is obtained.

6) The point of intersection of these two straight lines, shown in Fig. (6.8), should correspond to a point in the $[\hat{k},\hat{m}]$ plane for which the mass and stiffness values are exact.

In principle no more than two masses and frequencies are required but in practice the presence of experimental error may mean that an average result could be obtained using more than two frequencies.

The analysis has been restricted to steady-state sinusoidal excitation but it will be shown later by example that the lines may be obtained instead from narrow band frequency sweeps (i.e. when data are taken from the start of the excitation).

6.5.2. Extension of approach to a system with cubic stiffness nonlinearity.

As was pointed out earlier, the analytical extension of the approach to nonlinear systems will be restricted to the well known cubic stiffness nonlinearity for which the equation of motion may be written as

$$m\ddot{x} + c\dot{x} + k x + \beta x^3 = P \cos \omega t \qquad \ldots\ldots\ldots\ldots (6.29)$$

In general the periodic response of a nonlinear system to a steady-state sinusoidal excitation consists of three terms; the fundamental component at the excitation frequency, a series of superharmonic components at integer multiples of the excitation frequency and a series of subharmonic components at integer fractions of the excitation frequency [61]. It would be very difficult to obtain the full series solution to equation (6.29) in analytical form but fortunately it is common practice to reduce the form of the solution for particular nonlinearities by neglecting many of the series components in order to obtain an approximate solution.

In order to carry out an approximate analysis for the cubic stiffness problem, then for simplicity the undamped case will be considered, namely

$$m\ddot{x} + k x + \beta x^3 = P \cos \omega t \qquad \ldots\ldots\ldots\ldots (6.30)$$

and this is known as the Duffing equation. The dominant response of this could be made up of the fundamental and third superharmonic, so

$$x = X \cos \omega t + A \cos 3\omega t \qquad \ldots\ldots\ldots\ldots\ldots (6.31)$$

Though other terms could be included the analysis would become unwieldy and it is considered that this simplified assumed solution is sufficient to illustrate what happens when the sensitivity approach is used.

As in the linear case, curve fitting the estimated restoring force would yield

$$\hat{f}_c = \hat{k} x + \hat{\beta} x^3 = P \cos \omega t - \hat{m} \ddot{x} \qquad \ldots\ldots\ldots\ldots (6.32)$$

assuming a perfect fit. Then substituting equation (6.31) into (6.32), using the identity $\cos^3\theta = (3/4) \cos \theta + (1/4) \cos 3\theta$ and equating the terms in $\cos \omega t$ and $\cos 3\omega t$ gives the two equations

$$\hat{k} + (3/4)\, \hat{\beta}\, (X^2 + X A + 2A^2) = \frac{P}{X} + \omega^2 \hat{m} \qquad \ldots\ldots\ldots (6.33)$$

$$\hat{k} + (3/4)\, \hat{\beta}\, \left(\frac{X^3}{3A} + 2X^2 + A^2 \right) = 9\omega^2 \hat{m} \qquad \ldots\ldots\ldots (6.34)$$

The other trigonometric terms are ignored since they would lead to the coefficients of other harmonic terms not included in the solution.

Now, eliminating $\hat{\beta}$ from equation (6.33) and (6.34) leads to

$$\hat{k} = \left[\frac{R}{R-1}\ \frac{P}{X}\right] + \left[\frac{R-9}{R-1}\right] \omega^2\, \hat{m} \qquad \ldots\ldots\ldots\ldots (6.35)$$

where

$$R = \frac{(1/3) + 2\nu + 3\nu^3}{\nu + \nu^2 + 2\nu^3} \qquad \text{and} \qquad \nu = A/X$$

Following the same argument presented for the linear case it can be seen from equation (6.35) that the relationship between $\hat{k}$ and $\hat{m}$ is actually still linear for a particular excitation frequency, even though the system is nonlinear.

In this case the slope and intercept of the straight line differ to the values of ω^2 and $1/H$ $(=P/X)$ for a linear undamped system $(\phi=0)$ but when $A \longrightarrow 0$ then $R \longrightarrow \infty$ and the results are the same.

Although various approximations have been made, it would appear that the sensitivity approach will work for this nonlinear system, though the results may not be perfect if other harmonics are significant. Damping is not expected to make any substantial difference to the result.

No other nonlinearities have been considered analytically. It is not obvious to the author how the method could be proven for any general nonlinearity. Instead the approach will be investigated by examples to show that it does in fact work for different types and combinations of nonlinearity.

6.5.3. Examples of the sensitivity approach.

(a). Linear system.

The linear system considered earlier in section (6.3.1) is reconsidered here and the initial mass values were taken as $\hat{m}_1$ = 0.5 kg and $\hat{m}_2$ = 1.5 kg.

Following the procedure outlined in section (6.5.1), the estimated parameters corresponding to these two initial mass values and to two frequencies f_1 = 13 Hz and f_2 = 19 Hz are given in table (6.2)

Frequency	$\hat{m}$	$\hat{K}$	$\hat{c}$
f_1=13 Hz	0.5	6551.2	5.344
	1.5	13448.8	4.655
f_2=19 Hz	0.5	3237.6	5.349
	1.5	16762.4	4.650
Exact value	1.0	10000.0	5.000

Table (6.2). Estimated parameters for the linear example.

Fig. (6.9) shows a plot of $\hat{k}$ against $\hat{m}$ obtained by joining up the results for the two frequencies. The intersection of the resulting two straight lines corresponded to the values

$\hat{m}$ = 1.000001 and $\hat{k}$ = 9999.992

which are exactly equal to the true values to within the accuracy of the computer used.

(b). Nonlinear example with cubic stiffness.

A cubic stiffness element with $\beta = -10^6$ N/m^3 was added to the above system as for the example in section (6.3.2). The R.M.S. excitation force level was 20 N which, as seen in Fig. (6.3), will excite the nonlinear behaviour strongly. The mass estimation procedure was applied as in the above example but the force-state mapping identification included a cubic stiffness term in the fitted model. The results are shown in table (6.3).

Frequency	$\hat{m}$	$\hat{K}$	$\hat{c}$	$\hat{\beta}$
f_1=13 Hz	0.5	6837.5	5.343	-0.5253E7
	1.5	13162.5	4.656	0.3253E7
f_2=19 Hz	0.5	2712.9	5.367	0.9669E7
	1.5	17287.1	4.632	-0.1166E8
Exact value	1.0	10000.0	5.000	-0.1000E7

Table (6.3). Estimated parameters for the cubic stiffness example.

Fig. (6.10) shows a plot of $\hat{k}$ against $\hat{m}$ and the intersection of the two lines occurred at

$\hat{m}$ = 0.999997 and $\hat{K}$ = 9999.975

which are also very accurate when compared to the exact values. Clearly the approach has worked for this nonlinear example, notwithstanding the approximations in the attempt to demonstrate it analytically.

(c). Nonlinear example with quadratic damping.

The cubic stiffness element of the above example was replaced by a quadratic damping element with γ = 5 $N/m^2/s^2$. The R.M.S. force level was also 20 N. The fitted model included a special function to account for the nonlinearity. The results are shown in table (6.4).

Similarly, when $\hat{k}$ was plotted against $\hat{m}$ the intersection occurred at

$\hat{m}$ = 0.999996 and $\hat{k}$ = 9999.978

which are also nearly exact so the approach has worked for a different type of nonlinearity.

Frequency	$\hat{m}$	$\hat{K}$	$\hat{c}$	$\hat{\gamma}$
f_1=13 Hz	0.5	6591.8	7.676	1.194
	1.5	13408.2	2.323	8.805
f_2=19 Hz	0.5	3083.5	8.760	0.179
	1.5	16916.5	1.239	9.820
Exact value	1.0	10000.0	5.000	5.000

Table (6.4). Estimated parameters for the quadratic damping example.

(d). Nonlinear example with quadratic damping and cubic stiffness.

All the nonlinear examples considered so far in this chapter have included only one type of nonlinearity. In the following example the sensitivity procedure will be applied to estimate the mass for a nonlinear system having both cubic stiffness and quadratic damping elements. Clearly the presence of these two elements in a particular system would have a significant effect on its FRF since both damping and stiffness behaviour would change with force level.

The coefficients of these two elements were considered to be β=-10^6 N/m^3 and γ=5 N/m^2/s^2. The linear part of the system is the same as for the previous examples. The R.M.S. values of the input force was 20 N as before. The identification results obtained using the above two initial mass values are shown in table (6.5).

As before, a plot of $\hat{k}$ against $\hat{m}$ yielded the following values

$\hat{m}$ = 1.000003 and $\hat{k}$ = 1.0000.03

and again the results are encouragingly close to the exact values.

An interesting point about the sensitivity approach is that the linear relationship is not only valid between $\hat{k}$ and $\hat{m}$ but also

Frequency	$\hat{m}$	$\hat{K}$	$\hat{c}$	$\hat{\beta}$	$\hat{\gamma}$
f_1=13 Hz	0.5	6782.5	7.593	-0.4180E7	1.390
	1.5	13217.5	2.407	0.2180E7	8.609
f_2=19 Hz	0.5	2637.9	8.789	0.1058E8	0.109
	1.5	17362.1	1.210	-0.1258E8	9.890
Exact value	1.0	10000.0	5.000	-0.1000E7	5.000

Table (6.5). Estimated parameters for the 2 nonlinear element example.

between any of the estimated parameters and $\hat{m}$. In Fig. (6.11) each of the estimated parameters $\hat{c}$, $\hat{\beta}$ and $\hat{\gamma}$ for this example are plotted against $\hat{m}$. The corresponding points of intersection occurred at the following values

$\hat{m}$ = 1.000005 , $\hat{c}$ = 4.999956
$\hat{m}$ = 0.999997 , $\hat{\beta}$ = -0.999994E6
$\hat{m}$ = 1.000012 , $\hat{\gamma}$ = 5.000105

which are also very close to the exact values.

The author has found that the approach works very well for other types of nonlinearity such as friction, clearance etc and for more complicated systems, having coupling terms between velocity and displacement as in the Van der Pol oscillator.

6.5.4. Application of the sensitivity approach using nonparametric curve fit.

As has been shown, the implementation of the sensitivity approach requires that the estimated restoring force is curve fitted in terms of the states. However, in the above example it has been assumed that the type of nonlinearity is known and thus a parametric identification procedure has been carried out, with the exact number of terms being included in the fitted models. In

practice the type of nonlinearity present in a system would not be known precisely. Therefore it is more appropriate to use a nonparametric curve fit with a more general model; thus conforming to the original philosophy of the force-state mapping technique.

In accordance with this argument, the sensitivity approach was applied again to estimate the mass for the earlier example with two nonlinear elements. The procedure was carried out exactly as before but this time a nonparametric model of the form,

$$\hat{f}(x,\dot{x}) = a_1 x + a_2 \dot{x} + a_3 x^2 + a_4 \dot{x}^2 + a_5 x^2 \dot{x} + a_6 x \dot{x}^2 + a_7 x^3 + a_8 \dot{x}^3 + a_9 \dot{x}^2 \text{sign}(\dot{x}) + a_{10} \text{sign}(\dot{x}) \quad \ldots\ldots\ldots\ldots\ldots (6.36)$$

was used in the least squares curve fit. When the identified linear stiffness term was plotted against the mass, the intersection of the two lines occurred at $\hat{m}$=0.999995 and $\hat{k}$=9999.92 which are again very accurate. Also the corresponding cubic stiffness and quadratic damping terms were of similar accuracy. An interesting point is that even when the coefficient of a term not actually present in the data, such as friction, was plotted against the mass, the values $\hat{m}$=1.00018 and $\hat{a}_{10}$=0.00014 were obtained. This indicates that the system does not contain this type of nonlinearity since the coefficient is very small but the companion mass estimate is still surprisingly accurate.

6.5.5. Effect of systematic errors on the sensitivity approach.

In the previous chapter, it was shown that an analytical consideration of the effect of systematic amplitude and phase errors on the force-state mapping technique was useful. In this section the same philosophy will be applied to see how such errors affect the accuracy of the estimated mass obtained by the sensitivity approach.

In section (5.2) it was shown that, when systematic amplitude and phase errors were present, the least squares fit to the restoring

force of a linear system led to equation (5.12). This equation can be simplified to yield a relationship between the estimated stiffness $\hat{k}$ and the mass $\hat{m}$ assumed for the identification, namely

$$\hat{k} = \frac{k\,\alpha_p}{\alpha_d}\left[\,(1-\lambda^2)\,\Phi_{k1} - 2\,\zeta\,\lambda\,\Phi_{k2}\,\right] + \frac{\alpha_a}{\alpha_d}\,\Phi_{k3}\,\omega^2\,\hat{m} \qquad \ldots\ldots(6.37)$$

where the exact mass m has been replaced by $\hat{m}$ and k is the exact stiffness. All the other terms in this equation were defined in section (5.2). Clearly there is a linear relationship between $\hat{k}$ and $\hat{m}$ for each frequency and the slope and intercept are dependent upon the amplitude and phase errors. However, because the effect of these errors on the estimated mass is required, an expression for the point of intersection of the two lines corresponding to different frequencies, is needed. It can be easily shown that this expression is given by

$$\hat{m} = \frac{A_2 - A_1}{B_1 - B_2} \qquad \ldots\ldots(6.38)$$

where A_1 and A_2 are the intercepts and B_1 and B_2 are the slopes of the 2 straight lines corresponding to the two frequencies used. It is likely that any phase and/or amplitude errors will be present at both of the frequencies but they could be frequency dependent.

It will be assumed in the examples considered here that there are only relative errors between the acceleration and the force and that there are no integration errors.

Firstly, when only relative <u>amplitude</u> errors are present between the force and acceleration then it is reasonable to choose $\alpha_p = 1$ and $\alpha = \alpha_a = \alpha_v = \alpha_d \neq 1$ but all phase errors are zero so equation (6.37) becomes

$$\hat{k} = \frac{k}{\alpha}\,(1-\lambda^2) + \omega^2\,\hat{m} \qquad \ldots\ldots(6.39)$$

so only the intercept is affected and the damping is not involved. If the amplitude error α is the same for both the frequencies used

then from equation (6.39) and (6.38), the intersection occurs at

$$\hat{m} = \frac{k}{\alpha\ \omega_n^2} = \frac{m}{\alpha} \qquad \ldots\ldots\ldots\ldots\ldots\ldots\ldots (6.40)$$

so there is a direct relation between the error and the mass (e.g. α=1.02 means $\hat{m}$=0.98 m). The expression is more complex when the error varies with frequency but such a calibration error is unlikely to change much between two frequencies fairly close to resonance. Thus equation (6.40) provides a fair guideline and there are no worrying effects since α tends to cancell out when the restoring force is calculated using

$$\hat{f} = p - \hat{m}\ \ddot{x}_m = p - (m/\alpha)\ \alpha\ \ddot{x}$$

where $\ddot{x}_m$ and $\ddot{x}$ are the measured and exact acceleration respectively. However, when this <u>exact</u> restoring force is curve fitted in terms of the biased velocity and displacement signals then the resulting equation of motion will be

$$\hat{m}\ \ddot{x}_m + \hat{c}\ \dot{x}_m + \hat{k}\ x_m = p$$

where $\hat{c} = c/\alpha$ and $\hat{k} = k/\alpha$ so α is embedded in the signals and the identified parameters and hence this equation is able to predict the measured as opposed to true response. This is also the case for nonlinear systems where powers of α may be involved.

Secondly, when only phase errors are present between the measured acceleration and the force but integration errors are neglected then it is reasonable to take ε_p=0, $\varepsilon = \varepsilon_a = \varepsilon_v = \varepsilon_d$. As a result equation (6.37) reduces to

$$\hat{k} = k \left[(1-\lambda^2) \cos \varepsilon_{dp} - 2\ \zeta\ \lambda \sin \varepsilon_{dp} \right] + \omega^2\ \hat{m} \qquad \ldots\ldots (6.41)$$

As in the earlier case, the errors only affected the intercept,

but this time the damping of the system is involved. If the phase error is the same for both frequencies then from equations (6.41) and (6.38), the intersection occurs at

$$\hat{m} = m \left[\cos \varepsilon_{dp} + (\zeta / \bar{\lambda}) \sin \varepsilon_{dp} \right] \qquad \ldots\ldots\ldots\ldots\ldots (6.42)$$

where $\bar{\lambda}$ is the frequency ratio corresponding to the average of the two frequencies used (usually $\bar{\lambda} \approx 1$). It can be seen from this equation that the mass will be underestimated for low damping or for negative values of ε_{dp} but can be overestimated for higher dampings and positive values of ε_{dp}. However, inserting some values shows that the errors are extremely small even for significant phase errors (e.g. for $\zeta=0.05$, $\varepsilon_{dp}= +5^{0}$ gives $\hat{m}=1.0006m$ and $\varepsilon_{dp}=-5^{\circ}$ gives $\hat{m}=0.9918m$). The variation is clearly more complex when the error is frequency dependent but the results should still be fairly accurate.

Finally when only phase errors are present in the integration so that $\alpha_{p}=\alpha=1$, $\varepsilon_{p}=\varepsilon_{a}=0$ but $\varepsilon_{v}\neq\varepsilon_{d}\neq 0$ then equation (6.37) becomes quite complicated. However if for simplicity only phase error $\Delta\varepsilon$ is introduced at each integration then $\varepsilon_{v}=\Delta\varepsilon$ and $\varepsilon_{d}=2\Delta\varepsilon$ and equation (6.37) becomes

$$\hat{k} = \left[(1-\lambda^{2}) - 2\,\zeta\,\lambda \tan \Delta\varepsilon \right] + \omega^{2}\,\hat{m}$$

and hence the estimated mass from equation (6.38) is

$$\hat{m} = m \left[1 + (\zeta/\bar{\lambda}) \tan \Delta\varepsilon \right] \qquad \ldots\ldots\ldots\ldots\ldots\ldots (6.43)$$

so again the error in mass due to integration phase errors will be very small.

It seems that the sensitivity approach to mass estimation is fortunately fairly insensitive to systematic errors.

6.5.6. Effect of noise errors on the sensitivity approach.

Following the same philosophy adopted in chapter 5, it can be shown that the effect of random noise errors on the relationship between $\hat{k}$ and $\hat{m}$ for a linear system is given by the following expression

$$\hat{k} = \left(\frac{1}{1 + \gamma_d^2} \right) \frac{\cos \phi}{H} + \left(\frac{1 + \mu \gamma_a^2}{1 + \gamma_d^2} \right) \omega^2 \hat{m} \qquad \ldots\ldots (6.44)$$

where γ_a and γ_d are the noise to signal ratio for the acceleration and displacement signals respectively, $\mu = \omega^2/(\omega_L \omega_u)$ and ω_L and ω_u are the lower and upper frequency bounds of the noise spectrum. Equation (6.44) has been derived on the basis that noise errors are present only in the measured force and acceleration signals and that the velocity and displacement signals are obtained by integrating the acceleration.

Now for realistic tests, the noise to signal ratio for acceleration γ_a is less than 0.02 ($\gamma_a^2 < 0.0004$) and the value for the displacement is arguably is less than this when frequency domain integration is used. Also μ is likely to be of order unity. Thus an inspection of equation (6.44) shows that the effect of noise on the slope and intercept, and therefore on the mass estimate, is very small.

It would be interesting to see if this result is supported by the simulation carried out earlier using noise.

(a). Linear example.

The same linear example considered earlier in section (6.4.1) with two different Gaussian noise sequences added into the input and acceleration time histories, has been used again. The sensitivity approach was applied such that 7 force-state maps were produced at frequencies 13 to 19 Hz in 1 Hz step. In order to be consistent

with the previous results for the other methods, the noise to signal ratios were $\gamma_p=\gamma_a=2\%$ and 20 noise cases were considered for each frequency, each noise case having a different seed value. The average values of the intercepts and slopes were then calculated for the 7 lines derived from the stiffness estimated in the curve fits using $\hat{m}_1=0.5m$ and $\hat{m}_2=1.5m$. The resulting averaged plots of $\hat{k}$ against $\hat{m}$ are shown in Fig. (6.12). The 22 possible intersection points between the seven lines yielded mass estimates varying from a minimum value of 0.998m to a maximum value of 1.004m. The results are encouraging since the maximum error value was only 0.4% indicating that the approach is not sensitive to measurement noise for this example and there is no obvious bias. Averaging the mass estimates instead of the slopes and intercepts have yielded similar quality results.

(b). Nonlinear example.

The cubic stiffness nonlinear example from section (6.4.1) was also reconsidered and the identification process for the mass carried out in exactly the same manner as above. The resulting averaged lines corresponding to the 7 frequencies yielded mass estimates varying from a minimum value of 1.00004m to a maximum value of 1.006m and both are accurate. By comparison with the results obtained using the Crawley and O'Donnell approach for the same data, the sensitivity approach seems much less sensitive to noise in the measurements. The analytical results expressed in equation (6.44) has also been confirmed.

6.6. Estimation of generalised mass and modal matrices for multi-d.o.f. systems.

The natural extension of the force-state mapping to the identification of multi-d.o.f. systems requires that the modal and generalised mass matrices need to be used for estimating the modal restoring force vector of the system and for transforming from physical to modal coordinates.

So far in this thesis, it has been assumed that those two matrices are known exactly. Clearly for a practical application of the force-state mapping approach the matrices will need to be estimated, preferably using measured data rather than a theoretical model. In this and the following sections, the estimation of these matrices will be considered.

The author has chosen to obtain initial estimates for the generalised mass and modal matrices using a technique based on a linear theory. The initial estimate of the generalised mass matrix can then be refined using the sensitivity approach, which will be extended and applied to multi- d.o.f. systems in section (6.7).

As far as the author is aware, the problems of refining the initial estimate of the modal matrix or of obtaining a correct estimate of the modal matrix for nonlinear systems have not been investigated in connection with the force-state mapping technique. However some comments about the use of a wrongly estimated modal matrix have been given by Worden and Tomlinson [46]. This aspect is also considered in section (6.8).

The linear technique used for obtaining initial estimates of the generalised mass and modal matrices is based upon the use of appropriated multi-point monophase force distributions which are used for exciting pure normal modes of vibration when close modes are a problem. Force appropriation methods [62,63] make use of the measured FRF matrix in square or rectangular form. The matrix can be measured a column at a time by using a single exciter or alternatively using independent patterns of forces. It is important that the number of exciters e satisfies $e \geq r$, where r is the effective number of modes in the frequency range of interest. Once the FRF matrix has been measured at a number of discrete frequencies, the complex response to a set of sinusoidal excitation forces applied in monophase can be written as

$$\bar{\underset{\sim}{X}} = [\ A(\omega) + i\ B(\omega)\ ]\ \underset{\sim}{P} \qquad \ldots\ldots\ldots\ldots\ldots (6.45)$$

where $\underset{\sim}{P}$ is an (ex1) applied force vector, $[A(\omega)+iB(\omega)]$ is the (mxe) complex FRF matrix at frequency ω and m is the number of response stations. The method used in this work makes use of a square FRF matrix so m=e and the exciter and response stations need to be coincident.

The philosophy of the force appropriation methods is based upon the fact that a pure mode is one in which all displacement are in quadrature (i.e. $\pm\ 90^{\circ}$ phase) with the applied forces [62,63]. This implies that the real part of the complex response is zero, namely

$$A(\omega)\ \underset{\sim}{P} = 0 \qquad \ldots\ldots\ldots\ldots\ldots\ldots\ldots (6.46)$$

The frequencies at which this occurs are the undamped natural frequencies of the system and the corresponding vectors are the distributions required to excite the modes.

There are various approaches known as "direct methods" which can be used for obtaining the solution of equation (6.46); these include Asher's method, the modified Asher's method and Trail Nash's method [62,63]. The Trial Nash method used in this work assumes a solution

$$\bar{\underset{\sim}{X}} = \underset{\sim 0}{X}\ e^{-i\psi}$$

where ψ is a characteristic phase lag. When this solution is substituted into equation (6.45) and $\underset{\sim 0}{X}$ eliminated, the result is an eigenvalue problem of the form,

$$A(\omega)\ \underset{\sim}{P} = \mu\ B\ \underset{\sim}{P} \qquad \ldots\ldots\ldots\ldots\ldots\ldots (6.47)$$

where $\mu = -1/\tan\psi$. Clearly the solution of equation (6.46)

corresponds to μ=0. The eigenvalue problem is solved at the discrete frequencies for which the matrices are available. The natural frequencies, corresponding to μ=0, may be found by curve fitting and interpolating the eigenvalues which vary almost linearly in the resonant regions. The corresponding eigenvectors are the required force distributions which can be estimated by evaluating their individual elements at the natural frequencies by a similar curve fitting and interpolation process. once the natural frequencies and appropriated force distributions for the modes of interest have been obtained, it remains to use them to estimate the generalised mass and modal matrices.

It can be shown [64] that the jth mode shape can be estimated using

$$\underset{\sim}{\Phi}_j = \frac{1}{\gamma_j} [\, B(\omega_j)\, \underset{\sim}{P}_j \,] \qquad \ldots\ldots\ldots\ldots\ldots\ldots (6.48)$$

where $B(\omega_j)$ is the value of the imaginary part of the FRF matrix at the jth natural frequency and γ_j is a normalising factor used for normalising the jth mode shape with respect to its maximum value.

The diagonal generalised mass matrix can be obtained using

$$M_u(j,j) = \frac{-\frac{d}{d\omega}\,[S_{jj}(\omega)]_{\omega=\omega_j}}{2\,\gamma_j^2\,\omega_j} \qquad \ldots\ldots\ldots\ldots (6.49.a)$$

where $$S_{jj}(\omega) = \underset{\sim}{P}_j^t\, A(\omega)\, \underset{\sim}{P}_j \qquad \ldots\ldots\ldots\ldots (6.49.b)$$

and $\underset{\sim}{P}_j$ is the force distribution used to excite the jth mode and ω_j is the natural frequency of the jth mode. The numerator of equation (6.49.a) represents the slope of the function $S_{jj}(\omega)$ (known as the reactive energy) estimated at the jth natural frequency. It may be noted that for a single-d.o.f. system equation (6.48) reduces to $\gamma_j = B(\omega_j)$ and equation (6.49.a) to

(6.16). Clearly, it is possible to estimate the generalised stiffness matrix using

$$K_u(j,j) = \omega_j^2 M(j,j) \qquad \ldots\ldots\ldots\ldots\ldots\ldots (6.50)$$

Furthermore, it can be shown that the generalised damping matrix may be estimated using

$$C_u(i,j) = \frac{-T_{ij}(\omega_j)}{\omega_i \gamma_i \gamma_j} \qquad \ldots\ldots\ldots\ldots\ldots\ldots (6.51.a)$$

where $T_{ij}(\omega_j) = \underset{\sim}{P}_i^t B(\omega_j) \underset{\sim}{P}_j \qquad \ldots\ldots\ldots\ldots\ldots (6.51.b)$

is the active energy and the expression involves parameters for both the jth and ith modes. The direct damping terms are given when j=i. The off diagonal terms (j≠i) will be zero if the damping is proportional.

Example.

The author has found that the above technique works fairly well for linear systems. It is expected that incorrect estimates would be obtained by this technique for nonlinear systems. However, in order to illustrate the practical aspects of the technique and to indicate how it behaves for nonlinear systems, the two d.o.f. nonlinear example given in section (3.3.3), was reconsidered. A sample FRF plot for this system was shown in Fig. (3.3) for two force levels, namely 50 and 500 N. Clearly the nonlinearity had a significant effect on the FRF matrix.

Firstly, the eigenvalue problem of equation (6.47) was solved and the two eigenvalues obtained for each force level are shown varying with frequency in Figs (6.13.a and b). The undulations seen in the eigenvalues corresponding to the high force level case are caused by the nonlinear behaviour of the system. Typically, for a linear system the eigenvalue vary linearly with frequency.

The zero crossings of the eigenvalues were obtained by carrying out a simple curve fit through the four points nearest to the frequency axis using a first order polynomial and then interpolating to yield the following estimates for the natural frequencies of the two modes,

Force level 1 : $f_{n1} = 28.50$ Hz and $f_{n2} = 31.50$ Hz
Force level 2 : $f_{n1} = 28.75$ Hz and $f_{n2} = 31,68$ Hz

The results are exact for the first case but shifted somewhat for the second case.

The associated eigenvectors were estimated by curve fitting a second order polynomial through the corresponding four points for each element of these eigenvectors as shown in Fig. (6.14) for the high force level. The natural frequency estimates were then substituted into the resulting fitted polynomials to yield the following appropriated force distributions, normalised to a maximum value of unity,

Force level 1 : $\underset{\sim}{P}_1 = \begin{bmatrix} 0.997 \\ 1.000 \end{bmatrix}$ and $\underset{\sim}{P}_2 = \begin{bmatrix} 1.000 \\ -0.999 \end{bmatrix}$

Force level 2 : $\underset{\sim}{P}_1 = \begin{bmatrix} 0.762 \\ 1.000 \end{bmatrix}$ and $\underset{\sim}{P}_2 = \begin{bmatrix} 1.000 \\ -0.928 \end{bmatrix}$

compared to the exact vectors

$$\underset{\sim}{P}_1 = \begin{bmatrix} 1.000 \\ 1.000 \end{bmatrix} \quad \text{and} \quad \underset{\sim}{P}_2 = \begin{bmatrix} 1.000 \\ -1.000 \end{bmatrix}$$

It is clear that the nonlinearity has had an effect on the technique since the error in $\underset{\sim}{P}_1$ and $\underset{\sim}{P}_2$ for the high force level is significant.

Having obtained the natural frequencies and the appropriated force distributions, equations (6.48) to (6.51) can then be used to provide estimates for the modal, generalised mass, damping and stiffness matrices. Examples of the plots used to determine these

estimates are shown in Figs. (6.15) to (6.17).

The variations of the two elements of the vector $[B(\omega)\ \underset{\sim}{P}_1]$ with frequency are shown in Fig. (6.15) for the low force level case. It can be seen that these two elements are similar. For the estimation of the jth mode shape, a third order polynomial was curve fitted through the four points nearest to the natural frequency for each of the elements of the vector $[B(\omega)\ \underset{\sim}{P}_j]$. The natural frequency was then substituted into the fitted polynomials yielding the jth mode shape which was then normalised with respect to its maximum value.

Fig. (6.16) shows the variation of the function $S_{11}(\omega)$ with frequency. The evaluation of the slope of $S_{jj}(\omega)$ at the jth natural frequency was carried out simply by curve fitting a third order polynomial through the corresponding four points, differentiating the fitted polynomial and substituting for natural frequency. Equation (6.49) was then used for estimating the generalised mass matrix.

Finally, the variations of the two elements $T_{11}(\omega)$ and $T_{21}(\omega)$ with frequency are shown in Fig. (6.17). A similar curve fitting process was used for estimating the $T_{1j}(\omega)$ elements at the natural frequencies. The results were then substituted into (6.51.a) to yield the generalised damping matrix. The resulting matrices for the two force levels were

Force level 1 :

$$M_u = \begin{bmatrix} 2.003 & 0 \\ 0 & 1.997 \end{bmatrix} \qquad K_u = \begin{bmatrix} 64253.5 & 0 \\ 0 & 78250.6 \end{bmatrix}$$

$$C_u = \begin{bmatrix} 15.94 & -0.01 \\ -0.14 & 21.55 \end{bmatrix} \qquad \Phi = \begin{bmatrix} 0.997 & 1 \\ 1 & -0.998 \end{bmatrix}$$

Force level 2 :

$$M_u = \begin{bmatrix} 1.595 & 0 \\ 0 & 1.709 \end{bmatrix} \quad K_u = \begin{bmatrix} 52068.7 & 0 \\ 0 & 67721.1 \end{bmatrix}$$

$$C_u = \begin{bmatrix} 13.381 & -0.97 \\ -1.08 & 18.87 \end{bmatrix} \quad \Phi = \begin{bmatrix} 0.823 & 1 \\ 1 & -0.879 \end{bmatrix}$$

The exact matrices were given in the example considered in section (3.3.3). The results for the low force level are very accurate indicating that the force appropriation method is very suitable for estimating the generalised matrices for linear systems or systems in which the nonlinearity is not significantly excited. However the results obtained for the high force level are much more significantly in error indicating that the force appropriation method may not be sufficiently accurate for nonlinear systems where the nonlinearity strongly affects the measured FRF matrix used. Nevertheless the method may lead to reasonable estimates if the nonlinear behaviour can be kept acceptably low, especially if the mass can be refined using the sensitivity approach. Note that the damping and stiffness matrices are not needed as input to the force-state mapping method so are only presented for interest.

6.7. Estimation of the mass matrix for multi-d.o.f. nonlinear systems.

At the beginning of this chapter, a brief introduction to current techniques available for estimation of the mass matrix for multi-d.o.f. nonlinear systems was presented. Some workers were concerned with estimating the physical mass matrix needed for carrying out an identification purely in the physical space for lumped parameter systems [44]. Others were concerned with estimating the generalised mass matrix for carrying out the identification of general nonlinear systems in modal space [38] as explained in chapter 3.

In this work the latter philosophy has been adopted and thus the estimation of the generalised mass matrix for multi-d.o.f. nonlinear systems has been investigated. In particular, the sensitivity approach introduced earlier for single-d.o.f. mass estimation procedure has been extended to multi-d.o.f. systems. This extension of the sensitivity approach was possible provided the curve fitting of the modal restoring force is carried out with all the linear and nonlinear coupling terms between the modes included in the fitted model.

However it should be pointed out that no theoretical analysis has been developed to show that the identified parameters vary linearly with the mass for multi-d.o.f. nonlinear systems. Nevertheless the applications of the approach to simulated and real multi-d.o.f. nonlinear systems (see chapter 7) have shown that at least the relationship between the estimated generalised stiffness and mass is linear and thus the same procedure outlined in section (6.5.1) can be extended for estimating the generalised mass values of the ith mode as follows :

1) For an initial estimate of the generalised mass matrix $\hat{M}1$ (somewhat lower than that obtained from the linear approach in section (6.6)), the ith modal restoring force $\hat{h}_i$ is estimated using equation (3.14) at frequency ω_j which satisfies $\omega_{n(i-1)} < \omega_j < \omega_{ni}$ where $\omega_{n(i-1)}$ and ω_{ni} are the resonance frequencies of the (i-1)th and ith modes respectively. It is assumed for the moment that the correct modal matrix is available. It will be shown in section (6.8) that the use of wrong modal matrix will not affect the outcome of the approach.

2) $\hat{h}_i$ is curve fitted in terms of the modal velocity and displacement vectors $\dot{\underset{\sim}{u}}$ and $\underset{\sim}{u}$ (see section (3.3.2)) or in terms of $\dot{\underset{\sim}{u}}$ and $\underset{\sim}{u}$ and relative physical velocities and displacement (see section (3.4)). At this stage the generalised stiffness of the ith mode corresponding to the initial generalised mass becomes available.

3) For a second initial estimate of the generalised mass matrix $\hat{M}2$ (somewhat greater than the linear estimate), steps 1 and 2 are repeated in exactly the same manner yielding another estimate for the generalised stiffness of the ith mode.

4) The results $(\hat{K}1_i, \hat{M}1_i)$ and $(\hat{K}2_i, \hat{M}2_i)$ are then plotted in the $[\hat{K}, \hat{M}]$ plane and joined by a straight line L1.

5) Steps 1 to 4 are repeated for a different frequency ω_j which satisfies $\omega_{ni} < \omega_j < \omega_{n(i+1)}$ leading to a second straight line L2.

6) The intersection of L1 and L2 corresponds to the point in the $[\hat{K}\text{-}\hat{M}]$ plane at which the generalised stiffness and mass for the ith mode are exact.

7) The procedure can be repeated for all the modes of interest, resulting in a diagonal generalised mass matrix.

Example.

In this section the above procedure for the sensitivity approach is applied to the two d.o.f. nonlinear system considered earlier in section (6.6). The two initial values of the generalised mass matrix were considered to be

$$\hat{M}1 = \begin{bmatrix} 1 & 0 \\ 0 & 1 \end{bmatrix} \quad \text{and} \quad \hat{M}2 = \begin{bmatrix} 3 & 0 \\ 0 & 3 \end{bmatrix}$$

but there is no requirement for the elements to be equal.

For the estimation of the generalised mass value of the first mode, the two frequencies below and above the first resonance frequency of 28.5 Hz were selected to be 25 Hz and 30 Hz. The system was then excited at the selected frequency using a sinusoidal force, applied to the first mass, having R.M.S. value

of 2000 N. The physical response vectors $\ddot{\underset{\sim}{x}}$, $\dot{\underset{\sim}{x}}$ and $\underset{\sim}{x}$ were generated by a Runge-Kutta program which provided 256 data points for each of the time signals, the start of the excitation being used. The modal velocity and displacement vectors were estimated by equation (3.11) and the modal restoring force at each frequency and for each of the initial mass matrix were estimated using equation (3.14). Thus four modal restoring forces were ready for curve fitting.

It was shown in chapter 3 that the transformation of this two d.o.f. system into the modal space revealed that the two modes are coupled nonlinearily in quite a complicated manner. The curve fitting for each of the modal restoring forces was carried out in a single step by including all possible coupling terms between the modes in a large model (see section (3.3.2)) or by using the approach introduced in section (3.4) since in this case information about the relative physical velocities and displacements is available. The step-by-step approach of section (3.3.1) was considered too lengthy for the sensitivity approach.

In this example, these two approaches have been implemented, yielding similar results. The results obtained by the latter approach are presented in table (6.6).

Frequency	$\hat{M}1$	$\hat{K}1$	$\hat{C}1$	$\hat{\beta}1$
f_1=25 Hz	1	37867.1	5.54	7995.64
	3	90396.5	26.13	63069.40
f_2=30 Hz	1	32048.3	17.27	19867.50
	3	96215.7	14.40	51192.50
Exact value	2	64132.6	15.84	35530.00

Table (6.6). Estimated parameters for the 2 d.o.f. example.

When the $\hat{K}$ values were plotted against the $\hat{M}$ values as shown in Fig. (6.18) then the coordinates of the intersection between the resulting two straight lines were found to be

$$\hat{M}_1 = 1.99996 \qquad \text{and} \qquad \hat{K}_1 = 64130.1$$

which are very close indeed to the exact values.

For the second mode, the above procedure was repeated similarly except that the two excitation frequencies below and above the second resonance frequency of 31.5 Hz were 30 Hz and 37 Hz. Note that because the two modes are fairly close, it was possible to use the 30 Hz data for both modes. The results for the second mode are also shown in Fig. (6.18) and the intersection occurred at

$$\hat{M}_2 = 1.99997 \qquad \text{and} \qquad \hat{K}_2 = 78342.5$$

which are also very accurate. The author has also found that all the other identified parameters vary linearly with the mass and thus can yield accurate values for the mass.

The sensitivity approach clearly works for this multi-d.o.f. nonlinear system. Moreover, when other 2 d.o.f. examples with different types of nonlinearities or with more than one nonlinear element were tried, the method also worked accurately.

6.8. Effect of using an incorrect modal matrix in the force-state mapping technique.

The force-state mapping technique was originally introduced for single-d.o.f. systems. The extension to general multi-d.o.f. systems involved the equation of motion being transformed from physical to modal space. However, if the estimated modal matrix $\hat{\Phi}$ were incorrect, then the resulting transformed generalised equations would be, say,

$$M_c\ddot{q} + C_c\dot{q} + K_c q + f_c(q,\dot{q}) = p_c \qquad \ldots\ldots\ldots\ldots\ldots (6.52)$$

where $x = \hat{\Phi}\, q$, $p_c = \hat{\Phi}^t p$, $M_c = \hat{\Phi}^t M\, \hat{\Phi}$ etc and q are generalised, but not modal, coordinates. This is a valid and <u>consistent</u> transformation but the generalised mass, damping and stiffness matrices are not diagonal. Any model used on data transformed using $\hat{\Phi}$ would need to be expanded to take account of the linear coupling terms. Also the fully-populated consistent mass matrix M_c would need to be known and used to obtain the generalised restoring force vector.

It might be argued that the main purpose of the force-state mapping approach is to obtain a model that produces a physical, not generalised, response similar to that of the true system and not particularly to obtain correct equations in modal coordinates. Provided that the consistent mass matrix M_c is used and an adequate model fitted, then the consistent generalised equation (6.52) will provide a correct physical response.

However, unfortunately, the consistent generalised mass matrix M_c will not usually be known. If the <u>correct</u> diagonal modal mass matrix $M_u = \Phi^t M \Phi$ were assumed to be available and were used in place of M_c to estimate the generalised restoring forces then the equations would be inconsistent and the fitted model would not give the correct response. This point is illustrated in Fig. (6.19) in which the true sweep response of the two d.o.f. nonlinear system considered in section (6.7) is compared to the response of a model identified using the incorrect modal matrix $\Phi = \begin{bmatrix} 1 & 1 \\ 1.2 & -0.8 \end{bmatrix}$, having 20% error on the mode shapes, and the correct modal mass matrix. The responses are clearly quite different and the fitted model is unsatisfactory.

Since, in practice, the correct modal mass matrix will not be known a priori but will need to be estimated, it will be interesting to consider what happens when the sensitivity approach

to mass estimation is carried out using the incorrect modal matrix $\hat{\Phi}$. Will the estimated diagonal mass matrix compensate in any way for the error in the modal matrix ? The answer is rather surprising and is best illustrated by an example.

Consider again the two d.o.f. example used earlier in section (6.7) but for simplicity omit the nonlinear element. Now assume that the modal matrix is considerably in error, namely

$$\hat{\Phi} = \begin{bmatrix} 1 & 1 \\ 0.4 & -1.3 \end{bmatrix} \quad \text{compared to} \quad \Phi = \begin{bmatrix} 1 & 1 \\ 1 & -1 \end{bmatrix}.$$

The sensitivity approach to mass estimation is then applied as before using the transient data from single frequency excitation applied to the first mass only; three frequencies and two estimates for the generalised mass matrix were used in the approach. The plots of estimated stiffness against mass for the two equations identified led to the sensitivity approach mass estimate,

$$M_s = \begin{bmatrix} 1.3075 & 0 \\ 0 & 4.2475 \end{bmatrix}$$

The resulting model obtained using this mass matrix M_s and $\hat{\Phi}$ is

$$\begin{bmatrix} 1.3075 & 0 \\ 0 & 4.2475 \end{bmatrix} \ddot{\underset{\sim}{q}} + \begin{bmatrix} 10.5527 & 0.7572 \\ 2.9712 & 45.0010 \end{bmatrix} \dot{\underset{\sim}{q}} + \begin{bmatrix} 42418 & 1886.2 \\ 7457.4 & 164778 \end{bmatrix} \underset{\sim}{q} = \hat{\Phi}^t \begin{bmatrix} 1 \\ 0 \end{bmatrix} p(t)$$

.....(6.53)

The matrices are nonsymmetric and the equations look quite different to those corresponding to the consistent transformation in equation (6.52) where, for example,

$$M_c = \begin{bmatrix} 1.16 & 0.48 \\ 0.48 & 2.69 \end{bmatrix} \quad \text{and} \quad K_c = \begin{bmatrix} 38476 & 20295 \\ 20295 & 105053 \end{bmatrix}.$$

However, when equations (6.53) were transformed back into physical space using $\underset{\sim}{q} = \hat{\Phi}^{-1} \underset{\sim}{x}$ and then premultiplied by $[\hat{\Phi}^t]^{-1}$, the following equations were obtained,

$$\begin{bmatrix}0.99975 & 0.00026\\ 0.00026 & 1.92214\end{bmatrix}\ddot{\underset{\sim}{x}} + \begin{bmatrix}9.3331 & -1.4108\\ -2.7133 & 17.9326\end{bmatrix}\dot{\underset{\sim}{x}} + \begin{bmatrix}35608.8 & -3542.2\\ -6819.4 & 68461.0\end{bmatrix}\underset{\sim}{x}$$

$$= \begin{bmatrix}1\\ 0\end{bmatrix} p(t) \quad \ldots\ldots\ldots\ldots (6.54)$$

Now the exact physical equations, repeated here for clarity, are

$$\begin{bmatrix}1 & 0\\ 0 & 1\end{bmatrix}\ddot{\underset{\sim}{x}} + \begin{bmatrix}9.33 & -1.41\\ -1.41 & 9.33\end{bmatrix}\dot{\underset{\sim}{x}} + \begin{bmatrix}35619 & -3553\\ -3553 & 35619\end{bmatrix}\underset{\sim}{x} = \underset{\sim}{p}(t) \quad \ldots\ldots (6.55)$$

What is interesting is that when these two sets of equations are compared, the x_1 equation is essentially the same whereas the x_2 equation is more or less correct within a scaling factor of about 1.924; this is the factor required to make the equations symmetric. Since the force used for the identification was applied only to the first mass then the scaling will not affect the ability of the estimated equations to reproduce the response of the system very closely. This is illustrated in Fig. (6.20) in which the exact and estimated responses are seen to be virtually identical.

The same sort of behaviour was also seen when different estimated modal matrices were used and when nonlinearity was included in the system. What appears to have happened is that the sensitivity approach has effectively determined a modified set of generalised equations for which the generalised mass matrix is in fact diagonal, as opposed to the consistent equations for which the matrix is fully-populated. This diagonal matrix corresponds to allowing the unforced physical equation to be scaled. Thus, if the estimated modal matrix and the scaled physical mass matrix are $\hat{\Phi} = \begin{bmatrix}1 & 1\\ a & b\end{bmatrix}$ and $M_\mu = \begin{bmatrix}m_1 & 0\\ 0 & \mu m_2\end{bmatrix}$ respectively, where μ is the scaling factor and excitation is applied to m_1 only, then the generalised mass matrix for the scaled equations will be

$$\hat{\Phi}^t M_\mu \hat{\Phi} = \begin{bmatrix}m_1+\mu a^2 m_2 & m_1+\mu abm_2\\ m_1+\mu abm_2 & m_1+\mu b^2 m_2\end{bmatrix} \quad \ldots\ldots\ldots (6.56)$$

For this matrix to be diagonal then $\mu=-m_1/abm_2$ and so the matrix estimated using the sensitivity approach would be

$$M_s = \begin{bmatrix} m_1(1-a/b) & 0 \\ 0 & m_1(1-b/a) \end{bmatrix} \quad \ldots\ldots\ldots\ldots\ldots\ldots (6.57)$$

In the example considered, $m_1=m_2=1$, $a=0.4$ and $b=-1.3$ in which case $\mu=1.923$ and the diagonal elements of M_s are 1.30769 and 4.25, all values very close to those seen earlier. In practice the scaling factor could be obtained from the ratios of the off-diagonal damping and stiffness terms.

Since the sensitivity approach to mass estimation seems to compensate for an incorrect modal matrix when only a single force is used, it would be interesting to examine the more general case of forces applied to both masses. When a similar analysis was carried out for the excitation vector $\underset{\sim}{p} = \begin{bmatrix} 1 \\ 2 \end{bmatrix} p(t)$ then the resulting estimated mass matrix was

$$M_s = \begin{bmatrix} 0.9267 & 0 \\ 0 & 1.699 \end{bmatrix}$$

When this matrix was used with the same incorrect modal matrix as before and the fitted model transformed back into physical space then the resulting equations were

$$\begin{bmatrix} 0.63360 & 0.18169 \\ 0.18169 & 0.90850 \end{bmatrix} \ddot{\underset{\sim}{x}} + \begin{bmatrix} 5.6736 & 0.80610 \\ 0.4094 & 8.23159 \end{bmatrix} \dot{\underset{\sim}{x}} + \begin{bmatrix} 22010.72 & 4209.16 \\ 3241.29 & 31724.94 \end{bmatrix} \underset{\sim}{x}$$

$$= \begin{bmatrix} 1 \\ 2 \end{bmatrix} p(t) \quad \ldots\ldots\ldots\ldots (6.58)$$

This fitted model was also found to reproduce the correct system response, a rather interesting result. It is not obvious, how this equation (6.58) relates to the exact equation (6.55). There is no simple scaling relationship as before. However, upon closer examination it was seen that the equations are in fact related by a <u>scaling matrix</u>. Equations (6.58) are equal to the exact equation (6.55) premultiplied by the scaling matrix

$$W = \begin{bmatrix} 0.63360 & 0.18169 \\ 0.18160 & 0.90850 \end{bmatrix}$$

Also the matrix W is such that the force vector is unaffected (i.e. $W\begin{bmatrix}1\\2\end{bmatrix}=\begin{bmatrix}1\\2\end{bmatrix}$). Note that the effective scaling matrix for the simple example, with excitation at only one point, would be

$$W = \begin{bmatrix} 1 & 0 \\ 0 & \mu \end{bmatrix}$$

At this stage the basis of this scaling process will be presented in a more general form.

Consider the physical equation of motion for an n degree of freedom linear system premultiplied by the unknown scaling matrix W, namely

$$W M \ddot{\underset{\sim}{x}} + W C \dot{\underset{\sim}{x}} + W K \underset{\sim}{x} = W \underset{\sim}{p}(t) \quad \ldots\ldots\ldots\ldots\ldots (6.59)$$

When these equations are transformed to generalised space using $\hat{\Phi}$ then

$$[\hat{\Phi}^t W M \hat{\Phi}]\ddot{\underset{\sim}{q}} + [\hat{\Phi}^t W C \hat{\Phi}]\dot{\underset{\sim}{q}} + [\hat{\Phi}^t W K \hat{\Phi}]\ \underset{\sim}{q} = \hat{\Phi}^t W \underset{\sim}{P} \quad \ldots\ldots (6.60)$$

Because the sensitivity approach to mass estimation provides a diagonal generalised mass matrix M_s, a value of the scaling matrix W is implied such that

$$\hat{\Phi}^t W M \hat{\Phi} = M_s \quad \ldots\ldots\ldots\ldots\ldots\ldots\ldots (6.61)$$

Also, in order that the scaling should not affect the excitation force vector, then W must satisfy

$$W \underset{\sim}{P} = \underset{\sim}{P} \quad \ldots\ldots\ldots\ldots\ldots\ldots\ldots\ldots (6.62)$$

There are (n^2-n) equations in (6.61) for the off-diagonal mass values to be zero and n equations in (6.62). These could provide

the n^2 unknown elements in W if the physical mass matrix M were known. However, in practice the matrix W does not need to be known and will simply be implied by the sensitivity approach. The final equation (6.59) will reproduce the system response exactly for any number of degrees of freedom and any excitation vector. Note that the above analysis is also valid for nonlinear systems.

Thus the sensitivity approach has implied a scaling to the original physical equations such that no off-diagonal mass terms are present in the generalised mass matrix even though the modal matrix is incorrect. To understand this further, it should be recognised that the nature of the sensitivity approach is to provide parameter estimates that are <u>independent</u> of frequency because several frequency lines intersect at points corresponding to the generalised mass values used. The fitted models used do not include terms for any inertia coupling and therefore any off-diagonal mass contribution would introduce some bias into the fitted parameters. Since such bias would depend upon frequency then the intersection point in the sensitivity approach must correspond to there being no off-diagonal mass contribution in the equations.

The result of this section means really that <u>any</u> modal matrix may be assumed for a multi-d.o.f. nonlinear identification provided the sensitivity approach is used to obtain the corresponding generalised mass matrix.

<u>Comment on possible linear dependence.</u>

An important point which arose during the consideration of using an incorrect modal matrix and which should be highlighted is the problem of possible linear dependence of terms within the fitted model. This problem is encountered when multi-d.o.f. identification is carried out using steady-state data and linear coupling terms are included. The problem was pointed out earlier for linear single-d.o.f. systems when the acceleration and

displacement were linearly dependent for steady-state excitation.

Indeed, when the above 2 d.o.f. linear example was analysed using the exact Φ and M_u matrices and a model without linear coupling terms, then steady-state data yielded exact parameters. However, when linear coupling terms were included in the fitted model the estimated parameters were in error. It is thought that this is due to linear dependence between u_1 and u_2 and also $\dot{u}_1$ and $\dot{u}_2$ for steady-state data. This explanation was confirmed when good results were obtained for the same coupled fitted model using single frequency sweep data, in which transient components were present.

It is considered that the use of steady-state data should be avoided for the force-state mapping identification of multi-d.o.f. systems, especially where linear coupling terms can arise due to use of an incorrect modal matrix.

6.9. Conclusion.

In this chapter a new approach, called the sensitivity approach, for estimating the mass or generalised mass matrix for single and multi-d.o.f. nonlinear systems has been introduced. The approach has proved to be effective and useful in that it can provide accurate estimates for the generalised mass matrix, it is not sensitive to the presence of realistic systematic and random errors in the measurements and it can cope with systems having mixed nonlinearities.

A further interesting bonus is that the approach can provide an estimate for the generalised mass matrix that can be used with a wrongly estimated modal matrix in the force-state mapping technique to yield a model equivalent to the exact model of the system. This means that accurate estimates for the modal matrix are not essential for carrying out a force-state mapping identification.

Further consideration of the theoretical basis of the sensitivity approach would be beneficial in any future work.

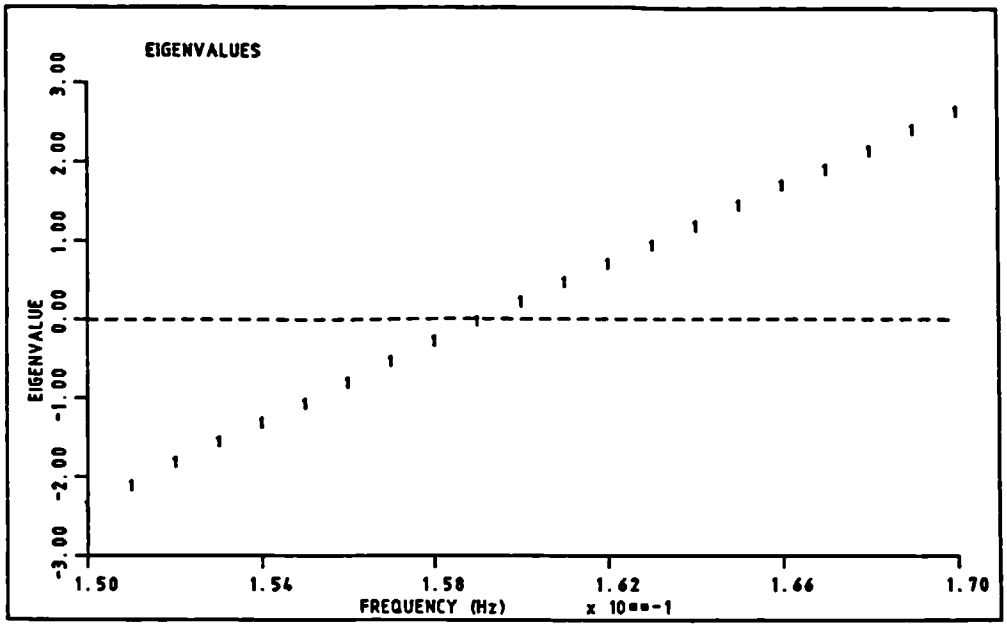

Figure 6.1. Variation of eigenvalue with frequency for a single-d.o.f. linear system.

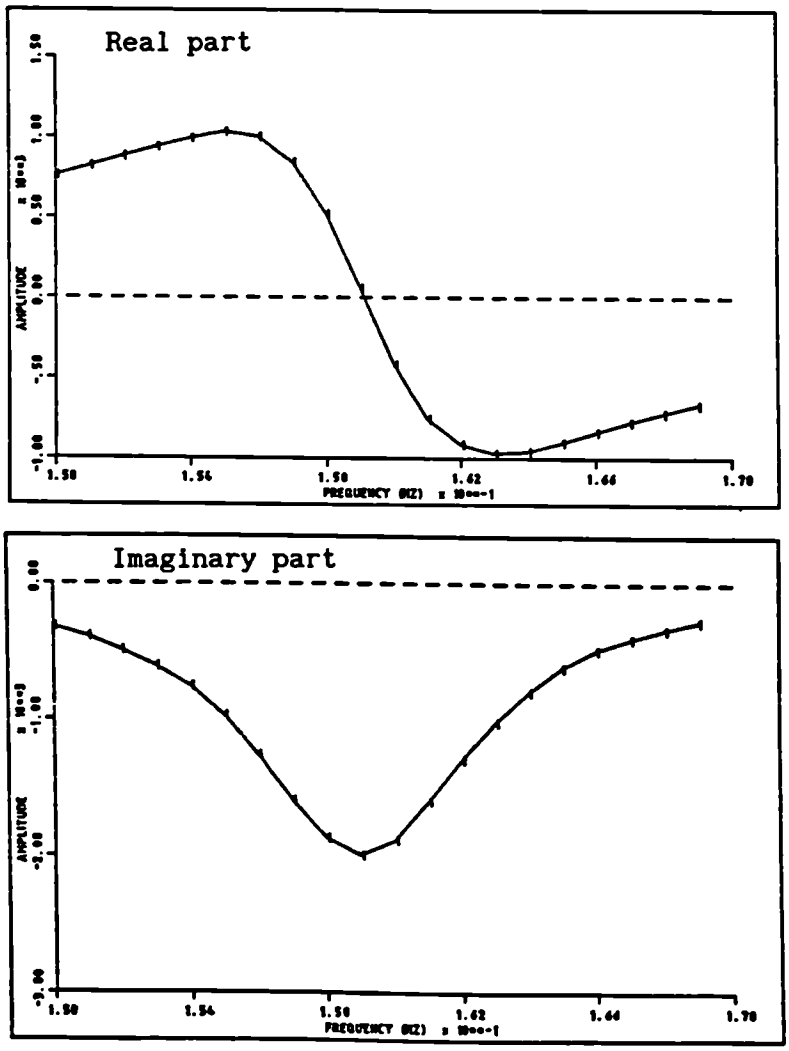

Figure 6.2. Real and imaginary parts used for estimating the mass for a single-d.o.f. linear system.

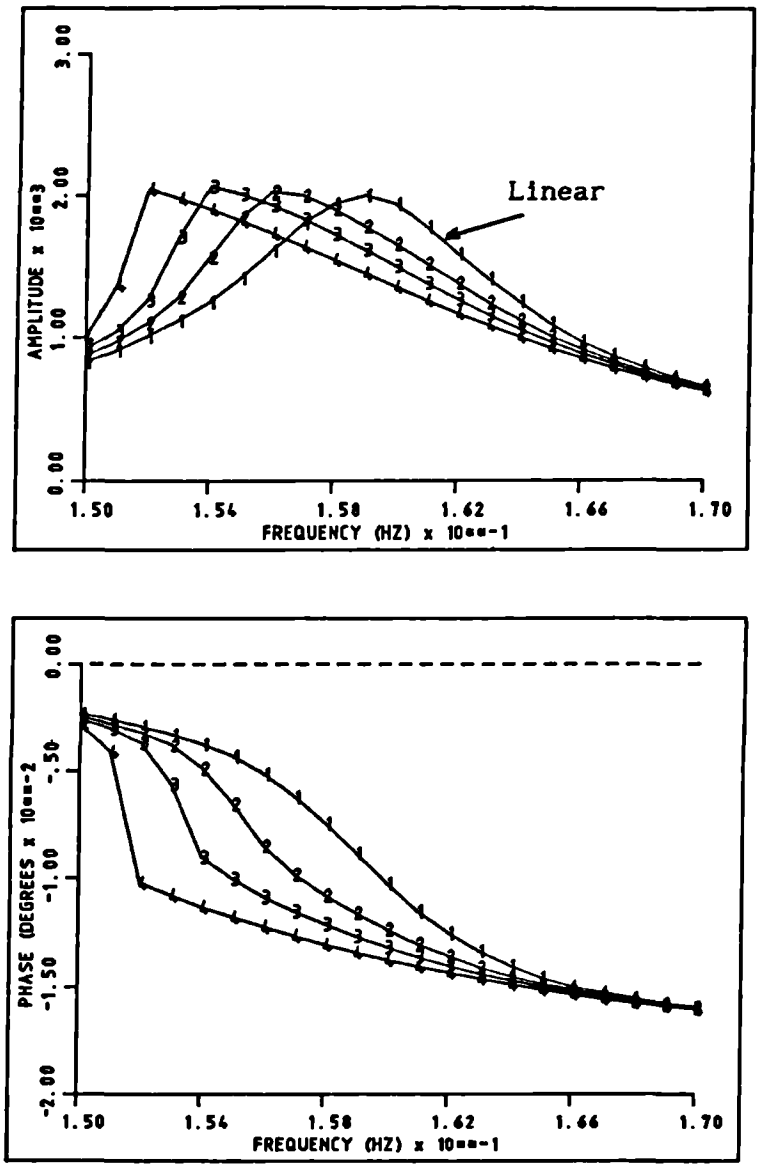

Figure 6.3. FRF of the nonlinear example given in section (6.3.2) for different force levels.

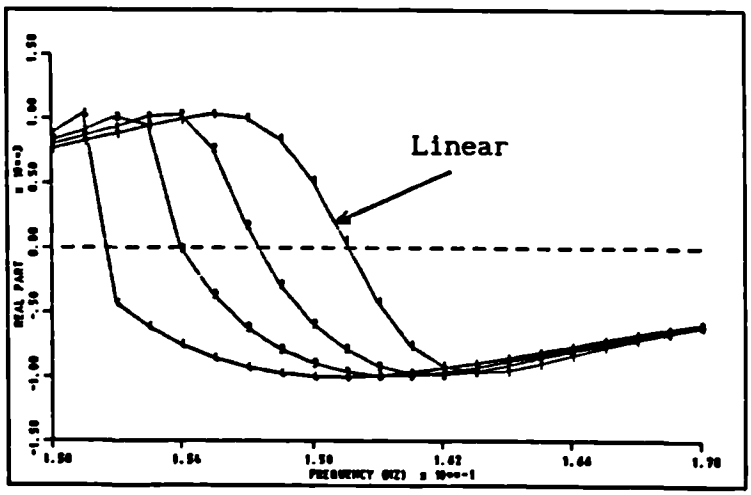

Figure 6.4. Real part of FRF of the nonlinear example at 3 force levels.

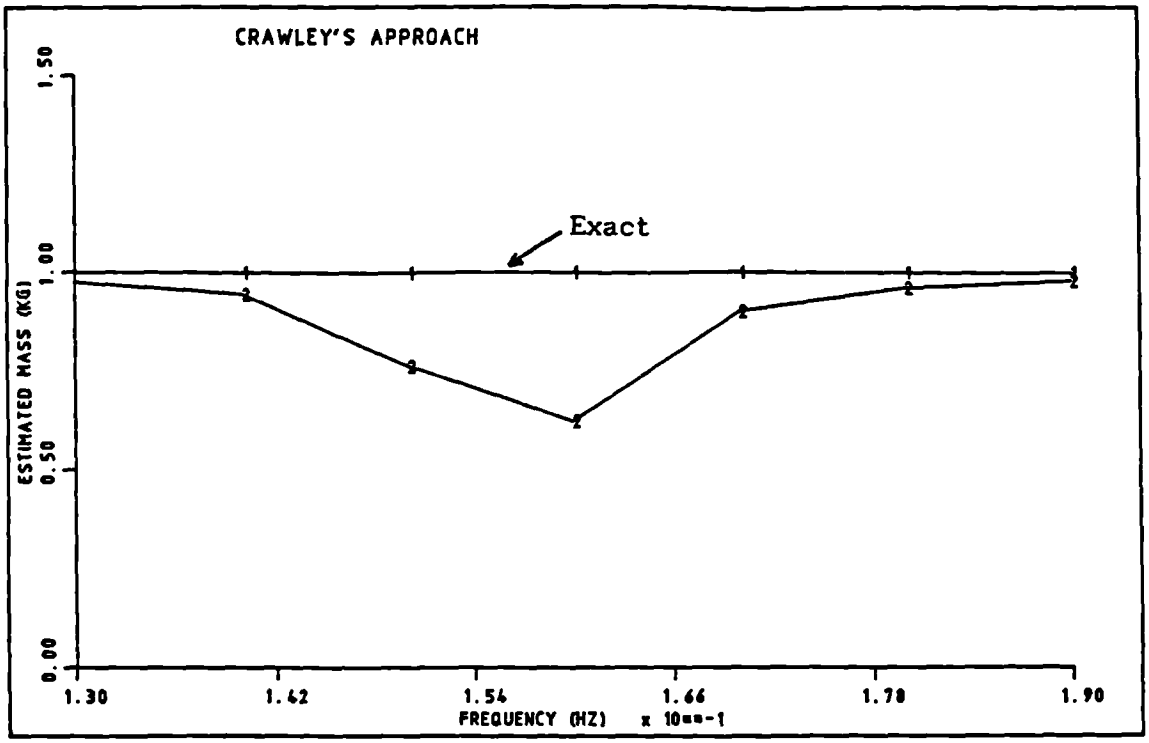

Figure 6.5. Variation of mass, obtained using Crawley's approach, with frequency for a linear example.

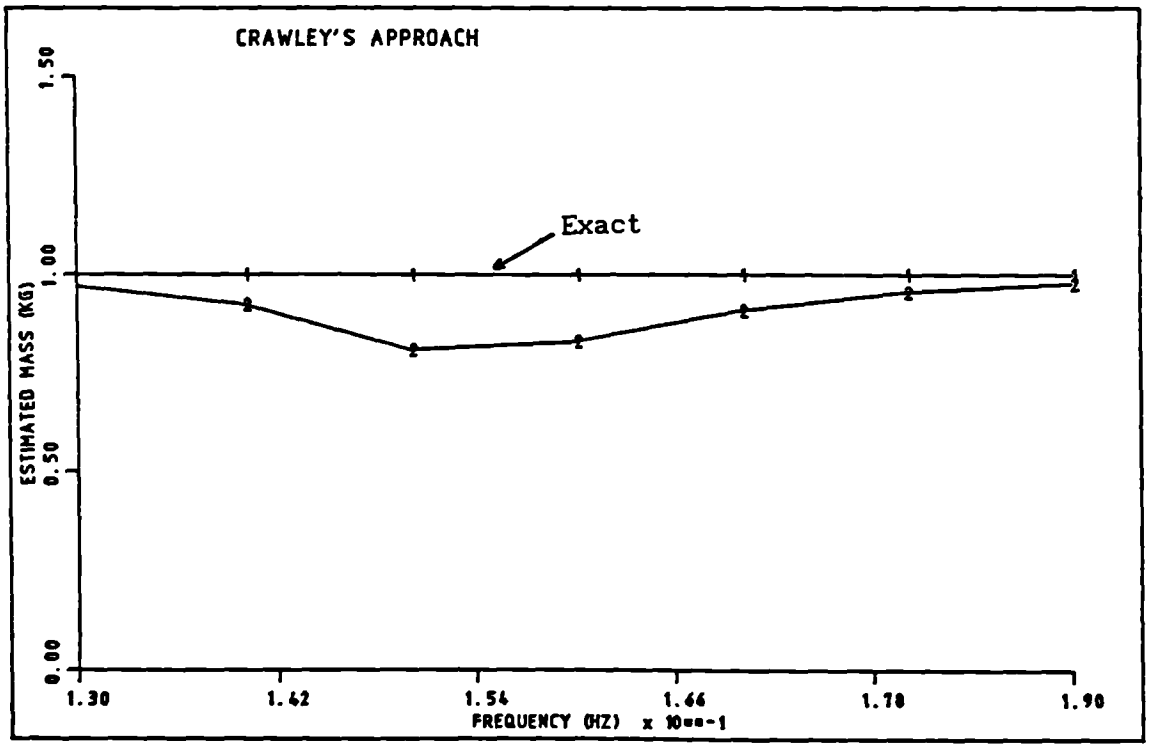

Figure 6.6. Variation of mass, obtained using Crawley's approach, with frequency for the nonlinear example of section (6.3.2).

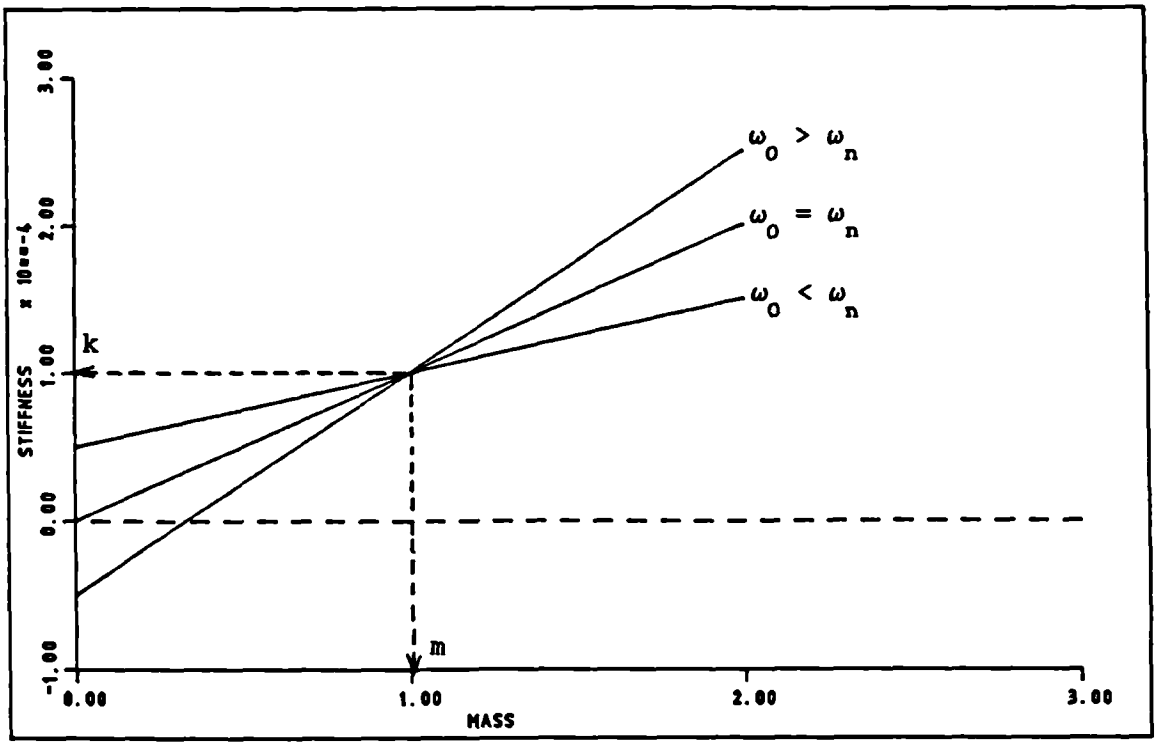

Figure 6.7. Variations of stiffness with mass for a linear system, for frequencies below, at and above the natural frequency.

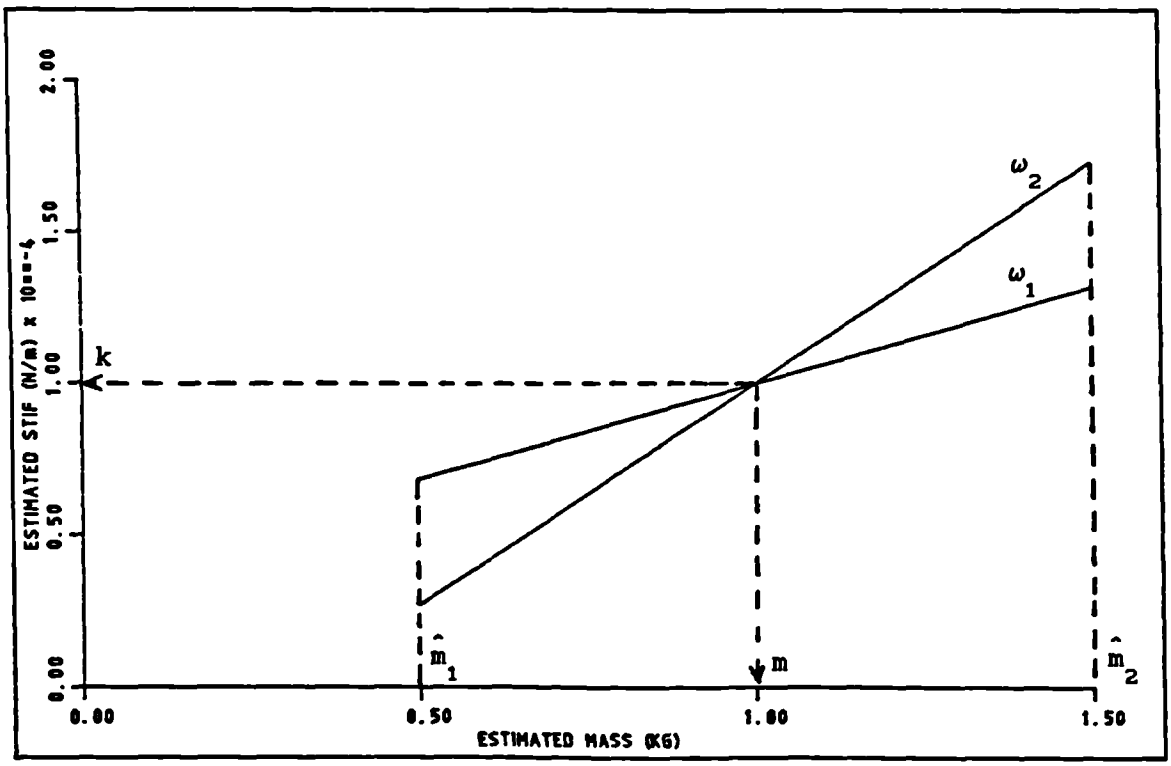

Figure 6.8. Illustration of the sensitivity approach procedure.

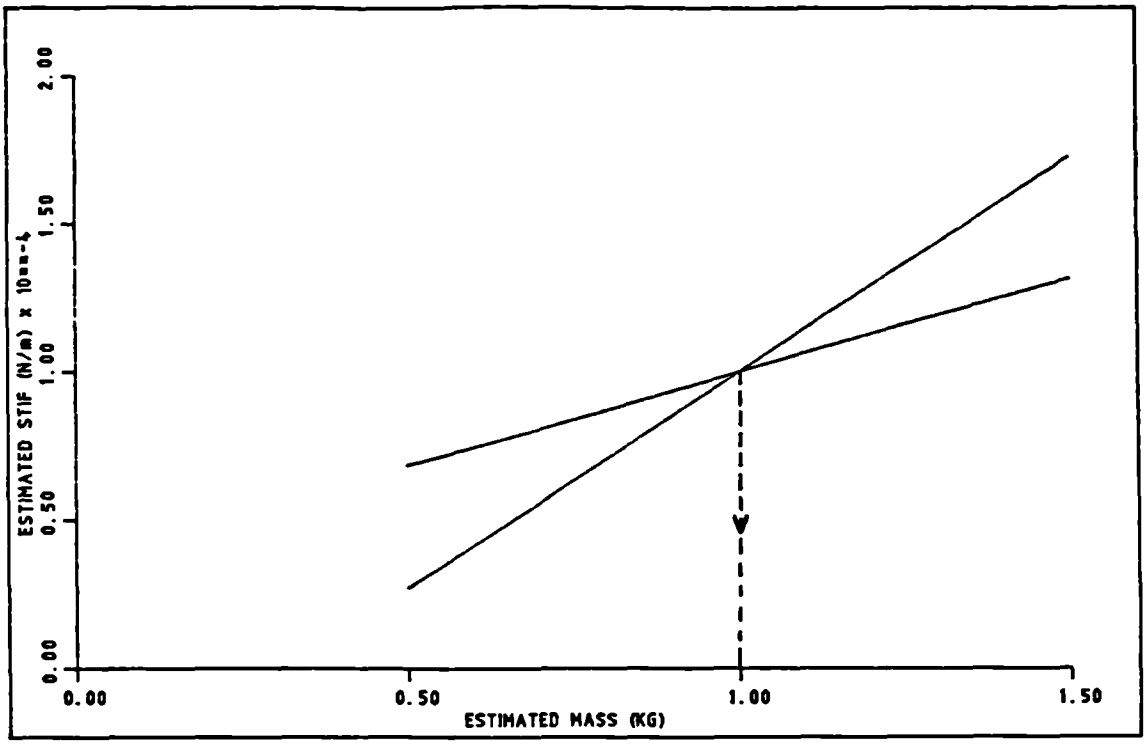

Figure 6.9. Mass estimation using the sensitivity approach for a linear system.

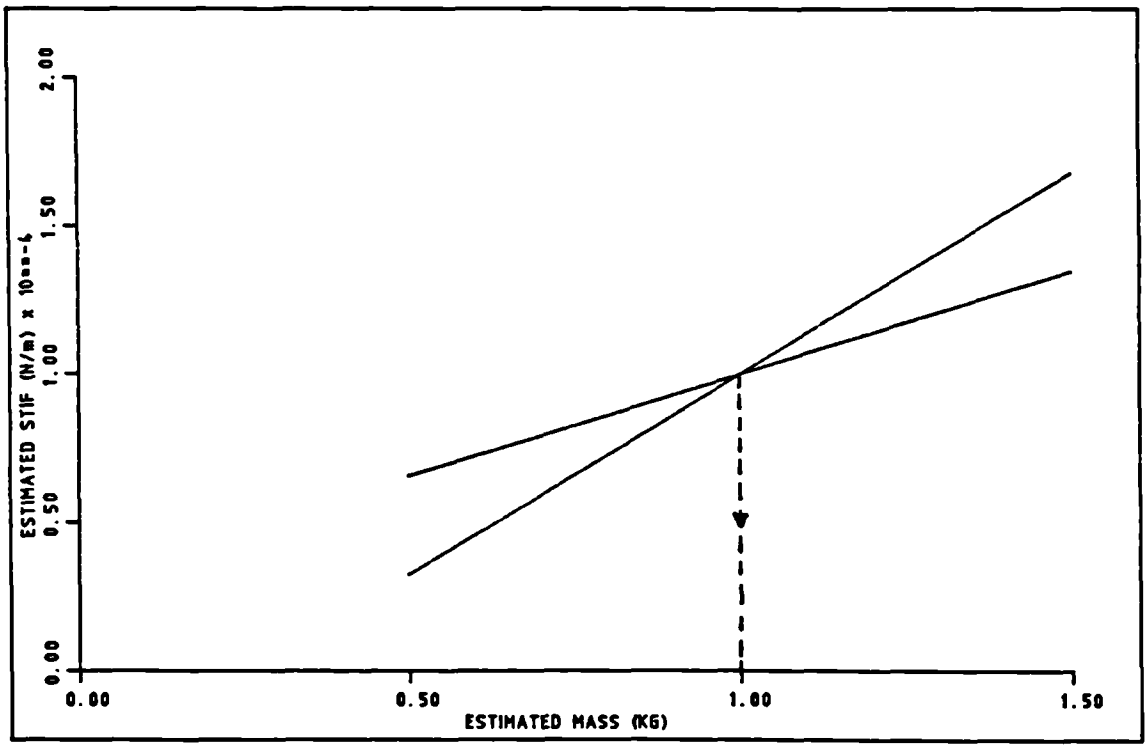

Figure 6.10. Mass estimation using the sensitivity approach for a cubic stiffness nonlinearity.

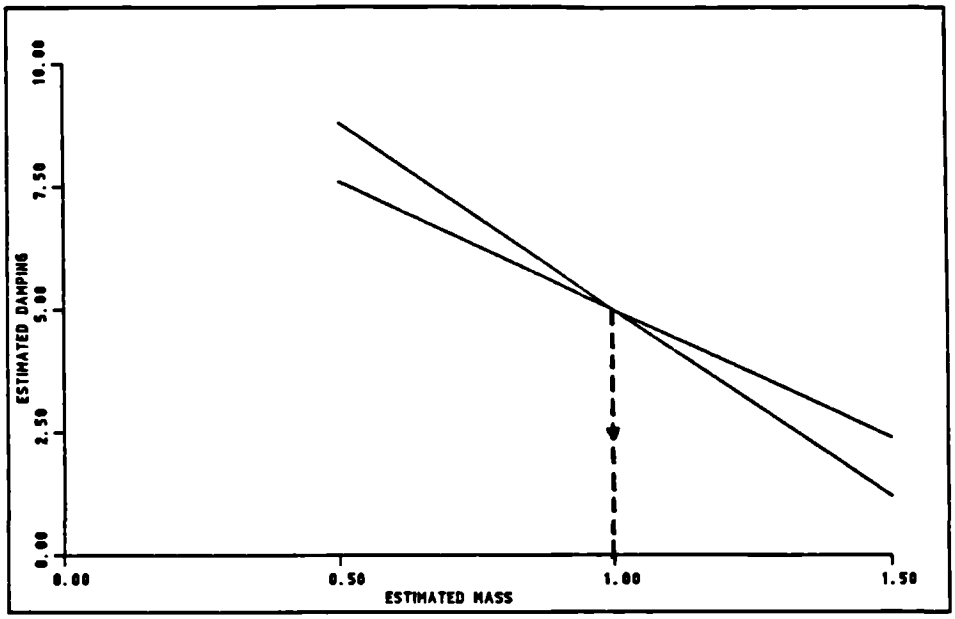

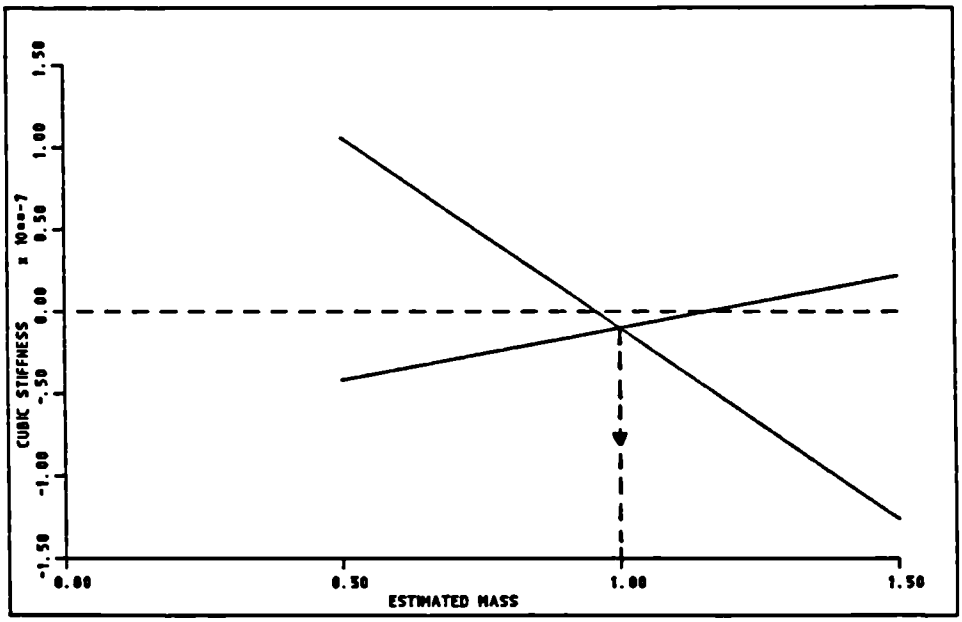

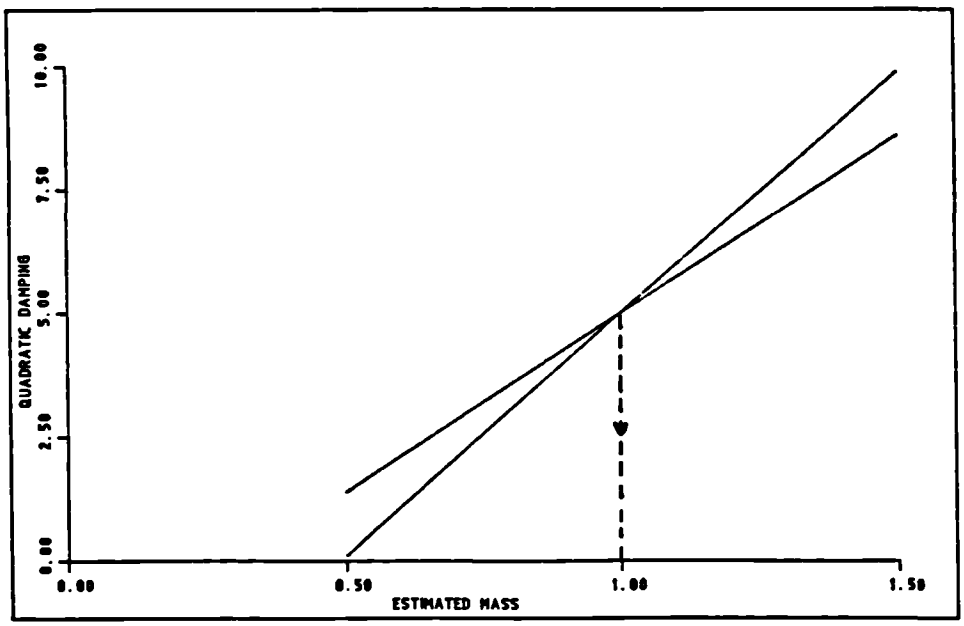

Figure 6.11. Mass estimation using the sensitivity approach for a nonlinear example with cubic stiffness and quadratic damping nonlinearity.

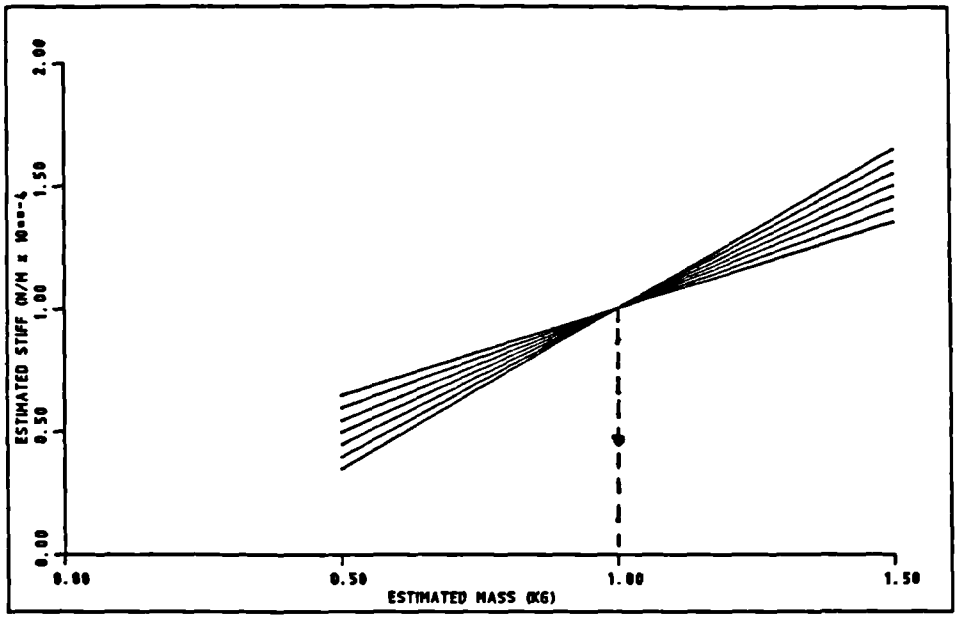

Figure 6.12. Effect of noise on the mass obtained by the sensitivity approach for a linear system.

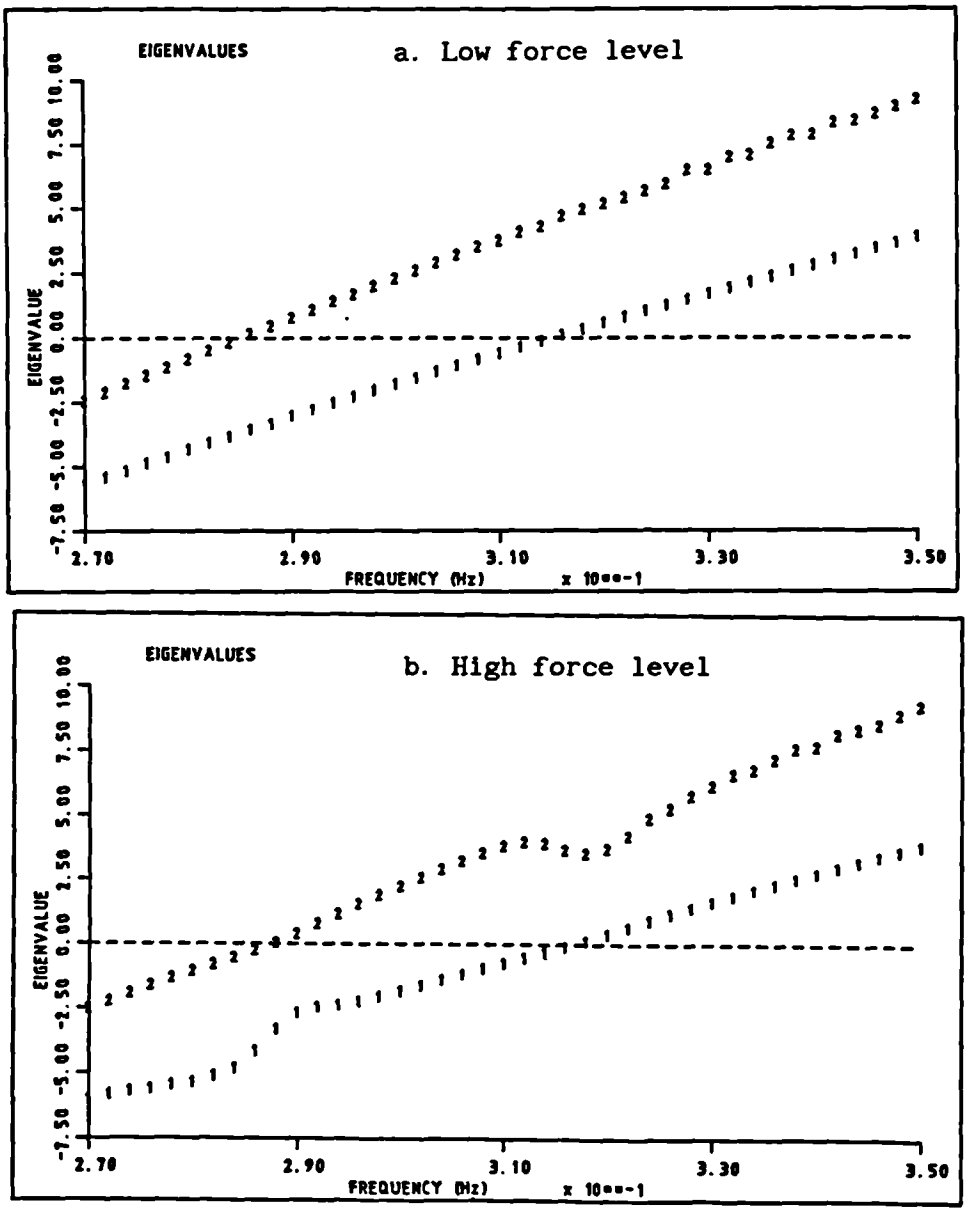

Figure 6.13. Variations of eigenvalues of the two d.o.f. nonlinear example, considered in section (6.6), with frequency for 2 force levels.

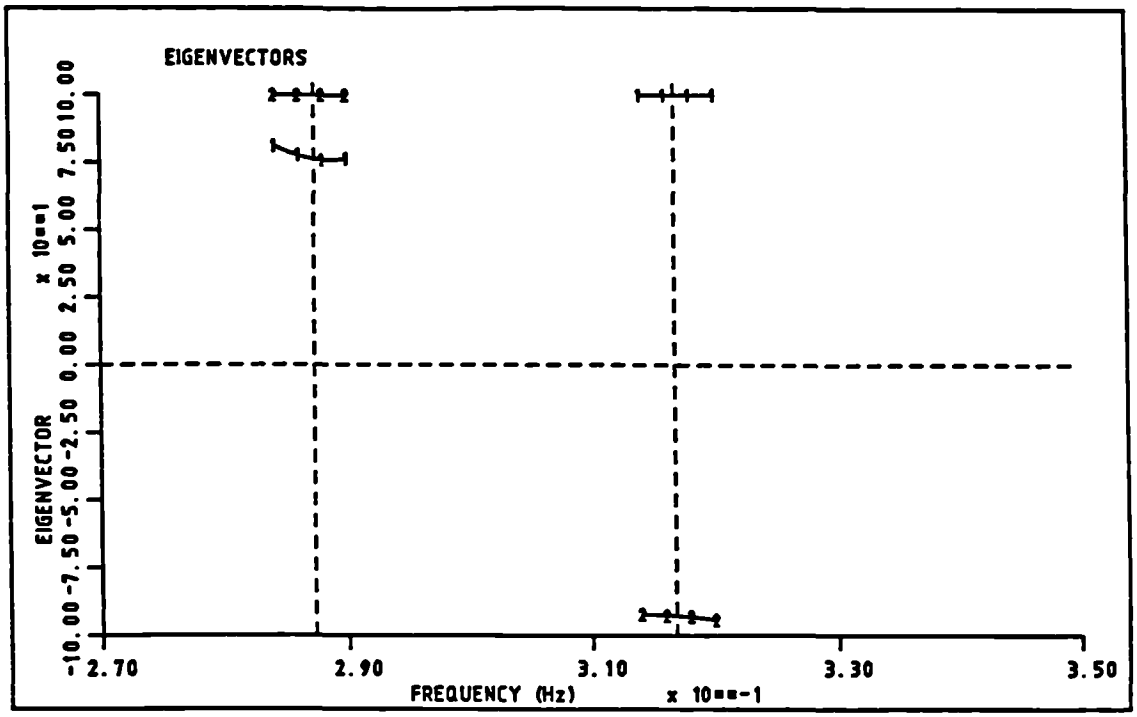

Figure 6.14. Eigenvectors corresponding to the eigenvalues of Fig. (6.13.b).

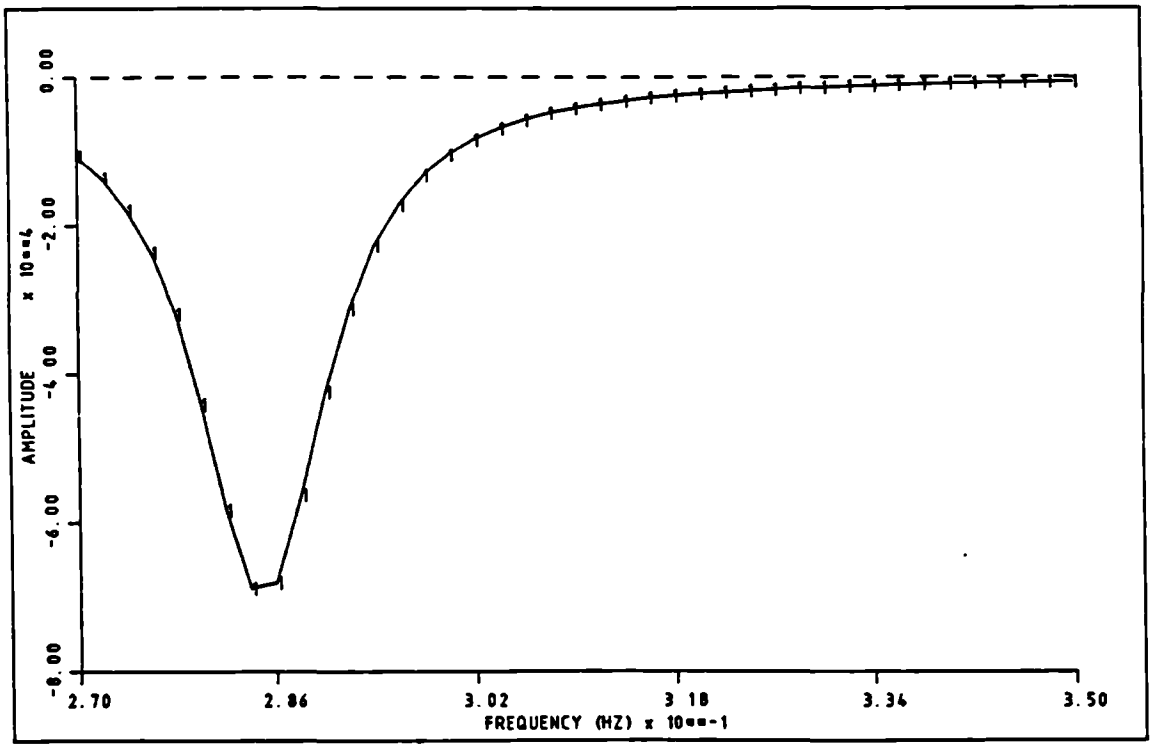

Figure 6.15. Sample plots used to estimate the first mode shape of the 2 d.o.f. example.

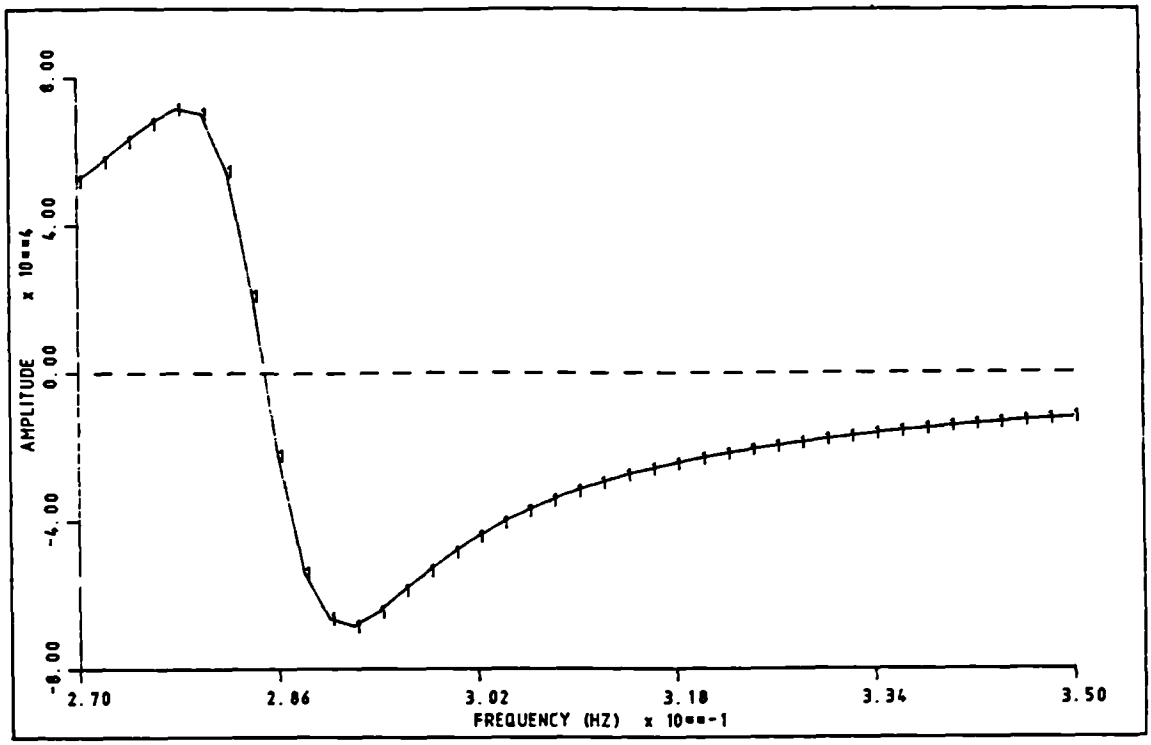

Figure 6.16. Sample plot of the S_{11} function used to estimate the generalised mass for mode 1.

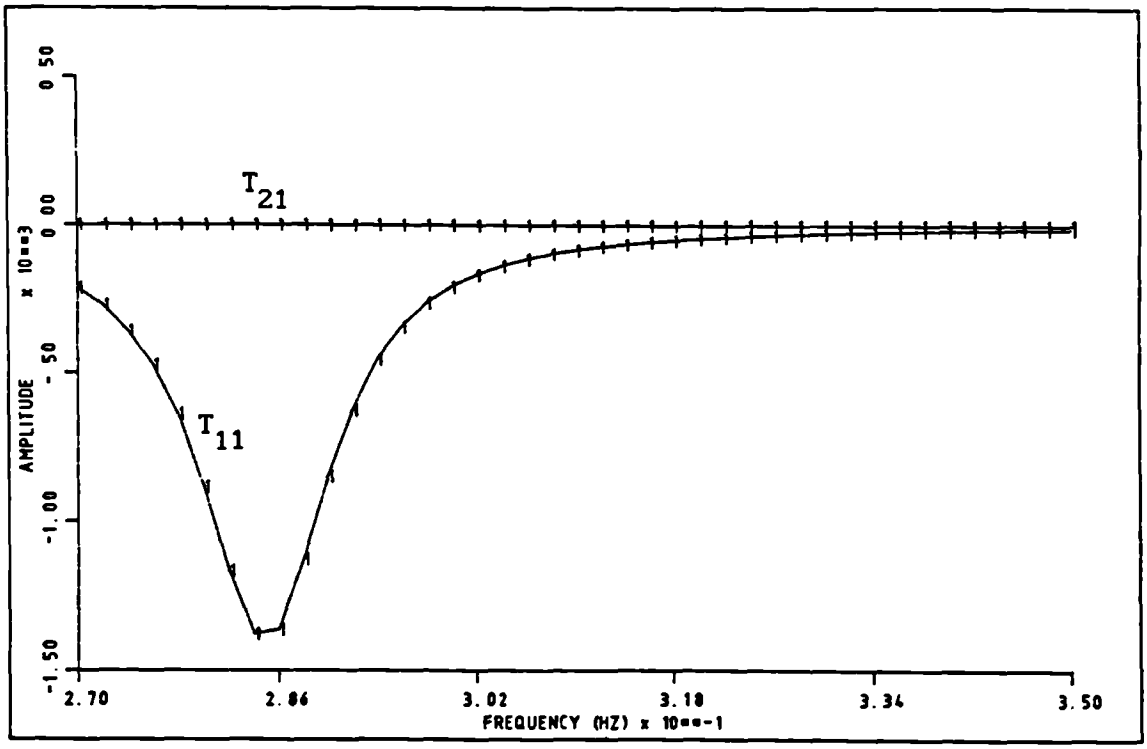

Figure 6.17. Sample plots for the T_{11} and T_{21} functions used to estimate the first column of the generalised damping matrix of the 2 d.o.f. example.

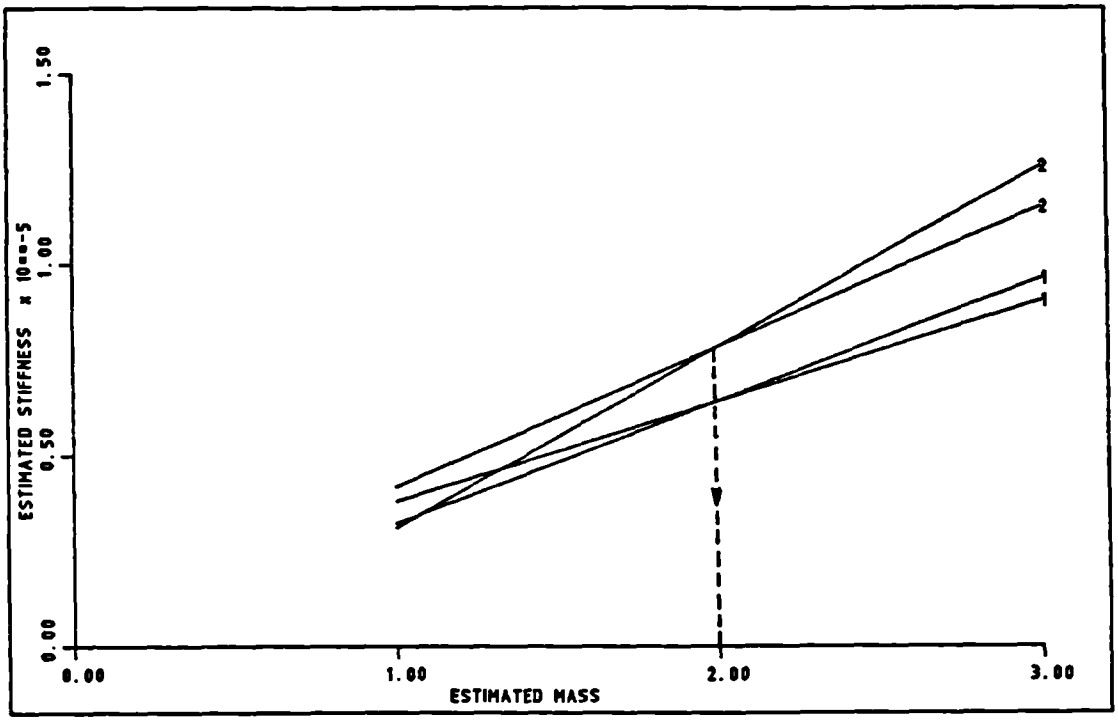

Figure 6.18. Estimation of generalised mass matrix of the 2 d.o.f. example using the sensitivity approach.

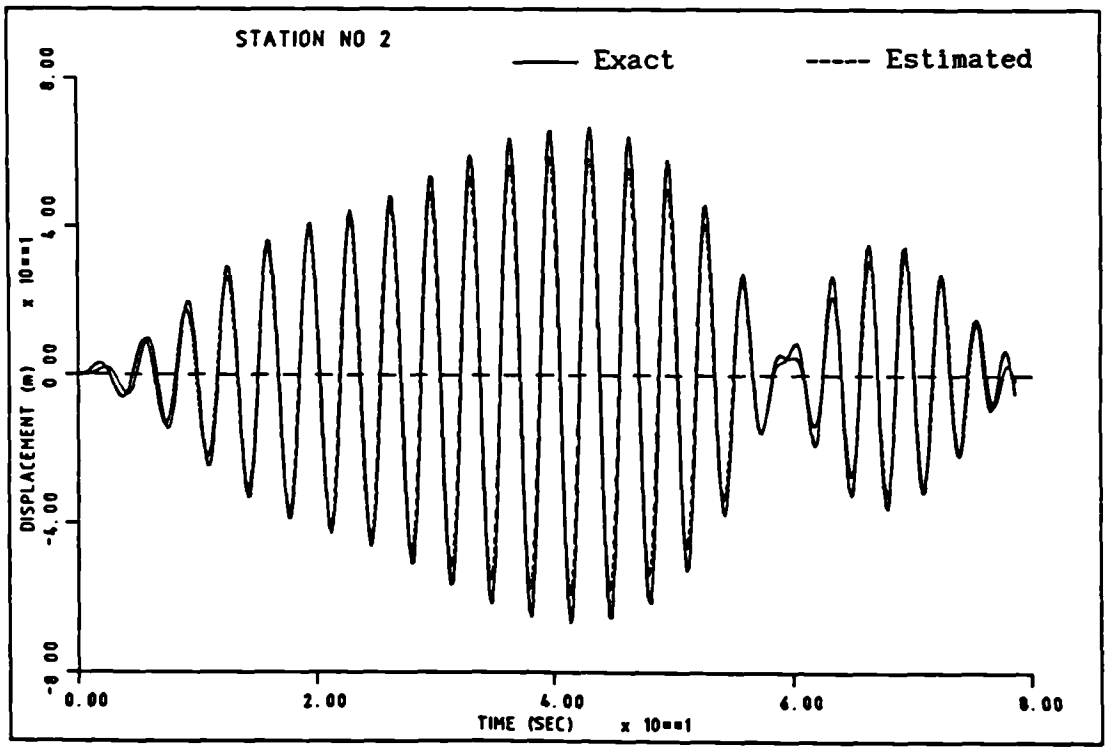

Figure 6.19. Comparisons of the exact responses of the 2 d.o.f. example and the responses of a model identified using an incorrect modal and the exact mass matrices.

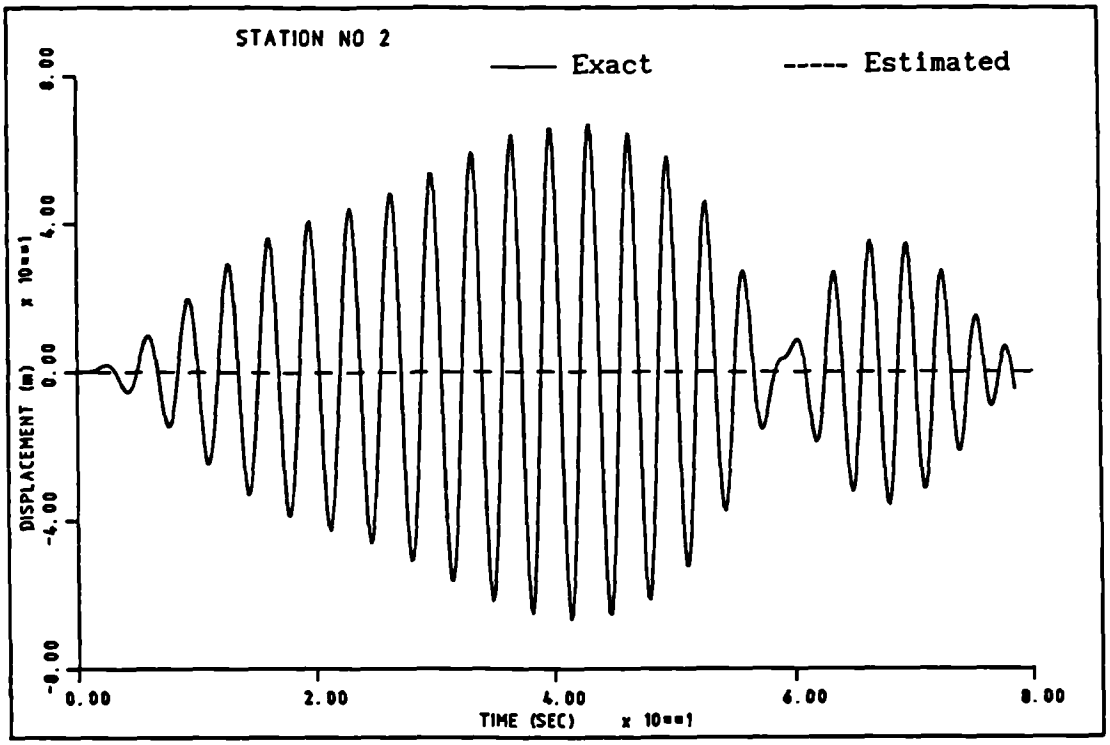

Figure 6.20. Comparison of exact response of the 2 d.o.f. example and the response of a model identified using an incorrect modal matrix but a mass matrix obtained using the sensitivity approach.

7. Application of the Force-State Mapping Technique to the Identification of Real Systems

7.1. Introduction.

It is sensible to start a particular investigation through the use of simulated data. However, an important question following a successful application to simulated systems, is how well the identification technique works when applied to real structures.

Some experimental work involving the force-state mapping has been carried out. In particular, Crawley et al [39-42] were the first who used the force-state mapping concept to investigate the nonlinear dynamic properties of truss joints in space structures. They idealised the joints, essentially, as a mass moving on flexure in one degree of freedom with some stiffness and friction nonlinearity. As a result it was shown that the application of the force-state mapping technique to single-d.o.f. real systems was possible but linear damping estimation was particularly difficult since, in some cases, negative values were obtained at high frequency tests. Worden and Tomlinson [52] have presented and curve fitted force-state maps for a cantilever beam with a clearance nonlinearity near the root, and for a vibration isolator. Also, Hunter et al [49] presented a map for a simple beam with base excitation and pointed out that the force-state mapping technique can provide a reasonable model for a single-d.o.f. system. It is understood that an application of the approach to a multi-d.o.f. system is being carried out by Worden and Tomlinson but as yet there are no published results.

In this chapter the application of the force-state mapping to a multi-d.o.f. T-beam structure shown in Fig. (7.1) is presented. The structure has been designed to exhibit properties involving at

least two types of common nonlinear elements. Also the relative natural frequencies of the primary bending and torsion modes could be controlled to some extent, simply by adding lumped masses to the structure. Thus it has been possible to separate these two modes sufficiently to enable the structure to be treated as a single-d.o.f. system or to bring them close together so that it can be treated as a two d.o.f. system. Some results for the single-d.o.f. identification of this T-beam have been already published in reference [54].

The main body of this chapter will be divided into two main parts. Firstly, a full description of the experimental set-up and software used will be given and some possible sources of systematic errors associated with the instrumentation and data acquisition are discussed. Secondly, some results from the identification of the bending and torsion modes, both when they are well separated and when they are close together, are presented.

It is important to point out that in the published experimental work of other authors, no attempt has been made to show how good the resulting model is compared to the actual behaviour of the structure. In this chapter, such comparisons will be made.

7.2. Description of test structure.

The structure considered in this work is a T-beam constructed from two lengths of thin-walled steal tube with a uniform square cross section. The two lengths were welded together and clamped horizontally to a large angle plate which in turn was fastened firmly to a strong floor. The clamp consisted of two pieces of angle and the tube was stiffened internally at the point of clamping. The general arrangement of the structure is shown in Fig. (7.1).

In order to introduce a source of nonlinear damping, as well as to

increase the damping in the lightly damped structure, a dashpot was attached to the structure. The position of the damper could be varied such that it was possible to introduce its damping into the primary bending mode only or into both the bending and torsion modes.

The dashpot arrangement consisted of a circular plate immersed in high viscosity oil and connected to the T-beam via a thin rod. The oil was contained in a beaker supported firmly by a wooden base which was in turn fastened to the floor. The size of the beaker was deliberately selected to be relatively large so that the damper plate was positioned far enough from the top and bottom surfaces of the oil for any surface effects to be unimportant when the plate oscillated. In addition, it was ensured that there was sufficient gap between the edge of the plate and the side of the beaker so as to minimize boundary effects.

The original idea of the root clamping arrangement was to be able to provide more flexible inserts to cause a stiffness nonlinearity. However once the basic structure was tested, the behaviour was sufficiently nonlinear for no inserts to be required!

7.3. Description of experimental set-up.

All the experimental, and indeed theoretical, investigations were carried out using a Computer Automation Alpha minicomputer. The computer was connected to a Cambridge Electronic Design CED 502 Analogue Interface unit, thus providing a data acquisition system. The system plus peripherals, power amplifiers and signal conditioning units were housed in a test cabin and linked to the test area by about 10-15 m of cabling.

A block diagram of the entire experimental set-up is shown in Fig. (7.2). The individual components are considered in the following subsections.

7.3.1. Computer.

The Alpha 2-40 computer was primarily FORTRAN based but some data acquisition routines supplied by CED were written in Assembler. The core memory of the computer was limited to only 64 Kbytes which limited the size of problems that could be tackled without resorting to overlaying or chaining. The standard integer word length was 16 bit and the floating point number were represented by a 24 bit mantissa and 8 bit exponent. In certain circumstances an increased precision (32 bit integer and 48 bit real) was used for calculation of inner products.

Although the computer was supported by existing libraries and programmes supplied by the manufacturer or written by previous users, a considerable software effort was expended by the author.

The peripherals associated with the computer were a floppy disc drive, a high resolution Westward 1015 alphanumeric/graphic visual display unit plus a keyboard, an Epson printer, an HP 7470A plotter and a CRT display unit.

7.3.2. Analogue Interface Unit (502 unit).

The Analogue Interface Unit was connected to the computer via a high speed link. It provided the excitation to the structure and acquired responses from it.

The main components of the interface unit used in the experimental investigation of the force-state mapping approach are described below.

(i) Buffer DAC [Digital to Analogue Converter].

Any excitation signal generated digitally in the computer can be stored with 8 bit amplitude resolution in the 2048 point memory of the Buffer DAC. The signal can then be output once or repeatedly

to the structure under the control of an internal 10 MHz clock. The number of clock counts between each stored point dictates the frequency of the output. The output is converted into an analogue signal proportional to the digital source, with ± 5 volts maximum range, and a low pass filter is used to smooth out the "steps" in the signal. The Buffer DAC was used primarily to provide steady-state or swept sinusoidal excitation.

(ii) Multiplying DACs.

Six 12 bit multiplying DACs were available in the interface unit. Each one allows the Buffer DAC output to be multiplied by a factor between 0 and ± 1 to a resolution of one part in 2048. They can be used for multipoint excitation or simply, as in this study, to control the force level applied to the structure.

(iii) ADC [Analogue to Digital Converter].

The analogue signals from the transducers and signal conditioning units can be converted to digital signals by the 12 bit ADC module provided in the interface unit. Signals entering the 16 data channels are sampled by the ADC in a multiplexed fashion using a "burst" mode data acquisition with a fixed delay of about 3.7 μsec between channels; the acquisition is synchronised with the Buffer DAC start. The resulting of sequence of 12 bit integers (+2048 corresponds to the +5 volts maximum) is stored in memory and demultiplexed later. The sampled signals were monitored using a CRT display with 4096 x 4096 resolution.

(iv) Anti-aliasing filter and programmable gain.

Basically the ADC sampler module mentioned above operates as a switch measuring the instantaneous amplitude of the analogue signal at a given sampling frequency. However if the analogue signal contains frequencies above half the sampling frequency (Nyquist frequency) then after sampling these high frequencies

will "fold back" into the lower frequency range, thus introducing errors into the frequency content of the digitised signal. The remedy for this problem, which is widely known as "aliasing" [1], is to use anti-aliasing filters to eliminate the frequency content above the Nyquist frequency in the original signal.

The analogue interface unit includes a programmable low pass filter for 8 of the input channels; the cut-off frequency can be set digitally. The filters are of switched capacitor type; analogue filters would be preferable in any future work. Unfortunately the filter chips in the unit were among the first used by CED and introduced a significant DC offset which had to be dealt with by using a high pass analogue filter with a 1 Hz cut-off.

A programmable gain facility was also available for 8 input channels in order to make reasonable use of the ADC range (± 5 volts). Thus if the analogue signal from the structure was very small then the signal could be amplified to use as much of the 5 volt range as possible. This would improve the amplitude resolution of the signal. The gain can be set independently on each channel in 7 discrete steps from 1 to 1000 (x1, 3, 10, 30, 100, 300, or 1000). A suitable gain value is chosen in an iterative fashion using software to asses the maximum value possible.

7.3.3. Other equipment.

(i) power amplifiers.

Six HH 500 Watt power amplifiers were available to be driven by the outputs from the multiplying DACs in order to provide sufficient current to the vibration exciters. Unfortunately the amplifiers were of the "constant voltage" output type which meant that the exciter back emf introduced by motion of the coil would affect the exciter current and hence the actual excitation force

measured at the structure would vary over the frequency range of interest. However it should also be pointed out here, apart from the exciter back emf, the influence of the exciter dynamic properties upon the structure behaviour would also contribute to the variation of the actual force particularly with lightly damped structures excited with oversized shakers where a significant force "drop out" around resonance regions is likely to occur [20,21].

(ii) Vibration exciters.

The electromagnetic exciters used were the LING 400 series, having a peak force of 90 N (uncooled). Although smaller exciters were available, the requirement to drive the structure well into the nonlinear range meant that they were probably inadequate, even though the use of a larger exciter increases the force drop out and therefore the current required to produce a large force at resonance. The larger exciter, however, proved satisfactory.

The exciter current was monitored using a voltmeter placed across a 1 ohm resistor. The exciter was connected to the structure via a fairly flexible thin rod. The exciter alignment and functioning was monitored by using an oscilloscope to view the analogue signals prior to sampling.

(iii) Transducers and signal conditioning.

The force and acceleration were measured using the well known PCB piezoelectric transducers which have a built-in amplifiers and are powered by a constant current source so that cable length is unimportant. These transducers operate fairly linearly over a wide frequency range and are fairly sensitive and stable.

The force gauge used throughout was a PCB 208A02, having a manufacturer's calibration of 11.236 mv/N, and the accelerometer was a PCB 308B with a calibration of 10.194 mv/m/s^2 at 100 Hz. An

additional pair of transducers with similar calibration factors was used for the two d.o.f. identification. The calibration of transducers will be discussed later.

The transducers were powered and coupled to the analogue interface unit via a compatible PCB 483A multi-channel signal conditioning unit.

7.4. Experimental procedure.

The experimental procedure for the force-state mapping investigation was carried out on the T-beam structure using the above equipment under the control of a FORTRAN programme with the flowchart given in Fig. (7.3). The flowchart shows that the programme can be used for generating the FRF of the structure using a stepped sine steady-state excitation or for obtaining the time history response of the structure under random or sine sweep excitation.

Any particular test was started by generating 2048 points of a specified excitation signal and storing the data in the Buffer DAC memory. The Buffer DAC clock was set up to provide the desired interval between points to be output. The low pass filter associated with the Buffer DAC output was set to have a cut-off at four times the maximum frequency of the signal.

The gains of the relevant multiplying DAC and ADC channels were set at suitable initial values. The anti-aliasing filters were set to have a cut-off frequency equal to 80% of the Nyquist frequency.

Sampling of the measured signals in the ADC was carried out at some chosen multiple (power of 2) of the Buffer DAC clock interval; this was due to memory limitations in the subsequent analysis programmes where the number of points had to be reduced. The ADC clock had to be set to provide the required sampling interval such that the two clocks were operating at consistent

rates. The Buffer DAC was used to trigger the data acquisition at the start of the excitation signal.

Once transducer data had been sampled and stored, the maximum value of each of the raw sampled signals was calculated. In order to make reasonable use of the ADC range these maximum values were compared with the maximum range of the ADC (±2048) and the gain adjusted in some suitable fashion. The process of data acquisition and gain adjustment was then repeated until the gains had converged and the incoming signals had been amplified as much as possible. This process of adjusting the gain is essential in order to minimise the quantization error introduced by the analogue to digital conversion (see section (7.5.1)).

In the case of sine sweep or random excitation, the signal in the Buffer DAC was only output once for each gain adjustment iteration. Once convergence was achieved the sampled time signals were extracted from the multiplexed data array, viewed on the CRT, calibrated and finally stored on a disc for further analysis.

In the case of steady-state sinusoidal excitation carried out at a number of discrete frequencies, the Buffer DAC contents were output repeatedly and acquisition of the data repeated so that the excitation force level to the structure could be kept constant, especially around resonance regions. The adjustment of the force was based on implementing a feed back loop in which the maximum value of the measured force was compared with the demanded maximum force. If the difference was not within the prescribed limits (usually ± 2%) then the voltage provided to the exciter was adjusted accordingly by modifying the multiplying DAC gain and the acquisition repeated.

Once the measured force level had converged to the demanded level, a digital Resolver process [65] was carried out by multiplying each signal with an internal sinusoidal reference array similar to that in the Buffer DAC and with one in quadrature with it. The

resolver outputs were the real and imaginary parts of the transfer function between the signal and the reference signal.

In order to ensure that the steady-state response of the structure was obtained at each frequency step, and not to have to specify a time delay before data acquisition in order to account for the transient, the resolver output components were used to indicate convergence by repeating the process until a prescribed accuracy criteria was achieved. The corresponding final results were calibrated and stored on disc for further analysis.

Before proceeding with the analysis phase, it is worthwhile considering and assessing the quality of the measured and processed response data and trying to pinpoint the possible sources of errors associated with the above experimental approach. Some errors are associated with the imperfection of the instrumentation and hardware and others are inherent in the experimental process.

7.5. Sources of experimental errors.

7.5.1. Quantization error.

In essence, the ADC sampling process produces fixed-point binary (i.e. integer) number representations of the original analogue signal, generally referred to as quantization of the analogue signal [22]. The difference between the actual floating point input value to the ADC and the fixed-point binary representation is commonly referred to as quantization noise as shown in Fig. (7.4).

The resolution of the ADC used in this study is one part in 2048 where 12 bits (including sign) are used for the conversion. The difference between adjacent quantization levels is then Q=1/2048 and hence the maximum possible quantization error is Q/2. However the error-to-signal ratio will depend upon the instantaneous

amplitude of the signal being sampled, i.e. the error will be more significant in the low amplitude regions.

Because any ADC has a limited resolution by definition, some quantization error is inevitable but its effect can be minimised by increasing the magnitude of the analogue signal as much as possible via the programmable gain.

7.5.2. Multiplexer error.

It was stated earlier that response data from the structure were acquired and sampled by the ADC in a multiplexed manner with a fixed delay between the input channels of 3.7 μsec. This time delay occurs because the ADC can only sample one signal at a time and it will clearly introduce phase shift errors between the measured signals.

The 3.7 μsec time delay is an inherent property of the multiplexer used in this particular test and thus it could not be minimised or avoided. The only way to eliminate this delay is to use a simultaneous sample and hold so that all channels are sampled at the same instant.

It can be shown that the phase shift in degrees introduced by a time delay $\Delta\tau$ between the Ith channel in the sampling sequence and the first channel may be given by

$$\varepsilon = \Delta\tau \; f \; (I-1) \; 360 \qquad \ldots\ldots\ldots\ldots\ldots (7.1)$$

where f (Hz) is the frequency of the signals. When only two channels are used, as for the single-d.o.f. identification, then with $\Delta\tau$ = 3.7 μsec the phase error will be $\varepsilon = 1.33 \times 10^{-3}$ f. The error is proportional to frequency but is only 0.133° at 100 Hz. When three channels are used, as for the two d.o.f. identification, the error will double. It was shown in chapter 5 that such errors could be significant for lightly damped

structures.

Whilst it is possible to correct the phase of any transfer function for this error, it would be difficult to correct time signals since some form of interpolation would probably be required [53].

7.5.3. Channel mismatch errors.

Ideally the signals from the structure should pass through identical hardware paths in the analogue interface unit. In practice, manufacturers seek to ensure that hardware is designed within specified tolerances given that individual components are not identical.

Because the ADC sampling process is common to all channels in the analogue interface unit, any mismatch between channels is only likely to occur in the programmable gain/filter unit where each channel is processed independently. Unfortunately, whereas the gain amplifiers used high precision components, the filters fitted were somewhat imperfect due to high variability in the chips used.

It is necessary, therefore, to carry out a simple test on the channels used in the experiment to see the differences in their amplitude and phase characteristics over the frequency range of interest. This simple test is described below.

A sinusoidal excitation signal was taken as an output from one of the multiplying DAC channels and presented as an input to all of the first four ADC channels. The usual processing described in section (7.4) was carried out for the four identical signals and the corresponding amplitude and phase of each channel with respect to the internal reference was obtained for a range of frequencies between 20 and 80 Hz. The excitation signal had 32 points per cycle so 64 cycles were involved in the resolver process. The Nyquist frequency for data acquisition was 8 times the signal

frequency.

If the hardware paths of the signals were identical then it would be expected that the resulting amplitude and phase values would be similar for all channels with only quantization and multiplexing errors present. Unfortunately this was not the case and some mismatch between channels was apparent. This mismatch is seen in Fig. (7.5) which shows the percentage amplitude and absolute phase errors with respect to the first channel, calculated for the Ith channel using

$$\alpha(I) = \frac{A(I) - A(1)}{A(1)} \times 100 \qquad \ldots\ldots\ldots\ldots\ldots (7.2)$$

$$\varepsilon(I) = \phi(I) - \phi(1) \qquad \ldots\ldots\ldots\ldots\ldots (7.3)$$

It can be seen that the third channel had the maximum amplitude and phase errors of about -2% and 1.5° respectively. These errors were considered to be too large to be accommodated by the force-state mapping technique and thus the third channel was not used. Fortunately, the errors in the remaining two channels were smaller with maximum values around -0.5% and 0.5° over the 30-80 Hz range used. Some variation with frequency is apparent.

However, when the test was repeated using an input signal having 1024 points per cycle, it is seen in Fig. (7.6) that the phase errors were smaller for all the channels and both errors were completely different to those found for the 32 points per cycle case.

The use of a larger number of points per cycle in the input signal meant that the cut-off frequency of the anti-aliasing filters was 32 times higher than that for the previous case. It would appear therefore that the phase and amplitude errors were dependent upon the cut-off frequency as might be expected and this fact was confirmed when similar results were obtained for both cases using a common cut-off frequency. The filter behaviour is rather complex

because a combination of digital low pass and an analogue high pass filter are involved.

The use of very large number of points per cycle is possible when steady-state excitation is used . However, for swept sine or random excitation, many cycles are usually needed in order to give sufficient time to sweep through the range of interest and then for the response to decay within the data window so as to minimise leakage effects. Since the number of points available in the Buffer DAC memory is limited to 2048, it is not possible to use a large number of points per cycle.

Although the phase errors can be reduced by increasing the number of points per cycle used, a more satisfactory solution is to seek to compensate for the amplitude and phase errors in some way. It is conceivable that a steady-state signal could be shifted by a suitable amount but even this would be difficult to carry out accurately since the shift would probably be less than one sampling interval. For more general signals containing a range of frequency components, correction would be even harder.

The compensation for amplitude mismatch errors between the Ith and the first channel is a fairly simple matter for a steady-state sinusoidal excitation. It can be carried out by curve fitting a polynomial $\hat{RI}(f_k)$ through the points given by

$$RI(f_k) = \frac{AI(f_k)}{A1(f_k)} \qquad (k=1,NF) \qquad \ldots\ldots\ldots\ldots\ldots\ldots (7.4)$$

where NF is number of frequency points used in the test and f_k is the frequency at a step k, AI and A1 are the amplitudes of the FRF for the Ith and the first channels respectively with respect to the reference signal, obtained from the test. The resulting polynomial can then be used in an actual experiment to modify the calibration factor for the Ith transducer at each excitation frequency using

$$\hat{TI}(f_k) = \hat{RI}(f_k) \times TI \qquad \ldots\ldots\ldots\ldots\ldots (7.5)$$

where TI is the nominal calibration factor of the Ith transducer. Clearly the assumption has been made that the first channel has no error which is unlikely to be true. However an absolute calibration of filters is not easy to carry out.

For a swept sine or random excitation the problem is not so simple since the response would contain a number of frequency components, each of which requires a different calibration. An approximate solution is to work out the average value of the amplitude error over the frequency range of interest using, for the Ith channel,

$$RI_{av} = \frac{1}{NF} \sum_{k=1}^{NF} RI(f_k) \qquad \ldots\ldots\ldots\ldots\ldots\ldots (7.6)$$

The calibration factor for the Ith transducer would then be adjusted using

$$\hat{TI} = RI_{av} \times TI \qquad \ldots\ldots\ldots\ldots\ldots\ldots\ldots\ldots (7.7)$$

Note that when using this approach, the variation of RI within the frequency range of interest should be reasonably small.

In further work it could be worth considering carrying out compensation in the frequency domain but a disadvantage of this is that the mismatch characteristics would need to be known over a wide frequency range.

7.5.4. Transducer errors.

The calibration considered so far have not included the signal conditioning amplifiers, cable connections and transducers used in the actual measurements.

The PCB transducers used are individually and carefully calibrated by the manufacturer. However, transducers can suffer internal damage due to shocks or misuse and this could modify their characteristics. A confirmation, or otherwise, of the manufacturer's calibration factors would therefore be helpful.

In modal testing, there are two types of calibration which can be made [1]. The first of these is an absolute calibration of individual transducers to check their sensitivity values with those specified by the manufacturer. This type of calibration is somewhat difficult to carry out since it relies heavily upon the use of an accurate reference signal provided by a calibrator device or by a transducer which has very stable and reliable characteristics. The accuracy of such a calibration is usually better than ± 2% when carried out by the manufacturer and this includes the influence of connection cables and the conditioning amplifier supplied with the transducers. It was decided not to attempt an absolute dynamic calibration for this study since high accuracy reference transducers were not readily available.

A simpler and more convenient approach is to use the alternative relative calibration philosophy. This is based on calibrating ratios between response and force levels for the whole measurement system. Such a calibration is ideal when seeking to measure ratios such as FRFs but not when the individual time signals are used in force-state mapping since one ratio can not be used to modify two calibration figures. In view of this it was originally decided to adopt the manufacturer's calibrations.

However, for interest and as a check on the whole instrumentation set-up, a ratio test was carried out by suspending an exciter and a known mass on cables as shown in Fig. (7.7). The mass was then excited horizontally and its (force/acceleration) transfer function obtained under steady-state conditions, using the manufacturer's calibration factors modified to compensate for the

amplitude error mismatch between anti-aliasing filters.

It can easily be shown that the amplitude of the force/acceleration transfer function provides an estimate of the shaken (or apparent) mass and the phase should ideally be zero. Fig. (7.8) shows typical apparent mass and phase plots measured at three force levels over the frequency range of interest for the accelerometer and force gauge used later. The apparent mass hardly varied with frequency or force level as might be expected but was slightly lower than the measured mass.

The phase curves had slightly different values and they all were within 0.75° except around 20-30 Hz. The behaviour of the 3 phase curves is probably due to some physical effect on the calibration rig which is not an ideal mass but a lightly damped pendulum with a low natural frequency. It is also possible that pitching or yawing of the mass could occur.

In order to gain some appreciation of the phase differences between accelerometers of the same type, the same test was repeated for the other accelerometer used in the actual experiment. The results in Fig. (7.9) show that there is quite good agreement in the amplitude but that the phase differs by around $1/3^{\circ}$ between the accelerometers.

It is clear that the experimental set-up could produce errors which are significant for state-mapping identification of lightly damped structures since the earlier sensitivity studies indicated that phase errors could have significant influence on the results. Amplitude errors are arguably less important.

In any future work, better filters would be essential and, if possible, an absolute amplitude and phase calibration of the transducers should be carried out. Frequency domain compensation would need to be considered.

The following sections consider the experimental results obtained using this imperfect test set-up for configurations with two well separated and two close modes.

7.6. Experimental application of the force-state mapping technique to the identification of well separated modes.

As stated earlier, the T-beam structure considered in this work has the advantage that the relative natural frequencies of the primary bending and torsion modes, sketched in Fig. (7.10.a), can be controlled by adding lumped masses to the structure as shown in Fig. (7.10.b).

The FRF of the T-beam, without any added masses or dashpot, is shown as the solid line in Fig. (7.11). It would be expected that the addition of significant masses M at the junction end of beam 1 would reduce the bending frequency significantly and the torsional frequency slightly, assuming that the beam stiffness was unaffected. However, as shown in Fig. (7.11) by the dotted line, the addition of 2.2 kg mass reduced the bending frequency by 13% but increased the torsion frequency by about 5%, presumably because the clamped masses increased the beam torsional stiffness locally. In any case the two modes are sufficiently well separated for each of them to be treated as a single-d.o.f. system.

Later on, by positioning the masses on beam 2 and increasing the distance L as shown in Fig. (7.10.b), the torsion frequency could be reduced whilst the bending frequency remains essentially constant. This leads to the two close modes configuration.

7.6.1. Identification of bending mode.

In order to increase the damping in the bending mode and to introduce a quadratic damping type of nonlinearity, the dashpot type arrangement described earlier was added at the junction of the T-beam as shown in Fig. (7.1).

A sample frequency response function for this mode at three force levels is shown in Fig. (7.12) for the structure with no oil in the dashpot. The natural frequency is around 40.5 Hz and there is clearly some nonlinear behaviour simply due to the root clamp; some softening stiffness nonlinearity is thought to be associated with local flexibility of the clamp altering the clamping action and some damping nonlinearity from rubbing within the joint. The damping is very low (< 1%) and is considered to be too small for the frequency shift with amplitude to be merely due to increased damping. The addition of oil to the dashpot introduced additional nonlinear damping and reduced the natural frequency to around 39.3 Hz due to the added mass of the oil; a FRF plot for this case will be shown later.

In this section, force-state maps will be produced using both steady-state and swept sine excitations. However, for single-d.o.f. identification, steady-state excitation can have further advantages over swept sine excitation in that

(i) a controlled constant force level can be used in order to avoid force drop out around resonance regions and allow the system to be excited at the required force level,
(ii) an integer number of cycles can be provided leading to periodic signals and hence to leakage-free integration in the frequency domain and
(iii) the selection of cut-off frequency for the frequency domain integration is easier since the spectrum usually contains only sharp peaks.

One drawback in using steady-state excitation is that at a particular force level the map will merely be a "ring" in the state space. This means that a large region in the state space will have no restoring force data; the curve fitting of such a map would tend to be more sensitive to errors in the measurements. It was therefore decided to build up the force-state map from several

rings each of which corresponds to a different force level. This will be illustrated shortly when some results are presented. An alternative approach would be to use rings obtained at different frequencies.

In order to proceed with the identification process, the effective mass of the system needed to be estimated. In the case of this continuous system the mathematical model would need to correspond to the force and response measured at one position so the mass is the effective mass of the structure in this mode as seen by the exciter. From the approach presented in section (6.3) using only 3N force the mass was approximately 5.3 kg. A complete set of results regarding the application of multi-point force appropriation to real systems will be presented later for the T-beam with 2 close modes. The mass estimate was then refined using the sensitivity approach. Data was acquired at five frequencies (36,38,39.4,41 and 42 Hz) and three force levels (typically 20, 40 and 80N) for each frequency using steady-state excitation. Maps were constructed by combining the three force results for each frequency and assuming a mass of firstly 3kg (<5.3) and then 8kg (>5.3); a curve fit using a nonlinear model was carried out for each frequency/mass combination.

The resulting variation of the estimated linear stiffness with the assumed mass values for the five frequencies is shown in Fig. (7.13). This result is encouraging since all the lines should intersect at the same mass value; in fact all the ten possible intersections lay in the range 5.8 - 6.6 kg with an average value around 6.0 kg, taken as the effective system mass.

A force-state map corresponding to the 38 Hz steady-state excitation at 20, 40 and 80N and the 6 kg effective mass was then constructed. In all cases The integrations were carried out in the frequency domain by transforming the integer number of cycles of the acceleration data defined at 32 points per cycle. Sample portions of the time histories for each of the three force levels are shown sequentially in Fig. (7.14). The corresponding map and

its projections onto the force-displacement and force-velocity planes are shown in Fig. (7.15).

Another version of the map was obtained using frequency sweep excitation around resonance with the sweep occupying only about 30% of the acquired data window in order to allow the response to decay sufficiently and so minimise leakage. The sweep amplitude was tailored by multiplying the excitation signal with a cosine taper window so as to avoid large transients. After frequency domain integration, every fourth point from the 1024 point data records was selected for the map, due to memory limitations. The corresponding time histories and the map and its projections are shown in Figs. (7.16) and (7.17).

The two versions of the map differ somewhat because the steady-state excitation produces a higher level of response than the sweep. There is no obvious reason for the apparent lack of symmetry in the steady-state map, as seen from the projection of Fig. (7.15). It may only be said that for a real structure the nonlinearity may not behave in an ideal way or that some experimental or integration error may be responsible. Any stiffness nonlinearity is clearly not large and is obscured by the thickness of the projection due to the damping; the map doesn't help much in this case.

A curve fit using a nonlinear model was carried out to each map. A nonparametric model was used and found to give better results than a parametric model with only a few terms. The fitted models are shown in table (7.1), together with the R.M.S. contribution of each term to the overall fit. Apart from the linear terms, dominated by the stiffness, a small cubic softening stiffness was consistently obtained, as well as a quadratic damping term. The other nonlinear terms helped to improve the fit and were presumably some representation of the non-ideal behaviour of the structure and the hardware used for carrying out the test.

Table (7.1): Identified models of bending and torsion modes

$$f(x,\dot{x}) = a_0 + a_1 x + a_2 \dot{x} + a_3 x\dot{x} + a_4 x^2 + a_5 \dot{x}^2 + a_6 x^2\dot{x} + a_7 x\dot{x}^2 + a_8 x^3 + a_9 \dot{x}^2 \, \mathrm{sign}(\dot{x})$$

A. Bending mode (steady-state model, 38 Hz, 20, 40 & 80 N, m=6 ,G=0.986)*

Term	a_o	a_1	a_2	a_3	a_4	a_5	a_6	a_7	a_8	a_9
Identified terms	-1.39	3.6E5	6.1	1.2E4	1.7E6	-28.8	1.8E6	-1.1E4	-3.3E8	67
R.M.S. contbn.+(%)	0.16	90.46	0.3	1.36	1.28	1.28	0.51	0.77	0.83	2.98

B. Bending mode (sweep model, m=6 ,G=0.963)

Term	a_o	a_1	a_2	a_3	a_4	a_5	a_6	a_7	a_8	a_9
Identified terms	-.159	3.6E5	1.3	6.6E3	2.6E6	-41.7	1.09E6	-1.8E4	-5.6E8	71
R.M.S. contbn. (%)	0.03	92.48	.08	0.51	1.43	1.38	0.16	0.71	0.78	2.4

C. Torsion mode (steady-state model,75.5 Hz, 5, 8, 10 & 15 N, m=4, G=.97)

Term	a_o	a_1	a_2	a_3	a_4	a_5	a_6	a_7	a_8	a_9
Identified terms	2.38	9.1E5	.47	6.8E3	-9.E5	-3.17	-2.8E6	-1.9E3	-2.9E9	15
R.M.S. contbn. (%)	0.25	97.	.02	0.30	0.15	0.11	0.16	0.52	0.81	.56

* G stands for goodness of fit (max=1) + contribution

The quality of the models was evaluated firstly by using Runge-Kutta simulation to obtain responses due to constant force steady-state excitation and hence frequency response functions. These are compared to measured results in Figs. (7.18) and (7.19) for the two fitted models at 4 force levels; the agreement is encouraging. A further check on the models is to compare the responses of the model and the structure to sweep and random excitations; some sample comparisons are shown in Figs (7.20) and (7.21) for the steady-state model and again show fairly good agreement over a range of excitation levels.

Clearly for this mode the nonlinear model is able to represent the behaviour of the structures fairly well. It is arguable that by increasing the level of damping, phase errors have not had a great effect.

In order to study the sensitivity of the results to any possible error in the mass the model was reproduced using different mass values and the simulation in the frequency domain repeated. The corresponding frequency response functions generated at 5N for the m =5.5, 6 and 6.5 kg cases are shown (dashed lines) in Fig. (7.22) and compared to the measured FRF (solid line). It can be seen that the variation of the mass hardly changed the FRF of the model around the peak while it had more effect away from resonance regions.

Similar analysis was also carried out in conjunction with the adoption of parametric and nonparametric models. The FRFs corresponding to a parametric model, which included linear stiffness, linear damping, cubic stiffness and quadratic damping terms, and to a nonparametric model given in table (7.1), were generated for m = 6 kg and P = 5N and compared with the measured FRF in Fig (7.23). It can be seen that the behaviour of the nonparametric model matches the behaviour of the test structure more closely.

7.6.2. Identification of torsion mode.

For this mode the behaviour without oil in the dashpot was fairly similar to that seen in Fig. (7.12) for the bending mode, except that the natural frequency was around 76.0 Hz. However in this case the addition of oil made very little difference as might be expected since the dashpot was located at an effective node and the only mechanism for damping would be the plate moving more or less in its own plane in the oil. Unfortunately this meant that the damping was much lower than that for the bending mode and therefore poorer results were expected for the identification of the torsion mode.

The initial effective mass estimate obtained from a FRF measured at 3N using the method in section (6.3) was 4 kg. The sensitivity approach was used again, this time for three frequencies (74, 75.5 and 79 Hz) each at four force levels and for assumed masses of 3 and 8 kg. The variation of stiffness with assumed mass is shown in Fig. (7.24). The intersections are at values 3.8, 4.3 and 5.5 kg and have an average of 4.5 kg. The scatter in values is believed to be larger due partly to the sensitivity problem and partly because the measured force near resonance at 75.5 Hz was corrupted by noise and harmonic content. In addition, the slopes of the straight lines for this mode are closer together because the ratio of 79/74 is less than that of 42/36 for the bending mode. This would make the intersection point more sensitive to errors and thus well separated frequencies should had been considered. Therefore the effective mass was taken to be equal to the 4 kg value estimated at low force level.

Some attempt was made to use sweep excitation to produce a map for fitting but difficulty was experienced in obtaining a leakage-free response due to the very low damping present; attempts to use time domain integration did not give good results. The high frequency problem of Simpson and Bode rules was encountered. The use of the trapezoidal rule and the cubic spline approach yielded unreasonable maps having apparent phase shift errors which could

have been introduced by the high-pass filtering, though the filter was used forward and backward.

Therefore the identification process was restricted to the steady-state excitation case. It was found that increasing the number of points per cycle from 32 to 512 seemed to improve the identification results since the phase shift error introduced by the mismatch in the anti-aliasing filters was smaller.

A typical force-state map and projection for 74 Hz and 4 force levels is shown in Fig. (7.25). It is narrower than the corresponding result for the bending mode, reflecting the lower damping, but still the nonlinear stiffness is not obvious since it is a very small proportion of the linear stiffness. A typical fitted model is shown in table (7.1.c). In this case the softening stiffness is apparent again but the nonlinear damping is much smaller as might be expected. The other nonlinear terms have only a small contribution.

Finally a comparison of frequency response functions obtained from the structure and fitted model are shown in Fig. (7.26); the agreement is not as good as for the bending mode, probably because it is very sensitive to the damping obtained. Nevertheless the basic reduction in amplitude and shift in peak is modeled. A sample comparison of structure and model responses to a random excitation is shown in Fig. (7.27). The apparent disagreement is believed to be due to the frequency shift between the FRFs of the structure and the model. This can be seen in Fig. (7.26) where at a particular frequency the difference between the amplitudes of the structure and the model is significant though the shape of the curves is reasonable.

For this mode the model obtained was fair but clearly the identification of very lightly damped structures is more sensitive, a feature known from even linear identification.

7.7. Experimental application of the force-state mapping to the identification of two close modes.

In this section the force-state mapping technique will be applied to the T-beam structure after its primary bending and torsion modes have been brought fairly close together. It can be seen from Fig. (7.10.b) that the addition of the lumped masses M on beam 2 will have the effect of reducing the natural frequencies for both modes, but that the torsion frequency should reduce as the distance L is increased. Fig. (7.28) shows the variation of the measured resonance frequencies for the two modes as the mass M added at each tip of beam 2 is increased. What is happening is that when the tip mass dominates the effective mass of the beams, then both frequencies are essentially proportional to $1/\sqrt{M}$. The only way to bring the frequencies any closer, or to bring the torsion mode below the bending mode, would be to increase L. However, the results for the largest mass were considered sufficiently close in frequency to proceed without extending beam 2.

In order to increase the damping in both modes and to introduce the nonlinear behaviour of the dashpot arrangement to both modes, the dashpot was attached at one tip of the T-beam as shown in Fig. (7.29). Fig. (7.30) shows a sample FRF for both modes at 3 force levels after adding a mass of 2.33 kg and attaching the dashpot at the tip. Clearly the two modes are fairly close and can be considered to have significant modal interaction. The nonlinear behaviour of the structure is also apparent.

7.7.1. Initial estimation of generalised mass and modal matrices.

In order to proceed with the identification of this 2 d.o.f. nonlinear system, the generalised mass and modal matrices of the system needed to be estimated. For such a continuous system the use of two transducers would be sufficient to characterise the bending and torsion modes. The location of these transducers is

shown in Fig. (7.29).

For the application of the multi-point force appropriation techniques described in chapter 6, the required 2x2 FRF matrix $[A(\omega)+iB(\omega)]$ was assembled column by column using the two exciters shown in Fig. (7.29). It should be pointed out that only one exciter was attached to the structure at a time to avoid the effective mass of the moving coil of the other exciter being added to the structure, i.e. the other exciter would actually input additional force to the structure even if no power was applied. The constant force level used to measure the FRF matrix was 5 N peak.

The eigenvalue problem of the Trial-Nash method introduced in section (6.6) was then solved yielding two eigenvalues and their associated eigenvectors. Fig. (7.31) shows the variation of the resulting eigenvalues against frequency. The eigenvalues crossing zero behaved sensibly but, as also seen in reference [62], the other eigenvalue was sometimes noisy.

A simple curve fitting and interpolation scheme involving a first order polynomial was then applied to the nearest 4 points to the frequency axis for each mode. The interpolated values corresponding to zero eigenvalues provided natural frequency estimates of f_1= 31.72 Hz and f_2= 35.29 Hz. Fig. (7.32) shows the variation of each element of the two normalised eigenvectors against frequency, corresponding to the points selected above. A second order polynomial was curve fitted through each set of points for all the individual elements of the eigenvectors. The resulting polynomials were estimated at the corresponding natural frequencies to yield the following two optimal or appropriated force distributions,

$$\underset{\sim}{P}_1 = \begin{bmatrix} -0.264 \\ 1.000 \end{bmatrix} \qquad \text{and} \qquad \underset{\sim}{P}_2 = \begin{bmatrix} -0.796 \\ 1.000 \end{bmatrix}$$

These are the force patterns which should be able to excite each

mode in isolation. Having obtained the natural frequencies and the optimal force distributions for the two modes it remains to use these values in the manner shown in section (6.6) to obtain initial estimates for the generalised mass and modal matrices.

The estimation of the generalised mass of the first mode required that the slope of the function $S_{11}(\omega) = [\underset{\sim}{P}_1^t \; A(\omega) \; \underset{\sim}{P}_1]$ be evaluated at the natural frequency. Fig. (7.33) shows the variation of the function S_{11} with frequency for the primary bending mode of the T-beam. The behaviour of the resulting curve is not completely consistent with the behaviour of a pure isolated mode since some variations of the curve around the region of the other mode can be seen. This is believed to be due to errors in the estimated optimal force distribution which has not been able to isolate the first mode. This is perhaps not surprising since a linear idea has been applied to nonlinear data but it is considered that the second mode has been sufficiently suppressed for an approximate value of the generalised mass of mode 1 to be estimated. Similarly, the variation of the function S_{22} for the second mode is shown in Fig. (7.34). Regarding the modal matrix, plots of $B(\omega)\underset{\sim}{P}_j$ for estimation of the first and second mode shapes are shown in Figs. (7.35) and (7.36) respectively.

The estimation of the required matrices from all these plots has been carried out in exactly the same manner as introduced for the two d.o.f. simulated system considered in section (6.6). The resulting estimated matrices were

$$M_u = \begin{bmatrix} 6.26 & 0 \\ 0 & 9.20 \end{bmatrix} \qquad \text{and} \qquad \Phi = \begin{bmatrix} 0.668 & 1.000 \\ 1.000 & -0.307 \end{bmatrix}$$

and the estimated mode shapes for the two modes are shown in Fig. (7.37). The shapes are not symmetric and there is bending/torsion coupling which is reasonable considering the added mass of the dashpot plate and oil. However it might be expected that the bending mode would have a smaller deflection on the dashpot side

of the junction but the torsion mode is satisfactory. The mode shapes will obviously include some errors but are clearly sensible.

As was shown in section (6.6) the force appropriation method can also provide an estimate for the generalised damping matrix. Although this estimate will not be used in conjunction with the force-state mapping technique, it would be useful to present some results in order to obtain some initial insight into the damping of the system and into the degree of nonproportionality. Figs. (7.38) show plots for the T_{11}, T_{21} and T_{12}, T_{22} elements used for estimating the generalised damping matrix. The use of equation (6.51) yielded

$$C_u = \begin{bmatrix} 25.22 & -17.50 \\ -17.62 & 41.57 \end{bmatrix}$$

and clearly the damping is nonproportional for this linear approximation and the matrix is very nearly symmetric.

All the above results were obtained for a force level of only 5 N peak in order for the data to be as linear as possible. However for higher force levels, the degree of nonlinearity would increase and as a result it would be expected that errors in these estimates would also increase. Fig. (7.39) shows the variation of the generalised mass estimates for both modes with the force level used to measure the FRF matrix. The variations of the other parameters showed similar behaviour. The change in the estimated parameters is not exceptionally large.

Clearly, because these estimates were obtained for real data, any errors in the results could also be due to experimental errors such as mismatch between channels, inaccuracies in transducer calibration factors, measurement noise etc.

7.7.2. Refinement of generalised mass matrix using sensitivity approach.

Having obtained an initial estimate for the generalised mass matrix, the sensitivity approach of chapter 6 was implemented to try and refine the estimate.

Data were acquired at five frequencies (30, 31.8, 33.5, 35 and 37 Hz) using a sinusoidal excitation applied at the first station on the structure. The excitation was essentially a single frequency "sweep". In order to minimise transients created by the sudden application of the force, the excitation signal was tailored by multiplying its time history with a cosine taper window. This process proved useful particularly in reducing the low frequency components in the measured input and response signals. The sweep of the excitation occupied only 30% of the acquired data window in order to minimise leakage. The single frequency sweep was used because its transient response covered the whole map with data points. Also the problem of linear dependence of u_1 and u_2 and also $\dot{u}_1$ and $\dot{u}_2$ was avoided. The maximum values of the force signals were 76.1, 71.1, 74.1, 69.6 and 88.3 N for the above five frequencies respectively. These high force levels ensured that the nonlinear behaviour of the structure was excited significantly.

The integration of the measured acceleration time histories was carried out in the frequency domain. Sample time histories for the acceleration and integrated velocity and displacement signals corresponding to the first response station and to the 31.8 Hz case are shown in Fig. (7.40).

The next step in the sensitivity approach was to estimate the modal restoring force vectors corresponding to the five frequencies using the estimated modal matrix and two initial estimates for the generalised mass matrix. The two initial mass estimates were selected such that they embraced the initial estimate obtained by the force appropriation method. Thus

$$\hat{M}1 = \begin{bmatrix} 3 & 0 \\ 0 & 3 \end{bmatrix} \qquad \text{and} \qquad \hat{M}2 = \begin{bmatrix} 10 & 0 \\ 0 & 10 \end{bmatrix}$$

The first mode restoring forces corresponding to the 30, 31.8 and 33.5 Hz tests were curve fitted using the "direct" curve fitting philosophy adopted in chapter 3. The author has found it much simpler and more effective to use this approach rather than the multi-step approach. The model used was nonparametric and included linear and nonlinear coupling terms between the 2 modes. The same form of model was also used to curve fit the second mode restoring forces for the 33.5, 35 and 37 Hz tests.

The resulting variations of the estimated linear stiffness with the assumed mass values for the two modes are shown in Fig. (7.41). The three possible intersections occurred at values of 6.75, 6.2 and 5.61 for the first mode and 10.21, 10.52 and 10.738 for the second mode. The average values yielded the following estimate for the generalised mass matrix

$$M_s = \begin{bmatrix} 6.19 & 0 \\ 0 & 10.49 \end{bmatrix}$$

Clearly the modal matrix does not need to be refined since the sensitivity approach will tend to compensate for any errors.

7.7.3. Identification of model.

For the identification phase of this two d.o.f. nonlinear system, the structure was excited at the first station using a tailored sinusoidal signal which swept through the range 30 to 37 Hz in 0.69 seconds. The sweep occupied 30% of the total length of the acquired data window which was 2.30 sec. Sample time histories for the input signal measured at the first station and the corresponding estimated velocity and displacement signals are shown in Fig. (7.42). A sample 2 dimensional force-state map for the first mode restoring force plotted with respect to the direct modal velocity and displacement signals, is shown in Fig. (7.43).

Clearly not much information can be deduced from such a plot.

Having obtained the restoring force vector, it remained to curve fit its individual elements in terms of the states. In section (3.3.2) it was shown that the direct approach required all possible linear and nonlinear coupling terms to be included in a single large model, given for a two d.o.f. system in equation (3.35). However, due to memory limitations, the smaller model given in table (7.2) was used.

The use of such a model yielded "goodness of fit" values around 0.99 for both modes indicating that the size of the model was adequate and that most of the necessary coupling terms were included. The identified parameters and their R.M.S. contributions to the total fits for both modes are shown also in table (7.2).

As for the single-d.o.f. case, the quality of the identified model can be examined by solving the equations numerically to obtain its physical response in the frequency or time domain, and comparing it with the response of the structure.

Fig. (7.44) shows a comparison between the FRF of the structure and of the identified model, both obtained using steady-state excitation applied at the first station for three force levels (5,10 and 15 N). For the second mode, it can be seen that the agreement between the structure and the model is reasonably good for both elements of the FRF matrix (H_{11} and H_{21}). It is possible that the damping terms may have been slightly overestimated. However, for the first mode, the agreement is rather poor due to errors in the identified terms contributing to the damping which seems to have been overestimated.

The fact that the goodness of fit figures were high indicates that the curve fit has provided a model which matches the measured maps well. It is most likely that the errors in the model, seen by the poor comparison of FRF results, are due to the effect of

Identified model:

$$\hat{h}_i(\underset{\sim}{u},\dot{\underset{\sim}{u}}) = a_1 + a_2u_i + a_3\dot{u}_i + a_4u_j + a_5\dot{u}_j + a_6u_i\dot{u}_i + a_7u_i^2 + a_8\dot{u}_i^2 +$$

$$a_9u_i^2\dot{u}_i + a_{10}u_i\dot{u}_i^2 + a_{11}u_i^3 + a_{12}u_i^2u_j + a_{13}u_iu_j^2 + a_{14}u_j^3 +$$

$$a_{15}\dot{u}_i\dot{u}_j + a_{16}u_i\dot{u}_j + a_{17}\dot{u}_i^2u_j + a_{18}\dot{u}_iu_j^2 + a_{19}\dot{u}_i^2\,\mathrm{sign}(\dot{u}_i)$$

	First mode (i=1, j=2) G = 0.989		Second mode (i=2, j=1) G = 0.994	
Term	Value	C^+ (%)	Value	C (%)
a_1	-0.090E0	0.03	0.320E0	0.06
a_2	0.246E6	87.15	0.507E6	94.08
a_3	0.376E2	2.72	0.324E2	1.29
a_4	-0.174E3	0.06	0.245E4	0.41
a_5	-0.285E2	2.42	-0.238E2	0.81
a_6	0.929E3	0.08	-0.816E3	0.03
a_7	0.680E6	0.50	-0.315E6	0.10
a_8	-0.747E1	0.23	0.888E1	0.13
a_9	0.372E7	0.60	0.211E7	0.12
a_{10}	0.217E4	0.07	-0.463E4	0.06
a_{11}	-0.812E9	1.44	-0.592E9	0.37
a_{12}	-0.971E9	0.70	-0.228E9	0.07
a_{13}	-0.147E10	0.97	-0.115E9	0.04
a_{14}	0.184E8	0.02	0.447E8	0.03
a_{15}	-0.184E2	0.30	-0.763E1	0.06
a_{16}	0.399E4	0.41	-0.330E4	0.15
a_{17}	-0.132E5	0.61	-0.465E5	0.80
a_{18}	-0.170E7	0.29	-0.631E7	0.69
a_{19}	0.419E2	1.31	0.421E2	0.63

+ R.M.S. contribution to total fit.

Table (7.2). Identified sweep model for the 2 d.o.f. configuration.

systematic phase errors in the measurements as discussed in chapter 5. Even though a dashpot is used, the damping in the two modes is actually still fairly low at the force levels used (typically 0.8% at 5 N) and the sensitivity to error is high for such lightly damped structure. In addition, the sensitivity of the force-state mapping to errors is likely to increase for multi-d.o.f. structures where more than two measurement channels are used.

It was decided to repeat the identification process using the different data obtained earlier using "sweeps" at discrete frequencies. The modal restoring forces for the bending and torsion modes were estimated using the 31.8 Hz and 35 Hz data respectively. The same nonparametric model given in table (7.2) was used in the direct curve fitting approach yielding the parameters shown in table (7.3). Fig. (7.45) shows a comparison between the FRFs of the structure and the identified model for the same three force levels. It can be seen that the agreement around the first mode for this model is much better than that for the model obtained from the conventional sweep but the nonlinear amplitude behaviour is still not represented accurately. Sample comparisons of structure and model response time histories to random excitations are shown in Fig. (7.46) for a low force level and in Fig. (7.47) for a high force level. The agreement for the lower force level is good but the discrepancies for the higher force level indicate errors in the nonlinear damping for this data. It is not obvious why the results from this single frequency "sweep" model should be better than the conventional sweep model.

Finally in order to show once again that the use of steady-state data is not ideal for multi-d.o.f. identification due to the linear dependence problem, other force-state maps were constructed using a series of "rings". The resulting models obtained for this version were very poor in that the R.M.S. contribution values of some of the nonlinear terms were higher than that of the linear

term and the damping term was negative!

	First mode (i=1, j=2) G = 0.989		Second mode (i=2, j=1) G = 0.993	
Term	Value	C^+ (%)	Value	C (%)
a_1	-0.110E0	0.02	-0.010E0	0.001
a_2	0.244E6	90.78	0.506E6	94.41
a_3	0.110E2	0.81	0.278E2	1.14
a_4	0.909E4	0.99	0.665E4	0.38
a_5	-0.182E2	0.40	-0.883E1	0.11
a_6	-0.941E3	0.10	-0.349E3	0.02
a_7	0.308E6	0.29	-0.264E6	0.12
a_8	-0.893E1	0.34	0.684E1	0.15
a_9	0.325E6	0.08	-0.103E7	0.14
a_{10}	0.574E4	0.29	-0.765E4	0.23
a_{11}	-0.152E9	0.44	-0.221E9	0.30
a_{12}	0.224E9	0.09	-0.892E9	0.17
a_{13}	-0.177E10	0.21	-0.261E10	0.17
a_{14}	-0.117E11	0.96	-0.563E10	0.26
a_{15}	-0.120E0	0.00	-0.214E2	0.08
a_{16}	-0.222E4	0.12	0.513E3	0.01
a_{17}	-0.222E5	0.71	0.425E4	0.08
a_{18}	0.232E8	1.14	-0.170E8	0.48
a_{19}	0.557E2	2.15	0.717E2	1.66

+ R.M.S. contribution to total fit.

Table (7.3). Identified single-frequency model for the 2 d.o.f. configuration.

Bearing in mind that the instrumentation used for data acquisition was far from perfect and that the structure was fairly lightly damped, some of the two d.o.f. identification results are quite reasonable. Identification at higher force levels might have helped improve the results by increasing the effective damping , introduced by the dashpot, of the data but any future work needs to use better quality equipment.

7.8. Conclusion.

In this chapter, some experimental results from the application of the force-state mapping approach to a T-beam structure have been presented, both for well separated and close mode configurations.

The model obtained from the single-d.o.f. identification of the bending mode was able to represent the nonlinear response of the structure very accurately. The model for the torsion mode was less accurate, because the method is more sensitive to error when the damping is lower.

The two d.o.f. identification provided some reasonable models but damping was not high and it appeared that the results were sensitive to instrumentation error. It is expected that better models could be obtained if better instrumentation was used. Particular attention should be paid to the use of more advanced hardware having channels with similar amplitude and phase characteristics and with a simultaneous sample and hold in order to minimise phase errors. Careful absolute calibration of transducers would also be necessary. Further experimental work using structures with controlled and known nonlinearities and even closer modes, is necessary.

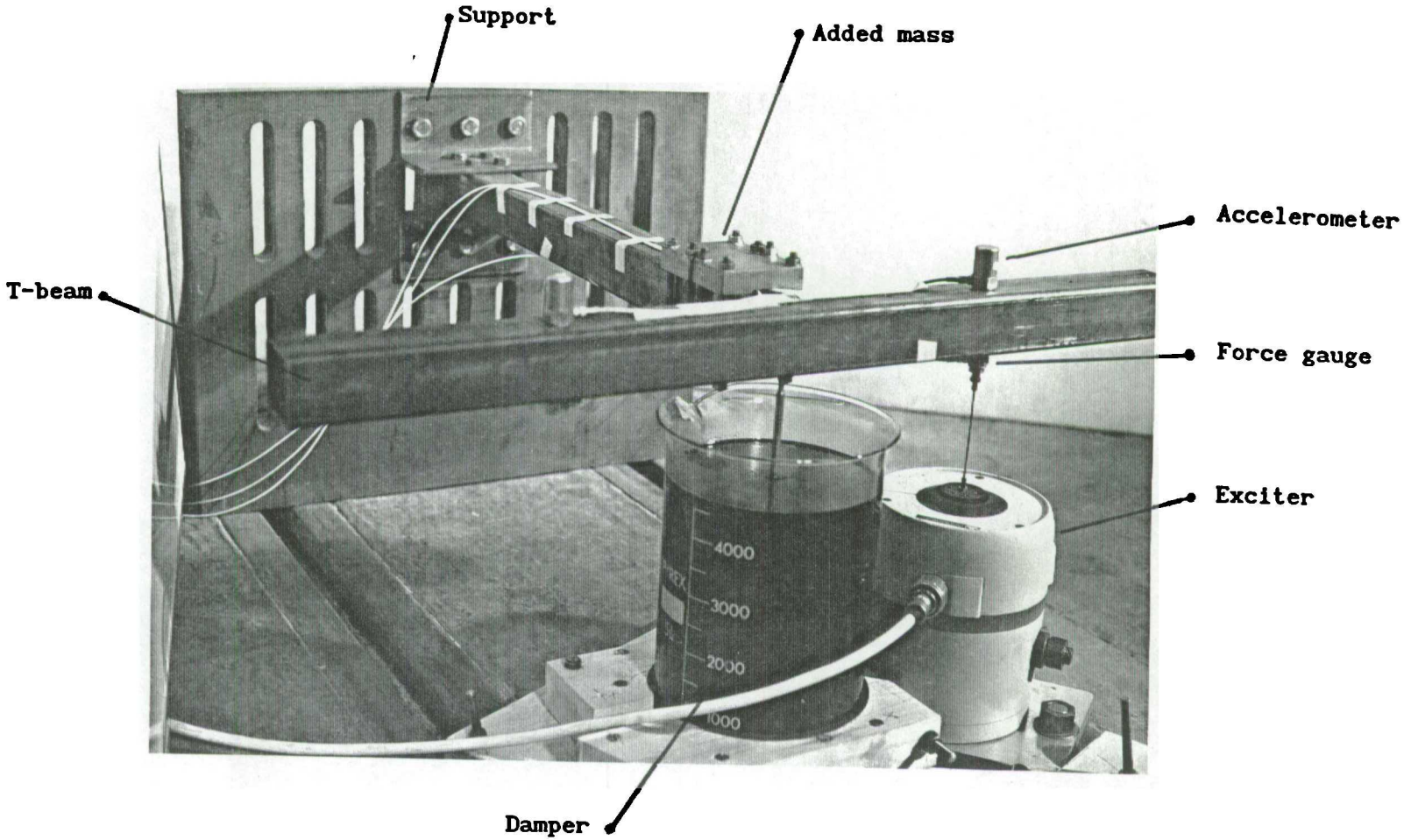

Figure 7.1. Photograph of experimental T-beam configuration.

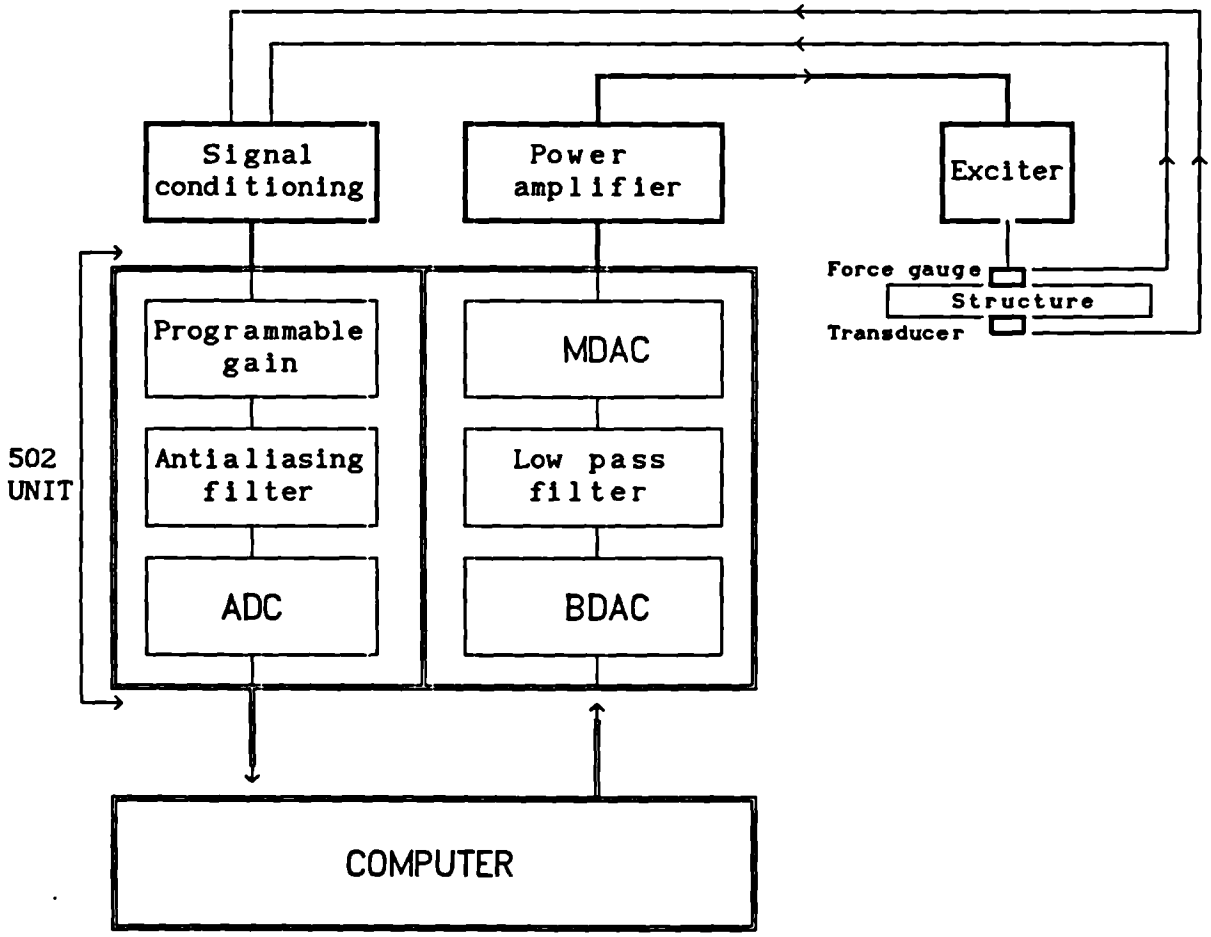

Figure 7.2. Block diagram of experimental set-up

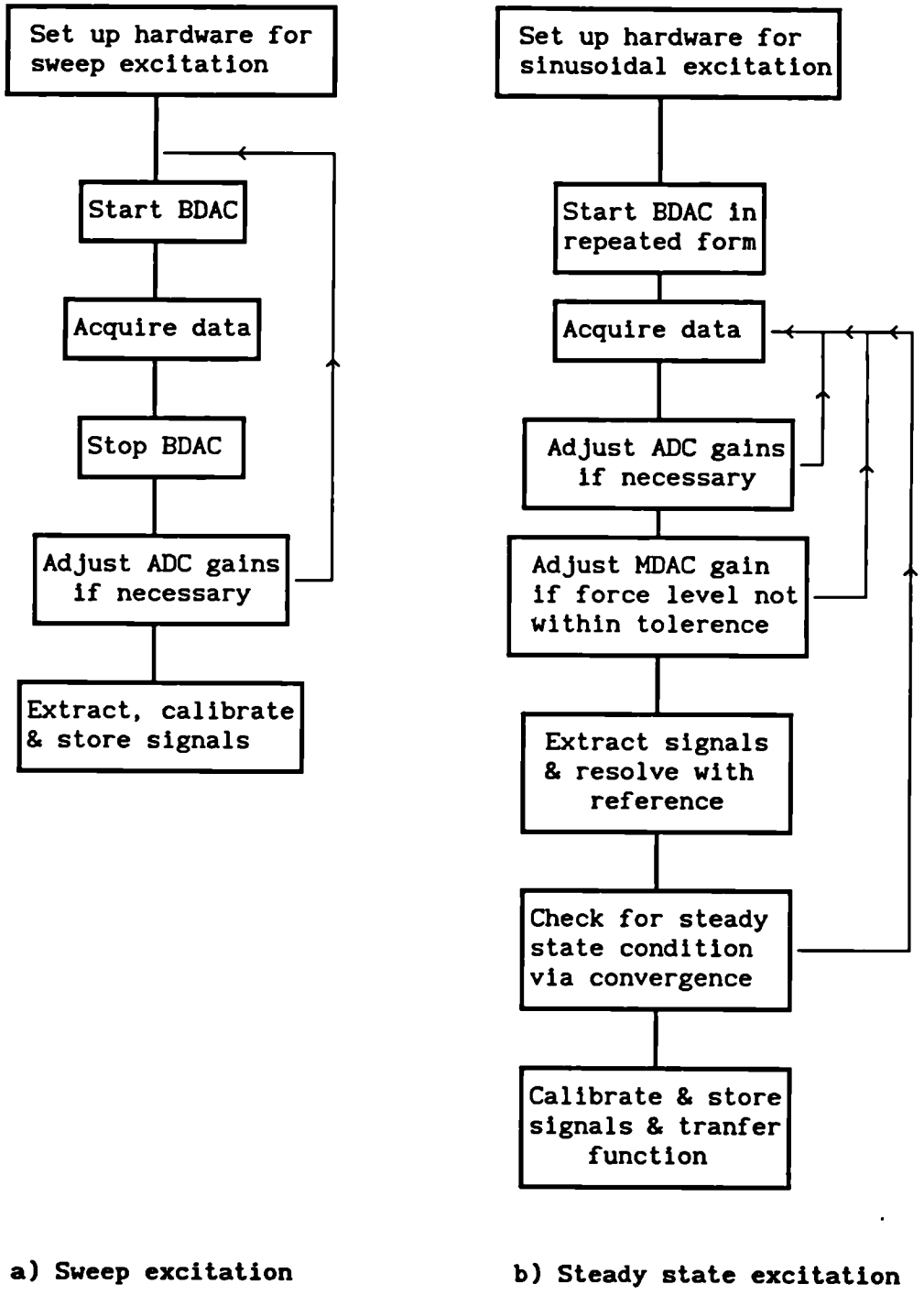

Figure 7.3. Flowchart of programme used for carrying out test.

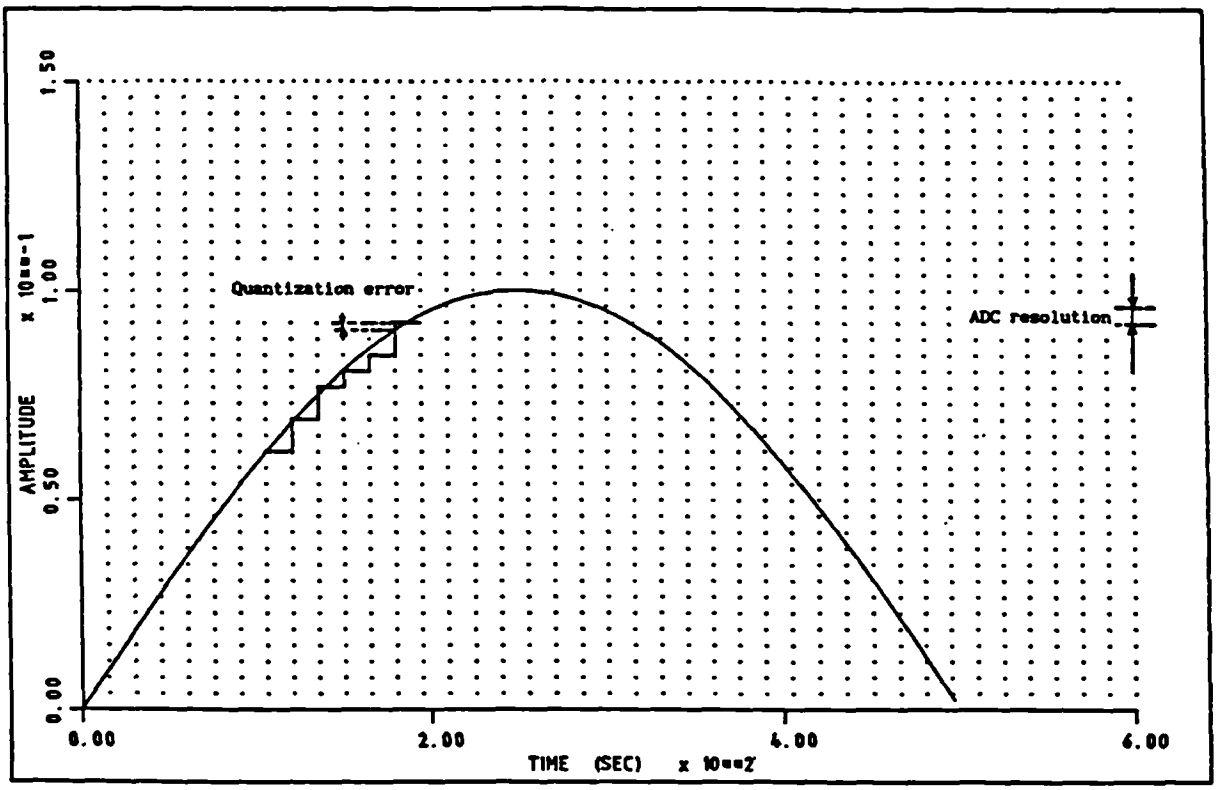

Figure 7.4. Illustration of quantization error problem.

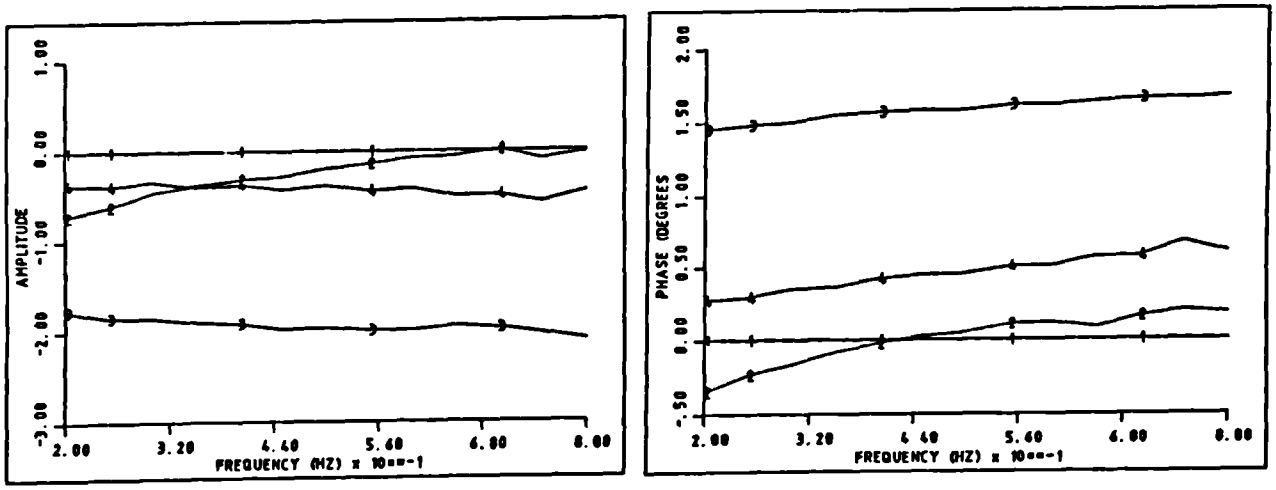

Figure 7.5. Amplitude and phase mismatch errors between channels for the 32 points/cycle case.

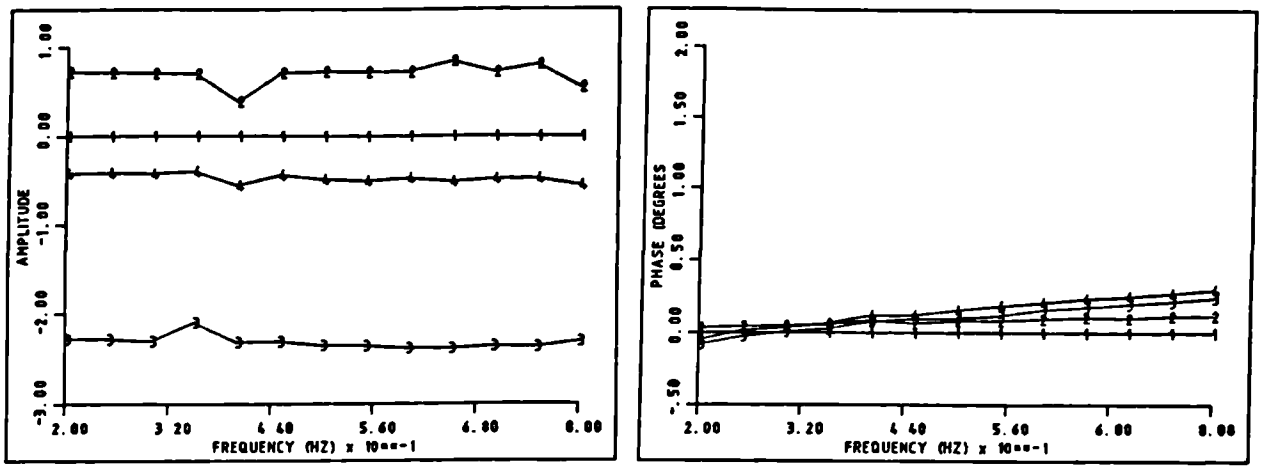

Figure 7.6. Amplitude and phase mismatch errors between channels for the 1024 points/cycle case.

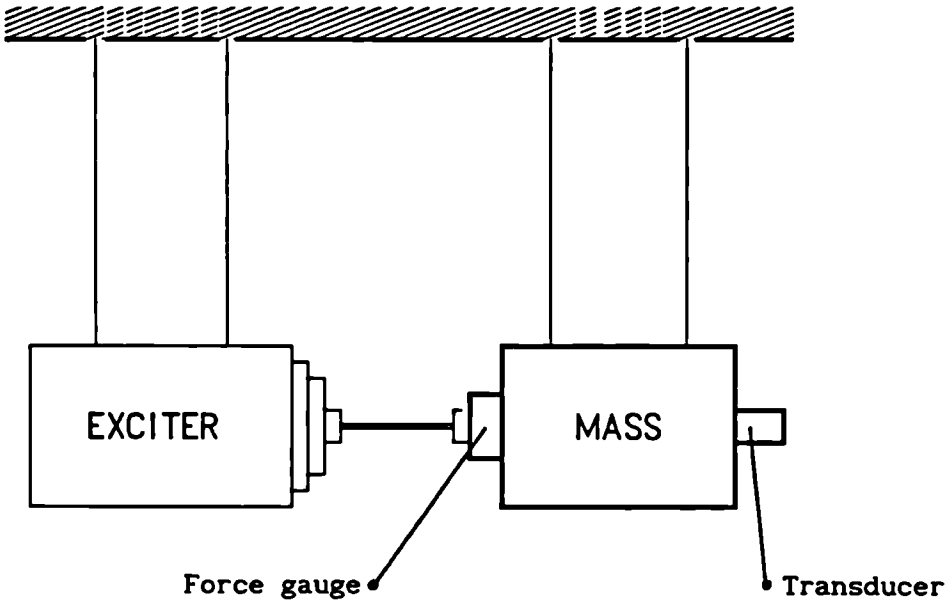

Figure 7.7. Transducer calibration set-up.

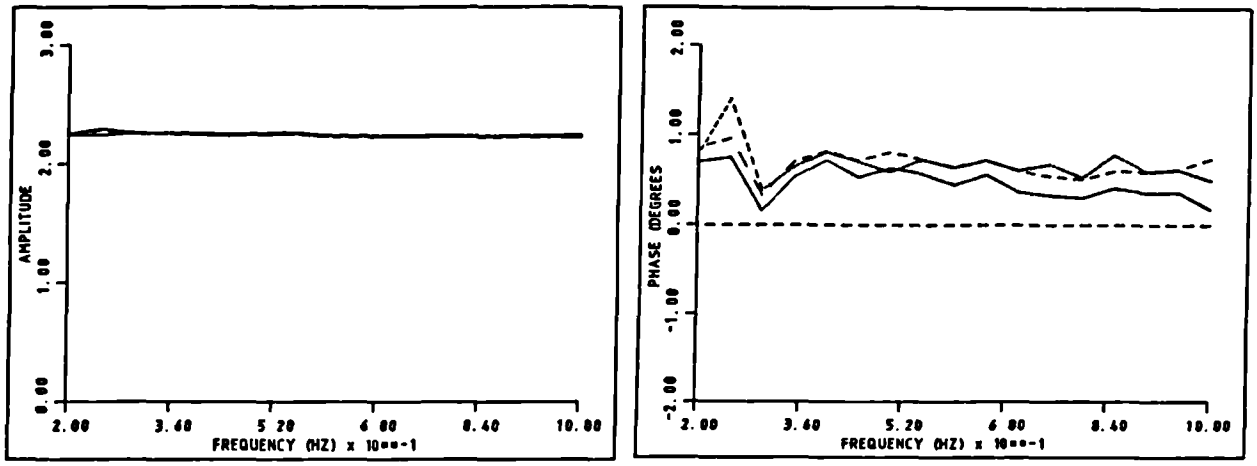

Figure 7.8. Apparent mass and phase plots measured at 3 force levels.

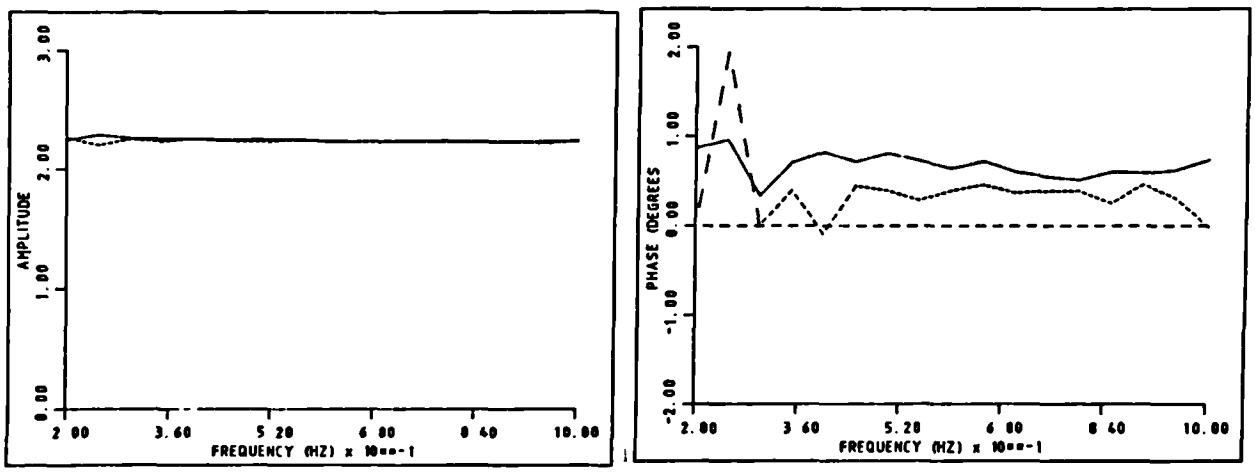

Figure 7.9. Apparent mass and phase plots for the 2 accelerometers used in the test.

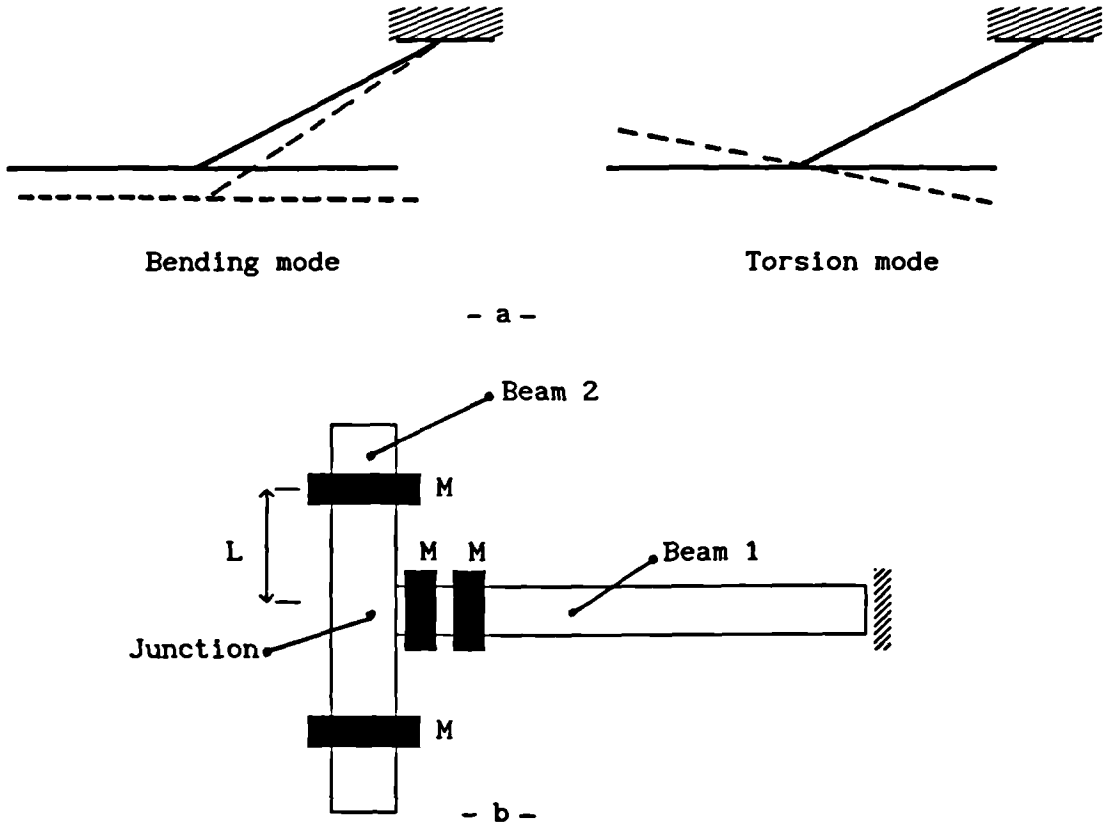

Figure 7.10. Sketch of the T-beam and its primary modes.

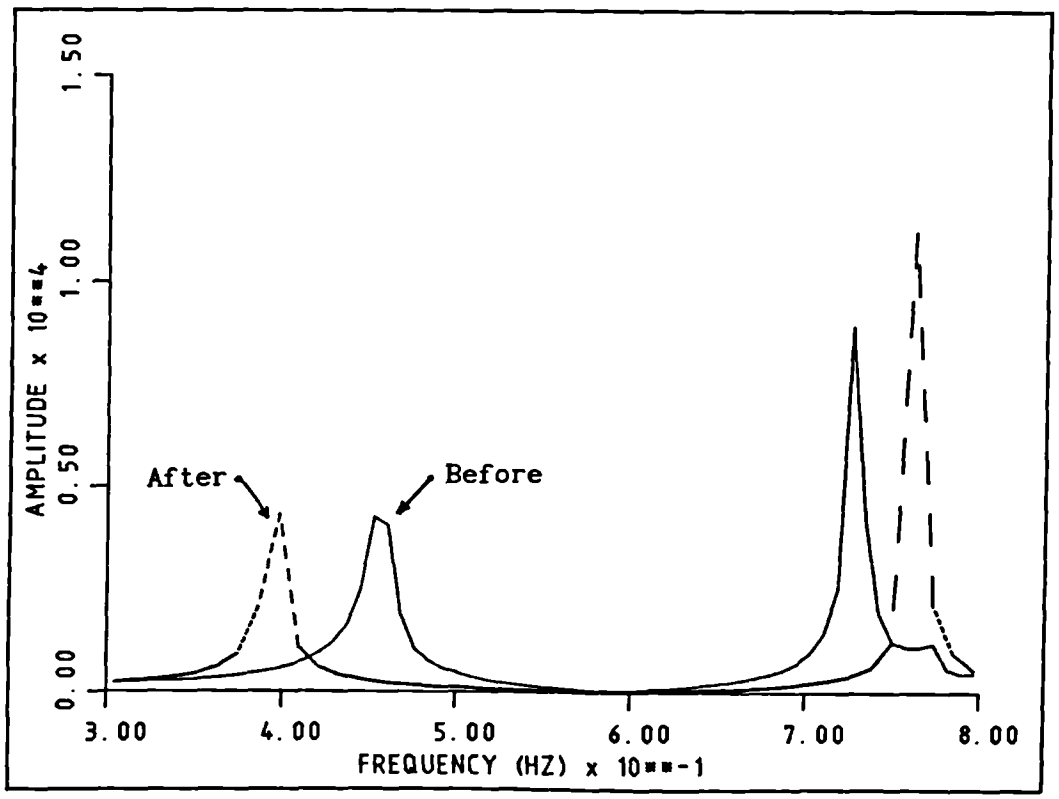

Figure 7.11. FRF of T-beam before and after adding a lumped mass at its junction.

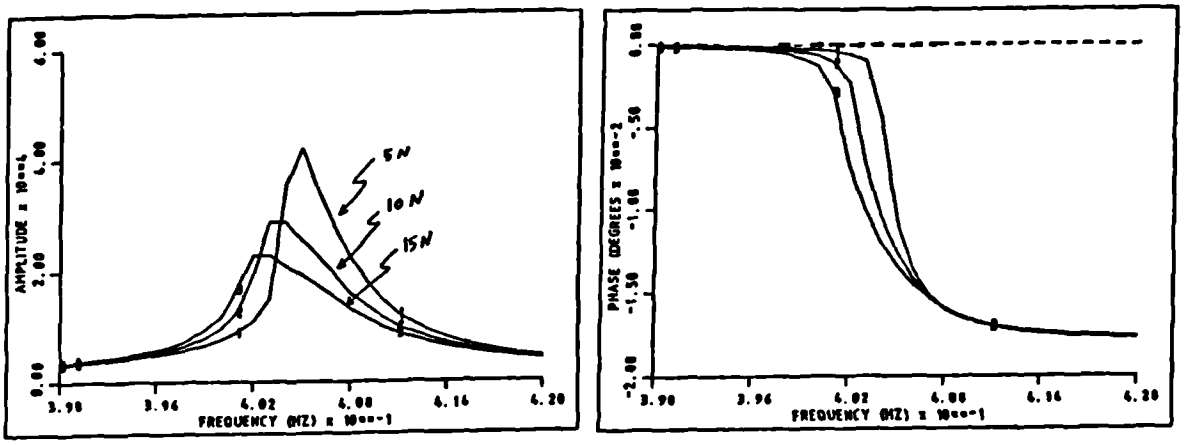

Figure 7.12. A sample FRF of bending mode at 3 force levels.

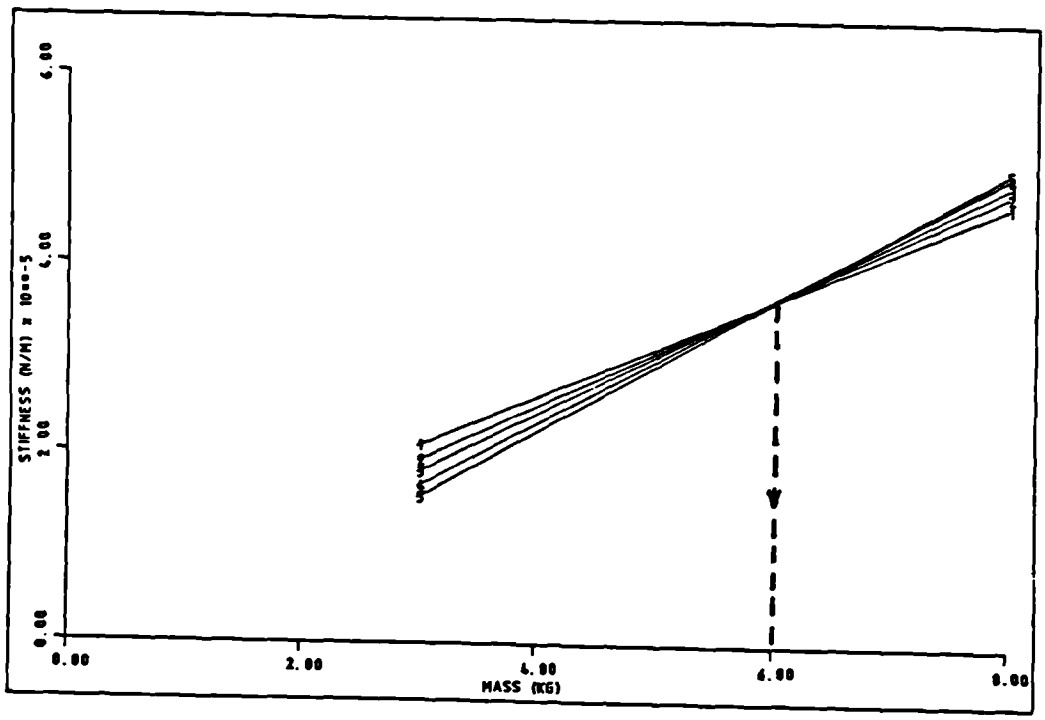

Figure 7.13. Mass estimation plot for the bending mode obtained using the sensitivity approach.

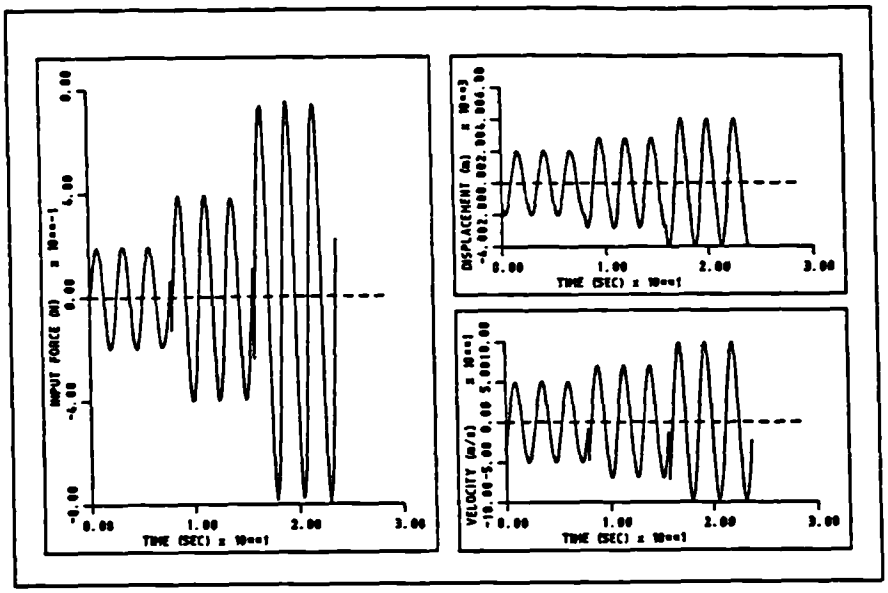

Figure 7.14. Sample portions of steady-state time histories at 3 force levels.

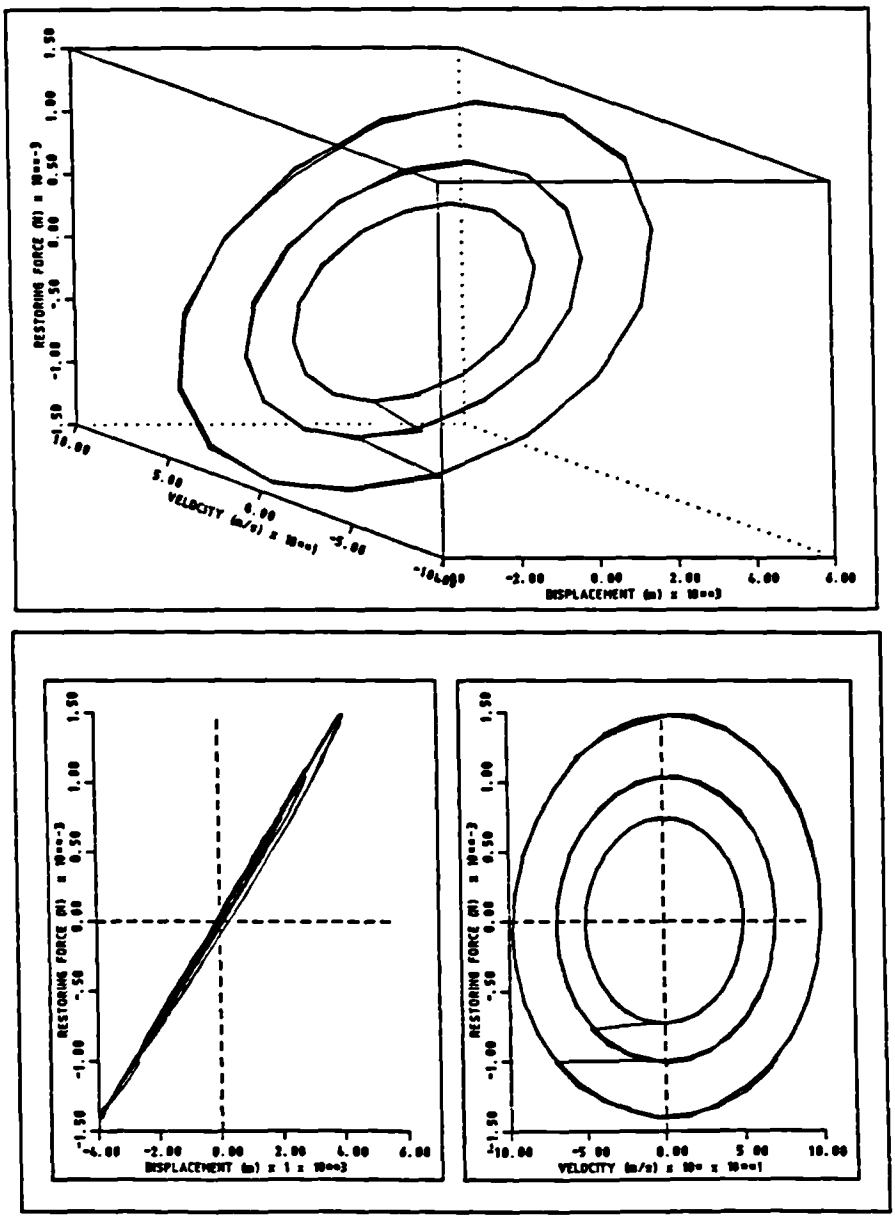

Figure 7.15. Force-state map generated at 3 force levels using steady-state excitation.

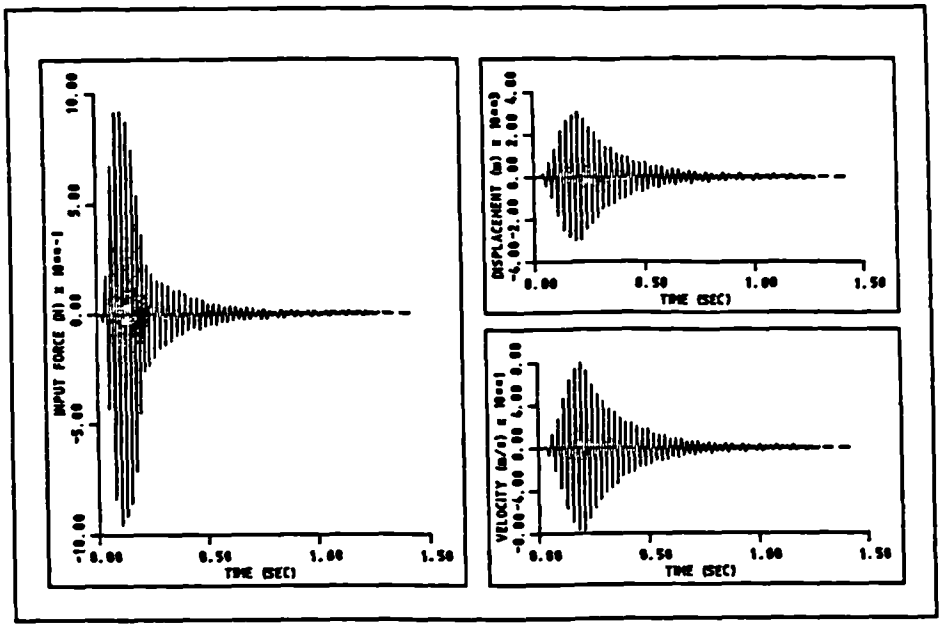

Figure 7.16. Sample measured and integrated time histories for sweep excitation.

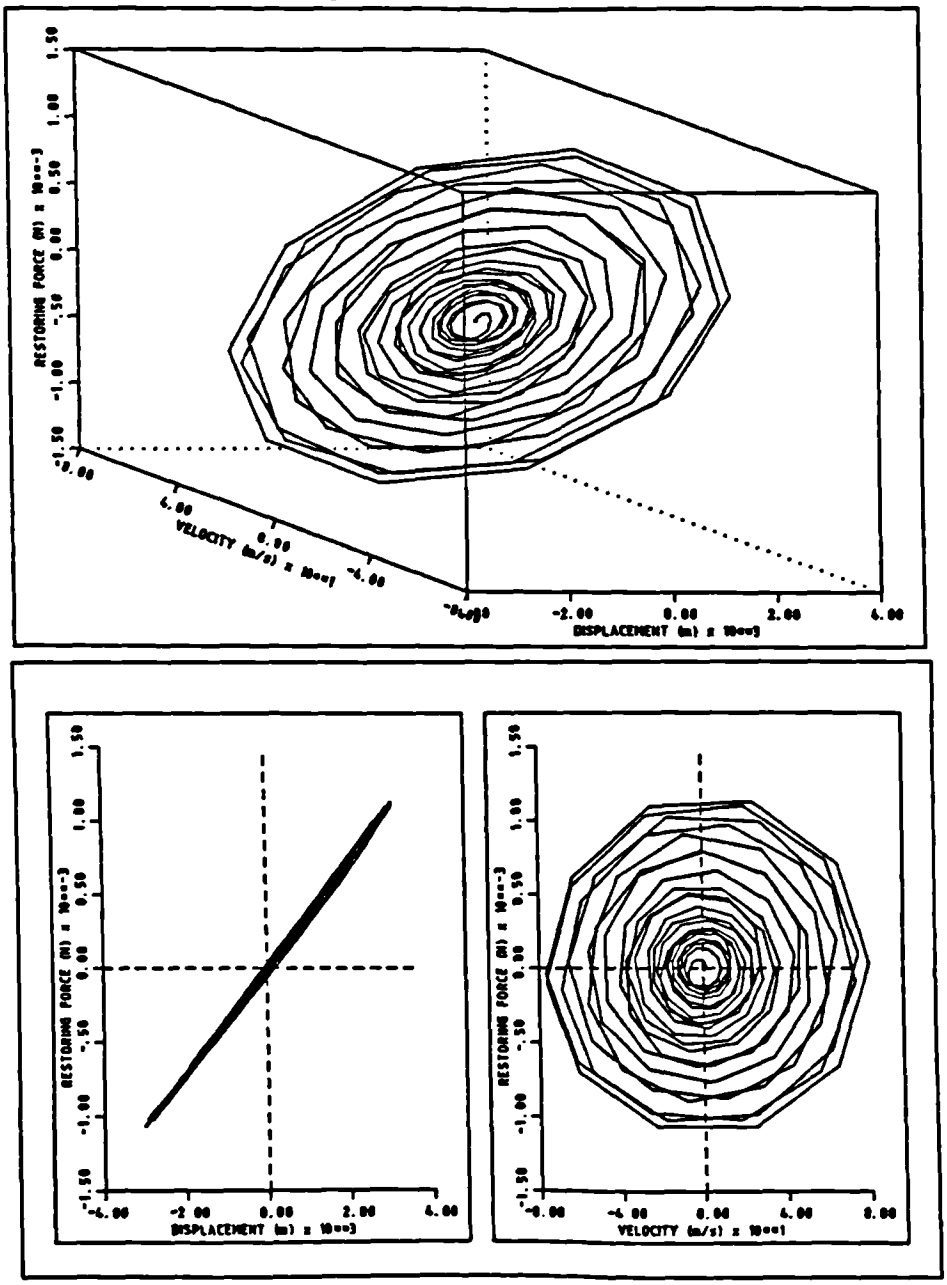

Figure 7.17. Force-state map generated using sweep excitation.

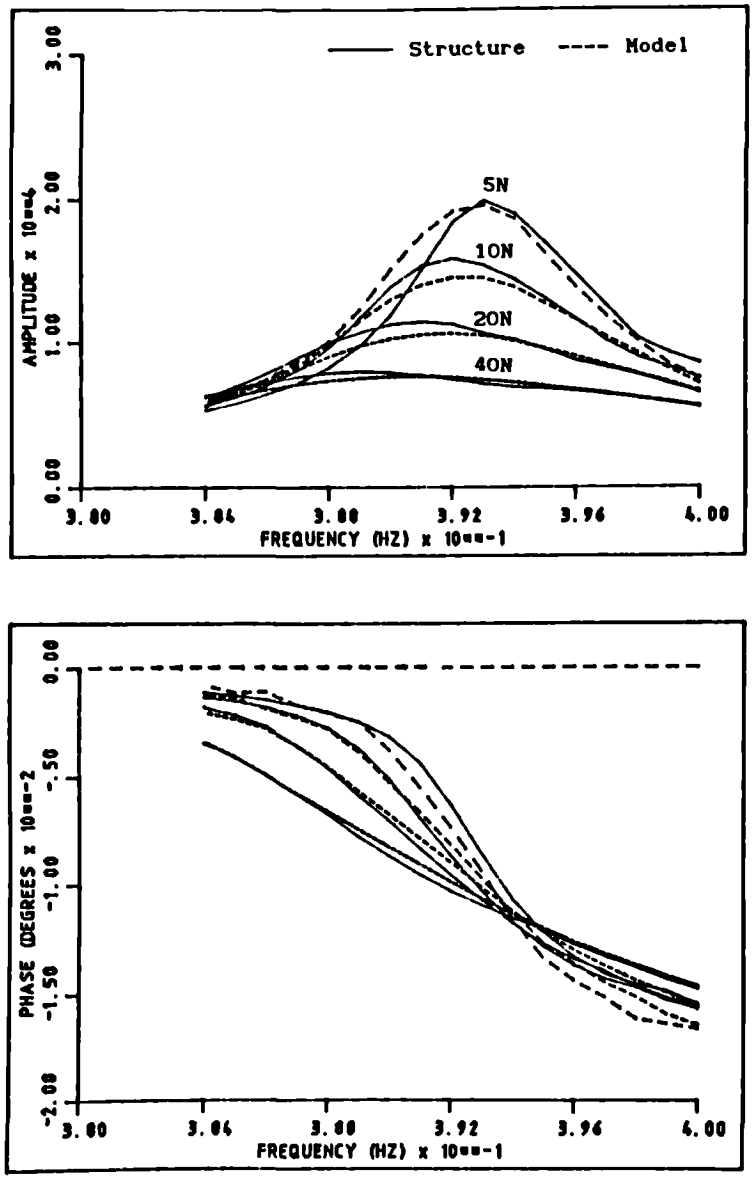

Figure 7.18. Comparison between FRFs of structure and identified steady-state model at 4 force levels.

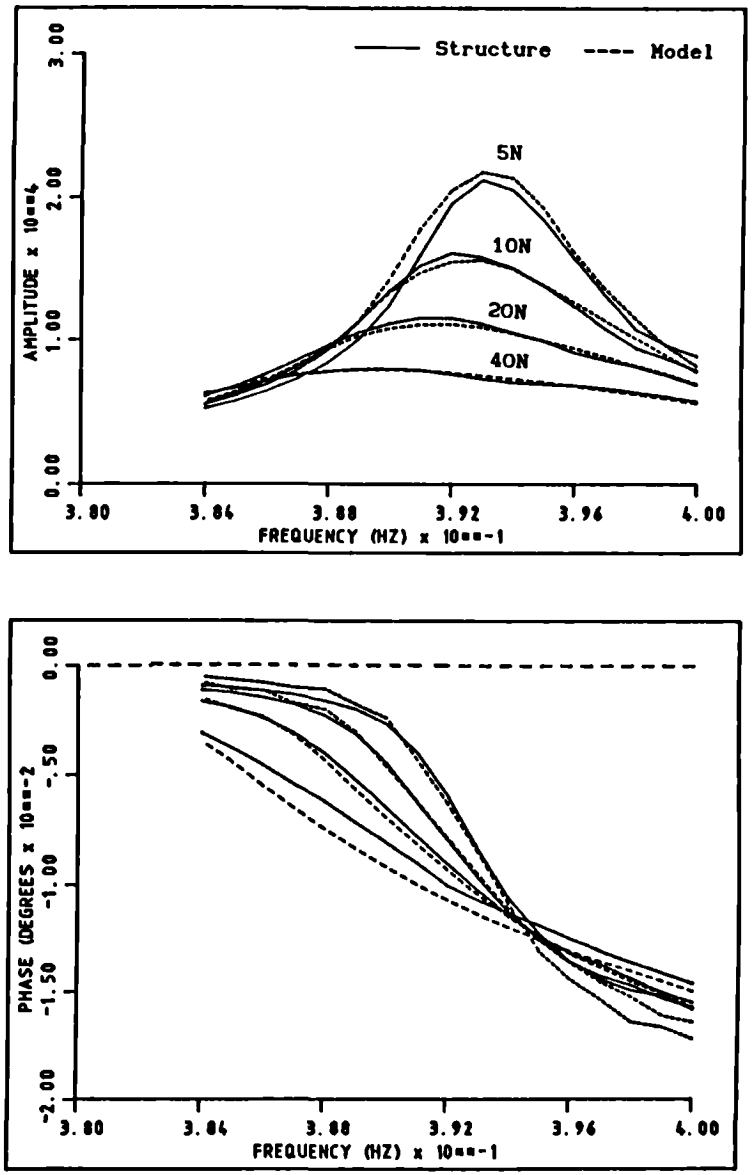

Figure 7.19. Comparison between FRFs of structure and identified sweep model at 4 force levels.

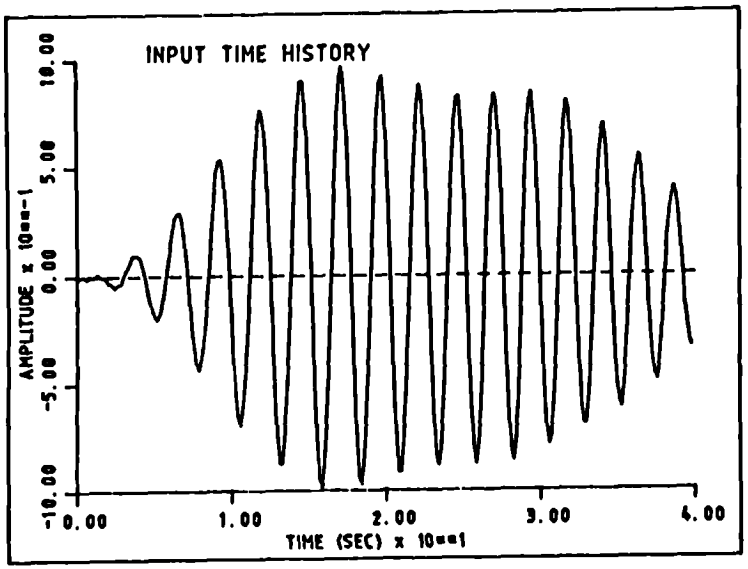

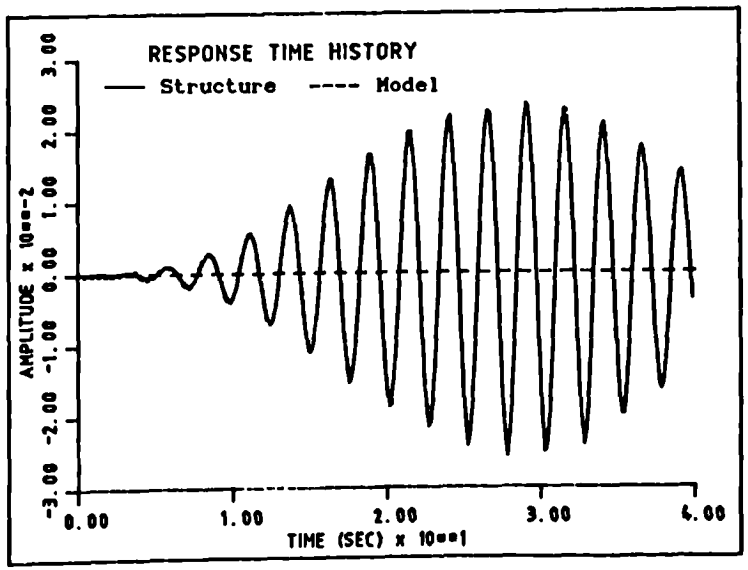

Figure 7.20. Comparison between responses of structure and steady-state model for sweep excitation.

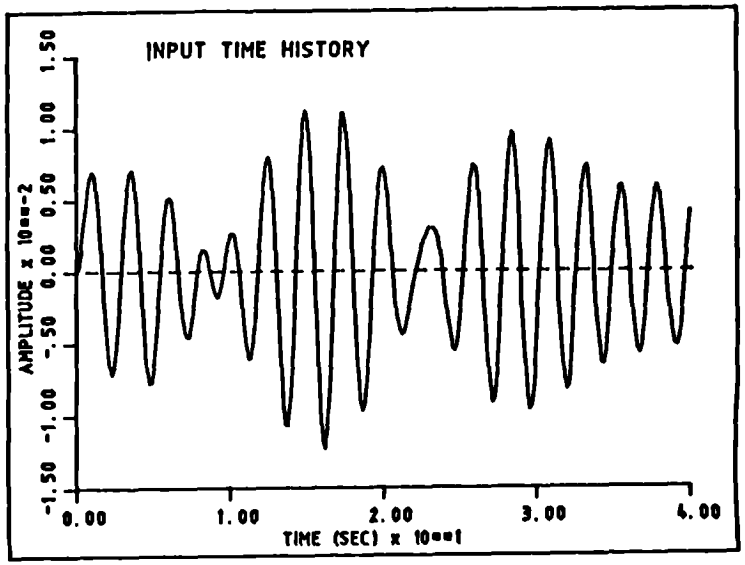

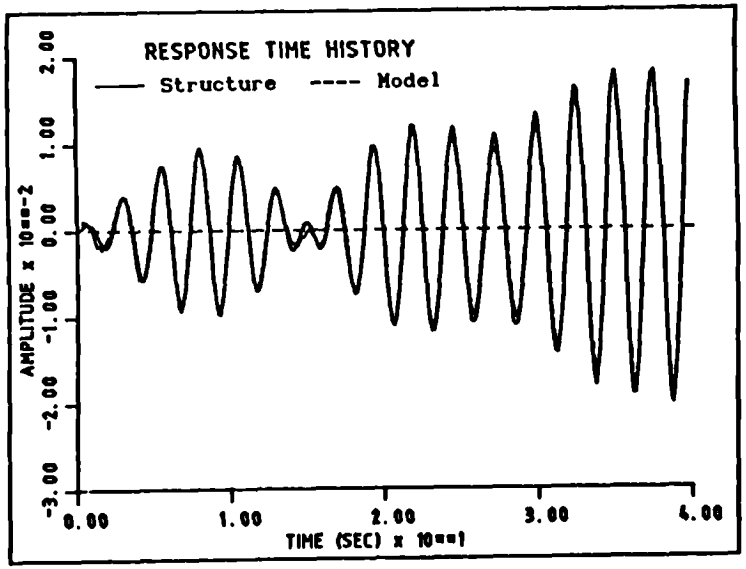

Figure 7.21. Comparison between responses of structure and steady- state model for random excitation.

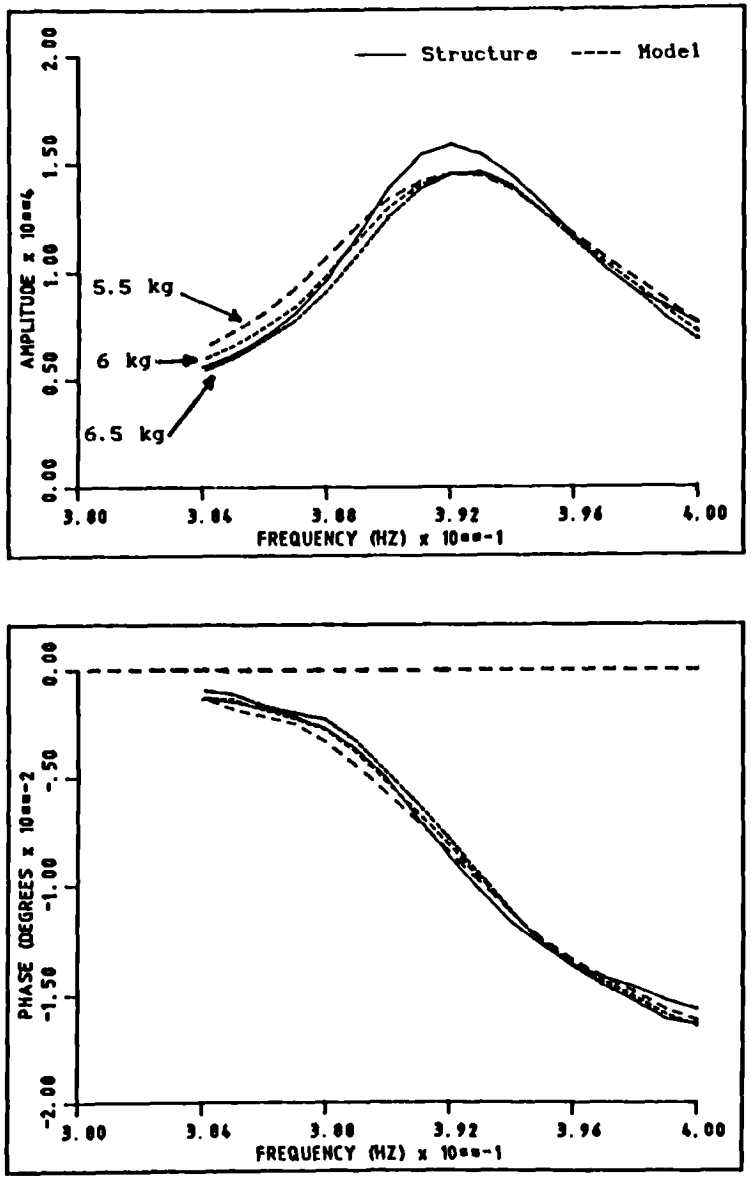

Figure 7.22. Comparison between FRFs generated from models using different mass values.

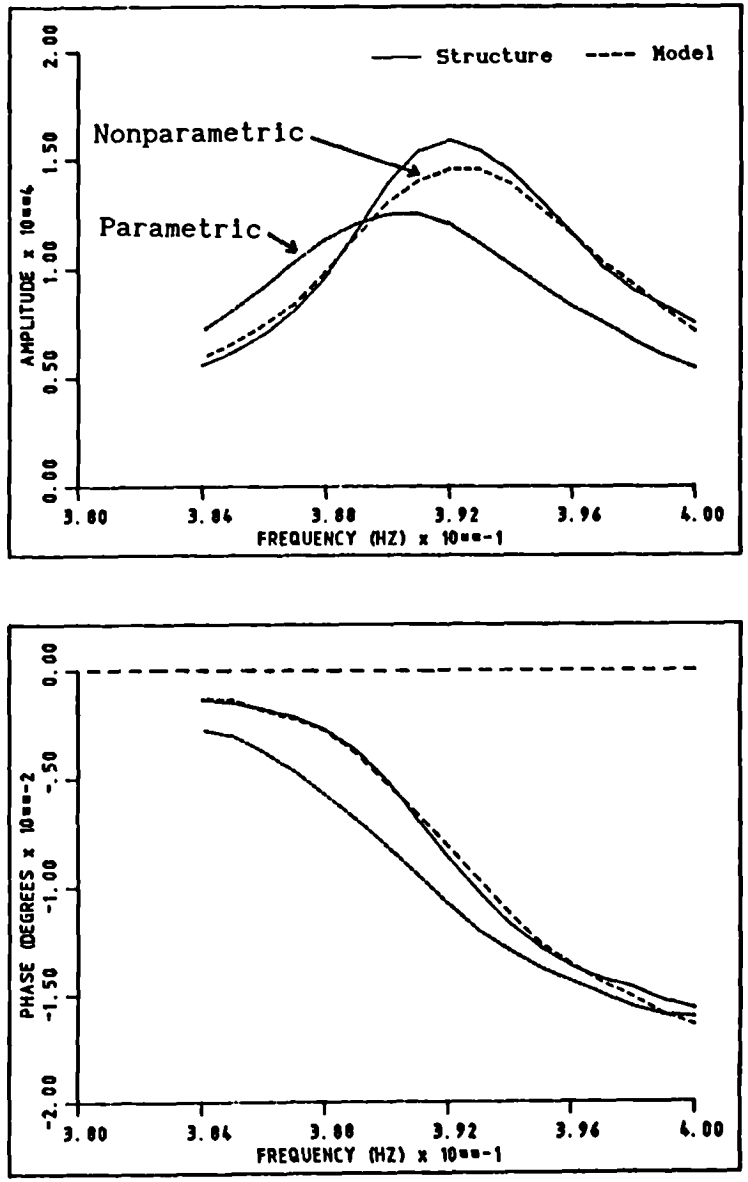

Figure 7.23. Comparison between FRFs generated from models using parametric and nonparametric approaches.

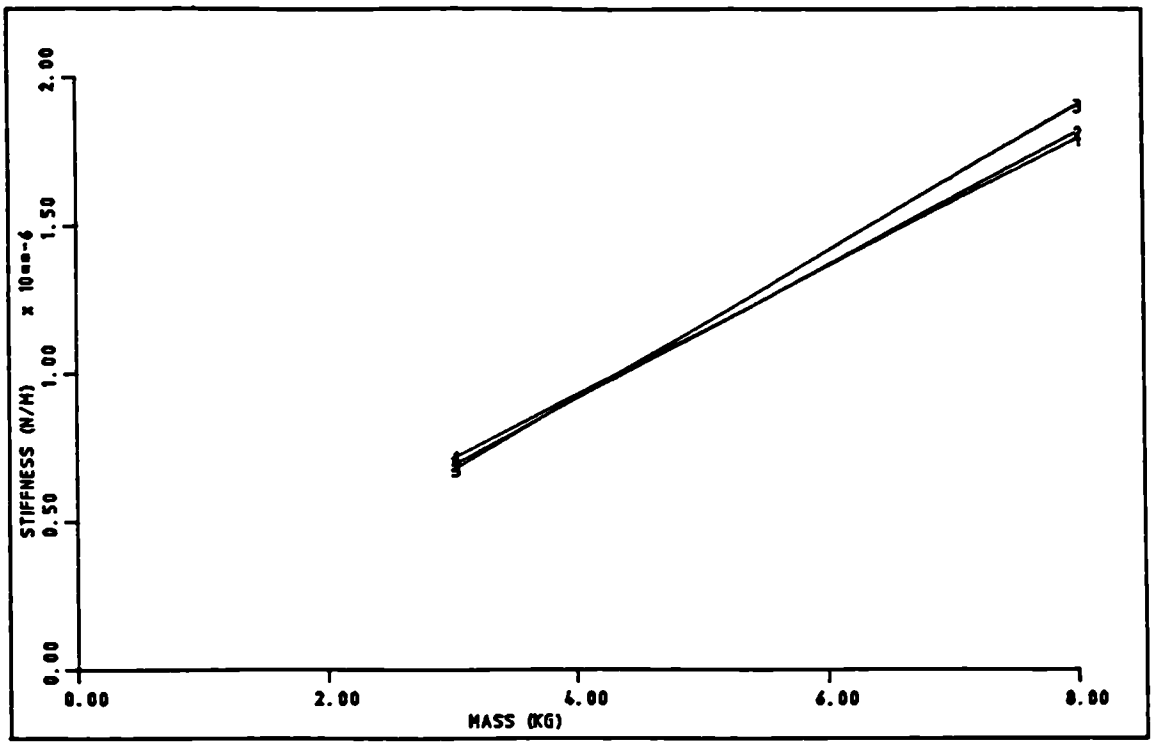

Figure 7.24. Mass estimation plot for torsion mode.

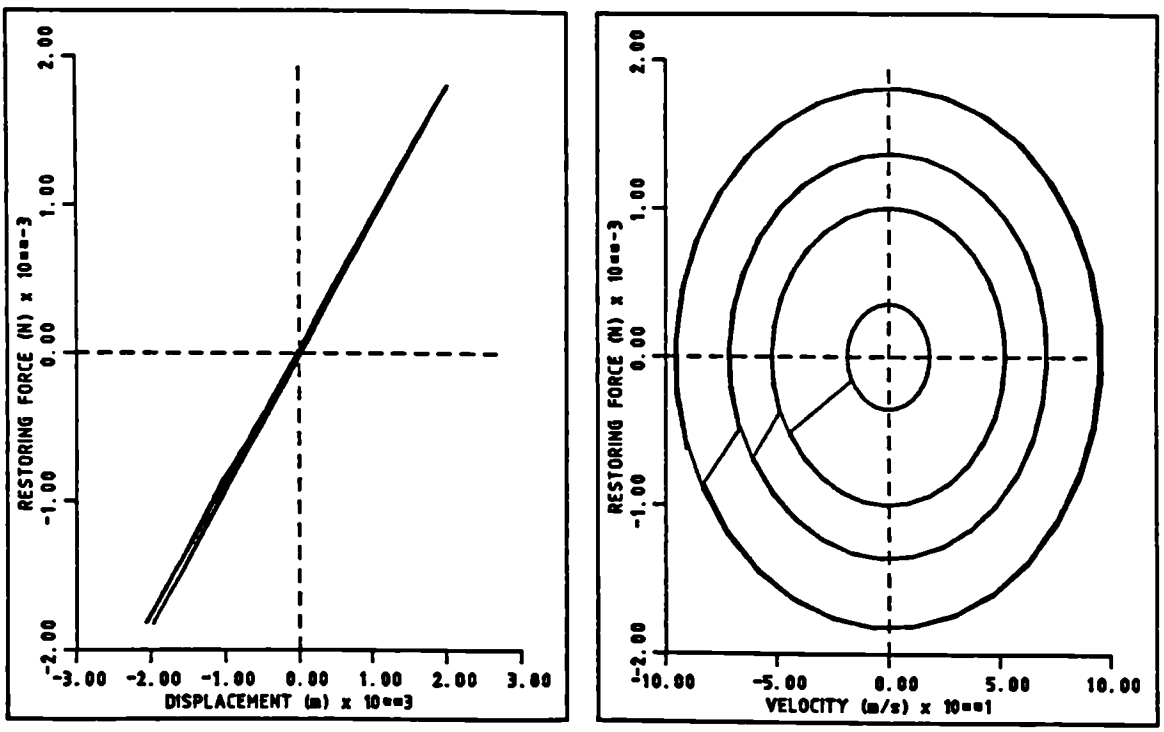

Figure 7.25. Two dimensional force-state map generated at 4 force levels for torsion mode.

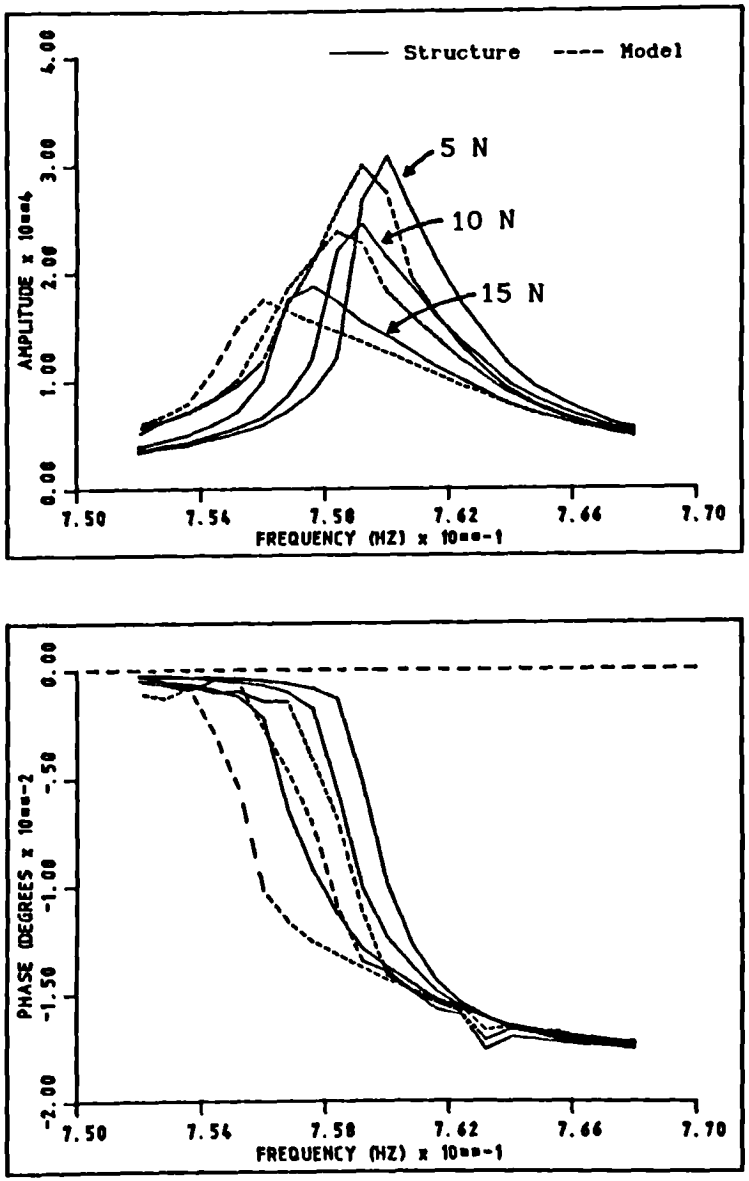

Figure 7.26. Comparison between FRFs of structure and model for torsion mode.

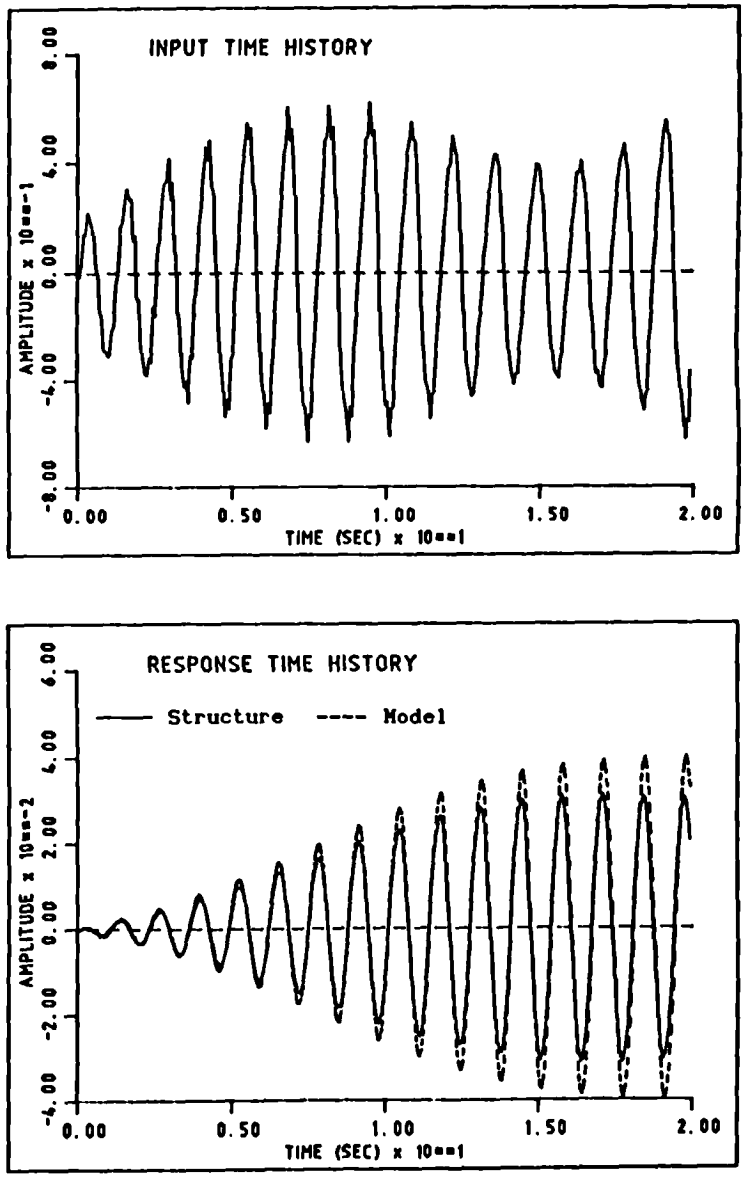

Figure 7.27. Comparison between responses of structure and model for random excitation.

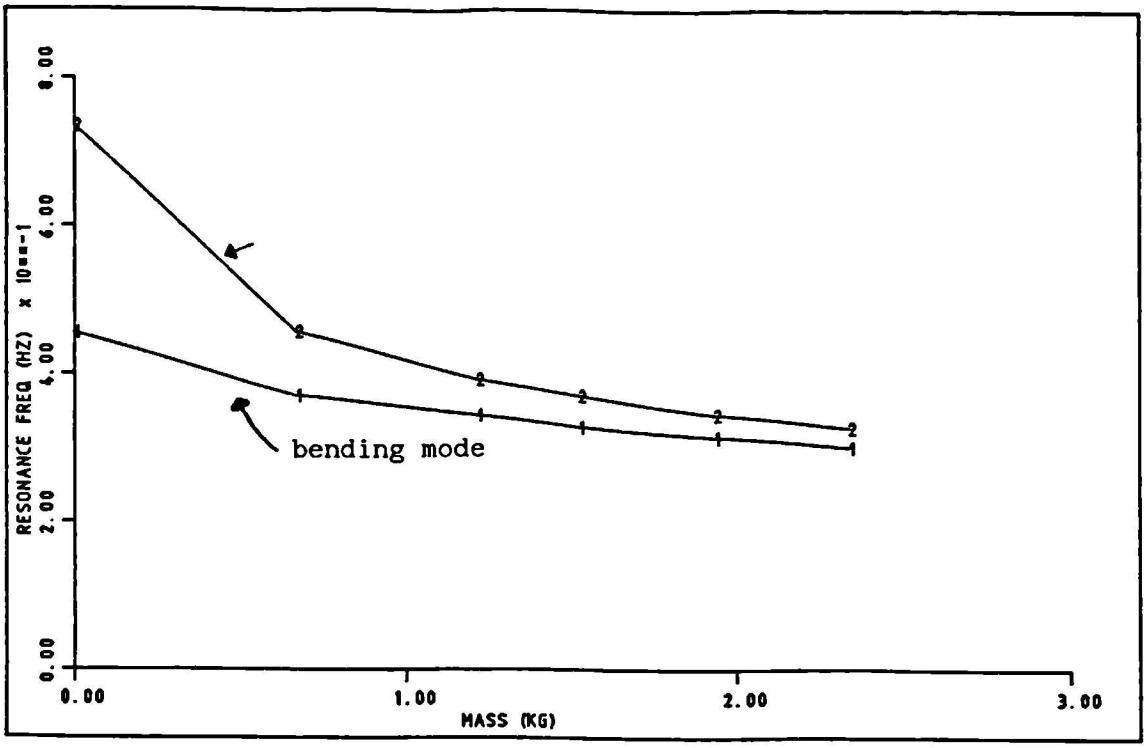

Figure 7.28. Variation of measured resonance frequencies with added mass for the 2 modes.

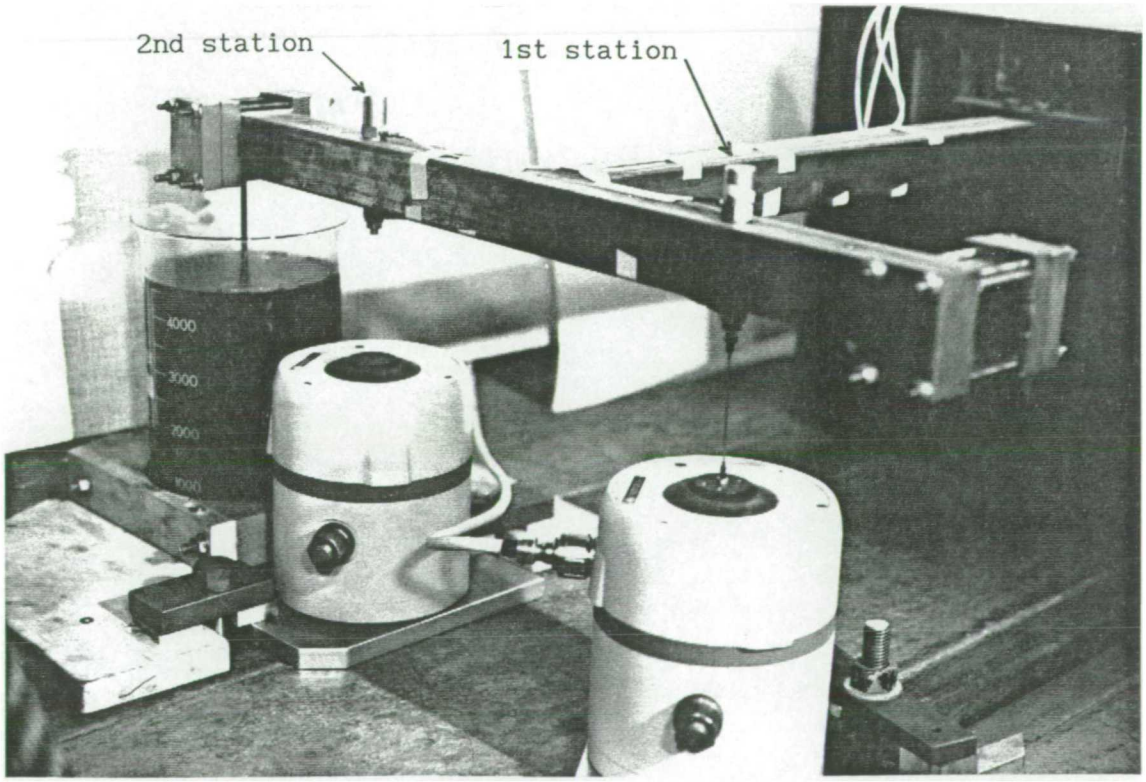

Figure 7.29. Photograph of experimental configuration for the 2 close mode case.

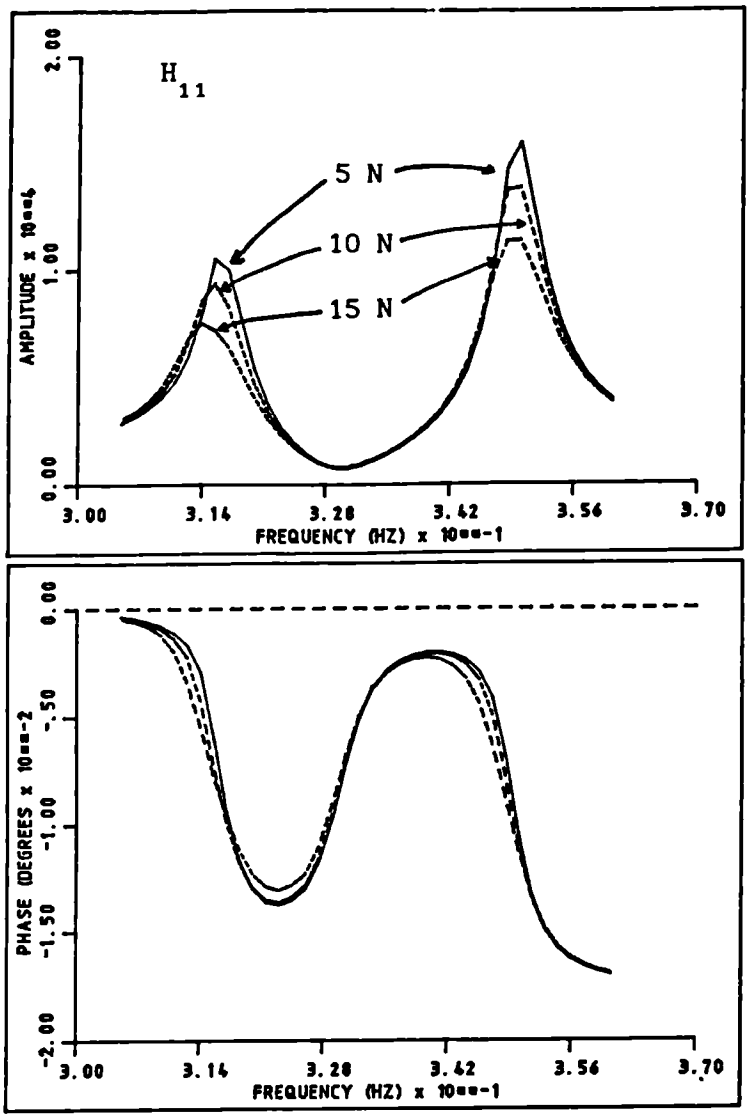

Figure 7.30. A sample FRF of 2 close mode configuration at 3 force levels.

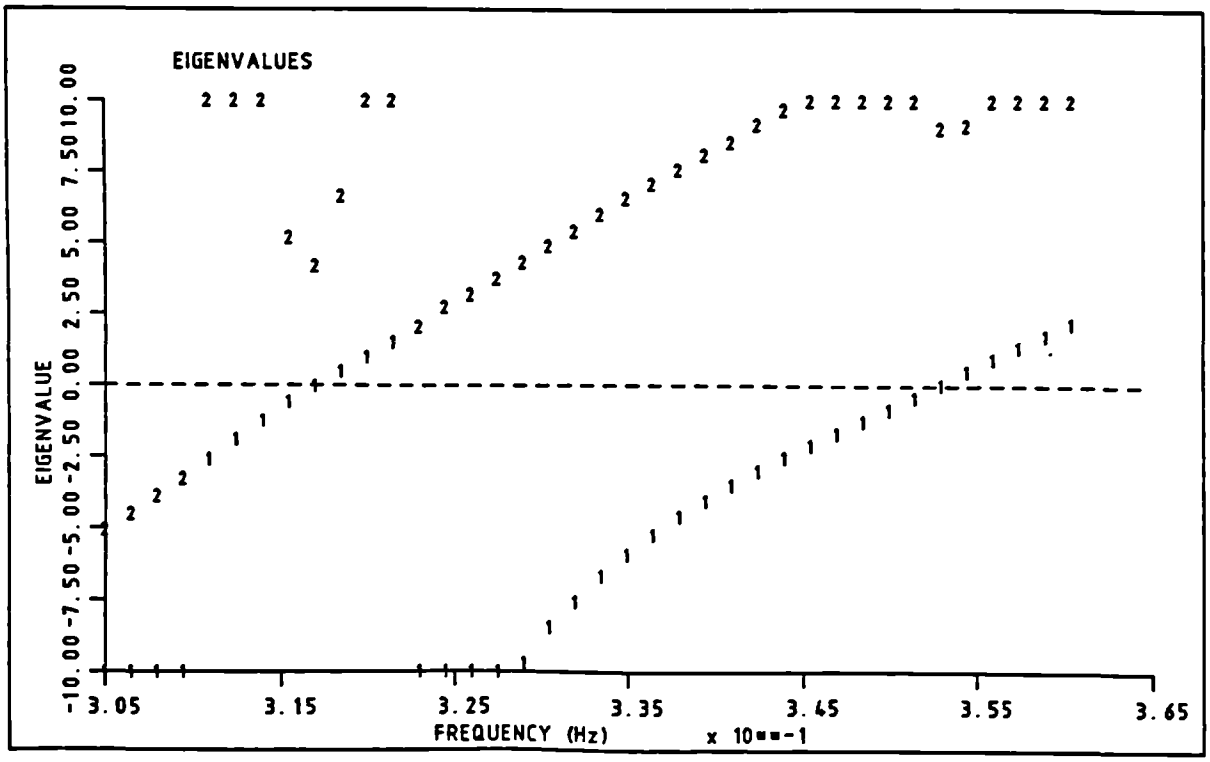

Figure 7.31. Variation of Trail Nash eigenvalues with frequency for the 2 d.o.f. case.

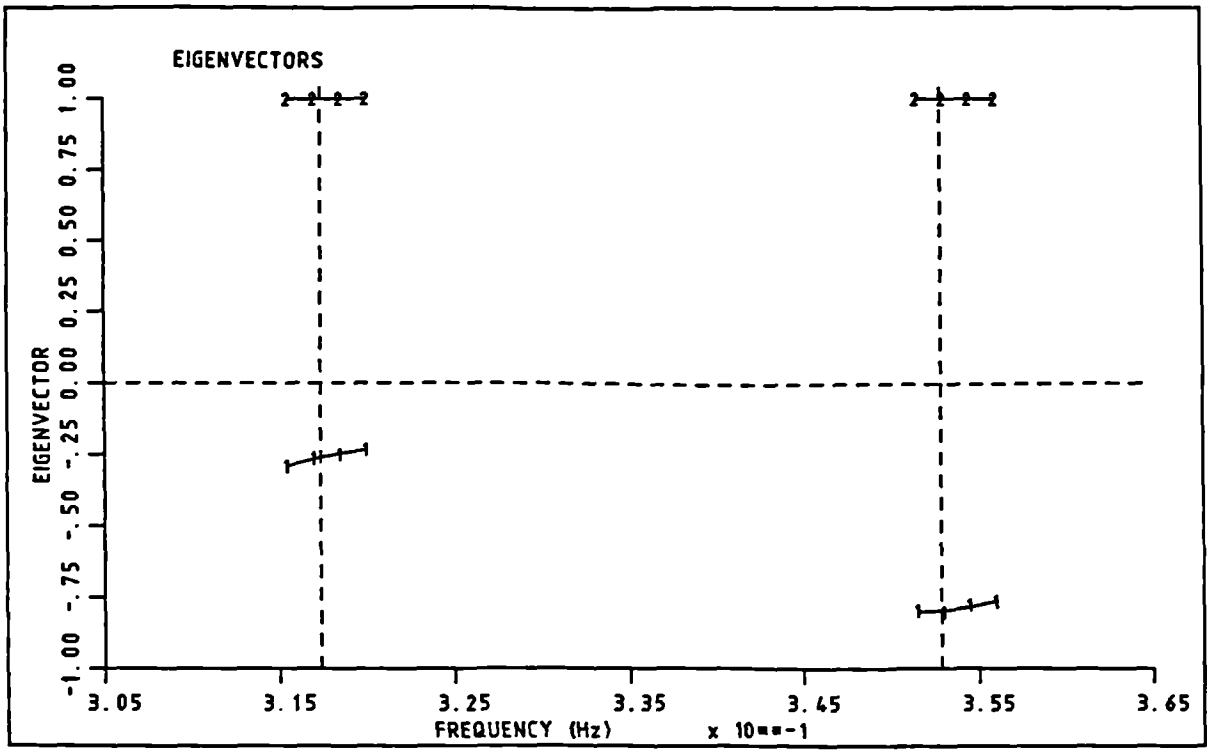

Figure 7.32. Variation of normalised eigenvector elements with frequency for the 2 d.o.f. case.

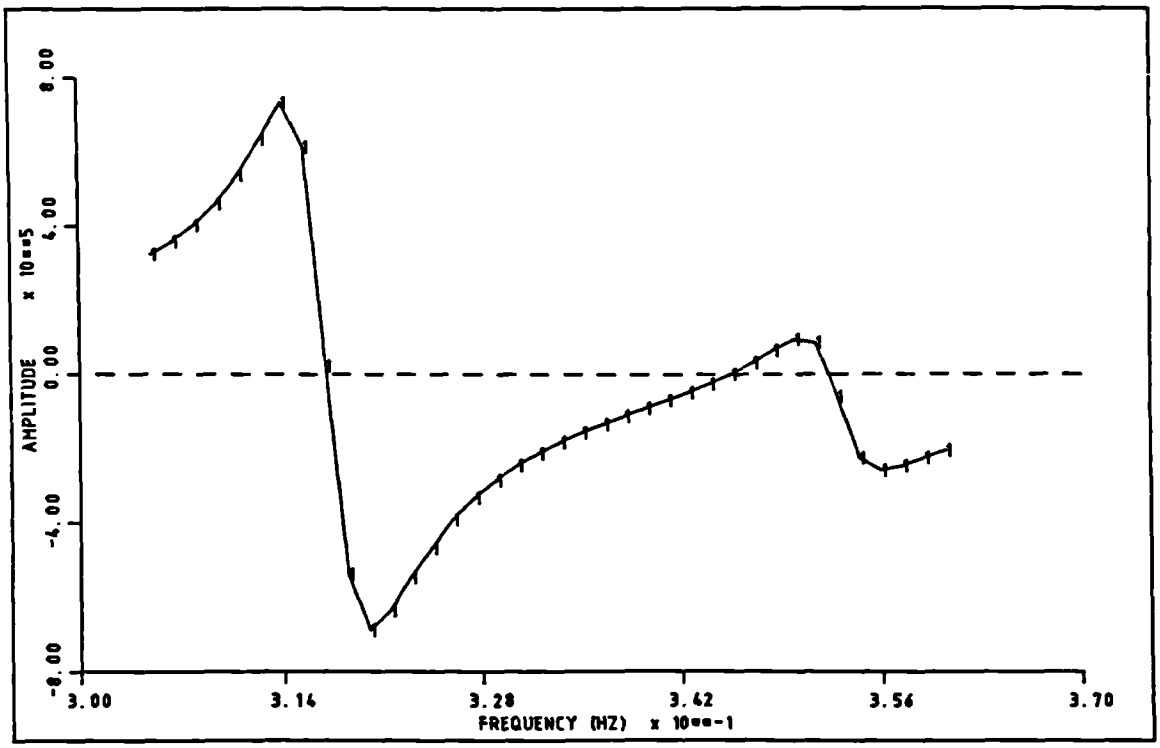

Figure 7.33. Variation of the S_{11} function with frequency for the primary bending mode.

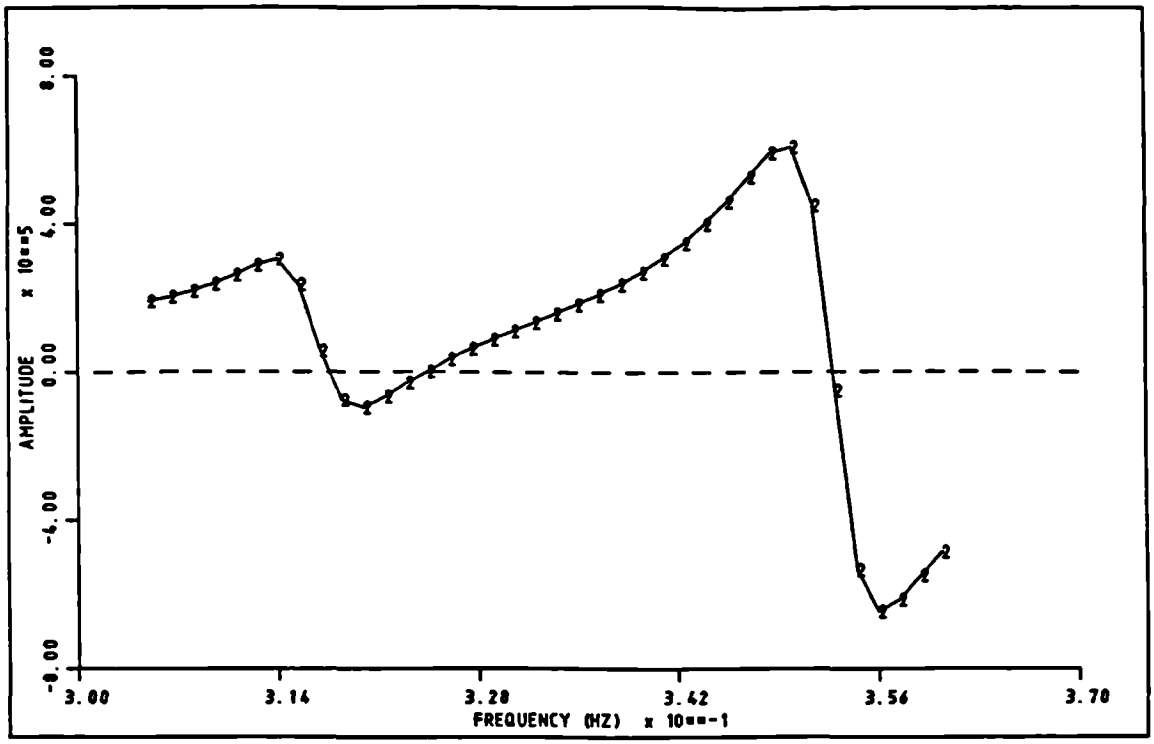

Figure 7.34. Variation of S_{22} function with frequency for the torsion mode.

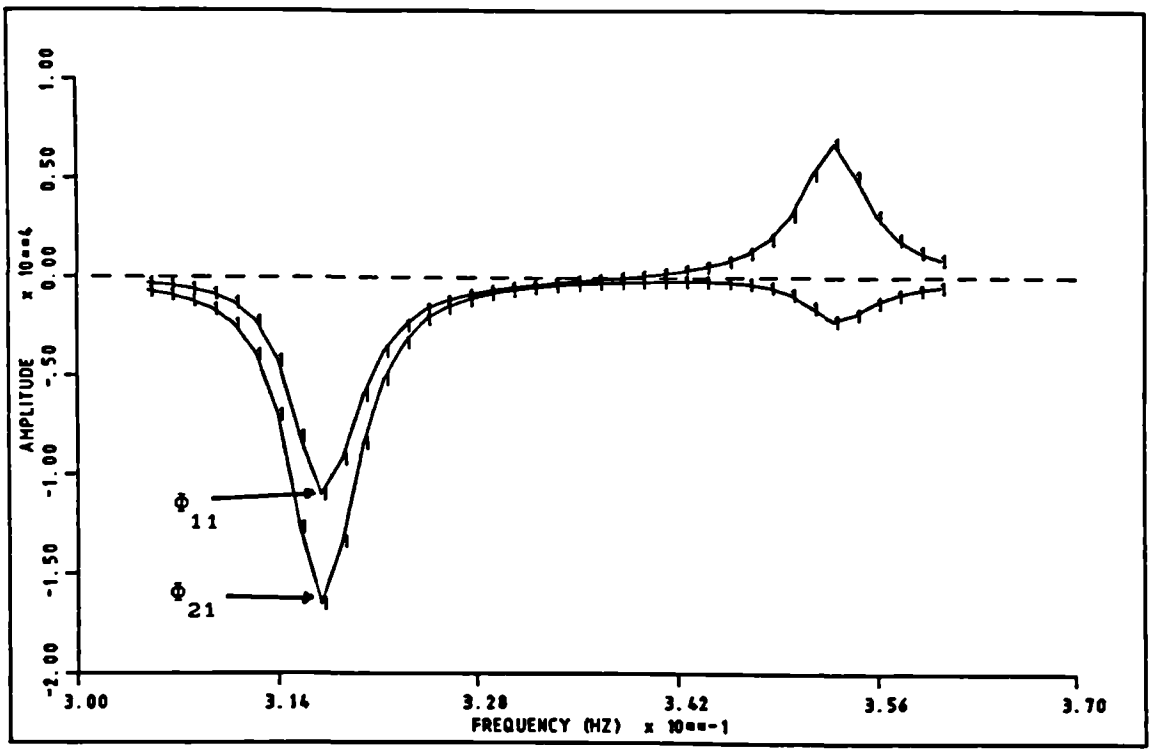

Figure 7.35. Variation of the mode shape parameter with frequency for the bending mode.

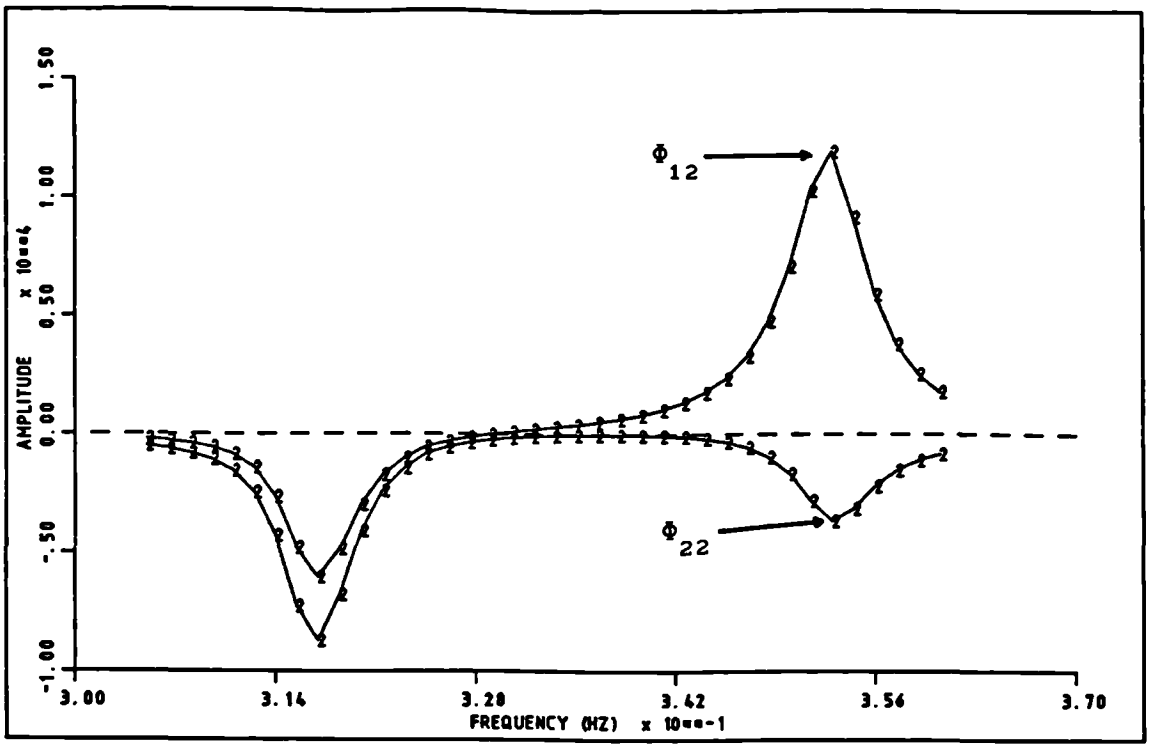

Figure 7.36. Variation of the mode shape parameter with frequency for the torsion mode.

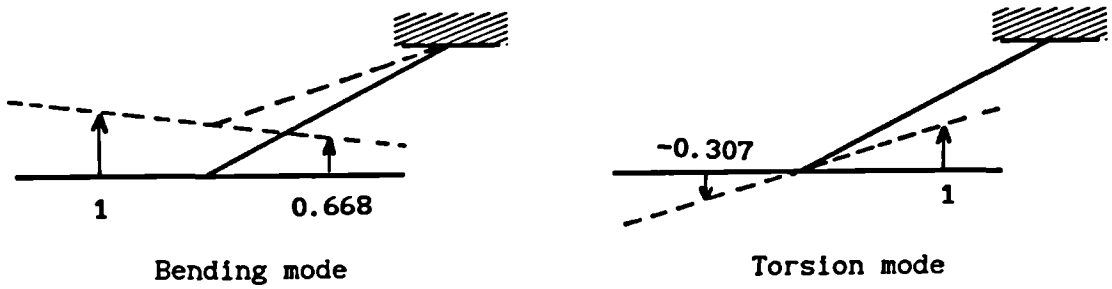

Bending mode

Torsion mode

Figure 7.37. A sketch of the estimated mode shapes for the 2 d.o.f. configuration.

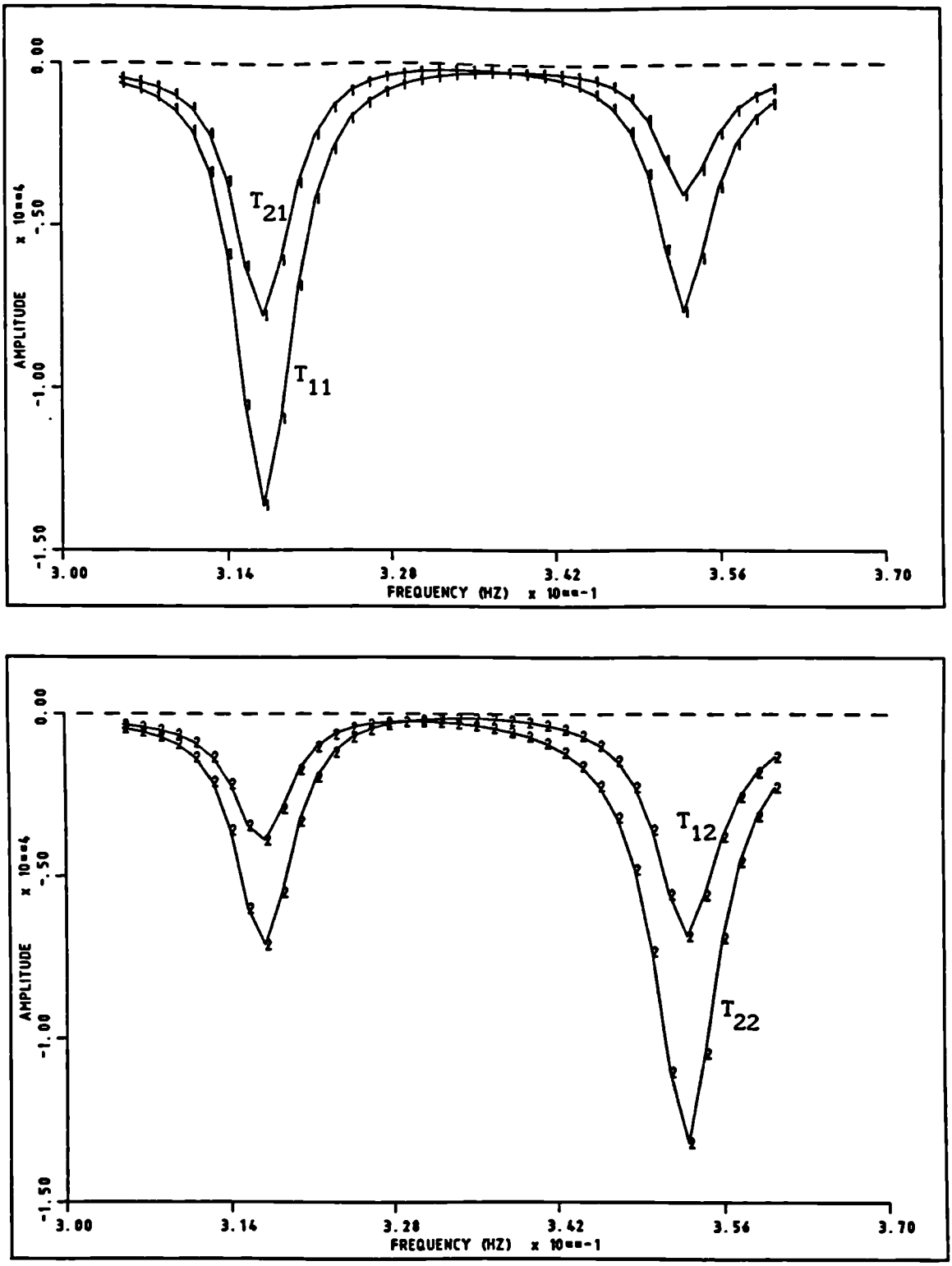

Figure 7.38. Variations of T_{11}, T_{21} and T_{12}, T_{22} functions with frequency for the 2 d.o.f. case.

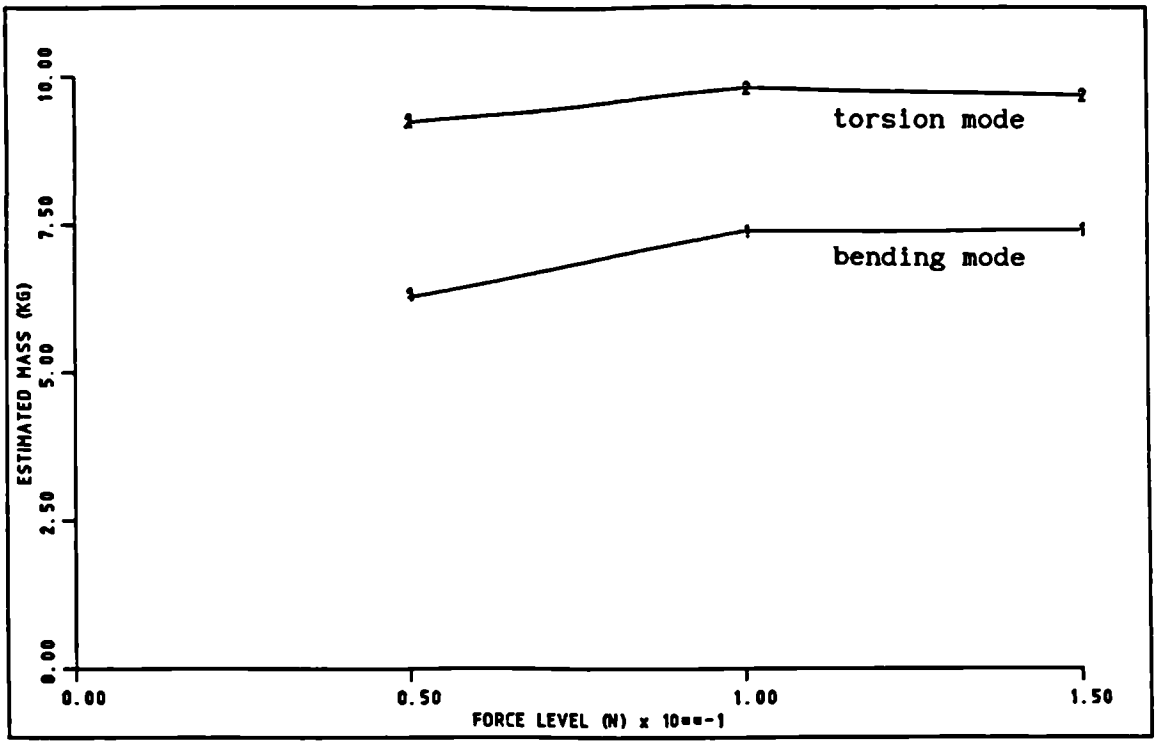

Figure 7.39. Variation of generalised mass estimates for both modes with force level.

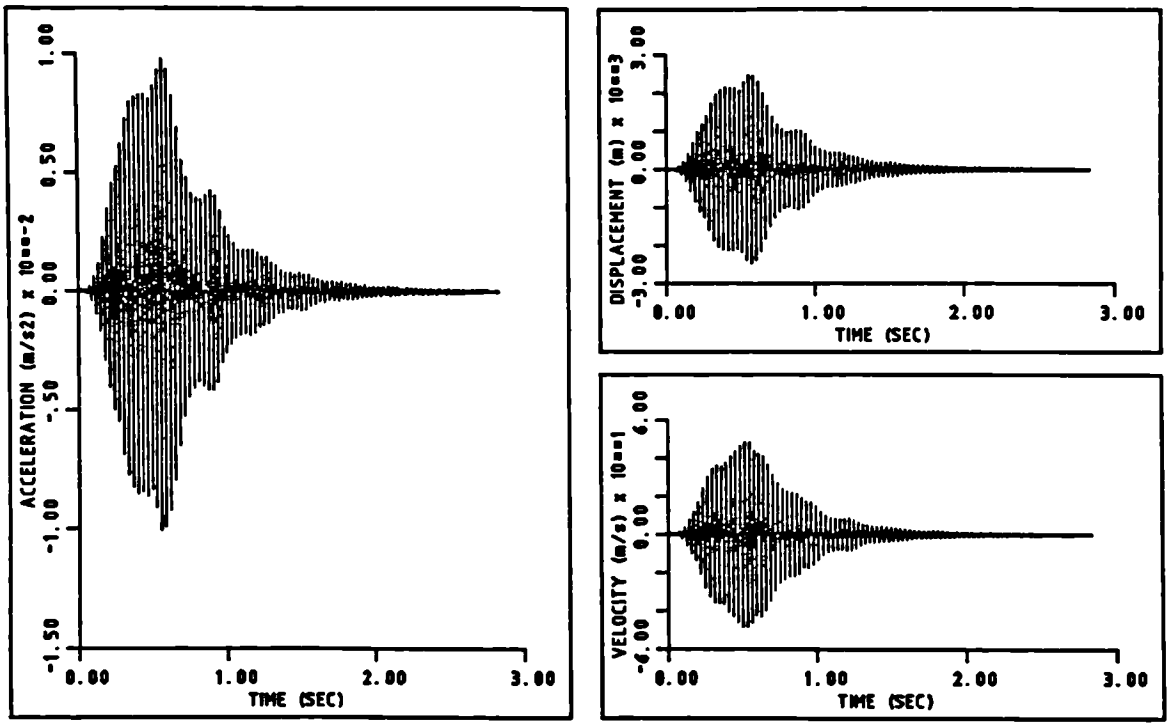

Figure 7.40. Sample time histories for the acceleration and integrated signals corresponding to first station.

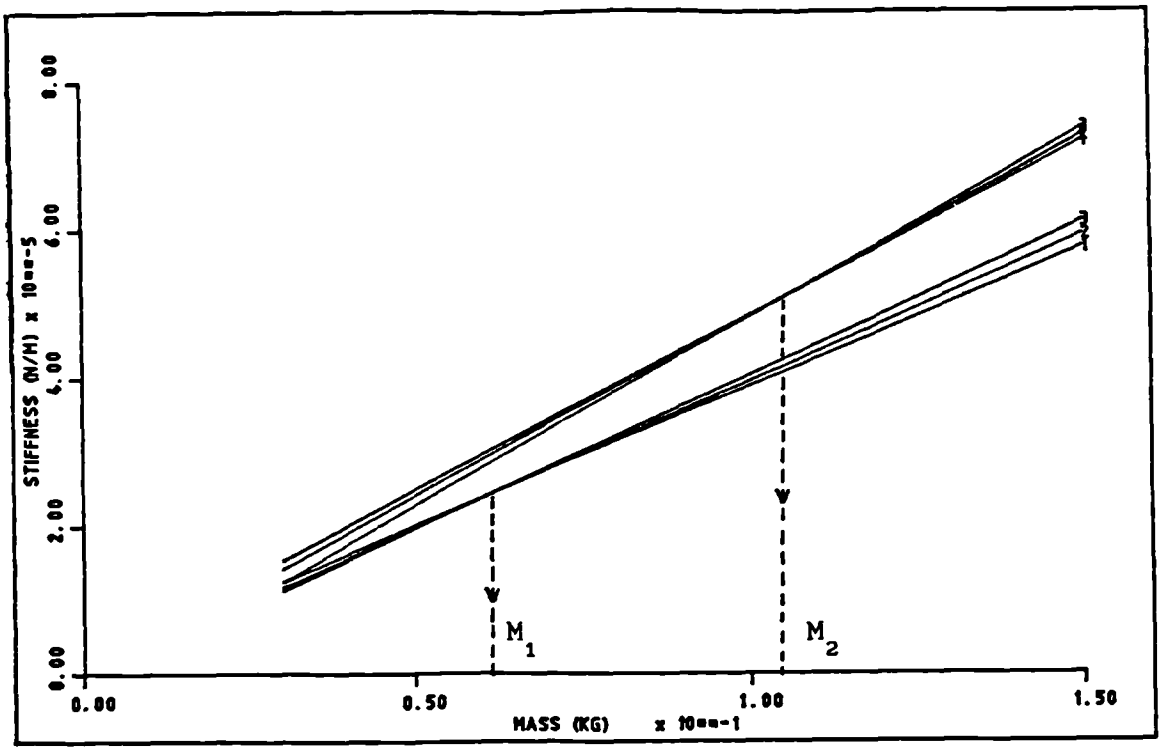

Figure 7.41. Mass estimation using the sensitivity approach for the 2 d.o.f. case.

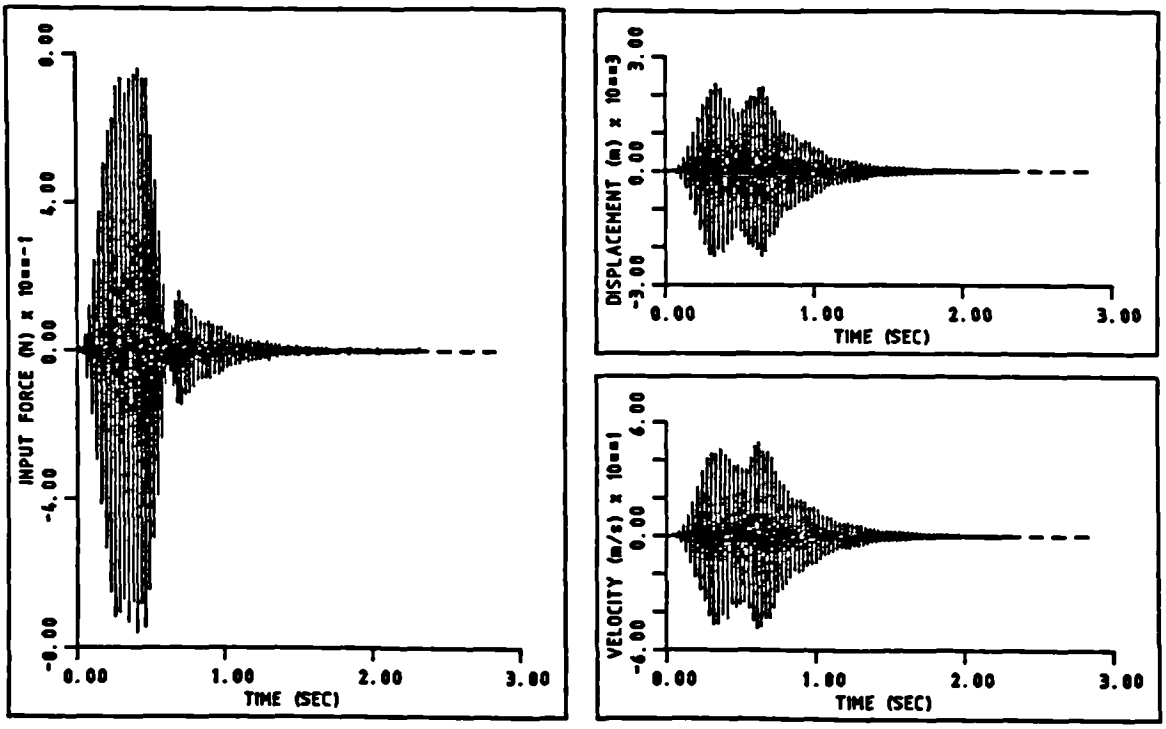

Figure 7.42. Sample sweep time histories used for identification of the 2 d.o.f. case.

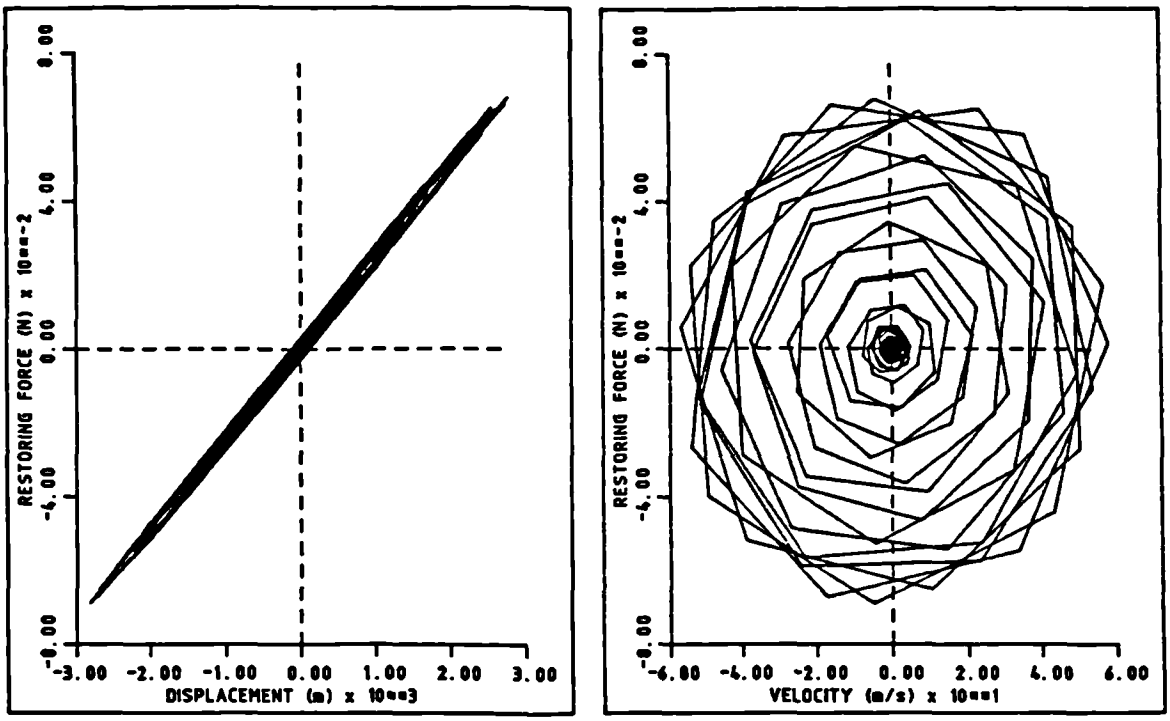

Figure 7.43. Sample sweep map used for identification of the 2 d.o.f. case.

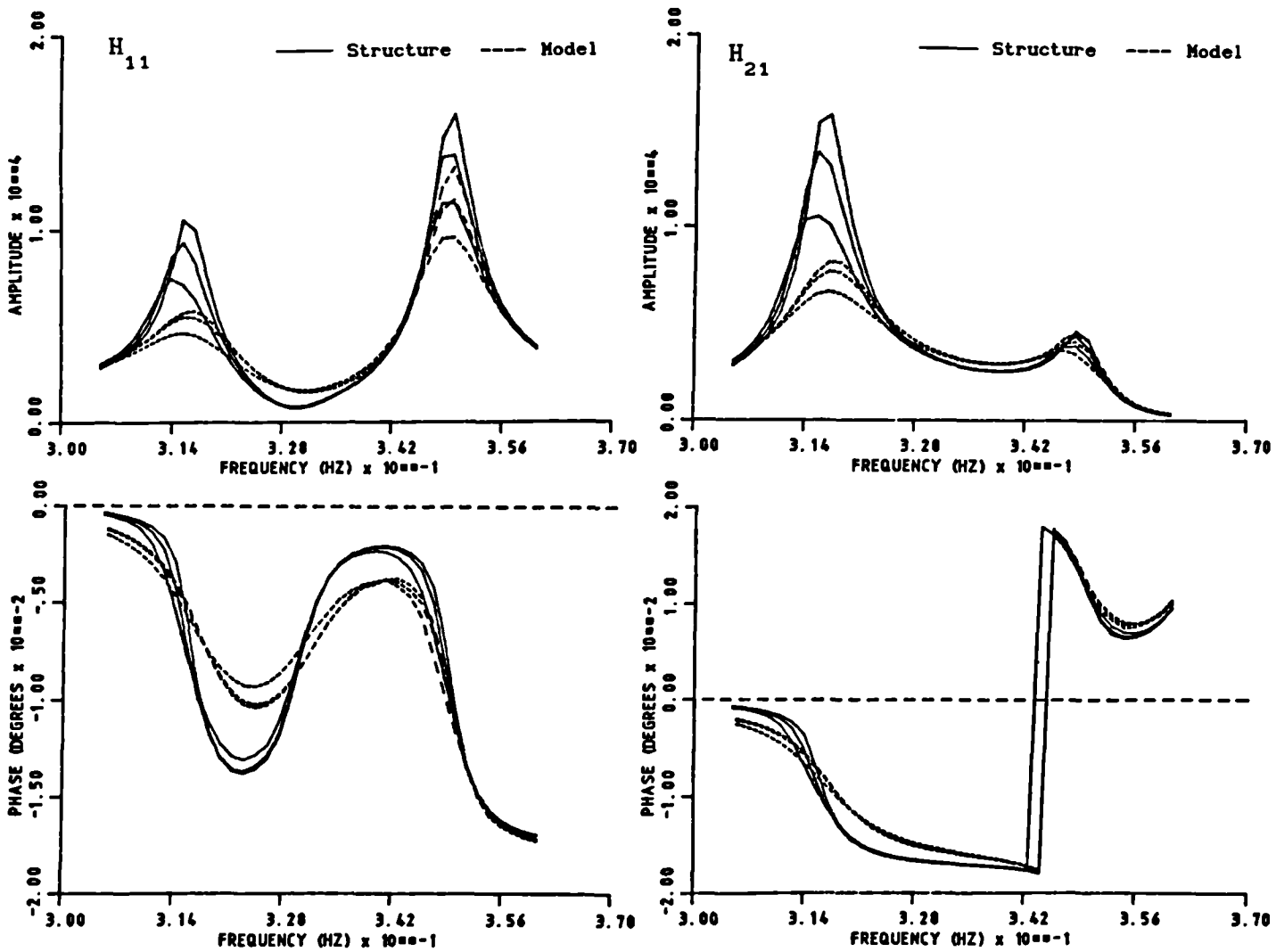

Figure 7.44. Comparison between FRFs of structure and identified sweep model at 3 force levels.

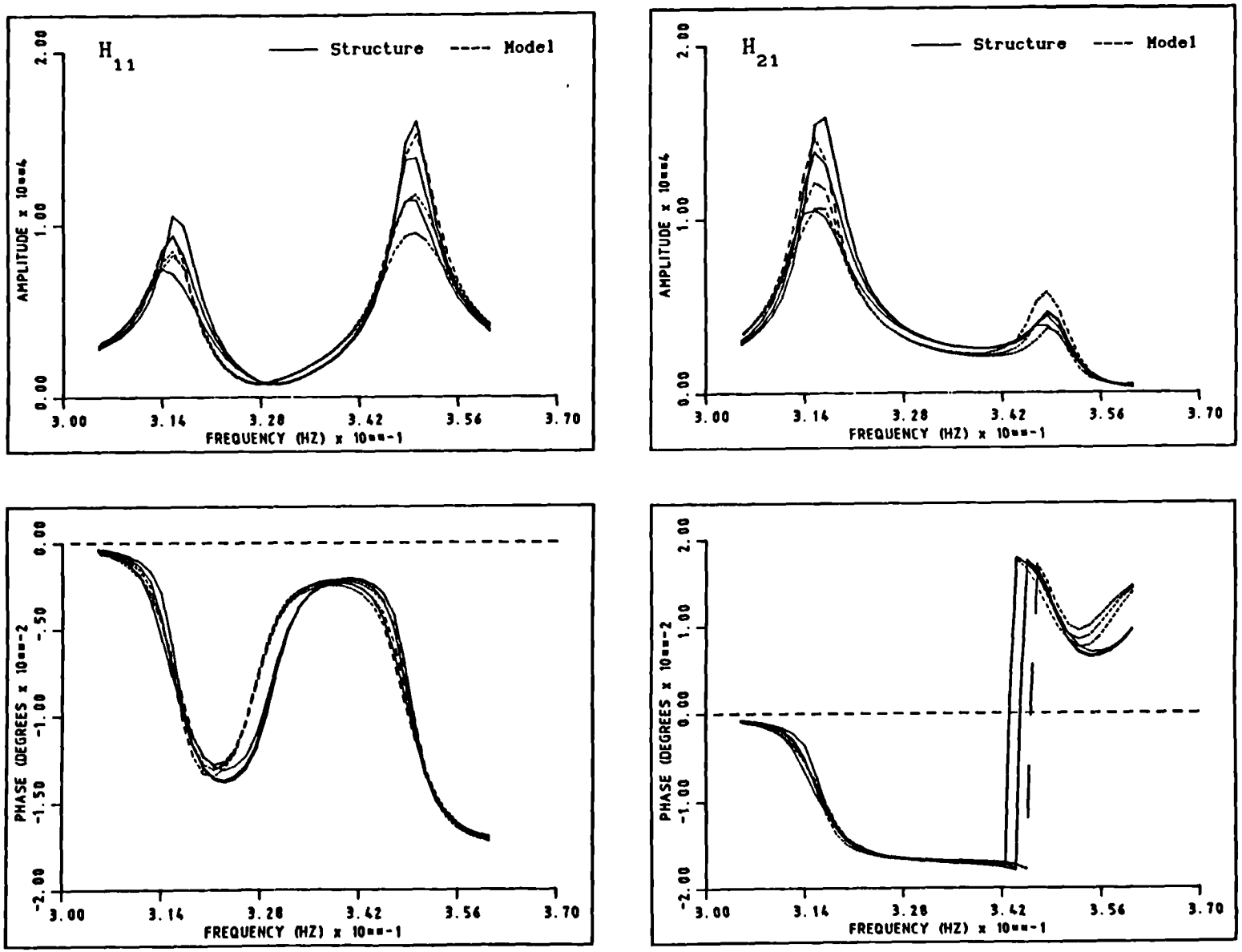

Figure 7.45. Comparison between FRFs of structure and identified single-frequency sweep model at 3 force levels.

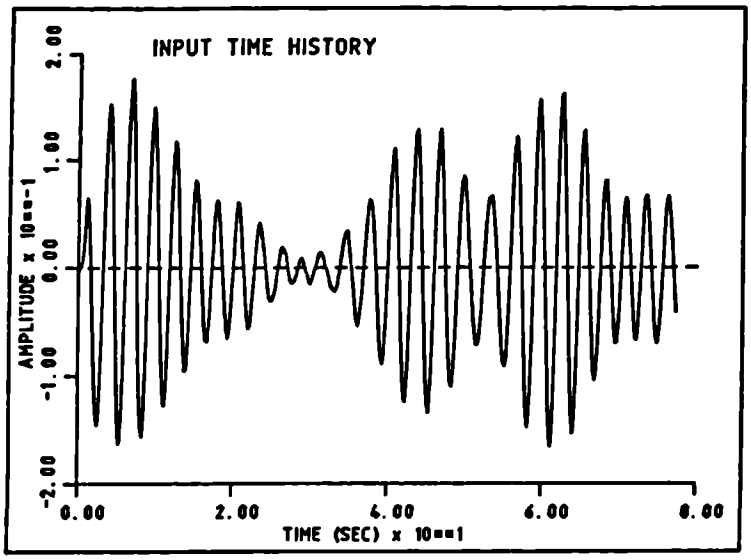

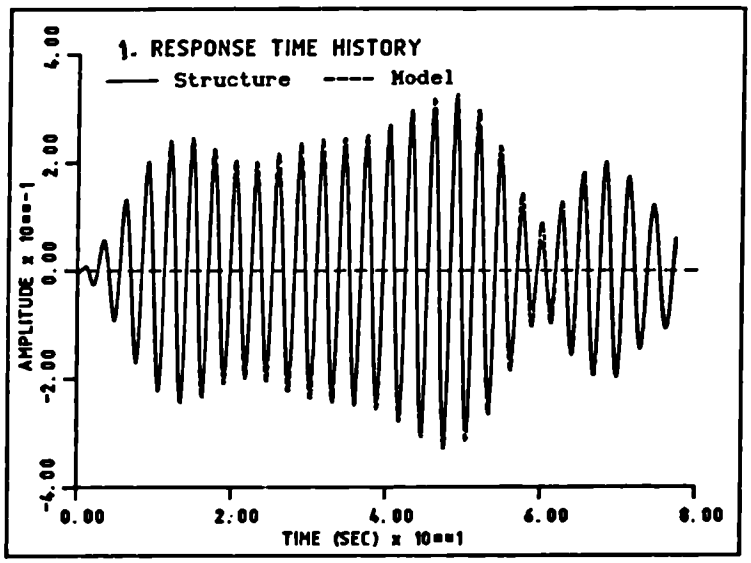

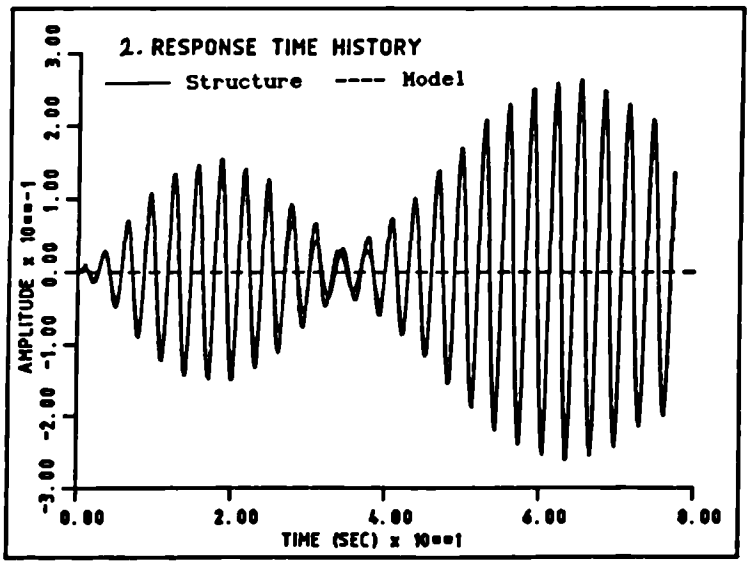

Figure 7.46. Sample comparisons between responses of structure and identified single-frequency sweep model using random excitation at low force level.

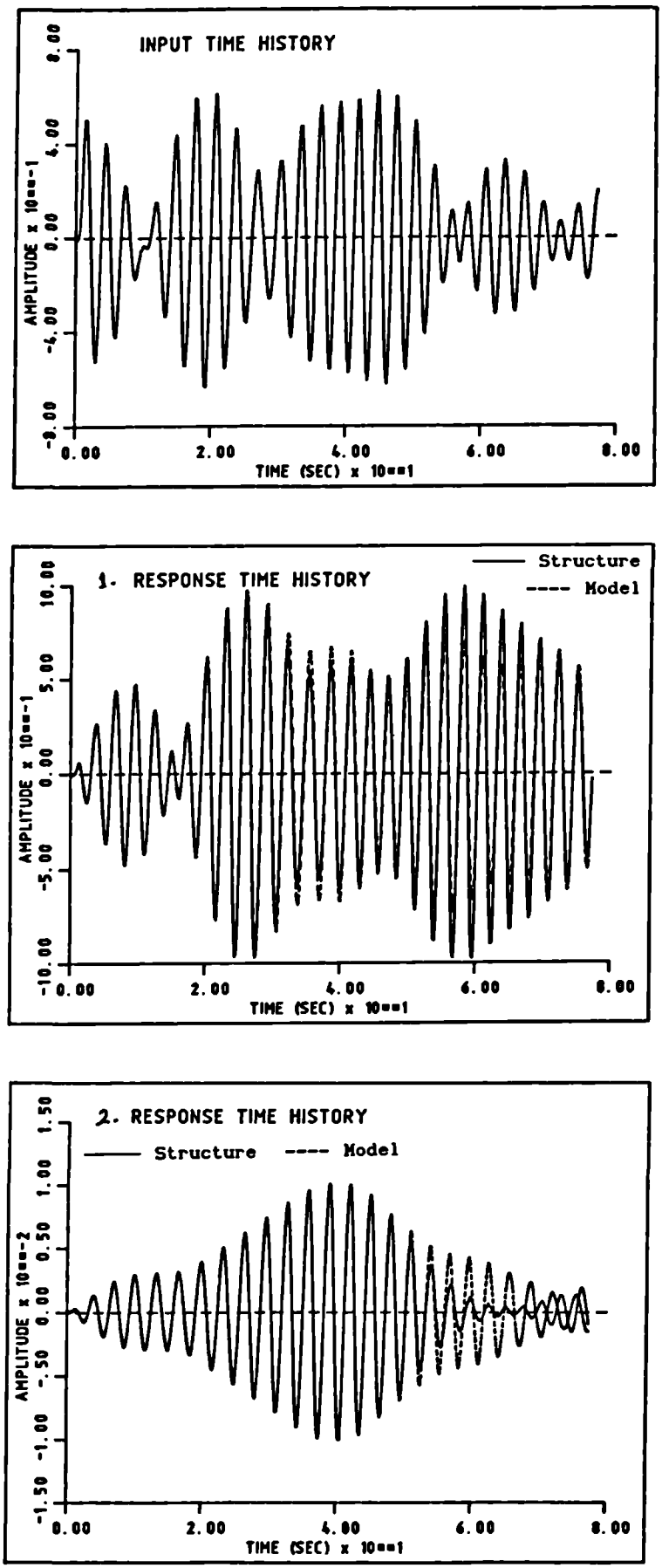

Figure 7.47. Sample comparisons between responses of structure and identified single-frequency sweep model using random excitation at high force level.

8. Conclusion and Suggestions for Future Work

A successful application of the force-state mapping approach relies upon two main aspects,

(i) the process of curve fitting the restoring force in terms of the states and
(ii) the quality of data used in the overall identification procedure.

(i) The current study was started by investigating the first aspect in chapters 2 and 3 where it was assumed that the exact data (acceleration, velocity and displacement signals and generalised mass and modal matrices) were available. This was possible by considering simulated systems.

The original curve fitting philosophy adopted by Masri and Caughey was shown to have certain practical restrictions and drawbacks due to the use of orthogonal Chebyshev polynomials. However ordinary polynomials were found to be superior to Chebyshev polynomials in this particular application in that they yielded a faster, simpler and more accurate identification procedure. Furthermore, the inclusion of special functions in the fitted model yielded a more accurate identification for nonpolynomial nonlinearities than the ordinary polynomial approach; the latter required a large number of terms to be used in order to approximate discontinuities in the maps.

The extension of the investigation to the identification of multi-d.o.f. systems showed that the restriction of fitting only two modal variables at a time, in each step of the Masri/Caughey iterative curve fitting philosophy, introduced bias errors in the identified parameters. These errors required that some of the steps be repeated several times in order to correct for the bias.

The process of curve fitting several modes would thus become involved and time consuming. However the adoption of the direct curve fitting philosophy, which included all possible linear and nonlinear modal coupling terms in a single model, avoided the bias problem and made the identification simpler and faster.

It was shown that the transformation of the equation of motion from physical to modal space lead to very involved modal equations, even for simple nonlinear systems. Also the transformation of nonpolynomial nonlinearities introduced complicated modal terms, the identification of which was impractical. Consequently, in order to overcome these problems, a new approach was developed in which the equation of motion was rewritten in a form such that the restoring force had a linear component expressed in terms of modal quantities and a nonlinear component expressed in terms of relative physical velocities and displacements. This form yielded a much simpler identification procedure. In addition, information regarding the physical locations of the identified nonlinear elements were obtained. Results from a two d.o.f. example with several nonlinearities of different types were accurate and encouraging. The idea is most suitable to lumped parameter systems but an extension to discrete nonlinear elements within continuous systems may be possible.

(ii) The aspect of obtaining a complete set of data from partial measurements and the sensitivity of the force-state mapping approach to errors in these data was then investigated in chapters 4, 5 and 6.

In chapter 4, it was considered that the most attractive practical approach to obtaining a complete set of response data was that the velocity and displacement signals are obtained by integration of the measured acceleration in the time or frequency domain. The most suitable time domain method for estimating the displacement seemed to be the cubic spline approach.

However, providing that the acceleration signal is periodic it was shown that the frequency domain integration approach has some advantages over the time domain integration and is arguably more attractive. In any case, it was possible to obtain reasonable quality parameter estimates from the force-state mapping identification when the velocity and displacement signals were estimated by either time or frequency domain integration.

The effect of systematic and random errors upon the force-state mapping approach was investigated in chapter 5. It was shown that there was a significant influence of systematic phase errors upon the accuracy of damping estimates when the system is lightly damped. Systematic errors in amplitude, and random errors, were far less important. Consequently, a great deal of attention should be paid towards reducing systematic phase errors as much as possible.

The estimation of the mass or generalised mass matrix from measurements was studied in depth in chapter 6 for single and multi-d.o.f. nonlinear systems. The sensitivity approach was developed and shown to provide accurate mass estimates for systems with mixed nonlinearities. It was not sensitive to the presence of realistic systematic and random errors in the measurements. The most interesting bonus of the sensitivity approach is that it can provide an estimate for the generalised mass matrix that can be used with a wrongly estimated modal matrix to yield an identified model equivalent to the exact model of the system. Accordingly, accurate estimates for the modal matrix were not essential for carrying out a force-state mapping identification.

The application of the overall study to a T-beam structure was considered in chapter 7 for well separated and fairly close mode configurations. The model obtained for the well separated bending mode was encouraging since it represented the nonlinear response of the structure very accurately. As expected, the model for the torsion mode was less accurate because its damping was lower.

Reasonable models for the close mode configuration were obtained but accurate identification of the linear and nonlinear damping was difficult since the response of the structure showed low damping and thus results were sensitive to systematic phase errors.

As a final conclusion, this study has shown that the force-state mapping technique is feasible for identifying single and multi-d.o.f. nonlinear systems. However, for real applications particular attention should be paid to the use of hardware with channels having well matched amplitude and phase characteristics and with a simultaneous sample and hold in order to minimise phase errors. In addition careful absolute calibration of all transducers is necessary.

Suggestions for future work.

It is suggested that future research in this area should include :

1. Consideration of continuous systems and, in particular, the identification and location of discrete nonlinearities, the use of more transducers than required modes and the residual effects of modes not included in the model.

2. Development of a fuller theoretical justification of the sensitivity approach to mass estimation for general single and multi-d.o.f. nonlinear systems.

3. Evaluation and development of experimental techniques using a real system, with closer modes and controllable nonlinearities, and using more advanced instrumentation.

4. Comparison of the technique with other modern nonlinear identification methods.

5. Application of the force-state mapping technique to real situations such as the identification of nonlinear model for the control surface behaviour of an airplane.

REFERENCES

1. Ewins D. J.
   Modal Testing : Theory and Practice
   Research Studies Press Ltd 1985.

2. Masri S. F. & Caughey T. K.
   A Nonparametric Identification Technique for Nonlinear Dynamic Systems
   Journal of Applied Mechanics, Vol. 46, PP 433-447, June 1979.

3. Tomlinson G. R.
   Detection Identification and Quantification of Nonlinearity in Modal Analysis - A Review
   Proc. 4th IMAC, Vol. II, PP. 837-843, 1986.

4. Tomlinson G. R. and Hibbert J. H.
   Identification of the Dynamic Characteristics of a Structure with Coulomb Friction
   Journal of Sound & Vibration, Vol. 64 (2), PP. 233-242, 1979.

5. Tomlinson G. R.
   An analysis of the Distortion Effects of Coulomb Damping on the Vector Plots of Lightly Damped Systems
   Journal of Sound & Vibration, Vol. 71 (3), pp. 443-451, 1980.

6. Martens M. et al
   Basic Rules of Reliable Detection Method for Nonlinear Dynamic Behaviour
   Proc. 10th International Seminar on Modal Analysis, Part IV, pp. 1-16, Sep-Oct 1985.

7. Mertens M. et al
   Detection of Nonlinear Dynamic Behaviour of Mechanical

Structures
Proc. 4th IMAC, Vol. I, pp. 712-719, 1986.

8. Mertens M. et al
Measuring and Evaluating Nonlinear Dynamic Behaviour of Mechanical Structures Using Sinusoidal Excitation
Proc. 5th IMAC, Vol. I, pp. 721-727, 1987.

9. Simon M. & Tomlinson G. R.
Use of the Hilbert Transform in Modal Analysis of Linear and Nonlinear Structures
Journal of Sound & Vibration, Vol. 96, No. 4, PP. 421-436, 1984.

10. Tomlinson G. R.
Using the Hilbert Transform with Linear and Nonlinear Multi-Mode Systems
Proc. 3rd IMAC, Vol. I, PP. 255-263, 1985.

11. Tomlinson G. R.
Recent Developments in the Identification of Nonlinearity in Modal Testing
2nd International Symposium on Aeroelasticity and Structural Dynamics, pp. 571-580, 1985.

12. Billings S. A.
Identification of Nonlinear Systems - A Survey
IEE Proc., Vol. 127, Pt. D, No. 6, PP. 272-285, Nov. 1980.

13. Gifford S. J. and Tomlinson G. R.
A functional Series Approach in the Identification of Nonlinear Structures
Proc. 5th IMAC, Vol. I, pp. 593-600, 1987.

14. Bendat J. S.
Statistical Errors for Nonlinear System Measurement Involving

Square law Operations
Journal of Sound & Vibration, Vol. 90 (2), pp. 275-282, 1983.

15. Choi D. W. et al
Application of Digital Cross-Bispectral Analysis Techniques to Model the Nonlinear Response of a Moored Vessel System on Random Seas
Journal of Sound & Vibration, Vol. 99 (3), pp. 309-326, 1985.

16. Leontaritis I. J. & Billings S. A.
Input Output Parametric Models for Nonlinear Systems. Part I - Deterministic Nonlinear Systems. Part II - Stochastic Nonlinear Systems
International Journal of Control, Vol. 41, PP. 303-344, 1985.

17. Natke H. G. , Juang J. N. & Gawronski W.
Identification of Nonlinear Mechanical Systems. A Brief Review
Proc. 6th IMAC, Vol. I, Feb. 1988.

18. Ewins D. J.
Modal Testing and the Linearity of Structures
9th International Seminar on Modal Analysis, Belgium, Sep. 1984.

19. Masri S. F. , Sassi H. & Caughey T. K.
Nonparametric Identification of Nearly Arbitrary Nonlinear Systems
Journal of Applied Mechanics, Vol. 49, PP. 619-627, 1982.

20. Tomlinson G. R.
Force Distortion in Resonance Testing of Structures with Electro-Dynamic Vibration Exciters
Journal of Sound & Vibration, Vol. 63 (3), pp. 337-350, 1979.

21. Tomlinson G. R.

A Simple Theoretical and Experimental Study of the Force Characteristics from Electrodynamic Exciters on Linear and Nonlinear Systems
Proc. 5th IMAC, Vol. II, pp. 1479-1486, 1987.

22. Terrell T. J.
Introduction to Digital Filters
The Macmillan Press Ltd, 1980.

23. Tomlinson G. R., Simon M., Vinh T. and Haoui A.
Applications of the Hilbert Transform to Nonlinear Systems
Euromech 131, University of Manchester.

24. Tomlinson G. R.
Beyond the Linear Model
Presented at Royal Aeronautical Society Workshop on Ground Vibration Testing of Aerospace Structures, 27th Nov 1986.

25. Tomlinson G. R. and Kirk N. E.
Modal Analysis and Identification of Structural Nonlinearity
2nd Symposium on Advances Structural Testing, 1983.

26. Tomlinson G. R.
A Global Approach to the Detection of Structural Nonlinearity
Proc. 6th IMAC, Vol. II, PP. 1439-1445, 1989.

27. Vinh T. et al
Extension of Modal Analysis to Nonlinear Structures by Using Hilbert Transform
Proc. 2nd IMAC, Orlando-Florida USA, 1984

28. Tomlinson G. R.
Vibration Analysis and Identification of Nonlinear Systems. Part I - Hilbert Transform Method
Short Course Notes (Heriot-Watt University), 16th to 18th Sep. 1987.

29. Vinh T.
Vibration Analysis and Identification of Nonlinear Structures - Hilbert transform (theory and practice)
Short Course Notes (Heriot-Watt University), 16th to 18th Sep. 1987.

30. Chouy Chai T. and Vinh T.
Analysis of Nonlinear Structure by Programmed Impact Testing and Higher Order Transfer Function
Proc. 4th IMAC, Vol. I, pp. 743-747, 1986.

31. Gifford S. J.
Vibration Analysis and Identification of Nonlinear Systems. Part II : The Volterra Series
Short Course Notes (Heriot-Watt University) 16th to 18th Sep. 1987.

32. Vinh T.
Mathematical Models for Higher Order Impulse Responses and Transfer Functions
Short Course Notes (Heriot-Watt University) 16th to 18th Sep. 1987.

33. Storer D. M. and Tomlinson G. R.
Identifying a Parametric Model of Nonlinear Systems Using Multi-dimensional Frequency Response Functions
European Forum on Aeroelasticity and Structural Dynamics, Aachen, April 17-19, 1989.

34. Hammond J. K. , Lo H. R. & Seager Smith J.
Identification of Nonlinearities in Vibrating Systems Using Optimal Control Techniques
Proc. 5th IMAC, Vol. II, pp. 1467-1473, 1987.

35. Clarkson P. M.

Adaptive Approaches to Signal Enhancement and Deconvolution
Ph. D. Thesis, Institute of Sound & Vibration Research, University of Southampton, England, 1983.

36. Thomas G.
Deconvolution and Linear Tracking Problems
Signal Processing, Vol. II, pp. 131-135, 1979.

37. Masri S. F. , Beckey G. A. & Sassi H.
Nonparametric Identification of a Class of Nonlinear Multi Degree Dynamic Systems
Journal of Earthquake Eng. Struct. Dynam. , Vol. 10, PP. 1-30, 1982.

38. Masri S. F. et al
Identification of Nonlinear Vibrating Structures. Part I - Formulation. Part II - Applications
Transactions of the ASME, Journal of Applied Mechanics, Vol. 54, PP. 918-929, Dec 1987.

39. Aubert A. C., Crawley E. F. and O'Donnell K. J.
Measurement of the Dynamic properties of Joints in Flexible Space Structures
Space Systems Laboratory, Massachusetts Institute of Technology, Cambridge, Rept. 35-83, Sep. 1983.

40. O'Donnell K. J. and Crawley E. F.
Identification of Nonlinear System Parameters in Space Structure Joints Using the Force-State Mapping Technique
MIT SSL Report # 16-85, July 1985.

41. Crawley E. F. and Aubert A. C.
Identification of Nonlinear Structural Elements by Force-State Mapping
AIAA Journal, Vol. 24, No. 1, pp. 155-162, Jan. 1986.

42. Crawley E. F. and O'Donnell K. J.
Identification of Nonlinear System Parameters in Joints Using the Force-State Mapping Technique
AIAA Journal, 86-1013, pp. 659-667.

43. Marquardt D. W.
An Algorithm for Least Squares Estimation of Nonlinear Parameters
Journal of the Society for Industrial and Applied Mathematics, Vol. 11, No. 2, pp. 431-441, 1963.

44. Yang Y. and Ibrahim S. R.
A Nonparametric Identification Technique for a Variety of Discrete Nonlinear Vibrating Systems
Journal of Vibration, Acoustics, Stress and Reliability in Design, Vol. 107, pp. 60-66.

45. Worden K. and Tomlinson G. R.
Developments in Force-State Mapping for Nonlinear Systems
Proc. 6th IMAC, Vol. II, pp. 1471-1479, 1988.

46. Worden K. and Tomlinson G. R.
Identification of Linear/Nonlinear Restoring Force Surfaces in Single and Multi-Mode Systems
3rd International Conference on Recent Advances in Structural Dynamics at Southampton, 1988.

47. Worden K. and Tomlinson G. R.
Vibration Analysis and Identification of Nonlinear Systems Part III-The Masri/Caughey Identification Procedure , Short Course Notes (Heriot-Watt University), 16th to 18th Sep. 1987.

48. Argoul P.
Une Methode D'Identification Des Structures Nonlineaires En Dynamique

French Mechanical Congress at Nates, 1987.

49. Hunter N. F. et al
Force-State Mapping Using Experimental Data
Proc. 7th IMAC, Vol. II, pp. 843-849, 1989.

50. Press W. H. et al
Numerical Recipes - The Art of Scientific Computing
Cambridge University Press, 1986.

51. Masri S. F. et al
Identification and modeling of Nonlinear Systems
Nuclear Engineering and Design, Vol. 72, pp. 235-270, 1982.

52. Worden K. and Tomlinson G. R.
Application of the Restoring Force Surface Method to Nonlinear Elements
Proc. 7th IMAC, Vol. II, pp. 1347-1355, 1989.

53. Worden K.
Data Processing and Input Design for Force Surface Identification
Progress Report No. 4, SERC Contract No. GR/D75809.

54. Al-Hadid M. A. and Wright J. R.
Application of the Force-State Mapping Approach to the Identification of Nonlinear Systems
European Forum on Aeroelasticity and Structural Dynamics, Aachen, April 17-19, 1989.

55. Williams D. A.
The Analysis of Random Data
AGARD Flight TEST Instrumentation Series, Vol. 14, AGARD, No. 160.

56. Hamming R. W.
Digital Filters
Second Edition, Prentice-Hall, 1983.

57. Stark P. A.
Introduction to Numerical Methods
Macmillan Publishing Co., Inc. New York.

58. Randall R. B.
Frequency Analysis
Brüel & Kjar Publications.

59. Newland D. E.
Random Vibrations and Spectral Analysis
Second Edition, Longman Group Ltd. , 1984.

60. Worden K.
Linear and Nonlinear Restoring Force Surface Identification
Progress Report No. 3, SERC Contract No. GR/D75809.

61. Harris C. M. & Crede C. E.
Shock and Vibration Handbook
Second Edition, McGraw-Hill, 1976.

62. Wright J. R. and Alexiou K.
Multi-Point Resonance Test Methods
Final Internal Report for MoD Contract No. 2042/077 XR/STR,
Department of Aeronautical Engineering, Q.M.C., May 1987.

63. Alexiou K. and Wright J. R.
Determination of Force Distribution in Multi-Point Resonance Testing Using Various Direct Methods
Second International Symposium on Aeroelasticity and Structural Dynamics, Aachen, 1985.

64. Rades M.

On Modal Analysis of Structures with Nonproportional Damping
Revue Roumaune Des Sciences Techniques Serie Mecanique Appliquee, Vol. 26 (4), pp. 605-622, 1981.

65. Wright J. R.
Flutter Test Analysis Methods
Ph. D. Thesis, University of Bristol, Dept of Aeronautical Engineering, 1975.

Application of the Force-State Mapping Approach to the Identification of Nonlinear Systems

by

M. A. Al-Hadid and J. R. Wright

Aeronautical Engineering Department,
Queen Mary College,
Mile End Road,
London E1 4NS.

Summary

In this paper the application of the force-state mapping approach to the identification of nonlinear structures is considered. The results of an experimental study of a T-beam structure are presented for the well separated bending and torsion modes. Mathematical models to represent the nonlinear stiffness and damping behaviour of the structure are obtained. Quite a good agreement between responses of the model and the structure is shown but the approach is more sensitive when the damping is low. A technique for estimating the effective mass prior to identification is also illustrated.

1. Introduction

The identification of the dynamic characteristics of linear dynamic systems is now commonplace but interest in nonlinear systems is increasing. Identification of nonlinear systems ranges from methods simply to detect the presence or type of a nonlinearity to those which seek to quantify the behaviour via some form of mathematical model. In this latter category is the force-state mapping approach proposed initially by Masri and Caughey [1,2].

In this approach, given an estimate for the system mass and measurements or estimates of the acceleration, velocity and displacement, the nonlinear restoring force is represented by a surface over the velocity-displacement plane and then a fit to the surface is carried out using an orthogonal Chebychev polynomial series expansion. An extension to multi-degree of freedom systems is possible.

Since the method was proposed, it has been the focus of development by other researchers [3-9]. Particular attention has been paid to the implementation of the curve fit to the restoring surface, where ordinary polynomials are superior to orthogonal polynomials, to the estimation of unmeasured states by integration or some form of optimal control, to the estimation of mass and to the location of nonlinearity within a multi-degree of freedom system.

Most of the work has understandably made use of simulated data but some experimental results have been presented. In particular O'Donnell and Crawley [4] have investigated the behaviour of nonlinear joints as essentially a lumped mass moving on a flexure in one degree of freedom with some stiffness and friction nonlinearity. They measured both acceleration and displacement and estimated velocity by an optimal state estimation process. Experimental force-state maps and estimated parameters were presented; results were encouraging. Worden and Tomlinson [6] have presented a force-state map for a cantilever beam with a clearance nonlinearity near the root; they used random excitation and integrated the measured acceleration in the time domain to estimate the other states. Also Hunter et al [8] have presented results using the same approach but for a simple beam with base excitation. The authors are not aware of any published experimental work on multi-degree of freedom systems.

One interesting omission in the experimental work presented so far is the comparison of responses of the system with those predicted using the fitted model, though this has been done for simulated systems.

In this paper, the application of force-state mapping to a T-beam with stiffness and damping nonlinearity is presented. Steady-state and swept sinusoidal excitation signals are used with integration of measured acceleration carried out in the frequency domain. A new approach for mass excitation, arguably less sensitive than those used so far, is presented. Comparisons of time responses and frequency response functions for the fairly well-separated bending and torsion modes are shown, treating each as if it was a single degree of freedom. Work on the identification of two closer modes is in progress.

2. Basic Philosophy of the Force-State Mapping Approach

The equation of motion for a single degree of freedom nonlinear system may be written as

$$m\ddot{x} + f(\dot{x}, x) = p(t) \qquad (1)$$

where m is the mass, $\ddot{x}$ is the acceleration, p(t) is the applied force and f(ẋ,x) is the restoring force which is a function of velocity ẋ and displacement x. The restoring force contains the linear stiffness and damping forces and also any additional nonlinear restoring forces.

It is possible to rewrite equation (1) in the form

$$f(\dot{x}, x) = p(t) - m\ddot{x} \qquad (2)$$

The idea of the force-state mapping approach is to obtain an estimate of the restoring force f(ẋ, x) from equation (2) using measured force and acceleration data and an estimated value of the mass. If the velocity and displacement can also be obtained, either by separate measurement or by integration of the acceleration, then a mathematical relationship between f(ẋ, x) and ẋ and x may be sought.

In practice, the force and acceleration signals will be sampled at discrete time intervals and therefore f(ẋ, x), ẋ and x will also be available as discrete values. A three-dimensional plot of f(ẋ, x) against ẋ and x is called a force-state map; it is often helpful to examine the projection of the map onto the force- displacement plane. A sample map for a single degree of freedom system, having a cubic stiffness nonlinearity and excited by a sinusoidal frequency sweep, is shown in Fig. 1. The map has a characteristic shape for different types of nonlinearity and can help indicate the type of nonlinearity present in a system if the nonlinearity is not "weak".

It is worth noting that any excitation signal that can excite the system in its nonlinear region may be used. Worden and Tomlinson [6] and Hunter et al [8] used random excitation whereas Crawley et al [3,4] made use of steady state sinusoidal excitation.

Once a measured map has been obtained, a mathematical model relating f(ẋ, x) to ẋ and x may be obtained using a least squares fit. Whereas Masri and Caughey [1,2] used a Chebychev polynomial representation there are significant disadvantages in using this approach as shown in reference [7] where a better model is considered to be

$$f(\dot{x}, x) \approx \hat{f}(\dot{x}, x) = \sum_{i=0}^{M} B_i F_i(\dot{x}, x) \qquad (3)$$

where B_i are unknown coefficients and $F_i(\dot{x}, x)$ are basis functions of ẋ and x.

This model caters for the linear part of the restoring force and also any "polynomial" nonlinearity (such as cubic stiffness) by using basis functions which contain simple powers of ẋ and x (e.g. $F_1 = x$, $F_2 = \dot{x}$, $F_3 = x^3$ etc).

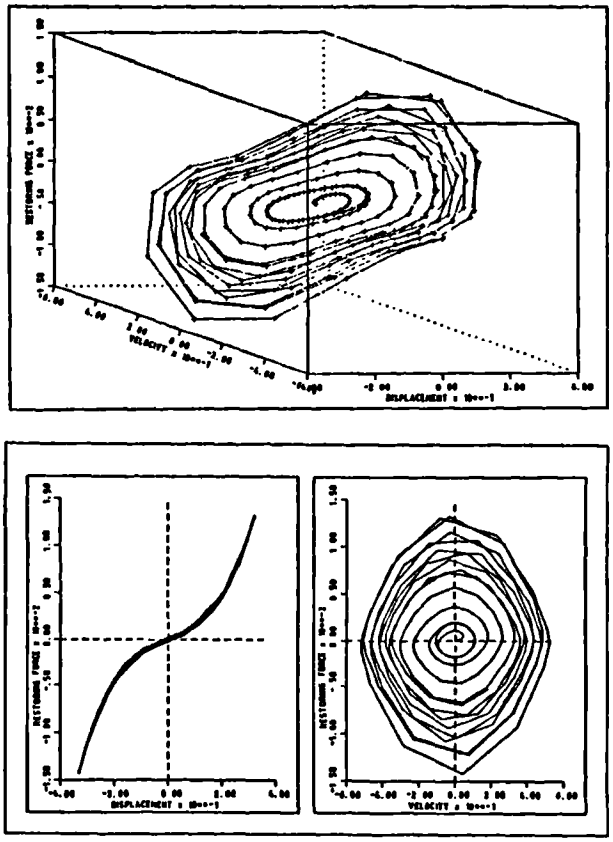

Figure 1: Sample map for a single dof system with cubic stiffness

However, whilst it is possible to model other types of nonlinearity such as friction, quadratic damping and piecewise stiffness (e.g. dead space) in an approximate manner using many terms in such a power series expansion, it is better to deal with them more precisely using special basis functions. For example, a quadratic damping effect could be represented by including a function

$$F_i(\dot{x}, x) = \dot{x}^2 \text{ sign } (\dot{x}) \qquad (4)$$

in the series of equation (3).

Once suitable terms have been included in the model, it can be fitted to the measured data in the map using a least squares process. Implementation using a singular value decomposition approach can help to avoid conditioning problems.

The authors have found it helpful to classify the model used as 'parametric', when terms in the series are only included if they can be easily related to known types of nonlinearity, and 'nonparametric' if additional terms with no obvious physical meaning (e.g. $\dot{x}^3$, x^2 etc) are included to improve the goodness of fit for real data. Masri and Caughey effectively adopt the latter approach by choosing to use Chebychev polynomials.

Once a mathematical model has been obtained then it can be used to simulate the behaviour of the system to different inputs. The quality of the model can be assessed by how well it is able to match measured time histories and frequency response functions obtained using constant force level over the frequency range of interest.

Finally, it should be pointed out that the method can be extended to identify multi-degree of freedom nonlinear systems [2,6-9] by effectively transforming the measured data into modal space using estimated generalised mass and mode shape information.

3. Estimation of Mass and Unmeasured States

The force-state mapping approach has been applied to simulated data by a number of authors [5-9] and found to work well. The main problems lie in estimating the mass and in accurate integration of the acceleration data if velocity and displacement data are not directly measured. Various approaches to these problems have been suggested.

O'Donnell and Crawley [4] suggest that the mass can be estimated by curve fitting the applied force and including an $\ddot{x}$ term in the fitted model, so in essence equation (1) is used. Worden and Tomlinson [6] suggested a similar approach in which the mass is guessed and the mass error estimated by including an $\ddot{x}$ term in the model fitted to the restoring force; the mass can then be updated and the analysis repeated until convergence occurs. The authors found that these methods were rather sensitive to simulated measurement noise and a different approach is adopted in this paper. The mathematical basis of the method and results of one and two degrees of freedom simulations will be published elsewhere.

The basic idea is to find a first estimate of the mass (or generalised mass for multi-degree of freedom systems) using, for example, a multi-point force appropriation type of method for data obtained at a low force level; for a single degree of freedom system this reduces to using the slope of the real part and the value of the imaginary part of the frequency response function at the undamped natural frequency. Then data is measured at two or more discrete frequencies or small frequency bands around resonance. For each set of data maps are produced corresponding to each of two or more different mass values which embrace the estimated mass. Once each map has been fitted, a typical parameter such as estimated linear stiffness can be plotted against the mass used. It can be shown that the relationship between a parameter such as stiffness, and the assumed mass is linear even for nonlinear systems, and the constant of proportionality depends upon the frequency. Thus lines obtained at different frequencies should intersect at a point corresponding to the correct mass value.

As regards the problem of obtaining $\ddot{x}$, $\dot{x}$ and x data, it is clearly possible to measure all three signals but this is not ideal. Perhaps the most attractive approach is to measure only $\ddot{x}$ and to obtain $\dot{x}$ and x by integration either in the time or frequency domains. The problem in both domains is that small low frequency components in the acceleration data are amplified relative to the components of interest when integration is carried out. Thus some form of high pass filtering is required. Frequency domain integration is affected by any leakage errors present.

Time domain integration of acceleration was rejected by O'Donnell and Crawley [4] in favour of a more involved approach in which $\ddot{x}$ and x are measured and $\dot{x}$ obtained in some optimal way using a state estimator to minimise bias effects in the measurements. However Worden and Tomlinson [6] and Hunter et al [8] have used time domain integration in conjunction with random excitation with some success. The authors, who have only used swept sine and single frequency sine excitation, have found frequency domain integration to be as good as if not better than time domain integration; use of these excitations can minimise leakage effects and low frequency components in the amplitude spectra can be eliminated without the phase shift problem associated with time domain high pass filtering. Simulated results for time domain integration were found to be sensitive to this effect.

4. Experimental Application of Force-State Mapping.

Clearly for any identification technique, the most important question is how well it works when applied to real problems. In this section results from a T-beam structure with two well separated modes are presented.

4.1. Experimental Setup

The structure investigated was a T-beam constructed from two lengths of steel tube welded together and clamped to an angle plate as shown in Fig. 2. This configuration was chosen because the relative natural frequencies of the primary bending and torsion modes could be controlled to some extent by adding lumped masses. Initially two well separated modes were required, essentially for single degree of freedom identification, but an investigation into a nonlinear configuration with two close modes is currently in progress. The natural frequencies for the configuration tested in this paper were approximately 40 and 76 Hz.

In order to increase the damping in the bending mode and to introduce a quadratic damping type of nonlinearity, a dashpot type arrangement of a circular plate immersed in oil of a high viscosity was added at the junction of the T-beam, as shown in Fig. 2. The relatively flexible root clamp also behaved nonlinearly as will be seen later.

Excitation was provided using a single LING 401 exciter and the force and acceleration signals measured using PCB transducers. A Cambridge Electronic Design data acquisition system was used to sample the data in a burst mode with under 4 μsec delay between channels so any phase errors at the frequencies considered were very small (<0.1°) and were ignored. The swept or single frequency sine excitation signals were generated from a Buffer DAC using a clock synchronised with that performing the ADC function. This meant that an integer number of cycles of data could be acquired for the single frequency sine and thus leakage in any subsequent Fourier Transform was avoided.

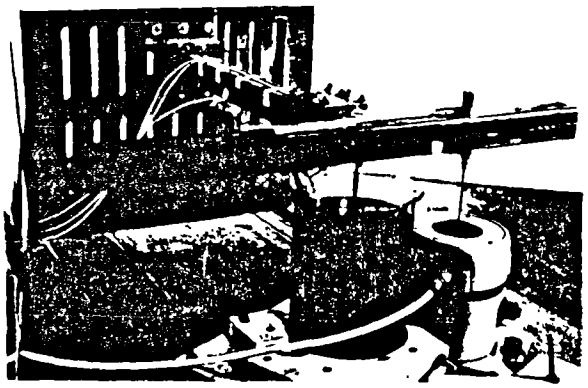

Figure 2: Photograph of experimental T-beam configuration

4.2. Identification of Bending Mode

A sample frequency response function for this mode at three force levels is shown in Fig. 3 for the structure with no oil in the dashpot. The natural frequency is around 40.5 Hz and there is clearly some nonlinear behaviour simply due to the root clamp; some softening stiffness nonlinearity is thought to be associated with local flexibility of the clamp altering the clamping action and some damping nonlinearity with rubbing within the joint. The damping is very low (<1%) and is considered to be too small for the frequency shift with amplitude to be merely due to increased damping. The addition of oil to the dashpot introduced nonlinear damping and reduced the natural frequency to around 39.3 Hz due to the added mass of the oil; a frequency response function for this case will be shown later.

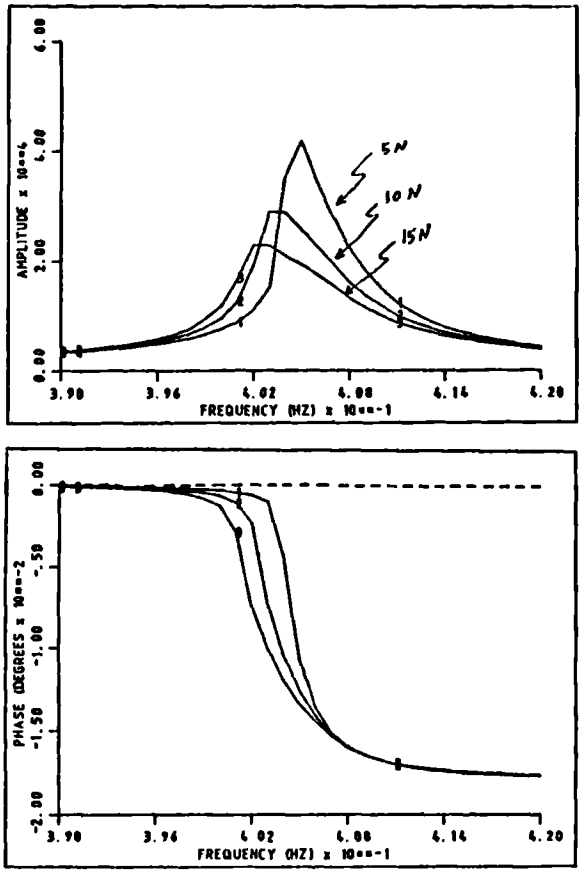

Figure 3: A sample FRF for bending mode at 3 force levels

In order to proceed with the identification process, the effective mass of the system needed to be estimated. In the case of this continuous system the mathematical model would need to correspond to the force and response measured at one position so the mass is the effective mass of the structure in this mode as seen by the exciter. From the multi-point force appropriation approach using only 3N force the mass was approximately 5.3 kg. This estimate was refined using the approach mentioned in Section 3. Data was acquired at five frequencies (36,38,39.4,41 and 42 Hz) and three force levels (typically 20, 40 and 80N) for each. Maps were constructed by combining the three force results for each frequency and assuming a mass of firstly 3kg (<5.3) and then 8kg (>5.3); a curve fit using a nonlinear model was carried out for each frequency/mass combination.

The resulting variation of the estimated linear stiffness with the assumed mass values for the five frequencies is shown in Fig. 4. This result is encouraging since all the lines should intersect at the same mass value; in fact all the ten possible intersections lay in the range 5.8 - 6.6 kg with an average value around 6.0 kg, taken as the effective system mass.

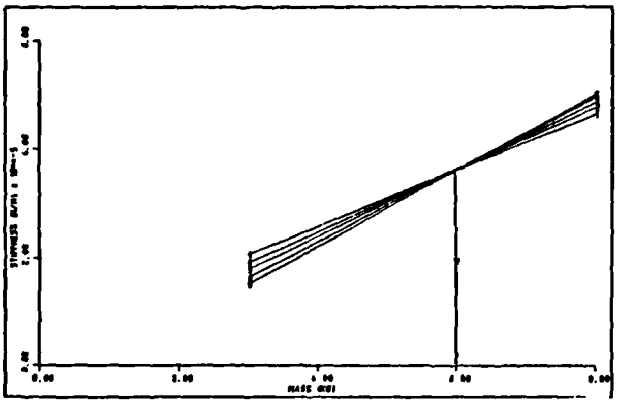

Figure 4: Mass estimation plot for bending mode

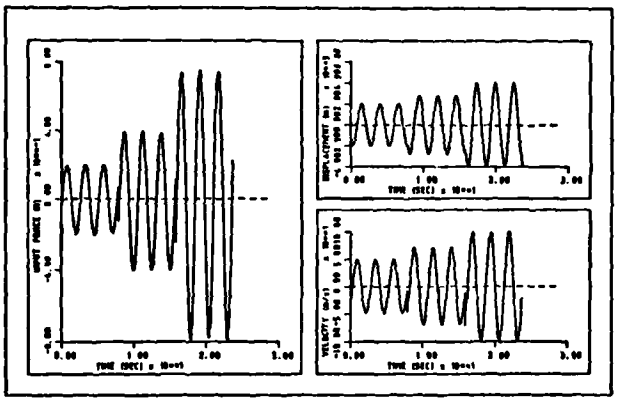

Figure 5: Sample portions of the steady-state time histories at 3 force levels

A force-state map corresponding to the 38 Hz steady-state excitation at 20, 40 and 80N and the 6 kg effective mass was then constructed. The integrations were carried out in the frequency domain by transforming the integer number of cycles of the acceleration data defined at 32 points per cycle. Sample portions of the time histories for each of the three force levels are shown sequentially in Fig. 5. The corresponding map and its projection onto the force-displacement plane are shown in Fig. 6.

Another version of the map was obtained using frequency sweep excitation around resonance with the sweep occupying only about 30% of the acquired data window in order to allow the response to decay sufficiently and so minimise leakage. The sweep amplitude was tailored so as to avoid large transients. After frequency domain integration, every fourth point from the 1024 point data records was selected for the map, due to memory limitations. The corresponding time histories and map and its projection are shown in Figs. 7 and 8.

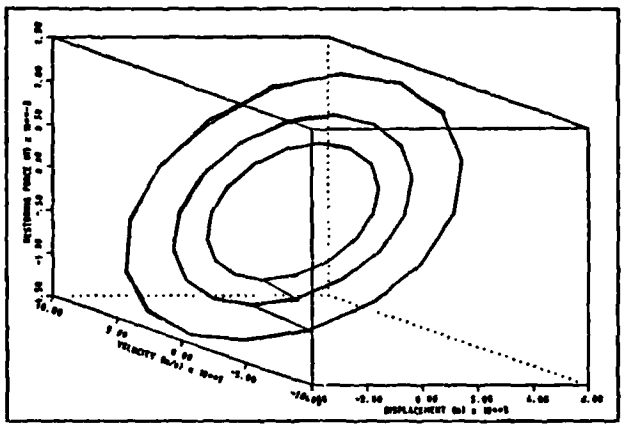

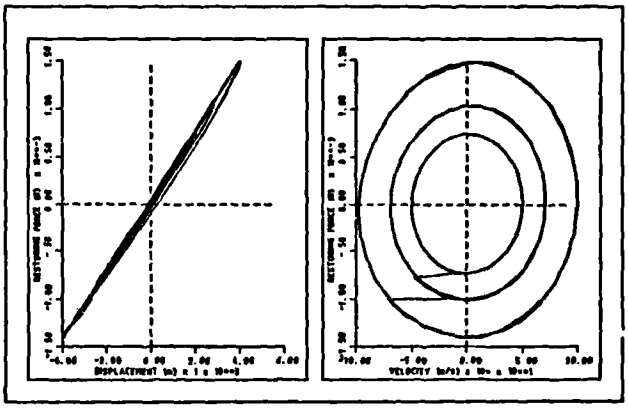

Figure 6: Force-state map generated at 3 force levels using steady-state excitation

The two versions of the map differ somewhat because the steady state excitation produces a higher response than the sweep. There is no obvious reason for the apparent lack of symmetry in the steady state map, as seen from the projection of Fig. 6. It may only be said that for a real structure the nonlinearity may not behave in an ideal way or that some experimental or integration error may be responsible. Any stiffness nonlinearity is clearly not large and is obscured by the thickness of the projection due to the fairly significant damping; the map doesn't help much in this case.

A curve fit using a nonlinear model was carried out to each map. A nonparametric model was used and found to give better results than a parametric model with only a few terms. The fitted models are shown in Table 1, together with the rms contribution of each term to the overall fit. Apart from the linear terms, dominated by the stiffness, a small cubic softening stiffness was consistently obtained, as well as a quadratic damping term. The other nonlinear terms helped to improve the fit and were presumably some representation of the non-ideal behaviour of the structure and the hardware used for carrying out the test.

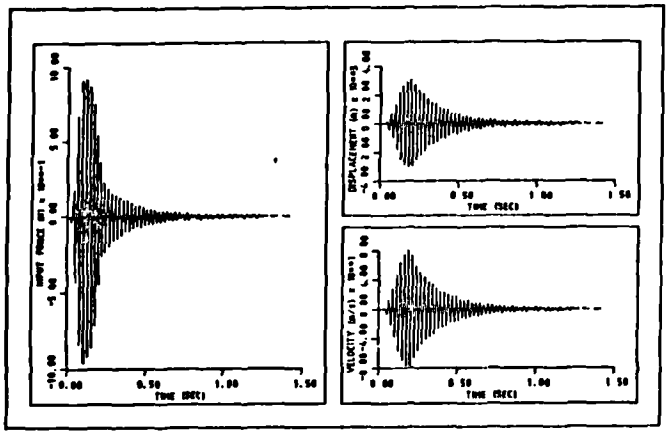

Figure 7: Sample measured and integrated time histories for sweep excitation.

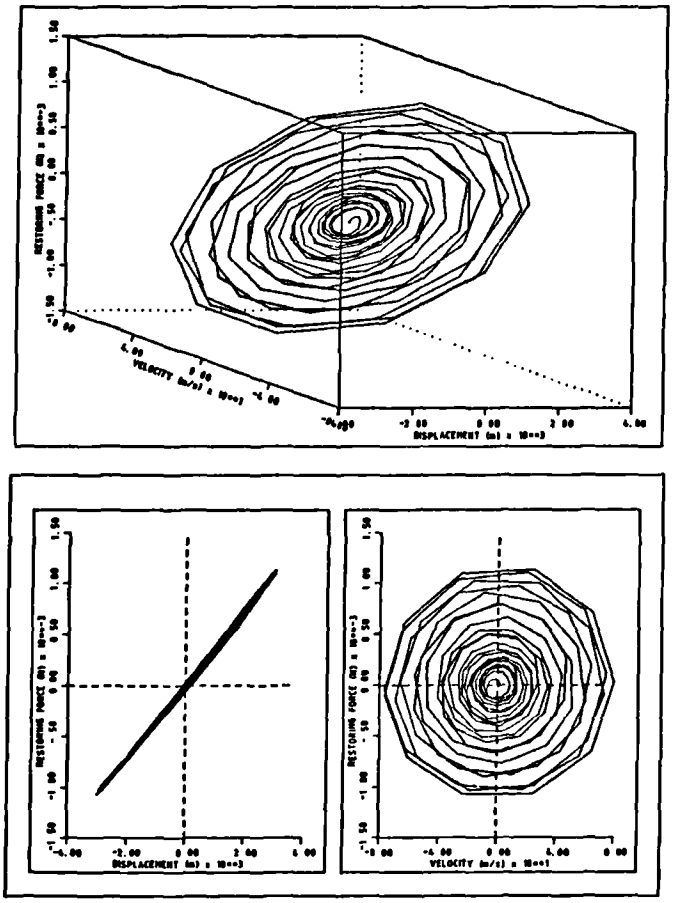

Figure 8: Force-state map generated using sweep excitation

The quality of the models was evaluated firstly by using Runge-Kutta simulation to obtain responses due to constant force steady state excitation and hence frequency response functions. These are compared to measured results in Fig s 9 and 10 for the two fitted models; the agreement is encouraging. A further check on the models is to compare the responses of the model and the structure to sweep and random excitations; some sample comparisons are shown in Fig s 11 and 12 for the steady-state model and again show fairly good agreement over a range of excitation levels.

Clearly for this mode the nonlinear model is able to represent the behaviour of the structure fairly well.

In order to study the sensitivity of the results to any possible error in the mass the model was reproduced using different mass values and the simulation in the frequency domain repeated. The corresponding frequency response functions generated at 5N for M =5.5, 6 and 6.5 kg cases are shown (dashed lines) in Fig. 13 and compared to the measured FRF (solid line). It can be seen that the variation of the mass hardly changed the FRF of the model around the peak while it had more effect around anti-resonance regions.

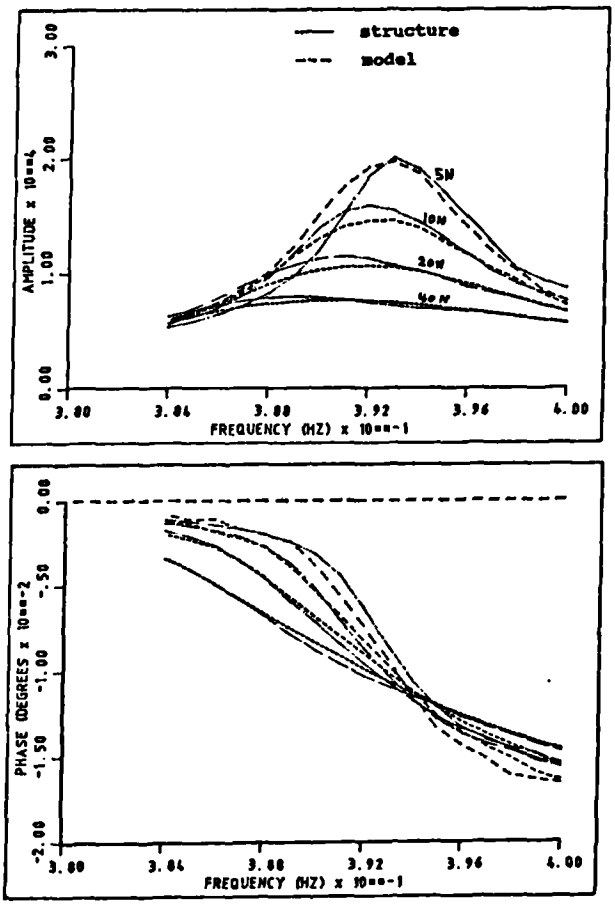

Figure 9: Comparison between FRFs of structure and identified steady-state model at 4 force levels

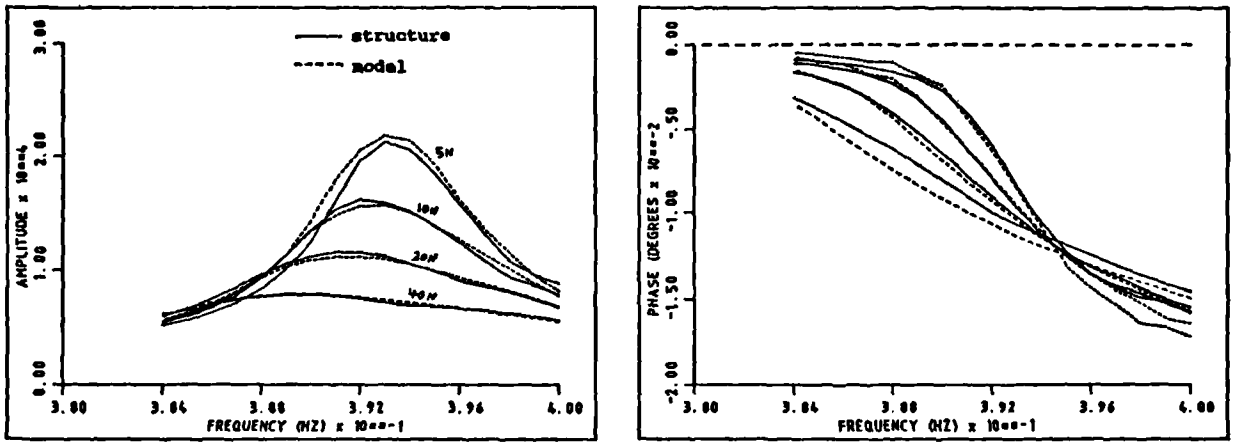

Figure 10: Comparison between FRFs of structure and identified sweep model at 4 force levels

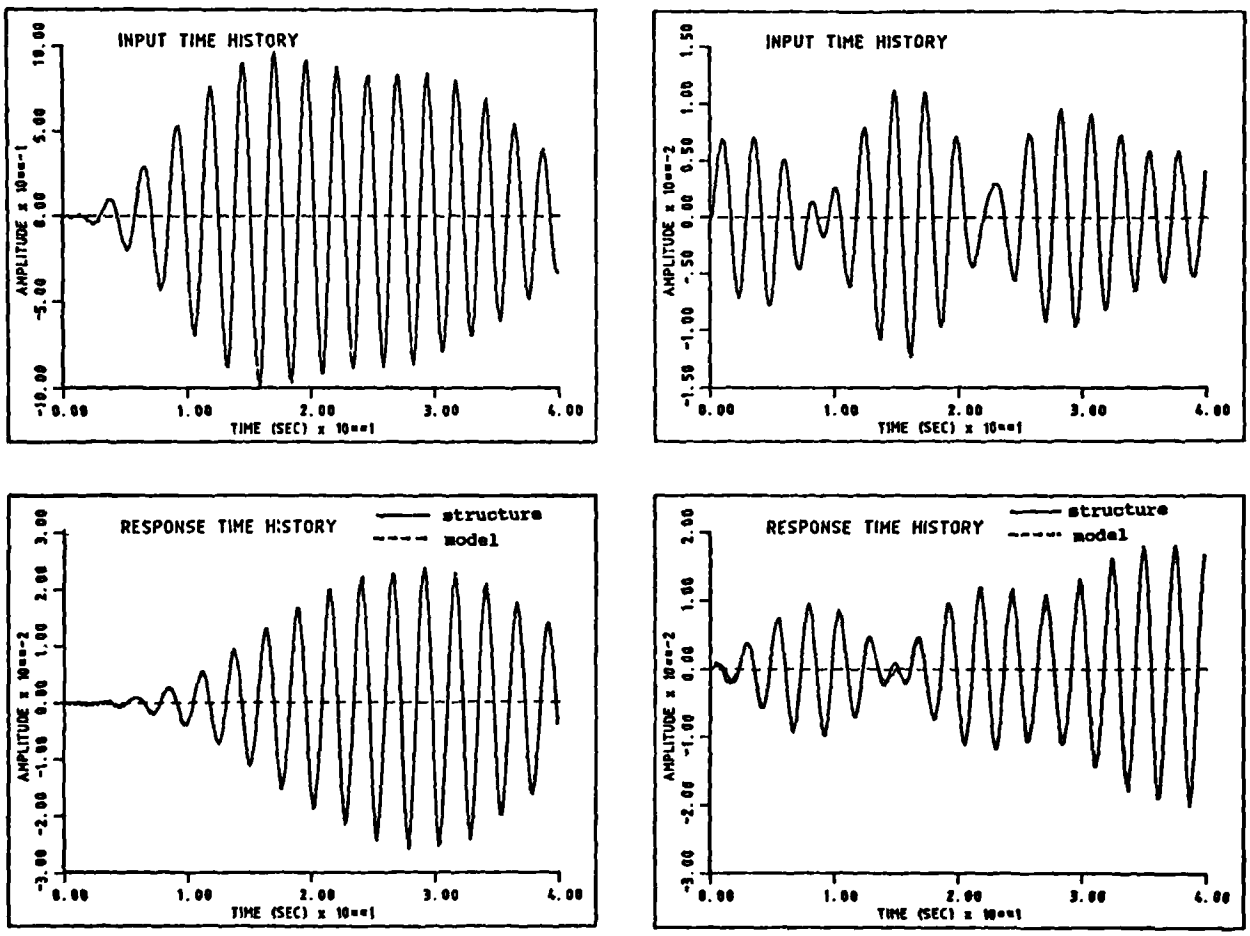

Figure 11: Comparison between responses of structure and steady-state model for sweep excitation

Figure 12: Comparison between responses of structure and steady-state model for random excitation

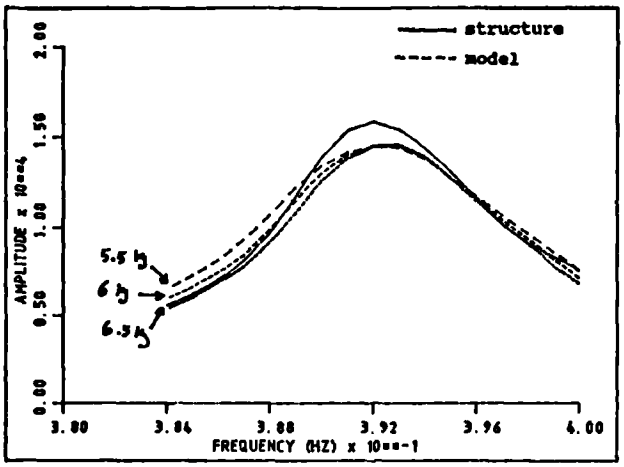

Figure 13: Comparison between FRFs generated using different mass values

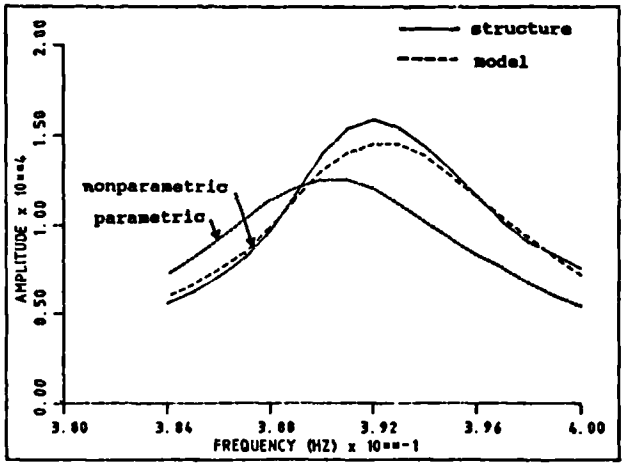

Figure 14: Comparison between FRFs generated using parametric and nonparametric approaches

Similar analysis was also carried out in conjunction with the adoption of parametric and nonparametric models. The FRFs corresponding to a parametric model, which included linear stiffness, linear damping, cubic stiffness and quadratic damping terms, and to a nonparametric model given in table [1.a], were generated for M = 6 kg and F = 5N and compared with the measured FRF given in Fig 14. It can be seen that the behaviour of the nonparametric model matches the behaviour of the test structure more closely.

4.3. Identification of Torsion Mode

For this mode the behaviour without oil in the dashpot was fairly similar to that seen in Fig. 3 for the bending mode, except that the natural frequency was around 76.0 Hz. However in this case the addition of oil made very little difference as might be expected since the dashpot was located at an effective antinode and the only mechanism for damping would be the plate moving more or less in its own plane in the oil. Unfortunately this meant that the damping was much lower than that for the bending mode. It can be shown that the force-state mapping process becomes much more sensitive to experimental error as the damping reduces and therefore poorer results might be expected.

As an example, Fig. 15 demonstrates the sensitivity of the damping estimate to the phase shift errors, between measured acceleration and force signals, with respect to frequency and critical damping. The Fig is generated for a simulated linear single degree of freedom system. It can be seen that for the lightly damped system (ξ = 1%, solid lines) the damping estimate, normalised with respect to the exact value, is very sensitive to the phase errors while for the second case (ξ = 5%, dashed lines) the damping estimate becomes much less sensitive to the same phase errors. Note also that the errors are more severe at higher frequencies; this may explain some of O'Donnell and Crawley's results [4] in which a negative

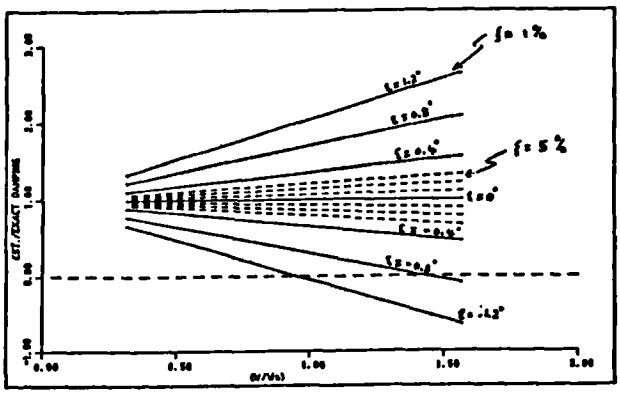

Figure 15: Sensitivity of damping estimate to phase-shift errors for simulated system

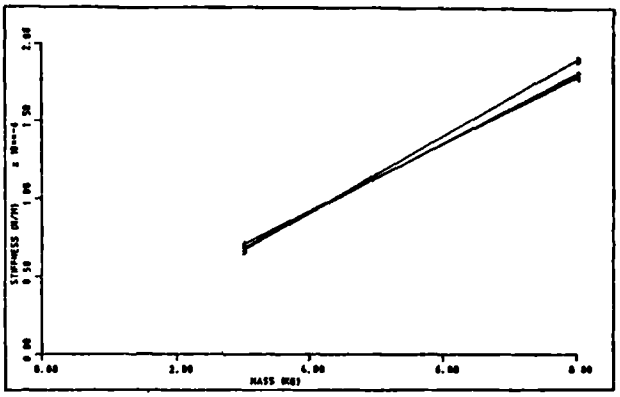

Figure 16: Mass estimation plot for torsion mode

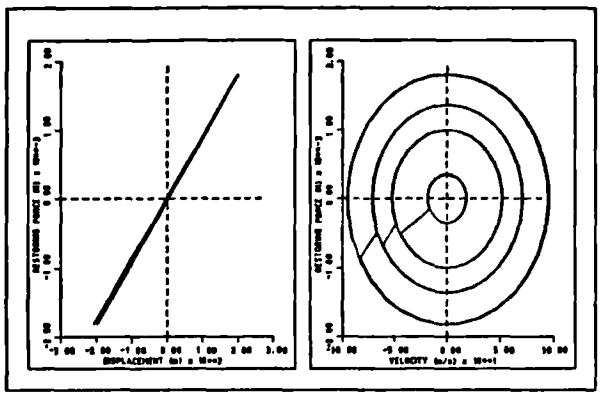

Figure 17: Force-state map projection generated at 4 force levels for torsion mode

damping was obtained at frequencies around and above the natural frequency for a linear system.

The initial effective mass estimate from a frequency response function measured at 3N was 4 kg. The intercept method described earlier was used again, this time for three frequencies (74, 75.5 and 79 Hz) each at four force levels and for assumed masses of 3 and 8 kg. The variation of stiffness with assumed mass is shown in Fig. 16. The intersections are at values 3.8, 4.3 and 5.5 kg and have an average of 4.5 kg. The scatter in values is believed to be larger due partly to the sensitivity problem and partly because the measured force near resonance at 75.5 Hz was corrupted by noise and harmonic content. Therefore the effective mass was taken to be equal to the 4 kg value estimated at low force level.

Some attempt was made to use sweep excitation to produce a map for fitting but difficulty was experienced in obtaining a leakage-free response due to the very low damping present; attempts to use time domain integration did not give good results.

Therefore the identification process was restricted to the steady state excitation case. It was found that increasing the number of points per cycle from 32 to 512 seemed to improve the identification results since the phase shift error intoduced by the mismatch in the anti-aliasing filters was smaller.

A typical force-state map projection for 74 Hz and four force levels is shown in Fig. 17. It is narrower than the corresponding result for the bending mode, reflecting the lower damping, but still the nonlinear stiffness is not obvious since it is a very small proportion of the linear stiffness. A typical fitted model is shown in Table [1.c] In this case the softening stiffness is apparent again but the nonlinear damping is much smaller as might be expected. The other nonlinear terms have only a small contribution.

Finally a comparison of frequency response functions obtained from the

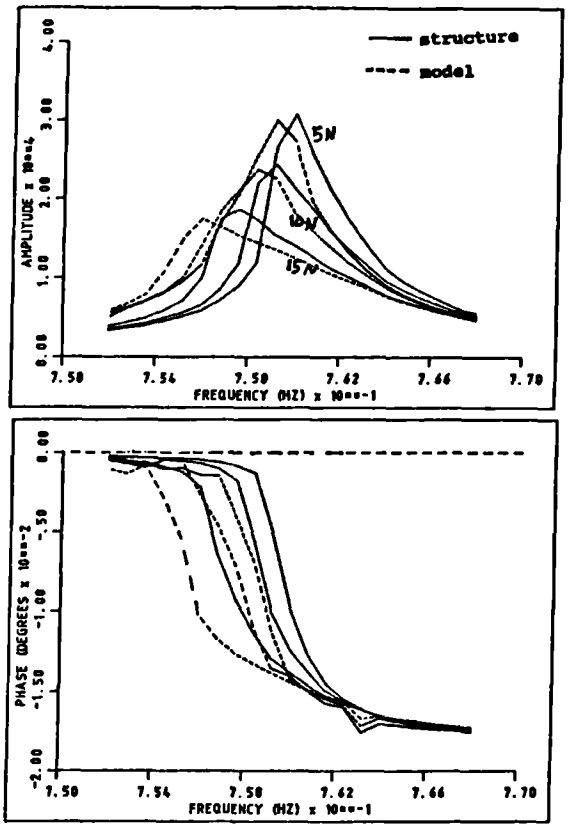

Figure 18: Comparison between FRFs of structure and model for torsion mode

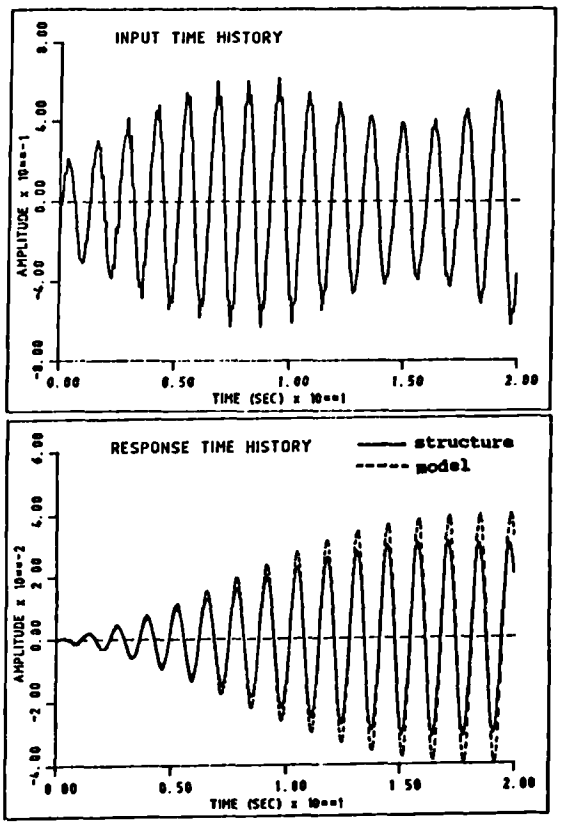

Figure 19: Comparison between responses of structure and model for random excitation

structure and fitted model are shown in Fig. 18; the agreement is not as good as for the bending mode, probably because it is very sensitive to the damping obtained. A sample comparison of structure and model responses to a random excitation is shown in Fig. 19. The apparent disagreement is believed to be due to the frequency shift between the FRFs of the structure and the model. This can be seen in Fig. 18 where at a particular frequency the difference between the amplitudes of the structure and the model is significant though the shape of the curves is reasonable.

For this mode the model obtained was fair but clearly the identification of very lightly damped structures is more sensitive, a feature known from even linear identification.

5. Conclusions

In this paper some experimental results from application of the force-state mapping approach to a T-beam structure have been presented. Mathematical models able to represent the nonlinear behaviour of the well separated bending and torsion modes were obtained. Quite good agreement between the models and the structure for different inputs was illustrated but the method becomes more sensitive for low damping. An approach for estimating the effective mass of each mode was also illustrated. The application to two closely spaced modes has yet to be presented.

Table 1: Identified models of bending and torsion modes

Model used:

$$f(x,\dot{x}) = a_0 + a_1 x + a_2 \dot{x} + a_3 x\dot{x} + a_4 x^2 + a_5 \dot{x}^2 + a_6 x^2\dot{x} + a_7 x\dot{x}^2 + a_8 x^3 + a_9 \dot{x}^2 \,\mathrm{sign}(\dot{x})$$

A. Bending mode (steady-state model, 38 Hz, 20, 40 & 80 N, m=6 ,G=0.986)*

Term	a_0	a_1	a_2	a_3	a_4	a_5	a_6	a_7	a_8	a_9
Identified terms	-1.39	3.6E5	6.1	1.2E4	1.7E6	-28.8	1.8E6	-1.1E4	-3.3E8	67
R.M.S. contbn.+(%)	0.16	90.46	0.3	1.36	1.28	1.28	0.51	0.77	0.83	2.98

B. Bending mode (sweep model, m=6 ,G=0.963)

Term	a_0	a_1	a_2	a_3	a_4	a_5	a_6	a_7	a_8	a_9
Identified terms	-.159	3.6E5	1.3	6.6E3	2.6E6	-41.7	1.09E6	-1.8E4	-5.6E8	71
R.M.S. contbn. (%)	0.03	92.48	.08	0.51	1.43	1.38	0.16	0.71	0.78	2.4

C. Torsion mode (steady-state model,75.5 Hz, 5, 8, 10 & 15 N, m=4, G=.97)

Term	a_0	a_1	a_2	a_3	a_4	a_5	a_6	a_7	a_8	a_9
Identified terms	2.38	9.1E5	.47	6.8E3	-9.E5	-3.17	-2.8E6	-1.9E3	-2.9E9	15
R.M.S. contbn. (%)	0.25	97.	.02	0.30	0.15	0.11	0.16	0.52	0.81	.56

* G stands for goodness of fit (max=1)
+ contribution

References

1. S.F. Masri and T.K. Caughey. 1979 Journal of Applied Mechanics 46, pp 433-447. A non-parametric identification technique for nonlinear dynamic problems.

2. S.F. Masri, H. Sassi and T.K. Caughey. 1982 Journal of Applied Mechanics 49, pp 619-627. Non-parametric identification of nearly arbitrary nonlinear systems.

3. E.F. Crawley and A.C. Aubert. 1986 AIAA Journal vol 24, pp 155-162. Identification of nonlinear structural elements by force-state mapping.

4. K.J. O'Donnell and E.F. Crawley. MIT Space System Laboratory report. SSL #16-85. Identification of nonlinear system parameters on space structure joints using the force-state mapping technique.

5. K. Worden and G.R. Tomlinson. 6th IMAC 1988, pp 1471-1479.Developments in force-state mapping for nonlinear systems.

6. K. Worden and G.R. Tomlinson. 7th IMAC 1989, pp 1347-1351. Application of the restoring force surface method to nonlinear elements.

7. M.A. Al-Hadid and J.R. Wright. Developments in the force-state mapping technique for nonlinear systems and the extension to the location of nonlinear elements in a lumped parameter system. accepted for publication in the Journal of Mechanical Systems and Signal Processing.

8. N.F. Hunter, T. Paez & D.L. Gregory. 7th IMAC 1989, pp 843-849
Force state mapping using experimental data.

9. Y. Yang and S.R. Ibrahim. Journal of Vibration, Acoustics, Stress and Reliability in Design, vol.107, pp 60-66. A non- parametric identification technique for a variety of discrete nonlinear vibrating systems.

Mechanical Systems and Signal Processing (1989) 3(3), 269-290

DEVELOPMENTS IN THE FORCE–STATE MAPPING TECHNIQUE FOR NON-LINEAR SYSTEMS AND THE EXTENSION TO THE LOCATION OF NON-LINEAR ELEMENTS IN A LUMPED-PARAMETER SYSTEM

M. AJJAN AL-HADID AND J. R. WRIGHT

Department of Aeronautical Engineering, Queen Mary College, Mile End Road, London E1 4NS, U.K.

(*Received June* 1988, *accepted June* 1989)

The implementation of the force-state mapping approach of Masri and Caughey to the identification of single- and multi-degree-of-freedom non-linear systems is considered. In particular it is shown that the use of two-dimensional orthogonal polynomials is unnecessarily restrictive and that a simpler approach based on ordinary polynomials and special functions provides a faster and more accurate identification for polynomial and non-polynomial types of non-linearity. The procedure for multi-degree-of-freedom systems is simplified. A method for identifying the type and location of discrete non-linear elements in a lumped-parameter system is presented.

1. INTRODUCTION

The identification of mathematical models to represent dynamic systems has attracted considerable attention in recent years. Most of the effort has been directed towards linear systems but interest in non-linear systems has been increasing. Some methods, such as the Hilbert transform [1], seek to indicate the presence of non-linearity in the system and in some circumstances can also give an idea of the type of non-linearity. Other approaches, such as the Volterra/Weiner series and non-linear autoregressive moving average model representations [1], aim to identify the system behaviour in a functional or non-parametric form i.e. the model does not easily yield physical parameters of the system but rather should behave in a similar way to the true system when subjected to a different input.

An interesting technique for non-linear identification has been suggested by Masri and Caughey [2]. Given an estimate of the system mass, the restoring force is represented by a surface over the velocity–displacement plane and a fit to the surface carried out using an orthogonal polynomial series expansion. The method is said to be non-parametric and to have advantages over other methods [2]. Masri and Caughey have also shown how the approach may be extended to multi-degree-of-freedom systems [3], yielding a model in modal space. They have applied the method to simulated lumped-parameter systems, representative of certain types of civil engineering structures.

In an independent study, Crawley *et al.* [4, 5] have developed a variant of the Masri/Caughey single-degree-of-freedom approach for investigation of joints in space structures. They used a least squares algorithm for the curve-fitting process, not involving orthogonal polynomials. This force-state mapping, as it is appropriately called, has been applied to experimental data from an idealised test article. Yang and Ibrahim [6] have also used ordinary polynomials, referred to relative velocities and displacements, for identification. It is of interest to note that Hammond *et al.* [7] have recently shown a

0888-3270 89 030269+22 $03.00 0

different way of obtaining restoring force surfaces using an approach based on optimal control theory.

The potential of the force-state mapping method for identification of single- and multi-degree-of-freedom non-linear modal systems has attracted attention from other researchers, namely Worden and Tomlinson [8, 9] and Argoul [10]. So far their published work has focused upon the implementation of the orthogonal polynomial curve-fitting process and will be discussed later.

In this paper, the curve fitting procedure involved in the force-state mapping approach will be considered. In particular, the use of orthogonal and ordinary polynomials will be compared. The ordinary polynomial approach will be seen to have a number of advantages over the orthogonal polynomial approach for this application in that it is more accurate, it allows inclusion of special functions to model non-polynomial types of non-linearity such as friction, clearance etc. and it simplifies the identification of multi-degree-of-freedom systems.

Finally, an approach for identifying not only the type but also the *location* of discrete non-linearities within lumped parameter systems will be introduced. The idea arose from releasing the constraint of using two-dimensional orthogonal polynomials. The authors are not aware of any published work in which a method for location of non-linearity in a multi-degree-of-freedom system is presented.

2. BASIC PHILOSOPHY OF THE FORCE-STATE MAPPING APPROACH FOR A SINGLE-DEGREE-OF-FREEDOM SYSTEM

The equation of motion of the single-degree-of-freedom non-linear system shown in Fig. 1 may be written as

$$m\ddot{x}+f(\dot{x}, x)=p(t), \tag{1}$$

where m is the mass, $\ddot{x}$ is the acceleration, $p(t)$ is the applied force and $f(\dot{x}, x)$ is the restoring force which contains both the linear and non-linear parts of the system and is a function of the velocity $\dot{x}$ and displacement x. For a linear system,

$$f(\dot{x}, x)=c\dot{x}+kx, \tag{2}$$

where c is the viscous damping constant and k is the stiffness.

The aim of the non-parametric identification approach being considered is to express the restoring force as a mathematical function of $\dot{x}$ and x, which can be referred to as the states of the system, by some curve-fitting process. In order to carry out such a curve fit it is necessary to obtain $f(\dot{x}, x)$, $\dot{x}$ and x as functions of time. In practice, test data is digitised and so the three values must be available at the same sampling instants. It is possible to rearrange equation (1) into the form

$$f(\dot{x}, x)=p(t)-m\ddot{x}, \tag{3}$$

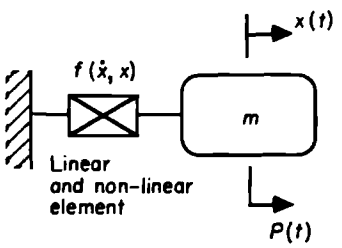

Figure 1. Single-degree-of-freedom non-linear system.

and thus it can be seen that an estimate of the restoring force may be obtained if the acceleration and force signals are measured for a particular test and if a good estimate of the mass is available. The velocity and displacement may be found by direct measurement [4] or by careful integration of the acceleration [5, 9].

In principle, any excitation may be used (for example random or sine sweep) so long as it is persistently exciting and large enough to excite any non-linearity present in the system.

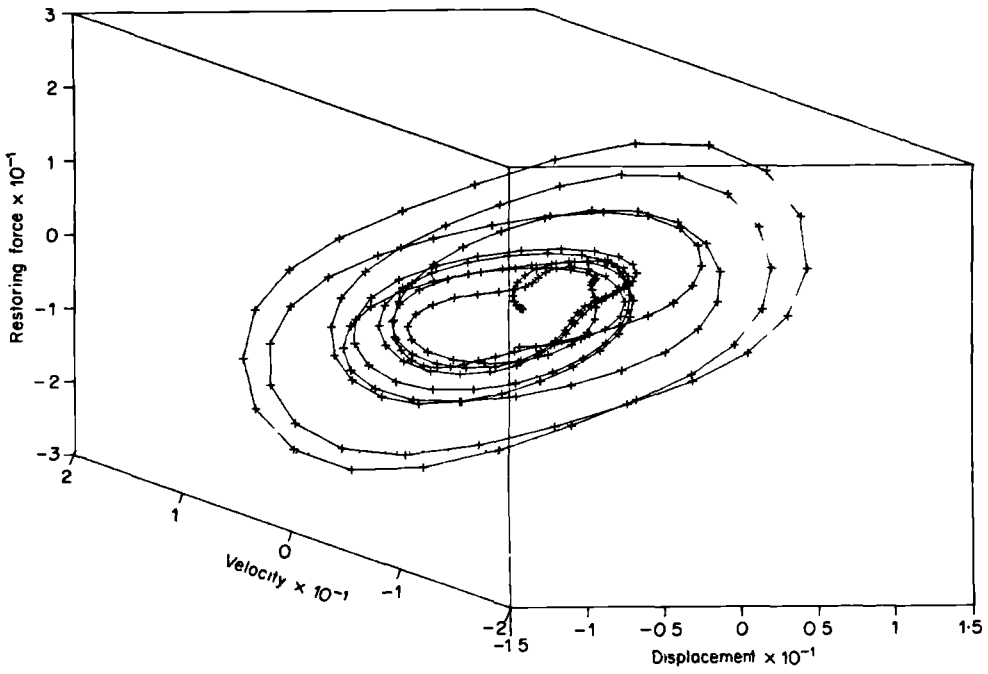

Figure 2. Force-state map of the raw data for a 1 dof system with cubic non-linearity.

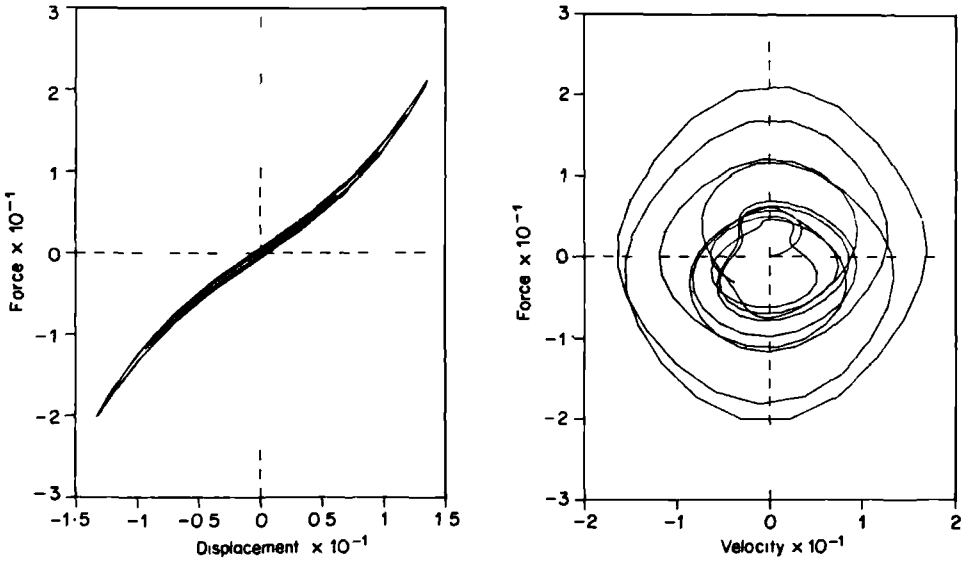

Figure 3. Projection of the map in Fig. 2 onto the force-displacement and force-velocity planes.

Once a sufficient number of values of the restoring force, velocity and displacement have been obtained at discrete times, the particular characteristics of the non-linearity may be seen by plotting $f(\dot{x}, x)$ against $\dot{x}$ and x in a three-dimensional form called a force-state map [4, 5], as shown in Fig. 2. It is often particularly helpful for lightly damped systems to plot the projection of the map onto the force-displacement plane as shown in Fig. 3. The force-velocity projection shown is not usually as useful. It has been shown that the shapes of the force-state map are unique and recognisable for most structural non-linearities. This feature will be illustrated later by examples.

3. CURVE FITTING THE RESTORING FORCE

Once the restoring force $f(\dot{x}, x)$, velocity $\dot{x}$ and displacement x are obtained as a set of values at discrete time instants, it remains to fit a suitable mathematical model for the restoring force.

3.1. MASRI/CAUGHEY APPROACH USING CHEBYCHEV POLYNOMIALS

The approach adopted by Masri and Caughey in their development of this non-parametric identification procedure [2] is to approximate the restoring force $f(\dot{x}, x)$ by a function expressed in terms of two-dimensional orthogonal polynomials. Thus

$$f(\dot{x}, x) \approx \hat{f}(\dot{\bar{x}}, \bar{x}) = \sum_{i=0}^{mv} \sum_{j=0}^{md} C_{ij} T_i(\dot{\bar{x}}) T_j(\bar{x}), \tag{4}$$

where T_i, T_j are Chebychev polynomials and C_{ij} are unknown coefficients to be determined by a least squares curve-fitting procedure. The values $\dot{\bar{x}}$ and $\bar{x}$ are velocity and displacement normalised to the region $[-1, +1]$. Chebychev polynomials were chosen because of their orthogonal property which meant that additional terms could be introduced into the series in equation (4) without needing to recompute earlier coefficients. An additional feature was the equal ripple approximation for the error.

The mathematical derivation of the curve fit procedure has been covered in several references [2, 8] and so will not be repeated in detail here. However the practical implementation of a Chebychev polynomial representation of the restoring force has several significant drawbacks which are important and will be discussed below.

(i) Since the normalisation process will usually involve an effective change of origin, any odd or even behaviour of the function to be fitted will be lost and also the resulting polynomial is not easy to interpret unless it is rewritten in terms of the original variables.

(ii) Because a weighting function is involved in the orthogonality integrals for the Chebychev polynomials, the data must be transformed from the $[\dot{\bar{x}}, \bar{x}]$ plane to the $[\phi, \theta]$ plane using $\phi = \arccos(\dot{\bar{x}})$ and $\theta = \arccos(\bar{x})$. The numerical integration procedure used in obtaining the coefficients C_{ij} requires restoring force data at equal intervals within the $[\phi, \theta]$ plane. In principle this requires both interpolation and extrapolation in two dimensions, the latter introducing potentially serious errors. The problem is exaggerated because the arccosine transformation makes the proportion of the plane over which extrapolation is required increase significantly. For example, in the linear case the proportion changes from around 21% for the $[\dot{\bar{x}}, \bar{x}]$ plane to around 50% for the $[\phi, \theta]$ plane as seen in Figs 4 and 5. Moreover, it is found that a significant number of integration points are required for adequate accuracy in the double integration, even for a simple linear surface.

Although the method is fairly time consuming, the requirement for interpolation and extrapolation is by far the most important disadvantage associated with the use of

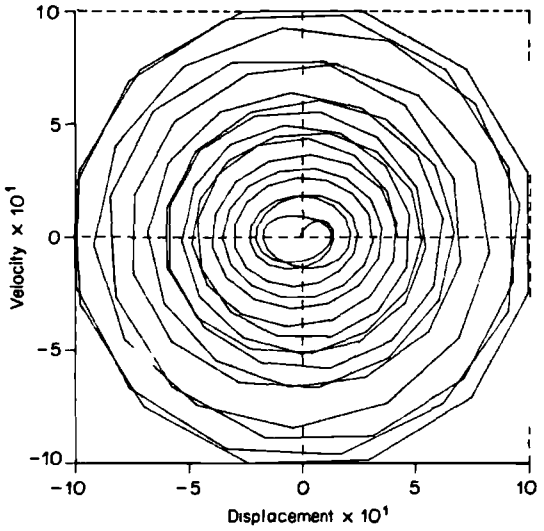

Figure 4. Projection of the force surface onto the $[\dot{x}, x]$ plane for a 1 dof linear system.

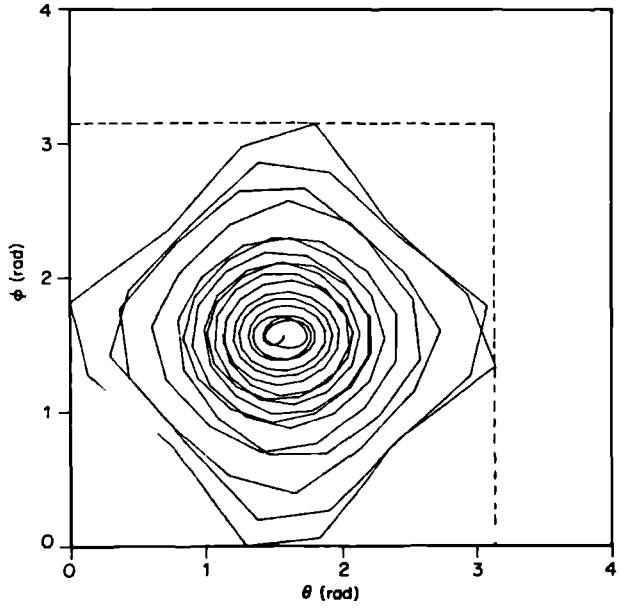

Figure 5. Projection of the force surface onto the $[\phi, \theta]$ plane for a 1 dof linear system.

Chebychev polynomials for this particular application. In fact, interpolation in the regions covered by measured data should be fairly accurate. However extrapolation into the empty corner regions in Fig. 5, in order to obtain equispaced data points for integration, will clearly give opportunity for significant errors to be introduced.

Masri and Caughey do not specify which two-dimensional interpolation scheme they use, but their extrapolation procedure [2] is based on the assumption that

$$f(\dot{x}, x) = f_D(\dot{x}) + f_S(x) \tag{5}$$

is a valid approximation. This assumption of no coupling between $\dot{x}$ and x is probably not too unreasonable in practice but it would not apply to the Van der Pol oscillator, for

example. Single-dimensional series expansions are found for $f_D(\dot{x})$ and $f_S(x)$ by using data in narrow bands around $\dot{x}=0$ and $x=0$ respectively. Worden and Tomlinson [7] describe a simple modification to this technique to account for a restoring force offset at the origin.

Worden and Tomlinson [7, 8] use an interpolation procedure for the irregularly spaced points based on the construction of the Dirichlet tesselation and the associated Delaunay triangulation. The process is rather involved and time consuming. Because it will not cope with extrapolation, the data zone has to be reduced until there are no empty corner regions. Obviously normalisation must then be referred to this reduced data area. There is clearly a major disadvantage in this procedure since a large quantity of data may be rejected and it is the very data associated with the significant non-linear excursions. It would then be expected that the fitted mathematical model would suffer in accuracy.

Argoul [9] has also implemented the method using Chebychev polynomials but has adopted an iterative approach to the extrapolation procedure. A function is first fitted within the reduced data region used by Worden and Tomlinson. The function is then used to extrapolate into a somewhat larger region and the fit repeated to update the function. Eventually the whole data area is covered. Argoul claims better results than Masri and Caughey for the Van der Pol example.

In the work carried out by the present authors on the Chebychev representation, a simpler approach was adopted for the interpolation and extrapolation. No data were discarded. Instead the $[\phi, \theta]$ plane was divided up into a number of equal size square "bins". Within each bin a two-dimensional fit using an ordinary polynomial series of first, second or third order was used to fit the restoring force. The resulting functions were used to generate equi-spaced data values for the subsequent Chebychev fit. The number of bins (typically 4–9) was chosen to ensure sufficient data points within each bin. The procedure worked fairly well as will be seen later when some examples are considered.

3.2. ORDINARY POLYNOMIAL APPROACH

In essence Crawley *et al.* [4, 5] and Yang and Ibrahim [6] made use of ordinary polynomials for fitting the restoring force. It is worth comparing the use of Chebychev and ordinary polynomials because it is believed that the former has provided an unnecessary restriction upon the identification process for this application which has limited several workers in this field, including the authors.

The series representation uses ordinary polynomials with powers of $\dot{x}$ and x, namely

$$f(\dot{x}, x) \approx \hat{f}(\dot{x}, x) = \sum_{i\ 0}^{mv} \sum_{j\ 0}^{md} A_{ij} \dot{x}^i x^j, \tag{6}$$

where A_{ij} are unknown coefficients. The series is then fitted directly to the $f(\dot{x}, x)$, $\dot{x}$ and x data by a linear least squares process. This is simple and rather obvious but nevertheless will be seen to be an important modification to the implementation of Masri and Caughey's idea. It is believed that the use of Chebychev polynomials has been an unnecessary restriction which has limited other workers in this area as well as the authors.

There are a number of advantages to using ordinary polynomials for this particular application, namely

(i) there is no need to extrapolate or interpolate because equispaced data points are not required,

(ii) all the data can be used,

(iii) the process is much faster and has lower computer storage requirements,

(iv) the series produced is easier to interpret, and
(v) odd or even behaviour of the restoring force function is preserved.

The absence of extrapolation and interpolation errors means that a better "goodness of fit" is achieved. However, a main feature which might be argued to be a disadvantage is that the terms in the series are not orthogonal. This means that the entire calculation has to be repeated when the number of terms in the series is modified. In fact the fit in the ordinary polynomial case is so much faster that this is not really a problem. A more serious feature of this lack of orthogonality is that ill-conditioning of the least squares solution can become a problem when the number of terms in the series is large. The likelihood of ill-conditioning occurring can be reduced by

(a) simple normalisation of the data by dividing through by maximum values,
(b) selection of odd or even powers of $\dot{x}$ or x in the series if appropriate, in order to reduce the number of terms in the fit, and
(c) the use of singular value decomposition [11] to solve the overspecified set of equations obtained in the least squares process.

3.3. THE USE OF SPECIAL FUNCTIONS

There is a further benefit to the simple approach in section 3.2. Because each Chebychev polynomial is essentially an ordinary polynomial series expansion (eg. $T3(x)=4x^3-3x$), then only polynomial type non-linearities such as cubic stiffness can be accurately represented. Non-polynomial non-linearities such as friction, velocity squared damping and piecewise stiffness (e.g. deadspace) can only be approximated by using a significant number of terms in the series. The result is then essentially non-parametric.

However, removing the Chebychev restriction allows the ordinary polynomial expansion of equation (6) to be rewritten more generally as

$$f(\dot{x}, x)=\hat{f}(\dot{x}, x)=\sum_{i=0}^{N} B_i F_i(\dot{x}, x) \tag{7}$$

where B_i are unknown coefficients and $F_i(\dot{x}, x)$ are basis functions that not only include the ordinary polynomial power terms (e.g. $1, x, \dot{x}, x^2, x\dot{x}\ldots$ etc.) but can also be special functions chosen to represent non-polynomial non-linearities.

A velocity-squared damping term could be represented by

$$F_j(\dot{x}, x)=\dot{x}^2 \operatorname{sgn}(\dot{x}) \tag{8}$$

and a Coulomb friction term by

$$F_k(\dot{x}, x)=\operatorname{sgn}(\dot{x}) \text{ or } \dot{x}/|\dot{x}|. \tag{9}$$

A piecewise non-linearity such as a deadspace of $x=\pm d$ would require

$$\begin{aligned} F_l(\dot{x}, x)&=0 && \text{for } |x| \leqslant d, \\ &=(x-d\cdot \operatorname{sgn}(x)) && \text{for } |x|>d, \end{aligned} \tag{10}$$

and clearly a value of d would need to be estimated from the force-state map. Other non-linearities may be dealt with in a similar way, except for memory dependent hysteresis. The curve fitting of such non-polynomial non-linearities has also been illustrated by Crawley *et al.* [4, 5].

Later in this paper it will be shown that the rejection of the Chebychev polynomial approach opens new possibilities for multi-degree-of-freedom identification.

4. SINGLE-DEGREE-OF-FREEDOM EXAMPLES

Several of the single-degree-of-freedom examples chosen are those used by Masri and Caughey [2].

4.1. LINEAR CASE

The parameters of the linear part of the model given in equation (1) and (2) are chosen to be

$m = 1$ kg (assumed known),

$c = 0{\cdot}1$ N/m/s (5% critical damping),

$k = 1$ N/m (undamped natural frequency 0·159 Hz),

and therefore the exact restoring force is given by

$$f(\dot{x}, x) = 0{\cdot}1\,\dot{x} + x.$$

The system was excited by a sinusoidal frequency sweep over the range 0·1 to 0·2 Hz in 128 sec, yielding 512 data points when sampled at 0·25 sec intervals. The force level was 1 N peak. This excitation was intended to be very similar to that in reference [2] around the resonant region, but did not extend over such a wide frequency range in order to reduce memory requirements. The response was obtained numerically using a fourth order Runge-Kutta integration and 256 data points of each of $\ddot{x}$, $\dot{x}$ and x emerged from the simulation.

The parameters obtained from several different approaches are shown in Table 1. The approaches refer to:

(a) Results deduced from the Chebychev coefficients obtained by Masri and Caughey [2] (an interpolation and extrapolation over a 100×100 grid was used).

(b) Results obtained from the Chebychev fit using fitting within bins to interpolate/extrapolate the data.

(c) Results obtained from the ordinary polynomial fit to the raw data, outlined in section 3.2.

The "goodness of fit" G is defined by reference to the measured data points as

$$G = 1 - (\text{rms error in fit/rms restoring force}) \tag{11}$$

and will have a value of 1·000 for a perfect fit.

The timings refer to the minicomputer used and are quoted to allow comparison of Chebychev and ordinary polynomial approaches.

The results in Table 1 indicate an improvement in the Chebychev fit when the alternative extrapolation approach was used. Also the ordinary polynomial results are more accurate and take considerably less time.

4.2. NON-LINEAR CASES

The above process was carried out for several different non-linear systems in turn, there being slight differences in the linear part of each system, the force level used and the sweep range.

TABLE 1

Parameters identified for linear case

Approach	Description	C	k	Goodness of fit	Time (sec)
—	Exact values	0·100	1·000	—	—
A	Chebychev polynomials $mv = nd = 2$ (ref [2])	0·082	0·999	0·923	—
B	Chebychev polynomials (alternative approach)	0·103	1·030	0·969	288
C	Ordinary polynomials	0·100	1·000	1·000	4

4.2.1. *Cubic hardening stiffness*

In this case the stiffness restoring force component includes a term which varies with the cube of the displacement, so that

$$m\ddot{x} + c\dot{x} + kx\beta x^3 = p(t). \tag{12}$$

In this example the exact restoring force was chosen to be

$$f(\dot{x}, x) - 0{\cdot}04\dot{x} + x + 0{\cdot}003x^3$$

and the sweep from 0·1 to 0·3 Hz used 4 N peak force.

Various views of the force-state map for the raw data are shown in Figs 2 and 3, as seen earlier. The fitted surface is shown in Fig. 6 and shows a characteristic shape. The identified parameters are presented in Table 2 where a similar behaviour is seen as in the linear case.

4.2.2. *Van der Pol oscillator*

This rather unusual non-linearity has become a fairly classical case for investigating non-linear identification schemes since velocity and displacement are coupled via an

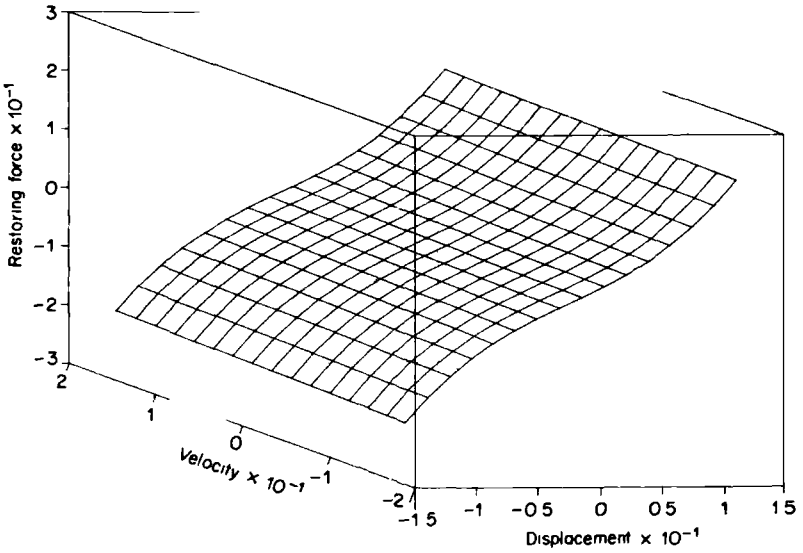

Figure 6. Force-state map of the fitted model of a 1 dof system with cubic stiffness non-linearity.

TABLE 2

Parameters identified for the cubic stiffness case

Approach	Description	C	k	β	Goodness of fit	Time (sec)
—	Exact values	0·04	1·000	0·003	—	—
A	Chebychev polynomials *mv* 2, *md* – 4 (ref. [2])	0·043	0·975	0·00296	0·991	—
B	Chebychev polynomials (alternative approach)	0·0404	1·008	0·003	0·993	672
C	Ordinary polynomials	0·04	1·000	0·003	1·000	8

amplitude dependent damping force. The equation of motion is

$$m\ddot{x} + \varepsilon(x^2 - 1)\dot{x} + kx = p(t). \tag{13}$$

The exact restoring force for this example was chosen to be

$$f(\dot{x}, x) = -0{\cdot}2\dot{x} + 0{\cdot}2x^2\dot{x} + x$$

and the sweep from 0·1 to 0·3 Hz used 4 N peak force.

This is a particularly difficult identification because if all the data are to be used, then there is a large amount of extrapolation necessary, as seen in Fig. 7. As might be expected, the ordinary polynomial fit only required three terms in the series and yielded almost the exact surface ($G = 0{\cdot}9999$), shown in Fig. 8.

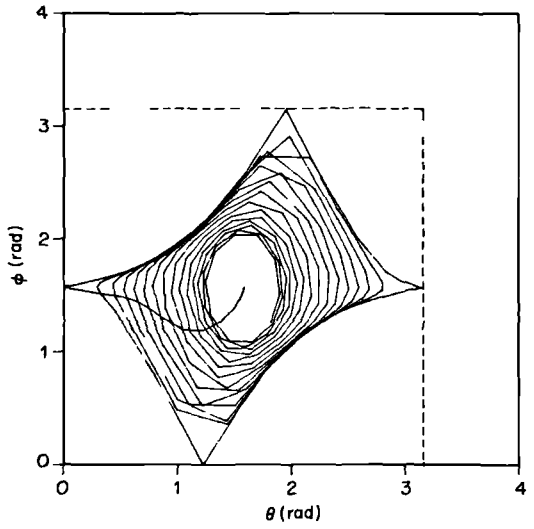

Figure 7. Projection of the force surface onto the $[\phi, \theta]$ plane for Van der Pol oscillator.

However, the results obtained using the Chebychev representation were rather poor due to extrapolation errors. The surface of interpolated and extrapolated values, shown in [2], displayed severe undulations which required a high-order model to provide a reasonable quality of fit. Indeed a total of 64 Chebychev coefficients had to be evaluated in order to achieve the fit shown in Fig. 9, generated from the results in [2]. It is clear that this differs significantly from the exact surface.

The equivalent 64-term Chebychev result using the alternative extrapolation procedure described in section 3.1 gave a much more realistic fit, as seen in Fig. 10. It is clear from the examples shown that the ordinary polynomial approach seems superior to the Chebychev representation in many ways and that the advantages outweigh the orthogonality and error ripple properties of the Chebychev polynomials in this particular application.

The remaining examples illustrate the use of special functions to identify non-polynomial non-linearities.

4.2.3. *Velocity squared (or quadratic) damping*

This type of damping may arise due to the action of fluid drag forces upon a body. The equation of motion is

$$m\ddot{x} + c\dot{x} + \eta\dot{x}^2 \operatorname{sgn}(\dot{x}) + kx = p(t). \tag{14}$$

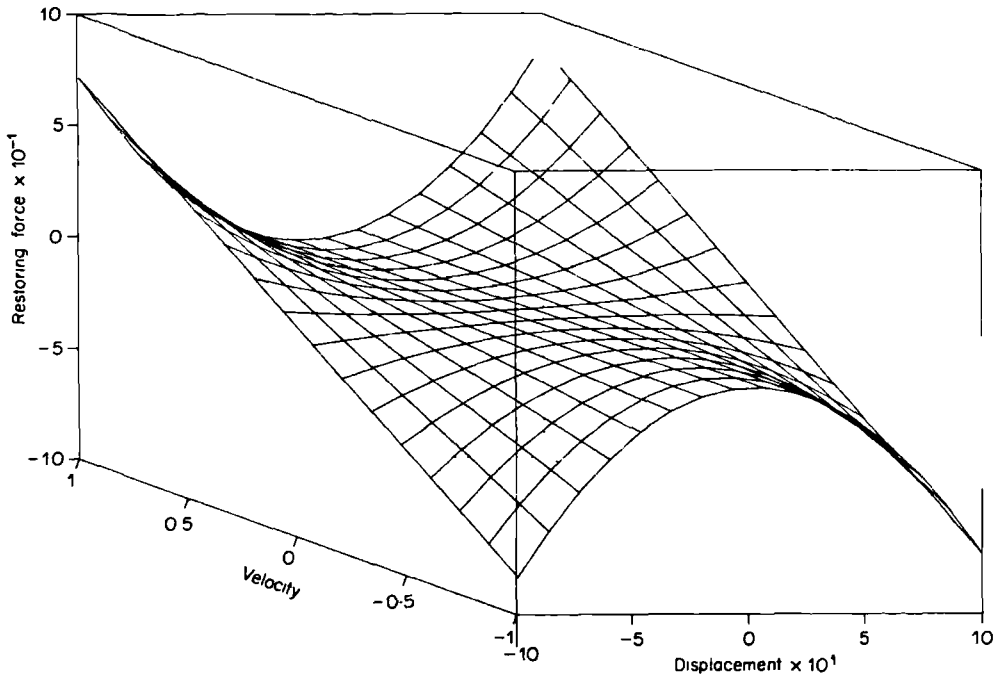

Figure 8. Exact force-state map of Van der Pol oscillator.

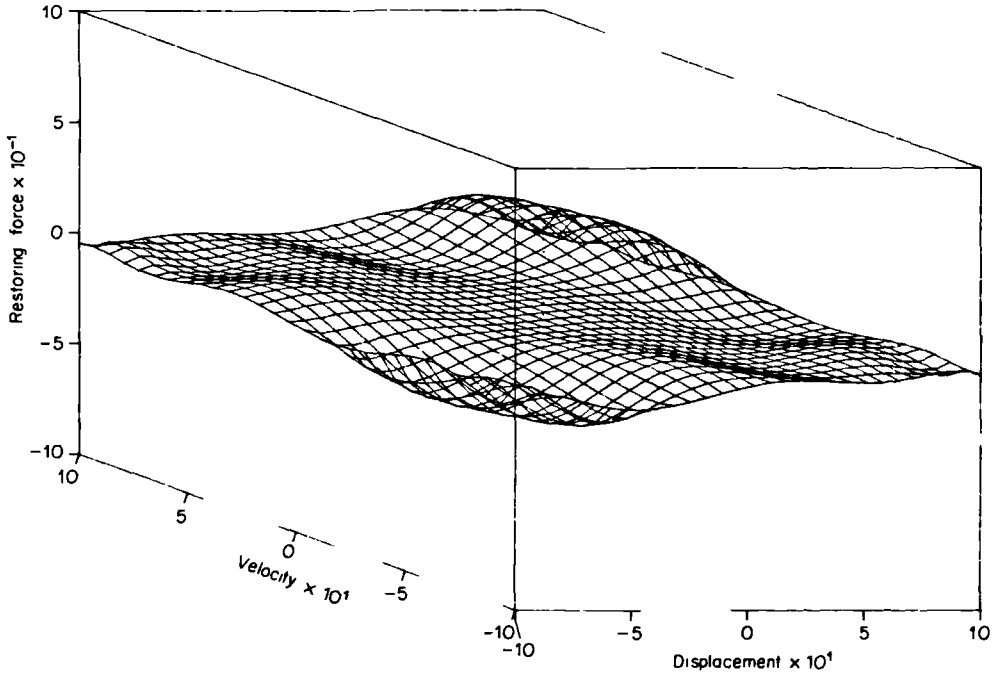

Figure 9. Force-state map of the fitted model of Van der Pol oscillator given in [2].

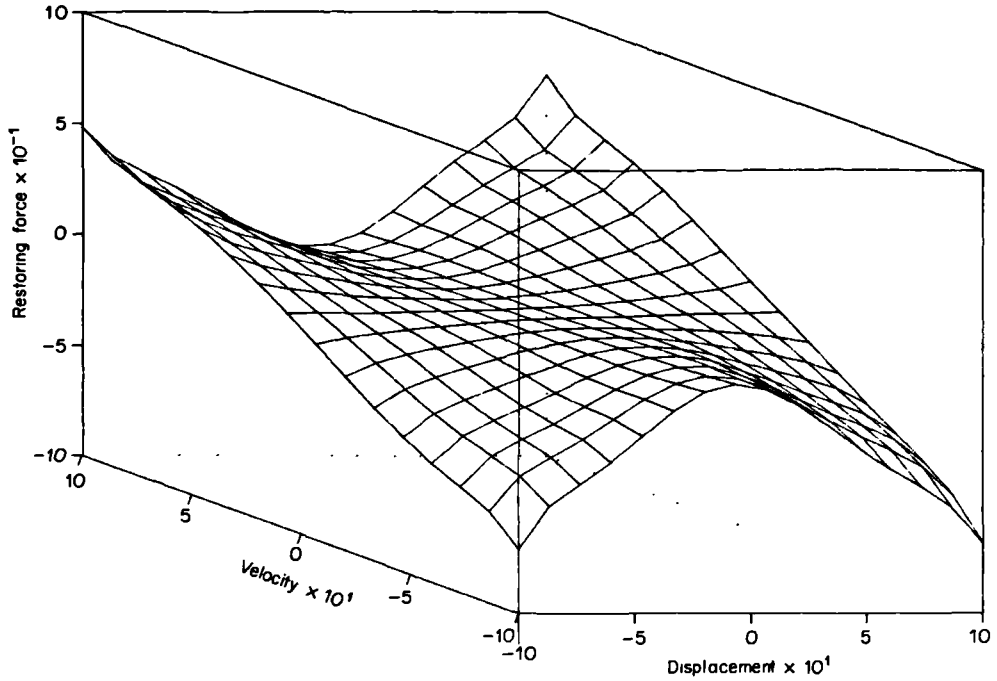

Figure 10. Force-state map of the fitted model of Van der Pol oscillator obtained using the alternative extrapolation procedure.

The exact restoring force for this example was chosen to be

$$f(\dot{x}, x) = 0{\cdot}04\dot{x} + 0{\cdot}04\dot{x}^2 \operatorname{sgn}(\dot{x}) + x$$

and a sweep excitation from 0·1 to 0·3 Hz was used with 2·8 N peak force.

The force-displacement variation for the raw data is shown in Fig. 11. Unlike previous plots, the damping is significant and makes this projection of the map more difficult to interpret. The identified parameters using a special function are obtained almost exactly ($k = 1$, $c = 0{\cdot}04002$, $\eta = 0{\cdot}039997$).

4.2.4. *Coulomb friction*

This common non-linearity leads to the single-degree-of-freedom equation of motion

$$m\ddot{x} + c\dot{x} + \alpha \operatorname{sgn}(\dot{x}) + kx = p(t), \tag{15}$$

where α is the friction force. In this example,

$$f(\dot{x}, x) = 0{\cdot}04\dot{x} + 0{\cdot}08 \operatorname{sgn}(\dot{x}) + x$$

and a sweep excitation from 0·1 to 0·3 Hz with 0·14 N peak was used.

The force-displacement and force-velocity variations for the raw data are shown in Fig. 12. The combination of friction and the stiffness restoring force gives rise to the classic hysteresis loop and the force-velocity variation also shows up the presence of friction.

The identified parameters using a special function are again obtained almost exactly ($c = 0{\cdot}04242$, $\alpha = 0{\cdot}0794$, $k = 1{\cdot}00001$) and the fitted map is shown in Fig. 13. Note that a large number of polynomial terms would have been required to give a reasonable fit to the step in the map.

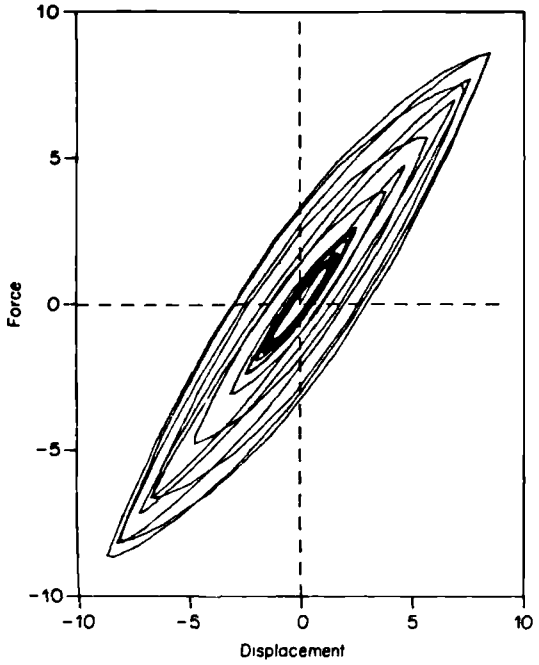

Figure 11. Projection of the force surface onto the force-displacement plane for a 1 dof system with quadratic damping non-linearity.

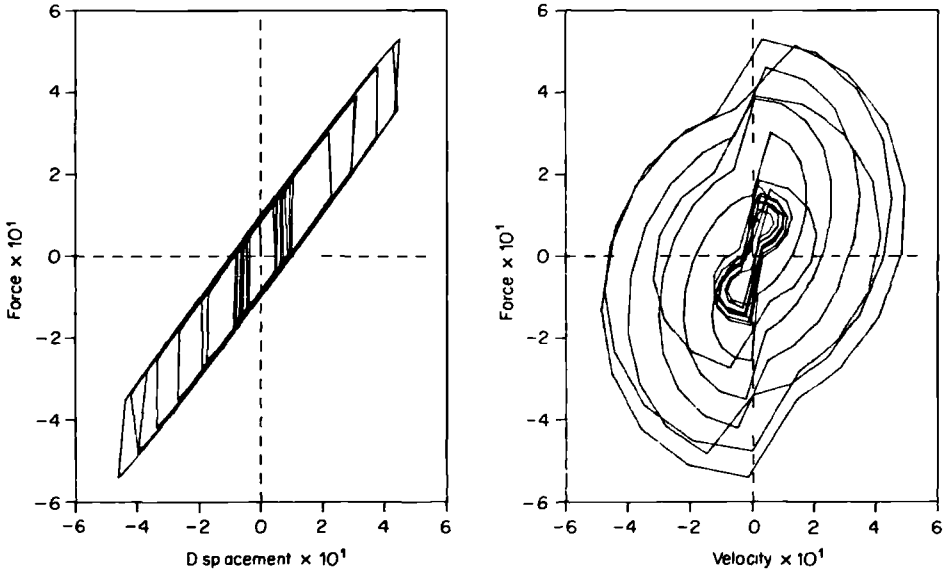

Figure 12. Projection of the force surface onto the force displacement and force-velocity planes for a 1 dof system with friction non-linearity.

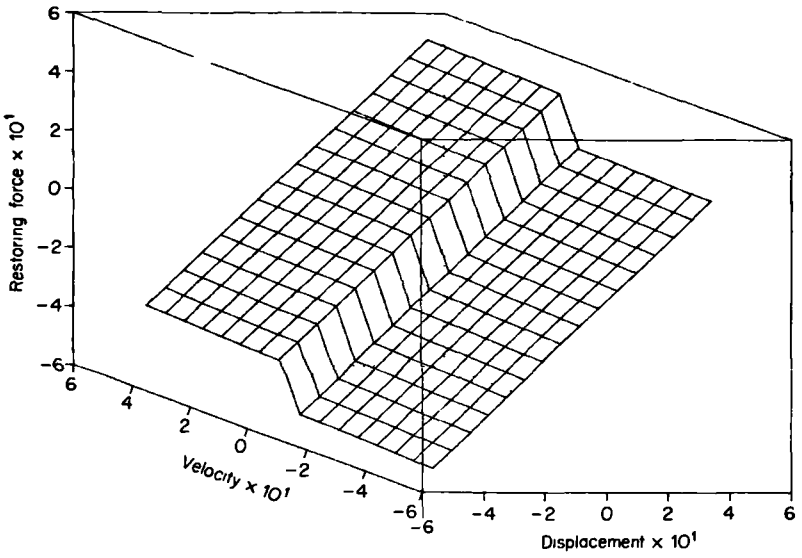

Figure 13. Force-state map of the fitted model of a 1 dof system with friction non-linearity.

4.2.5. *Clearance type non-linearity*

This common non-linearity which may be encountered in aircraft structures, can be described by,

$$m\ddot{x} + c\dot{x} + kx + F(x) = p(t), \tag{16}$$

$$F(x) = 0 \qquad \text{for } |x| \leq d,$$

$$F(x) = k_c(x - d \cdot \operatorname{sgn}(x)) \qquad \text{for } |x| > d,$$

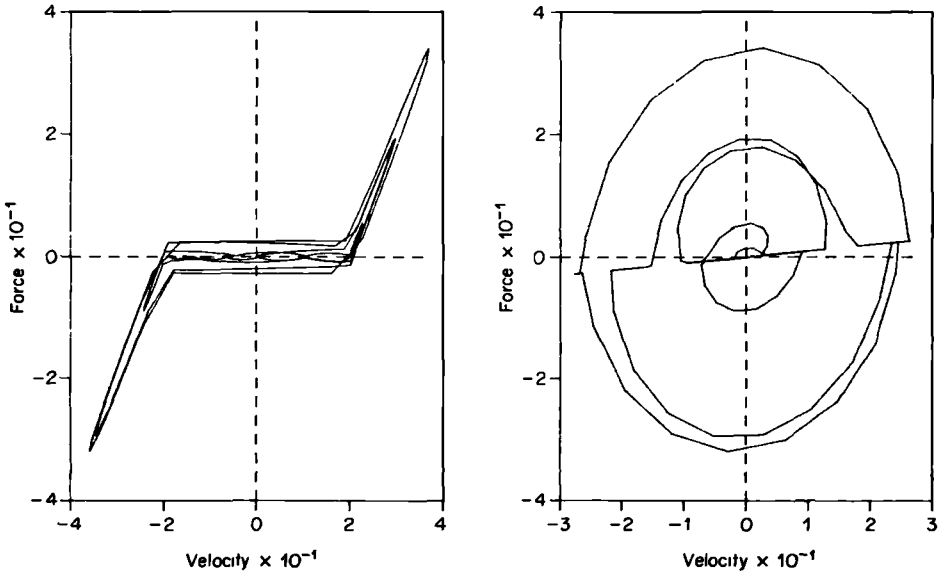

Figure 14. Projection of the force surface onto the force-displacement and force-velocity planes for a 1 dof system with clearance non-linearity.

where d is the clearance (deadspace) value and k_c the piecewise stiffness to be identified. The exact restoring force was considered to be

$$f(\dot{x}, x) = 0{\cdot}04\dot{x} + 2(x - 20 \cdot \mathrm{sgn}(x))$$

with $k = 0$. A sweep excitation from 0·1 to 0·4 Hz was used with 5·7 N peak force.

The force-displacement and force-velocity variations for the raw data are shown in Fig. 14. It can be seen that the clearance value can be estimated directly from the force-displacement plot. The identified parameters using the corresponding special function are obtained exactly ($c = 0{\cdot}04$, $k_c = 2$), assuming the exact d value is available.

5. APPLICATION OF FORCE-STATE MAPPING TO MULTI-DEGREE-OF-FREEDOM SYSTEMS

Masri and Caughey have shown [3] how the force-state mapping approach may be extended to cater for multi-degree-of-freedom systems. Again the theory has been fully covered elsewhere [3], so will only be outlined here.

The equation of motion of a general non-linear multi-degree-of-freedom system may be written as

$$M\ddot{\mathbf{x}} + \mathbf{f}(\dot{\mathbf{x}}, \mathbf{x}) - \mathbf{p}(t), \tag{17}$$

where M is the $(n \times n)$ mass matrix, $\mathbf{x}$ is the $(n \times 1)$ vector of displacements, $\mathbf{f}$ is the linear/non-linear restoring force vector and $\mathbf{p}$ is the excitation force vector.

The equation may be transformed into modal co-ordinates (or modal space) using

$$\mathbf{x} = \Phi\mathbf{u}, \tag{18}$$

where Φ is the $(n \times r)$ modal matrix, $\mathbf{u}$ is the modal displacement vector and r is the number of modes to be considered. Substituting (18) into (17) and premultiplying by Φ' yields

$$M_u\ddot{\mathbf{u}} + \mathbf{h}(\dot{\mathbf{u}}, \mathbf{u}) = \Phi'\mathbf{p}, \tag{19}$$

where $M_u = \Phi'M\Phi$ is the diagonal mass matrix and $\mathbf{h}$ $\Phi'\mathbf{f}$ is the generalised restoring-force vector.

Since from equation (18) the modal displacements are

$$\mathbf{u} = [\Phi'\Phi]^{-1}\Phi'\mathbf{x} - R\mathbf{x}, \tag{20}$$

then the modal restoring force may be expressed using equations (19) and (20) as

$$\mathbf{h}(\dot{\mathbf{u}}, \mathbf{u}) \quad \Phi'\mathbf{p} - M_uR\ddot{\mathbf{x}}. \tag{21}$$

This is the multi-degree-of-freedom equivalent of equation (3) and allows the modal restoring force vector to be estimated, provided that estimates for the generalised mass and modal matrices are available and that $\mathbf{p}$ and $\ddot{\mathbf{x}}$ have been measured. Once modal velocities $\dot{\mathbf{u}}$ and displacements $\mathbf{u}$ have been calculated from $\dot{\mathbf{x}}$ and $\mathbf{x}$ then a mathematical model for $\mathbf{h}$ may be sought.

It will be assumed in this paper that M_u and Φ matrices are known. A later paper will show how they might be estimated from non-linear measured data. Also only lumped parameter systems, for which $r - n$, will be considered; the extension to "continuous" systems is possible in principle but no examples have yet appeared in the literature. Note that Worden and Tomlinson [8] have pointed out that it is preferable to use Φ^{-1} in place of Φ' when obtaining equation (19) in case the estimated modal matrix is non-orthogonal.

Two approaches to obtaining a mathematical model for $h_i(\dot{\mathbf{u}}, \mathbf{u})$, the i-th mode component of the modal restoring force vector, will be considered.

5.1. ITERATIVE APPROACH

This approach was proposed by Masri and Caughey [3] and sought to build up a series representation of $h_i(\dot{\mathbf{u}}, \mathbf{u})$ by carrying out a sequence of Chebychev type curve fits using two modal variables at a time. It is possible to introduce ordinary polynomials instead, without altering the idea.

The first step in the sequence is to fit h_i against the direct modal velocity $\dot{u}_i$ and displacement u_i via a series

$$h_i(\dot{\mathbf{u}}, \mathbf{u}) \approx h_i^{(1)}(\dot{u}_i, u_i) = \sum_k B1_k F_k(\dot{u}_i, u_i), \tag{22}$$

where F_k are the basis functions introduced in section 3.3.

Since the "modes" will usually be coupled non-linearly, there will be error in the curve fit, not only in that a residual will be present but also that the parameter values will be biased by the influence of terms not included in the fit. Subsequent steps in the sequence seek to include these other terms in the model. For example, the next step could include the modal displacement coupling between u_i and u_j (j usually restricted to $i-1$ and $i+1$) by curve fitting the residual from the fit in equation (22) as

$$\begin{aligned} \Delta h_i^{(1)} &= h_i(\dot{\mathbf{u}}, \mathbf{u}) - h_i^{(1)}(\dot{u}_i, u_i) \\ &\approx h_i^{(2)}(u_i, u_j) = \sum_k B2_k F_k(u_i, u_j), \end{aligned} \tag{23}$$

where the basis functions will, in general, be different. Note that this residual will also be biased due to earlier parameter bias. A further residual

$$\Delta h_i^{(2)} = \Delta h_i^{(1)} - h_i^{(2)}(u_i, u_j) \tag{24}$$

may be calculated and the cumulative goodness of fit examined. If the fit is incomplete then the latest residual may be fitted by a further series involving a different pair of coupling terms. The sequence is said to be completed when all significant couplings have been included.

The final approximate representation for the ith mode restoring force is the sum of the separate fits,

$$h_i(\dot{\mathbf{u}}, \mathbf{u}) \approx h_i^{(1)}(\dot{u}_i, u_i) + h_i^{(2)}(u_i, u_j) + h_i^{(3)}(\dot{u}_i, \dot{u}_j) + \cdots. \tag{25}$$

In the published work on this process [3], it seems to have been assumed that, once sufficient coupling combinations have been included, the fit will be good and the parameters in the model accurate. However, the above process does not account for bias in the parameter estimates encountered because only two variables at a time are fitted to a function of many variables.

It has been the experience of the authors that some of the steps may have to be repeated several times in order to correct for the bias. This point will be illustrated in an example later.

The particular problem of bias has arisen primarily from the restriction to fitting two variables at a time which is an outcome of using two-dimensional Chebychev polynomials. However, the simpler curve fit philosophy adopted for single-degree-of-freedom identification in sections 3.2 and 3.3 can also be extended to overcome the bias problem and to simplify the procedure.

5.2. DIRECT APPROACH

The problem of bias in the multi-step procedure can be removed in principle by carrying out the entire curve fit to $h_i(\dot{\mathbf{u}}, \mathbf{u})$ in a single step. This is made possible by increasing the

number of modal variables present in the fitted model to more than two. In essence the model shown in equation (25) is fitted so that, for example,

$$h_i(\dot{\mathbf{u}}, \mathbf{u}) \approx \hat{h}_i(\dot{\mathbf{u}}, \mathbf{u}) = \sum_k B1_k F_k(u_i, \dot{u}_i) + \sum_k B2_k F_k(u_i, u) + \sum_k B3_k F_k(\dot{u}_i, \dot{u}) + \cdots, \tag{26}$$

where the basis functions are chosen carefully to account for likely linear and non-linear direct and coupling terms, given that some idea of the type of non-linearity should be available from observation of the effect of force amplitude upon the frequency response function etc. Note that all possible modal coupling terms may be included in a single fit. However, if the goodness of fit is not close to 1, then some terms are probably missing and the fit should be repeated including the missing terms.

Once parameters have been obtained from the fit, the contribution of each term in the series to $h_i(\dot{\mathbf{u}}, \mathbf{u})$ may be examined to see which are negligible. The significance of the k-th term, for example, may be found from the ratio

$$(\text{rms term } k) \Big/ \sum_{j\ 1}^{N} (\text{rms term } j),$$

where N is the number of terms in the fitted model. The rms values are calculated using the raw data values and the fitted parameters. If necessary the fit may be repeated with an appropriately reduced model to obtain better results.

6. MULTI-DEGREE OF FREEDOM EXAMPLE

The multi-degree-of-freedom identification procedure described in section 5 will now be illustrated on the two degree of freedom lumped parameter model shown in Fig. 15.

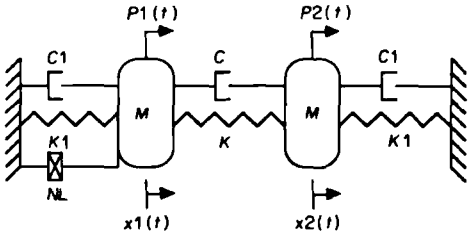

Figure 15. Two-degree-of-freedom system with cubic stiffness non-linear element between the first mass and the earth.

The equations of motion in both physical and modal coordinates are shown in Table 3. The correct modal matrix was assumed. The cubic stiffness non-linearity between mass 1 and "earth" leads to modes coupled non-linearly in quite a complicated manner. The undamped natural frequencies of the system are 28·5 and 31·5 Hz. A sample frequency response function, obtained by single frequency sinusoidal excitation, is shown in Fig. 16 for different force levels.

Data for the identification were obtained by applying a 27 to 37 Hz frequency sweep input to mass 1 and evaluating the responses numerically to provide 256 data points. The modal responses were computed using the exact generalised mass matrix.

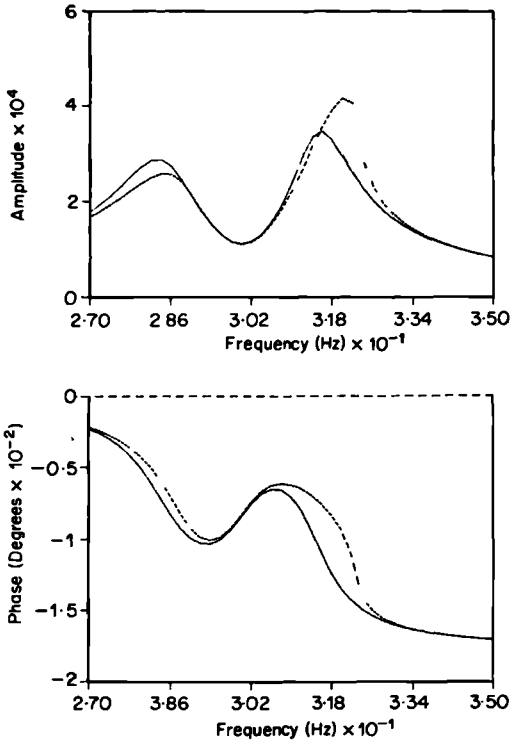

Figure 16. A sample frequency response function of the 2 dof system given for different excitation levels.

TABLE 3

Equation of motion of the 2 dof system

Physical co-ordinates

$$\begin{bmatrix} 1 & 0 \\ 0 & 1 \end{bmatrix}\begin{bmatrix} \ddot{x}_1 \\ \ddot{x}_2 \end{bmatrix} + \begin{bmatrix} 9{\cdot}33 & 1{\cdot}41 \\ 1{\cdot}41 & 9{\cdot}33 \end{bmatrix}\begin{bmatrix} \dot{x}_1 \\ \dot{x}_2 \end{bmatrix} + \begin{bmatrix} 35\,619 & -3553 \\ -3553 & 35\,619 \end{bmatrix}\begin{bmatrix} x_1 \\ x_2 \end{bmatrix} + \begin{bmatrix} 35\,530 & x_1^3 \\ 0 & \end{bmatrix} = \begin{bmatrix} F_1 \\ F_2 \end{bmatrix}$$

Modal matrix

$$\Phi = \begin{bmatrix} 1 & -1 \\ 1 & 1 \end{bmatrix}$$

Modal co-ordinates

$$\begin{bmatrix} 2 & 0 \\ 0 & 2 \end{bmatrix}\begin{bmatrix} \ddot{u}_1 \\ \ddot{u}_2 \end{bmatrix} + \begin{bmatrix} 21{\cdot}48 & 0 \\ 0 & 15{\cdot}84 \end{bmatrix}\begin{bmatrix} \dot{u}_1 \\ \dot{u}_2 \end{bmatrix} + \begin{bmatrix} 64\,132 & 0 \\ 0 & 78\,344{\cdot}6 \end{bmatrix}\begin{bmatrix} u_1 \\ u_2 \end{bmatrix}$$

$$+ \begin{bmatrix} 35\,530 & -106\,590 & 106\,590 & -35\,530 \\ 35\,530 & -106\,590 & 106\,590 & -35\,530 \end{bmatrix}\begin{bmatrix} u_1^3 \\ u_1^2 u_2 \\ u_1 u_2^2 \\ u_2^3 \end{bmatrix} = \begin{bmatrix} F_{u_1} \\ F_{u_2} \end{bmatrix}$$

(1) The iterative approach was applied to the data using ordinary polynomials. The sequence of steps used the following pairs of modal quantities for $h1$, namely ($u1$, $\dot{u}1$), ($u1$, $u2$), ($u1$, $u2$) and ($\dot{u}1$, $\dot{u}2$) where sufficient terms were included in each series to allow for the coupling present. The sequence was repeated more than three times and the cumulative parameter values after each sequence are shown in Table 4. It is seen that the sequence needs to be repeated in order for the main effect of the bias to be overcome.

(2) The direct approach was applied to the $h1$ data using the rather excessively large model shown in Table 5. The results of the fit using singular value decomposition are also shown in the table and significant terms are obvious having been identified accurately and quickly.

TABLE 4

The 2 dof example iteration

No.	Sequence	Terms used	Cumulative (K11)	Cumulative (C11)	Cumulative value of a non-linear parameter
1	1	$u1$, $\dot{u}1$	74 110·5	31·25	—
2		$u1$, $u2$	64 247·9	—	33 156·5
3		$\dot{u}1$, $u2$	—	24·33	—
4		$\dot{u}1$, $\dot{u}2$	—	24·47	—
5	2	$u1$, $\dot{u}1$	64 120·5	24·47	—
6		$u1$, $u2$	64 097·4	—	34 793·9
7		$\dot{u}1$, $u2$	—	22·54	—
8		$\dot{u}1$, $\dot{u}2$	—	22·48	—
9	3	$u1$, $\dot{u}1$	64 102·7	22·48	—
10		$u1$, $u2$	64 107·9	—	35 280·3
11		$\dot{u}1$, $u2$	—	21·88	—
12		$\dot{u}1$, $\dot{u}2$	—	21·83	—
13	4	$u1$, $\dot{u}1$	64 120·8	21·83	—
14		$u1$, $u2$ and so on	64 122·6	—	35 440·3

Exact values: K11 = 64 132·6, C11 = 21·48, NL = 35 530.

TABLE 5

Identification results of the 2 dof example obtained by the direct method via the singular value decomposition approach

$$h_1(\dot{\mathbf{u}}, \mathbf{u}) = B_1 + B_2u_1 + B\ \dot{u}_1 + B_4u_1\dot{u}_1 + B_5u_1^2 + B_6\dot{u}_1^2 + B_7u_1^2\dot{u}_1 + B_8u_1\dot{u}_1^2 + B_9u^3 + B_{10}\dot{u}_1^3 + B_{11}u_1u\ + B_{12}u_1u_2^2 + B_{13}u_2^3 + B_{14}\dot{u}_1u_2 + B_{15}u_1\dot{u}_2$$

Identified parameters:

$B_1 - 0{\cdot}0221$	$B_9 - 35\,531{\cdot}16$
$B_2 = 64\,131{\cdot}25$	$B_{10} - -0{\cdot}294\text{E}{-}06$
$B_3 = 21{\cdot}4831$	$B_{11} = -106\,593$
$B_4 = 0{\cdot}00111$	$B_{12} = 106\,593$
$B_5 = -0{\cdot}433$	$B_{13} = -35\,528{\cdot}63$
$B_6 = -0{\cdot}814\text{E}{-}06$	$B_{14} = -0{\cdot}1286\text{E}{-}05$
$B_7 = -0{\cdot}0149$	$B_{15} = 0{\cdot}1825\text{E}{-}03$
$B_8 = 0{\cdot}6039\text{E}\ \ 04$	

7. METHOD FOR IDENTIFICATION OF THE TYPE AND PHYSICAL LOCATION OF NON-LINEARITIES FOR A LUMPED PARAMETER MULTI-DEGREE-OF-FREEDOM SYSTEM

The adoption of a simpler approach to fitting the force-state map has led to a simple way of determining the physical location of non-linear elements in a lumped parameter system.

Consider an n-degree-of-freedom lumped parameter system in one dimension with m possible locations for non-linear elements. Consider further for simplicity in developing the approach that any non-linearities are of the cubic stiffness type. Then the equation of motion may be written with linear and non-linear terms separated as follows,

$$M\ddot{\mathbf{x}} + C\dot{\mathbf{x}} + K\mathbf{x} + \delta\mathbf{q} = \mathbf{p}(t), \tag{27}$$

where C is the damping matrix, K is the stiffness matrix, δ an $(n \times m)$ matrix of parameters defining the strength of the non-linearities and $\mathbf{q}$ is an $(m \times 1)$ vector containing functions of the relative physical displacements corresponding to each of the possible locations for non-linearity. In this case the function is a cubic so for example,

$$\mathbf{q} = [(x_1 - x_0)^3, (x_2 - x_0)^3, (x_2 - x_1)^3]^T \tag{28}$$

would be the relevant vector for the two-degree-of-freedom example in Fig. 15, where x_0 corresponds to the displacement of "earth" and is actually zero. The δ matrix will have null columns corresponding to locations where there is no non-linearity, so again for the earlier example where the non-linearity is located between mass 1 and "earth" then

$$\delta = \begin{bmatrix} 35\,530 & 0 & 0 \\ 0 & 0 & 0 \end{bmatrix}.$$

Now having established the equations written in this particular form, the transformation to modal space may be carried out largely as shown in section 5 but leaving $\mathbf{q}$ untransformed. Thus the result is

$$M_u\ddot{\mathbf{u}} + C_u\dot{\mathbf{u}} + K_u\mathbf{u} + \Phi'\delta\mathbf{q} = \Phi'\mathbf{p}(t), \tag{29}$$

where C_u and K_u are generalised damping and stiffness matrices. The modal restoring force vector may then be written

$$\mathbf{h}(\dot{\mathbf{u}}, \mathbf{u}) = C_u\dot{\mathbf{u}} + K_u\mathbf{u} + \Delta \cdot \mathbf{q} \tag{30}$$

where $\Delta = \Phi' \cdot \delta$ is an $(r \times m)$ matrix.

In the above example the Δ matrix is given by

$$\Delta = \begin{bmatrix} 35\,530 & 0 & 0 \\ -35\,530 & 0 & 0 \end{bmatrix},$$

In equation (30) the force has a linear component in terms of modal quantities and a non-linear component in terms of relative physical displacements. A model may now be fitted to the modal restoring force for each mode in order to identify C_u (diagonal if damping proportional), K_u (diagonal) and Δ. For the proportional damping case then, for the i-th mode,

$$h_i(\dot{\mathbf{u}}, \mathbf{u}) \approx \hat{h}_i(\dot{\mathbf{u}}, \mathbf{u}) = c_{ii}\dot{u}_i + k_{ii}u_i + \Delta_{i1}(x_1 - x_0)^3 + \Delta_{i2}(x_2 - x_1)^3 + \Delta_{i3}(x_2 - x_0)^3 + \cdots \tag{31}$$

and the curve fit is possible because information about the physical and modal states are assumed to be available. Obviously, for the non-proportional damping case, linear velocity dependent coupling terms would be included in equation (31).

The likely location of non-linearities will then correspond to the position in the Δ matrix of columns where the identified parameters are of significant magnitude compared with other columns.

When this process was carried out on the earlier two-degree-of-freedom example, the identified matrix was

$$\Delta = \begin{bmatrix} 35\,529.9 & -0{\cdot}30 & 0{\cdot}564 \\ -35\,529\,8 & -0{\cdot}077 & -0{\cdot}593 \end{bmatrix}$$

and it is obvious that the non-linearity is located between mass 1 and earth by reference to the $\mathbf{q}$ vector in equation (28). Since Φ is assumed to be known it is also possible to obtain the actual non-linear parameters in δ from Δ. The method has been shown to work where more than one non-linear element is present, even when mixed non-linearities are included in the same system.

The application to more than two degrees of freedom and to more than one dimension is straightforward but the number of possible locations increases.

For other types of non-linearity, the form of the $\mathbf{q}$ vector is different. In the friction case a typical element in the vector might be sgn $(\dot{x}_i - \dot{x}_j)$. Note that such a non-linearity would be extremely difficult to identify in modal space. If more than one type of non-linearity is thought to be present the $\mathbf{q}$ vector would need to be extended to include all possible terms. Any non-linearity included in the fitted model but not actually present in the real system will have small coefficients in the fit. Hopefully the length of the vector could be reduced if certain locations and types of non-linearity can be eliminated from consideration using other arguments.

Note that a cubic stiffness type of model should give an indication of the presence of other types of stiffness non-linearity such as piecewise stiffness, since there will be a dominant cubic term. Once the non-linearity has been located, the curve fit could be repeated with the behaviour at that location modelled more thoroughly.

Finally it should be pointed out that the approach taken by Yang and Ibrahim [6], where relative velocities and displacements are used for identification in physical space, would allow location of non-linearity in a similar way to the approach developed independently by the authors. However the formulation in model space can in principle allow the extension to the location of discrete non-linear elements in continuous systems.

8. CONCLUSION

Some of the drawbacks of the Masri/Caughey identification procedure are overcome by removing the restriction of using two-dimensional orthogonal polynomials. Because interpolation and extrapolation of the force surface are unnecessary if a simple ordinary polynomial fit is employed, a more accurate and faster identification is obtained. Further extending the fitted model to include special functions and more than two variables can cater for non-polynomial non-linearities such as friction, quadratic damping, deadspace, etc. and also improve multi-degree-of-freedom identification.

Finally, a method for identifying the location as well as the type of discrete non-linearities in lumped parameter systems has been presented and demonstrated in a simple example.

REFERENCES

1. G. R. TOMLINSON 1986 *Proceedings of the Fourth International Modal Analysis Conference*, pp. 837-843. Detection, identification and quantification of nonlinearity in modal analysis—a review.

2. S. F. MASRI and T. K. CAUGHEY 1979 *Journal of Applied Mechanics* **46**, 433–447. A nonparametric identification technique for nonlinear dynamic problems.
3. S. F. MASRI, H. SASSI and T. K. CAUGHEY 1982 *Journal of Applied Mechanics* **49**, 619–627. Nonparametric identification of nearly arbitrary nonlinear systems.
4. E. F. CRAWLEY and A. C. AUBERT 1986 *AIAA Journal* **24**, 155–162. Identification of nonlinear structural elements by force-state mapping.
5. E. F. CRAWLEY and K. J. O'DONNELL *AIAA paper 86-1013*, pp. 659–667. Identification of nonlinear system parameters in joints using the force-state mapping technique.
6. Y. YANG and S. R. IBRAHIM 1985 *Journal of Vibration, Acoustics, Stress and Reliability in Design* **107**, 60–66. A nonparametric identification technique for a variety of discrete nonlinear vibrating systems.
7. J. K. HAMMOND, H. R. LO and J. SEAGER SMITH 1987 *Proceedings of the 5th International Modal Analysis Conference*, pp. 1467–1473. Identification of nonlinearities in vibrating systems using optimal control techniques.
8. K. WORDEN and G. R. TOMLINSON To be presented at the *3rd International Conference on Recent Advances in Structural Dynamics at Southampton.* Identification of linear/nonlinear restoring force surfaces in single and multi-mode systems.
9. K. WORDEN and G. R. TOMLINSON 1988 *Proceedings of the 6th International Modal Analysis Conference*, pp. 1471–1479. Developments in force-state mapping for nonlinear systems.
10. P. ARGOUL 1987 *French Mechanical Congress at Nantes.* Une methode d'identification des structures non lineaires en dynamique.
11. W. H. PRESS *et al.* 1986 *Numerical Recipes—The Art of Scientific Computing.* Cambridge: Cambridge University Press.